Mechanisms of Isostatic Compensation in Areas of Lithospheric Extension: Examples from the Aegean

by

Trevor Alan King

Submitted in accordance with the requirements for the degree of

Doctor of Philosophy

The University of Leeds,

Department of Earth Sciences

February 1998

The candidate confirms that the work submitted is his own and that appropriate credit has been given where reference has been made to the work of others.

Mechanisms of Isostatic Compensation in Areas of Lithospheric Extension: Examples from the Aegean

The results of previous studies in the Aegean have greatly influenced our understanding of continental extensional tectonics. However, although lithospheric rheology is known to exert a significant control on tectonic style, it had not been assessed across the province. The effective elastic thickness, T_e, provides a good measure of lithospheric rheology. Through analyses of the isostatic mechanism, the spatial variability in rheology across the Aegean is examined.

A crucial step in the process is to obtain a good gravity dataset. This study compiles new and existing gravity data across both onshore and offshore regions to produce the best gravity dataset currently available for the Aegean region. Short wavelength components of the Bouguer gravity (less than ~80 km) are seen to correlate with surface geological features. Longer wavelength components are coherent with topographic features, which may be interpreted in terms of the lithosphere's isostatic response to loading.

The amplitudes of Bouguer anomaly minima across the sedimentary basins of central Greece are used to estimate the depth to basement. A model is derived for the gravitational signature of buried sedimentary strata whose porosity decreases exponentially with burial depth. The model results are presented in graphical form which may have general application. The resulting depth estimates for the eastern Gulf of Corinth (2.7 to 3.7 km) are used along with a seismic depth conversion and erosional marine terrace geometries to model the generation of topography across an active rift segment. These boundary element elastic models estimate the local rift-flank T_e as ~6 km.

The primary objective of this thesis - to assess the spatial variability in lithospheric rheology - is achieved through the analysis of gravity coherence. Windowed (short time) Fourier transforms are used, and the observed coherence is modelled with a thin elastic plate to estimate T_e. Across the Aegean extensional province, T_e is between 10 and 20 km, and values of between 8 and 10 km are observed across the extending Rhodope metamorphic core complex. The broad pattern is similar to that in measured surface heat flow, indicating that geothermal gradient is an important factor in controlling lithospheric rheology.

This thesis presents the first comparison between the conventional Fourier transform method and the wavelet transform method in a coherence analysis. Due to the locali-

sation properties of the continuous wavelet transform, an improved spatial resolution of the variability in coherence is observed. The weakest lithosphere across the Rhodope complex is observed to occur in a narrow zone (~100 km wide) trending parallel to normal faulting, where a T_e of less than 5 km is predicted. These features are not resolved with the Fourier method.

The results of this thesis are then compared to observations across the Basin and Range and the Tibetan Plateau. It is argued that rheological similarities between these collapsing orogens account for similarities in the tectonic style. A scheme is subsequently suggested for the evolution of the Aegean province since approximately 20 Ma.

Contents

List of Figures

List of Tables

List of Abbreviations

AGP	African Gravity Project (GETECH)
CMT	Centroid moment tensor
CWT	Continuous wavelet transform
DEM	Digital elevation model
DMA	Defense Mapping Agency (USA)
GPS	Global Positioning System
EAF	East Anatolian Fault
ETOPO5	5 minute grid of topography and bathymetry
FFT	Fast Fourier transform
HMGS	Hellenic Military Geographic Service
IGME	Institute of Geology and Mineral Exploration (Greece)
IGSN71	International Gravity Standardisation Net of 1971
ITRF89	International Terrestrial Reference Frame of 1989
MRA	Multi-resolution analysis
NAF	North Anatolian Fault
OSU91A	Ohio State University geoid model of 1991
TM	Transverse Mercator
WGS84	World Geodetic System 1984

List of Symbols

In a handful of cases, a particular symbol has been used to represent two different quantites. Both definitions are listed here, and confusion is avoided as the correct meaning should be obvious from the context.

B	Mechanical strength of the lithosphere
	Fourier transform of Bouguer anomaly
BA	Complete Bouguer anomaly
BC	Bouguer correction
CC	Curvature correction
D	Flexural rigidity
E	Young's modulus
E_0	Reference Young's modulus (1×10^{11} Pas)
$\mathcal{F}$	Fourier transform
FAA	Free air anomaly
FAC	Free air correction
F_b	Buoyancy force
F_d	Tectonic driving force, forming part of $\mathbf{N}$
F_{min}	Minimum F_d required for deformation
G	Gravitational constant (6.672×10^{-11} $\mathrm{Nm^2km^{-2}}$)
GPE	Gravitational potential energy
H	Fourier transform of topography (h) and bathymetry (b)
L	Thickness of the mechanical lithosphere
M	Bending moment
	Mass of the Earth
MR	Gravity meter reading
N	Geoid height
$\mathbf{N}$	2D in-plane tectonic force, comprising F_d and $\Delta\Gamma$
N_x	1D in-plane tectonic force
P	Pore fluid pressure
Q	Admittance
R	Universal gas constant

T	Absolute temperature
TC	Terrain correction
T_c	Crustal thickness
T_e	Effective elastic thickness
T_s	Seismogenic thickness
W	Fourier transform of moho topography
$\mathcal{W}$	Wavelet transform
a	Half-width of model basin
	Wavelet dilation
b	Water depth (bathymetry)
	Wavelet position
c	Gravity meter calibration constant
	Porosity decay exponent
	The convolution integral
d	Mineral grain size
e	Strain
	Fractional erosion in footwall
$\dot{e}$	Strain rate
f	Load ratio
g	Gravitational acceleration (9.81 ms^{-2})
g_{obs}	Observed (absolute) gravity
g_{base}	Absolute gravity at a base station
g_ϕ	Theoretical (reference) gravity on the WGS84 ellipse
h	Topography
h_e	Effective topography
h_I	Surface topography prior to isostatic compensation
$\mathbf{k}, k$	Wavenumber (2D, 1D)
$\bar{k}$	Average wavenumber in annular bin
l	Combined surface and sub-surface load
l_t	Top (surface) load
l_b	Bottom (sub-surface or moho) load
m	Mass

n	Number of Fourier components within a discrete waveband
	Wavelet order
p	Mean normal stress (or pressure)
q_s	Surface heat flow
r	Equivalent rock layer thickness
	Distance from centre of Earth
s	Sediment thickness
s'	Amount ot hanging-wall subsidence
t	Actual thickness of elastic plate
t_τ	Time since onset of rifting
v	Time averaged extensional velocity across a rift or fault
w	Flexural deformation
w_I	Bottom (or moho) topography prior to isostatic compensation
x	In-plane horizontal coordinate
y	Out-of-plane horizontal coordinate
z	Vertical coordinate
z'	Depth relative to neutral plane
z_0	Depth from surface to neutral plane
z_m	Moho depth

ΔD	Gravity meter drift
ΔT	Gravitational tidal correction
ΔT_c	Difference in crustal thickness between two lithospheric columns
Δg_c	Coseismic gravity change
Δh_c	Coseismic elevation change
$\Delta\Gamma$	Difference in Γ between two Airy-compensated lithospheric columns
$\Delta\rho$	Sediment-basement density contrast
Γ	Gravitational potential energy per unit area
Φ	Fractional porosity
Φ_0	Depositional fractional porosity
Φ_a	Gaussian smoothing function of width a
$\Psi_a^{(n)}$	Gaussian derivative wavelet of dilation a and order n

β	Extension factor
	Wavenumber exponent for topographic power
γ^2	Coherence
δg_A	Atmospheric gravity correction
ε	Error
η	Viscosity
κ	Isotropic stress
	Thermal diffusivity
λ	Wavelength
λ_c	Coherence characteristic wavelength
μ	Coefficient of static friction
ν	Poisson's ratio (0.25)
ρ	Density
ρ_B	Bouguer density (2670 kg/m^3)
ρ_c	Crustal density
ρ_{uc}	Upper crustal density
ρ_{lc}	Lower crustal density
ρ_m	Mantle density
ρ_f	Asthenosphere density ($\equiv \rho_m$)
σ	Stress
$\overline{\sigma}$	Depth averaged stress
σ_{Fb}	Buoyancy force per unit area
σ_b	Brittle yield stress
σ_d	Ductile yield stress
σ_e	Unloading stress across footwall due to erosion
σ_s	Loading stress due to sediment and water in the hanging wall
σ_y	Yield stress
τ	Deviatoric stress
$\overline{\tau}$	Depth averaged deviatoric stress
τ_{xx}^N	In-plane stress, resulting from N_x
τ_{xx}^w	Bending stress
ϕ	Geodetic latitude

Acknowledgments

This thesis has benefited from discussions with Cindy Ebinger, Richard Collier, Colin Stark, Evgene Burov, Anthony Lowry, Roger Buck, Jon Stewart, Gerald Roberts, Roger Clark and Dave Gubbins. My understanding of continental tectonics was much improved after discussions in the field with Richard Collier, Geoff King and Philip England. Colin Stark provided the wavelet analysis code, and Geoff King the boundary element flexure code. Duncan Hawksbee and Denizar Blitzkow advised on the processing of GPS data. Stelios Chailas, Evangelos Lagios, Roger Hipkin, Mike Brooks and GETECH are each thanked for supplying gravity and topography data for the Aegean region.

Fieldwork benefited from the assistance of Cindy, Pete, Mike and my dad. IGME in Greece are thanked for allowing field studies to go ahead, whose written word proved useful in the office of the Athens airport police and in convincing the Patras police department that a gravity meter is not sensitive to the location of buried treasure. Nikos Melis and Theodor Doutsos in Patras provided short but welcome breaks from the field. Pann and Chris in Kamari are thanked for helping with accommodation during my first visit. Athens became a brighter place to be thanks to the guidance of Stelios, and the man with the big mallet in Karpenissi is thanked for fixing the hire car.

Fellow students in the department ensured that study here was, for the most part, enjoyable and stimulating. In particular, office mates Nigel, Roberta, Tim, Frank, Nick, Shafkit, Aoife, Alex and Graeme. Invaluable computing support was provided throughout by Stuart Borthwick and Nick Barber. Toby is thanked for keeping me thinking about oil related problems, and Steve for many things mathematical.

Outside the department, Bert, Bobby Velve, Wild Ed, Steve, Jo (Foxey Lady), Tore (Norwegian pop-star), and Jimi Hendrix are each thanked for their musical distraction. Long live the Weird Chicken! Many fine beer moments were experienced in the company of Bert, Ed, M-C, Toby, Jon, Chris, Al and Sime. Housemates throughout my time in Leeds - Nick, Paul, Kath, Jim, Rich, Bert, Ed, Chris (and Sarah), Shona, Toby, Andy L., Wilma, Andy B., Kath, Max, Chris and Craig - are each thanked. Marie-Claire deserves special thanks for providing many pleasant distractions.

Funding for this project and trips to Greece, Strasbourg, Rennes and San Francisco came from the Natural Environmental Research Council and Richard Collier. Innumerable top-ups were provided by my parents, who have encouraged me throughout my undergraduate degree and my research.

Fall mountains, just don't fall on me.

From *"If 6 was 9"*, J. M. Hendrix, 1968

Chapter 1

Introduction

The theory of plate tectonics came largely from analyses of oceanic regions, where surface motions may be described by the rigid body rotation of a small number of plates. Earthquake locations show that the deformation is limited to narrow regions across oceanic plate boundaries. Strictly speaking, the original tenets of plate tectonics do not apply to the continents, where crustal deformation can occur across regions of several hundreds or even thousands of kilometers. Gaining a greater understanding of the dynamics of continental deformation - that is the relationship between tectonic force, rheology and deformation style - is the subject of much current research and has provided the motivation for this thesis.

Areas of lithospheric extension are critical to our understanding of lithospheric dynamics. Significant variations occur in the accommodation of extensional strain, which is manifest as variations in

- the depth-distribution of earthquakes (i.e., the seismogenic thickness)
- the spacing of individual rift basins
- the size and shape of rift basins
- the lengths of their bounding faults.

Each of these parameters is sensitive to lithospheric rheology, the assessment of which is the subject of many recent and ongoing studies.

In general, the weaker the lithosphere, the more diffuse its deformation. It is the analysis of weak collapsing orogenic belts - such as the Tibetan Plateau, the Basin and Range, and the Aegean - that has led to a notion that continental lithosphere deforms

as a continuum (e.g., *Davies et al.* [1997], *England and Molnar* [1997b], *Jones, Unruh and Sonder* [1996]). However, this view is contested by some (e.g., *King, Oppenheimer and Amelung* [1994]), and the nature of strain localisation through the lithosphere as a whole is still uncertain.

The nature of strain localisation in the upper-most brittle crust is more easily observed. Understanding these processes provides the platform from which we can address problems in structural geology, geomorphology and sedimentology, critical to the exploration for hydrocarbon reserves. This is especially true in extensional settings. The results from previous studies of the Aegean province have greatly influenced our understanding of surface processes, and yet lithospheric rheology had not been assessed prior to this study.

This thesis therefore aims to answer the following questions:

- What is the rheology of the Aegean lithosphere?
- How does the Aegean compare to other areas of lithospheric extension?
- What is the relationship between rheology and tectonics across the province?
- What are the major controls on lithospheric rheology in the Aegean?

These questions will be addressed by focusing on the following objectives:

- to compile new and existing gravity data across Greece and the Aegean Sea, and qualitatively evaluate the patterns observed across the extensional province
- to estimate the depth to basement beneath the rift basins of Greece
- to assess the nature of isostatic rift-flank uplift, and isolate its contribution across a broadly deforming zone
- to map the spatial variability in effective elastic thickness, T_e, across the Aegean province

The mechanism of isostatic compensation is dependent on lithospheric rheology. Consequently, the study of isostasy in areas where the kinematics of extension are well constrained should provide a greater understanding of the rheological control on extensional style, as well as the causes of vertical crustal movements. The theory behind these ideas is discussed in Chapter 2, where the importance of rheology on the style of crustal deformation is highlighted. The concept of *effective elastic thickness*, T_e, is introduced

and is shown to provide a reliable indication of lithospheric rheology. T_e estimates may be made across both weak and strong areas, whether deforming or not, which allows comparisons to be made across a variety of distinct provinces.

The Aegean region is one of the most rapidly deforming parts of the Alpine-Himalayan belt, and has been the site of continental extension since ~20 Ma. Recent results from global positioning system experiments, in which the author has participated, mean that the overall kinematic motions are well constrained [*Clarke et al.*, 1997; *Davies et al.*, 1997]. In addition, there are many earthquakes with a long record of historical seismicity, and there is an abundance of structural, geomorphological and sedimentological data on land. The Aegean therefore provides an excellent locale to address the problems outlined above. Chapter 3 reviews the results of past and present research, and analyses them in the context of the discussion presented in Chapter 2.

Isostasy deals with vertical displacements of the surface and of horizons within the lithosphere. Gravity and topography data are therefore well suited to analyses of the isostatic mechanism. Furthermore, gravity data may be forward modelled to assess the geometry of basins at depth, so providing a useful constraint on the dynamics of rifting. Previous to this study, gravity data have been used to map variations in the lithosphere's mechanical strength across the extensional terrains of the Basin and Range [*Lowry and Smith*, 1994; *Lowry and Smith*, 1995], East African [*Ebinger et al.*, 1989; *Upcott et al.*, 1996], and Baikal [*van der Beek*, 1997; *Petit, Burov and Déverchère*, 1997]. The results of these analyses have greatly improved our understanding of the dynamics of the extensional process, and have clearly established the importance of the mechanical lithosphere in controlling the geometry and morphology of rift basins and flanks. This thesis presents the first systematic analysis of the isostatic mechanism across the Aegean province.

Gravity data were collected across mainland Greece as part of this thesis. As well as providing a detailed transect across the Gulf of Corinth Rift, this allows for the evaluation of the quality of numerous existing datasets both across mainland Greece and offshore across the Gulf of Corinth. In order to increase the maximum lengthscale of analysis, the satellite derived gravity data of *Sandwell and Smith* [1997] are used to extend the data coverage to the entire Aegean. These data are supplemented by a five minute Bouguer gravity grid to extend the cover into the continental region north of the Aegean. Chapter 4 presents the results of the gravity fieldwork and describes the process

by which individual datasets are combined and re-processed. The final combined dataset represents the best currently available for the Aegean region. Nonetheless, the analysis of gravity data in isolation is limited by the non-unique (or inverse) problem. This may be suppressed by the simultaneous use of topographic data, and Chapter 4 also describes the 2 km and 5 minute digital elevation models used in this thesis. The final datasets are presented, and qualitative interpretations are performed from the inspection of both maps and profiles.

Gravity data are used in a more quantitative way in Chapter 5. The gravitational signal resulting from the Neogene sediments in the rift basins of central Greece is separated from that of deeper sources through the application of a series of wavenumber domain filters. This residual gravity anomaly is first analysed in map view, and compared to geological and structural features. A mathematical model is then derived for the gravitational effect of buried sedimentary strata. Predicted magnitudes are calculated as a function of water depth and sediment thickness, and are compared to the observed gravity anomalies. The recognition that residual separation may not entirely eliminate the gravitational effect of deeper layers leads to the identification of a maximum basin sediment response, and subsequently to maximum estimates for basin depth. In light of these results, elastic modelling of erosional marine terraces on flexurally uplifted crust is performed to assess the wavelength and amplitude of the isostatic response to extensional loading. This allows for the estimation of extensional velocity and of rift-flank T_e.

In Chapter 6, topographic and gravity data are used to constrain the vertical loads emplaced on the lithosphere. Through the adoption of a thin elastic plate model, the nature of the isostatic response to vertical loading is assessed throughout the Aegean. This spectral domain technique - the coherence analysis - therefore allows for the estimation of T_e and its spatial variability across the Aegean province.

Conventional coherence analyses adopt the windowed (or short time) Fourier transform which, because of its sinusoidal basis functions, has poor resolution in the space domain. Wavelet analysis is a branch of mathematics that has come about in the last decade to deal with problems that are not resolved by the Fourier transform, such as the analysis of local properties of a function. Continuous wavelet transforms are therefore used in addition to the conventional windowed Fourier transform. The extent of any improvement in resolution is tested on both synthetic and the Aegean datasets.

Chapter 7 brings together the results from all previous chapters and discusses them in the context of the aims of this thesis, outlined at the start of this introduction. The conclusions from all chapters are summarised at the end of Chapter 7.

Chapter 2

Isostasy, Rheology and Extensional Tectonics

2.1 Introduction

Isostasy is the process by which the elevation of the earth's surface is adjusted in response to surface and sub-surface loads in order to bring about a uniformity in vertical normal stress at some *compensation depth*. Below the compensation depth, the vertical normal stress at a given depth is constant as the state of stress is hydrostatic.

Classical ideas on isostasy assume that loads are only applied at the Earth's surface (i.e., topographic loading). With the Airy mechanism [*Airy*, 1855], surface topography is compensated by thickness variations in a constant density outer shell. Alternatively, the Pratt mechanism [*Pratt*, 1855] assumes a constant depth to the base of the outer shell (i.e., a constant compensation depth), and compensation is achieved by lateral variations in density. Both of these are simple applications of the Archimedes' principle, and as such require the load and its compensation to be vertically coincident. They are consequently referred to as *local* mechanisms of isostatic compensation. Whereas the Pratt mechanism may be applied to oceanic settings, an Airy-type mechanism is more appropriate for the continents.

It was recognised by *Barrell* [1914] that there are deviations from local isostasy at shorter wavelengths due to the rigidity of the Earth's outer shell. In this *regional* (or *flexural*) mechanism, loads are partially supported by the elastic strength of the outer shell, which overrides a weak layer. This idea is a modification of the Airy hypothesis, and was first developed quantitatively by *Vening-Meinesz* [1931]. He believed that the

outer shell corresponded to the crust, which floats on a weak mantle.

It is now understood that the upper mantle can have considerable strength (e.g, *Goetze and Evans* [1979]) - meaning that we must consider the *mechanical lithosphere* as Meinesz's outer shell - and that the lower crust may flow at geologically rapid strain rates (e.g., *Kirby and Kronenberg* [1987]). To understand how isostasy works, the rheology of the lithosphere must first be understood.

It is shown that the effective elastic thickness, T_e, provides a good measure of lithospheric rheology. The importance of rheology and of gravitational potential energy in controlling the style of extensional tectonics is highlighted. We therefore expect the style of deformation to show a relation with T_e. The chapter ends with a summary of T_e estimates across extensional provinces of varying style.

2.2 The Rheology of Continental Lithosphere

There has been some confusion in the literature over what is meant by the term *lithosphere* (e.g., *Anderson* [1995]). Conventionally, the thermal lithosphere is defined as that portion of the Earth's outer shell where heat transfer occurs by conduction. It is decoupled from the adiabatically convecting deeper mantle, and is defined as the depth to a constant isotherm. The potential temperature that is commonly used to define the base of the thermal lithosphere is ~1280°C [*McKenzie and Bickle*, 1988].

Numerous recent studies (e.g., *Burov and Diament* [1995a], *Kooi* [1991], *Lavier and Steckler* [1997]) refer to a *mechanical* lithosphere which is defined on rheological grounds. The base of the mechanical lithosphere is the depth at which significant amounts of deviatoric stress[1] are unable to accumulate because of rapid ductile strain. In the mantle, this corresponds to a temperature of between 800 and 900°C (*Kirby and Kronenberg* [1987] and Figure 2.1). The mechanical lithosphere is thus that portion of the Earth above this depth[2]. This definition is adopted in this study.

The mechanical behaviour of oceanic lithosphere shows a good relation to age [*Bodine, Steckler and Watts*, 1981] that reflects the plate cooling model of *Parsons and Sclater* [1977]. As oceanic crustal thicknesses do not normally exceed 7 km (i.e., for normal mantle potential temperatures), lithospheric rheology is controlled by that of the upper mantle. The rheology of continental lithosphere is complicated by its thick quartz-rich crust, its more complex thermal and tectonic history, and its compositional heterogeneity (e.g., *Kirby and Kronenberg* [1987]).

2.2.1 Rheological layering

In numerical analyses of lithospheric deformation, rheology is commonly approximated by *yield stress envelopes* [*Goetze and Evans*, 1979]. The minimum deviatoric stress (τ) that is required to cause rock to irrecoverably (i.e., inelastically) strain at a given depth is called the *yield stress*, σ_y. This is taken to be the lesser of two stresses: that required to induce brittle failure, σ_b, and that to cause ductile flow, σ_d. Where τ lies within the envelope of positive and negative σ_y, the strain is elastic and entirely recoverable.

Brittle yield stress, σ_b, is derived from Byerlee's law [*Byerlee*, 1978] and increases

[1] Deviatoric stress, τ, is defined as the sum of a principal stress, (σ_{xx}, σ_{yy}, or σ_{zz}), and the mean normal stress (p). See Appendix A.

[2] Note that the lithosphere may include weak zones, such as the lower crust.

with depth beneath the Earth's surface (z). Such frictional behaviour of rock is relatively insensitive to composition, to shear strain rate and to temperature up to ~400°C [*Kohlstedt, Evans and Mackwell*, 1995]. For compressional regimes ($\tau < 0$),

$$\sigma_b = -\left[(\sqrt{\mu^2+1}-\mu)^{-2}-1\right]\sigma_{zz}\left[1-(P/\sigma_{zz})\right] \tag{2.1}$$

and for tensional regimes ($\tau > 0$),

$$\sigma_b = \left[1-(\sqrt{\mu^2+1}-\mu)^{2}\right]\sigma_{zz}\left[1-(P/\sigma_{zz})\right] \tag{2.2}$$

where μ is the coefficient of static friction, σ_{zz} is the vertical normal stress and $P(z)$ is the pore fluid pressure at depth z [*Lowry and Smith*, 1995]. As μ typically varies between 0.2 and 0.7, brittle rocks are stronger in compression than in tension. P can greatly reduce the brittle strength of lithospheric materials.

As temperature increases with depth, there comes a point where σ_d is less than σ_b, and rocks can flow without fracturing. If this ductile creep is assumed to occur at constant strain rate ($\dot{e}$), σ_d can be described by a power law relationship. For both compressional and tensional deviatoric stress,

$$\sigma_d = \left(\frac{\dot{e}}{A}\right)^{1/n} d^{m/n} \exp\left(\frac{H}{nRT}\right) \tag{2.3}$$

where d is the mineral grain size, R is the universal gas constant and T is absolute temperature [*Ranalli*, 1987]. The parameters A, H, n, and m are experimentally determined parameters that are specific to both the material under stress and to the actual mechanism of ductile creep.

Two creep mechanisms are believed to be important in lithospheric deformation: *dislocation creep*, which involves the migration of dislocations in the crystalline structure, and *diffusion creep*, which involves the diffusion of atoms through the crystal grains. Diffusion creep is more efficient than dislocation creep for small d [*Hopper and Buck*, 1993] though is only important for low τ and low $\dot{e}$ [*Carter and Tsenn*, 1987; *Kirby and Kronenberg*, 1987]. Consequently, plastic deformation of the lithosphere is usually modelled as steady state dislocation creep (e.g., *Brace and Kohlstedt* [1980], *Buck* [1991], *Burov and Diament* [1995a], *Kusznir and Park* [1987], *Lavier and Steckler* [1997], *Sonder et al.* [1987]). This mechanism is independent of d (i.e., $m = 0$), so Equation 2.3 simplifies

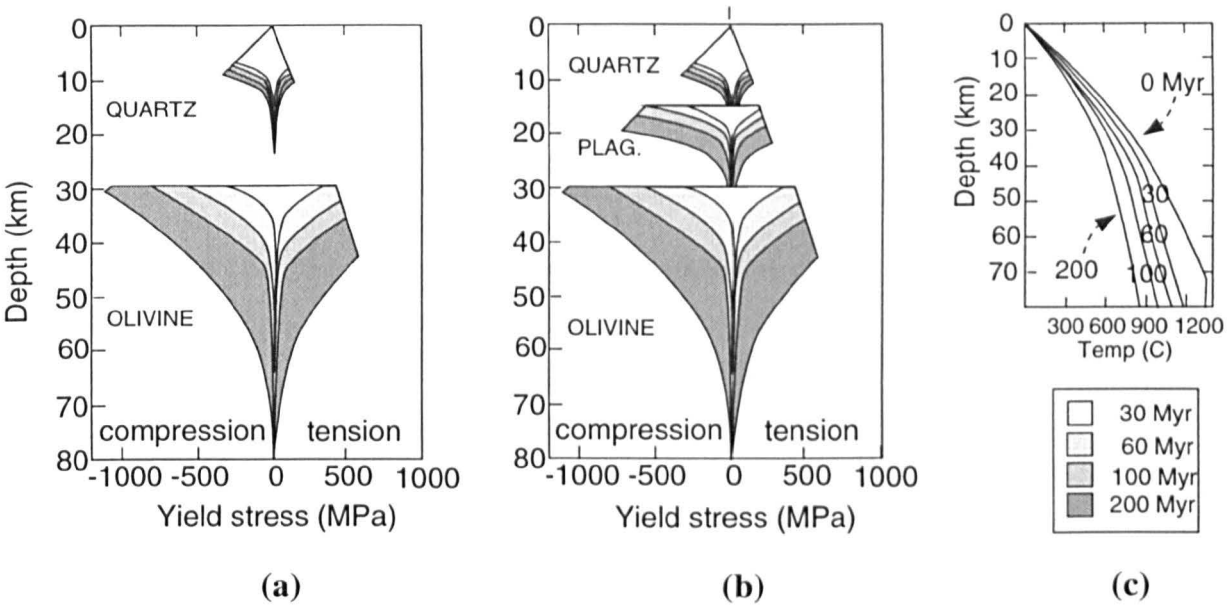

Figure 2.1: Continental yield stress profiles as a function of lithospheric thermal age, after *Beekman* [1994]. (a) Two layer model with dry quartz overlying dry olivine (i.e., $P(z) = 0$). (b) Three layer model, with an intermediate (dry plagioclase) layer. The intermediate layer significantly increases the integrated strength of the lithosphere (B). (c) Typical thermal profiles for lithospheric thermal ages up to 200 Myr.

to

$$\sigma_d = \left(\frac{\dot{e}}{A}\right)^{1/n} \exp\left(\frac{H}{nRT}\right) . \tag{2.4}$$

Table 2.1 presents typical values for A, n and H, and Figure 2.1 shows typical yield stress profiles for continental lithosphere.

2.2.2 Total Mechanical Strength of the Lithosphere

Hopper and Buck [1993] define the total mechanical strength of the lithosphere as the depth integral of yield stress:

$$B = \int_0^L \sigma_y(z)\, dz \tag{2.5}$$

where L is the thickness of the mechanical lithosphere. In the absence of gravitational potential energy (see Section 2.9), this would equal the force required to cause large scale deformation. Although most models of lithospheric extension assume that dislocation creep controls ductile deformation in the lithosphere, *Hopper and Buck* [1993] speculate that diffusion creep could be important during the early stages of extension. If grain

	A ($MPa^{-n}s^{-1}$)	n	H ($kJ\ mol^{-1}$)
Upper crust	10^{-6} to 10^{-3}	2.0 to 3.0	150-230
Lower crust	10^{-3} to $10^{-2.5}$	3.0 to 3.2	230-270
Upper mantle	10^{3} to $10^{4.5}$	3.0 to 4.0	470-535

Table 2.1: Typical creep parameters for lithospheric layers, from *Ranalli* [1997].

size is small or may be reduced, then B may be significantly smaller than the values conventionally assumed.

2.2.3 Factors Controlling Lithospheric Yield Stress

2.2.3.1 Geothermal Gradient

The geothermal gradient (alternatively expressed by some authors as a lithospheric thermal age - or time since the last reheating - as shown in Figure 2.1) greatly influences the strength of the lithosphere because ductile rheologies are strongly temperature dependent. From Equation 2.4 and Figure 2.1, it is seen that lithosphere is weaker for greater geothermal gradients. From a theoretical approach, *Burov and Diament* [1995a] show that temperature variations are the most important factor controlling lithospheric yield stress (see also Figure 2.2).

2.2.3.2 Crustal Thickness

It is clear from Figure 2.1 that, for a given thermal profile, thicker crust results in a reduction in upper mantle yield stress values. The effect of this on lithospheric strength was modelled by *Buck* [1991], and is illustrated in Figure 2.2.

2.2.3.3 Composition

Continental rheologies are typically modelled with two single-phase layers, with a bulk quartz rheology for the crust, and an olivine rheology for the mantle. Some recent models have incorporated a layer with an intermediate composition to approximate a stronger lower crust (e.g., *Bassi* [1995] and Figure 2.1b) though there is little observational evidence to support or contradict this.

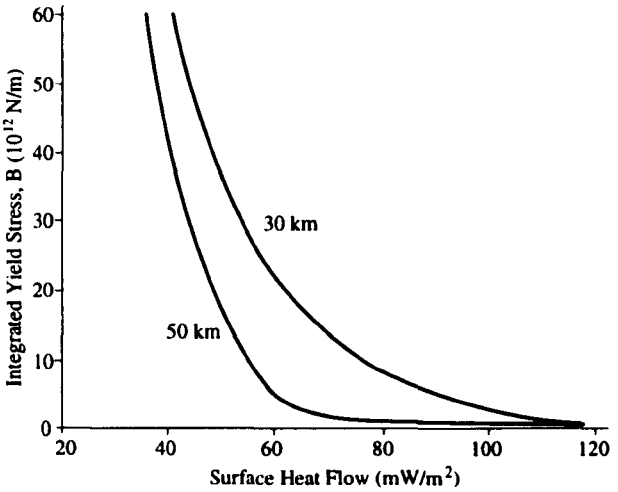

Figure 2.2: The integrated yield stress (B) as a function of surface heat flow for two crustal thicknesses. Under cold conditions, the integrated strength of the lithosphere is large, even for thick crust. Modified from *Buck* [1991].

2.2.3.4 Strain Rate

The laws that govern ductile creep are derived for steady-state conditions. From Equation 2.4, a higher $\dot{e}$ results in a greater ductile yield stress. For dislocation creep, the stress exponent (n) for lithospheric materials is between about 2 and 4 (Table 2.1). Therefore, an increase in $\dot{e}$ of three orders of magnitude will result in roughly one order of magnitude increase in the ductile yield stress. The stress exponent, n, for diffusion creep is lower (e.g., *Karato, Paterson and Fitzgerald* [1986]), so the dependence of σ_d on $\dot{e}$ is greater than for dislocation creep.

2.2.4 Uncertainties in Yield Stress Estimates

Uncertainties exist with yield stress profiles for the lithosphere. The material constants in Equation 2.3 are usually derived for single phase lithologies, and variability in these experimentally determined parameters alone represents a large source of uncertainty. Analyses of the rheology of two-phase mixtures currently exist for only highly idealised phase distributions which may not be applicable to the continental lithosphere [*Kohlstedt, Evans and Mackwell*, 1995].

Further difficulties result from uncertainties in the geothermal gradient (e.g., the timing and magnitude of thermal events, radiogenic heat generation) and variations in composition. The weakening effect of water is also an important factor controlling rock rheology [*Bassi*, 1995; *Hopper and Buck*, 1996; *Kirby and Kronenberg*, 1987]. Changing

a rheology from dry to wet reduces both the brittle and the ductile yield stress (e.g., *Bassi* [1991]).

Observations made under laboratory conditions are extrapolated to the far higher stresses and lower temperatures that are expected to occur deep within the lithosphere. *Kirby, Durham and Stern* [1991] suggest that Byerlee's law of brittle failure may not apply at depths greater than ~50 km. *Carter and Tsenn* [1987] also suggest that the power law behaviour of ductile flow (Equation 2.3) breaks down at low temperature and high stress, and weaker deformation mechanisms prevail for which strength is relatively insensitive to $\dot{e}$ and temperature. The influence of other weaker deformation mechanisms - particularly semi-brittle behaviour [*Kirby and Kronenberg*, 1987; *Scholz*, 1988] and diffusion creep [*Cooper and Kohlstedt*, 1986; *Hopper and Buck*, 1993] - may also be important.

Byerlee's law predicts that frictional stress acting on faults increases with depth, and that the magnitude at the base of the crust brittle is greater than ~100 MPa. However, earthquake stress drops are nearly always less than 10 MPa, regardless of depth. This implies that the frictional stress on faults are reduced, perhaps because of P, and that the value of 10 MPa may only be regarded as a lower limit of the strength of the upper crust.

Constraints on rock rheology are therefore poor. Research is ongoing to reduce the magnitude of some of the uncertainties outlined here (see *Kohlstedt, Evans and Mackwell* [1995]). However, even with those that remain, experimentally determined rheologies and the yield stress profiles derived from them are robust enough to be applied to tectonic problems (e.g., *Buck* [1991], *Cloetingh et al.* [1995], *Hopper and Buck* [1996]).

2.2.5 Alternative Expressions for Lithospheric Rheology

An alternative approach is to express lithospheric rheology as a depth average, either by estimating a bulk lithospheric viscosity or a flexural rigidity. To estimate viscosity, displacements must be accurately measured over a time scale of several decades. This may only be applied to regions deforming rapidly and on a regional scale which - as will be shown in this chapter - is only the case for hot, weak lithosphere. A smooth velocity field is extracted from the measured displacements, and modelled in terms of a viscous flow in response to some constrained tectonic force, **N** (e.g., *Davies et al.* [1997], *England and Molnar* [1997b]). Furthermore, spatial resolution is very poor since

only single estimates for entire provinces are possible. However, some sense of spatial rheological variations may be obtained from the misfit of local measurements to the smooth, regional velocity field.

Estimates of flexural rigidity may be made from gravity and/or topography data with far greater efficiency, and may be performed on a more local scale such that spatial variations in rheology may be resolved. Further, flexural rigidity may be estimated for stable cratons as well as for tectonically active regions. This enables quantitative comparisons to be made between regions of different tectonic style, so giving a potentially greater insight into the dynamics of extensional tectonics.

Recent studies have shown that estimates of lithospheric yield stress may be used to derive a theoretical flexural rigidity, and moreover that these values are consistent with those obtained from analyses of gravity and/or topography [*Burov and Diament*, 1995a; *Lavier and Steckler*, 1997]. This relationship, the reasons for which are outlined in Sections 2.4 and 2.5, justifies the approach taken in this thesis.

2.3 Flexural Rigidity

2.3.1 Bending Stress and Flexural Rigidity in 1D

Figure 2.3 considers a simple 1D flexure of a perfectly elastic plate of thickness t. When subjected to a vertical load, $l(x)$, and a horizontal in-plane force, N_x, the plate will deform, described by the function $w(x)$. Note that $l(x)$ is the sum of a top load, $l_t(x)$, and a bottom load, $l_b(x)$. This in turn generates deviatoric bending stresses, $\tau_{xx}^{w}(z)$, which are compressional towards the upper surface and tensional towards the lower surface in Figure 2.3. For a perfectly elastic rheology, τ_{xx}^{w} is linearly related to distance from a neutral plane within the plate (Figure 2.4a). Strictly speaking, $w(x)$ defines the deformation of the neutral plane, but thin plate theory assumes that all horizontal planes deform by $w(x)$. From *Love* [1944],

$$\tau_{xx}^{w} = \frac{E}{(1-\nu^2)} \frac{d^2w(x)}{dx^2} \, z' \tag{2.6}$$

where E is Young's modulus, ν is Poisson's ratio and z' is depth relative to the neutral plane.

Where a plate is deflected downwards (and $N_x = 0$), its upper portion will be under a deviatoric compression ($\tau_{xx} < 0$) and its lower portion under a deviatoric tension

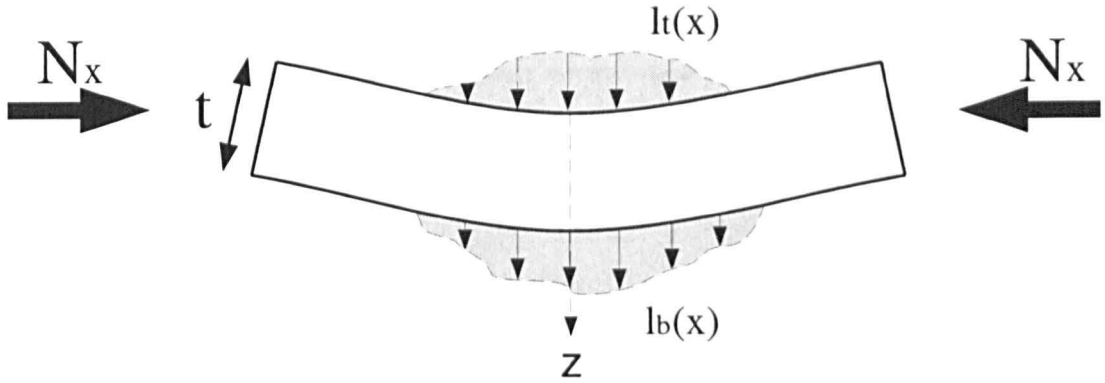

Figure 2.3: The 1D flexure of a perfectly elastic thin plate of thickness h. $l_t(x)$ is the load imparted on the upper surface of the plate, and $l_b(x)$ is that on the base. N_x is the in-plane force. The amplitude of flexure from its undeformed state is described by $w(x)$.

$(\tau_{xx} > 0)$. The net effect of this is to exert a bending moment (M) on the cross-section of the plate. It is calculated as the vertical integral of τ_{xx}^{w} weighted by distance from the neutral plane. If t is the thickness of the plate and z_0 the depth of the neutral plane from the top of the plate, then

$$M = \int_{-z_0}^{t-z_0} \tau_{xx}^{w}\, z'\, dz' \,. \tag{2.7}$$

For a perfectly elastic plate, we can substitute Equation 2.6 into 2.7 to give

$$\begin{aligned} M &= \frac{E}{(1-\nu^2)} \frac{d^2w(x)}{dx^2} \int_{-z_0}^{t-z_0} z'^2\, dz' \\ &= \frac{E}{3(1-\nu^2)} \frac{d^2w(x)}{dx^2} (t^3 - 3z_0t^2 + 3z_0^2t) \,. \end{aligned} \tag{2.8}$$

The depth z_0 is defined as that depth at which $M = 0$ for $\frac{d^2w}{dx^2} = 0$ [*Kooi*, 1991]. As $z_0 = \frac{t}{2}$ for perfectly elastic plates, Equation 2.8 becomes

$$M = \frac{Et^3}{12(1-\nu^2)} \frac{d^2w}{dx^2} \,. \tag{2.9}$$

It is seen that for the perfectly elastic case, M is directly proportional to the second derivative of $w(x)$. The constant of proportionality is called the *flexural rigidity* (D, in Nm). **The smaller the value of D, the tighter the curvature of flexure for a given M.** This is a very important observation, and shows that the wavelength of flexure for a given load is greater for more rigid plates. This is the basis for both the

elastic modelling in Chapter 5, and the coherence analysis in Chapter 6. The flexural rigidity is therefore a measure of the plate's resistance to bending. Thus,

$$M = D\frac{d^2w}{dx^2} \tag{2.10}$$

where

$$D = \frac{Et^3}{12(1-\nu^2)} \, . \tag{2.11}$$

Equation 2.11 shows that the flexural rigidity of a perfectly elastic plate is proportional to Young's modulus and to the cube of its thickness.

2.3.2 The Thin Plate Equations

In two-dimensions, the partial differential equation governing the flexure of a thin elastic plate, $w(x,y)$, of variable flexural rigidity, $(D(x,y))$ subjected to a vertical load $l(x,y)$ and an in-plane force (N) is

$$\nabla^2(D\nabla^2 w(x,y)) = N_x\frac{\partial^2 w(x,y)}{\partial x^2} + N_y\frac{\partial^2 w(x,y)}{\partial y^2} + N_{xy}\frac{\partial^2 w(x,y)}{\partial x \partial y} + l(x,y) \tag{2.12}$$

where $\nabla^2 = \frac{\partial^2}{\partial x^2} + \frac{\partial^2}{\partial y^2}$. All terms have units N/m^2. The load $l(x,y)$ is the resultant vertical normal stress imparted on the thin plate. For topographic loads,

$$l(x,y) = g\int_0^L \Delta\rho(x,y,z)\, dz \tag{2.13}$$

where $\Delta\rho(x,y,z)$ is the density contrast function, relative to the unloaded and unflexed lithosphere. Thus, for initial surface topography $h_I(x,y)$ and bottom topography $w_I(x,y)$,

$$\begin{aligned} l_t(x,y) &= g\rho_c h_I(x,y) \\ l_b(x,y) &= g(\rho_m - \rho_c)w_I(x,y) \end{aligned} \tag{2.14}$$

where ρ_c and ρ_m are the densities of the crust and mantle respectively.

Many studies of extensional tectonics have applied thin plate theory to lithospheric deformation (see Section 2.7), and most consider N to be zero. In this case, the thin

plate equation becomes

$$\nabla^2(D\nabla^2 w(x,y)) = l(x,y) \ . \tag{2.15}$$

Expanding the left hand side gives

$$D\frac{\partial^4 w(x,y)}{\partial x^4} + D\frac{\partial^4 w(x,y)}{\partial y^4} + 2D\frac{\partial^4 w(x,y)}{\partial x^2 \partial y^2} + \frac{\partial^2 D}{\partial x^2}\frac{\partial^2 w(x,y)}{\partial x^2} + \frac{\partial^2 D}{\partial x^2}\frac{\partial^2 w(x,y)}{\partial y^2}$$
$$+\frac{\partial^2 D}{\partial y^2}\frac{\partial^2 w(x,y)}{\partial x^2} + \frac{\partial^2 D}{\partial y^2}\frac{\partial^2 w(x,y)}{\partial y^2} = l(x,y) \tag{2.16}$$

and many simplify this further by assuming D to be spatially invariant such that

$$D\frac{\partial^4 w(x,y)}{\partial x^4} + D\frac{\partial^4 w(x,y)}{\partial y^4} + 2D\frac{\partial^4 w(x,y)}{\partial x^2 \partial y^2} = l(x,y) \ . \tag{2.17}$$

Equation 2.17 is the bi-harmonic thin plate equation of *Bodine, Steckler and Watts* [1981]. In 1D considerations, loads and resulting deflections are assumed to be constant in y, such that

$$D\frac{d^4 w(x)}{dx^4} = l(x) \ . \tag{2.18}$$

2.3.3 The Effect of In-Plane Force on $w(x)$

In-plane tectonic force, **N**, is difficult to estimate, and because it has no effect on D in the purely elastic case (see Section 2.4.3), it has been the convention to assume $\mathbf{N} = 0$ [*Turcotte and Schubert*, 1982]. Compressional in-plane force will lead to amplification of flexural topography $w(x)$, and tensional to a reduction in the amplitude [*Cloetingh and Kooi*, 1993]. However, the effect on the *wavelength* of flexure is small [*Kooi and Cloetingh*, 1992], so estimates of D from the difference in phase between the topography and gravity (see Chapter 6) will not be affected.

2.4 Flexural Rigidity of Continental Lithosphere

2.4.1 The Influence of Yield Stress

Bending stresses can only accumulate where the magnitude of the yield stress is greater than zero, and the maximum $\tau_{xx}^{w}(z)$ at any one depth is limited to $\sigma_y(z)$. Therefore, the factors controlling the magnitude of $\sigma_y(z)$ - geothermal gradient, crustal thickness,

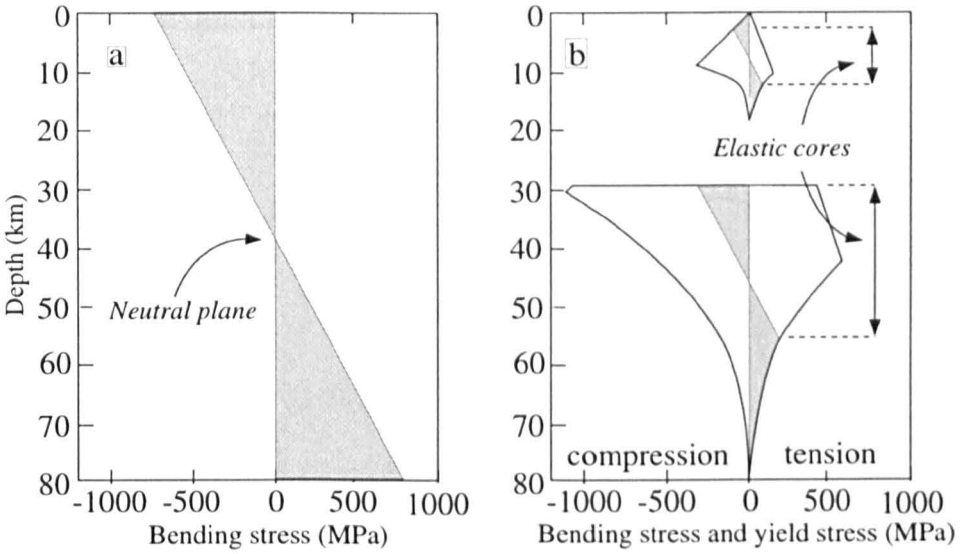

Figure 2.4: (a) Bending stresses in a perfectly elastic plate for a downward flexure. (b) The bending stresses in a lithosphere flexed to the same radius of curvature. The bending moment is less than in (a), so the flexural rigidity is smaller (see Equation 2.10). The *elastic cores* correspond to the depths where bending stress is not limited by yield stress. Adapted from *Lowry and Smith* [1995].

composition and strain rate (Section 2.2.3) - also control D [*Burov and Diament*, 1995a; *Lavier and Steckler*, 1997] The portions of the crust and mantle where strain is entirely elastic are referred to as the *elastic cores* (Figure 2.4). Above the elastic cores, bending stress is relaxed by brittle sliding, and beneath by ductile creep, resulting in a reduced bending moment and so a lower D.

2.4.2 The Effect of Lithospheric Curvature

As τ_{xx}^{w} is limited by σ_y, the bending moment (M) does not increase linearly with $\frac{d^2w}{dx^2}$ as in the perfectly elastic case. Where the bending stress due to plate flexure reaches its local yielding limit, zones of inelastic behaviour appear. In areas under greater loads - such as beneath a mountain chain - the lithosphere might be expected to flex with a reduced D [*Burov and Diament*, 1995b]. This theory has been born out by observations of oceanic lithospheric flexure at trenches [*McAdoo, Martin and Polouse*, 1985]. The effect of this process for a realistic continental rheology is shown in Figure 2.5. Due to the asymmetry in σ_y (i.e., brittle rock is stronger under compression than tension), D is expected to be stronger for a downward flexure than for an upward flexure.

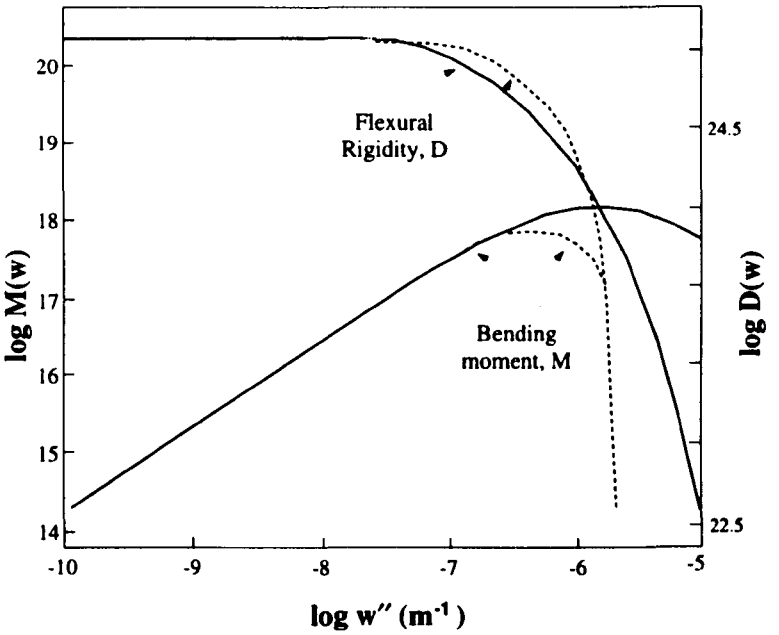

Figure 2.5: The dependence of D on $\frac{d^2w}{dx^2}$ for a layered continental rheology. For a curvature tighter than 10^{-7} m^{-1}, the departure from linear elasticity becomes increasingly significant. As a result, D decreases on increased flexure. Feint lines show the purely elastic behaviour. Downward flexure (i.e., convex down) is shown by solid lines, and upward flexure by the dashed lines. Adapted from *Burov and Diament* [1992].

2.4.3 The Effect of In-Plane Stress

For perfectly elastic plates, the tectonic force (N_x) has no effect on lithospheric rigidity. This is not the case for lithospheric rheologies as the resulting in-plane deviatoric stress (τ_{xx}^N) directly affects lithospheric rigidity. A mathematical analysis is not developed here, though the process is clearly illustrated for the single-layered rheology in Figure 2.6. The bending stress is now added to by the in-plane stress. The deviatoric stress may therefore be expressed as

$$\tau_{xx}(z) = \tau_{xx}^w(z) + \tau_{xx}^N(z) \; . \tag{2.19}$$

It is clear that the thickness of the elastic core reduces, so D decreases.

This process may become increasingly more significant with time for a constant N_x. *Bott and Kusznir* [1984] and *Kusznir and Park* [1987] describe the process of *stress amplification* whereby stresses are concentrated in the stronger portions of the lithosphere as a consequence of creep and stress relaxation in the weaker layers.

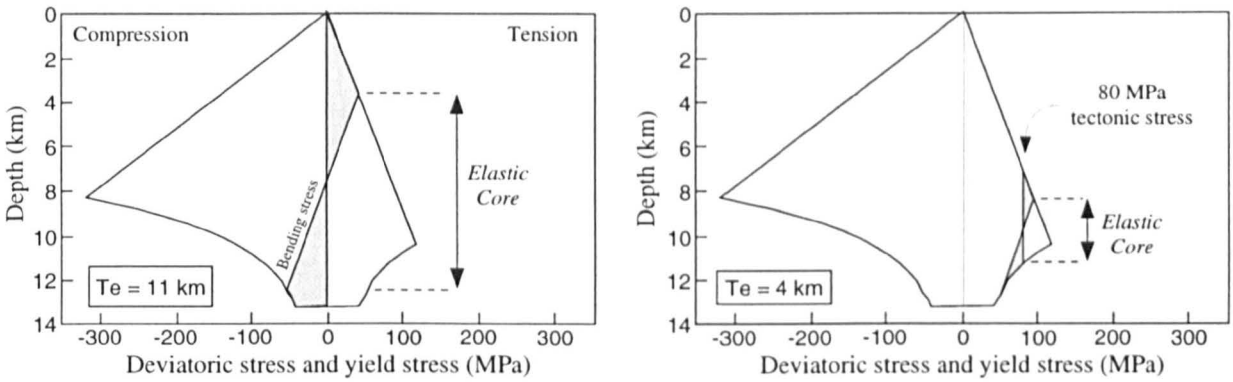

Figure 2.6: The effect of in-plane stress (τ_{xx}^N) on D for a brittle-ductile rheology. The bending stress (τ_{xx}^w) is reduced because of the stress. Adapted from *Lowry and Smith* [1995]. The effect of upward flexure under compressive in-plane stress and downward flexure under tensional in-plane stress is not discussed in the literature reviewed for this thesis.

2.5 The Effective Elastic Thickness

Flexural rigidities (in units of Nm) are rarely cited for the earth's lithosphere as authors prefer to define the equivalent or *effective elastic thickness* (T_e). Once D has been estimated, average lithospheric values for E and ν are assumed (1×10^{11} Pa and 0.25 have become standard values), and used in Equation 2.11 to find T_e.[3] Irrespective of the true stress distribution, one can always find - either by forward modelling or by spectral methods - an *effective* elastic thickness which, for a layered rheology, will not correspond to any single layer.

T_e provides a good measure of the integrated lithospheric strength, which may be compared from region to region. Moreover, the spatial variability of T_e within a single province provides a good handle on the spatial variability in lithospheric rheology. In some continental provinces, it has been shown that T_e variability is related to that in the measured surface heat flow, used as a proxy for geothermal gradient (e.g., *Lowry and Smith* [1994] for the Basin and Range). From Section 2.2.3.1, it is clear that reduction in yield stress due to ductile weakening can explain this. However, to fully understand spatial T_e variability, variations in lithospheric composition, crustal thickness, extensional strain rate, plate curvature and in-plane stress must also be considered (Sections 2.2.3 and 2.4).

Burov and Diament [1995a] and *Cloetingh and Burov* [1996] analyse continental T_e

[3]For perfectly elastic materials, T_e will be equal to t (if E and ν are correctly assigned) because τ_{xx}^w is not limited by σ_y.

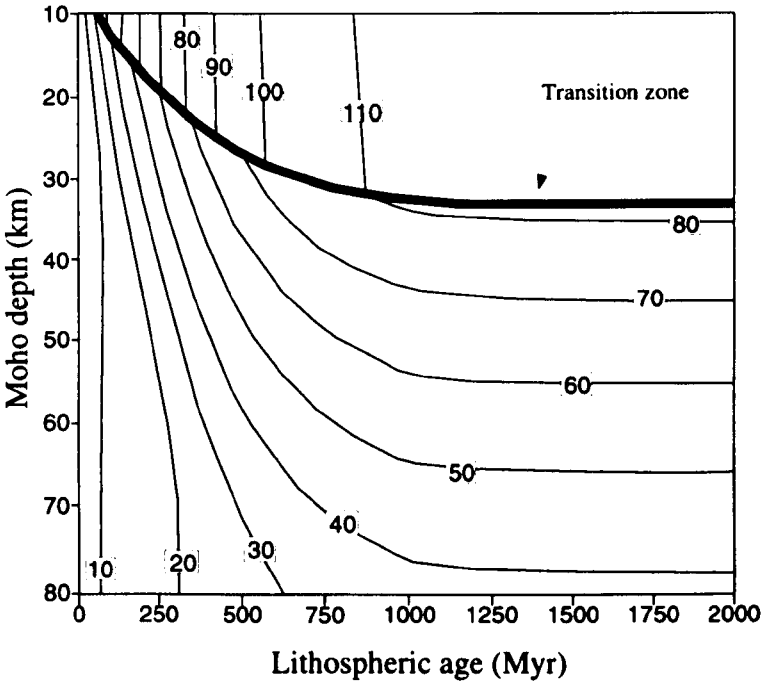

Figure 2.7: The dependence of T_e on moho depth and lithospheric age (or geothermal gradient). Fixed parameters are composition (quartz and olivine), $\dot{e}$ (3×10^{-15} s^{-1}), w'' (that of the earth) and τ_{xx}^N (0). For a given geothermal gradient, there is a critical moho depth where the yield stress in the lower crust becomes zero. *Burov and Diament* [1995a] refer to the effect of this on T_e as the *transition zone*.

values from around the Earth. They deduce that for all but a few estimates - those across old and cold cratons - T_e values indicate that yield stress in the lower crust decreases to zero. *McKenzie and Fairhead* [1997] go so far as to propose that the rheology of the lower crust is so weak that it may be thought of as an inviscid fluid. They suggest that this is the case everywhere, including beneath cratonic regions.

Burov and Diament [1995a] model the dependence of T_e on crustal thickness (or moho depth) and lithospheric thermal age for a two-layer lithosphere (quartz crust and olivine mantle), assuming a strain rate of 3×10^{-15} s^{-1}, a curvature equivalent to that of the earth, and zero in-plane stress. Figure 2.7 shows the predicted T_e for combinations of moho depth and lithospheric thermal age. The main feature of this plot is the *transition zone*. Beneath the transition zone, the yield stress (and so also the bending stress) in the lower crust decreases to zero. Above the zone, T_e values are significantly greater. It is also seen that for lithospheric ages less then 500 Ma, the geothermal gradient is the most important factor controlling T_e.

For very young lithosphere, the integrated lithospheric strength is dominated by the strength of the upper crust only, as the mantle yield stress is small. *Cloetingh and Burov* [1996] present yield stress profiles for the European lithosphere, and the weakest profiles

are shown to exist beneath the thermally young Alpine mountain chain. A yield stress profile for the Aegean is presented for the first time in Chapter 7.

As lithospheric flexural strength is derived primarily from that of the elastic cores, *Burov and Diament* [1995a] argue that

$$T_e \approx \sqrt[3]{\sum_{i=1}^{m} t_i^3} \tag{2.20}$$

for m elastic cores of thickness t_i. This assumes that both the entire crust and the mantle flex with the same curvature.[4] The results of *Burov and Diament* [1995a], which are summarised by Figure 2.7, therefore represent an end-member case (see Figure 2.10a). Lower crustal compensation (Figure 2.10c) is the other end-member, and is discussed in Section 2.7.2.

2.6 Airy Isostasy

With the Airy hypothesis, T_e is zero so loads and their isostatic compensation are vertically coincident. Surface loads (l_t) cannot be distinguished from sub-surface loads (l_b) as their phase spectra are identical. Figure 2.8 shows the lithosphere loaded at the surface by topography of crustal density (ρ_c) and amplitude $h_I(x)$. This results in an increase in the vertical normal stress (σ_{zz}) directly beneath the load. If the lower crust is assumed not to flow, the stress gradient persists to the base of the lithosphere and the moho deforms with its base (Figure 2.8).

Studies of post-glacial isostatic rebound (e.g., *Hager* [1991], *Mitrovica* [1996]) indicate that effective viscosity of the asthenosphere is $\sim 10^{20}$ to 10^{21} Pa s. Loads are therefore isostatically compensated by flow beneath the lithosphere on the order of 10^4 to 10^5 years until the horizontal gradients in σ_{zz} at the base of the lithosphere are zero. This is effectively instantaneous when compared to the rate of geological loading processes.

Figure 2.8b shows that the entire lithosphere beneath the load will shift by an amount $w(x)$ until the upward *buoyancy force* is equal and opposite to the load. From the Archimedes principle, the buoyancy force (F_b) is equal to the weight of fluid displaced. The buoyancy force per unit area, $\sigma_{Fb}(x,y)$, which is the vertical normal stress on the

[4] In this respect, their use of the term *decoupling* to describe a situation of zero lower crustal yield stress is potentially misleading and is not adopted here.

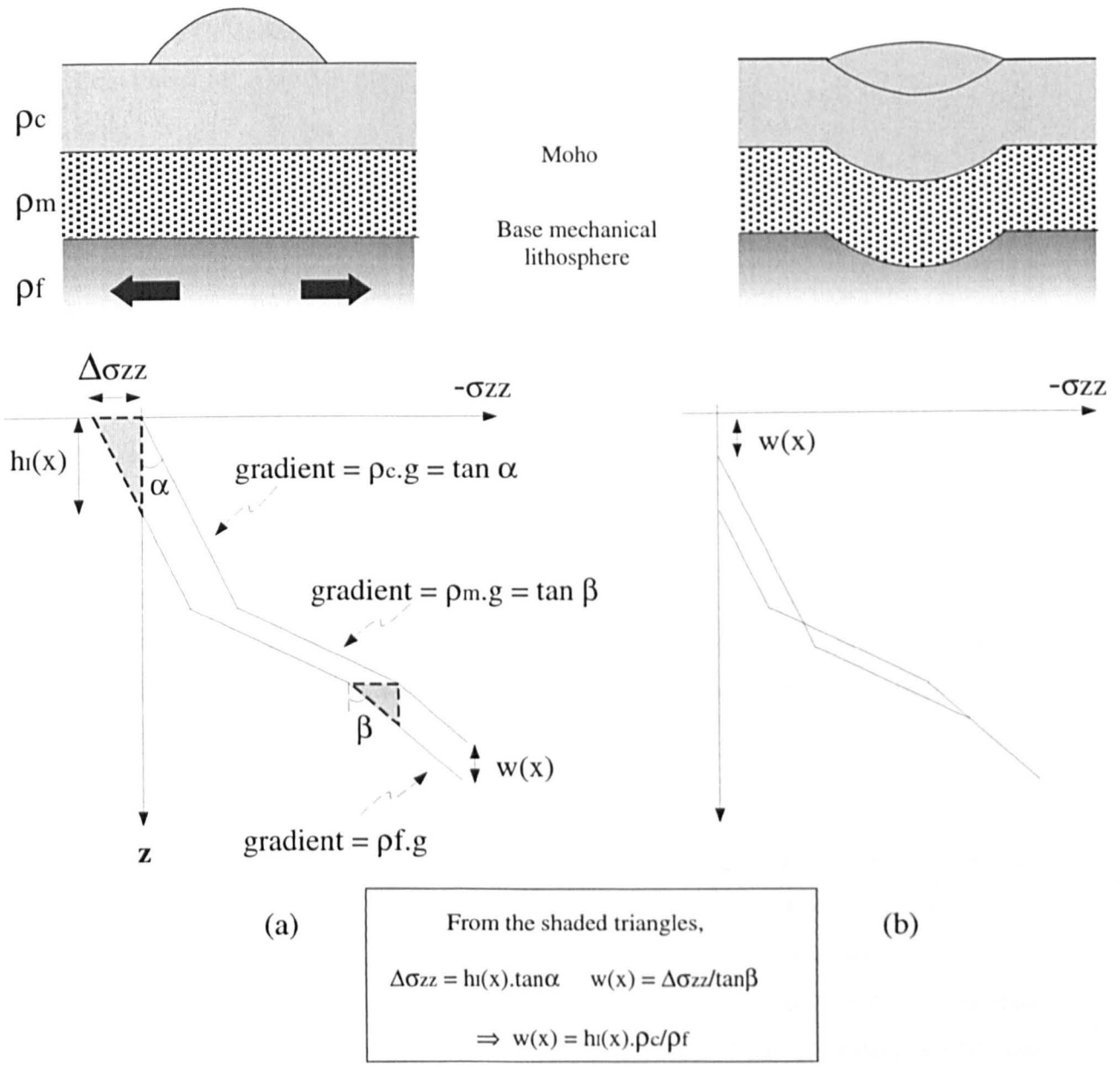

Figure 2.8: Airy isostatic compensation in response to topographic loading. (a) A topographic load results in horizontal gradients in the vertical normal stress (σ_{zz}) which drive flow in the asthenosphere. (b) Vertical motion ensues and compensation is achieved by a displacement of w, such that $\Delta\sigma_{zz}$ is reduced to zero beneath the lithosphere. If $\rho_f = \rho_m$, $\Delta\sigma_{zz}$ would be zero beneath the crust. Note that σ_{zz} values are negative, i.e., compressional.

plate resulting from the F_b, will be a function of position such that

$$\sigma_{Fb}(x,y) = g\rho_f w(x,y) \ . \tag{2.21}$$

If $l(x,y)$ is created by a topographic load of crustal density and amplitude $h_I(x,y)$ (Equation 2.14), then for Airy isostasy,

$$\begin{aligned} l(x,y) &= \sigma_{Fb}(x,y) \\ g\rho_c h_I(x,y) &= g\rho_f w(x,y) \end{aligned} \tag{2.22}$$

and so

$$w(x,y) = \frac{\rho_c}{\rho_f} \ h_I(x,y) \tag{2.23}$$

which is also derived in Figure 2.8. The final topography, $h(x)$, will be

$$h(x,y) = h_I(x,y) + w(x,y) \ . \tag{2.24}$$

Most studies of isostasy assume that crustal and mantle density (ρ_c and ρ_m) are constant, and that asthenospheric density $\rho_f = \rho_m$. These assumption is also adopted here.

2.7 Regional Isostasy

Studies of thin plate lithospheric flexure fall into two broad groups. The first involves forward modelling of gravity and/or topography data (e.g., *King, Stein and Rundle* [1988], *King and Ellis* [1990], *Weissel and Karner* [1989], *van Wees and Cloetingh* [1994], *Stewart and Watts* [1997]), usually in one dimension. In these, the equations describing plate flexure are solved for $w(x)$ within specific boundary conditions and with observational constraints on $l(x)$. This approach is applied to profiles in the Aegean in Chapter 5.

The second group analyses the statistical relationship between gravity and topography as a function of wavenumber (e.g., *Dorman and Lewis* [1970], *Forsyth* [1985], *Lowry and Smith* [1994], *Stark and Hartley* [1994], *Scheirer, Forsyth and Hosford* [1995]) and is usually carried out in 2D. The 2D thin plate equation (Equation 2.25) is used to model the *observed admittance* or *observed coherence* between gravity and topography within a specified area to find the best fit T_e for that area. These methods are compared in

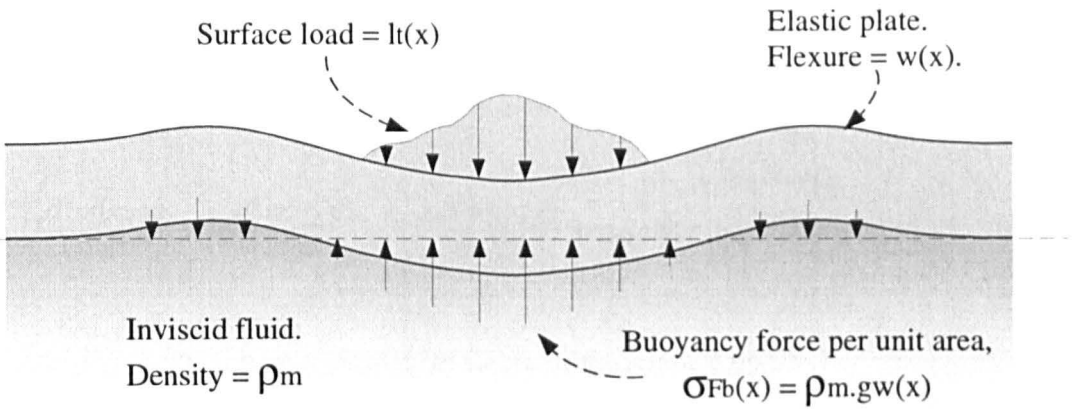

Figure 2.9: A schematic illustration of the thin plate approximation for the flexural isostatic compensation of a surface load. Surface load, $l_t(x, y)$, and buoyancy, $\sigma_{Fb}(x, y)$, are represented by arrows.

Chapter 6, and applied to the Aegean region.

With both methods, isostatic compensation may be assumed to occur either at the base of the lithosphere (i.e., whole lithospheric flexure) or within the lower crust (upper crustal flexure), and the wavelength of flexure for any load $l(x)$ is a function of the effective elastic thickness. Short wavelength components of $l(x)$ are supported by the rigidity of the plate, whereas longer wavelength components will flex the plate. At very long wavelengths, the deformation approximates the Airy mechanism. The wavelength of transition is a finction of T_e, and this idea is used in Chapter 6 to estimate T_e across the Aegean province.

2.7.1 Whole Lithospheric Flexure

The continental lithosphere's long-term response to loading can be modelled as a thin elastic plate overlying an inviscid substratum. There is therefore a vertical buoyancy force term (Equation 2.21) to add to the thin plate equations that is proportional to $w(x, y)$ (Figure 2.9).

The 2D thin plate equation (Equation 2.17) becomes

$$D\frac{\partial^4 w(x,y)}{\partial x^4} + D\frac{\partial^4 w(x,y)}{\partial y^4} + 2D\frac{\partial^4 w(x,y)}{\partial x^2 \partial y^2} + \rho_m g w(x,y) = l(x,y) \ . \tag{2.25}$$

and the 1D equation (Equation 2.18) becomes

$$D\frac{d^4 w(x)}{dx^4} + \rho_m g w(x) = l(x) \tag{2.26}$$

where ρ_m is the density of the inviscid asthenosphere. Assuming $l(x,y)$ to be a topographic surface load with amplitude $h_I(x,y)$, then from Equation 2.14, the 2D thin plate equation becomes

$$D\frac{\partial^4 w(x,y)}{\partial x^4} + D\frac{\partial^4 w(x,y)}{\partial y^4} + 2D\frac{\partial^4 w(x,y)}{\partial x^2 \partial y^2} + \rho_m g w(x,y) = \rho_c g h_I(x,y) \ . \tag{2.27}$$

It is seen that as $D \rightarrow 0$, Equation 2.27 tends to Equation 2.23.

2.7.2 Upper Crustal Flexure

Kirby and Kronenberg [1987] use the prediction of low yield stress in the lower crust to suggest the concept of a *crustal asthenosphere*. Even where the upper mantle is strong, the upper crust may strain independently. *Jin, McNutt and Zhu* [1994] present evidence for such a decoupling of the Tibetan crust and upper mantle, and the presence of a flexurally strong mantle beneath Tibet is supported by the observation of sub-crustal earthquakes [*Molnar and Chen*, 1983].

There is a growing body of evidence to support the idea that lower crustal isostatic compensation also occurs in some extensional settings, particularly where surface heat flow is high and the crust is thick [*Ruppel*, 1995]. Models for extensional processes within the Tibetan Plateau [*Bird*, 1991; *Masek, Isacks and Fielding*, 1994] and the Basin and Range [*Block and Royden*, 1990; *Kaufman and Royden*, 1994; *King and Ellis*, 1990; *Kruse et al.*, 1991] have assumed a lower crust that flows in response to loads created by upper crustal extension.

With the Airy and whole lithospheric flexure models, horizontal gradients in σ_{zz} exist to the base of the mechanical lithosphere where rapid lateral flow occurs. However, if the lower crust is viscous, σ_{zz} differences will induce flow above the moho. The level of isostatic compensation would then gradually shift from the mantle asthenosphere to the viscous lower crust [*Kaufman and Royden*, 1994] (Figure 2.10).

If the viscosity of the lower crust is very low prior to loading, isostatic compensation may occur entirely within the crust, and the moho will not deform [*McKenzie and Fairhead*, 1997] (Figure 2.10c). Crustal flexure would then be described by the equation

$$D\frac{\partial^4 w(x,y)}{\partial x^4} + D\frac{\partial^4 w(x,y)}{\partial y^4} + 2D\frac{\partial^4 w(x,y)}{\partial x^2 \partial y^2} + \rho_{lc} g w(x,y) = l(x,y) \tag{2.28}$$

where ρ_{lc} is the lower crustal density, and D is the flexural rigidity of the upper crust.

2.7.3 The Isostatic Scheme

The ideas of crustal flexure and whole lithospheric flexure - which are used in Chapters 5 and 6 respectively - are now analysed together. For given crustal and mantle densities, the rate at which the lower crust flows to achieve isostatic compensation depends on three factors [*Kaufman and Royden*, 1994]:

- the viscosity
- the thickness of the lower crustal channel
- the wavelength of loading.

In provinces where extension is occurring in thickened crust, the effective viscosity of the lower crust is expected to be low. *Masek, Isacks and Fielding* [1994] suggests that the effective viscosity of the lower crust beneath the extensional grabens of the Tibetan Plateau is less than $\sim 10^{22}$ Pas and indicate that the narrow rift structures are entirely compensated within the crust. Lower crustal viscosities of between 10^{18} Pas and 10^{20} Pas have been proposed for similar wavelength features in the Basin and Range [*Kaufman and Royden*, 1994; *Kruse et al.*, 1991].

If the crust were entirely elastic, the whole lithosphere would flex at a wavelength determined by its T_e. If the effective viscosity of the lower crust is low, compensation of short wavelength loads will shift from the asthenosphere to lower crust with time.[5] This idea is shown schematically in Figure 2.10.

The two isostatic models adopted in this thesis are end-members in Figure 2.10. Both ignore the wavelength dependence of viscosity and assume that all loads are compensated about a single interface: either the base of the lithosphere or the base of the brittle crust. Transient effects due to viscous flow are ignored, and the only wavelength dependence on isostatic compensation is assumed to be that due to flexure (see Equation 2.10).

2.8 Regional Isostasy and Models for Rift Geometry

Rift flank uplift is common to all styles (see Section 2.10) of continental extension. There are four distinct classes of mechanism to explain this phenomenon: (1) thermal, either

[5] Note that there may be a lag in time such that topography may appear overcompensated.

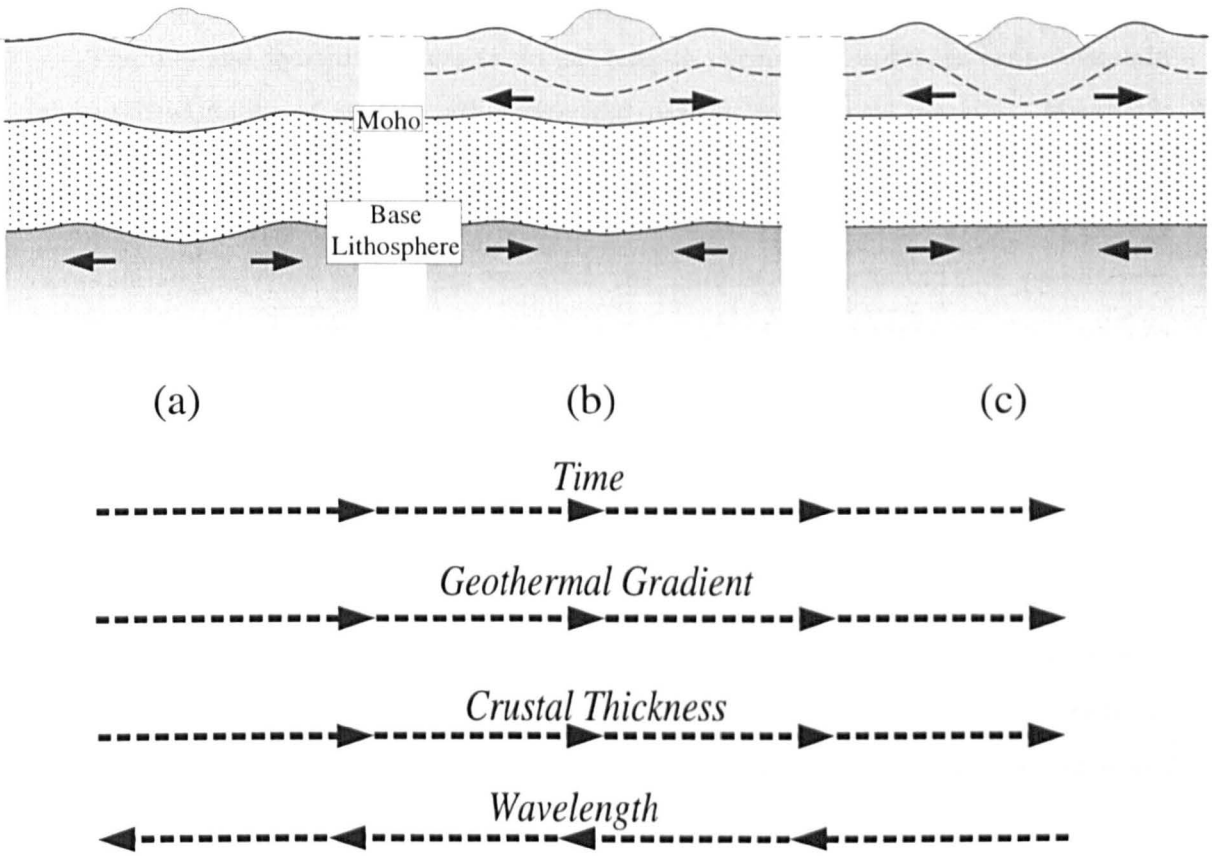

Figure 2.10: The shifting depth of compensation from asthenospheric mantle to viscous lower crust, in response to a surface load. (a) Whole lithospheric flexure. Lateral gradients in σ_{zz} persists to the base of the mechanical lithosphere, so the crust and mantle flex together with a combined T_e, as envisaged by *Burov and Diament* [1995a]. (b) The lower crust begins to flow, reducing the stress gradients in the mantle. The crust begins to flex independently, and less stress is transferred to the base of the lithosphere. As a result, the mantle starts to un-flex. (c) Upper crustal flexure. Crust is decoupled form the mantle, and all σ_{zz} gradients beneath the lower crust are hydrostatic. The rate at which this process occurs depends on geothermal gradient (or surface heat flow), crustal thickness and the wavelength of the load.

by conduction [*Alvarez, Virieux and Le Pichon*, 1984; *Buck et al.*, 1988; *Cochran*, 1983; *Royden and Keen*, 1980] or advection [*Buck*, 1986; *Keen*, 1985]; (2) dynamic support due to viscous stresses [*Bassi*, 1991; *Wdowinski and Axen*, 1992; *Zuber and Parmentier*, 1986]; (3) magmatic underplating [*McKenzie*, 1984; *Mutter, Buck and Zehnder*, 1988]; (4) flexural support of extensional loads [*Braun and Beaumont*, 1989; *Weissel and Karner*, 1989].

Thermal and dynamic processes do not lead to permanent uplift, so cannot explain the uplifted flanks of ancient rift basins and passive continental margins. Magmatic underplating thickens crust and can lead to permanent uplift. Although the contribution of underplating is difficult to assess, flexural uplift in response to extensional unloading is a potentially universal mechanism to explain the uplift of rift flanks and their persistence.

Because of their complexity, most dynamic models of continental extension - such as those described in Section 2.10 - do not include a flexural response to extensional loads. Models of lithospheric flexure require the load to be defined, and the regional isostatic response is modelled within specific boundary conditions. Two classes of these *kinematic* models have been applied to the process of rift flank flexure. These are lithospheric necking models (e.g., *Braun and Beaumont* [1989], *Kooi* [1991], *Kooi, Cloetingh and Burrus* [1992]) and simple shear models (e.g., *Bott* [1997], *Buck* [1993], *Forsyth* [1992], *King and Ellis* [1990], *King, Stein and Rundle* [1988]). Some models incorporate both, with simple shear in the upper crustal and pure shear beneath [*Kusznir, Marsden and Egan*, 1991; *Weissel and Karner*, 1989].

2.8.1 Pure Shear Necking Models

In the lithospheric necking model, the entire lithosphere is assumed to deform by pure shear by an extension factor β. The depth of necking, z_n, describes the level in the lithosphere that would remain horizontal in the absence of gravity. The initial (kinematic) surface and sub-surface loads (l_t, l_b) are therefore controlled by β and z_n. The pure shear model of *McKenzie* [1978a] assumed z_n to be at the surface such that $l_t = 0$, but *Braun and Beaumont* [1989] show that a rheologically layered lithosphere will neck about its strongest portion. For levels of necking that create a surface depression deeper than the level predicted by local isostasy, an upward buoyancy force acts at the base of the rift. If the lithosphere has a finite T_e, flexural uplift occurs (Figure 2.11).

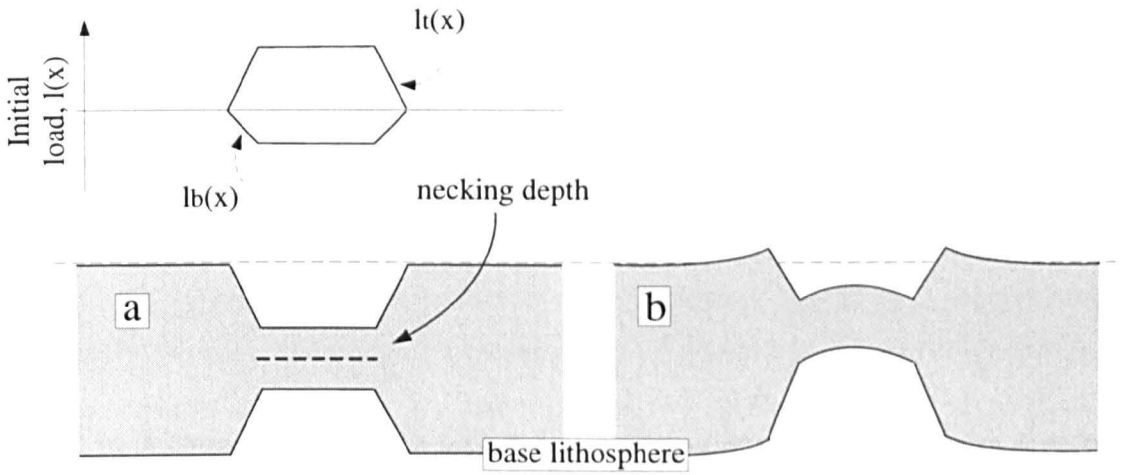

Figure 2.11: The lithospheric necking model, conceptually broken down into two stages: the kinematic deformation and the isostatic response. (a) The necking depth (z_n) is deep such that the surface depression is deeper than that which would result after local isostatic relaxation. (b) An upward flexure results if the (modulus of the) surface load is greater than the (modulus of the) subsurface load. The loads are calculated as in Equation 2.13. Modified from *Braun and Beaumont* [1989].

2.8.2 Simple Shear Models

Half grabens are a common extensional feature of continental regions, and are the dominant surface expression of many rift systems. They are characteristically bounded by planar faults that dip between 40° and 60° which penetrate to mid-crustal depths. Faulting then gives way to distributed plastic deformation, where the rate of flow depends on the effective viscosity.

King, Stein and Rundle [1988] model the flexural response to short wavelength loads resulting from normal faulting and show that unless the viscosity is very high, a model of an elastic upper crust overlying an inviscid half-space (Equation 2.28) adequately describes the first-order dynamics. Studies of Tibet and the Basin and Range suggest that the lower crustal viscosity is very low such that this assumption is valid, and numerous authors have adopted this idea in their models of rift geometry (e.g., *Bott* [1997], *Buck* [1993], *Forsyth* [1992], *Hassani and Chéry* [1996], *King and Ellis* [1990]).

In cooler regions, the viscosity of the lower crust may be high enough that the earth's surface is coupled with the moho. This may be incorporated by including a pure shear necking of the lower crust and mantle whose necking depth is assumed to coincide with the base of the brittle crust, so simulating a mid-crustal detachment [*Kusznir, Marsden and Egan*, 1991; *Weissel and Karner*, 1989].

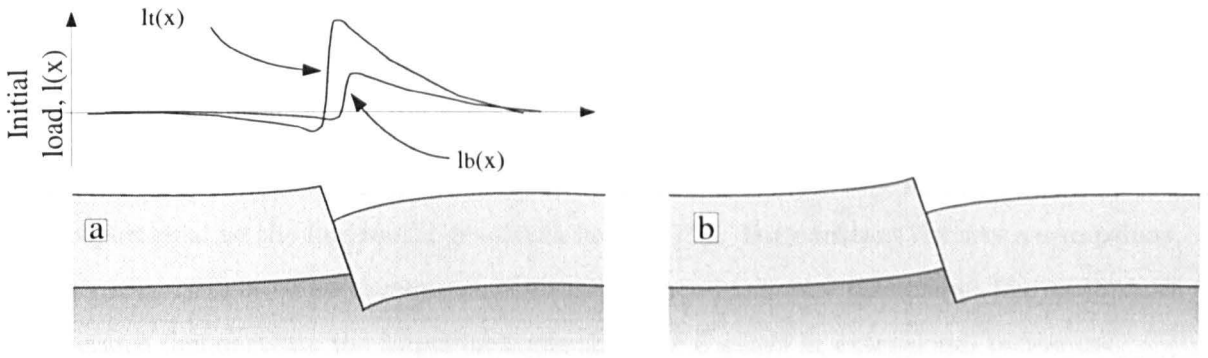

Figure 2.12: A Simple shear model for flexural compensation of rifts, conceptually broken down into two stages: the coseismic deformation and the isostatic response. (a) Coseismic response calculated for a semi-infinite plate, given a defined fault dip (θ) and slip. (b) Post-seismic relaxation is modelled as a continuous plate flexure given a defined T_e.

2.9 Gravitational Potential Energy

Local isostatic balance does not imply a complete stress balance within the lithosphere. Regions of isostatically compensated lithosphere may be in a state of tensional deviatoric stress (i.e., $\tau > 0$) if their gravitational potential energy (GPE) exceeds that of their surroundings. Regions of high GPE usually correlate with regions of greater surface elevation, although as GPE is proportional to the integral of the *product* of density and depth, this need not be so. In general however, elevated crust and its compensating root store GPE. It might be expected therefore that elevated regions should extend.

If we assume that the density of the crust and mantle are constant, and that the density of fluid asthenosphere is the same as the lithospheric mantle, horizontal GPE gradients will result solely from lateral thickness variations in the crust (Figure A.1 and 2.13). Analyses of GPE from various provinces have provided an attractively simple explanation for broad-scale tectonic features such as the simultaneous occurrence of reverse and normal faulting in mountainous regions [*Dalmayrac and Molnar*, 1981; *England and Houseman*, 1989; *Molnar and Lyon-Caen*, 1988], and the spatial distribution of surface strain within extensional provinces [*Buck*, 1991; *Hopper and Buck*, 1996].

Appendix A presents the theory behind these ideas for the 1D case, which is often vague in the literature. This leads to the important relationship

$$\begin{aligned} \Delta\overline{\tau_{xx}} &= \frac{1}{2L}\Delta\Gamma \\ &= \frac{g\rho_c}{4L}\left(1-\frac{\rho_c}{\rho_m}\right)(\Delta T_c)^2 \end{aligned} \tag{2.29}$$

where τ_{xx} is the horizontal deviatoric stress (the overbar indicates a depth average for the lithosphere), Γ is GPE per unit area, T_c is crustal thickness and Δ indicates a difference between two locally compensated columns of lithosphere. This states that the horizontal gradients in deviatoric stress required to deform a thin viscous sheet are proportional to the horizontal gradients in its GPE. For constant density assumptions, this may be related to the square of the difference in crustal thickness. The next three sections demonstrate the important role that GPE plays in extensional tectonics.

2.9.1 The Tibetan Plateau

Normal faulting plays a major role in the active tectonics of the Tibetan Plateau (e.g., *England and Molnar* [1997a], *Mercier et al.* [1987]). *Molnar, England and Martinod* [1993] show that normal faulting is confined to the highest parts of the plateau, between ~4 km and 5.5 km above sea-level, whereas thrust faulting continues to thicken the crust at lower elevations. The onset of normal faulting at ~8 Ma is thought to be associated with a rapid change in GPE due to convective removal of a cold lithospheric root [*England and Houseman*, 1989; *Molnar, England and Martinod*, 1993].

If $\overline{\sigma_{zz}}\,|_{h=4}$ represents the average vertical normal stress beneath the plateau at an elevation of 4 km, then

$$\overline{\sigma_{xx}} = \overline{\sigma_{zz}}\,|_{h=4} \quad . \tag{2.30}$$

From this,

$$F_d + F_x = \int_0^L \sigma_{zz}|_{h=4}\; dz \tag{2.31}$$

such that the resultant in-plane force, N_x, is zero. F_d is the driving force resulting from the collision between India and Eurasia, and F_x is the horizontal force that is present in the absence of such a driving force which is expressed in Equation A.14, and L is the thickness of the lithosphere.

From Equation A.15, if $F_d = 0$,

$$\begin{aligned} 2\,\overline{\tau'_{xx}}(A) &= \overline{\sigma_{xx}} - \overline{\sigma_{zz}}(A) \\ &= \frac{1}{L}F_x - \frac{1}{L}\int_0^L \sigma_{zz}(A)\; dz \end{aligned} \tag{2.32}$$

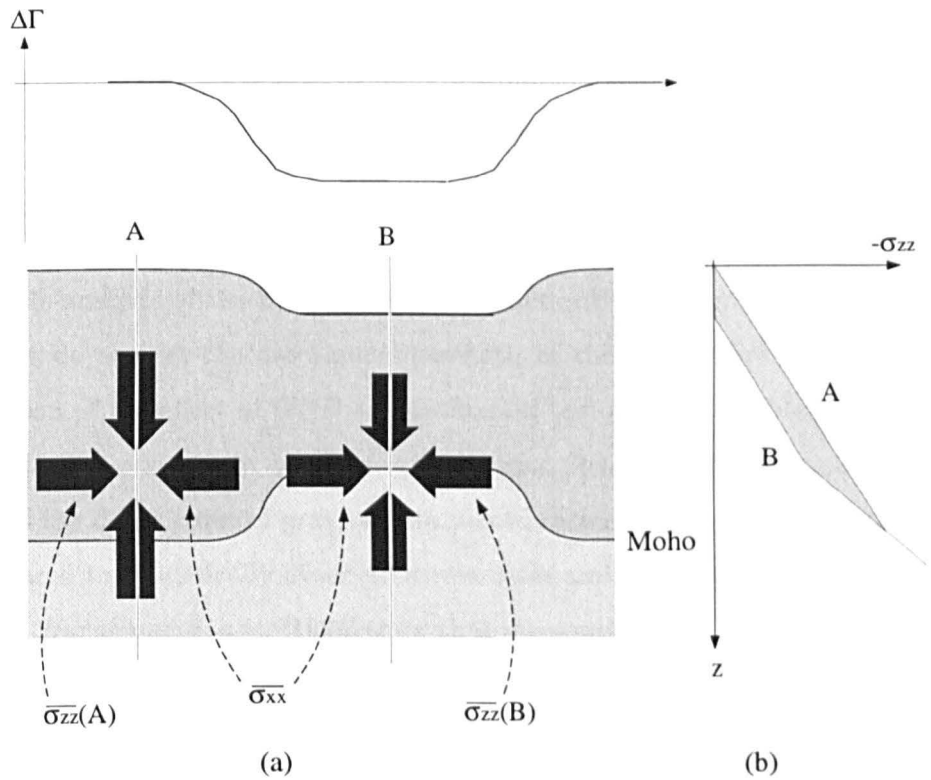

Figure 2.13: (a) $\overline{\sigma_{xx}}$ is constant across the system, such that the vertically averaged horizontal deviatoric stress ($\overline{\tau_{xx}}$) varies and controls the deformation of the region. $\Delta\Gamma$ describes the difference in GPE relative to that at reference column A. (b) Profiles of vertical normal stress, assuming $\rho_f = \rho_m$. Density differences due to thermal effects are ignored in this sketch.

where A refers to column A in Figure A.1, and $\overline{\tau'_{xx}}(A)$ represents the average horizontal deviatoric stress at A if there were no driving force. From Equations 2.31, 2.32 and A.25, the driving force resulting from the collision between India and Asia is expressed as

$$\begin{aligned} F_d &= \int_0^L \sigma_{zz}\big|_{h=4}\ dz - \int_0^L \sigma_{zz}(A)\ dz - 2L \int_0^L \tau'_{xx}(A)\ dz \\ &= \int_0^L \Delta\sigma_{zz}\ dz - 2L \int_0^L \tau'_{xx}(A)\ dz \\ &= -\Delta\Gamma - 2L \int_0^L \tau'_{xx}(A)\ dz. \end{aligned} \tag{2.33}$$

Thus, the driving force needs to overcome the GPE in the system. This comprises the excess GPE resulting from the elevated plateau plus a general level of GPE. From this, it can be seen why $\Delta\Gamma$ is sometimes referred to as a horizontal deviatoric force [*Buck*, 1991; *Molnar, England and Martinod*, 1993]. *England and Molnar* [1997b] show

that the spatial variations in Γ across the Tibetan Plateau correlate with variations in strain rate, which leads to a bulk viscosity estimate of 10^{22} Pas (see also *Haines* [1998]). This is only 10 to 100 times greater than the viscosity of the asthenosphere beneath.[6]

2.9.2 The Basin and Range

This simple analysis of the dynamics of the Tibetan Plateau ignores the work that the force must do against the mechanical strength of the lithosphere. A more thorough investigation of the effect of GPE on continental tectonics is possible in the Basin and Range, and was carried out by *Jones, Unruh and Sonder* [1996]. Seismic velocity estimates and the dense cover of gravity data provide a means of mapping Γ. These results are compared to geodetically observed strain rates and measured surface heat flow.

Jones, Unruh and Sonder [1996] show that the spatial GPE variations are capable of producing virtually all active deformation observed throughout the province, other than the strike-slip motion between the Pacific and North American plates. More specifically, those regions with the greatest GPE are extending at the highest rates. However, some regions with high GPE - such as the Colorado Plateau and the Rocky Mountains - do not extend as rapidly as others. From the heat flow data, the rheology of the lithosphere in these areas is expected to be stronger, and so resist the horizontal deviatoric stresses that arise from isostatic compensation. This is supported by *Lowry and Smith* [1994] who observe that regions of low T_e correlate with regions of high surface heat flow and regions that are pervasively faulted.

Jones, Unruh and Sonder [1996] therefore demonstrate that for a given driving force, *rheology* and GPE ultimately control the tectonic deformation in the Basin and Range province. Equation 2.33 may therefore be modified to

$$F_d = F_L - \Delta\Gamma - 2L \int_0^L \tau'_{xx}\, dz \tag{2.34}$$

where F_L is some measure of the lithospheric yield strength. Thus, in order to strain the lithosphere, the driving force must work against gravitational potential energy and a lithospheric mechanical strength.

[6] It is interesting to note that for thin elastic plate models, N_x is commonly assumed to be zero such that deviatoric stress (τ) results solely from elastic bending stresses (τ^w_{xx}). Analyses of gravitational potential energy such as these assume Airy isostasy. As a consequence, bending stress is zero, and τ results solely from N_x, i.e,. from a driving force (F_d) and lateral variations in vertical normal stress ($\Delta\Gamma$).

2.9.3 GPE across Rift Basins

Localised extension of a cross-section of continental lithosphere produces lateral density anomalies and thus horizontal gradients in Γ. Figure 2.13 shows that, if Airy isostasy prevails, rift basins will tend to be associated with relative lows in GPE.

The manner in which Γ changes as a region extends was modelled by *Buck* [1991] and *Hopper and Buck* [1996]. These authors separate the effects of crustal thickness changes (*crustal buoyancy*) and thermal anomalies (*thermal buoyancy*) on Γ, and calculate their magnitudes as a function of surface heat flow, crustal thickness and strain rate.

If the rheology of the lower crust is very weak, flow may occur within it in response to the horizontal gradients in σ_{zz} (see Section 2.7.2). Thicker crust and higher heat flow will increase the rate at which lower crustal flow reduces the differences in σ_{zz} and restores crustal thickness within the extended region. Thus, changes in the crustal buoyancy effect will be less for regions of thicker crust and higher heat flow (Figure 2.14). *Buck* [1991] does not model the effect of lower crustal flow on the thermal buoyancy effect, though *Hopper and Buck* [1996] state that the process is almost isothermal.

From Equation 2.34, we see that the driving force must work against gravitational potential energy and the mechanical strength. *Buck* [1991] uses the integrated yield strength (B) as a measure of F_L (Section 2.2.2). The right hand side of Equation 2.34 can be thought of as a combined lithospheric strength, or the minimum driving force required for deformation to occur (F_{min}). Thus, the change in lithospheric strength at a single position between two times may be expressed as

$$\tilde{\Delta}F_{min} = \tilde{\Delta}B - \tilde{\Delta}\Delta\Gamma \tag{2.35}$$

where $\tilde{\Delta}$ refers to a change with respect to time. *Buck* [1991] and *Hopper and Buck* [1996] calculate the change in $\Delta\Gamma$ and B between two stages of rifting. Figure 2.14 shows these changes as a function of surface heat flow for $\beta = 1$ to 1.25. If $\tilde{\Delta}F_{min}$ is positive, the rift strengthens with time. Conversely, the rift weakens through time if $\tilde{\Delta}F_{min}$ is negative.

Thus it has been shown that *spatial* (horizontal) gradients in GPE are sufficient to drive the extensional tectonics of the Tibetan Plateau and the Basin and Range, both of which are known to be rheologically weak. On a more local scale, *temporal* variations in GPE are seen to play an important role in the evolution of a rift's strength. The

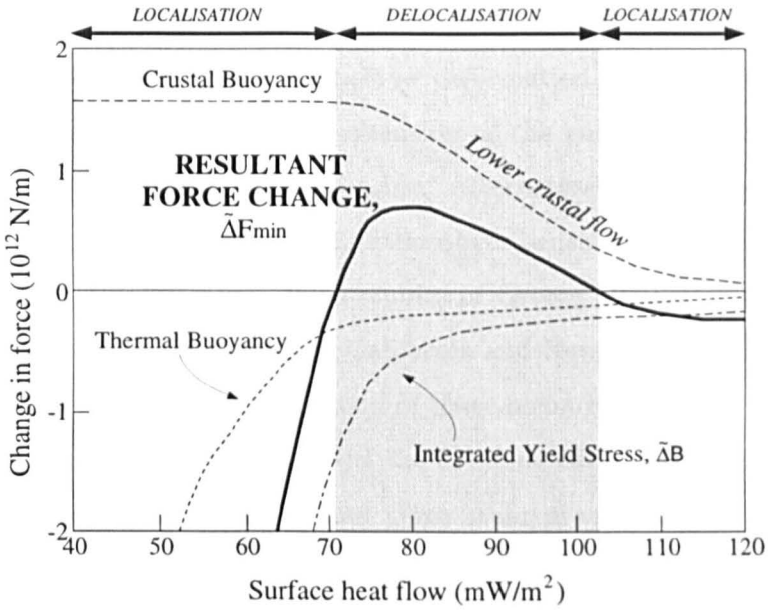

Figure 2.14: Changes in gravitational energy per unit area ($\Delta\Gamma$) and integrated yield stress (B) as a function of surface heat flow for an initial crustal thickness of 40 km, extending at a strain rate of 8×10^{-15} s^{-1}. $\Delta\Gamma$ comprises a crustal buoyancy effect and a thermal buoyancy effect. The rift is strengthening if $\tilde{\Delta}F_{min}$ is positive, resulting in the delocalisation of strain (shaded region). Strain is localised for negative $\tilde{\Delta}F_{min}$. Modified from *Buck* [1991].

implications of this on the style of rifting are discussed in the following section.

2.10 Rheology, Strain Localisation and Extensional Style

The continental lithosphere is observed to extend in three distinct modes: the discrete (or narrow) rift mode, the diffuse (or wide) rift mode, and the core-complex mode [*Buck*, 1991; *Hopper and Buck*, 1996; *Ruppel*, 1995] (Figure 2.15). Discrete rift systems are localised zones of lithospheric extension less than 100 km across, such as the East African Rift, the Baikal Rift, the Rhine Graben and the Rio Grande Rift. The archetypal discrete rift, the East African Rift, consists of long en-echelon normal faults that bound wide grabens and half grabens.

Diffuse rifts systems are broad zones of lithospheric extension, such as the Basin and Range Province. Upper crustal deformation occurs across the broad zone, often over 400 km wide, and strain is localised on a series of sub-parallel individual rifts structures. These are ~20 km wide and spaced at ~35 km.

Core complex rift systems, such as those that formed in the Basin and Range province between about 20 and 10 Ma, are generally narrow, localised areas of upper crustal extension. Where the amount of extension is very high, the exhumation of mid to lower

crustal metamorphic rocks can occur.

It is a matter of current debate as to how deformation beneath the upper crust is accommodated. One view is that the extension of the entire lithosphere is localised in narrow shear zones beneath the rift basins. Alternatively, strain localisation could simply be a surface phenomenon, and the lithosphere beneath deforms in a distributed, continuous fashion. Recent results from studies of Greece [*Davies et al.*, 1997], Tibet [*England and Molnar*, 1997b], Southern California and New Zealand [*Bourne, England and Parsons*, 1998] may support the second of these scenarios.

Many studies have attempted to model the dynamic effects of lithospheric rheology on the style of extensional tectonics, and three main processes have been described. These are

- the development of necking instabilities (Section 2.10.1)
- the process of conductive cooling (Section 2.10.2), and
- the generation of gravitational potential energy (Section 2.10.3).

2.10.1 Necking Instabilities

Examples of *boudinage* - the extension of a rock layer by the development of regularly spaced pinch and swell structures - are commonly seen at outcrop scale in the field. These structures form when a strong layer is embedded in a weak matrix, and the system is extended. This idea has been applied on a crustal and lithospheric scale to examine the effects of a layered lithospheric rheology on large-scale extensional deformation.

Analyses of lithospheric rheology and the seismicity from extending provinces suggests that a realistic strength stratification for regions of thickened crust and/or high heat flow consists of a strong upper crust and a weak lower crust. *Fletcher and Hallet* [1983], *Zuber and Parmentier* [1986] and *Zuber, Parmentier and Fletcher* [1986] approximate such rheological layering with power-law fluids, and examine the response to extensional stress.

Artemjev and Artyushkov [1971] and *Zuber and Parmentier* [1986] show how extensional strain can concentrate about an initial strength perturbation, and that the lithosphere will neck at some dominant wavelength. However, *Zuber and Parmentier* [1986] also point out the importance of the width of such a perturbation. If the width is wider than the dominant necking wavelength, then deformation develops *periodically* at

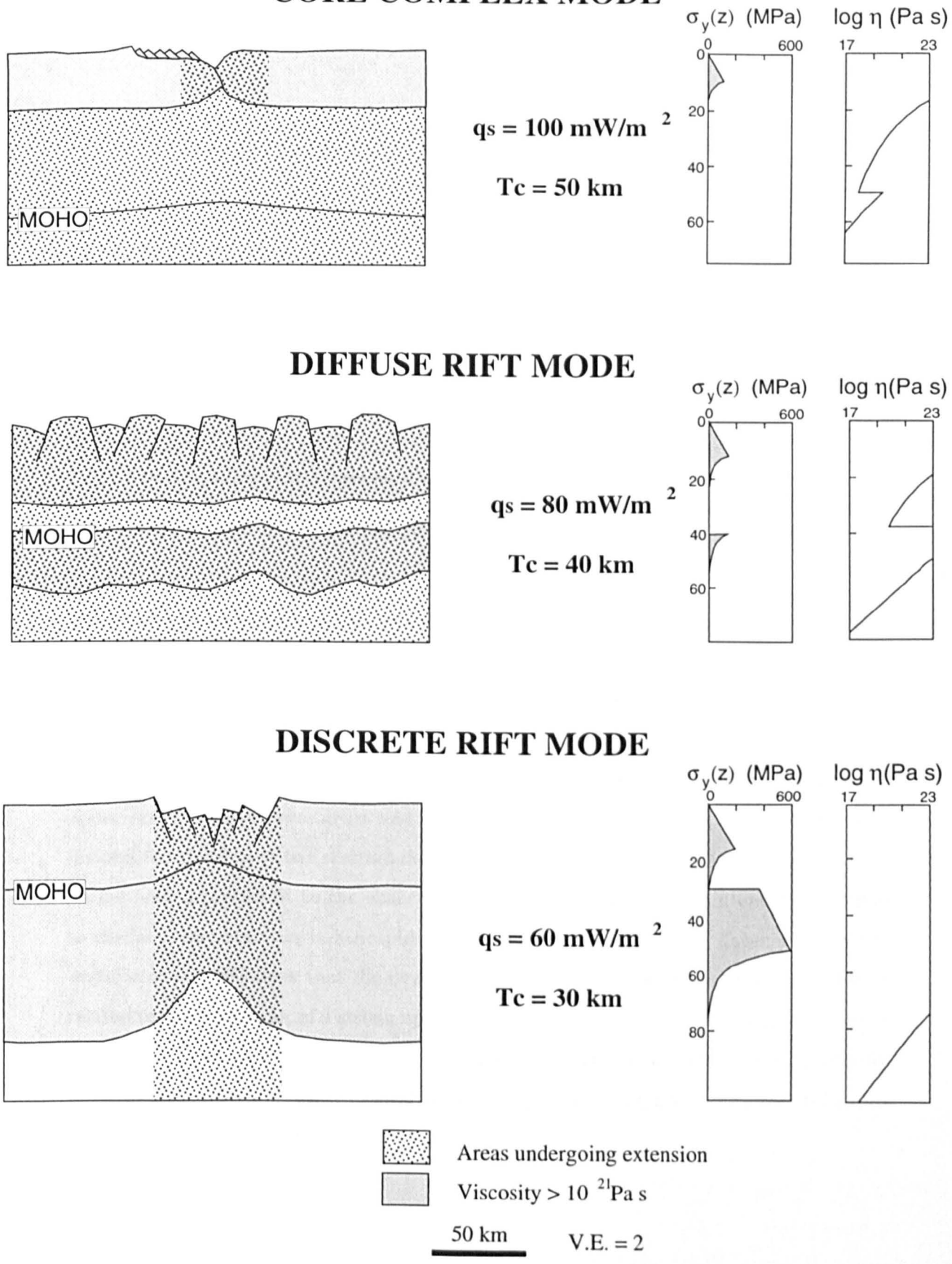

Figure 2.15: The lithosphere in the three modes of extensional deformation and the initial extensional yield stress profiles (for $\dot{e} = 8 \times 10^{-15}$ s^{-1}). Lithosphere here is taken correspond to depths where effective viscosity is greater that 10^{21} Pa s. (a) The core complex mode. Crustal thickness is 50 km. Lower crust has a viscosity lower than 10^{21} Pa s. (b) The wide rift mode. Crustal thickness is 40 km. (c) The narrow rift mode. Crustal thickness is 30 km. After *Buck* [1991].

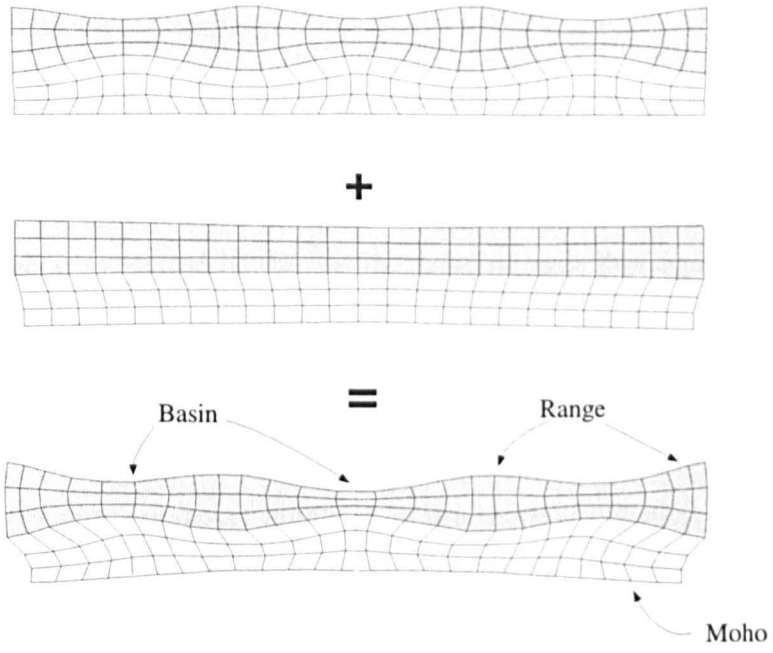

Figure 2.16: Displacement fields associated with the long, short and combined wavelengths of necking instability, from *Zuber, Parmentier and Fletcher* [1986]. The basins are spaced at roughly 3 times the upper crustal thickness. The long wavelength instability is due to the presence of a strong upper mantle layer.

the dominant wavelength in the region above the perturbation. The modern Basin and Range consists of rifts that are regularly spaced at an average of ~35 km [*Fletcher and Hallet*, 1983]. *Zuber and Parmentier* [1986] therefore suggest that this could indicate the presence of a very broad initial strength perturbation.

The three-layer model of *Zuber, Parmentier and Fletcher* [1986] comprises a strong upper crust, a weak lower crust and a strong upper mantle. Upon extension, necking instabilities develop at two distinct dominant wavelengths (Figure 2.16). Although they do not seek a precise fit to the observed wavelengths across the Basin and Range (due to the large uncertainties in lithospheric rheology, see Section 2.2.4), *Zuber, Parmentier and Fletcher* [1986] show that the development of the longer wavelength of instability is related to a the presence of a strong upper mantle, separated from the strong upper crust by a weak lower crust (Figure 2.16). Dominant wavelengths are determined primarily by layer thickness, and upper crustal necks are spaced at roughly three times thickness of the strong upper crust.

2.10.2 Conductive Cooling

The ductile yield stress, and so the mechanical strength of the lithosphere, is strongly dependent on geothermal gradient (Section 2.2.3.1). Three processes control lithospheric temperature: thermal conduction (or diffusion), thermal advection, and radioactive heat generation. This is expressed in the one dimensional heat flow equation [*Turcotte and Schubert*, 1982],

$$\frac{\partial T(z,t)}{\partial t} = \kappa \frac{\partial^2 T(z,t)}{\partial z^2} - u(z)\frac{\partial T(z,t)}{\partial z} + H(z) \tag{2.36}$$

where $T(z,t)$ is the temperature profile, κ is the thermal diffusivity, $u(z)$ is the vertical velocity of material that upwells due to thinning, and $H(z)$ represents the crustal radiogenic heat production.

It is seen from Equation 2.36 that thermal conduction and advection work in opposition. If the rate of thermal conduction is large, the temperature profile will change little from its initial state. The thinned area would become stronger as mantle rheologies replace weaker crustal rheologies (see Figure 2.2). Conversely, if the rate of conduction is low, then the geothermal gradient will increase and thermal weakening will dominate the evolution of lithospheric strength.

England [1983] shows that the extensional strain rate ($\dot{e}$) determines which is the dominant process. This is also observed by *Kusznir and Park* [1987] and *Bassi* [1991] who go on to show that for a strengthening rift, the locus of extension will shift to adjacent and weaker portions of the lithosphere, and the rifted area will widen through time. *Bassi* [1995] shows that this delocalisation of strain is more prone to happen where the lithosphere is warmer and weaker. *Buck* [1991] is more precise in quantifying the change in integrated yield stress that includes the effect of strain rate discussed in Section 2.2.3.4. For an initial crustal thickness of 40 km, B increases on extension for strain rates slower than $\sim 3\times10^{-16}$ s^{-1} (Figure 2.17).

2.10.3 Gravitational Potential Energy

Buck [1991] and *Hopper and Buck* [1996] model the evolution of gravitational potential energy during extension and conclude that horizontal differences in GPE are the dominant control on the style of continental rifting. Their model also accounts for the development of the core complex mode of extension that previous models could not.

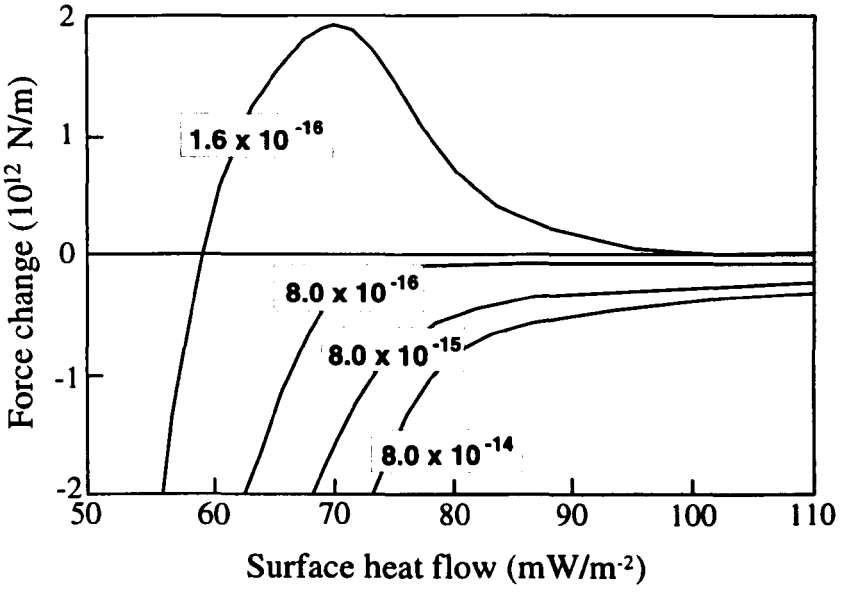

Figure 2.17: The change in integrated yield stress (B) as a function of surface heat flow for a series of extensional strain rates, from *Buck* [1991]. Initial crustal thickness is 40 km. Dislocation creep is assumed to operate. The plot applies to the first 25% of extension.

Nonetheless, the principle is the same as that of *Kusznir and Park* [1987] and *Bassi* [1991]: the style of rifting is determined by whether an extending region is becoming stronger or weaker with time.

The changes in the magnitude of B and $\Delta\Gamma$ are calculated for an assumed initial crustal thickness, initial surface heat flow and constant strain rate (Figures 2.14 and 2.18). *Buck* [1991] considers only the force changes for a β value of 1.25, and *Hopper and Buck* [1996] develop the model and examine the evolution of an extending region through time. They demonstrate that a core-complex may evolve to become a diffuse rift, and finally to the discrete rift in the space of several million years.

The idea that lower crustal flow and its influence on GPE controls the style of rifting is supported by the analogue models of *Benes and Davy* [1996]. The lower crust is modelled with silicone putty, and all three modes are reproduced as its viscosity is altered.

2.11 T_e and Style of Rifting

Coherence estimates across the cratonic lithosphere surrounding the East African Rift indicate that T_e is as high as 80 km [*Ebinger et al.*, 1989], and that the lithosphere decreases in rigidity towards the rift. *Ebinger, Karner and Weissel* [1991] and *Upcott et*

Discrete rifts								
	T_e estimates (km)		T_s (km)	q_s (mW/m^2) ‡	Tc (km) ‡	$\dot{e}$ (s^{-1})	t_r (Ma)	β
	Coherence ‡	Forward models						
Baikal	70 - 90	30 - 50	30	35 - 50	40 - 45		30 - 35	
East Africa	70 - 80	25	35	40 - 60	35 - 40		15 - 40	
Rhine	-	-	20	70 - 80	30 - 40		45	
Rio-Grande	-	15 - 30	20	60 - 80	30 - 40		20 - 30	
Diffuse and Core Complex rifts								
	Coherence	Forward models	T_s (km)	q_s (mW/m^2)	Tc (km) ‡	$\dot{e}$ (s^{-1})	t_r (Ma)	β
Aegean	†	†	10 - 15	50 - 100	40 - 50	2×10^{-15}	10	< 2.0
Basin & Range	5 - 15	2 - 4	10 - 15	90 - 110	40 - 50	3×10^{-16}	40	< 2.0
Tibet	-	2 - 4	10 - 12	90 - 150	60 - 70	10^{-16} - 10^{-15}	15	< 1.1

Table 2.2: Rheological and extensional parameters for different extensional provinces. q_s = surface heat flow. Tc = crustal thickness. $\dot{e}$ = strain rate. T_s = seismogenic thickness. t_r = time since onset of extension. '-' indicates that estimates were not be found in the literature reviewed for this thesis. † indicates values that are estimated in this thesis. ‡ indicates estimates made away from areas of extension, and are taken to be representative of pre-extensional values.

Values taken from *van der Beek* [1997], *Petit, Burov and Déverchère* [1997], *Kogan et al.* [1994], *Ruppel, Kogan and McNutt* [1993], *Logatchev and Zorin* [1987], *Lysak* [1987], *Keller et al.* [1995], *Ebinger et al.* [1989], *Upcott et al.* [1996], *Nyblade et al.* [1990], *Jestin, Huchon and Gaulier* [1994], *Braile et al.* [1995], *Prodehl, Meuller and Haak* [1995], *Bechtel et al.* [1990], *Lowry and Smith* [1994], *Stark and Stewart* [1997], *King and Ellis* [1990], *Sonder et al.* [1987], *Zoback, Anderson and Thompson* [1981], *Blackwell and Steele* [1992], *DeMets et al.* [1990], *Morgan and Meissner* [1989], *Jones et al.* [1992], *Parsons* [1995], *Masek, Isacks and Fielding* [1994], *Molnar, England and Martinod* [1993] and *Francheteau et al.* [1984]. See Chapter 3 for Aegean references.

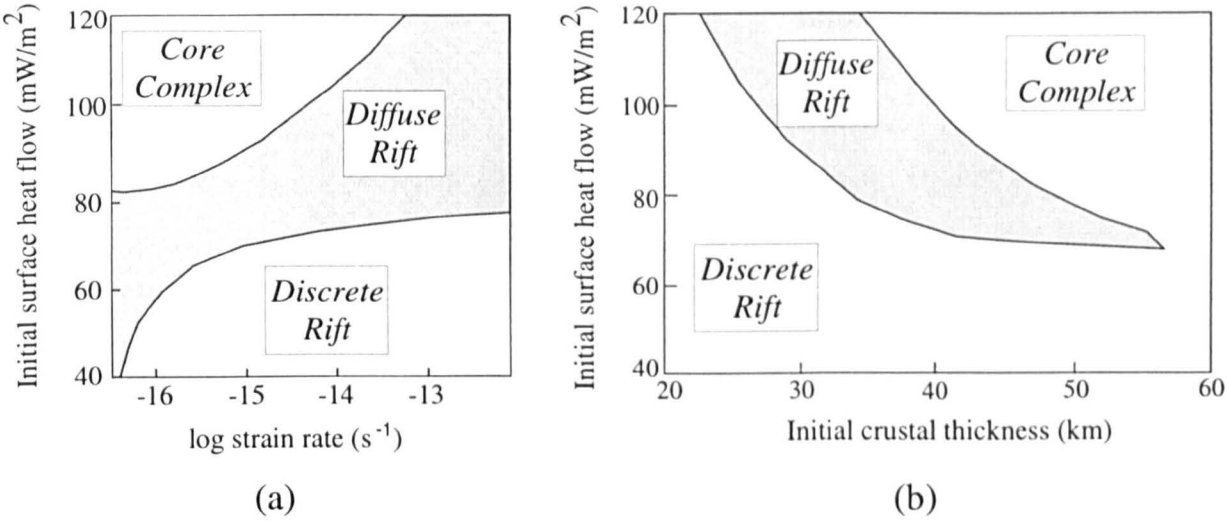

Figure 2.18: (a) Extensional mode boundaries in strain rate-initial heat flow space for an initial crustal thickness of 40 km. (b) Mode boundaries in initial crustal thickness-initial heat flow space for a strain rate of 8×10^{-15} s^{-1}. Shaded areas correspond to the field of surface strain localisation. From *Buck* [1991].

al. [1996] use the pure shear/simple shear (detachment) model of *Weissel and Karner* [1989] to reproduce the observed rift flexure, and deduce that T_e falls to ~25 km at the rift (Table 2.2). Similarly, T_e estimates across the Siberian craton suggest that the T_e prior to the formation of the Baikal rift may have been as large as 70 to 90 km [*Kogan et al.*, 1994]. Forward modelling results across individual rift structures using both pure shear and detachment models give T_e values of between 30 and 50 km [*van der Beek*, 1997; *Petit, Burov and Déverchère*, 1997].

A similar pattern is seen for the diffuse Basin and Range province. Spatial T_e variability mapped from coherence shows a good correlation to that in heat flow [*Lowry and Smith*, 1994], and values fall to below 10 km where surface heat flow is in excess of 100 mW/m^2. *King and Ellis* [1990] model a number of fault-controlled structures in the Basin and Range, and suggest that T_e is approximately 2 to 4 km across seismogenically active structures.

It is obvious from Table 2.2 that clear differences exist between the T_e estimates for discrete and diffuse rifts. It will be shown in Chapter 6 that the spatial resolution of T_e estimates obtained from the coherence between Fourier transforms of Bouguer gravity and topography depends on T_e, and is at best ~200 km for the Aegean. More local estimations are possible with the modelling of individual rift structures. Thus, if a decrease in T_e is observed across a rift, then one could infer that rheology is locally

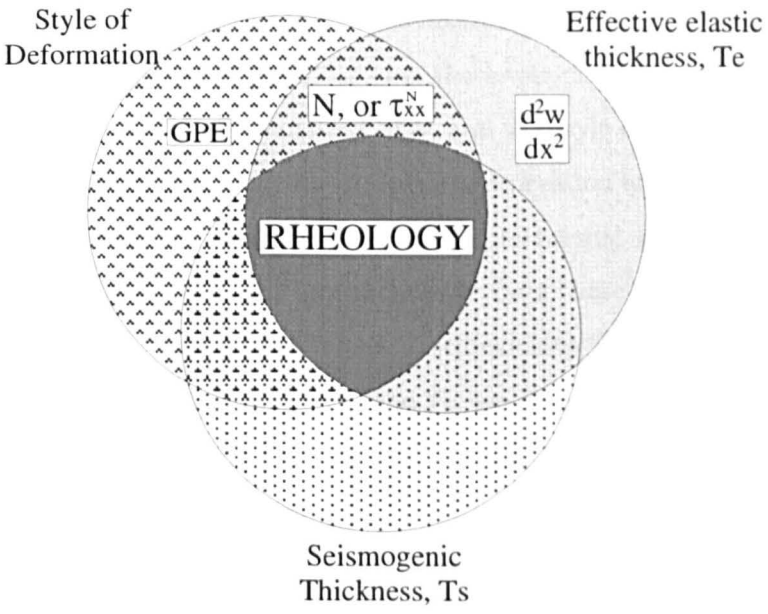

Figure 2.19: Diagram showing the factors that control the style of rifting, the effective elastic thickness (T_e) and the seismogenic thickness (T_s). Each depends on lithospheric rheology, commonly expressed as yield stress ($\sigma_y(z)$), which in turn depends on temperature (T), crustal thickness (T_c), composition and strain rate ($\dot{\epsilon}$). Note that the extent to which gravitational potential energy (GPE) controls rifting style is a function of (lower crustal) rheology. N_x is the horizontal in-plane force, τ_{xx}^N is the in-plane stress, and $\frac{d^2w}{dx^2}$ is plate curvature.

weakened due either to

- thermal weakening (Section 2.2.3.1), or
- curvature increase across the rift flanks (Section 2.4.2)

2.12 Summary

It has been shown that lithospheric rheology may be approximated by profiles of yield stress, and that these are robust enough to be applied to problems in tectonics and flexure. The effective elastic thickness, T_e, has been shown to provide a good indication of lithospheric rheology. Figure 2.7 showed that T_e depends strongly on the rheology of the lower crust. The style of rifting (i.e., the localisation of strain) also depends on the rheology of the lithosphere, and particularly that of the lower crust (Figure 2.19). We therefore expect the style of rifting to show a correlation with T_e.

It is clear from Table 2.2 that T_e estimates for various extensional provinces are consistent with the idea that rheology controls the style of rifting. Where T_e is high, the yield stress in the lower crust is finite and able to support bending stress. The strength

evolution is therefore dominated by thermal weakening, and the rifting style is discrete. Where the rheology is weak and the T_e is low, the lower crust may be weak enough to flow in response to horizontal gradients in GPE, and the style of rifting becomes diffuse.

The seismogenic thickness, T_s, is an alternative expression of rheology, and has been shown by *Molnar and Chen* [1983] to depend on geothermal gradient. As the strain rates associated with earthquakes are much greater than those associated with isostatic compensation, it might be expected that the contribution to T_e *from the crust* is less than T_s. Where observed T_e is similar to or less than T_s, some authors state that upper crustal flexure might be assumed to operate (e.g., *McKenzie and Fairhead* [1997]). However, this argument is simplistic, and returned to again in Chapter 7.

Chapter 3

Aegean Tectonics

3.1 Introduction

This chapter reviews the main tectonic observations in the Aegean extensional province, and discusses them in the context of rheology which, as seen in the previous chapter, controls the style of lithospheric extension. Surface heat flow data are presented, which may provide information on the thermal structure of the lithosphere. The structure and sedimentology of the main rift basins of central Greece are introduced, which will be used to constrain the modelling carried out in Chapter 5.

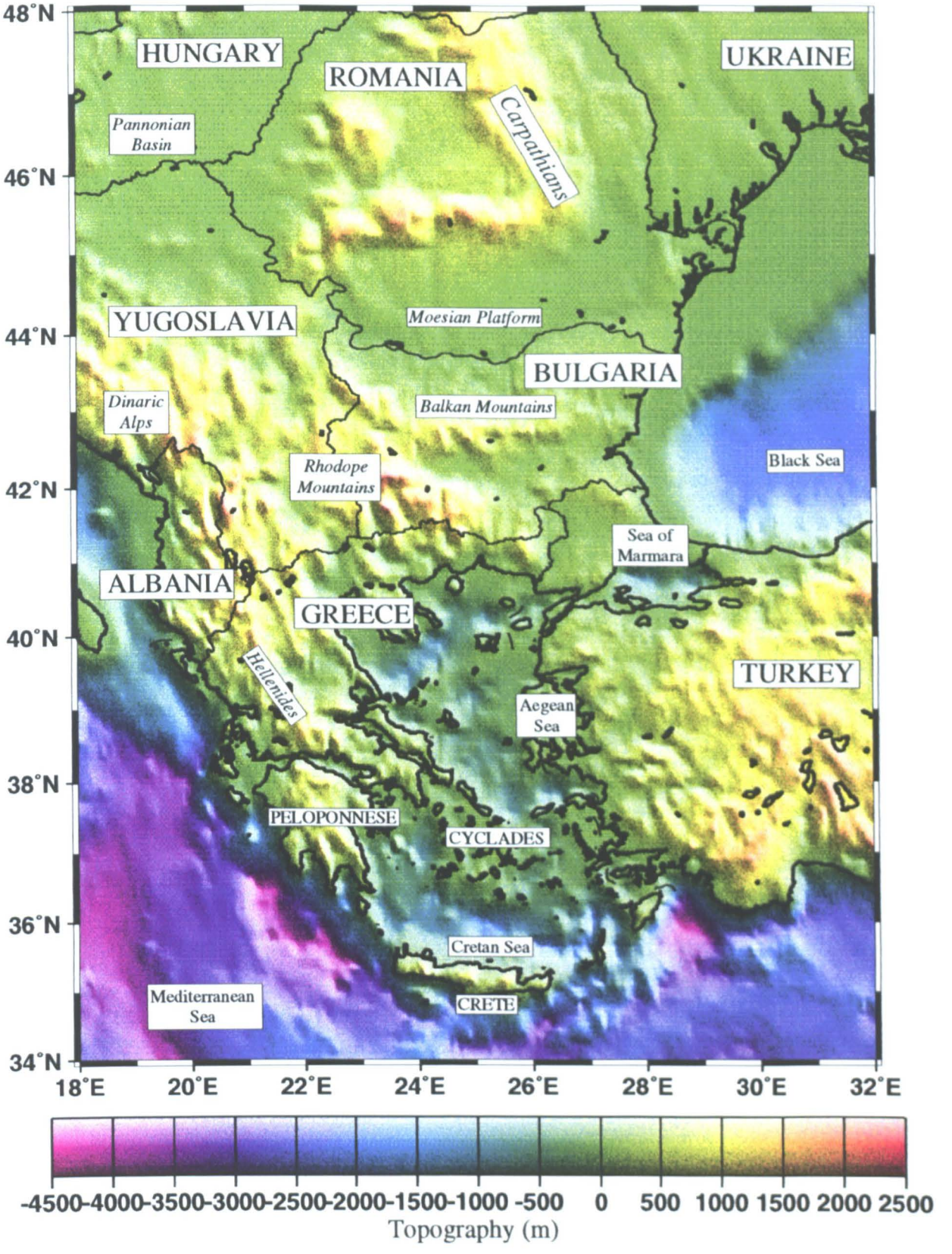

Figure 3.1: ETOPO5 digital elevation model, showing major geographical features.

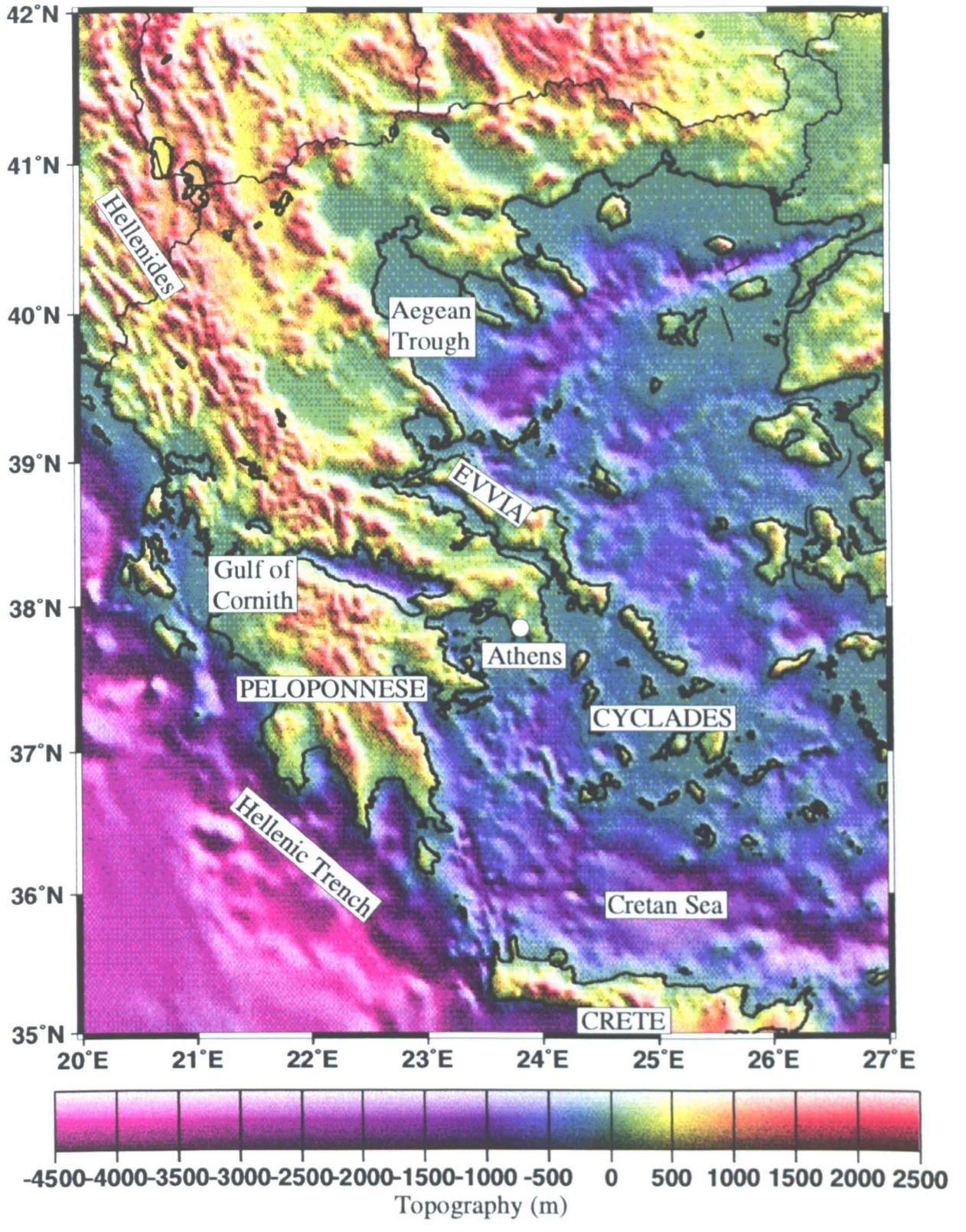

Figure 3.2: 2 km digital elevation model, showing major geographical features.

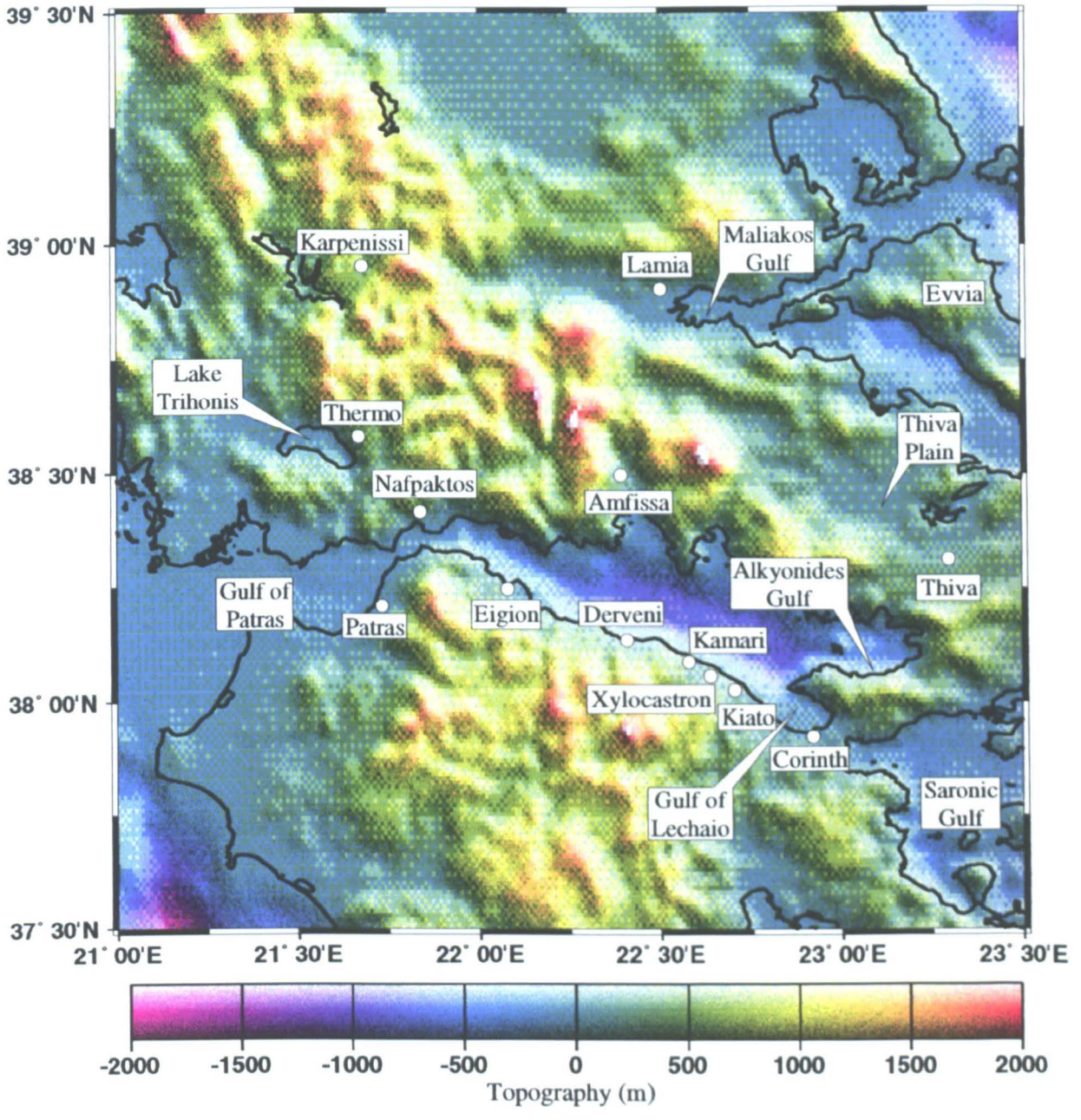

Figure 3.3: 2 km digital elevation model, showing place names referred to text.

3.2 Boundary Conditions for Present-day Tectonics

The Aegean region is one of the most rapidly deforming parts of the Alpine-Himalaya belt. Although the African and Eurasian plates are currently converging at a rate of 10 mm/yr [*Jackson*, 1994], the present-day surface deformation of the Aegean is dominated by extensional and strike-slip faulting. There is general agreement that the Hellenic Trench marks the site of subduction of the African oceanic lithosphere beneath the continental Aegean province (Figure 3.4), although a few authors believe that it lies south of the Mediterranean Ridge [*Lallemant et al.*, 1994; *Mascle and Chaumillon*, 1997; *Truffert et al.*, 1993] (see Figure 3.5).

The Benioff zone extends to a depth of ~150 km (e.g., *Comninakis and Papazachos* [1980]). Beneath the Peloponnese (Figure 3.2), the zone of earthquakes dips gently (15°) for 200 km, before steepening to 30° at the Gulf of Corinth. Beneath the Dodecanese in the eastern Aegean Sea, *Hatzfeld and Martin* [1992] recognise that the slab dips more steeply than beneath the Peloponnese. This is shown by the contours of the depth to the Benioff zone on Figure 3.4. However, *Hatzfeld and Martin* [1992] do not comment on the apparent change in tectonic style of the trench east of Crete (Figure 3.4). It seems the angle of dip is relatively constant along the azimuth of relative motion between Africa and the Southern Aegean (see Section 3.9).

Spakman, Wortel and Vlaar [1988] present tomographic images of the crust and mantle beneath the Aegean. Zones of anomalously high mantle velocity (Figure 3.5) are interpreted as subducted oceanic lithosphere, suggesting that the slab penetrates to a depth of at least 600 km. As with the Benioff zone, the slab appears to be kinked beneath the northern Peloponnese, although the steeper dip is closer to 45° (Figure 3.5). The tomographic study of *Papazachos and Nolet* [1997] reveals a similar structure. *Yoshioka and Wortel* [1995] model this geometry as a tear in the subducted slab which is propagating from the north-west along the strike of the slab. Appendix B presents a possible alternative to this idea.

At about 39°N on the western coast of Greece, the dextral Kephalonia transform fault (Figure 3.4) links oceanic subduction with active continental collision [*Anderson and Jackson*, 1987; *Hatzfeld et al.*, 1995; *Kahle et al.*, 1993]. Some authors argue that subduction in the southern-most Hellenic Trench has evolved to the stage where the southern Aegean has begun to collide with the northern margin of continental Africa [*Armijo, Lyon-Caen and Papanastassiou*, 1992; *Hatzfeld et al.*, 1997; *Le Pichon et al.*,

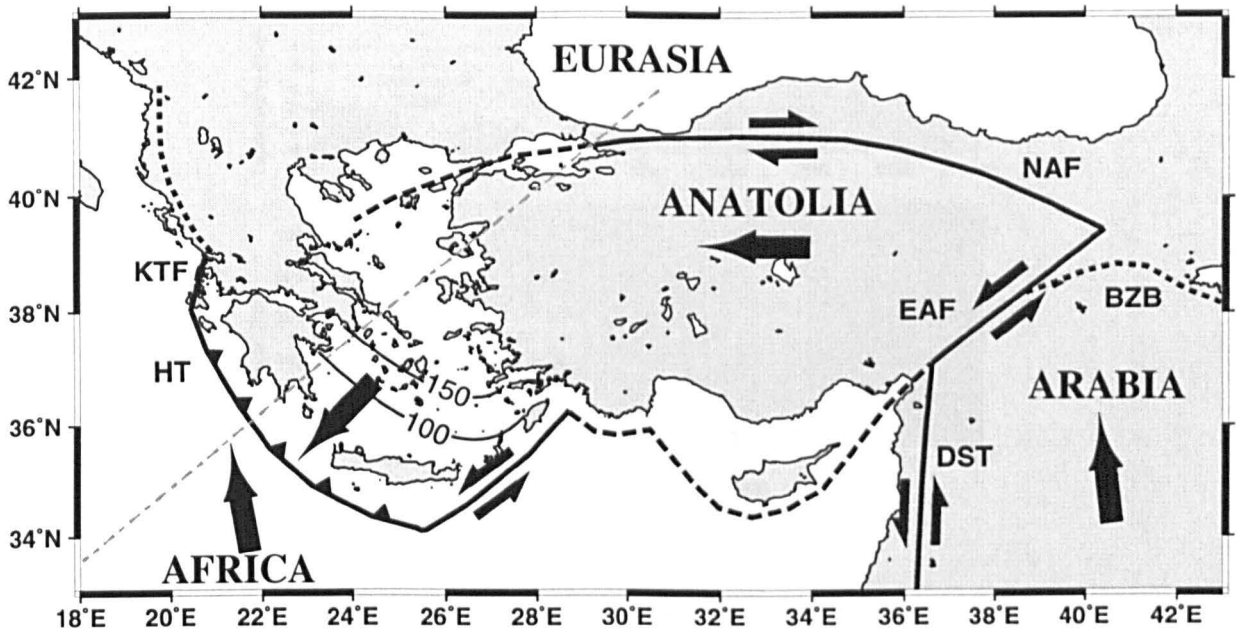

Figure 3.4: Major active tectonic elements that dominate Aegean kinematics. The 100 km and 150 km contours represent depths to the top of the Benioff zone, from *Hatzfeld and Martin* [1992]. HT: Hellenic Trench. NAF: North Anatolian Fault. EAF: East Anatolian Fault. DST: Dead Sea Transform. BZB: Bitlis-Zagros Belt. KTF: Kephalonia transform fault. The large arrows represent the direction of motion with respect to Eurasia. Dotted lines represent major continental thrusts. Feint dashed line refers to the tomography section of Figure 3.5.

1995; *Lyon-Caen et al.*, 1988].

An E-W trending zone of thrusting - the Bitlis-Zagros Belt - marks the zone of collision between Arabia and Eurasia (Figure 3.4). To the west of this, shortening is accommodated by right-lateral shear across the North Anatolian Fault (NAF) and left-lateral shear along the conjugate East Anatolian Fault (EAF) (Figure 3.4). These structures accommodate a counter-clockwise rotation af Anatolia.

3.3 Surface Heat Flow

Chapter 2 showed that the rheology of lithosphere is strongly dependent on its thermal structure. Surface heat flow provides information on this, although near-surface processes, such as groundwater circulation, may complicate the picture. Figure 3.6 shows a map of measured surface heat flow across the Aegean [*Pollack, Hurter and Johnson*, 1993], averaged in 1° by 1° bins. Although the distribution of data is poor, it is seen that the heat flow across the central and southern Aegean is in excess of 100 mW/m^2, comparable to that measured across the Basin and Range province and the Tibetan Plateau (Table 2.2). This probably accounts for the low P-wave velocity observed beneath the

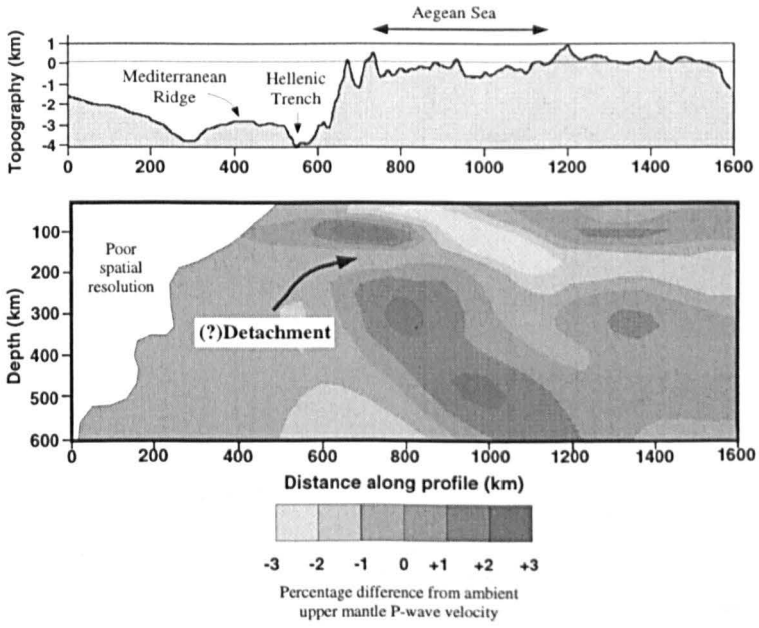

Figure 3.5: Vertical cross section of the tomographic image of the upper mantle, from *Spakman, Wortel and Vlaar* [1988]. The subducted slab is visible to a depth of at least 600 km, and appears to be detached at the change in dip. For location, see dashed line on Figure 3.4 and the topographic section.

Aegean Sea in Figure 3.5. Although there are few data points to the immediate north of the Aegean, there is a suggestion that heat flow values across the Rhodope Mountains is also high. Across mainland Greece, heat flow increases from ~40 mW/m^2 on the western coast to ~70-80 mW/m^2 on the eastern coast.

3.4 Pre-extensional Tectonic History

The tectonics of the Late Mesozoic to Mid Tertiary (i.e., prior to the onset of extension) was dominated by a series of Alpine collisional events (e.g., *Alberello et al.* [1997], *Robertson and Dixon* [1984]). This is responsible for the structural grain which is evident in the onshore pre-Neogene geology (Figures 3.7 and 3.9). The NW-SE trending zones of similar sedimentary and metamorphic facies were first defined by *Aubouin* [1965] who used the term *isopic zones.* Similarly trending deposits of well-bedded flysch represent the foreland basins that formed west of westward-verging, thin-skinned thrust sheets. Some authors argue that a NW-SE geological fabric influences the present-day fault geometries (e.g., *Lyon-Caen et al.* [1988], *Taymaz, Jackson and McKenzie* [1991], *Jackson, Haines and Holt* [1992]).

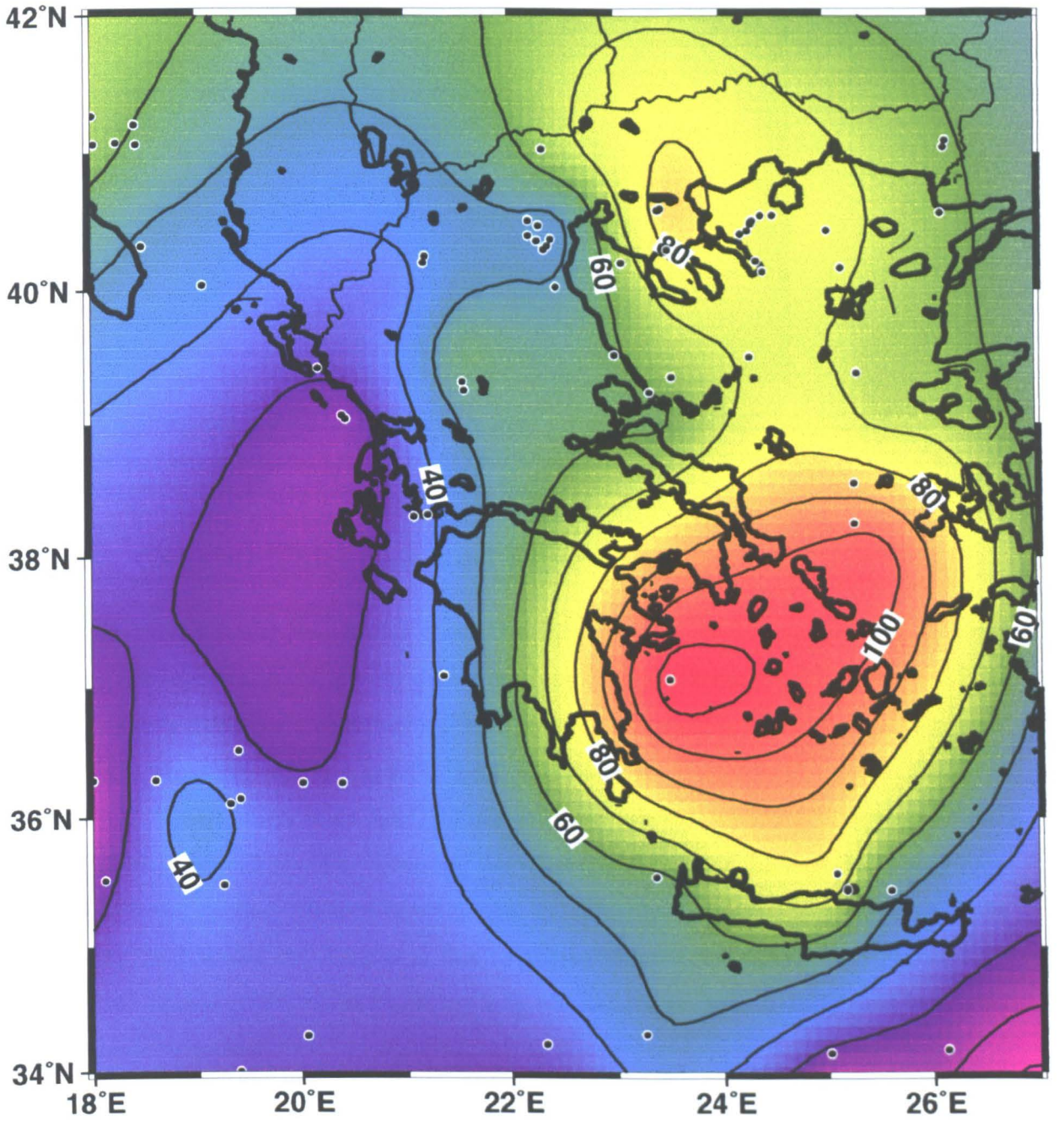

Figure 3.6: Surface heat flow across the study area. Location of measurements are shown by the black on white dots. Data are averaged within 1° by 1° bins prior to gridding. Contour interval = 10 mW/m^2. Data from *Pollack, Hurter and Johnson* [1993].

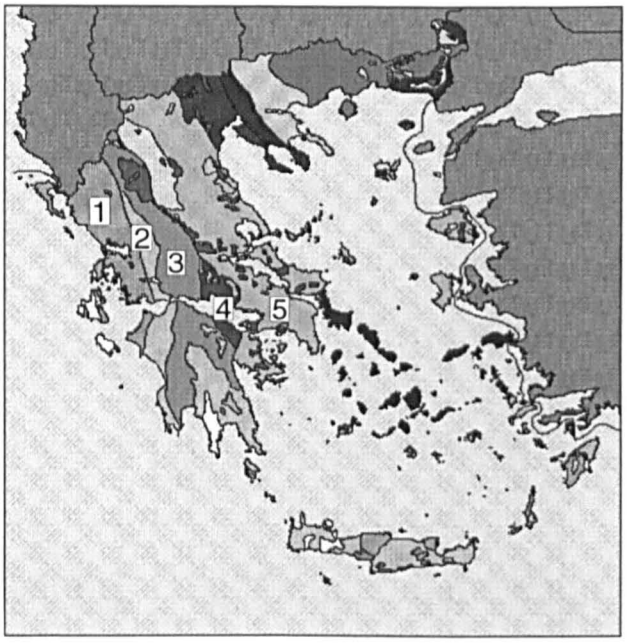

Figure 3.7: The trend of the isopic zones of Greece, first defined by *Aubouin* [1965] as zones of similar sedimentary and metamorphic facies. Zones mentioned in the text are labelled 1 to 5. 1: Ionian Zone. 2: Gavrovo Zone. 3: Pindos Zone. 4: Parnassos Zone. 5: Pelagonian Zone.

3.5 Crustal Thickness and Stretching Factors

The first estimates of present-day crustal thickness were derived by simultaneously modelling the seismic and the gravity data along long (100 to 500 km) seismic refraction lines (see *Makris* [1984] for a summary). These results were then extrapolated across the entire Aegean using only the gravity data, and must be treated with caution for three reasons. Firstly, there were only five non-reversed seismic refraction lines to constrain the gravity forward models. Secondly, the reference datum for the onshore gravity data was different to that offshore (see Chapter 4). Thirdly, a significant proportion of the gravity field across the Aegean is due to the subducted lithosphere (see Figure 5.2), whereas *Makris* [1984] assigned all the long wavelength Bouguer gravity field to crustal thickness variations.

Figure 3.8 is taken from *Papazachos et al.* [1995] who describe it as a preliminary map that is based on the results of numerous studies, including that of *Makris* [1984]. The moho beneath the Aegean coastline is at ~32 km and deepens to over 40 km beneath the Hellenide mountains. Beneath the Sea of Crete, the moho has been mapped to shallow to 25 km. In their tomographic study, *Papazachos and Nolet* [1997] show that the crust thickens to over 45 km beneath the Hellenides, and is thinnest beneath the Aegean Trough (~25 km) and the Sea of Crete (~30 km).

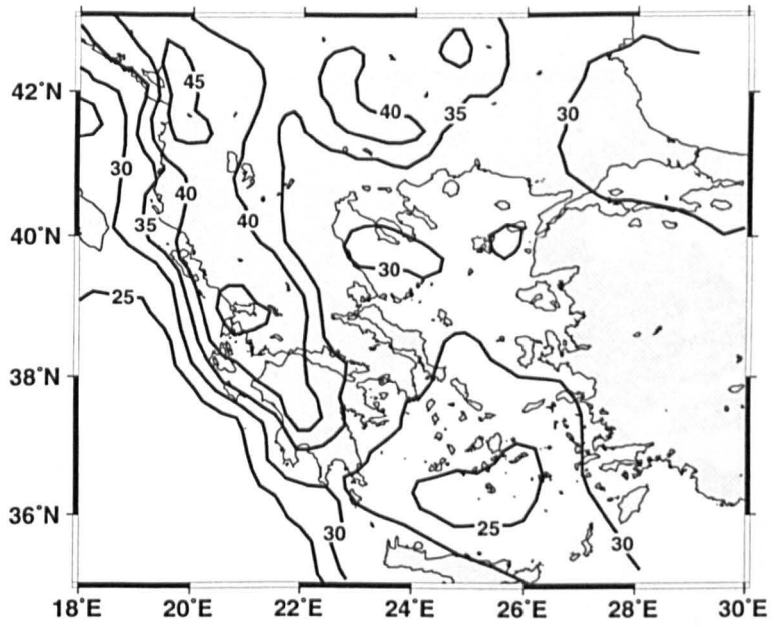

Figure 3.8: The moho depth map of *Papazachos et al.* [1995]. Contours are in km.

If one assumes Airy isostasy and homogeneous pure-shear deformation (e.g., *McKenzie* [1978a]), then present-day crustal thickness is a function of the *pre-extensional crustal thickness* and the *stretching factor* (β). Both are expected to vary spatially. It is for this reason that estimates of β based solely on present-day crustal thickness variations must be treated with caution. This problem becomes more serious if magmatic underplating and lower crustal flow are important processes.

Kinematic estimations of stretching may therefore be more reliable, and assume that the concave shape of the Hellenic Trench evolved from a linear one because of extension over the African plate. This idea is supported by rotations observed across the Aegean in palaeomagnetic data [*Kissel et al.*, 1993; *Kissel and Laj*, 1988]. The reconstruction of *Le Pichon and Angelier* [1979] implies an average β for the Aegean of 1.3. This locally increases to 1.5 over the southern Aegean and reaches a maximum of 2.0 across the Sea of Crete. A similar pattern of increasing β towards the trench was observed by *de Bremaecker, Huchon and Le Pichon* [1982], whose model suggests 1.7 for the Sea of Crete. From Figure 3.8, the pre-extensional crustal thickness may have been as great as 50 km across the southern and central Aegean.

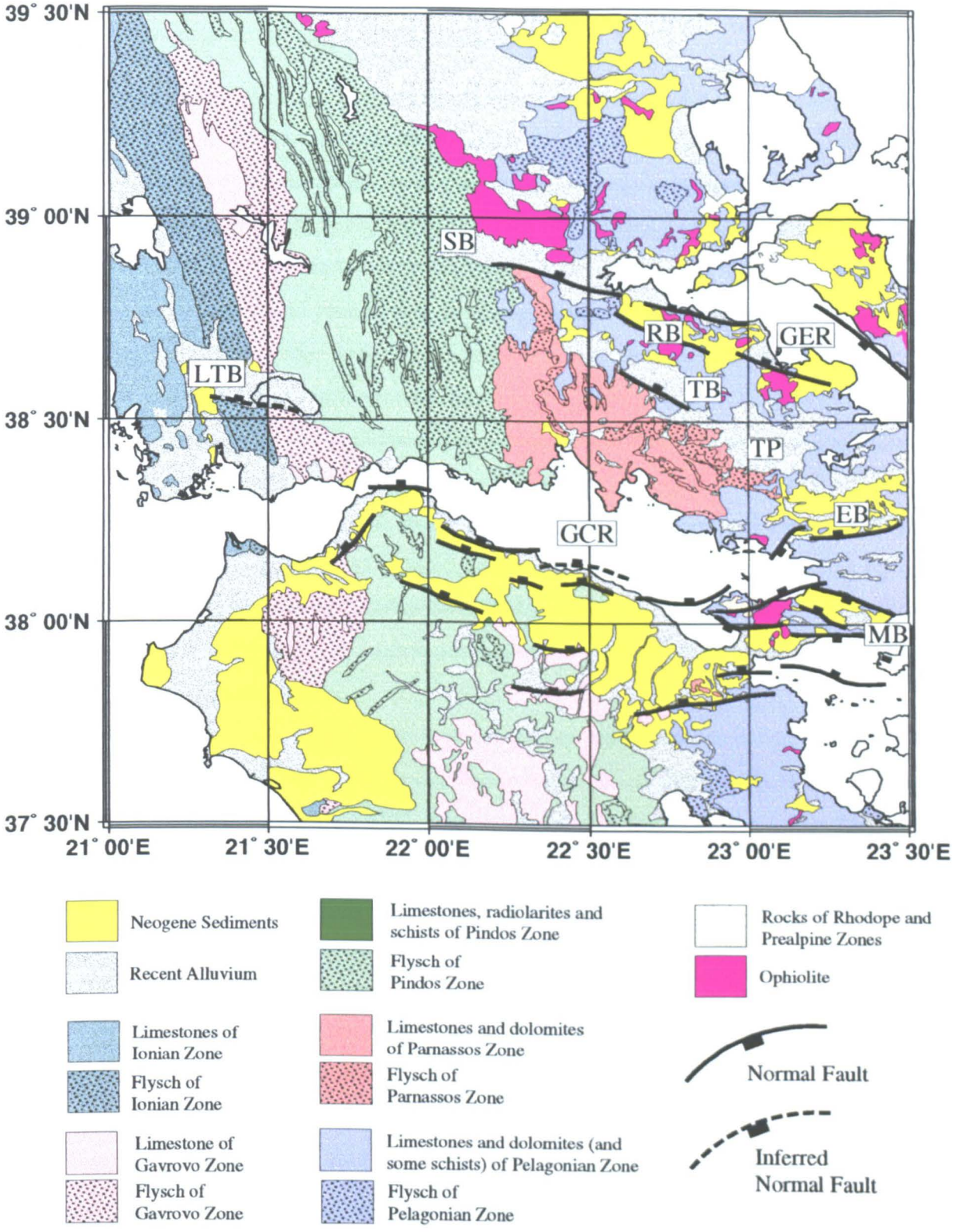

Figure 3.9: Geology map of central Greece. GCR: Gulf of Corinth Rift. LTB: Lake Trihonis Basin. GER: Gulf of Evvia Rift. SB: Sperchios Basin. RB: Renginion Basin. TB: Tithoria Basin. TP: Thiva Plain. EB: Erithres Basin. MB: Megara Basin.

3.6 Tectonics of the Aegean

3.6.1 Evolution of Aegean Extension

There is a considerable range of estimates for the time of onset of Aegean extension, and the most extreme come from analyses of ductile deformation fabrics. *Gautier and Brun* [1994] examine ductile lineations in the metamorphic core complexes of the Cyclades and Evvia and deduce that deformation occurred in response to a N-S oriented regional extensional stress. Radiometric and stratigraphic data constrain the minimum age of this extension to be between 19 and 22 Ma. Similarly, *Jolivet et al.* [1994] examined Miocene stretching lineations in the Aegean and proposed that the azimuth of the minimum compressional stress (σ_3) has been consistent since ~25 Ma.

Most analyses of the brittle deformation across mainland Greece and western Turkey suggest that Aegean extension commenced at some stage between 5 Ma and 16 Ma (e.g., *Angelier et al.* [1982]; *Jackson and McKenzie* [1988]; *Mercier, Sorel and Vargely* [1989]). *Seyitoğlu, Scott and Rundle* [1992] dated granitic rocks which were described to occur along a normal fault in western Turkey as early Miocene (~25 Ma). However, the details put forward are vague, and the fault is not one of the major E-W trending grabens, but a NE-SW trending structure.

It seems then that metamorphic core complexes were accommodating extensional strain at least 5 to 10 Myr prior to the development of the distributed rift structures we see onshore today (Figure 3.12). From the apparent length of the subducted slab seen in tomographic images, subduction at the Hellenic Trench appears to have initiated between 20 and 40 Ma[1] (Appendix B). It is likely therefore that Aegean extension has always occurred within a back-arc setting. As discussed in Chapter 2 (Section 2.10), *Hopper and Buck* [1996] show that a change in boundary conditions is not necessary to account for a changes in the style of rifting through time.

3.6.2 The Westward Motion of Anatolia

The North Anatolian Fault (NAF) is a right-lateral strike-slip fault that is over 1000 km in length, and has propagated from eastern Turkey into the Aegean. From the age of the sedimentary fill in basins associated with the NAF, the eastern part of the NAF

[1]This is considerably greater than the estimates based on the length of the Benioff zone - 5 to 13 Ma - of *Le Pichon and Angelier* [1979], *McKenzie* [1978b] and *Mercier* [1981].

is constrained to have started to propagate towards the west at ~10 Ma. *Barka* [1992] estimates that strike-slip faulting had reached the present-day Aegean Sea by ~5 Ma, and *Dinter and Royden* [1993] propose that the NAF reached the northern Aegean no sooner than ~2 Ma. East of ~31°E, there is little deformation south of the NAF (Figure 3.11). The kinematics of this region appear to be accurately described by a solid-body rotation about a pole located close to the Nile delta [*Oral et al.*, 1995]. It is clear then that the influence of Anatolian motion across the Aegean was felt long after the general extensional setting had been established.

From the observed pattern of focal mechanism and centroid moment tensor solutions (Figure 3.10), *Jackson* [1993] argues that west of 31°E, the NAF splays into a series of sub-parallel dextral strike-slip faults that cross NW Turkey and the northern Aegean with NE to ENE strikes. However, *Dewey and Şengör* [1979] and *Armijo et al.* [1996] argue that such evidence is not conclusive, and believe the strike-slip motion to be localised on just two branches of the NAF. *Barka and Reilinger* [1997] indicate that the NAF splays into three strands across the northern Aegean, and GPS results indicate that 60% of motion occurs on the northern-most strand. *Armijo et al.* [1996] go on to argue that a continuation of a southern branch has directly influenced the evolution of the Gulf of Evvia and the Gulf of Corinth rifts.

3.6.3 Distribution of Active Faulting

The distribution of crustal earthquakes throughout the Aegean reveal a diffuse pattern of deformation, although the southern and central Aegean is seismically less active than surrounding regions. Most studies of the faulting in the Aegean have concentrated on the E-W to ENE-WSW striking faults of Greece and western Turkey that bound half grabens which continue into the Aegean Sea. In Greece the Gulf of Corinth Rift and the Gulf of Evvia Rift (the onshore part of which is called the Sperchios Basin) are the most obvious (Figure 3.12), and have been the subject of numerous structural and sedimentological studies.

Roughly north-south trending normal faults have been mapped along the southern-most Aegean. In the southern Peloponnese, these bound the Gulf of Messinia and the Gulf of Argos. *Lyon-Caen et al.* [1988] describe a series of normal faults running from the southern Peloponnese to Crete. They explain that the E-W extension is partly accommodated on reactivated NW-SE trending structures, but mostly on newly-formed

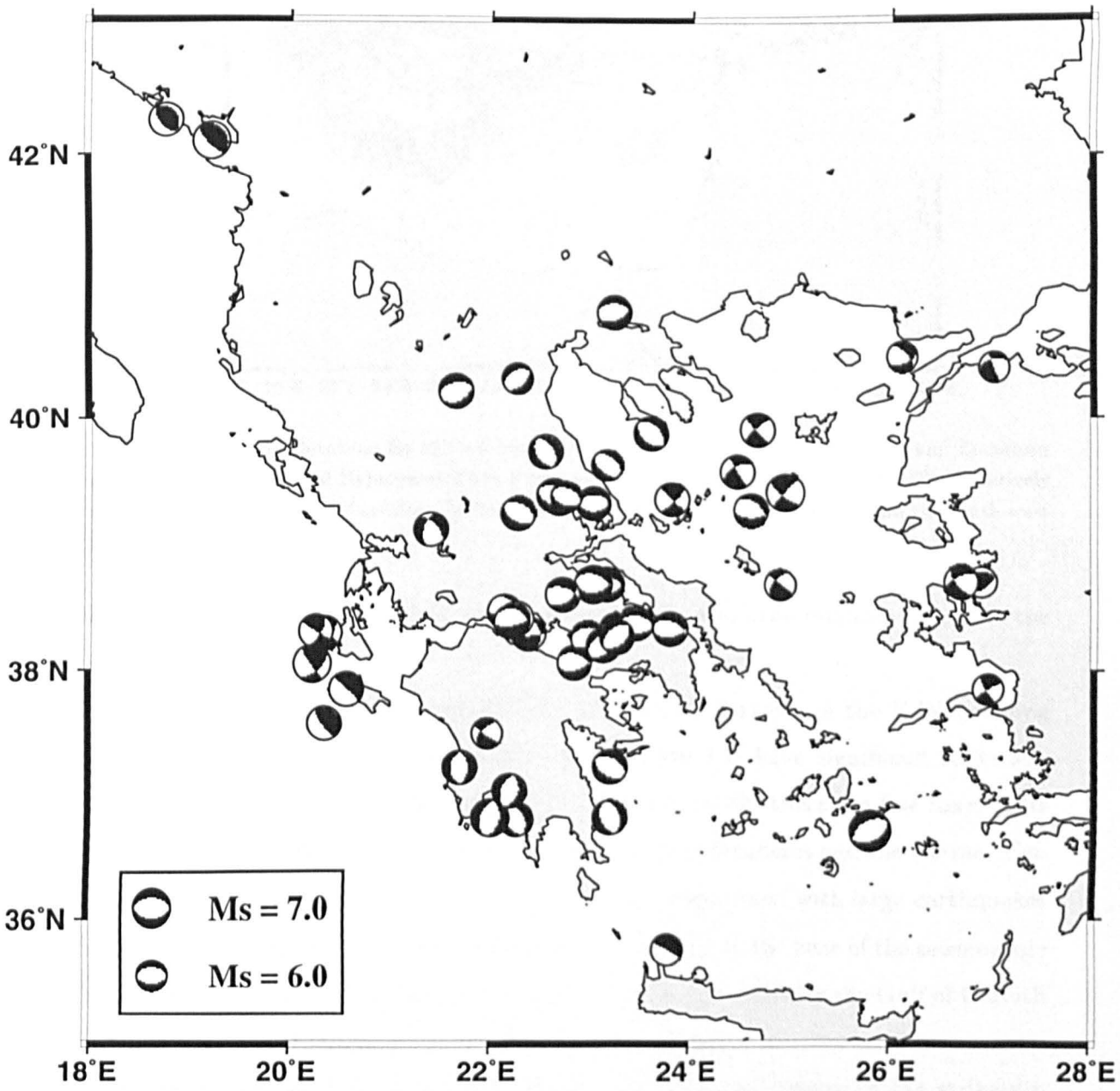

Figure 3.10: Focal mechanism and CMT solutions for earthquakes with $M_s \geq 6.0$. Events date from 1893 to 1995. Data from *Curtis, England and Davies* [1997], *Baker et al.* [1997] and the Harvard CMT catalogues.

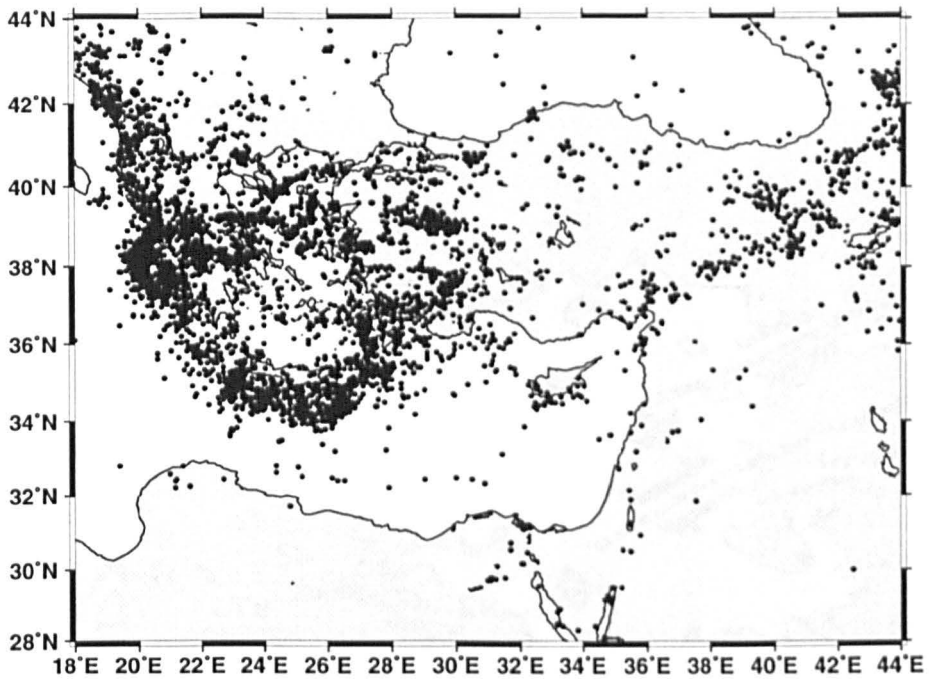

Figure 3.11: Epicentral locations for $M_s > 4.0$ earthquakes, with depths shallower than 50 km. Locations are from the USGS Global Hypocenter Data Base, and events date from 1933 to 1992. Two relatively aseismic zones within the diffuse Aegean deformation are observed: central Turkey and the south-west Aegean.

N-S trending structures. Similarly trending faults have also been mapped on and to the east of Crete (Figure 3.12).

The most prominent structural features of western Turkey are the E-W trending grabens. Those close to the Sea of Marmara (Figure 3.1) have significant strike-slip components due to the influence of the NAF. Further south, there are five major rifts (Figure 3.12): the Edremit Gulf, Simav, Alasehir, Büyük Menderes and the Kerme. *Eyidogan and Jackson* [1985] analyse the normal faulting associated with large earthquakes from these rifts, and propose a planar fault geometry down to the base of the seismogenic layer at 8 ± 2 km. This geometry is very similar to that proposed for the Gulf of Corinth Rift (see Section 3.7.1), suggesting similar crustal rheology.

There is a change from extensional faulting on mainland Greece to the strike-slip faulting in the northern Aegean (Figure 3.10). Figure 3.11 shows that the central plateau of Anatolia is a relatively aseismic region which is bound to the north by the NAF. East of the Marmara Sea the position of the NAF is mapped as a narrow band of right-lateral shear. However, there is uncertainty about the manner in which the strike-slip faulting and Anatolian motion is accommodated in the Aegean (Section 3.6.2).

The active normal faulting in northern Greece has been described by *Dinter and*

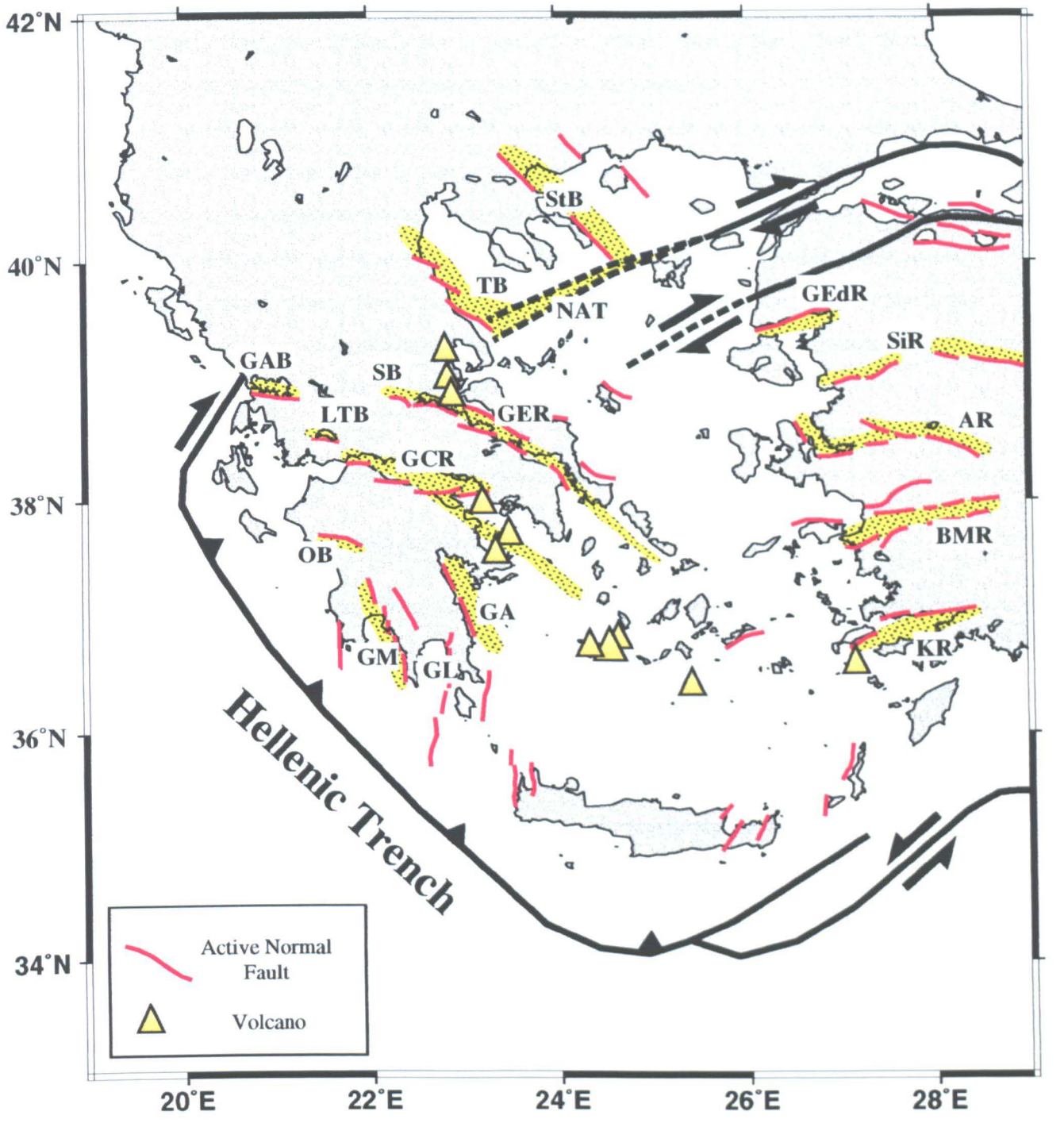

Figure 3.12: Map of active faults in the Aegean region. The major seismogenically active rifts are shaded in yellow. GCR: Gulf of Corinth Rift. GER: Gulf of Evvia Rift. SB: Sperchios Basin. LTB: Lake Trihonis Basin. GAB: Gulf of Amvrakia Basin. OB: Olympia Basin. GL: Gulf of Laconia. GM: Gulf of Messinia. GA: Gulf of Argos. KR: Kerme Rift. BMR: Büyük Menderes Rift. AR: Alasehir Rift. SiR: Simav Rift. GEdR: Gulf of Edremit Rift. NAT: North Aegean Trough. TB: Thermaikos Basin. StB: Strymon Basin.

Royden [1993]. They propose that the Thermakios and Strymon Basins are linked at depth by a low-angle detachment fault, which is rooted at the orthogonally trending North Aegean Trough. The scheme suggested by *Dinter and Royden* [1993] is largely based on analogies to models for Basin and Range deformation.

The precise nature of deformation beneath the central and southern Aegean Sea is not certain, due in part to the apparent lack of seismicity (Figures 3.10 and 3.11). However, the region appears to be significantly extended. The crust is thin (Figure 3.8), and seismic reflection experiments presented by *Mascle and Martin* [1990] show series of 5 to 20 km wide tilt blocks. This fault spacing is similar to that observed on the southern flank of the modern-day Gulf of Corinth Rift. If the central and southern Aegean Sea is accommodating strain today, it is doing so aseismically.

3.7 The Rifts of Central Greece

3.7.1 The Gulf of Corinth Rift

Throughout this thesis, the term *Gulf of Corinth* refers to that body of water which separates the Peloponnese from central Greece. The term *Gulf of Corinth Rift* refers to the rift which began at some stage during the Miocene, and has narrowed or shifted northwards through time. Thus, the Gulf of Corinth roughly equates to the present-day location of the Gulf of Corinth Rift.

The Gulf of Corinth Rift (Figure 3.12) is the best-exposed rift in Greece, and rates of extension increase from 8 mm/yr in the eastern gulf to 12 mm/yr in the west [*Davies et al.*, 1997]. In broad terms, the rift has a half-graben geometry, with normal faults on the southern coast of the gulf. Exposed deltas, marine terraces and notches across the northern Peloponnese indicate uplift, and submerged notched along the more irregular northern coast indicates subsidence.

The structure and the sediments have been described in numerous studies and the main results, which are summarised in this section, provide good constraints on the structural evolution. Furthermore, the area is one of great seismic hazard. Four large earthquakes ($M_s > 6.0$) have occurred since 1980, shown in Figure 3.13. The western Gulf of Corinth appears to display a huge deficit of seismic strain - equivalent to several $M_s > 6.5$ earthquakes - compared to that measured with the GPS [*Clarke et al.*, 1997]. For these reasons, the Gulf of Corinth provides a focus for this study with the aim of

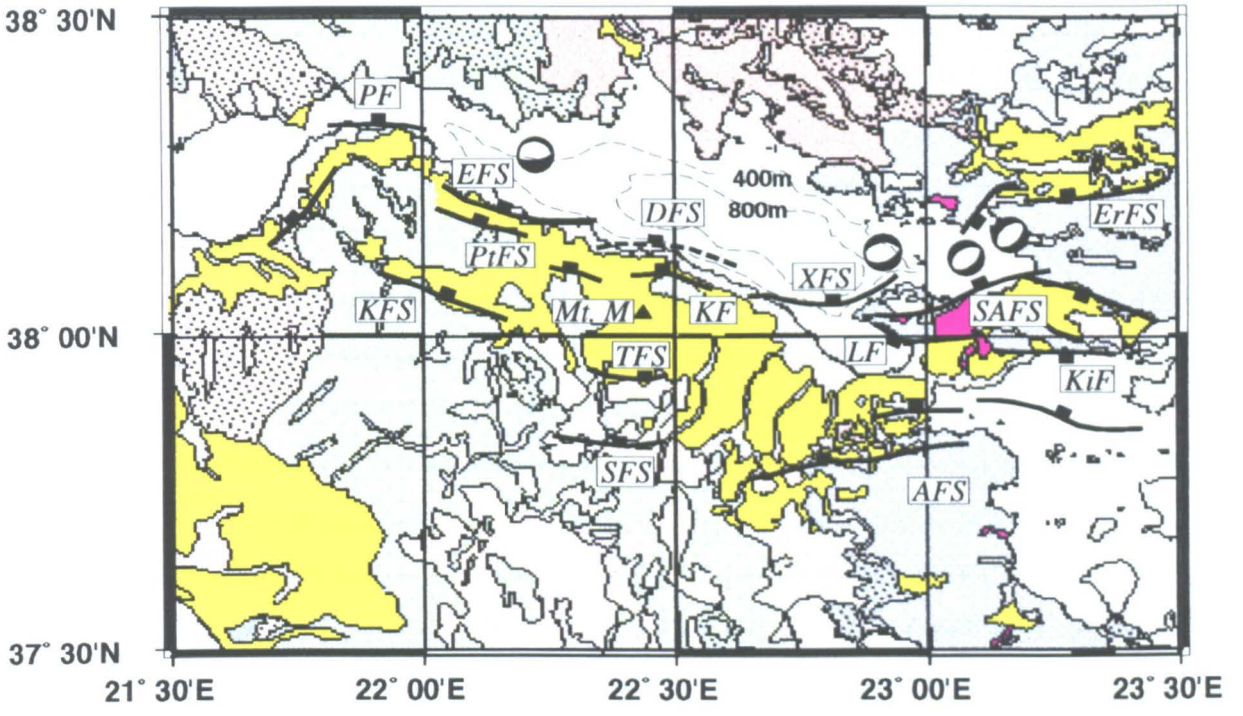

Figure 3.13: The structure of the Gulf of Corinth Rift. *PF*: Psathopyrgos fault. *EFS*: Eigion fault segment. *DFS*: Derveni fault segment. *XFS*: Xylocastron fault segment. *SAFS*: South Alkyonides fault segment. *KFS*: Kalavrita fault segment. *PtFS*: Pteri fault segment. *KF*: Kamari fault. *TFS*: Trikala fault segment. *SFS*: Stymfalia fault segment. *LF*: Loutraki fault. *AFS*: Athikia fault segment. *KiF*: Kineta fault. Mt.M: Mt. Mavron. Modified from *Roberts and Koukouvelas* [1996], on the basis of field observations. See Figure 3.9 for key to geological information.

understanding more about its dynamics and to assess the nature of vertical motions in response to normal faulting.

3.7.1.1 The Structure of the Gulf of Corinth Rift

The most thorough mapping of the onshore faults of the Gulf of Corinth Rift is presented by *Roberts* [1996b] and *Roberts and Koukouvelas* [1996]. The positions and dimensions of fault segments within the Gulf of Corinth Rift were identified by analysing the spatial variability in observed fault displacement and kinematic indicators measured on fault planes (Figure 3.13). This led to the mapping of *fault segments* of up to 35 km in length. These are distinct from the considerably shorter *earthquake segments*, which are less than 15 km for the Gulf of Corinth Rift [*Jackson et al.*, 1982; *Schmidt*, 1881]. Thus, a single earthquake will only rupture along part of its fault segment. The location of this earthquake segment along the fault segment is random, and so a characteristic-type offset pattern (*sensu Scholz* [1989]) develops over time for the fault segment.

A sequence of three earthquakes occurred in the Alkyonides Gulf in 1981 (Figure

3.13). *Jackson et al.* [1982] combined surface and seismological observations from these events to constrain the style of normal faulting. They concluded that the border faults are planar, and dip at 45° from the surface to a depth of 8 ± 2 km. At this depth, the dip significantly shallows to ~10°. Although motion on these low-angle faults cannot be observed directly, *Eyidogan and Jackson* [1985] present seismological evidence for motion along such faults in western Turkey. A very similar geometry exists here with steep, planar rift-bounding faults that penetrate to 8 ± 2 km. These faults exist as discrete surfaces for short time periods immediately after large earthquakes.

Chapter 2 showed that the seismogenic layer thickness is controlled by crustal rheology, and is loosely defined as the depth to which microseismicity is active. *Rigo et al.* [1996] measured microseismicity over of a six-week period during 1991 (i.e., long before the 1995 Eigion earthquake) in the western Gulf of Corinth. A network of 51 seismometers was deployed, spanning the Gulf of Corinth across the Eigion fault segment. Most of the microseismic activity is concentrated between 6 and 8 km depth, and 95% of the events were shallower than 14 km. In a similar study across the Alkyonides Gulf (Figure 3.3), *King et al.* [1985] showed that of the aftershocks following the 1981 sequence of events, more than 96% were shallower than 15 km.

West of the Alkyonides Gulf, the border faults strike at between 090° and 105°, and dip at around 50°. However, in the Alkyonides Gulf itself, the currently active faults trend at between 70° and 90° and cross-cut the earlier trend of rifting (e.g., the Megara Basin, Figure 3.9). There is also an abrupt shallowing of water depth at the entrance to the Alkyonides Gulf (~22.9°) from ~800 m to ~400 m.

The width of the currently subsiding zone varies along strike, and reaches a maximum of 30 km at the Xylocastron fault segment. This coincides with the deepest bathymetry (~800 m) in the gulf (Figure 3.13). Width and bathymetry may be used to qualitatively assess the variation in total strain along the rift. It seems then that less strain has accumulated across the Alkyonides Gulf than across the Xylocastron fault segment. Further west, the amount of strain decreases more gradually, suggesting that the Gulf of Corinth Rift is propagating towards the west.

The timing for the onset of rifting in the Gulf of Corinth is unclear as the sediments cannot be accurately dated. Most estimates in the literature are based on regional considerations, and so range between between 5 and 16 Ma (see Section 3.6.1). This matter remains uncertain, though something *can* be said about the present-day border

faults. Since the rift's inception, the border faults of the Gulf of Corinth rift have migrated northwards by 25 to 30 km (Figure 3.13). The currently active faults not only cross-cut old compressional structures, but also undeformed Neogene sediments deposited in the hanging walls to older faults. This implies that the present-day border faults have been active mostly during the Quaternary (i.e., the last 2 Myr).

3.7.1.2 The Sediments of the Gulf of Corinth Rift

The exposed and uplifted Gulf of Corinth Rift sediments across the northern Peloponnese have been studied by numerous authors (e.g., *Ori* [1989], *Ori, Roveri and Nichols* [1992], *Seger and Alexander* [1993]). The oldest exposed Gulf of Corinth Rift sediments are lacustrine and continental muds, silts and sands. At some stage, subsidence had accumulated such that the depositional environment became marine. Marls were deposited in the sea that formed, with large Gilbert-type fan deltas forming along the shoreline. As the bounding faults migrated northwards, younger deltas offlapped the older ones. West of Xylocastron, these large, coarse-grained deltas are now exposed onshore up to an maximum elevation of 1756 m (on Mt. Mavron, Figure 3.13).

It is not certain when the lake to marine transition occurred. *Westaway* [1996] suggests that the transition occurred at oxygen isotope stage 13 (approximately 500 ka), but his data are poorly constrained. *Armijo et al.* [1996] say that marine bands may exist up to elevations of 1756 m.

East of Xylocastron, the style of sedimentation is very different. Deltas are less-well developed and so marine marls dominate the succession. Uplift in the footwall to the rift bounding fault segments has resulted in the formation of erosional marine terraces, creating a step-like topographic profile (Figure 3.14). They are around 30 km long, rise to an elevation of over 400 m, and can be traced between Xylocastron and Corinth (Figure 3.3) as surfaces which dip gently towards the sea, trending parallel to the modern coastline. The inner edge of each terrace corresponds to the base of an ancient cliff face which formed at a eustatic highstand[2]. Consequently, a curve through a trace of any one inner-edge defines a palaeo-horizontal surface. This forms an important constraint for the elastic models for rift-related topography in Chapter 5.

These terraces were first described by *Sébrier* [1977], though *Armijo et al.* [1996]

[2]More precisely, inner edges form just prior to the highstand, but the errors in this approximation are small.

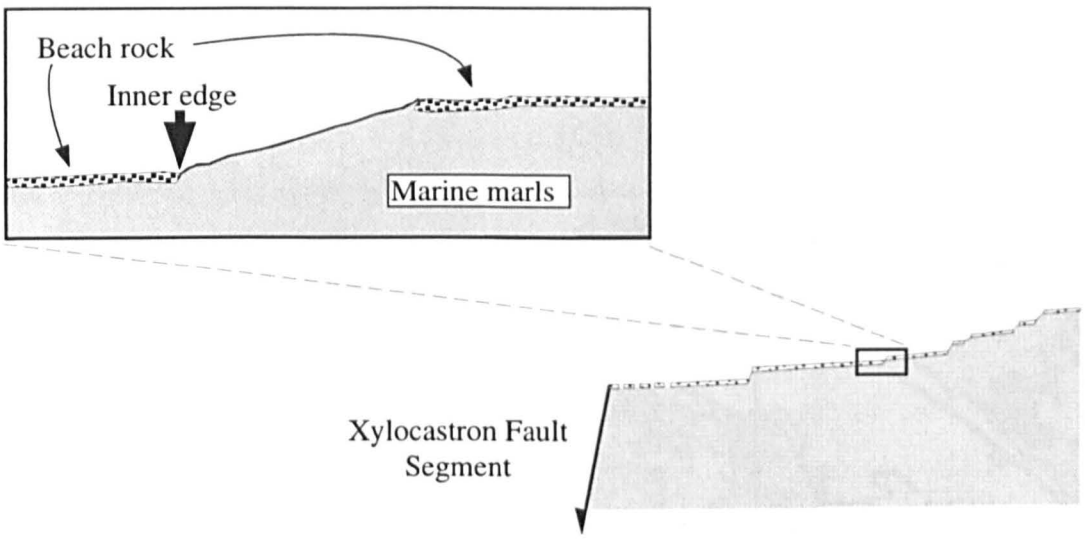

Figure 3.14: Schematic for the deformation of the erosional marine terraces in the footwall to the Xylocastron fault segment.

present their best description to date. Field observations and the use of SPOT satellite imagery allowed for detailed mapping and correlation of twelve terraces. Some of the terraces could be assigned an age from U/Th dating of molluscs and corals, and subsequently assigned to specific eustatic highstands. Those terraces which could not be dated directly were seen to fit in with the rest of the Pleistocene sea-level curve. Thus, the marine terrace inner-edges provide us with a series of dated palaeo-horizontal surfaces which are now deformed in the footwall to the Gulf of Corinth Rift.

3.7.2 The Gulf of Evvia Rift

The Gulf of Evvia Rift is approximately 85 km long and 15 km wide, making it the second largest extensional feature in central Greece. It is similar to the Gulf of Corinth in that it is dominated by roughly east-west trending normal faults on its southern flank. There is also evidence for a northward propagation of these rift-bounding faults. However, unlike the present-day marine sedimentation within Gulf of Corinth Rift, deposition within the present-day depocentre is sub-aerial in the west (the Sperchios Basin) and marine in the east (Figure 3.15). Despite the excellent exposure of normal fault scarps and sub-aerial depositional geometries, the Gulf of Evvia Rift has received little attention compared to that for the Gulf of Corinth. This may be due to the occurrence of fewer large earthquakes through the last century (see Figure 3.10), consistent with the slower extensional velocities compares to the Gulf of Corinth (Figure 3.21).

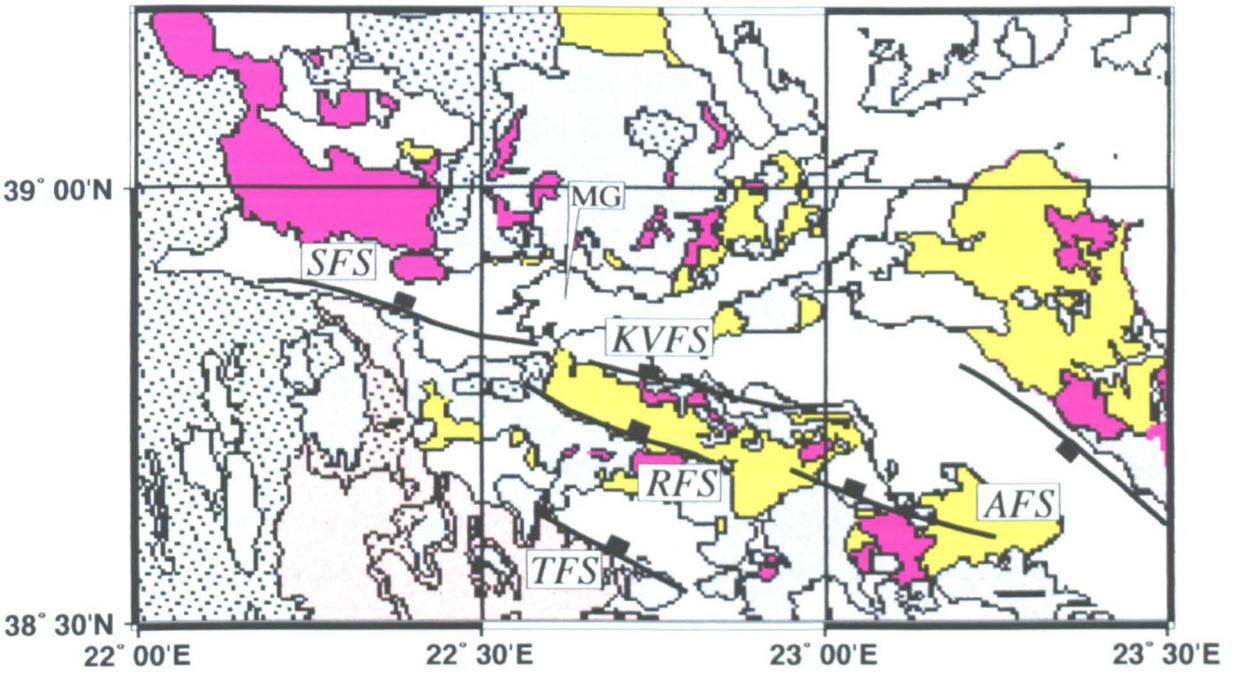

Figure 3.15: The structure of the Gulf of Evvia Rift. *SFS*: Sperchios fault segment. *KVFS*: Kamena Vourla fault segment. *RFS*: Renginion fault segment. *AFS*: Atalanti fault segment. *TFS*: Tithoria fault segment. MG: Maliakos Gulf. See Figure 3.9 for key to geological information.

3.7.2.1 The Structure of the Gulf of Evvia Rift

The sub-aerial portion - referred to as the *Sperchios Basin* - displays a classic half-graben geometry. In the central and eastern portions of the rift, a history of northward fault migration is observed. The faults controlling the Gulf of Evvia rift were first mapped by *Roberts* [1988] (see also *Roberts and Jackson* [1991]), and later by *Eliet and Gawthorpe* [1995]. G. Roberts (University College London, personal communication, 1997) grouped the faults on the southern margin into five kinematic fault segments (Sperchios, Kamena Vourla, Renginion, Atalanti and Tithoria - see Figure 3.15). The increasingly simple geometry of the Gulf of Evvia towards the west suggests that the rift is propagating in this direction.

3.7.2.2 The Sediments of the Sperchios Basin

Along the sub-aerial Sperchios Basin, the Sperchios river flows from west to east. Its position within the half-graben is influenced by the presence of low-angle alluvial fans [*Eliet and Gawthorpe*, 1995] at the southern margin. The river discharges into the Maliakos Gulf (Figure 3.15). Here, both tidal and wave action is low, and a bird's-foot delta forms [*Galloway and Hobday*, 1983]. There is no exposure in the hanging wall to

the Kamena Vourla fault segment.

In the hanging wall to the Tithoria fault segment, the sediments are largely covered by Quaternary to recent fluvial and alluvial deposits. Exposure in the north - towards the footwall of the Renginion fault - reveal a series of marls, claystones and conglomerates that dip towards the south. Similar lithologies are exposed across the uplifted Renginion basin.

3.7.3 The Lake Trihonis Basin

Very little sedimentological or structural work has been done on the Lake Trihonis Basin. Although exposure is poor and extensional structures cannot be mapped, *Doutsos, Komtopoulos and Frydas* [1987] infer that a 30 km long normal fault bounds the basin to the south. The idea that the basin is extensional may be supported by the GPS measured strain shown in Figure 3.21.

Doutsos, Komtopoulos and Poulimenos [1988] devise a tectonic scheme for central Greece where the Lake Trihonis Basin represents a westward extension of the Gulf of Corinth. Based on the spatial distribution of micro-seismicity, *Brooks et al.* [1988] and *Melis, Brooks and Pearce* [1989] take this idea further. They propose a scheme where a system of normal and strike-slip faults links the Gulf of Corinth, the Gulf of Patras, the Lake Trihonis Basin and the Gulf of Amvrakia Basin (see Figure 3.12).

3.8 Active Tectonics North of the Aegean

The metamorphic rocks exposed across the Rhodope Mountains (Figure 3.1) of northern Greece and southern Bulgaria had been interpreted as a pre-Mesozoic element that was tectonically stable throughout the Tertiary. However, the palaeomagnetic data presented by *Atzemoglou et al.* [1994] indicate that western Rhodope has rotated since 25 Ma, and *Sokoutis et al.* [1993] suggest that the metamorphic rocks are exposed due to the isostatic response to high extensional strain. *Mposkos and Liati* [1993] show that their P-T paths are similar to those for the core complexes across the Cyclades.

To the north of the Rhodope complex are the Balkan Mountains (Figure 3.1). *Doglioni et al.* [1996] suggests that this narrow chain resulted from compression during the Palaeogene, and has been characterised by extensional tectonics since the Neogene, controlled by steeply dipping normal faults. However, *Roy et al.* [1996] model the topography in their footwalls and suggest that all of the topography can be explained by flexural foot-

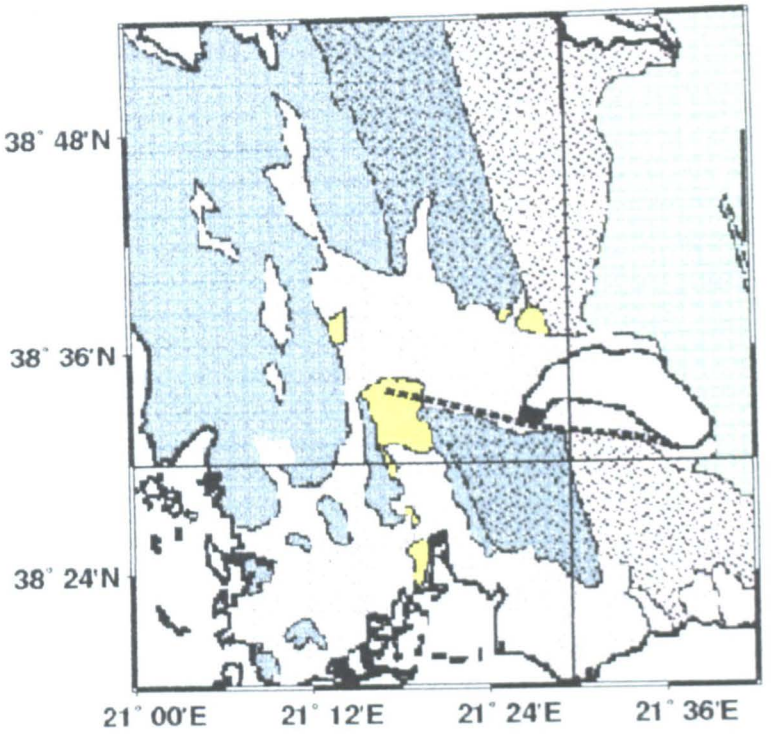

Figure 3.16: The structure of the Lake Trihonis Basin. Dotted line shows the inferred location of the bounding fault.

wall uplift. Using forward models of topography and gravity data, the T_e across the Moesian Platform is estimated to be ~12 km, which decreases to 3 km across the steep slopes of the narrow range.

Roy et al. [1996] also point out that Rhodope complex immediately to the south is bound by Neogene (and older) normal faults that dip towards the north, away from the mountains. They suggest that flexural uplift of similarly weak upper crust could contribute to the topography.

Stewart and Watts [1997] use forward models of gravity and topography to estimate the T_e across the east-west trending Southern Carpathians. They obtain T_e values of between 10 and 30 km across the range, and 20 to 30 km across the Moesian Platform (see Figure 3.1).

3.9 The Kinematics of Aegean Deformation

A prerequisite to understanding the dynamics of a region is an accurate description of the kinematics. The regional deformation field has been analysed in three ways. In chronological order, these have been from analyses of regional plate motions, of regional

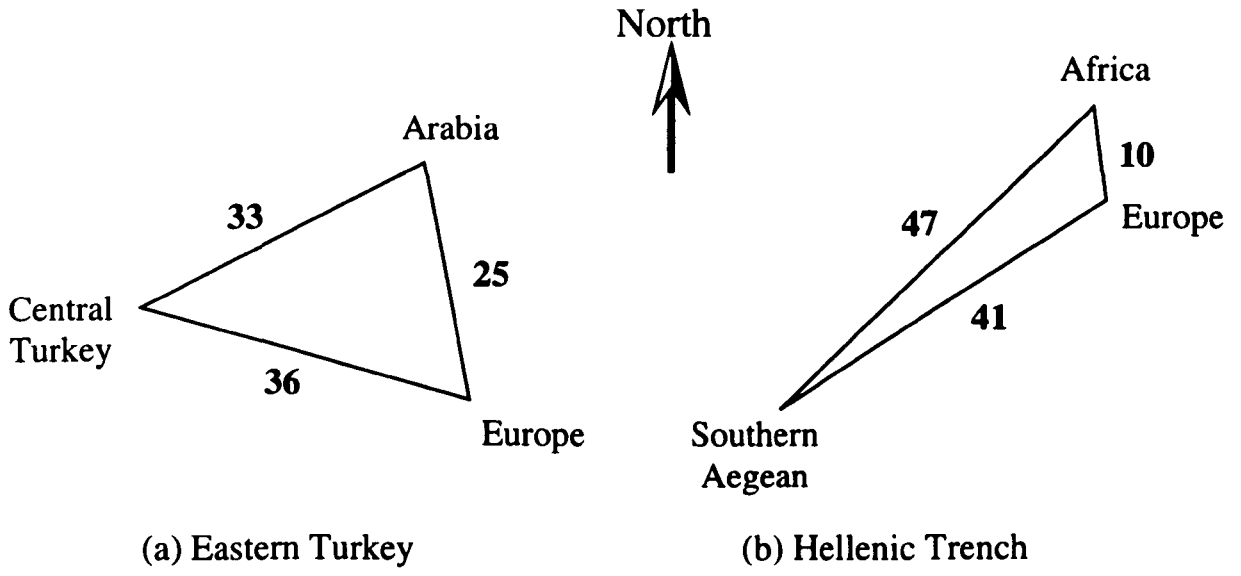

Figure 3.17: Velocity triangles for (a) eastern Turkey (at 41°E) and (b) the Hellenic Trench. All velocities are in mm/yr. From *Jackson* [1994].

seismicity, and most recently of geodetic observations. These reveal different and sometimes conflicting aspects of Aegean kinematics.

3.9.1 Plate Motions

The basic tenets of plate tectonics do not apply to regions where deformation occurs in diffuse zones rather than in the narrow bands which define oceanic plate boundaries (e.g., *England and Jackson* [1989]). However, in addition to Africa, Arabia and Eurasia, Figure 3.11 shows that there are two relatively aseismic areas - sometimes referred to as *micro-plates* - within the broad zone of Aegean deformation: central Anatolia and the southern Aegean.

McKenzie [1972] was the first to construct velocity triangles for these five regions. Those presented in Figure 3.17 are based on recent revisions of global plate motions (see *Jackson* [1994] for details). Figure 3.17a shows an estimated rate of slip along the NAF at 41°E of 36 mm/yr. As Africa and Europe are converging, the southwestern motion of the southern Aegean is accommodated by shortening at the Hellenic Trench. Figure 3.17b shows that the southern Aegean is moving away from Europe at 41 mm/yr towards the southwest. Thus, the rate of subduction is largely controlled by the rate of Aegean motion rather than the rate of the overall convergence.

3.9.2 Aegean Seismicity

Aegean seismicity is restricted to the upper 10-15 km of the crust. Based on the pattern of north Aegean seismicity, *Taymaz, Jackson and McKenzie* [1991] believed the deformation of the northern Aegean to be dominated by two effects: the accommodation of the motion of Anatolia by diffuse right-lateral faulting, and N-S extension. Believing these to be linked, *Taymaz, Jackson and McKenzie* [1991] presented the *slat model* for the kinematics of Aegean deformation.

A simple consideration of timing shows that the extension predates any Anatolian influence and that the strike-slip faulting is superimposed on a well established extensional regime. Furthermore, the slat model does not reproduce the N-S extension in western Turkey, and the predicted rotations are different to those measured by global positioning system (GPS) experiments [*Davies et al.*, 1997].

At horizontal length scales comparable to or larger than the thickness of the lithosphere, *England and Jackson* [1989] argue that surface deformation is controlled by the lithosphere as a whole rather than by that of the thin seismogenic layer on top, and that this deformation field may be approximated by a continuum. In other words, the spatially and temporally averaged surface deformation equates to the velocity field of the distributed deformation of the entire lithosphere.

Jackson, Haines and Holt [1992] applied this concept to derive a continuous velocity field by summing all earthquake moment tensors between 1909 and 1983 in 1.5 by 1.5 degree bins. A similar dataset to the one used is presented in Figure 3.10, which also shows events associated with shortening at the Hellenic Trench. The result was then smoothed by fitting a fifth-order polynomial to give the velocity field shown in Figure 3.18. The main features of this are

- E-W shortening in the northern Aegean
- N-S extension in the central Aegean, Greece and Turkey, and
- clockwise rotation of western Greece.

As only the largest earthquakes were used ($M_s > 6.0$) and because the length of the seismic record is shorter than the seismic cycle, the velocities shown in Figure 3.18 are likely to be underestimates. This argument is summarised by a vector sum of velocities,

$$v = v_{M>6} + v_{M<6} + v_{ANAT} \tag{3.1}$$

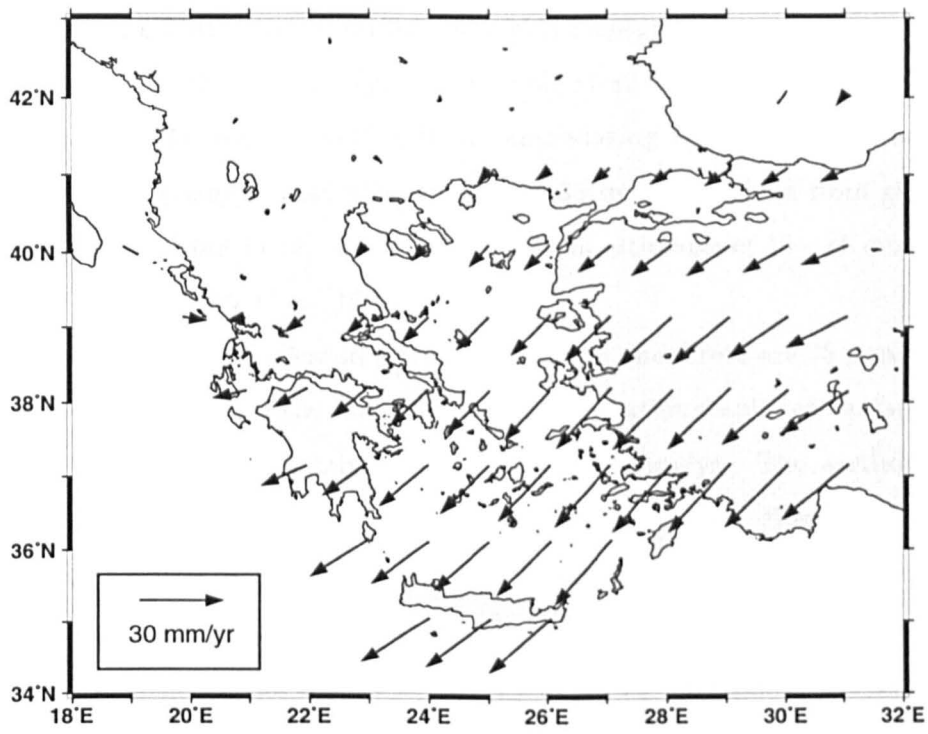

Figure 3.18: A velocity field in the Aegean Sea relative to Eurasia, derived from seismic moment tensors for earthquakes during 1909-1983. Spatial averaging performed with a 1.5° bin, following by smoothing with a fifth order polynomial. Only earthquakes with $M_s \geq 6.0$ were used. Arrow length is proportional to velocity. From *Jackson, Haines and Holt* [1992].

where v is the velocity at a point with respect to Eurasia, $v_{M>6}$ is the velocity measured by *Jackson, Haines and Holt* [1992], $v_{M<6}$ refers to the deformation occurring with earthquakes with $M_s < 6$ (including aseismic strain) and v_{ANAT} is some component of motion transferred directly from Anatolia. Geodetic observations aim to measure v directly.

3.9.3 Geodetic Observations

3.9.3.1 Satellite Laser Ranging Experiments

Satellite Laser Ranging (SLR) experiments began in the Aegean region in 1985 to estimate the displacements of individual SLR tracking sites (see *Smith et al.* [1994] for survey details). The most recent solution for ten of the SLR sites across the Aegean and Anatolia are presented by *Le Pichon et al.* [1995] to give a purely geodetic expression of the regional kinematics with respect to Eurasia.

The stations in Anatolia east of 31°E appear to move coherently. Similar results are obtained by *Oral et al.* [1995], who combine the SLR velocities with GPS observations

across Turkey. The best fitting rigid rotation with respect to Eurasia of this block is a counter-clockwise rotation at 1.72°/yr about a pole at 32.0°E and 32.7°N. This predicts that east of 31°E, the NAF is currently accommodating shear with a velocity of 28 mm/yr, considerably slower than the estimate of 36 mm/yr derived from global plate motions (Figure 3.17) but faster than the longer term estimates of 13 - 21 mm/yr based on geological data [*Hubert et al.*, 1997].

The SLR velocity of the sites on south-west Greece and Crete are 35 mm/yr and 30 mm/yr respectively, whereas the seismic moment summation results of *Jackson, Haines and Holt* [1992] are approximately 20 mm/yr and 30 mm/yr. The earthquake data provide a measure of strain, and the SLR data of displacement. However, the quality of these SLR velocities is limited by the short time period of measurements: a nine year period may not be enough to resolve the long-term displacement rates with respect to Europe. Their spatial resolution is also poor, so any anomalies occurring in the immediate region of the SLR stations (e.g., transient response to earthquakes) will not be resolved.

3.9.3.2 Terrestrial Geodetic Observations

Veis et al. [1992] calculated displacements of stations established in the 1890s from the results of a retriangulation carried out in 1975 but, because their choice of scale, tectonic deformation was not best resolved. To analyse the deformation within Greece, *Le Pichon et al.* [1995] reprocess the measurements to obtain the strain at 78 points across mainland Greece and the Cyclades. The SLR results were used to define the velocity at each point with respect to Eurasia (Figure 3.19).

Le Pichon et al. [1995] seek a kinematic interpretation involving the rotations of rigid plates and argue that the velocity field may be described by rotations about two poles. The pole for a counter-clockwise rotation of an area to the north of the Gulf of Corinth lies in the Adriatic Sea (Figure 3.1), which is similar to the results of *Jackson, Haines and Holt* [1992] (see third bullet in Section 3.9.2). For the Peloponnese and the Cyclades, the pole for a clockwise rotation lies close to that for the Anatolian rotation shown in Figure 3.20. Thus, *Le Pichon et al.* [1995] imply that the westward motion of Anatolia is transferred through the southern Aegean and directly to the trench.

The difference between two radially symmetrical vector fields gives a third radially symmetrical vector field whose pole lies on the great circle joining the poles of the two

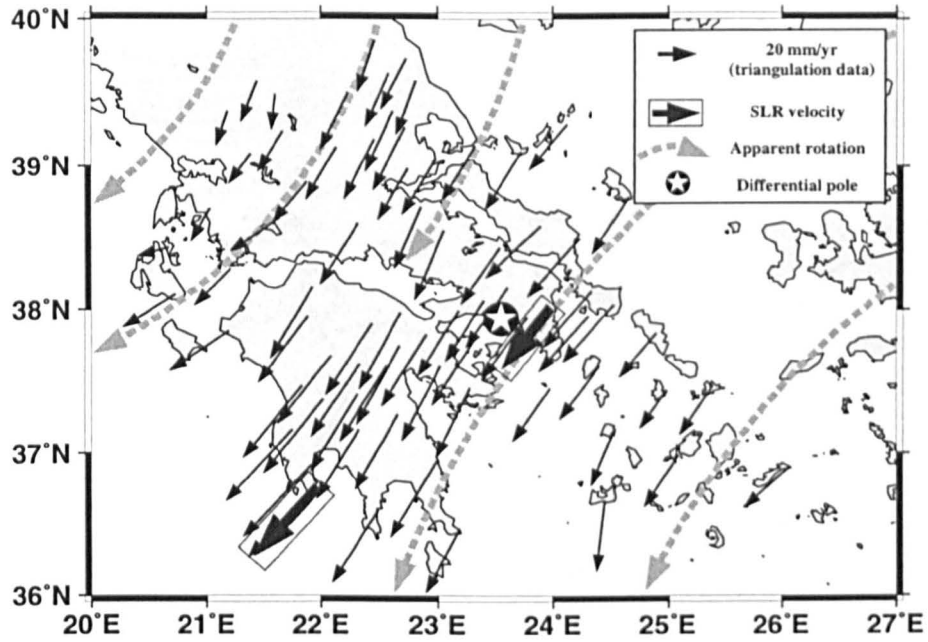

Figure 3.19: The velocity field with respect to Eurasia. The thick dashed lines represent two solid-body rotations, and the star represents the pole for their *differential rotation* (see text). Adapted from *Le Pichon et al.* [1995].

constituent fields. The pole for the relative rotation of central Greece away from the Peloponnese and Cyclades lies close to Athens, as shown in Figure 3.19. *Le Pichon et al.* [1995] believe that the extension between the two plates results in extensional deformation, accommodated on E-W trending faults. However, the authors fail to explain why the E-W trend is favoured, mention nothing of the Gulf of Evvia Rift, and provide no explanation for the E-W extension across the Gulf of Messinia (~7 mm/yr) and the Gulf of Laconia (~4 mm/yr) (see Figure 3.12).

Le Pichon et al. [1995] compile a velocity field for the whole of the Aegean area, obtained by supplementing the SLR and triangulation data with GPS data from the Marmara Sea region and the north-west Aegean Sea [*Straub and Kahle*, 1994] (Figure 3.20). A solid-body rotation fits the observations across central Anatolia, which corresponds to the aseismic region east of 31°E. Across the Aegean,

- the NAF zone appears to widen towards the west, becoming more diffuse as it enters the Aegean Sea (i.e., splaying of velocity contours), which might support the idea that strike-slip faulting in the northern Aegean is diffuse in nature [*Jackson, Haines and Holt*, 1992; *Taymaz, Jackson and McKenzie*, 1991]

- across the southern and central Aegean, the regional rotation of Anatolia is added

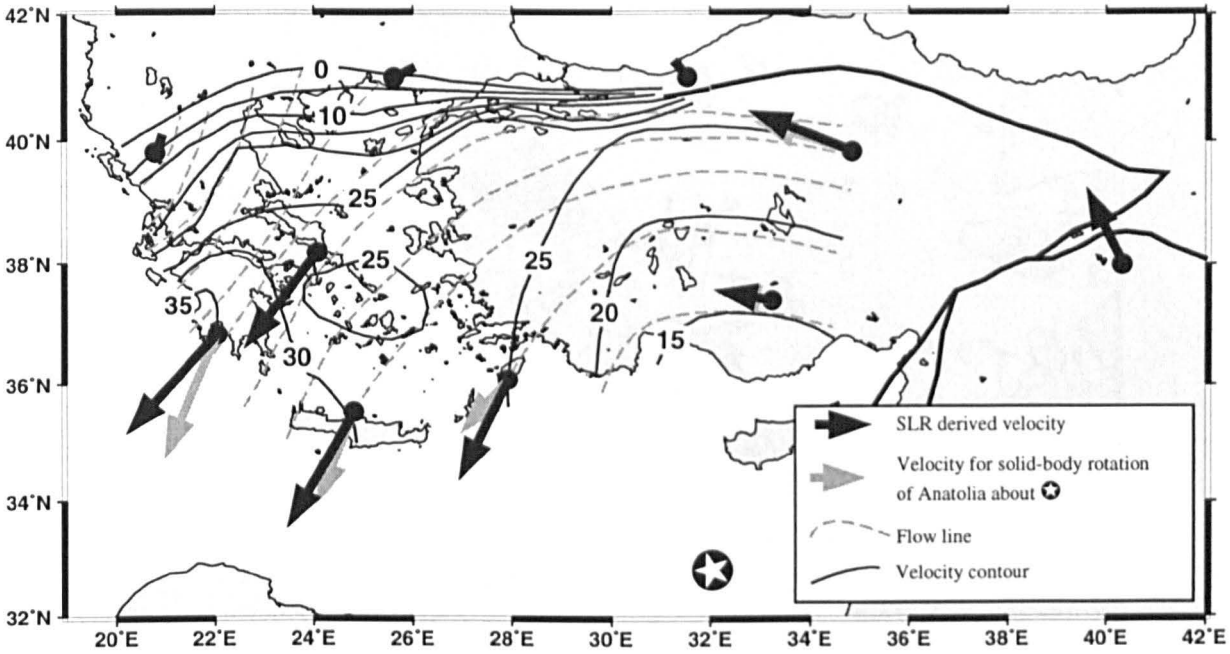

Figure 3.20: Aegean velocity field with respect to Eurasia, incorporating SLR observations, terrestrial geodetic observations across Greece, and GPS observations in northern Turkey. The star is the pole to the counter-clockwise rotation at a rate of 1.72°/yr. Dashed lines are flow lines, and solid lines are velocity contours. Areas of extension exist where velocities increase along flow-lines, and where flow-lines diverge. Adapted from *Le Pichon et al.* [1995].

to by extensional deformation

- there is a minimum in velocity across the Cyclades, consistent with the reduced seismicity
- velocities increase towards the southwest, and reach a maximum of 35 mm/yr in the southwest Aegean.

3.9.3.3 Global Positioning System Experiments

The first Global Positioning System (GPS) experiment in the area was carried out in central Greece to determine the strain between 1900 and 1988 [*Billiris et al.*, 1991]. The GPS station network was later expanded to cover central Greece, the Peloponnese and the Cyclades [*Davies et al.*, 1997], one third of the Aegean extensional province. Work is currently ongoing to extend the network to cover the entire Aegean.

Several baselines exhibit no length change over the last century, and three non-deforming regions are recognised. These are shaded in Figure 3.21. The central Peloponnese is rotating counter-clockwise with respect to the zone near Athens, which corresponds to the opening of the Gulf of Corinth. The highest velocities are observed

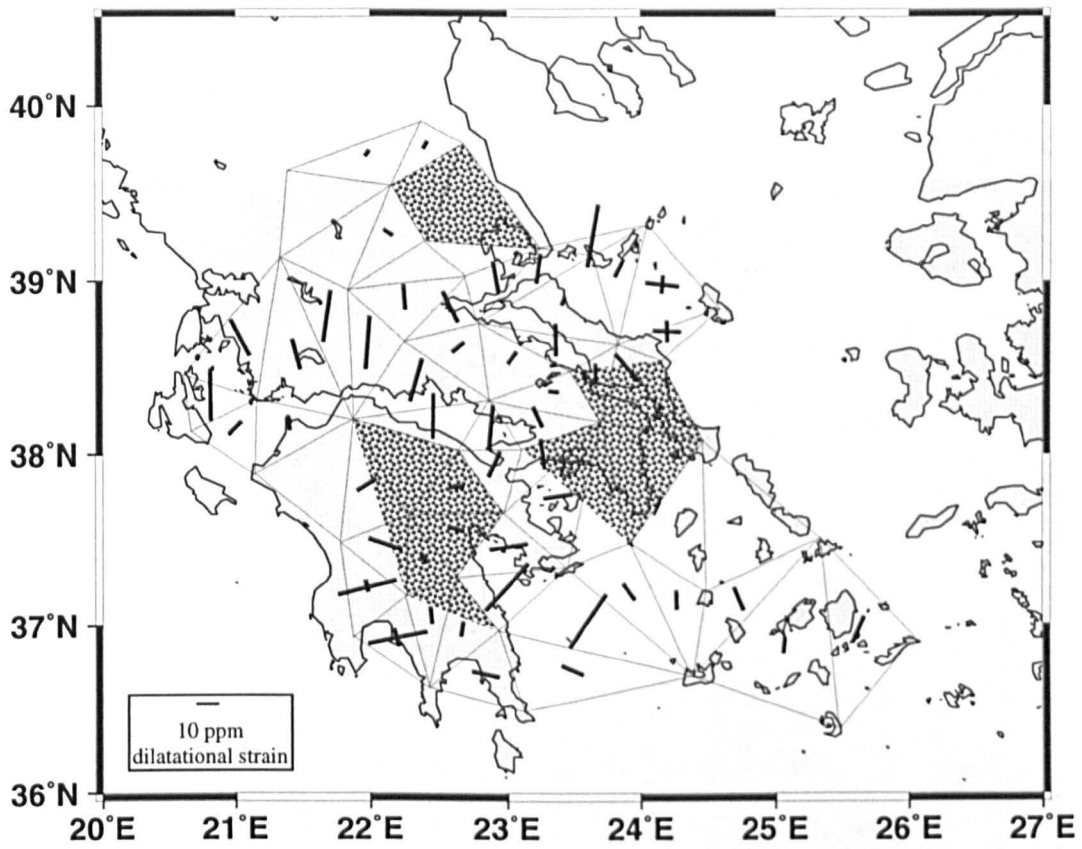

Figure 3.21: Extensional strain across Greece from GPS, averaged over the last century. Shaded regions are shown to be comoving. Taken from *Davies et al.* [1997].

across the Gulf of Corinth (Figure 3.21): approximately 8 mm/yr in the east, and 12 mm/yr in the west. This north-south extension gives way to east-west extension across the Peloponnese (Figures 3.10 and 3.21). In the southern Peloponnese, this is consistent with the seismologiocal and structural evidence, although there is no such expression in the northern and western Peloponnese (Figures 3.10 and 3.12).

To estimate the velocity field, the GPS observations are supplemented by the terrestrial observations of *Veis et al.* [1992], reprocessed such that the assumptions of scale and orientation are consistent (Figure 3.22). The Peloponnese is seen to be moving towards the south-west away from Eurasia at 50 mm/yr, ~30 mm/yr faster than that deduced by *Jackson, Haines and Holt* [1992] from seismic strains, and ~15 mm/yr faster than shown in Figure 3.19. *Davies et al.* [1997] find that for the region of the GPS network as a whole, only 20-50% of the observed deformation can be accounted for by recorded earthquakes with $M_s > 6.0$.

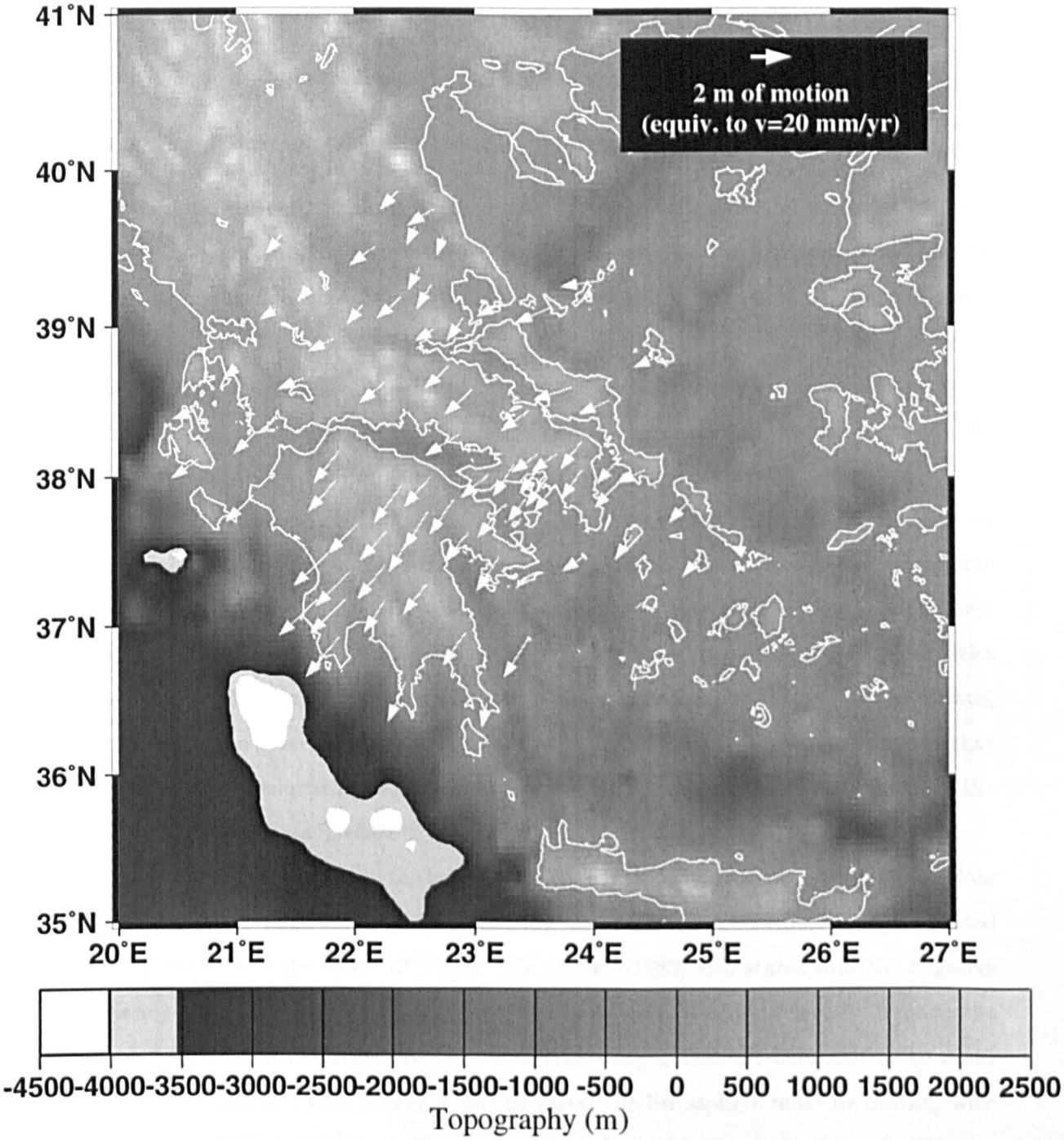

Figure 3.22: The averaged velocities of GPS stations for the interval 1892 to 1992, taken from *Davies et al.* [1997]. The deepest portion of the Hellenic Trench is shaded white.

3.10 Summary: The Dynamics of Extension

3.10.1 Tectonic Force

The kinematics of the Aegean province are dominated by two processes:

- the large scale westward motion of Anatolia, and
- diffuse extension across the Aegean.

There is some agreement among authors that the westward motion of Anatolia is driven by the difference in GPE between the elevated region of eastern Anatolia and the topographically low Hellenic Trench (i.e., *body forces*) [*Davies et al.*, 1997; *Hatzfeld et al.*, 1997; *Le Pichon*, 1982; *McKenzie*, 1978b]. Other authors, however, liken the motion to the squeezing of a pip (i.e., *boundary forces*). East of the Aegean, Anatolian motion is accommodated by the NAF and the EAF. The velocity of motion increases towards the southwest, and this extension is accommodated by diffuse rifting.

England and Jackson [1989] argue that a continuous velocity field that is smooth on a lengthscale greater than lithospheric thickness defines the deformation of the lithosphere as a whole. *Davies et al.* [1997] show that a quadratic velocity function is adequately smooth and fits the observed strains within the errors of the observations. Velocities increase from 30 mm/yr in the northeast of the network to 50 mm/yr at the trench, corresponding to a strain rate of 2×10^{-15} s^{-1}. This is consistent with the idea that GPE drives extensional deformation in Greece, with velocities increasing towards the low across the Hellenic Trench (Figure 3.22).

As shown in Appendix A, the magnitude of this tectonic force will roughly correlate with topographic relief. Assuming a stretching factor (β) of 2, *Le Pichon* [1982] estimated that the force is of the order 10^{12} N/m. *Le Pichon* [1982] also states that the negative buoyancy of the slab beneath the Aegean Sea could also contribute up 10^{13} N/m to the buoyancy force at the trench. *Davies et al.* [1997] argue that for deformation to occur in response to these forces at the observed rates, the lithosphere must be flowing with a viscosity of 10^{22} to 10^{23} Pas. This is similar to the viscosities derived for the Tibetan Plateau by *England and Molnar* [1997b].

Further support that GPE drives extension comes from recent analogue modelling (*Hatzfeld et al.* [1997]; P. Gautier, Université de Rennes, personal communication, 1997). A three-layer model of sand, silicone putty, and honey is prepared in a box. A gate in

one of the sides is opened, and the system is allowed to flow and deform in response to the drop in GPE across the gate. The observed deformation patterns resemble the broad-scale extensional features seen across the Aegean province. Horizontal gradients in GPE could also account for the E-W extension in the southern Peloponnese and towards Crete, although this may simply be accommodating a radial expansion as the Aegean expands southwards.

3.10.2 Implications for Aegean Rheology

It is clear that extensional strain across the Aegean is accommodated by diffuse rifting. From the models of *Buck* [1991] and *Hopper and Buck* [1996] discussed in Chapter 2, this suggests that the viscosity of the lower crust is low enough to flow and partially restore the horizontal GPE gradients created by rifting.

The occurrence of core complexes across the central Aegean may indicate that lower crustal rheology across the region was very weak. However, both earthquake and geodetic observations show that this area is not extending rapidly at present. This has been explained by *Le Pichon et al.* [1995] by the onset of continental collision. Little evidence exists for this, and temporal changes in rheology may provide a more simple explanation. A quantitative assessment of lithospheric rheology is carried out in this thesis, and mapping its spatial variability is a primary objective.

Chapter 4

Topography and Gravity Data

4.1 Introduction

The compilation of both the topography and the gravity datasets is described in this chapter. To ensure that separate gravity data sources are compatible, additional data were collected on mainland Greece. Details of this fieldwork are provided here. All pre-existing gravity data were then reprocessed to ensure compatibility. The reduction procedure - which includes the automated calculation of terrain corrections from the digital elevation models - is presented. The magnitude of the errors in the gravity data are estimated before the presentation of gravity maps and regional profiles, and a qualitative description of these data.

4.2 Digital Elevation Models

4.2.1 The 2 km Digital Elevation Model

A 2 km Digital Elevation Model (DEM) for onshore and offshore Greece was compiled by geophysicists at the University of Athens [*Lagios et al.*, 1994]. The 1:50,000 series topographic maps were used to estimate the average topography within adjacent 2 km boxes. A map of these elevations - given to the nearest metre above sea-level - is shown in Figure 4.1.

4.2.2 The ETOPO5 Digital Elevation Model

Beyond the limits of the 2 km DEM, the ETOPO5 DEM was used[1]. This 5 minute grid of topography is presented in Figure 4.2.

4.3 The Pre-existing Gravity Datasets

Prior to this study, there were six sources of gravity data available. These are referred to as the Greek onshore gravity data, the Greek offshore gravity data, the African Gravity Project (AGP) data, the satellite gravity data, the Gulf of Corinth gravity data and the regional gravity grid.

4.3.1 The Greek Onshore Gravity Data

4.3.1.1 Compilation

The first publically accessible gravity data across mainland Greece were collected between 1971 and 1974 [*Makris*, 1977]. This regional scale survey deployed G-series LaCoste-Romberg gravity meters, and altimeters were used to estimate the elevation of each gravity station. This survey covered all of mainland Greece, Crete, and the Greek Aegean Islands. Subsequently, a further twelve more localised surveys have been carried out by various universities and energy companies and added by *Lagios et al.* [1994] to the initial regional data to form the Greek onshore gravity database.

The Greek Institute of Geology and Mineral Exploration (IGME) and the University of Athens agreed to provide this project with some of these data, restricted to certain coordinate limits (Figure 4.3). The stations comprising the regional gravity dataset are

[1]Supplied by GETECH at the University of Leeds.

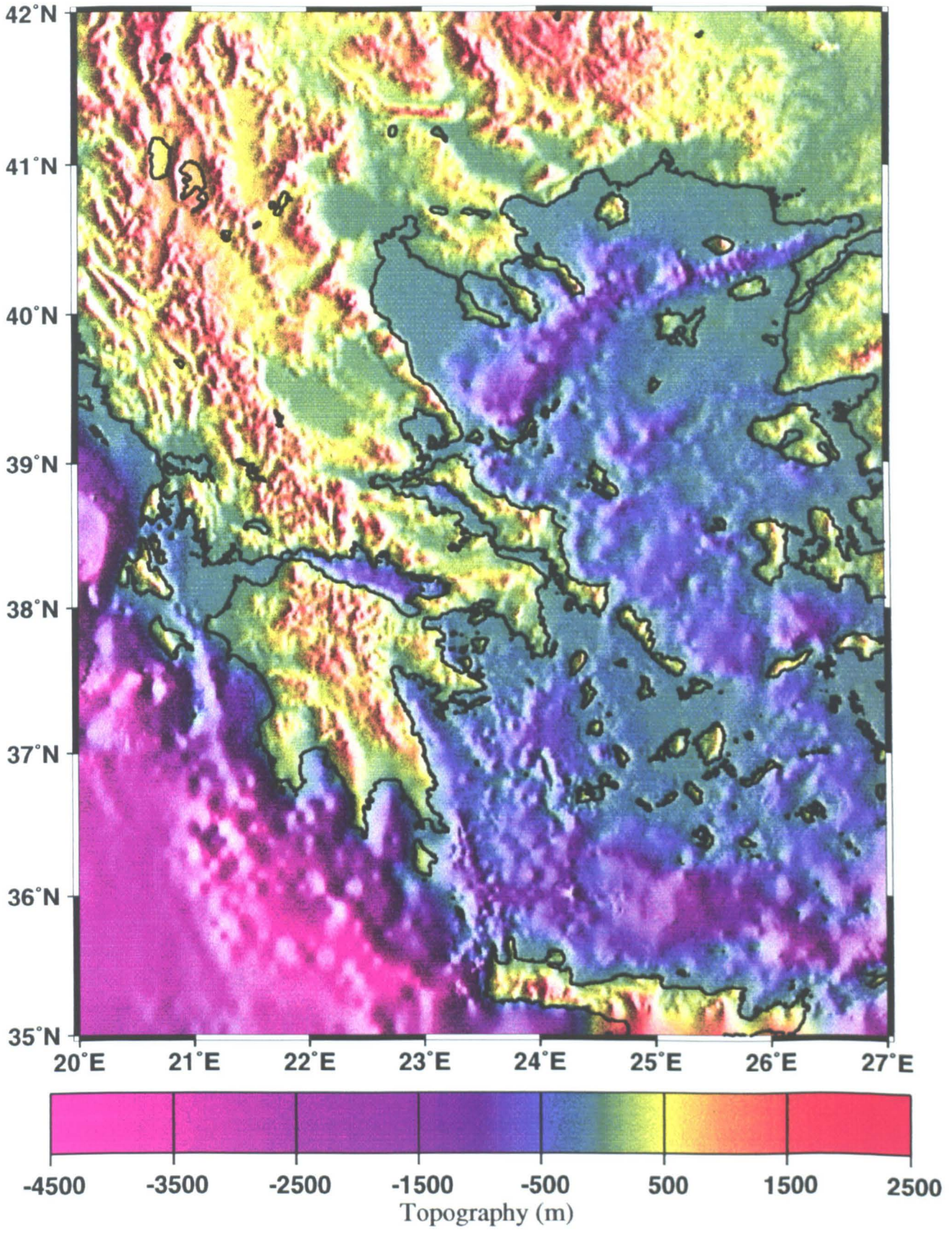

Figure 4.1: The 2 km digital elevation model.

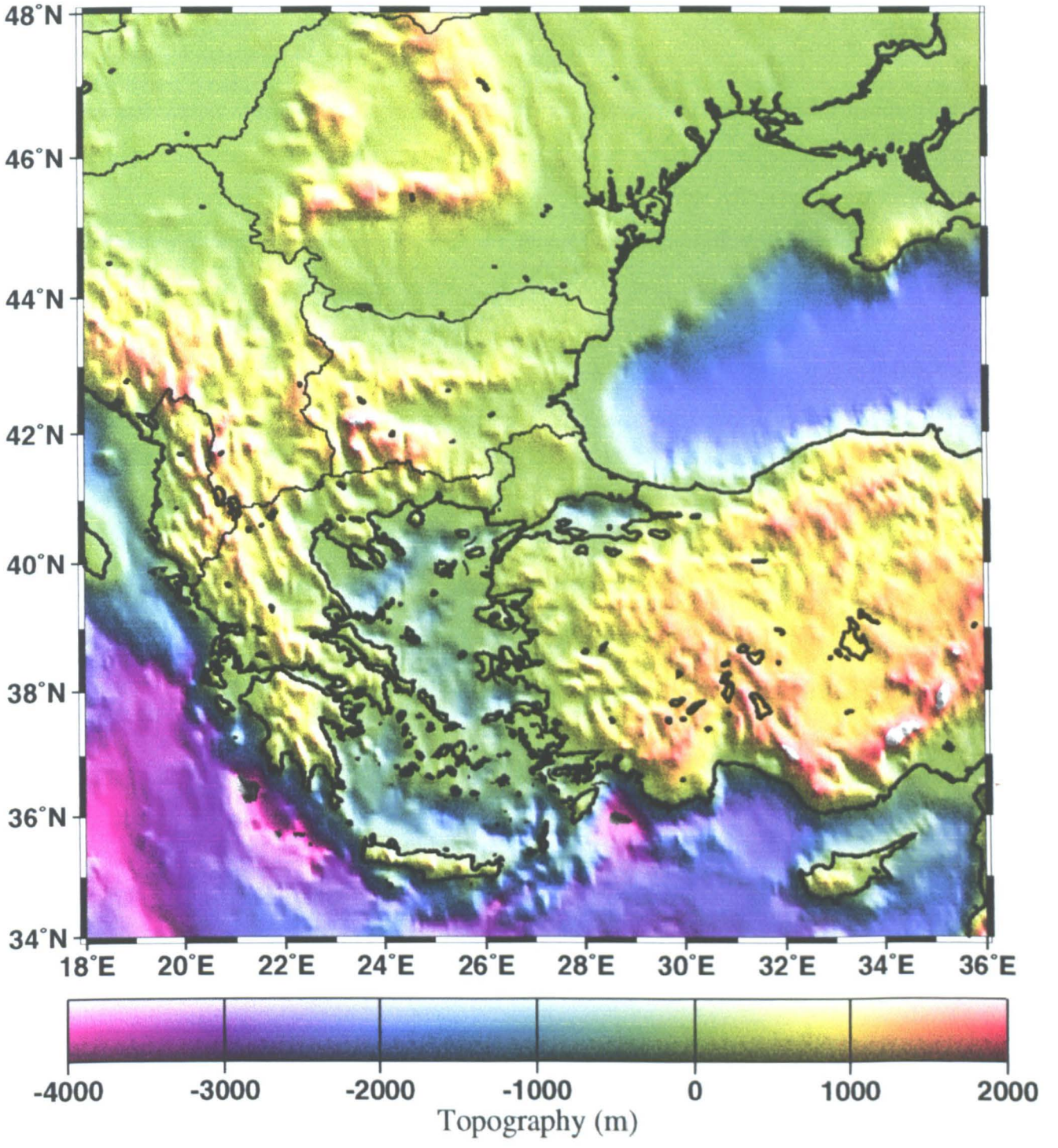

Figure 4.2: The ETOPO5 digital elevation model.

spaced at ~5 km across the whole of the region. From Fourier theory, the smallest resolvable wavelength is therefore 10 km. The black patches in Figure 4.3 indicate more localised surveys whose stations are spaced at between 100 and 500 m.

4.3.1.2 Errors

An estimation of the errors in the existing gravity data was carried out by *Lagios et al.* [1994]. The error in the observed gravity (ε_{obs}) was assumed to result from errors in meter reading, base-station absolute gravity estimates, gravity meter drift approximations and the meter scaling factors. These combined to give an estimated error of ±0.035 mGal.

An assumed location uncertainty of 10 m would result in an error of roughly ±0.01 mGal in the theoretical gravity value (ε_{ϕ}). The error in the free-air correction and the Bouguer correction (i.e., ε_{FAC} and ε_{BC}) were assumed to result from an expected 2 m uncertainty in station elevations. This would result in errors of ±0.62 mGal and ±0.22 mGal respectively. Finally, an error in the terrain correction (ε_{TC}) of ±0.8 mGal was arbitrarily estimated as 10% of their mean value across mainland Greece, so errors will be higher in areas of extreme relief.

From the laws of error propagation (e.g., *Barford* [1985]), the combined error in the free-air anomaly and Bouguer anomaly are calculated as

$$\varepsilon_{FAA} = \pm\sqrt{{\varepsilon_{obs}}^2 + {\varepsilon_{\phi}}^2 + {\varepsilon_{FAC}}^2} \tag{4.1}$$

and

$$\varepsilon_{BA} = \pm\sqrt{{\varepsilon_{obs}}^2 + {\varepsilon_{\phi}}^2 + (\varepsilon_{FAC} - \varepsilon_{BC})^2 + {\varepsilon_{TC}}^2}. \tag{4.2}$$

From these equations, ε_{FAA} was estimated to be ±0.62 mGal, and ε_{BA} to be ±0.89 mGal. On the basis of the fieldwork and gravity data reduction carried out as part of this thesis, the estimate of ±0.89 mGal represents a conservative one. An error analysis for the data used in this study is presented in Section 4.11.

Lagios et al. [1994] state that the data are referenced to the IGSN71 standard. The results of my fieldwork show that this is not the case, though there are no dc shifts between the sub-sets that comprise the Greek onshore gravity database (see Section 4.10). However, the Bouguer Anomaly values were incompatible as different Bouguer densities were used in the different sub-sets.

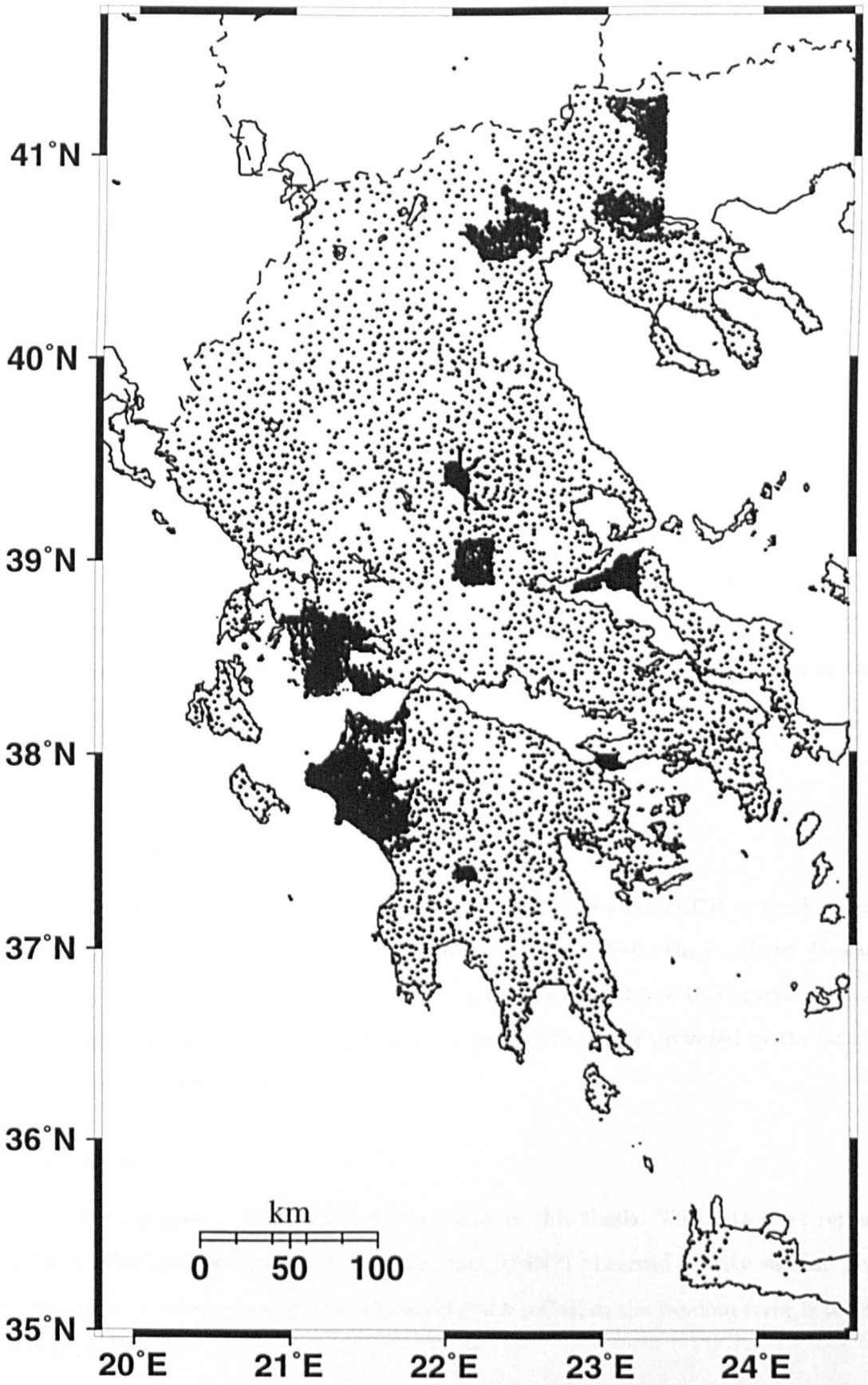

Figure 4.3: The 11969 stations comprising the Greek onshore gravity dataset made available for this study.

4.3.2 The Greek Offshore Gravity Data

4.3.2.1 Compilation

The University of Athens also supplied part of their offshore gravity dataset for use in this thesis. The data were collected during the late 1960s, but were not available to *Lagios et al.* [1994]. Instead, they used maps of Bouguer gravity anomaly, and the points shown in Figure 4.4 simply represent locations where a 10 mGal gravity anomaly contour intersected a ship path. The spacing is very coarse, and the smallest resolvable wavelength is approximately 50 km.

4.3.2.2 Errors

The random errors in this dataset cannot be estimated directly. Moreover, *Lagios et al.* [1994] assumed that these data were referenced to the same datum as the Greek onshore gravity data. My analyses show that these data are consistent with the IGSN71 standard (Section 4.10.2). Indeed, the Bouguer gravity maps were published in 1975 [*Morelli, Pisani and Gantar*, 1975], and C. Morelli was the key figure in establishing the IGSN71 standard [*Morelli et al.*, 1974].

4.3.3 The African Gravity Project Data

4.3.3.1 Compilation

These data were compiled from numerous existing datasets by GETECH at the University of Leeds. The cover extends far enough north to cover Crete, the southern Aegean islands and the southern Peloponnese. By comparing Figure 4.5 with Figures 4.3 and 4.6, it is seen that the AGP data fill some of the gaps in the cover provided by the Greek onshore and satellite datasets.

4.3.3.2 Errors

The supplied Bouguer gravity values are not used in this thesis. The data were reprocessed from the latitude, longitude, elevation and IGSN71 observed gravity values. The observed gravity values are quoted to the nearest 0.1 mGal, so the random error is taken to be ± 0.05 mGal.

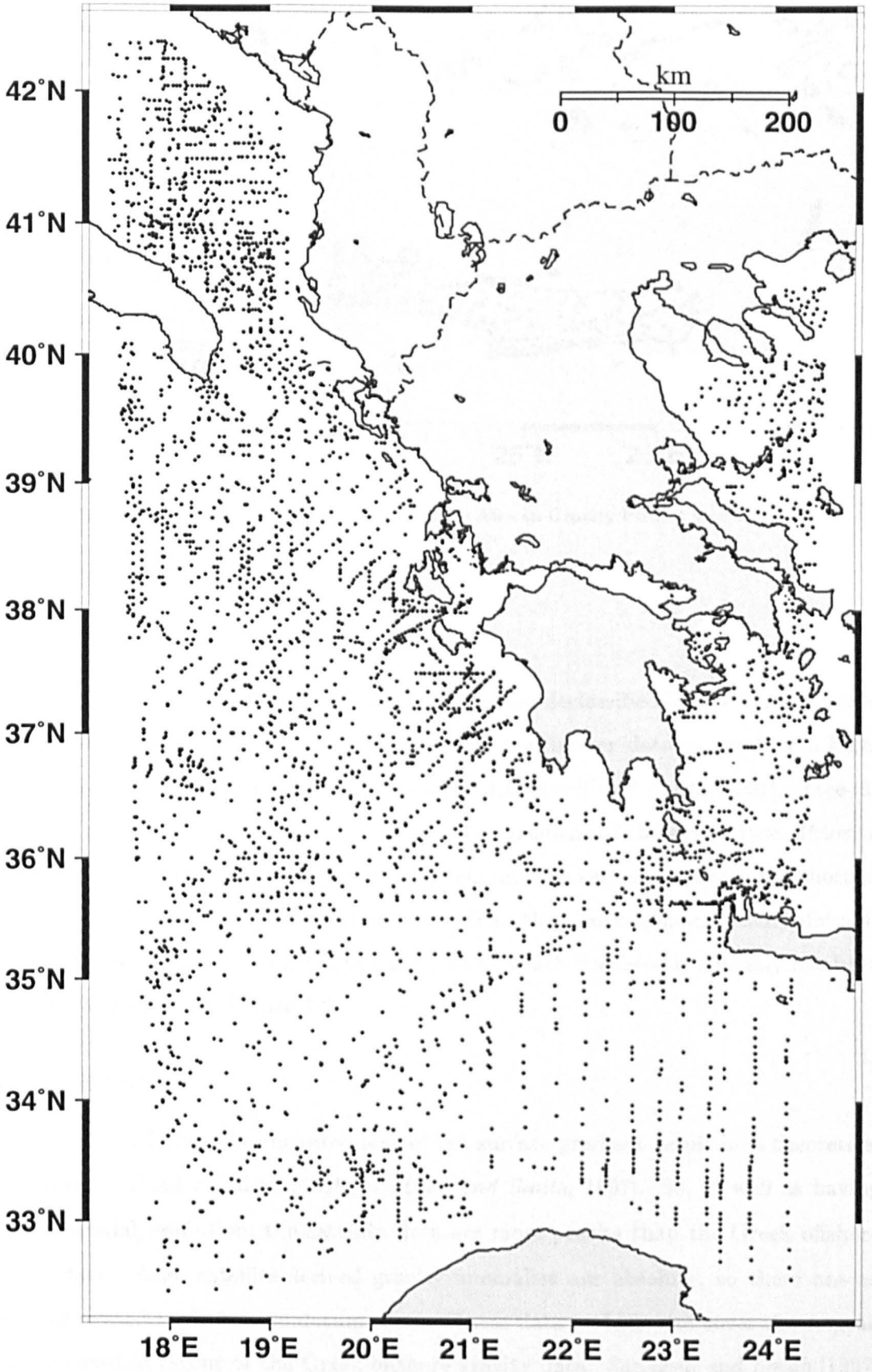

Figure 4.4: The locations of offshore gravity anomaly values made available for this study.

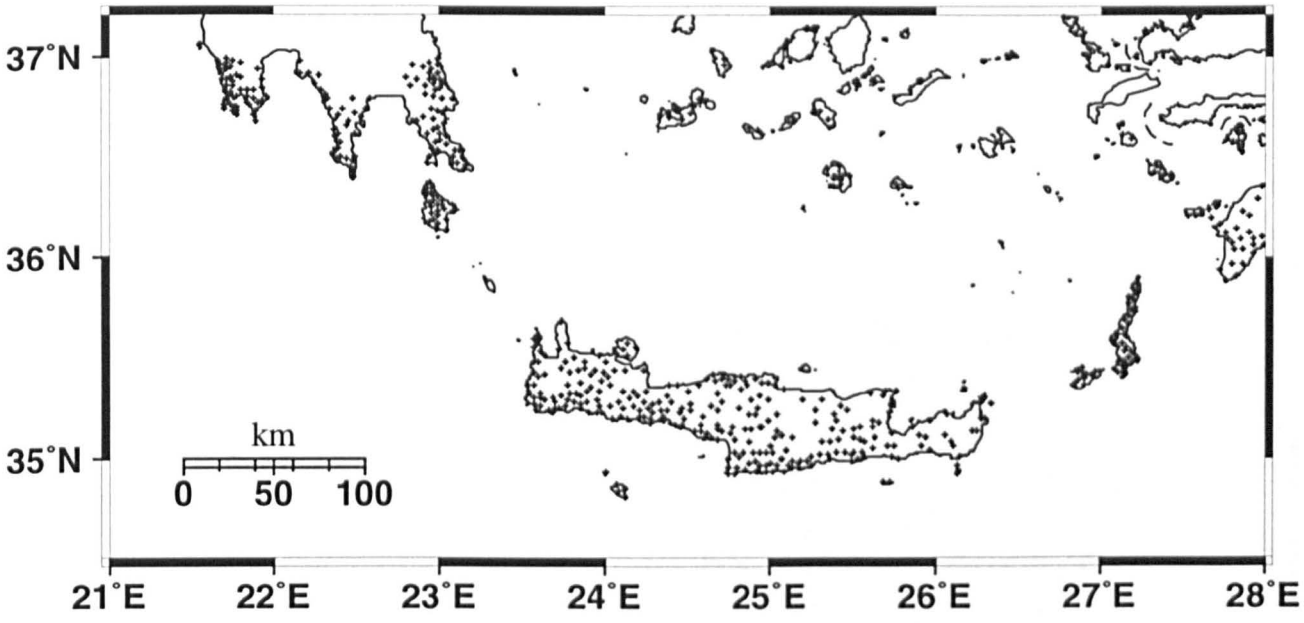

Figure 4.5: The locations of the 540 stations from the African Gravity Project used in this study.

4.3.4 The Satellite Gravity Data

4.3.4.1 Compilation

In June of 1995, all of the Geosat altimeter data were declassified by the United States Navy. These data were combined with the ERS-1 altimeter data to produce a high-density dataset across all of the world's oceans [*Sandwell and Smith*, 1997]. Free-air gravity anomalies are calculated directly from the gradient of the sea-surface. Prior to gridding, all along-track data were filtered to eliminate noise. As a result, the shortest resolvable wavelength is 20 km which is better than the Greek offshore gravity dataset. The satellite data exist as a grid, and the nodes at which the free-air anomaly has been calculated are shown in Figure 4.6.

4.3.4.2 Errors

Errors associated with the measurement of sea-surface gradient result in a theoretical random error of ±4 mGal in *FAA* [*Sandwell and Smith*, 1997]. So, as well as having a better spatial resolution, the satellite data are more precise than the Greek offshore gravity data. Also, satellite-derived gravity anomalies are absolute, so there are no problems related to drift or to datum errors. These data - which also cover the Aegean Sea - are used in favour of the Greek offshore gravity data. *Sandwell and Smith* [1997] compared the satellite data to profiles of conventional offshore data in the Atlantic

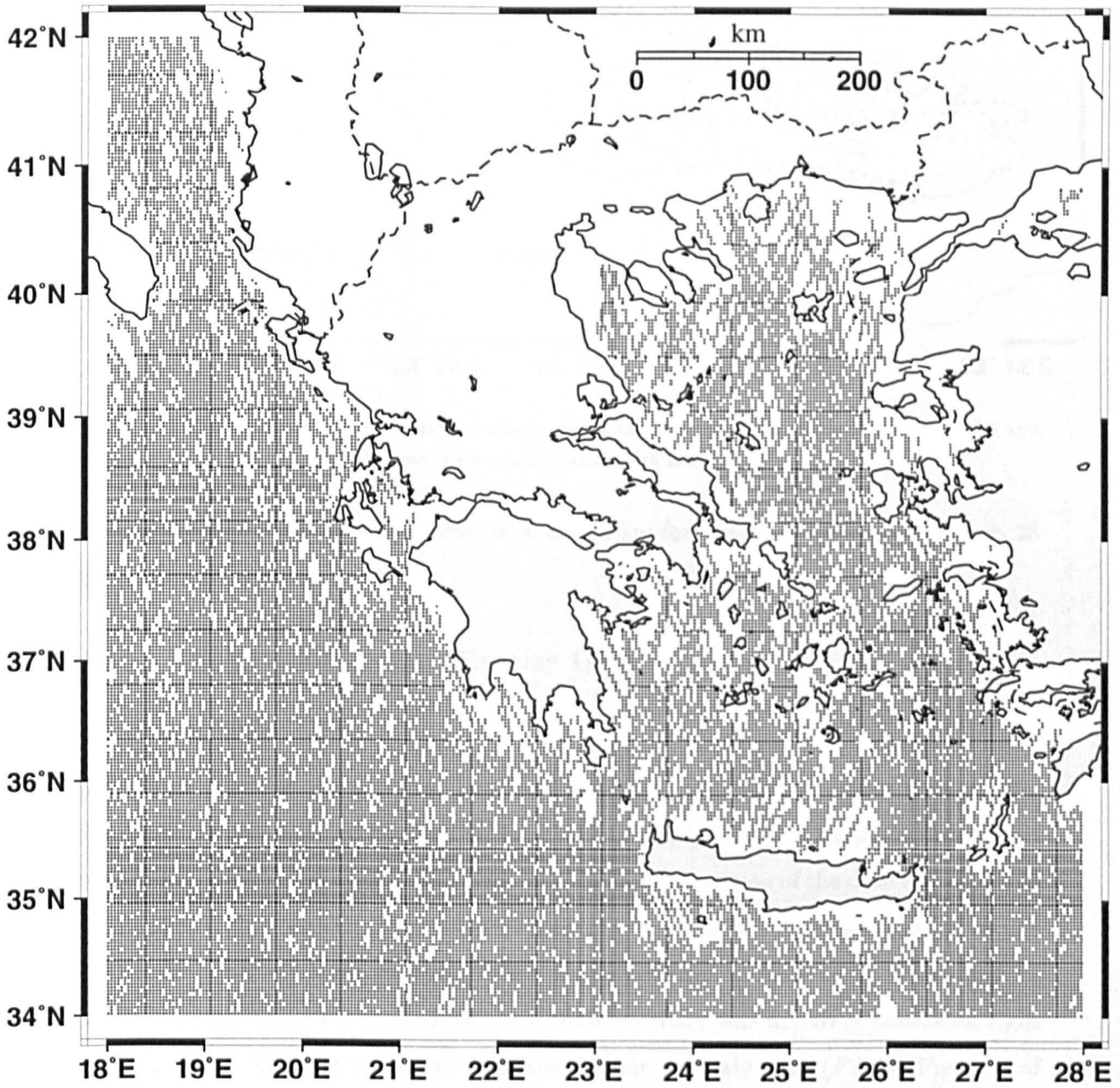

Figure 4.6: The 37356 locations of satellite free-air gravity anomaly values.

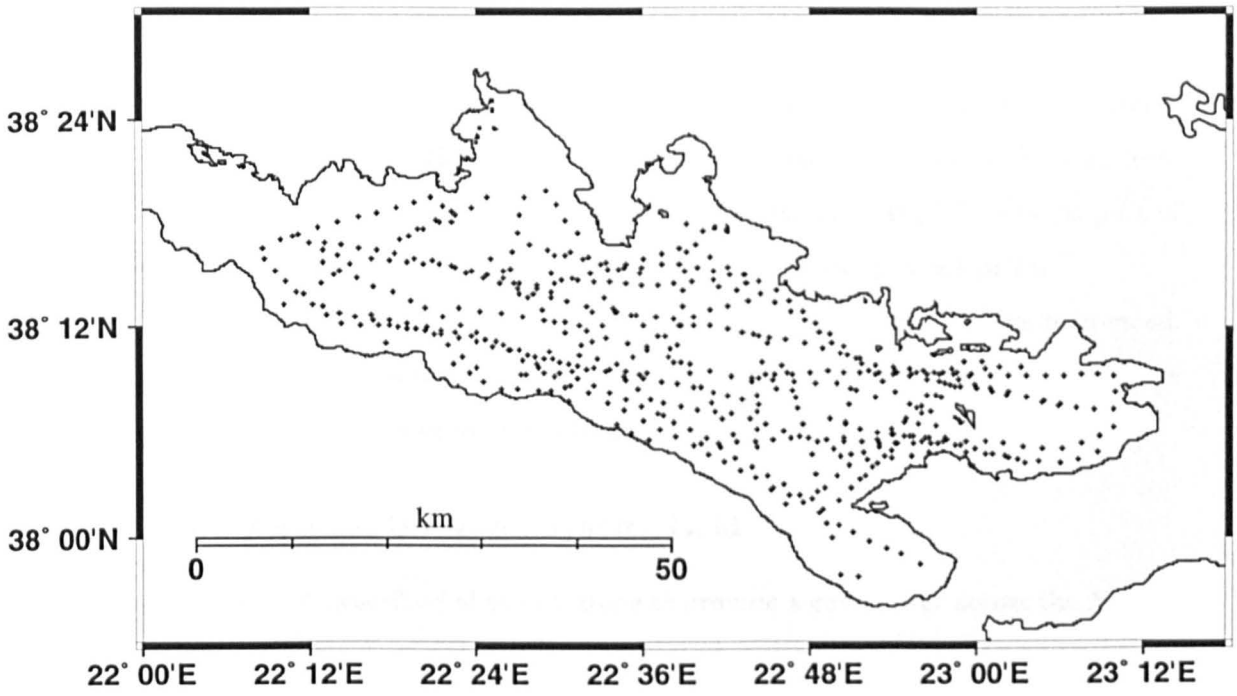

Figure 4.7: The location of the 544 gravity measurements made on the Gulf of Corinth where FAA and bathymetry are known. Measurements were made during 1982 and 1983.

Ocean, and found that the rms error is 3 to 6 mGal for wavelengths of greater than 20 km, as the theory suggests.

4.3.5 The Gulf of Corinth Gravity Data

4.3.5.1 Compilation

Gravity data across the Gulf of Corinth, the Gulf of Patras and further west around Kephalonia were collected during two cruises in the early 1980s. All reports and details concerning these surveys have since been lost, and only a portion of the data remain: that within the Gulf of Corinth. These were supplied by M. Brooks (formerly at the University of Cardiff, personal communication, 1996), though careful analyses and processing were required before these data could be used. Indeed, there was apparent confusion right from the start: the first presentation of the free-air anomaly data (FAA) (Figure 5 of *Brooks et al.* [1988]) is actually of the Bouguer anomaly. The points at which both FAA and bathymetry are known are shown in Figure 4.7.

4.3.5.2 Errors

The supplied Bouguer anomaly gravity values (BA) are not used in this study. Instead, BA is derived from FAA, so the errors in FAA are discussed here. As can be seen from Figure 4.7, many of the ship lines cross. A cross-over analysis was performed as part of the analyses. The mean cross-over error (ε_{cross}) in FAA is roughly ± 1 mGal.

A major problem with these data concerned the datum to which they are referenced. All records of the way in which the data were tied to gravity base stations on land are lost. This problem is returned to and solved in Section 4.10.3.

4.3.6 The Regional Bouguer Gravity Grid

The five data sources described above combine to provide a good cover across the Aegean Sea and mainland Greece. To extend the cover across the continental areas to the north and east, these data were merged with a regional gravity grid. This was supplied by GETECH, and comprises Bouguer values at a spacing of 5 minutes. Free-air gravity data were not available. The Bouguer gravity data are consistent with the IGSN71 standard, and are not reprocessed. No data exist across most of Turkey and the central parts of former Yugoslavia.

4.4 Resolution and Isostasy

From Fourier theory, the separation between adjacent gravity stations should be less than half the wavelength of the gravity signal which is to be resolved. Studies of isostasy analyse those gravitational signals originating from the moho. The coherence between gravity and topography (see Chapter 6) for a very weak lithosphere ($T_e = 5$ km) is predicted to be zero for wavelengths shorter than 50 km [*Forsyth*, 1985]. Thus, the onshore and offshore resolutions of 10 km and 20 km respectively should resolve the gravitational signal of the isostatic mechanism.

4.5 Gravity Fieldwork

New gravity data were collected during the summers of 1994 and 1995 to evaluate the quality of the existing data, and to check for datum shifts between separate sets. A single G-series LaCoste-Romberg gravity meter (serial number G-471), Magellan NAV 5000 PRO GPS receivers and AIR digital altimeters were deployed. The survey concentrated

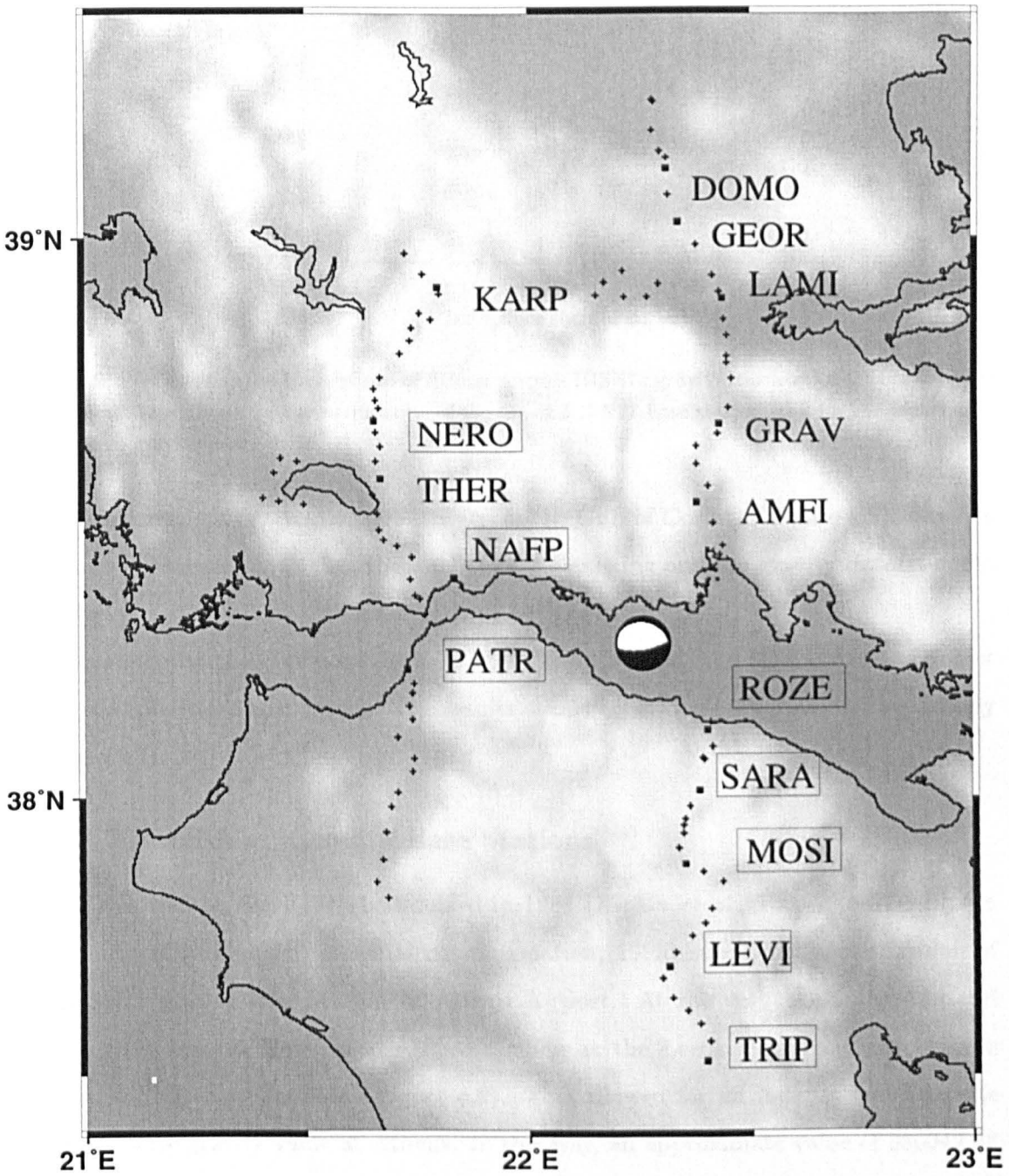

Figure 4.8: The location of the gravity stations occupied during the 1994 and 1995 field campaigns. The squares represent base stations, and those labelled with a box were established by myself. The CMT solution in the Gulf of Corinth is that for the Eigion earthquake (15 June 1995, $M_s = 6.5$).

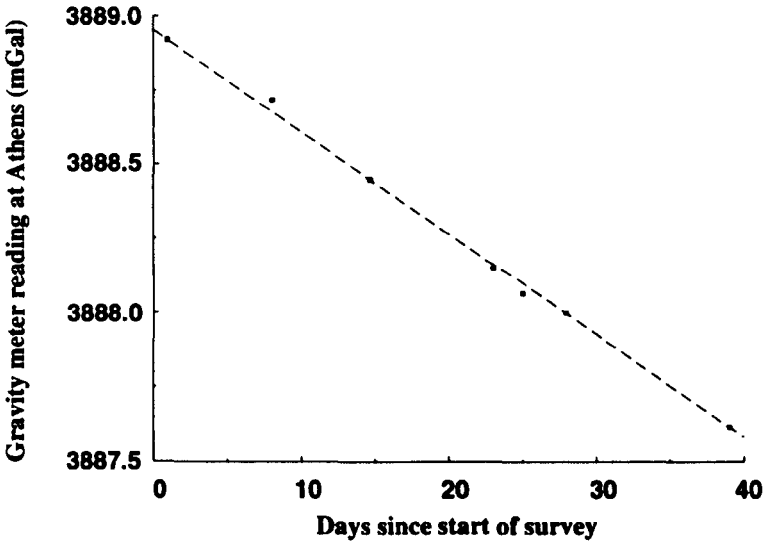

Figure 4.9: Plot showing the occupations of Athens Airport IGSN71 gravity base station during the 1995 field season. This allows for the verification of the Greek IGSN71 base station, and for the monitoring of long term gravity meter drift.

along two north-south trending profiles across the Gulf of Corinth (Figure 4.8). Gravity stations were located such that the quality of the existing onshore gravity dataset could be tested.

Subsequent to the Eigion earthquake of 15 June 1995 ($M_s = 6.5$), the stations closest to the epicentre were re-surveyed. The results of this experiment are presented separately (Appendix I).

4.5.1 Establishing Gravity Base Stations

Greece was tied to the IGSN71 standard in 1986 [*Hipkin et al.*, 1988], and R. Hipkin (University of Edinburgh, personal communication, 1995) supplied the description of the IGSN71 gravity base station at Athens Airport. At the very beginning and end of each field season, meter readings were made at the Leeds University and Athens Airport IGSN71 base stations (Figure 4.9). This allowed for an independent estimate of the absolute gravity value at Athens. In this way, an approximate value of 980042.63 mGal is obtained, so the quoted value of 980042.605±0.010 mGal [*Hipkin et al.*, 1988] is confidently adopted for this study.

Throughout mainland Greece there are two networks of gravity base stations: one for central Greece [*Lagios*, 1985], and one for the Peloponnese [*Georgadas and Lagios*, 1982]. Details of each were supplied by E. Lagios (University of Athens, personal communication, 1995). For the central Greece network, absolute gravity values were determined

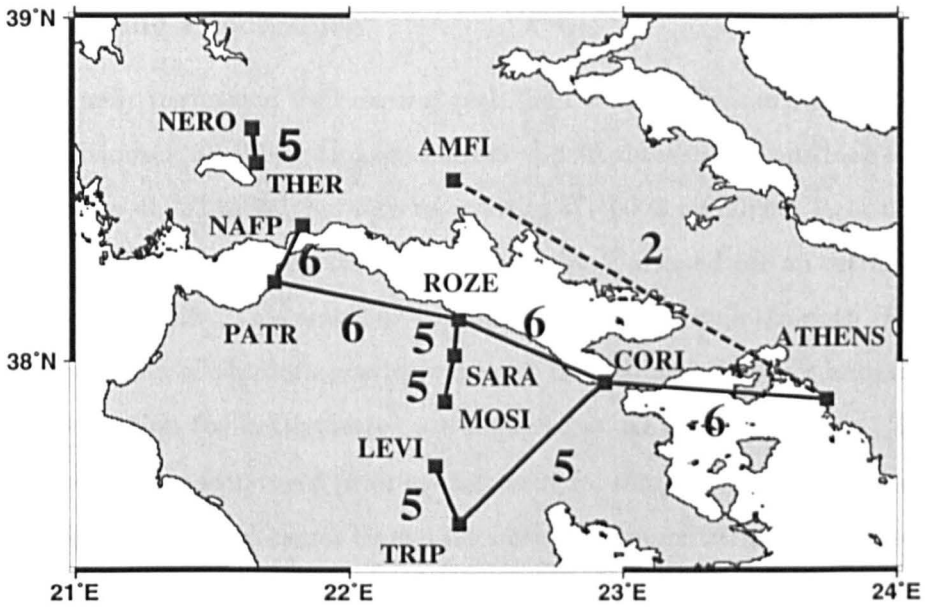

Figure 4.10: Gravity base station ties made during the 1994 and 1995 field campaigns. The numbers show the number of estimates for each gravity difference.

during 1982, and are given as differences relative to a Potsdam base station in Athens. However, details of this station have since been lost. Therefore, to obtain an IGSN71 gravity base-station network across central Greece, at least one of the stations had to be tied with Athens Airport. For the Peloponnese base station network, only site descriptions were supplied. Thus, every base station used throughout the Peloponnese had to be tied with Athens Airport (Figure 4.10). Base stations were located such that survey loop periods were less than three hours, and each is described in Appendix C.

Figure 4.10 shows how the base-stations used in this study were established. To establish an accurate tie it is necessary to average over 5 estimates, which requires six consecutive journeys between two base stations. This is therefore a time consuming process. Of the details supplied, the closest base station of the central Greece network to ATHENS is AMFI. The journey between these is 3 hours, and so establishing an absolute gravity value at AMFI directly from ATHENS was impractical. Thus, the central Greece network was tied to ATHENS at NAFP via PATR (requiring seven consecutive boat trips across the Gulf of Corinth), ROZE and CORI. Only one additional site (NERO) was necessary in Central Greece. In the Peloponnese, stations CORI and TRIP belong to the Peloponnese network [*Georgadas and Lagios*, 1982].

4.5.2 Surveying Proceedure

The gravity meter performed well during each field season. Precautions were made to minimise vibrations at all times, and the measured drift rates in any one loop varied from 0.012 mGal/hr to -0.022 mGal/hr, with an average of -0.002 mGal/hr. Reoccupations of the Athens Airport base station throughout the survey allowed for an estimate of long term gravity meter drift. This was found to be linear and $\sim$1 mGal/month (Figure 4.9).

For the reduction of absolute gravity values to free-air and Bouguer anomaly values, estimates of elevation (or bathymetry) are required at all gravity stations. The height above sea-level had been surveyed prior to this study for some of the gravity base stations. Additional elevation control comes from a network of trigonometric beacons, established by the Hellenic Military Geographic Service (HMGS). Their elevations above sea-level are quoted to the nearest metre on the 1:50,000 scale topographic maps.

To supplement these sites of elevation control, differential GPS surveying was carried out using Magellan NAV 5000 PRO GPS equipment. This requires the simultaneous recording of carrier phase data at two sites from the same four (or more) satellites. The accuracy of the position fix at a remote site will depend on the accuracy to which the control site coordinates are known. After recent GPS surveys [*Billiris et al.*, 1991; *Davies et al.*, 1997], a network of GPS sites exists throughout mainland Greece whose geodetic coordinates - referenced to the International Terrestrial Reference Frame 1989 (ITRF89) ellipse - are known with centimetric accuracy. The precise locations of a number of these were provided by G. Veis (National Technical University, Athens, personal communication, 1995), and were used as the first order control sites for this GPS surveying. Five second order GPS sites were established such that sites of elevation control (i.e., gravity base stations, trigonometric beacons and GPS sites) exist at regular intervals along the two north-south profiles. All have a clear view of the sky and can be easily reoccupied (Appendix D).

In this way, over 20% of the 112 gravity stations have elevation estimates accurate to $\pm$1.3 m. Elevations for the remaining gravity stations were estimated by single-base differential barometric levelling. Two digital AIR altimeters were deployed, and the air-pressure was sampled at 10 minute intervals at a single site of known elevation. Figure 4.11 shows a schematic representation of a typical day's barometric variation. Whenever possible, surveying was carried out during the morning and early afternoon when the rate of barometric change is most constant. Remote measurements at the regularly

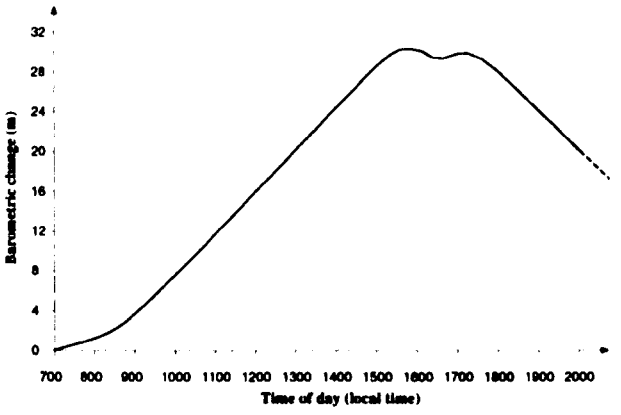

Figure 4.11: A schematic representation of recorded barometric variations during a typically warm and calm day.

spaced control points allowed for the calibration of the barometric curves.

The gravity surveying and the barometric levelling were carried out simultaneously, and loop periods were never greater than 3 hours. This regular reoccupation of gravity base stations throughout each day defined the drift of the gravity meter. The assumed meter drift curve was constructed from linear interpolations between successive base station readings.

4.6 Differential GPS Post-processing

All GPS data were initially post-processed in the field. The Magellan post-processing software uses the World Geodetic System 1984 (WGS84) ellipse as its reference. Subsequent to the fieldwork, the quoted ITRF89 coordinates for the first order sites were converted to WGS84[2]. Upon performing the conversions, it was found that the required correction vectors are less than 1 mm.

For a given satellite constellation, the accuracy of a differential GPS position fix is inversely proportional to the length of observation time. The Magellan post-processing software is capable of working with a maximum of 20 minutes of overlapping data. Further, the assumption of equal atmospheric delay at both sites breaks down for receiver separations greater than 50 km. In all cases, there was in excess of 15 minutes of overlapping data, and the average baseline length was 20 km. As the control site locations are known with centimetric accuracy, the accuracies of remote site geodetic coordinates

[2]The algorithm for this was supplied by D. Hawksbee, Trimble Navigation Europe Ltd., Hampshire, UK.

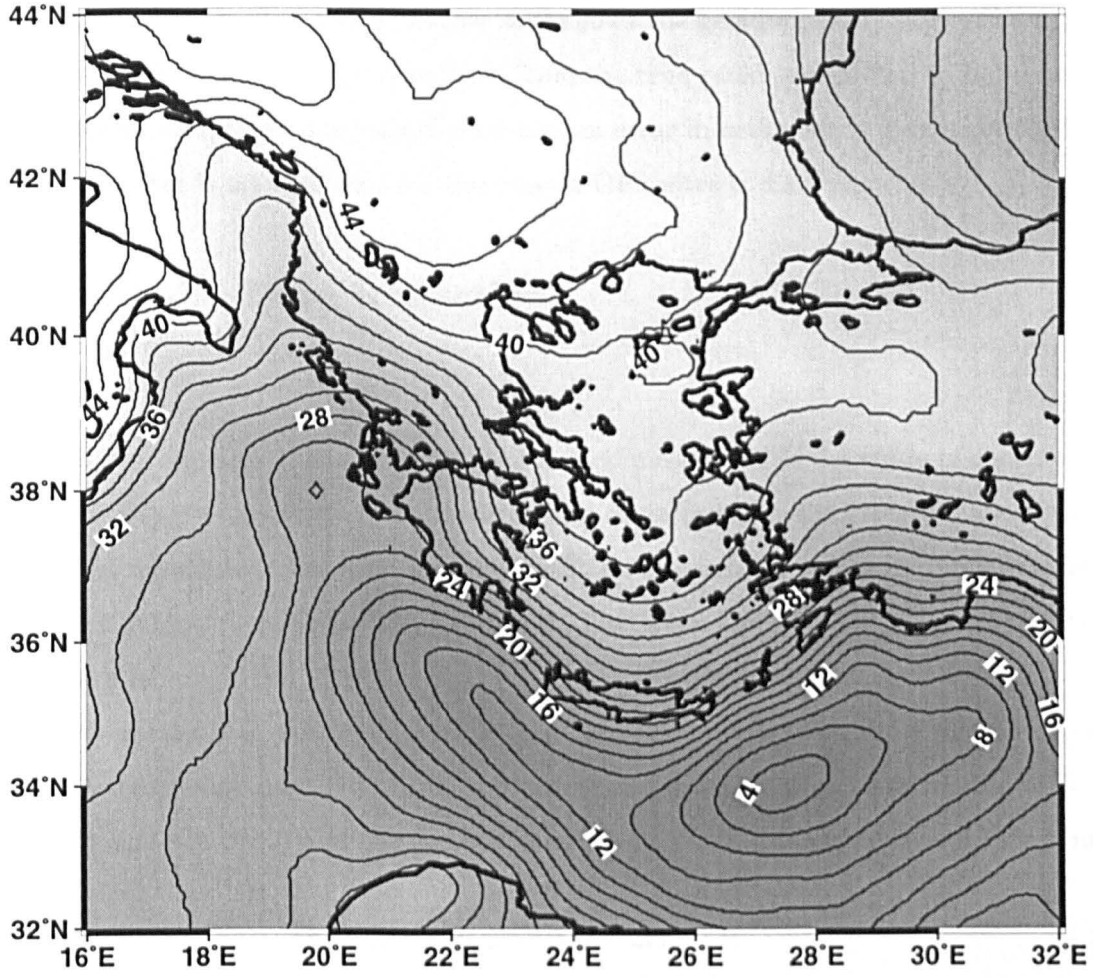

Figure 4.12: Height of the OSU91A geoid above the WGS84 reference ellipse.

are better than ±0.9 m [*Magellan*, 1992].

The repeatability of the GPS results was tested by the reoccupation of two baselines. The difference in the estimated geodetic heights were 5 cm and 1 cm. The absolute accuracy was tested over a baseline between two first order GPS sites. The quoted difference in geodetic elevation is 44.03 m, and the results from the post-processing gave a difference of 43.84 m. The manufacturer's claim of sub-metre accuracy appears to be justified.

The reduction of gravity data requires station elevations above the geoid (i.e., orthometric elevation). Consequently, the geoid anomaly must be subtracted from the geodetic heights obtained from the GPS. Various geoid models exist, and on the advice of G. Veis (personal communication, 1994), the Ohio State University geoid model of 1991 (OSU91A) was adopted. The algorithm for computing the height of this geoid above the WGS84 ellipse was supplied by D. Blitzkow (University of São Paulo, Brazil,

personal communication, 1994). Figure 4.12 shows the geoid anomaly map. The departure of the OSU91A model (Figure 4.12) from the true geoid is expected to be less than 1 m [*Hipkin*, 1995]. Subsequently, the maximum error in orthometric heights of the first order GPS sites is ±1.0 m, and for the remote GPS sites is ±1.3 m.

4.7 Gravity Data Reduction

4.7.1 Gravity Anomalies

The Bouguer anomaly is the quantity that is used most often in the study of continental tectonics. Despite this, there is a certain amount of confusion in the literature about what it actually represents. The true meaning must be understood before its interpretation, so the reduction procedure is fully described. The procedure laid out by *LaFehr* [1991b] is followed here.

The observed (i.e., absolute) gravity (g_{obs}) at each station is found by measuring the difference in gravity relative to a base station, and making corrections for the drift of the gravity meter (ΔD) and the gravitational effect of the sun and moon (ΔT)[3]. Thus,

$$g_{obs} = (MR_{stat} - MR_{base})c + g_{base} - \Delta D - \Delta T \tag{4.3}$$

where MR_{stat} and MR_{base} are gravity meter readings at the station and the base respectively, c is the calibration factor of the gravity meter and g_{base} is the IGSN71 absolute gravity value at the base station.

The free-air anomaly (FAA) is then found by subtracting the theoretical gravity value (g_ϕ) from g_{obs}, and adding the free-air correction (FAC) and the atmospheric gravity correction (δg_A) [*DMA*, 1987].

$$FAA = g_{obs} - g_\phi + FAC + \delta g_A \tag{4.4}$$

Onshore, FAA contains the gravitational signal of the rock between the gravity station and sea-level. That portion of the signal resulting from a rock density of 2670 kg/m^3 is removed with the Bouguer slab (or Bullard A) correction (BC), the curvature (or Bullard B) correction (CC) and the terrain (or Bullard C) correction (TC). CC is added to BC to modify the infinite slab to a spherical cap of radius 167 km [*LaFehr*,

[3]This leaves the gravitational effect of solid earth tides, which can be up to 15% of ΔT

1991a]. TC corrects for the gravitational effect of topography of density ρ_B about the upper surface of this cap.

A gravitational effect of rock between the station elevation and sea-level with a density other than 2670 kg/m^3 remains in the signal and must be dealt with at the interpretation stage. The only significance of the datum plane is that all of the mass below the datum contributes to BA, whereas only deviations from 2670 kg/m^3 are included above the datum. The statement that BA represents a reduction to sea-level (e.g., *Dobrin and Savit* [1988], *Telford, Geldart and Sheriff* [1990]) is therefore misleading.

In the offshore, FAA is highly correlated with bathymetry. *Sandwell and Smith* [1997] point out that the satellite free-air gravity data can be used to examine the topographic features associated with oceanic ridges and transform faults. This effect is removed in the calculation of BA. The combined BC and CC replace a curved slab of sea-water with rock of density 2670 kg/m^3, and TC corrects for topography on the lower surface of this slab. Thus, a signal from any lower density sea-bottom sediments will be present in the Bouguer anomaly.

The complete Bouguer anomaly for onshore gravity stations is given by

$$BA = g_{obs} - g_\phi + FAC + \delta g_A - (BC + CC) + TC \tag{4.5}$$

and for offshore gravity stations by

$$BA = g_{obs} - g_\phi + \delta g_A + (BC + CC) + TC \tag{4.6}$$

4.7.2 The Reduction Procedure

The most recent expression for g_ϕ was published in 1987 [*DMA*, 1987], and is the reference gravity field on the WGS84 ellipse,

$$g_\phi = 978032.67714 \frac{1 + 0.00193185138639 \sin^2 \phi}{\sqrt{1 - 0.00669437999013 \sin^2 \phi}} \tag{4.7}$$

where ϕ is the geodetic latitude.

Because the earth's radius is large compared to the elevations of gravity stations above sea-level (h), FAC has conventionally been taken as being proportional to h (Equation 4.8). However, *Robbins* [1981] shows that such an approximation results in artificial gravity anomalies which correlate with h, although the difference from Equation

4.8 at Aegean latitudes is nearly zero (and far less than sources of error in the data). Further, there has been recent discussion about the validity of the expression presented by *Robbins* [1981]. Consequently, Equation 4.8 is adopted.[4] .

$$FAC = 0.3086h \tag{4.8}$$

δg_A is an empirically derived expression for the gravitational attraction of the atmosphere (Equation 4.9) [*DMA*, 1987]. For the range of elevations in mainland Greece, δg_A varies between 0.7 and 0.9 mGal.

$$\delta g_A = 0.87e^{-0.116\left(h/1000\right)^{1.047}} \tag{4.9}$$

The infinite slab Bouguer correction is calculated for a Bouguer density (ρ_B) of 2670 kg/m^3. For onshore gravity stations,

$$BC = 2 \times 10^5 \pi G \rho_B h \tag{4.10}$$

and for offshore gravity stations,

$$BC = 2 \times 10^5 \pi G (\rho_B - \rho_w) b \tag{4.11}$$

where ρ_w is the density of sea-water (taken here at 1030 kg/m^3) and G the gravitational constant. Onshore, BC is equivalent to a gradient of 0.1119 mGal per metre of topography, and offshore to 0.0688 mGal per metre of bathymetry (b).

The curvature correction is rarely referred to in the literature, though *LaFehr* [1991a] presents an approximation that is accurate to $\sim$1 μGal at a latitude of 45^o (Equation 4.12).

$$CC = 1.46308 \times 10^{-3}h - 3.52725 \times 10^{-7}h^2 + 5.1 \times 10^{-14}h^3 \tag{4.12}$$

[4]All parameters in the gravity reduction formulae are in SI units, apart from values of gravity which are in mGal.

Although not discussed by *LaFehr* [1991b], the offshore CC is given by

$$CC = \frac{\rho_B - \rho_w}{\rho_B}\left(1.46308 \times 10^{-3}b - 3.52725 \times 10^{-7}b^2 + 5.1 \times 10^{-14}b^3\right) \tag{4.13}$$

This expression for CC is for a spherical cap out to 167 km. *LaFehr* [1991a] shows that CC is positive for a slab thickness less than ~4150 m. For the elevations and bathymetries encountered across this study area, CC is always positive and ranges between 0 and 1.4 mGal.

4.7.3 The Gravity Terrain Correction

To ensure compatibility with this reduction procedure, TC must also be calculated out to a distance of 167 km on a curved earth. Topography beyond this distance is ignored as its gravitational effect is negligible compared to other errors in the BA. This is a convention recommended by *LaFehr* [1991b].

Terrain corrections were supplied with the Greek onshore and the AGP data, though there is no record of how they were calculated. Further, it is probable that they were calculated differently for each sub-set. Terrain corrections were not available for either the satellite or the Gulf of Corinth data. To ensure the six separate datasets are compatible, their terrain corrections must be calculated in the same way.

As part of this thesis, a FORTRAN77 programme was written to calculate the terrain corrections from the DEMs for a curved earth out to a distance of 167 km. The programme is presented in Appendix E. The best DEM available has a resolution of 2 km. This was resampled to a 1 km grid using the GRDSAMPLE algorithm of GMT, and TC is calculated for the topography between 1 and 167 km from each gravity station.

The major error in TC will therefore result from omitting the immediate topography about each gravity station. On a flat earth, the TC is always positive. Although this is not the case for a curved earth, the omitted TC for the 1 km surrounding each station will be positive, so the error is not strictly random.

To estimate the errors, I consider a synthetic topography out to 1 km and calculate its gravitational attraction. This is shown in Figure 4.13a. In a cylindrical coordinate system (r, z, θ), the vertical gravitational attraction of an element of volume $\delta r \delta z \delta \theta$ and

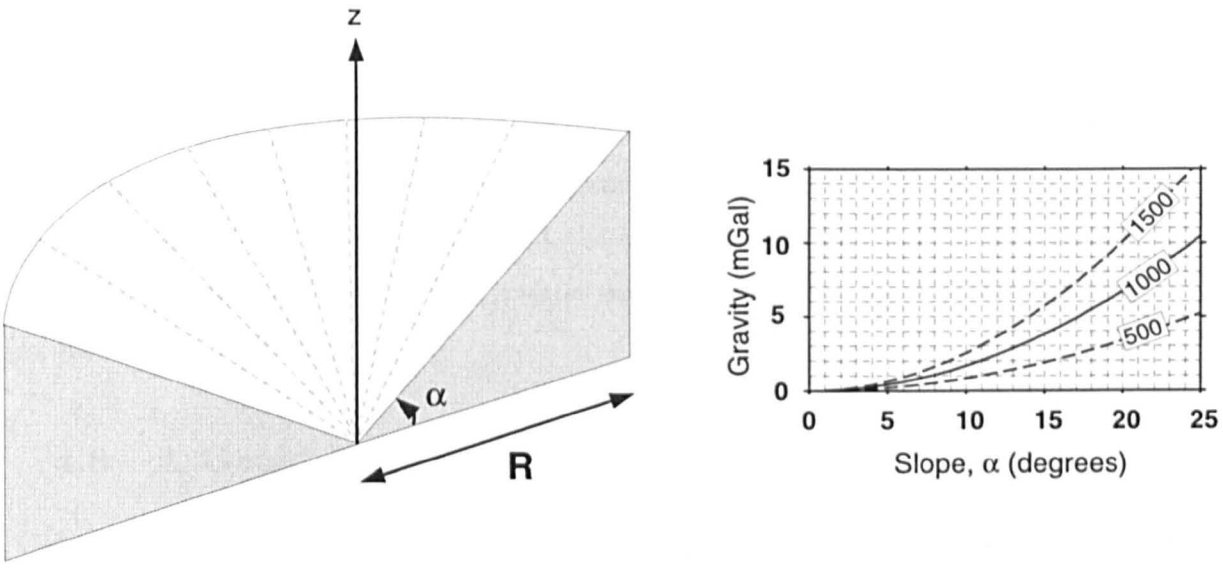

(a) (b)

Figure 4.13: (a) Sketch of half of the sloping topography used to estimate the error in the terrain correction. (b) The error in the terrain correction as a function of topographic slope, for the R = 500, 1000 and 1500 m.

density ρ_B at a distance $(z^2 + r^2)^{\frac{1}{2}}$ is given by

$$\Delta g_{element} = \frac{10^5 \times G\rho_B rz}{(z^2 + r^2)^{\frac{3}{2}}} \delta\theta\delta z\delta r \ . \tag{4.14}$$

This is then integrated through the topography shown in Figure 4.13 (Equation 4.15).

$$\Delta g_{topo} = \int_0^R \int_0^{r\tan\alpha} \int_0^{2\pi} \frac{10^5 \times G\rho_B rz}{(z^2 + r^2)^{\frac{3}{2}}} d\theta dz dr \ . \tag{4.15}$$

The result is an expression for the vertical gravitational attraction as a function of its slope (α) and its radius (R).

$$\Delta g_{topo} = 2\pi \times 10^5 G\rho_B R\left(\frac{1 - (1 + \tan^2\alpha)^{\frac{1}{2}}}{(1 + \tan^2\alpha)^{\frac{1}{2}}}\right) \tag{4.16}$$

The curve of Equation 4.16 is shown in Figure 4.13b. The 1:50000 topographic maps indicate that the topographic slope in the 1 km surrounding any one point rarely exceeds 20°. From Figure 4.13, if the topography dips in all directions by this amount the maximum error in the estimated TC is ~7 mGal.

The error in TC is greatest in mountainous regions where gravity stations are located

on steep slopes and in valleys (though usually on the flattest portions). These are equivalent as far as the terrain correction is concerned, so a more realistic representation of the topography in the inner 1 km might be a single gradient. The gravitational effect of this is approximately half that of the cone described above. Thus, the error in the TC is taken to be 4 mGal. Note that the actual error will be less for the offshore, as the density is lower and the bathymetric variations are more remote from the point of observation.

4.8 A Geoid Height Correction

Conventionally, all gravity reduction procedures stop here, and many are not as thorough as that presented above. g_ϕ is the theoretical gravity value *on the WGS84 reference ellipse*. A further FAC, BC and CC should be made for the height of the geoid above the ellipse, N. (TC due to the geoid undulation is negligible.) After Equations 4.4 and 4.5 or 4.6 have been applied, a geoid height correction (g_N) should be subtracted for positive N.

$$g_N = 0.3086N - (2 \times 10^5 \pi G \rho_B N + 1.46308 \times 10^{-3} N \\ -3.52725 \times 10^{-7} N^2 + 5.1 \times 10^{-14} N^3) \quad (4.17)$$

However, this correction is not a standard one. Papers on the meaning of the Bouguer anomaly [*Chapin*, 1996; *Ervin*, 1977] and on standardisation in gravity data reduction [*LaFehr*, 1991b] make no reference to it. Moreover, the wavelength of the correction is far greater than features of interest, so it is not adopted in this study.

4.9 Reprocessing the Pre-existing Gravity Data

Five different data sources are to be processed: the new data collected during 1994 and 1995, the Greek onshore data, the AGP data, the satellite data, and the Gulf of Corinth data. To ensure that these can be merged to form one dataset, the four pre-existing datasets must be re-processed.

The Greek onshore gravity data and the AGP data were supplied with g_{obs} and h. The satellite gravity data are supplied as gridded FAA, so b was found by interpolating the DEM to these grid nodes using the GRDTRACK algorithm of GMT. Finally, the

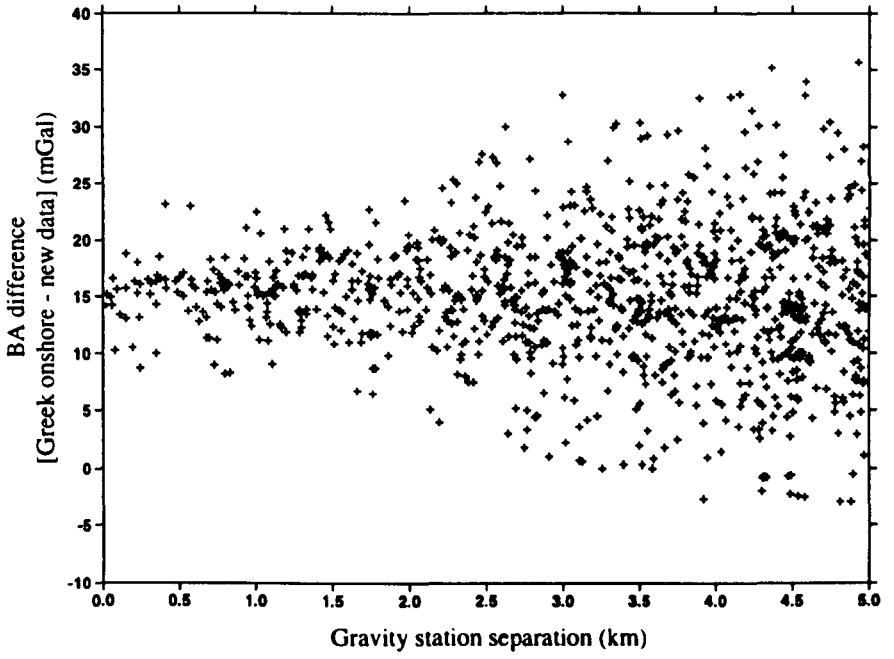

Figure 4.14: A plot of the difference between the complete Bouguer anomaly values of the new and the pre-existing gravity data, as a function of station separation. As the station separation approaches zero, this difference narrows and converges on a value of roughly 14 mGal.

Gulf of Corinth data were supplied as FAA and b data points. From these gravity and elevation/bathymetry data, reduction was carried out as described in Section 4.7.

4.10 Datum Shifts

4.10.1 Greek Onshore Gravity Data

By comparing BA values of the regional onshore gravity data sub-set [*Makris*, 1977] against those of the subsequent denser surveys, it is clear that the sources comprising the Greek gravity dataset are all referenced to the same datum. However, when compared to the new onshore BA data, the pre-existing data were found to be ~14 mGal too large (Figure 4.14).

There are three separate points where the separation in Figure 4.14 is zero, and the quoted and measured g_{obs} values differ by 14.142, 14.194 and 14.390 mGal. The best estimate of the datum shift is the average of these: 14.242 ±0.01 mGal (i.e., the error in the datum shift, (ε_{shift}), is ±0.01 mGal).

The obsolete Potsdam System is known to be ~14 mGal too high [*Morelli et al.*, 1974], and Greece was tied to the IGSN71 network in 1986 [*Hipkin et al.*, 1988]. Although *Lagios et al.* [1994] state that this datum correction has since been made, I show here

that this seems unlikely (Figure 4.14). Thus, 14.242 mGal were subtracted from all g_{obs} values of the Greek onshore gravity data.

4.10.2 Satellite and Greek Offshore Gravity Data

Analysis to check the reference datum of the satellite gravity data is not required. However, BA values were computed for the Greek offshore gravity data by adding δg_A, CC and TC to the supplied simple Bouguer anomaly values. Profiles through these and the satellite BA data are compared in Figure 4.15. As expected, the satellite gravity values show a better spatial resolution. Furthermore, there is no dc shift between the two datasets. The Greek offshore data are thus referenced to the IGSN71 datum.

4.10.3 Gulf of Corinth Gravity Data

A similar analysis was undertaken for the Gulf of Corinth data, and the result is shown in Figure 4.16. The situation is less clear as there is no apparent narrowing as the station separation decreases. The average difference is 8.3 mGal. As these data were collected before Greece was tied to the IGSN71 network, it is probable that the Gulf of Corinth data are referenced to the Potsdam datum.

The question to address is 'What accounts for the 6 mGal difference with respect to an expected shift of 14 mGal?' Seismic reflection profiles in the Gulf of Corinth have penetrated to depths of ~1 km beneath the sea-bed and have not imaged Mesozoic basement [*Brooks and Ferentinos*, 1984]. There will be a signal from these sediments in the BA data. If this 1 km of sediment - which *Brooks and Ferentinos* [1984] assumed to be Quaternary in age - has an average density contrast of 250 kg/m^3, then from Equation 4.10, the gravitational effect with respect to the Bouguer density will have a maximum negative amplitude of 10 mGal. The sediment thickness at distances greater than 5 km from the shore is likely to be thicker than 1 km. However, it is clear that the apparent 6 mGal anomaly is easily explained. Detailed gravity modelling across the Gulf of Corinth is undertaken in Chapter 5.

4.11 Error Analysis

The final dataset comprises six different sources. The errors in each are different and are independently assessed. In all cases, the final error estimate represents the maximum

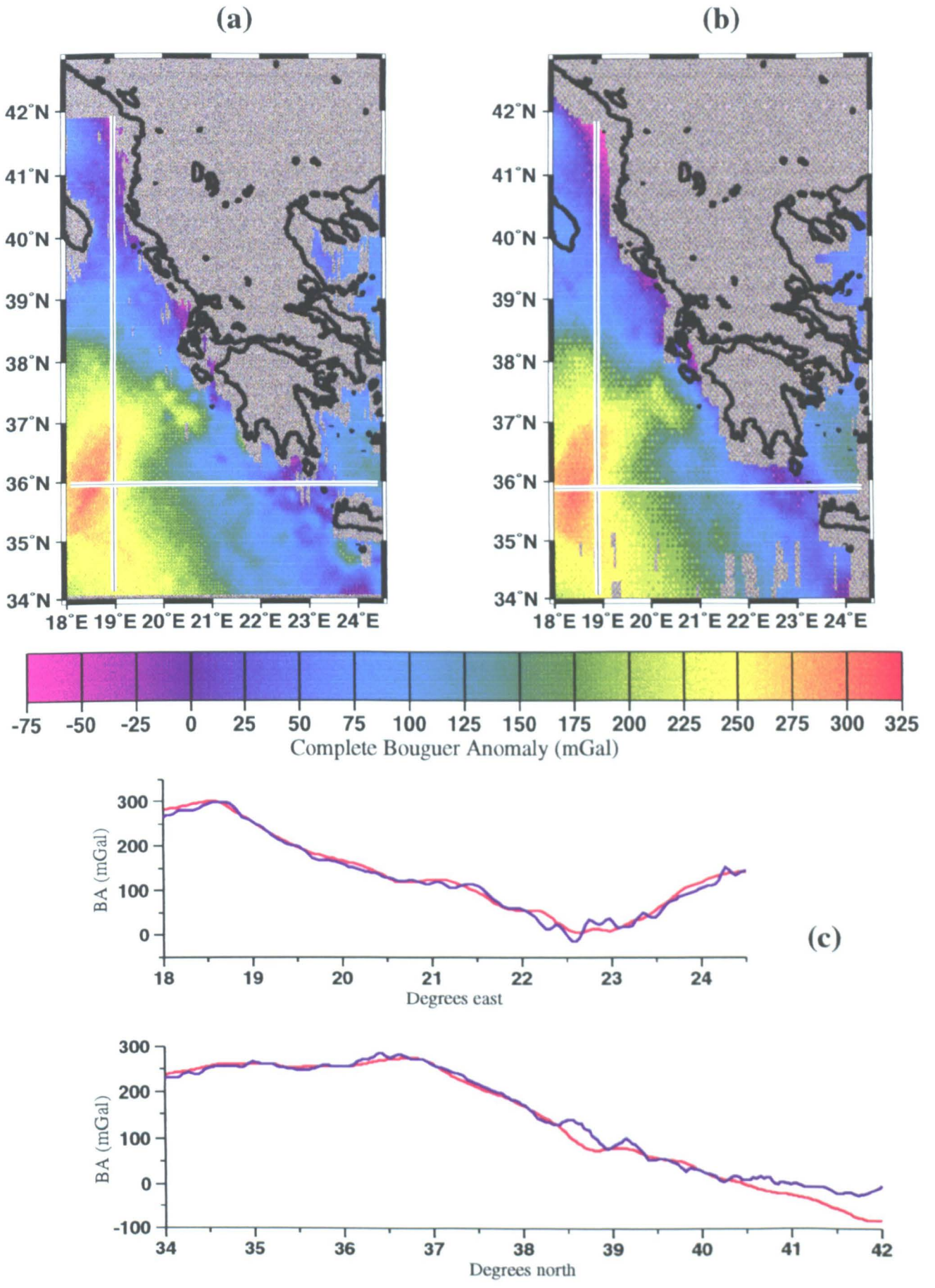

Figure 4.15: (a) Satellite Bouguer anomaly map. (b) Greek offshore Bouguer anomaly map. (c) Profiles through the Greek offshore (red) and satellite (red) Bouguer anomaly data. The latter displays superior resolution.

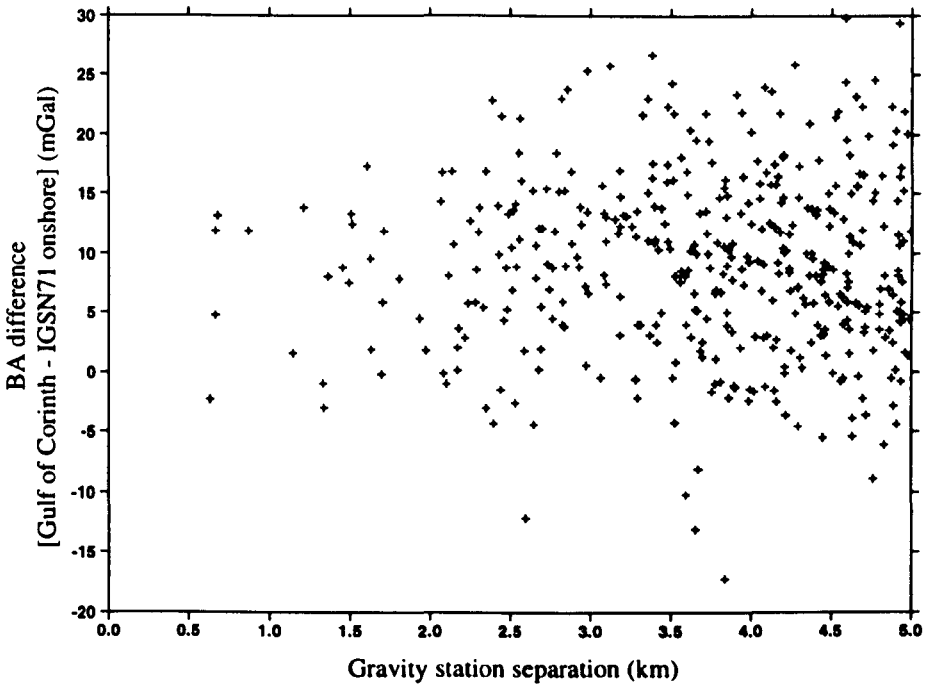

Figure 4.16: A plot of the difference between the IGSN71 Bouguer anomaly values of the onshore (combined new and pre-existing) and Gulf of Corinth Bouguer anomaly values.

Source	New	Old Onshore	AGP	Satellite	Gulf of Corinth
ε_{FAA}	±0.5	±0.6	±0.6	±4.0	±1.0
ε_{BA}	±4.0	±4.0	±4.0	±6.0	±4.2

Table 4.1: The total error in the Bouguer and free-air gravity anomaly values, in mGal.

random error. Figure 4.17 summarises the sources of error in the gravity measurements, and Table 4.1 summarises the results of the error analysis.

4.11.1 Errors in the New Onshore Gravity Data

Each of the terms in Equations 4.4 and 4.5 have errors associated with them. The error in the observed gravity value (ε_{obs}) is assessed by considering the errors in each of the terms in Equation 4.3. At both the base station and the gravity station, meter readings were made until two were in agreement to within ±0.005 mGal. The error in the Athens IGSN base station value (ε_{ATH}) is ±0.01 mGal [*Hipkin et al.*, 1988], and all other base station gravity differences relative to Athens have an error of less than ±0.01 mGal. Thus, the maximum error in the g_{base} values (ε_{base}) is ±0.014 mGal. Loop periods were never greater than 3 hours, so assuming that the meter drift was linear on this time-scale, the maximum error in ΔD (ε_D) is ±0.005 mGal. Finally, *Cartwright and Tayler*

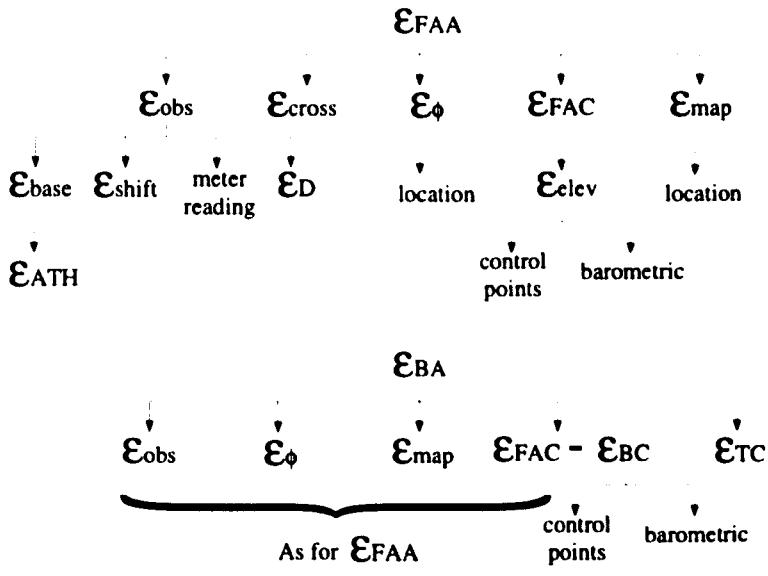

Figure 4.17: The contributions to the error in the gravity anomaly values. Symbols are explained in the text.

[1971] show that the error in ΔT is only significant adjacent to oceans with a large tidal range. As the Gulf of Corinth and the Aegean Sea have a low tidal range, this effect is considered negligible. Thus,

$$\begin{aligned} \varepsilon_{obs} &= \pm\sqrt{0.005^2 + 0.014^2 + 0.005^2} \\ &= \pm 0.016 \text{ mGal} . \end{aligned} \tag{4.18}$$

The WGS84 latitude and longitudes of each station were established with single Magellan GPS receivers, accurate to ±20 m (or ±0.0002°) [Magellan, 1992]. This results in two errors. Firstly, from Equation 4.7, a location error of ±0.0002° would result in a maximum error in the WGS84 reference ellipse gravity (ε_ϕ) of ±0.017 mGal. A second error results from the gravity anomaly value being mapped at a location shifted from the true location of that anomaly (ε_{map}). From Figure 4.14, the maximum gradient in the BA is ~4 mGal/km, so ε_{map} is ±0.08 mGal.

Over 20% of the gravity stations are located at either GPS sites (first order and second order), trigonometrical beacons or surveyed gravity base stations. There are two types of error to consider here. Firstly, systematic errors will exist due to lateral variations in air pressure across the field area. This was responsible for observed discrepancies of up to 10 m where remote readings were made at control sites. These systematic errors were corrected for by calibrating the drift curves at locations of pre-determined elevation.

Random errors were estimated by observing the scatter of the points about a smooth (usually linear - see Figure 4.11) trend. Such scatter is due to localised rapid fluctuations in air pressure, and as such would not correlate with similar variations at the remote site. The associated random error is estimated at ±0.5 m. The maximum random error associated with the elevation estimates is therefore

$$\begin{aligned} \varepsilon_{elev} &= \pm\sqrt{1.3^2 + 0.5^2} \\ &= \pm 1.4 \text{ m} . \end{aligned} \tag{4.19}$$

This error will effect two terms in Equation 4.4, four in Equation 4.5 and three in Equation 4.6. However, the errors in CC and δg_A are negligible, and the error in FAC (ε_{FAC}) and BC (ε_{BA}) - ±0.463 mgal and ±0.168 mGal - partially cancel.

The errors in TC were discussed in Section 4.7.3, and although the estimate of 4 mGal is not random, it shall be considered here as ±4.0 mGal such that the theory of error propagation may be applied. Thus, the errors in FAA and BA for the new gravity data are given by

$$\begin{aligned} \varepsilon_{FAA} &= \pm\sqrt{\varepsilon_{obs}^2 + \varepsilon_{\phi}^2 + \varepsilon_{map}^2 + \varepsilon_{FAC}^2} \\ &= \pm\sqrt{0.016^2 + 0.017^2 + 0.08^2 + 0.463^2} \\ &\approx \pm 0.5 \text{ mGal} \end{aligned} \tag{4.20}$$

and

$$\begin{aligned} \varepsilon_{BA} &= \pm\sqrt{\varepsilon_{obs}^2 + \varepsilon_{\phi}^2 + \varepsilon_{map}^2 + (\varepsilon_{FAC} - \varepsilon_{BC})^2 + \varepsilon_{TC}^2} \\ &= \pm\sqrt{0.016^2 + 0.017^2 + 0.08^2 + (0.463 - 0.168)^2 + 4.0^2} \\ &\approx \pm 4.0 \text{ mGal} . \end{aligned} \tag{4.21}$$

The error in the Bouguer anomaly is dominated by that in the terrain correction.

4.11.2 Errors in the Greek Onshore Gravity Data

The errors in the existing Greek onshore gravity data are calculated in a similar way. As the gravity surveying may have been carried out less precisely, the error in the Potsdam observed gravity value from Section 4.3.1 - ±0.035 mGal - is adopted. Additional errors in the observed gravity are ε_{ATH} (±0.01 mGal) and ε_{shift} (±0.01 mGal). The error in

the observed gravity is therefore

$$\begin{aligned}\varepsilon_{obs} &= \pm\sqrt{0.035^2 + 0.01^2 + 0.01^2} \\ &= \pm 0.038 \text{ mGal} .\end{aligned} \tag{4.22}$$

Also, as the barometric surveying may have been less precise, the elevation error of ±2.0 m is also used here, resulting in values for ε_{FAC} and ε_{BA} of ±0.617 mGal and ±0.224 mGal.

The values for ε_{ϕ} (±0.017 mGal), ε_{map} (±0.08 mGal) and ε_{TC} (±4.0 mGal) are taken from Section 4.11.1. The errors in the FAA and the BA for the Greek onshore gravity data are

$$\begin{aligned}\varepsilon_{FAA} &= \pm\sqrt{0.038^2 + 0.617^2 + 0.017^2 + 0.08^2} \\ &\approx \pm 0.6 \text{ mGal}\end{aligned} \tag{4.23}$$

$$\begin{aligned}\varepsilon_{BA} &= \pm\sqrt{0.038^2 + (0.617 - 0.224)^2 + 0.017^2 + 0.08^2 + 4.0^2} \\ &\approx \pm 4.0 \text{ mGal} .\end{aligned} \tag{4.24}$$

4.11.3 Errors in the AGP Data

Few details were provided with the AGP data. The reprocessing procedure is identical to that for the Greek onshore gravity data, so the magnitude of error is assumed to be the same.

4.11.4 Errors in the Satellite Gravity Data

The error in FAA is given by *Sandwell and Smith* [1997] as ±4.0 mGal (see Section 4.3.2.2). To find the error in BA, estimates of ε_{BC} and ε_{TC} must be made. The bathymetry offshore was found from the DEMs, using the GRDTRACK algorithm in GMT. Error in the bathymetry estimate (ε_b) will occur due to smoothing, and were assessed by comparing the estimated values at the elevations of the new gravity data, known to ±1.4 m. ε_b is seen to be very large: up to ±50 m.

Using a slab formula (Equation 4.11), the value for ε_{BC} would be ~3.5 mGal. However, this will be corrected for by the TC for distances greater than 1000 m. Thus, ε_{BC} is equivalent to the gravity of a vertical cylinder of radius (R) 1000 m. The expression

for this is found by changing the limits of integration in Equation 4.15, and using a different density.

$$\Delta g_{topo} = \int_0^R \int_d^{d+\varepsilon_b} \int_0^{2\pi} \frac{10^5 G(\rho_B - \rho_w) r z}{(z^2 + r^2)^{\frac{3}{2}}} d\theta dz dr \ . \tag{4.25}$$

If bathymetry is an overestimate of the true water depth (d), (i.e., ε_b = 50 m) then

$$\varepsilon_{BC} = \pm 2 \times 10^5 \pi G(\rho_B - \rho_w)\left(\varepsilon_b + \sqrt{d^2 + R^2} - \sqrt{(\varepsilon_b + d)^2 + R^2}\right) . \tag{4.26}$$

and if b is and underestimate (ε_b = -50 m),

$$\varepsilon_{BC} = \pm 2 \times 10^5 \pi G(\rho_B - \rho_w)\left(|\varepsilon_b| + \sqrt{(d - |\varepsilon_b|)^2 + R^2} - \sqrt{d^2 + R^2}\right) . \tag{4.27}$$

The average water depth across the Aegean Sea is ~1000 m (Figure 4.1). So, for a true water depth d = 1000 m, both equate to ±1.0 mGal.

It is noted here that the same correcting effect of TC also applies for onshore gravity data. However, topography here occurs on the upper-surface of the spherical cap so d is zero and $\varepsilon_h \ll R$. It is seen that the expression for ε_{BC} will approximate that of an infinite slab of thickness ε_h.

The error in TC for a given slope (α) will be less than that onshore because of the difference in density and because the bathymetric variations are more distant. However, the same value of ±4.0 mGal will be used. Assuming ε_{map} is negligible, the error in the BA is calculated as

$$\begin{aligned} \varepsilon_{BA} &= \pm\sqrt{4.0^2 + 1.0^2 + 4.0^2} \\ &\approx \pm 6.0 \text{ mGal} \ . \end{aligned} \tag{4.28}$$

4.11.5 Errors in the Gulf of Corinth Gravity Data

The cross-over error (ε_{cross}) in the supplied FAA is ±1 mGal (Section 4.3.5.2). Further errors are ε_{ATH} (±0.01 mGal), ε_{base} (±0.04 mGal) and ε_{shift} (±0.01 mGal), such that

$$\begin{aligned} \varepsilon_{FAA} &= \pm\sqrt{1.0^2 + 0.01^2 + 0.014^2 + 0.01^2} \\ &\approx \pm 1.0 \text{ mGal} \ . \end{aligned} \tag{4.29}$$

Equitorial radius (km)	6378206.4
Square of eccentricity	0.00676866
Meridian of projection	21.0 °E
Scale of meridian	0.996
False Easting (km)	500.0
False Northing (km)	-3499.72

Table 4.2: The parameters used for converting latitude and longitude in to TM coordinates.

The supplied bathymetry was estimated using sonar depth sounding but estimates of the error were not supplied. However, errors are expected to result from non-vertical reflections. Seismic profiles reveal a smooth shape to the floor of the Gulf, with a maximum dip (α) of around 15° [*Higgs*, 1988]. The average water depth (d) in the area of the survey is ~600 m. Thus, the error in depth is calculated as

$$\begin{aligned} \varepsilon_b &= dcos\alpha - d \\ &\approx 20 \text{ m} . \end{aligned} \tag{4.30}$$

Although this error is only ever negative, the maximum error is taken as ±20 m.

The error in BC is calculated in a similar way to Section 4.11.4. Using ε_b as 20 m and d as 600 m, Equation 4.27 equates to 0.7 mGal. Thus, assuming a 4 mGal TC error, the BA error is calculated as

$$\begin{aligned} \varepsilon_{BA} &= \pm\sqrt{1.0^2 + 0.7^2 + 4.0^2} \\ &\approx \pm 4.2 \text{ mGal} . \end{aligned} \tag{4.31}$$

4.12 Gravity Anomaly Maps and Profiles

This section presents maps of the Bouguer and free-air gravity data that are used throughout the rest of the thesis. The data have been transformed into Transverse Mercator (TM) coordinates using the parameters shown in Table 4.2.

Flexural isostasy has been shown to depend on wavelength. Short wavelength loads are supported by the strength of the plate, whereas large wavelength loads are isostatically compensated. Intermediate wavelength loads are only partially supported, and the wavelength of transition is a function of T_e. Therefore, uncompensated surface loads will be associated with (or *coherent* with) free-air gravity anomalies, and compensated

surface loads will be coherent with Bouguer anomalies. It will be shown in Chapter 6 that, with the additional consideration of sub-surface loads, this idea can be used to systematically estimate lithospheric rigidity across a region. A qualitative examination is performed here prior to the application of the numerical techniques.

4.12.1 The Free-Air Anomaly

Figure 4.18 shows the map of FAA for the five combined datasets across the Aegean. A contoured version of this and the Bouguer gravity map are presented in Appendix G. The most obvious feature is the deep low immediately south of the Aegean continental lithosphere. FAA values decrease to less than -200 mGal to the south of the Peloponnese (see Profiles 1 and 2 of Figure 4.20), and these are likely to be maintained on such a broad wavelength by the stresses associated with plate subduction.

Coherence between FAA and topography is clearly observed for short wavelength positive topographic features through the eastern half of mainland Greece that correspond to the peaks of broadly elevated regions. Values decrease away from the peaks, indicating isostatic compensation at longer wavelengths.

Sedimentary rift basins are seen in the FAA as short wavelength, negative anomalies. The Gulf of Corinth and Gulf of Evvia rifts are clearly observed, as are the NNW striking rifts on the southern Peloponnese. This is due to the combined effect of low/submerged topography and the low density sedimentary infill. The gravity across the rift basins of central Greece is examined in Chapter 5.

The FAA across the Hellenides is negative. Values decrease to less than -150 mGal, and these minima are displaced westwards with respect to the topography of the Hellenide mountains. This is clearly seen on Profile 1 of Figure 4.20. Similar features have been reported for the Alpine mountain system i.e., Pyrenees-Apennines-Carpathians-Dinarides (e.g., *Giese et al.* [1982]). *Karner and Watts* [1983] model the development of mountain belts, and show that maximum topographic elevations need not correlate with maximum crustal thicknesses. This indicates the presence of sub-surface loads acting on flexurally strong lithosphere. *Karner and Watts* [1983] obtain T_e estimates for the Alps of between 20 and 50 km.

The Cyclades in the central Aegean show positive FAA values in the region of 100 mGal, as seen on Profile 3 (Figure 4.20). This correlates with *broad*, shallow bathymetry (Figure 4.19). This observation is inconsistent with the flexural isostatic model, and

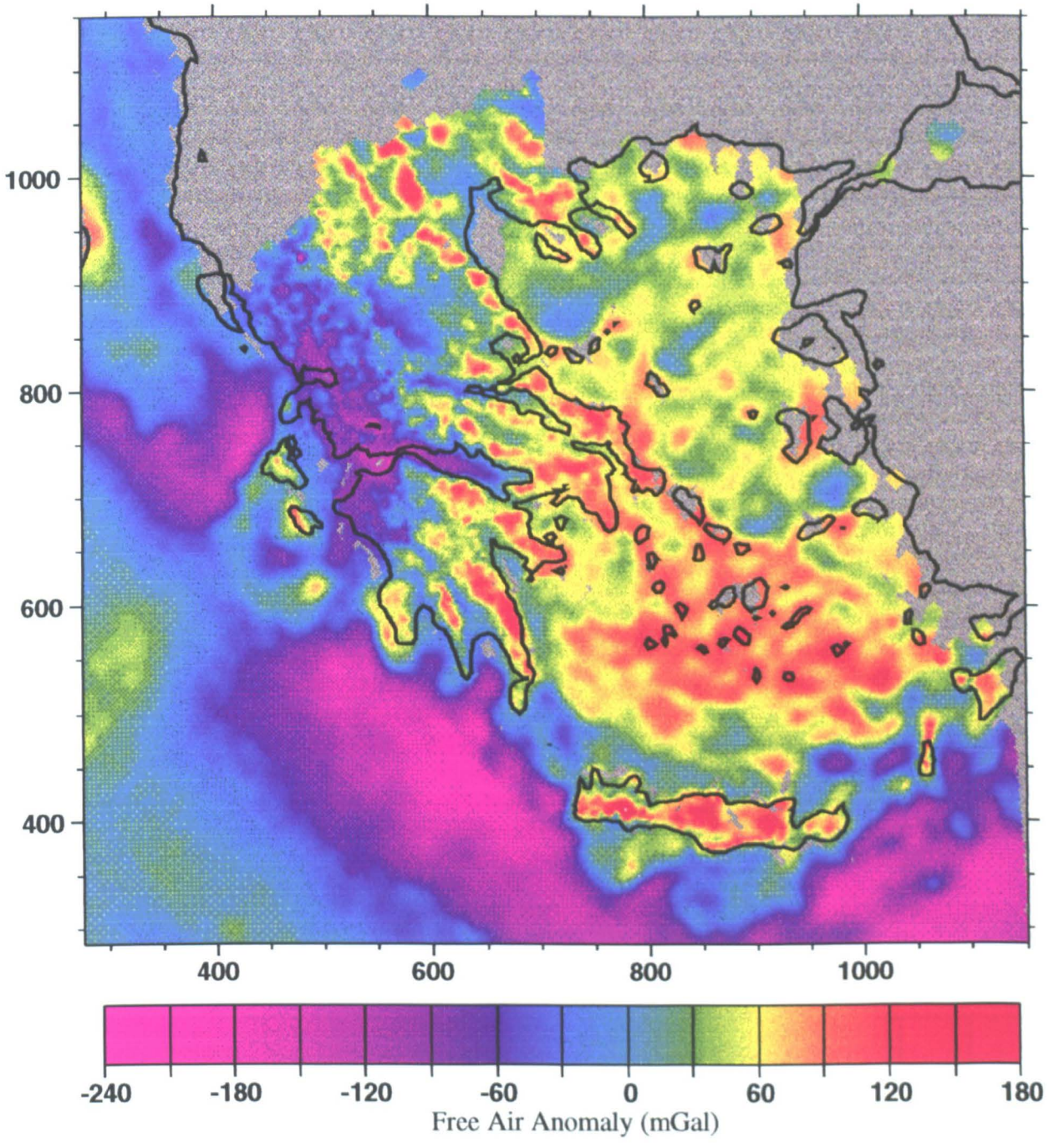

Figure 4.18: The free-air gravity anomaly map.

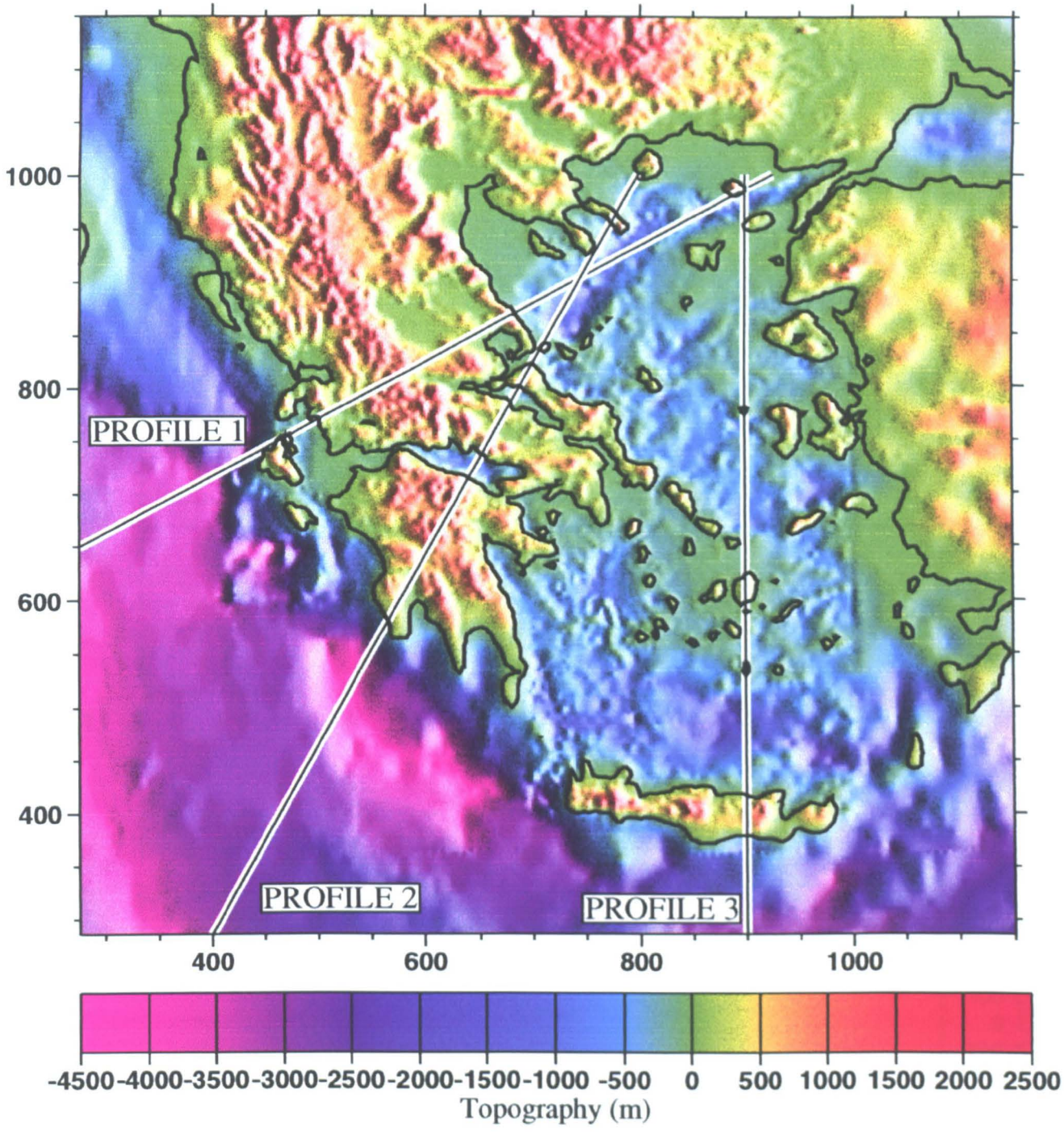

Figure 4.19: Topography map to show location of profiles in Figures 4.20 (FAA) and 4.22 (BA).

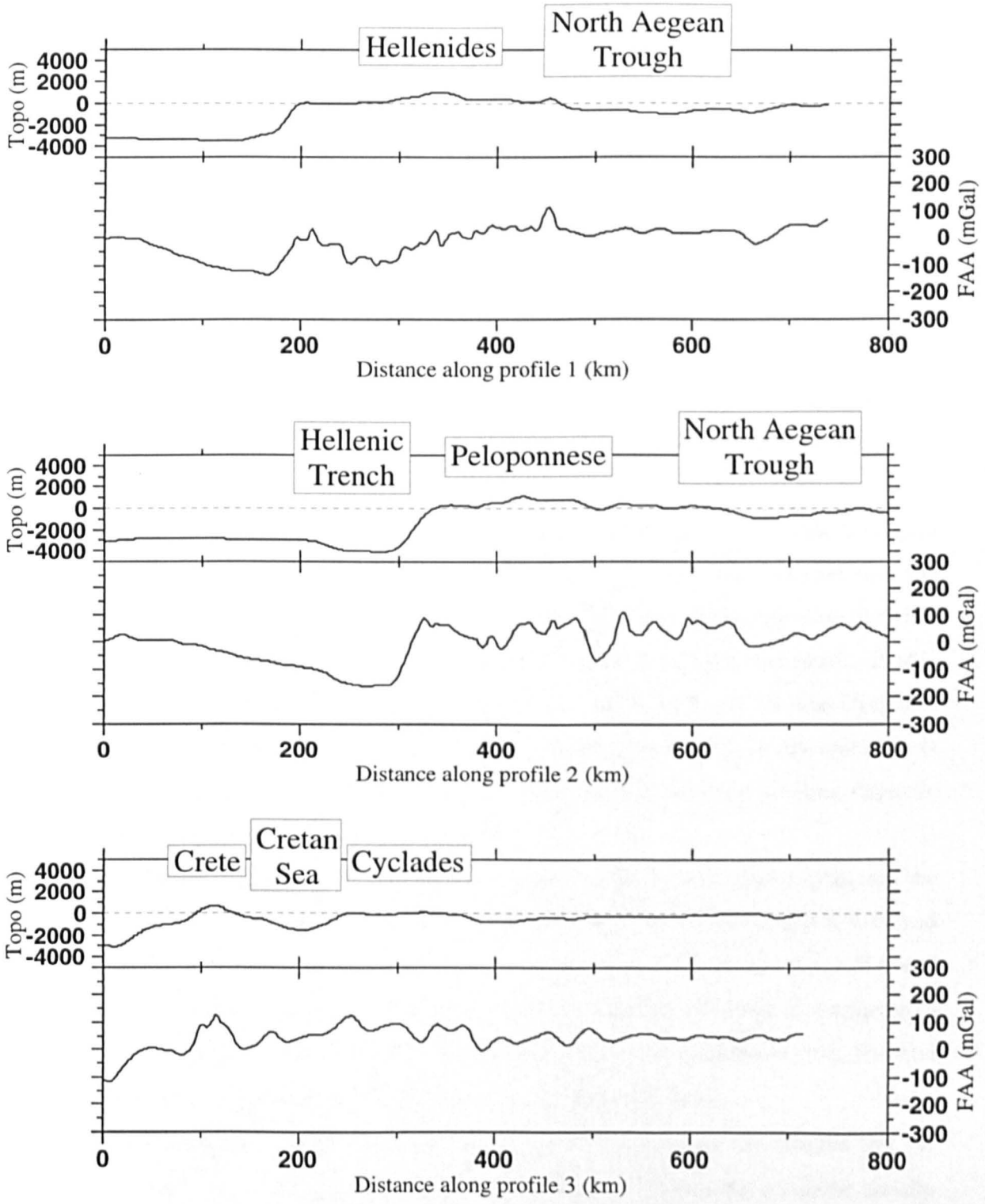

Figure 4.20: Profiles of topography and free-air gravity. All profiles run from west/south to east/north.

may therefore indicate the action of dynamic compensation mechanisms.

4.12.2 The Bouguer Anomaly

The most striking feature of the BA map is the gravity low across western Greece, the minima for which (~125 mGal) is displaced relative to the topographic maximum (see Profiles 1 and 2, Figure 4.22). The lack of correlation at these broad wavelengths is again indicative of a relatively strong plate. The low Bouguer gravity is seen to continue south of the Peloponnese and east through Crete. This suggests the presence of a crustal root along this length that is not immediately apparent in the topography.

Across Crete, the topographic high is vertically coincident with the BA low. If the same sub-surface loading processes are in operation here as across the Hellenides, then surface and sub-surface loads are spatially correlated. In such cases, a strong plate masquerades as a weaker one [*Forsyth*, 1985; *Macario, Malinverno and Haxby*, 1995]. This phenomenon is discussed further in Chapter 6.

The general trend in the BA across the Aegean is clearly seen in Profile 3 (Figure 4.22), and is one of a gradual increase from north to south. This suggests that that the moho is becoming more shallow from north to south. Isostatic considerations predict that this should correlate with gradually deepening bathymetry towards the south. Profile 3 in Figure 4.22 shows that this might be the case, if it were not for the Cyclades. This broad topography is apparently not supported by a deflection at the moho. It is difficult to explain this lack of coherence on a regional scale without invoking dynamic (i.e., non-isostatic) compensation mechanisms.

These Bouguer gravity data were supplemented by the regional gravity grid, and the composite map is shown in Figure 4.23. Three profiles are examined (Figures 4.24 and 4.25). The first shows that an apparently good coherence exists between the BA and topography across the Rhodope Mountains. Towards the east, the Black Sea appears to be floored by thinner crust. However, the tectonics of the this region are complex, and not of interest to this thesis. The Black Sea is no longer discussed.

The second profile shows the regional crustal thinning across the Aegean sea. A series of east-west profiles such as this were examined. Assuming a mantle density contrast of 500 kg/m^3 [*Makris*, 1984], the extensional factor (β) was obtained for an assumed crustal thickness of 40 km. Values between 1.2 and 1.5 were obtained. These results are not presented in full due to the problems associated with the pre-extensional

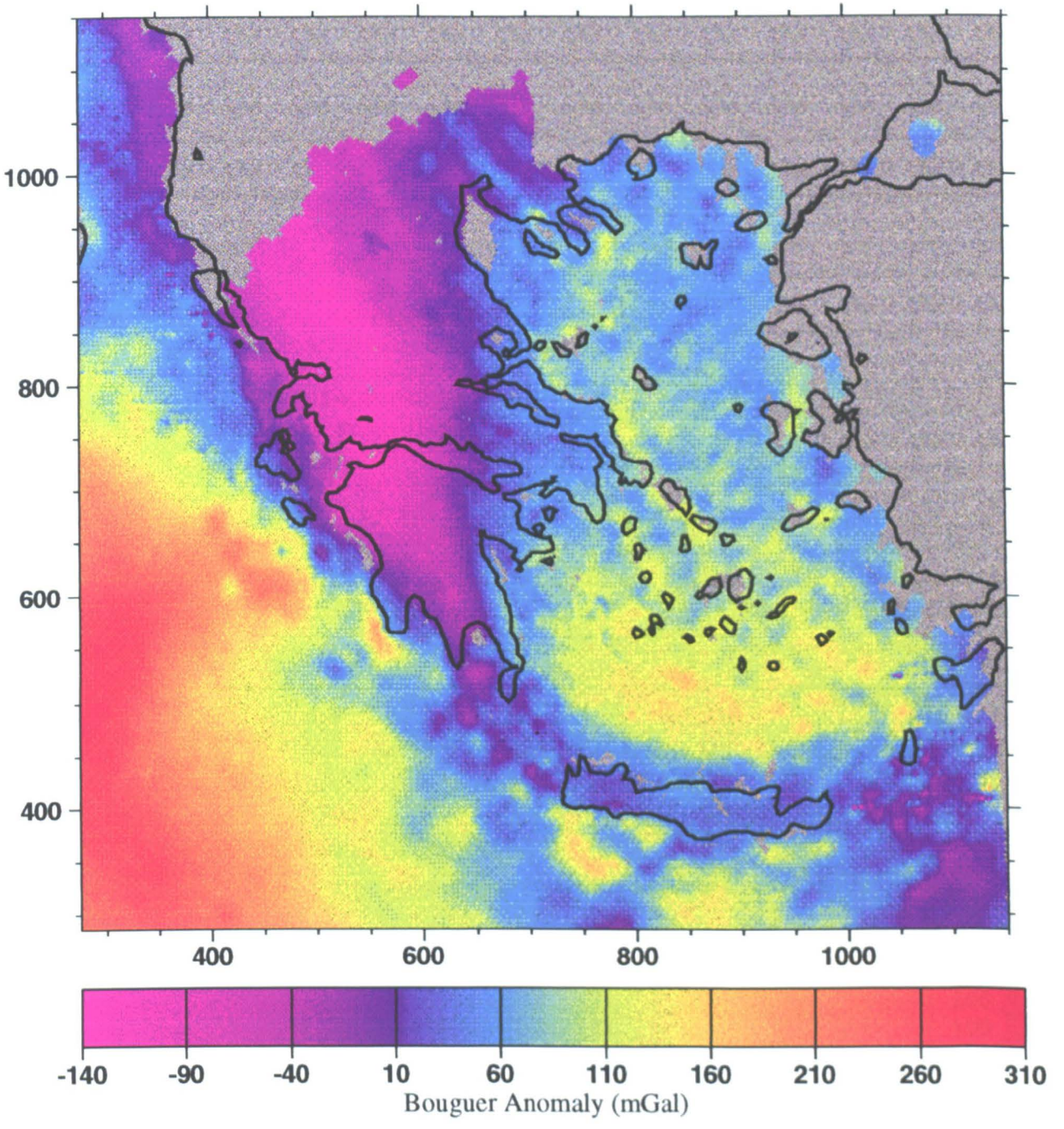

Figure 4.21: The Bouguer anomaly gravity map.

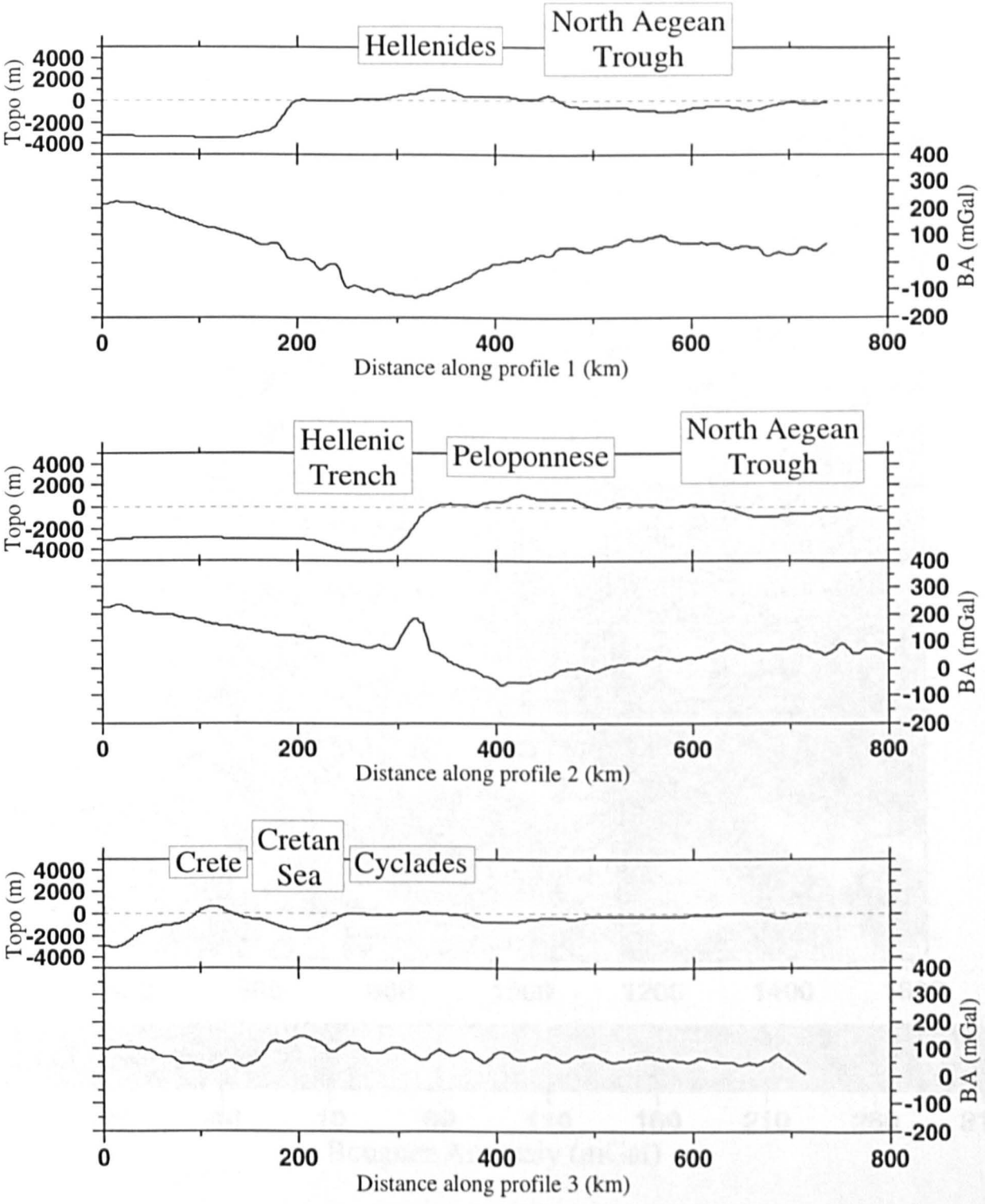

Figure 4.22: Profiles of topography and Bouguer gravity. All profiles run from west/south to east/north.

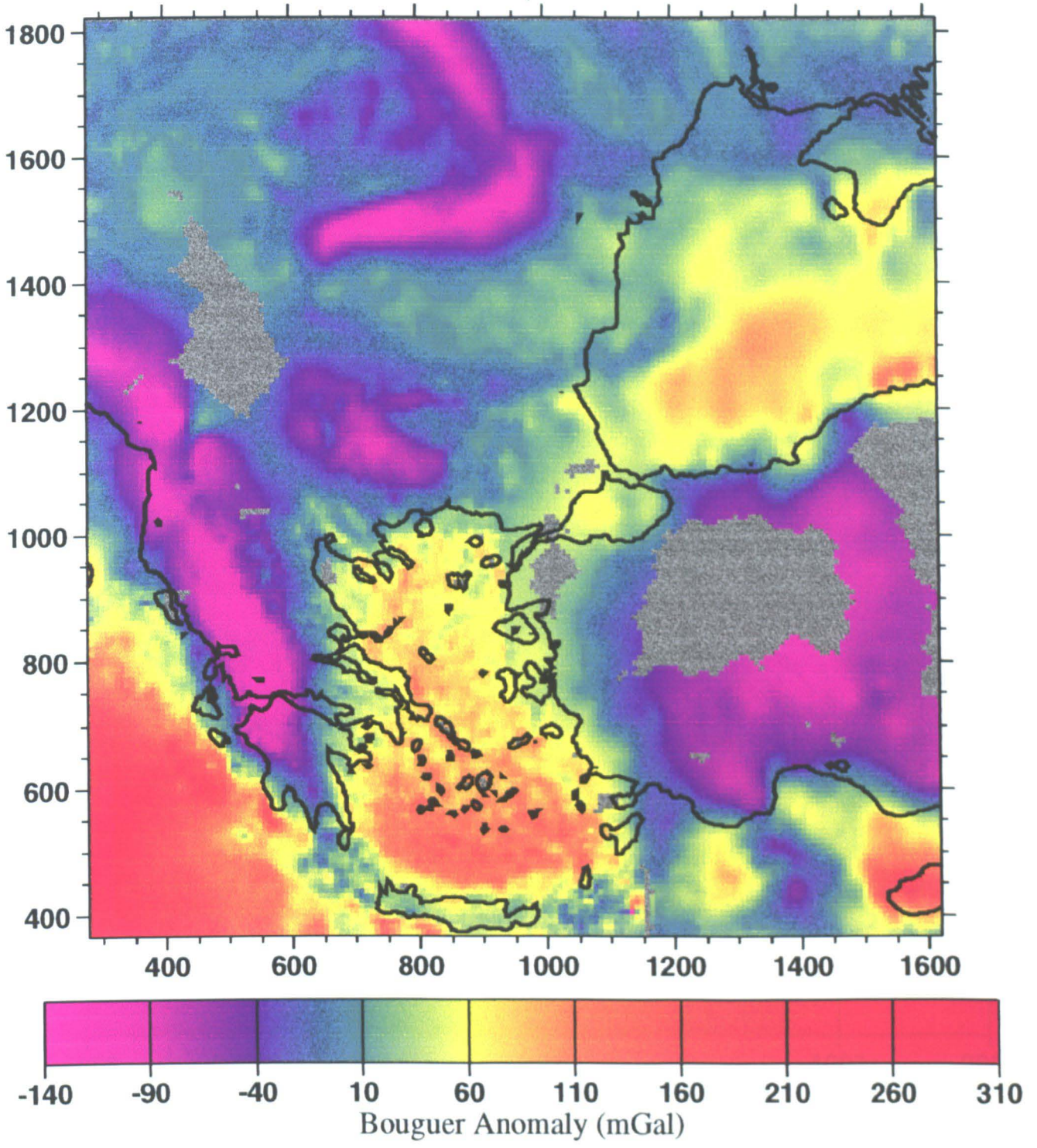

Figure 4.23: The Bouguer anomaly map, merged with the regional Bouguer gravity grid. These data are gridded with an 4 km cell size, and are used for the Fourier coherence analysis of Chapter 6.

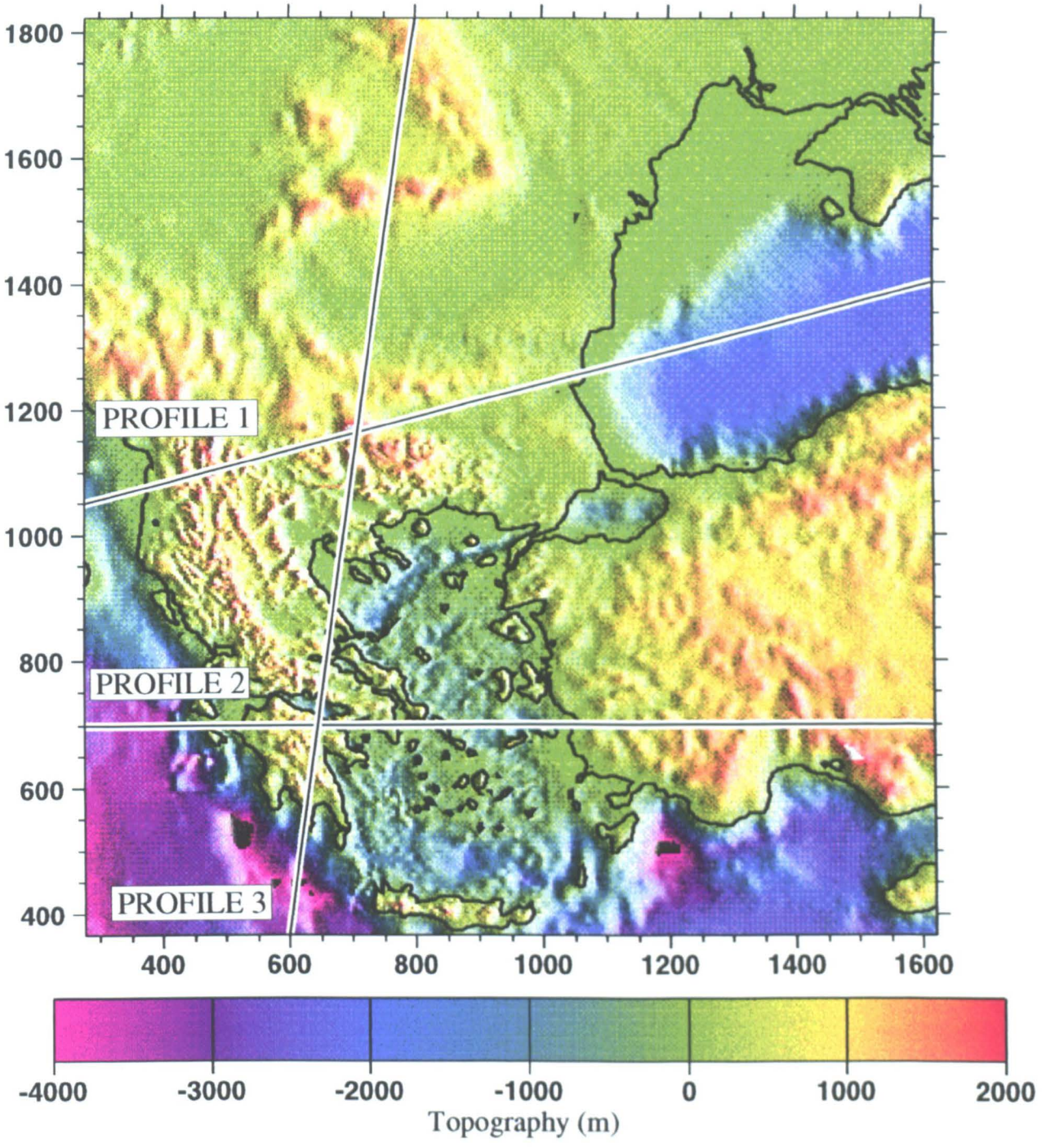

Figure 4.24: The 2 km DEM, merged with the ETOPO5 grid. These data are gridded with an 4 km cell size, and are used for the Fourier coherence analysis of Chapter 6.

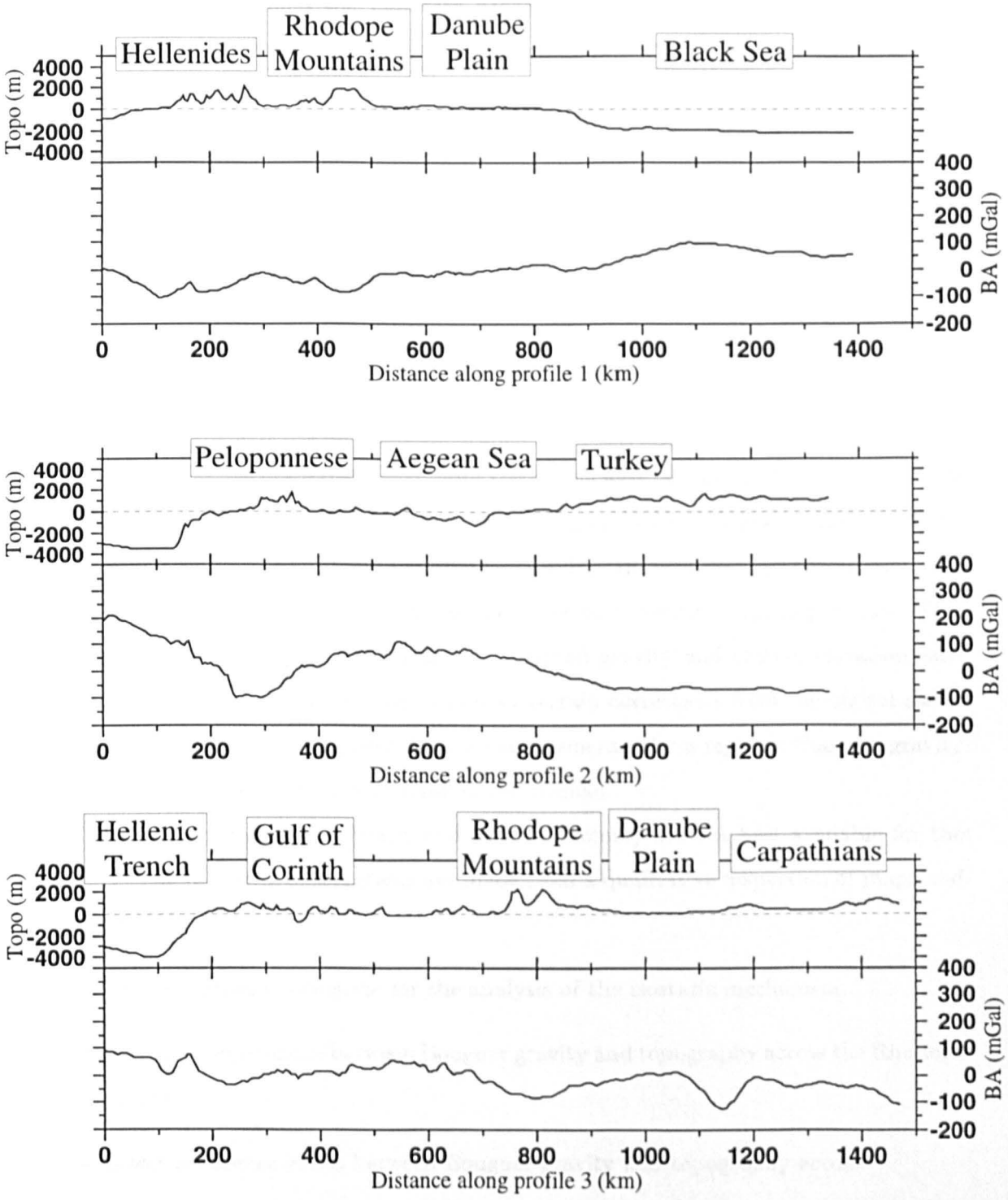

Figure 4.25: Regional profiles of topography and Bouguer gravity. All profiles run from west/south to east/north.

crustal thickness that were highlighted in Chapter 2. However, they are consistent with estimates based on kinematic reconstructions (Section 3.5).

Profile 3 again shows the apparent coherence between the gravity and topography across the Rhodope Mountains (see Figure 3.1). Further to the north across the Carpathian Mountains, the Bouguer gravity low is displaced by ~50 km south of the topographic maximum, as observed by *Karner and Watts* [1983]. *Stewart and Watts* [1997] presents flexural forward models of the gravity and topography across the Carpathians and estimates that T_e is between 10 and 30 km. T_e estimates will be obtained for this same region from the relationship between Bouguer gravity and topography in Chapter 6.

4.13 Conclusions

The collection of gravity data in mainland Greece allowed for both a check on the Greek IGSN71 gravity base station value, and the calibration of existing gravity datasets both onshore and across the Gulf of Corinth. The satellite derived gravity data of *Sandwell and Smith* [1997] are incorporated to extend cover to the entire Aegean province. This combined dataset is reprocessed from the observed gravity and station elevation estimates, and includes the calculation of gravity terrain corrections from the digital elevation models (Appendix E). These data are supplemented by a regional Bouguer gravity grid to extend cover to areas surrounding the Aegean.

The resulting maps of Bouguer and free-air anomaly are the best available for the Aegean. The following observations are made from a qualitative inspection of maps and profiles:

- The resolution is adequate for the analysis of the isostatic mechanism.
- High coherence exists between Bouguer gravity and topography across the Rhodope Mountains.
- Lower coherence exists between Bouguer gravity and topography across
    1. the Hellenide mountain chain
    2. the southern Carpathian mountain chain
    3. the southern and central Aegean.

- The anomalous behaviour across the southern and central Aegean is coincident with low P-wave velocities (Figure 3.5), high surface heat flow (Figure 3.6) and a positive geoid anomaly (Figure 4.12).
- The crustal root of the Hellenide chain continues south and east through Crete.
- There is no clear gravitational signature of the different isopic zones (Figure 3.7).

Chapter 5

Gravity and Topography Across the Rifts of Central Greece

5.1 Introduction

Knowledge of the amount of subsidence in a rift basin and the location of its depocentres can provide valuable constraints on its kinematics and dynamics. Previous analyses of the Gulf of Corinth Rift (e.g., *Roberts and Koukouvelas* [1996], *Armijo et al.* [1996]) have used surface information - i.e., geology, topography and bathymetry - to infer the likely nature of the rift at depth. Interpretation of the Bouguer gravity field provides a more direct, but clearly non-unique, means.

The insensitivity of the Bouguer anomaly to structural detail makes the gravity method useful in dealing with complex structures for which only simple answers are required, such as interpreting regional basin forms. This chapter analyses the Bouguer gravity across the rift basins of Central Greece. Once the gravity signal of the basin has been identified, it is compared to a digitised geology map to assess the location and dimensions of depocentres.

A general model is then derived for the gravitational response of buried sediment. The depth to the pre-rift basement in the rifts of central Greece is then assessed by comparing the magnitude of observed residual Bouguer anomalies to the model results.

Finally, the rift-related topography across the eastern Gulf of Corinth is analysed. Boundary element elastic models that assume upper-crustal flexure are constrained by marine terrace elevations and the gravity modelling results, and an estimate for rift-flank T_e is obtained.

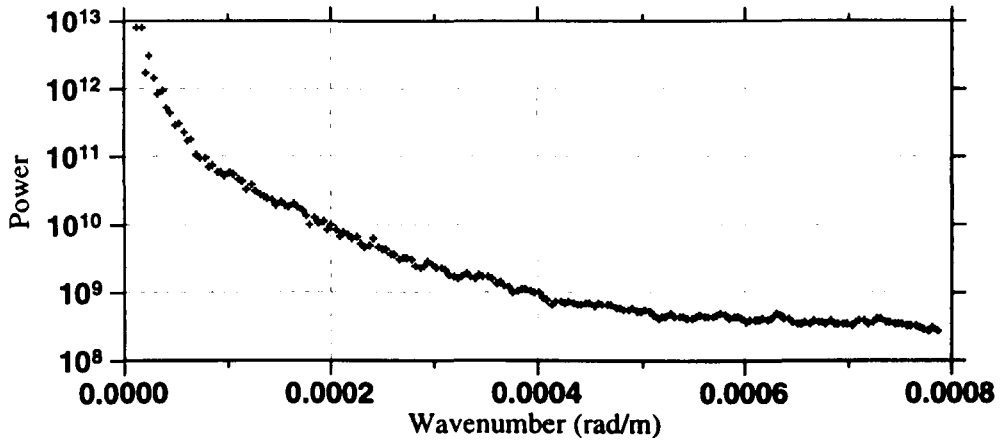

Figure 5.1: The radially averaged power spectrum for the complete Bouguer gravity dataset for longitudes 20 to 30 E and latitudes 34.5 to 44 N. Found using the GRDFFT algorithm of GMT.

5.2 Regional-Residual Separation

The first and critical step in the process is to eliminate the gravity signal of all unwanted sources, leaving only that due to the structure of interest. This may be done in either the space domain or the wavenumber domain.

The methods of *Spector and Grant* [1970] and *Pawlowski* [1995] assume that bulk density is discontinuous with depth. The depths to these discontinuities may then be found from the gradients of linear segments in gravity power spectra. From this, high-pass filters may be designed to isolate the gravitational signal from the desired depths.

Figure 5.1 shows the radially averaged power spectrum for the complete Bouguer anomaly across the Aegean region. Rather than being segmented, its smooth form is consistent with the findings of *Maus and Dimri* [1996] who argue that potential field power spectra are dominated by self-similar properties of their source distributions, and so contain only limited depth information. The methods of *Spector and Grant* [1970] and *Pawlowski* [1995] are not applied here.

Tsokas and Hansen [1997] consider the Bouguer gravity field across Greece and the Aegean as a superposition of three signals: that from the subducted slab, the moho and the upper-crustal geology. *Tsokas and Hansen* [1997] use a multiple source Werner deconvolution technique with the Bouguer gravity data of *Lagios et al.* [1988] to map the upper surface of the subducted slab. Chapter 3 (Section 4.10.2) shows that the offshore data of *Lagios et al.* [1988] are shifted by ~14 mGal with respect to the onshore data. Nonetheless, the calculated slab depths agree well with the tomographic images of *Papazachos and Nolet* [1997]. *Tsokas and Hansen* [1997] then calculate the gravity field

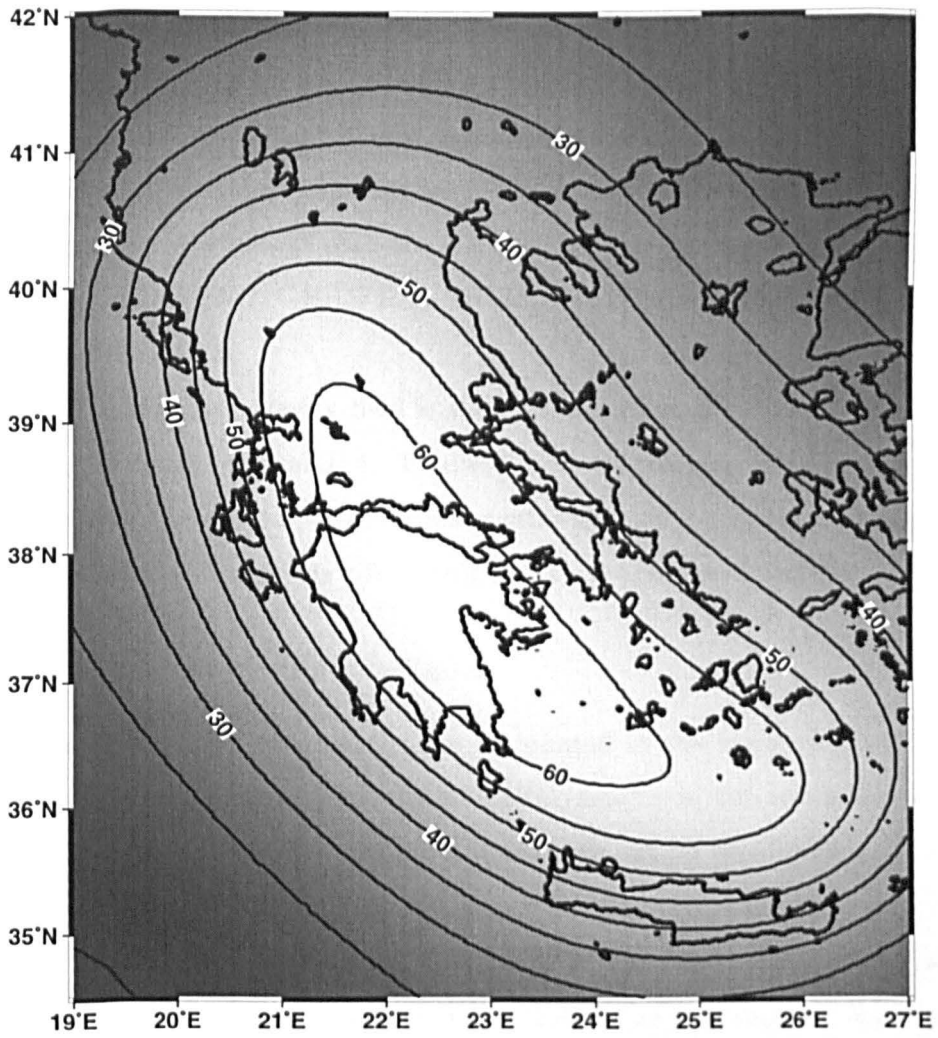

Figure 5.2: The gravity field of the subducted slab as derived by *Tsokas and Hansen* [1997]. Data were supplied by G. Tsokas (Aristotle University of Thessaloniki, personal communication, 1997).

of the dipping slab assuming a density contrast of 55 kg/m^3 (Figure 5.2).

Tsokas and Hansen [1997] use the same technique to derive a map for moho topography. However, there are some features in their results that require complicated explanation, and it is likely that the datum step produces artifacts at moho depths. Their moho depth map - and its gravity anomaly - are not used in this study. The gravity of the subducted slab may be subtracted from the BA in the space domain, but this would leave the gravitational effect of the moho to be removed by another process.

5.2.1 Two Dimensional Filtering

The separation of regional and residual Bouguer gravity signals is performed by wavenumber domain filtering. Before low-pass filtering, a first order trend is removed which is cal-

culated from the edge points of the rectangular data grid. The data are then transformed into the wavenumber domain with a fast Fourier transform algorithm. The filter is then applied to the transformed dataset, and the result is subjected to an inverse fast Fourier transform. Finally, the removed trend is replaced to obtain a regional Bouguer gravity data. This process is achieved with the RANGRID algorithm of GEOSOFT, and the GRIDTRND, GRIDXPND, GRIDFILL, FFTIN, FILTER, FFTOUT and GRIDBOOL algorithms of MAGMAP.

The residual Bouguer gravity field is then calculated as the difference between the complete BA and the regional BA. Figure 5.3 shows the effect of filtering the data. From the map that retains all wavelengths greater than 50 km, it is clear that the Gulf of Corinth and the Gulf of Evvia rifts continue into the region of the Cyclades islands.

5.2.2 Isolating the Sediment Signal

In order that the correct wavelengths are eliminated in the regional - and all of the signal due to the sediment in a particular basin remains in the residual - a series of low-pass filters were applied with regularly decreasing cut-off wavelengths. The process is demonstrated for the Gulf of Corinth, the largest of the rift basins in central Greece.

The regional field across the Gulf of Corinth is represented by the general north-south trend in the BA contours (Figure 5.4). This is due to a regional thinning of the crust towards the Aegean Sea from the thickened crust above the subduction zone. The residual signal of the Gulf of Corinth results from the low density sediment infill, and creates a deflection to the east in the contours. It is this negative gravity anomaly that we wish to separate and analyse.

Figure 5.5 shows the results for four different low-pass filters. The central wavelengths are 90 km, 80 km, 70 km and 60 km (i.e., 6.981×10^{-5} rad/m, 7.854×10^{-5} rad/m, 8.976×10^{-5} rad/m, and 1.047×10^{-4} rad/m respectively). A band-pass filter was seen to produce artifacts in the residual gravity at lengthscales similar to that of the cut-off wavelength. After performing a series of tests - the results of which are not presented here - filters with a $\pm 5\%$ wavelength roll-off were seen to best limit ringing in the space domain and retain a sharp roll-off in the wavenumber domain. Figure 5.5e shows the form of the radially symmetric cosine-squared function used for all low-pass filtering.

The negative deflection of the regional contours begins to be seen in Figure 5.5c, so the regional field is defined by that in Figure 5.5b. Figure 5.6 shows the residual

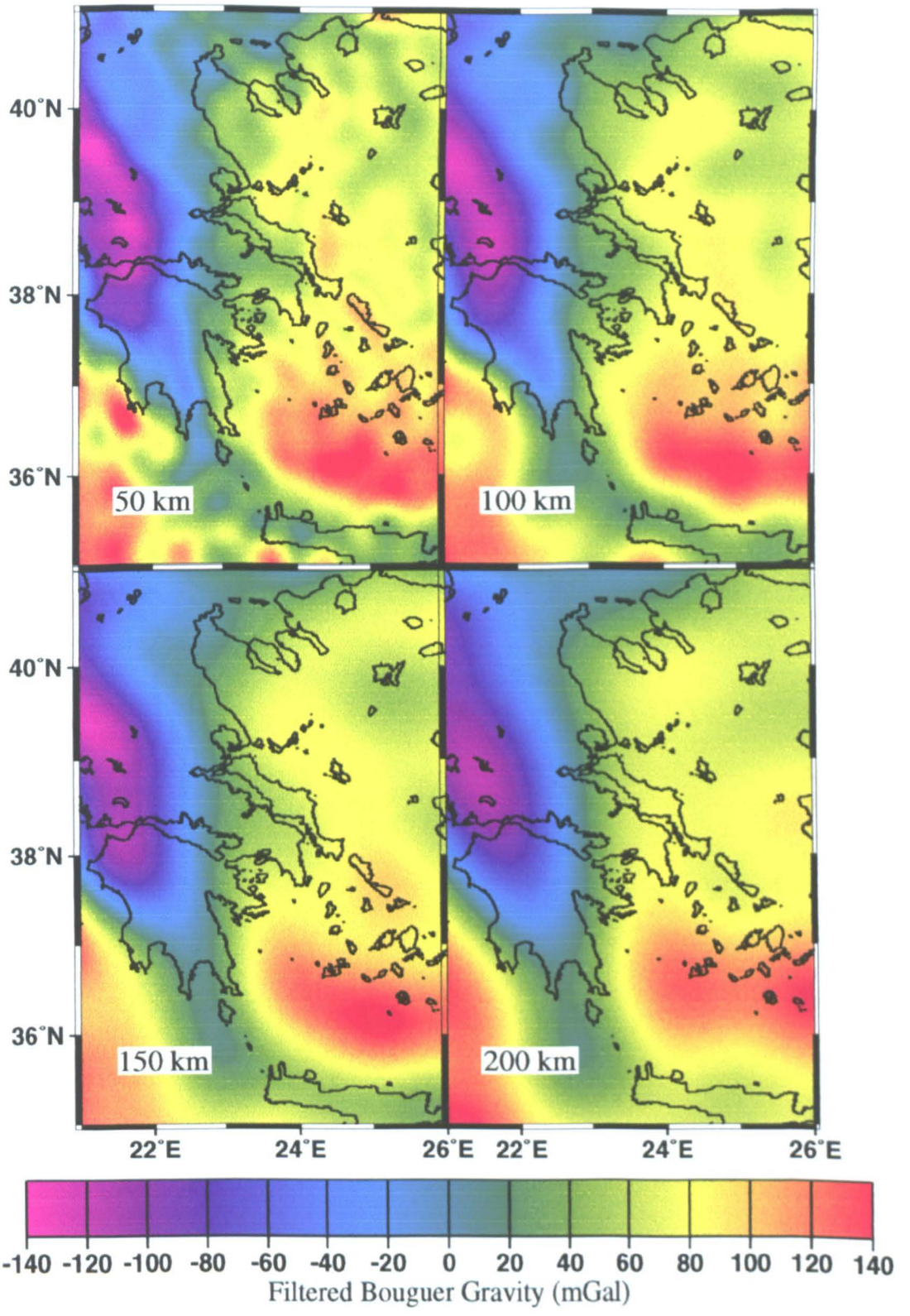

Figure 5.3: Low-pass filtering of the Bouguer anomaly across the Aegean. The cut-off wavelength is shown in each plot. Data are gridded and filtered to 2° beyond the limits of the area shown to avoid edge effects.

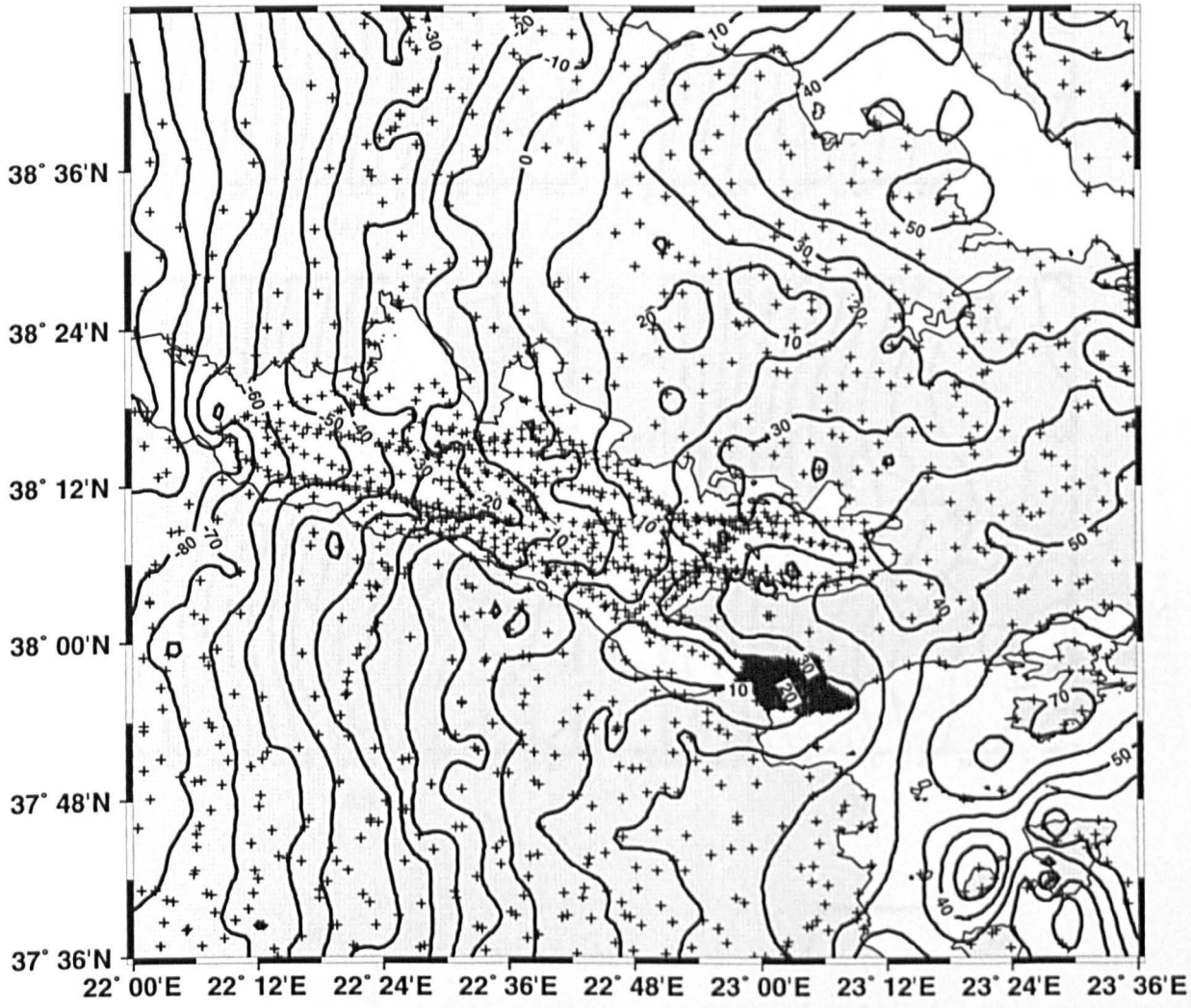

Figure 5.4: The complete Bouguer anomaly across the Gulf of Corinth. Note that the low density sediments within the Gulf will result in a negative residual Bouguer gravity anomaly.

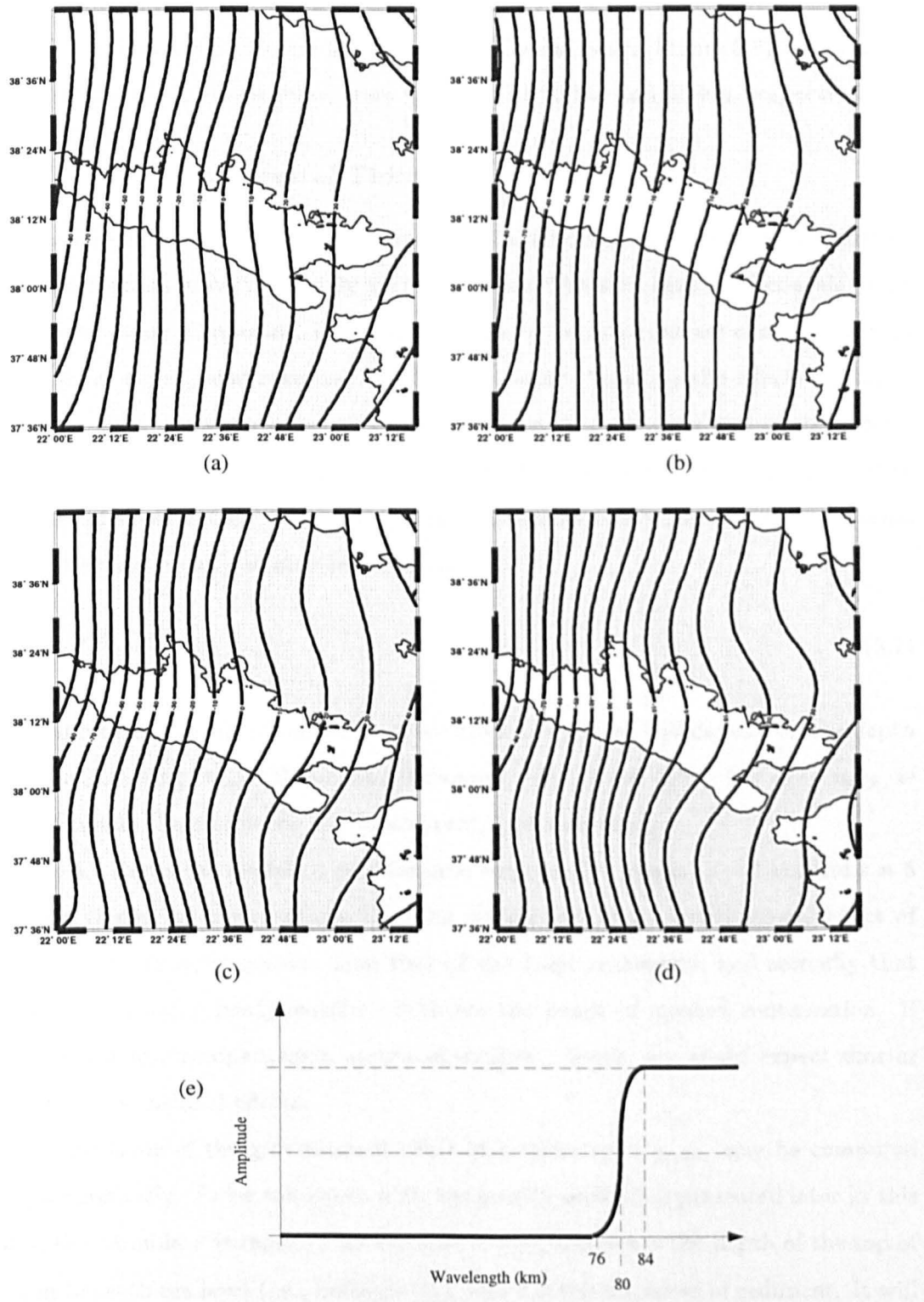

Figure 5.5: The low-passed Bouguer anomaly across the Gulf of Corinth. The four maps represent the results of four different filters: (a) 85.5 km to 94.5 km (b) 76.0 km to 84.0 km (c) 66.5 km to 73.5 km, and (d) 57.0 km to 63.0 km. The negative signature of the Gulf of Corinth begins to be seen in map (c), so the regional Bouguer gravity across the Gulf of Corinth is defined by map (b). (e) The form of the radially symmetric cosine-squared low-pass filter used to produce the regional field, with a central wavelength of 80 km.

Bouguer gravity map for the Gulf of Corinth. Similar analyses were carried out for the smaller Gulf of Evvia Rift (Figure 5.7) and Lake Trihonis Basin (Figure 5.8). The central wavelengths for the low-pass filters were found to be 50 km and 30 km, respectively.

5.2.3 The Effect of Crustal Thinning

Although there is no evidence of the regional crustal thinning away from the subduction zone in the residual gravity anomaly maps, we cannot be sure that smaller-scale moho depth variations are eliminated. Beneath the negative density contrast of a sedimentary basin, positive density contrasts are expected to occur. Ignoring the effects of simple shear, these form in response to two processes: pure shear necking and isostatic compensation. For a T_e of zero, the amplitude of a moho anti-root, w, is simply related to the amount of subsidence, s'. Given values for the density of the basin fill (ρ_i), the crust (ρ_c) and the mantle (ρ_m), w may be calculated as

$$w = s' \frac{\rho_c - \rho_i}{\rho_m - \rho_c} \; . \tag{5.1}$$

For $T_e > 0$, the magnitude of an anti-root for given subsidence will depend on the depth of pure shear necking, z_{neck} [*Braun and Beaumont*, 1989; *Kooi*, 1991]. For deep z_{neck}, w will overestimate the amplitude of the anti-root, and vice versa.

Figure 5.9 shows the modelled gravitational response for basins ($s = 3$ km and $s = 5$ km). Two things are clear: firstly that the wavelength of the gravitational effect of the moho is significantly greater than that of the basin sediments, and secondly that its magnitude is significantly smaller. Both are the result of upward continuation. If necking or isostatic compensation occurs at shallower levels, we would expect shorter wavelength gravitational effects.

The magnitude of the gravitational effect of a moho root, g_{root}, may be computed more systematically. To be consistent with the gravity modelling presented later in this chapter, the variable s' is replaced by the sum $(b + s)$, where b is the depth of the top of the basin beneath sea level (i.e., bathymetry), and s is the thickness of sediment. It will be shown in Section 5.7.1.2 that the gravitational attraction of an infinitely thin strip of width $2a$ in x and infinite length in y is found as

$$g_{strip} = 4G(\rho_m - \rho_c)\delta z \left(\arctan \frac{a}{z}\right) \; . \tag{5.2}$$

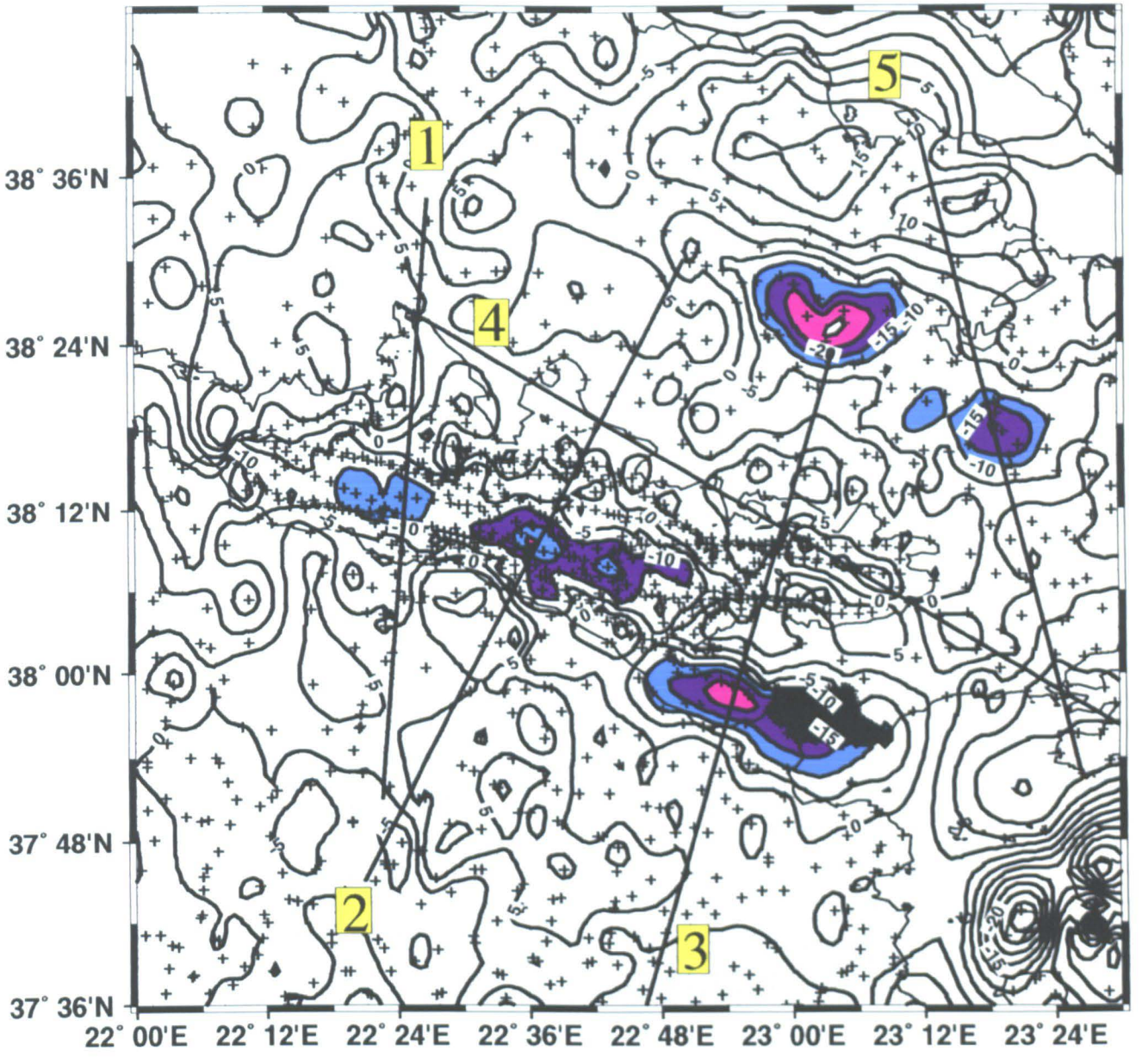

Figure 5.6: The residual Bouguer anomaly across the Gulf of Corinth Rift. The crosses indicate the stations where gravity measurements have been made. Note that four distinct lows are observed: two in the main Gulf of Corinth, one in the Alkyonides Gulf and one across the Gulf of Lechaio-Corinth Isthmus. There are also negative residuals across the Thiva Plain and the Erithres Basin. Profiles 1, 2 and 3 correspond to the location of the geological sections of Figures 5.14, 5.15 and 5.16. These are extended in both directions for the gravity profiles in Figure 5.11. Profiles 4 and 5 correspond to the gravity profiles in Figure 5.12. These anomalies are shaded where the magnitude is greater than 10 mGal.

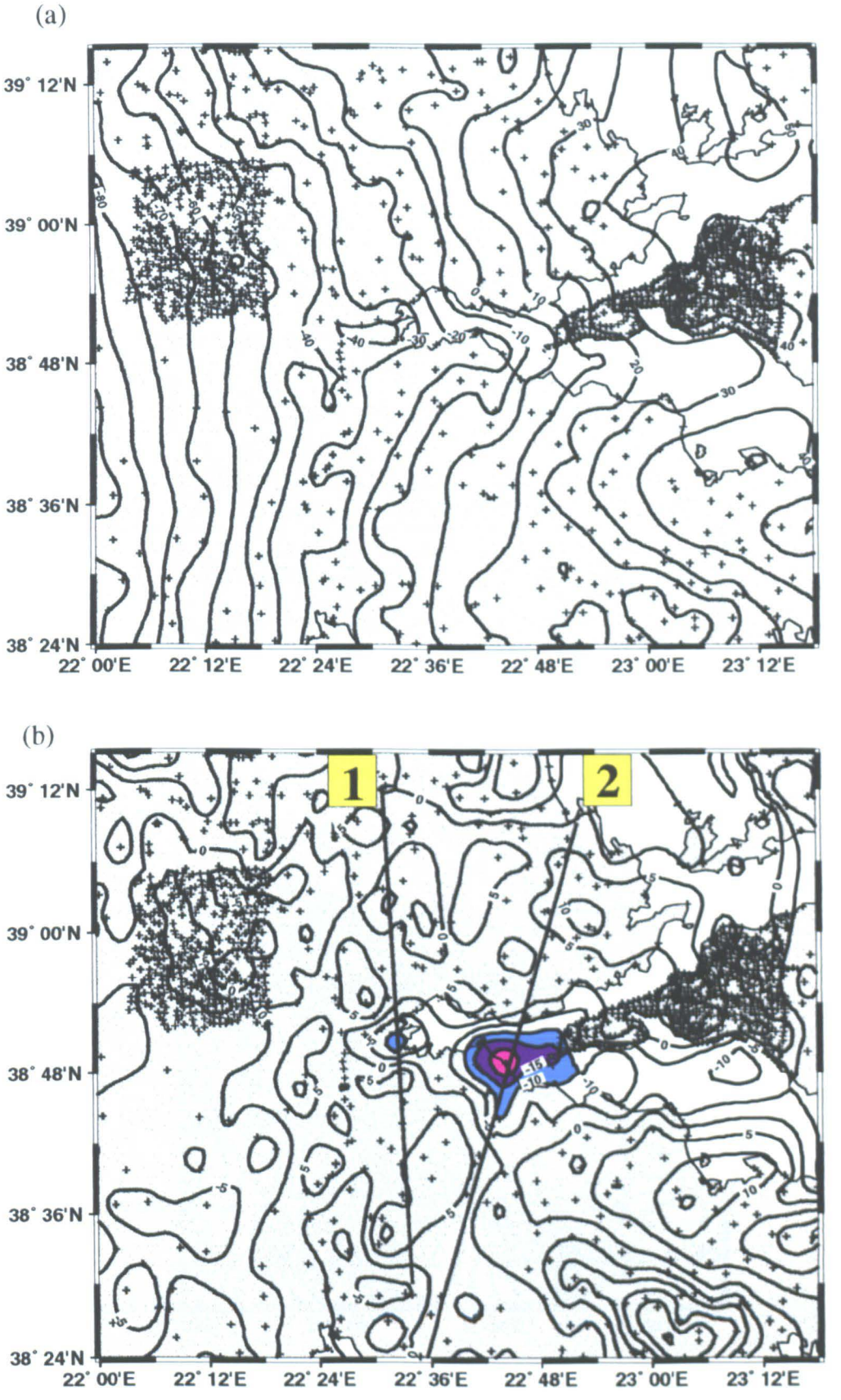

Figure 5.7: (a) The complete Bouguer anomaly across the Gulf of Evvia. (b) The residual Bouguer gravity anomaly the Lake Trihonis Basin. The crosses indicate the stations where gravity measurements have been made. The two lines show the locations of the sections presented in Figures 5.17 and 5.18. Anomaly magnitudes greater than 10 mGal are shaded.

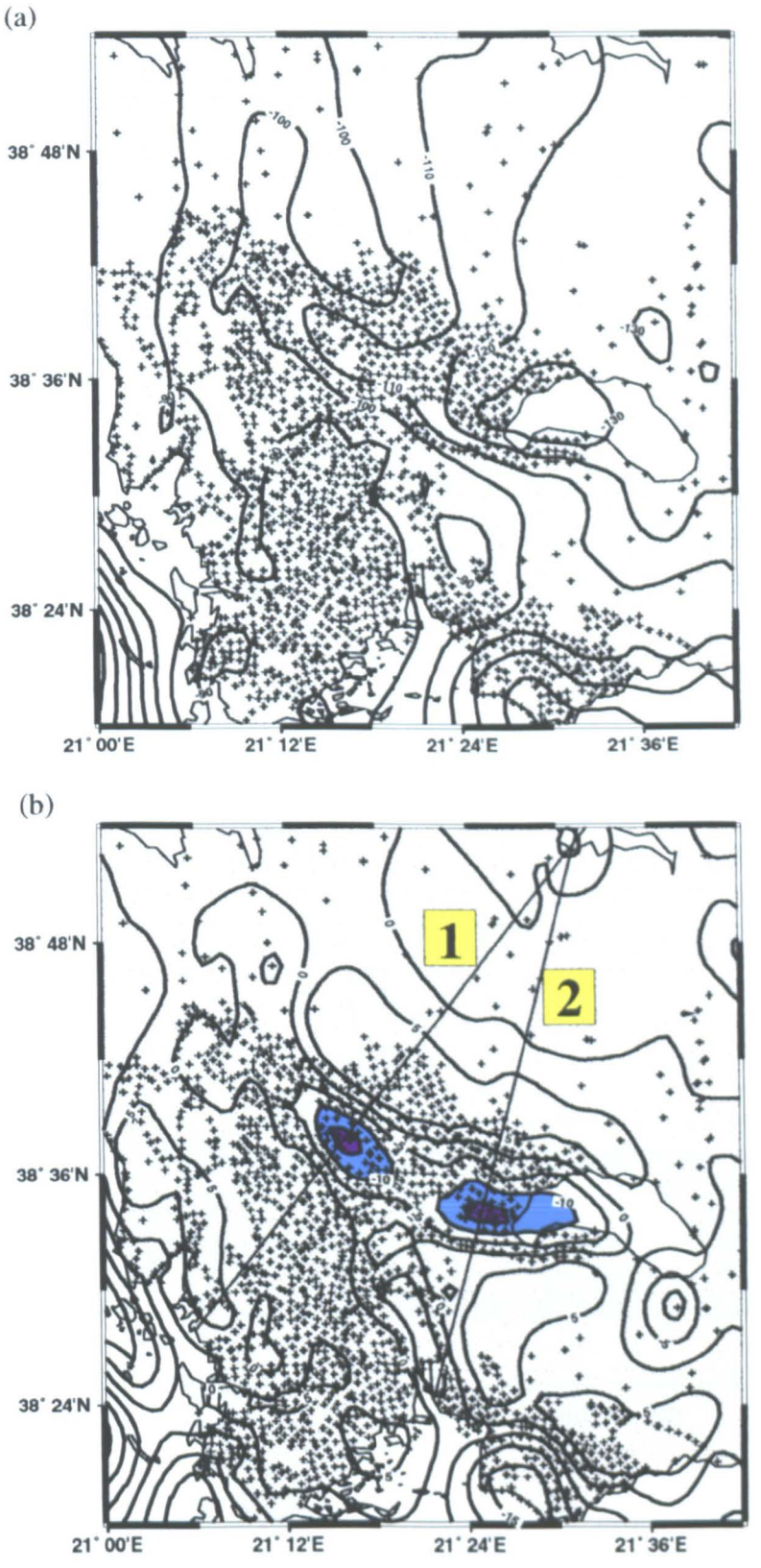

Figure 5.8: (a) The complete Bouguer anomaly across the Lake Trihonis Basin. (b) The residual Bouguer anomaly across the Lake Trihonis Basin. The crosses indicate the stations where gravity measurements have been made. The two lines show the locations of the sections presented in Figures 5.19 and 5.20. These anomalies are shaded where the magnitude is greater than 10 mGal.

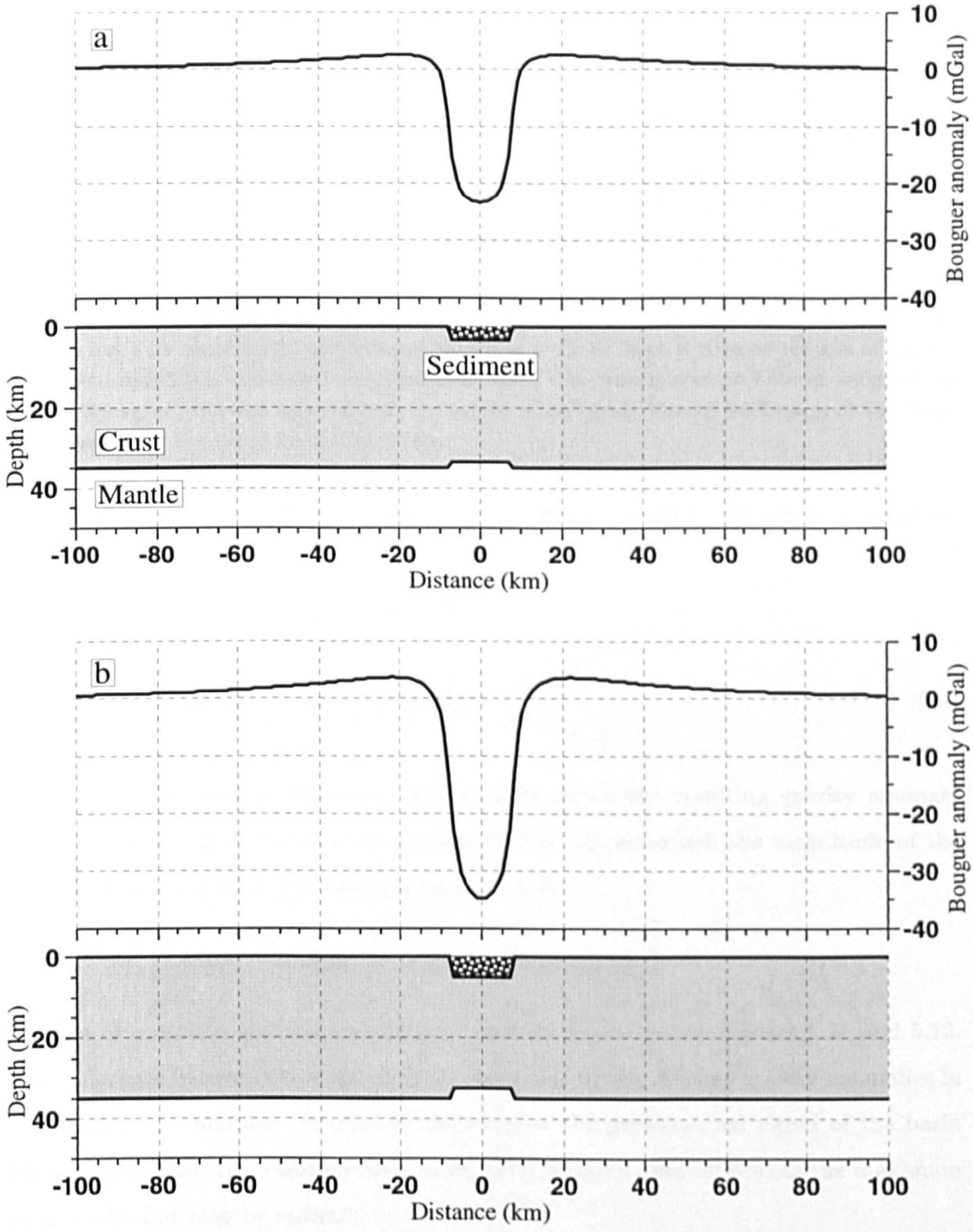

Figure 5.9: The modelled gravitational response of a sedimentary basin formed by pure shear for $T_e = 0$. Density contrast between sediment and crust is 250 kg/m^3, and that between crust and mantle is 500 kg/m^3. (a) Basin depth of 3 km. (b) Basin depth of 5 km. Width of basin and anti-root is 15 km in both cases. Crustal thickness is 35 km. Gravity profiles were calculated with forward modelling software GM-SYS.

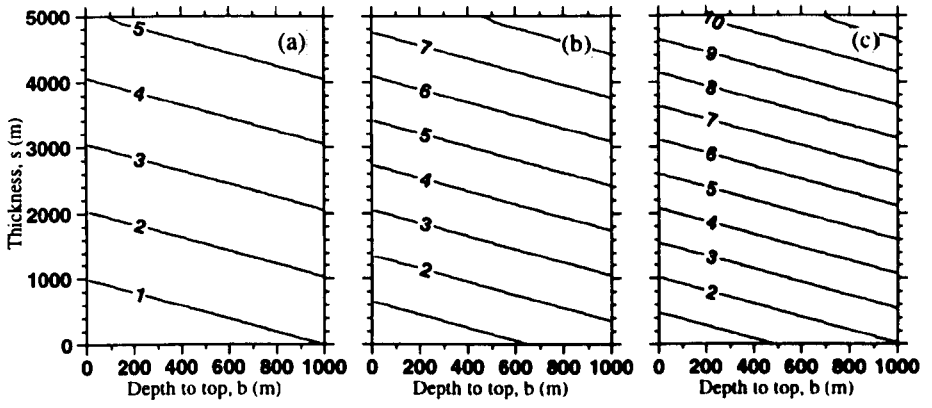

Figure 5.10: The magnitude of the gravitational signal from the moho, in mGal, as a function of depth to basin top, b (or water depth) and sediment thickness, s. Basin depth is given by the sum of b and s. The sedimentary basin is modelled with pure shear for $T_r = 0$. Density contrast between sediment and crust is 250 kg/m^3, and that between crust and mantle is 500 kg/m^3. Crustal thickness is 35 km. Basin widths are (a) 10 km, (b) 15 km and (c) 20 km.

Thus, the gravitational effect of the anti-root of width $2a$ and amplitude w is found as

$$g_{root} = 4G(\rho_m - \rho_c) \int_{T_c - w}^{T_c} \arctan \frac{a}{z}\, dz$$

$$= \left[z \arctan \frac{a}{z} - a \ln \frac{a}{z} + \frac{a}{2} \ln \left(1 + \frac{a^2}{z^2} \right) \right]_{T_c - w}^{T_c} \tag{5.3}$$

where T_c is the crustal thickness. Figure 5.10 shows the resulting gravity anomaly magnitudes for basin widths of 10, 15 and 20 km. As expected, the magnitude of the gravity anomaly is directly proportional to $(b + s)$.

5.2.4 Magnitudes of Effect of Basin Sediment

Profiles of complete and regional Bouguer gravity are shown in Figures 5.11 and 5.12. The difference between these two fields corresponds to the *residual* gravity anomalies in Figures 5.6, 5.7 and 5.8. It may be argued that the gravitational signal of the basin fill is greater than this residual magnitude. The stippled area represents the maximum magnitude that may be assigned to the basin fill.

The residual BA and the magnitude of the stippled portions of the curves are taken here as minimum and maximum estimates for the gravitational signal of sediment. Table 5.1 shows these estimates. The difference between them is always less than 10 mGal, which is consistent with Figure 5.10.

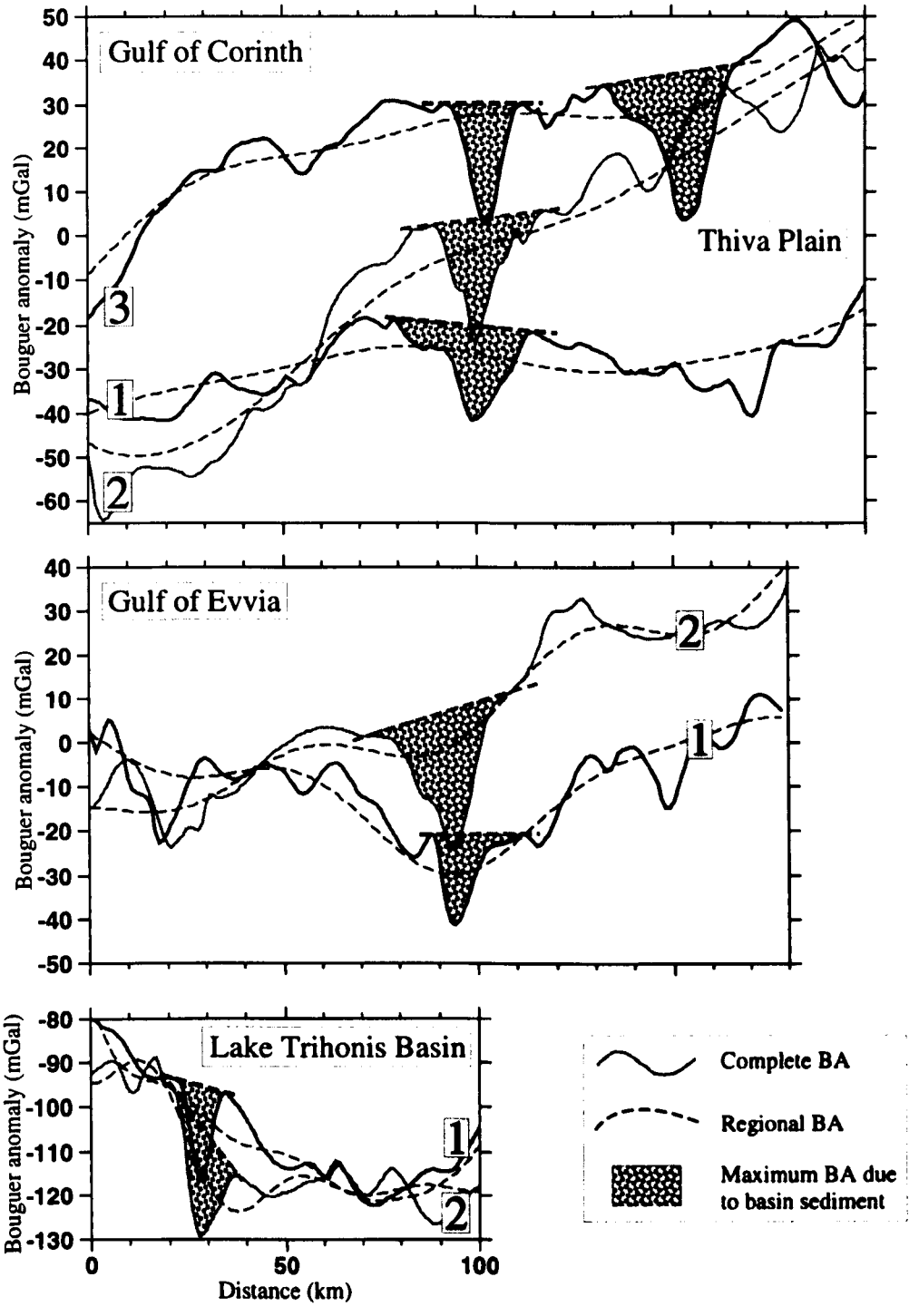

Figure 5.11: Profiles of complete Bouguer anomaly and the regional field (black dashed lines). The difference between the two corresponds to the residual anomaly presented in Figures 5.6, 5.7 and 5.8. The maximum amplitude gravity anomaly that may be assigned to basin sediment is indicated by the stippled pattern. Profiles of geology and residual gravity are presented in Figures 5.14 to 5.20.

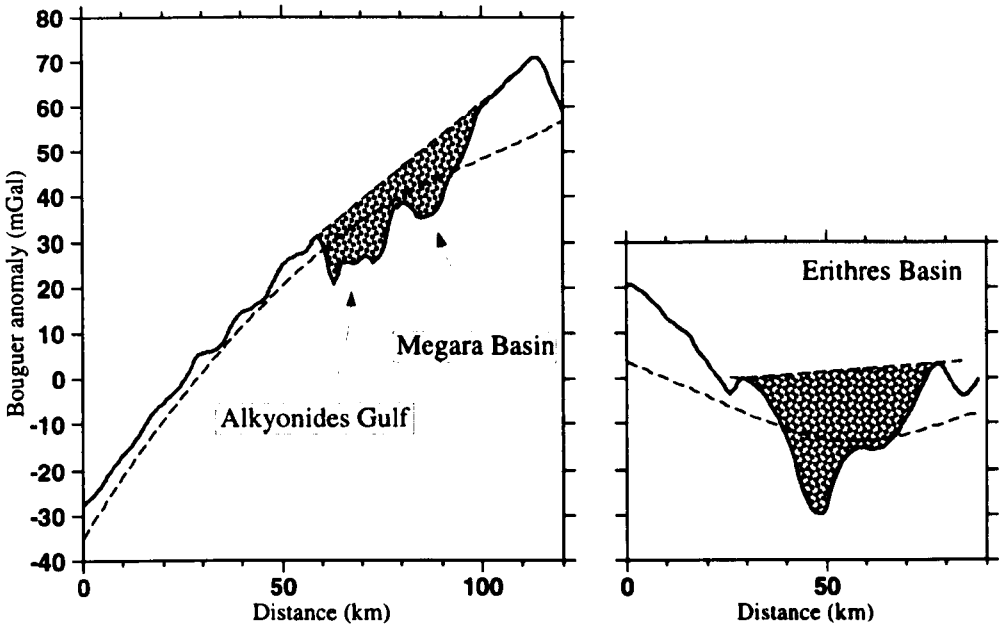

Figure 5.12: Profiles of complete Bouguer anomaly and the regional field across the Alkyonides Gulf, the Megara Basin and the Erithres Basin. The maximum amplitude gravity anomaly that may be assigned to basin sediment is indicated by the stippled pattern.

Anomaly	*BA* (mGal)		2*a* (km)	*b* (m)
	Min	Max		
Corinth 1	15	21	20	800
Corinth 2	21	27	20	800
Corinth 3	23	28	10	150
Alkyonides	10	16	10	0
Evvia 1	12	20	10	0
Evvia 2	23	32	10	0
Trihonis 1	16	22	10	0
Trihonis 2	16	25	10	0
Thiva	25	34	15	400
Erithres	17	26	10	0
Megara	7	16	10	0

Table 5.1: Observed magnitudes of the gravitational effect of basin sediments. Basin widths, 2*a*, are constrained from geological, topographic and bathymetric observations. *b* is the depth to the top of the basin fill.

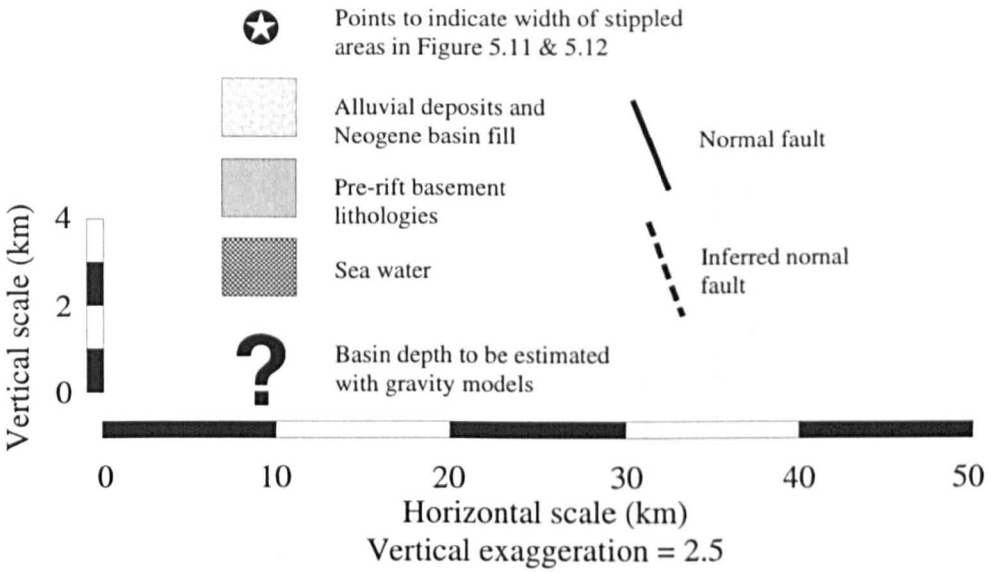

Figure 5.13: Key and scale for the seven geological and residual gravity profiles.

5.2.5 Profiles of Geology and Residual Bouguer Anomaly

The profiles presented in Figures 5.14 to 5.20 are constructed through these anomalies. Their trends are perpendicular to the strike of the basin, though the precise locations were chosen to pass through or near as many gravity stations as possible. The geological sections were constructed at 1:50,000 scale, scanned and reduced in size to be displayed along with the profiles of residual gravity. The geological information comes from a combination of field observations made during the summer of 1995, the 1:50,000 scale geological maps published by IGME, and fault maps from the published literature (e.g., *Roberts* [1996b]). The seven geological sections[1] each have the same scale and key (Figure 5.13).

5.3 The Residual Bouguer Anomaly and Surface Geology

The residual Bouguer anomaly is expected to show correlations with the surface geology map of Figure 3.9. Within a basin, the residual Bouguer anomaly might be expected to reflect lateral variations in sediment thickness. However, sediment bulk density is expected to increase with depth, such that the observed anomaly will reflect the shallower structure more that the deeper structure (see Section 5.4).

If there are no systematic lateral variations in density, local minima in the resid-

[1]No sections are presented for the Alkyonides Gulf, the Megara Basin, the Thiva Plain or the Erithres Basin.

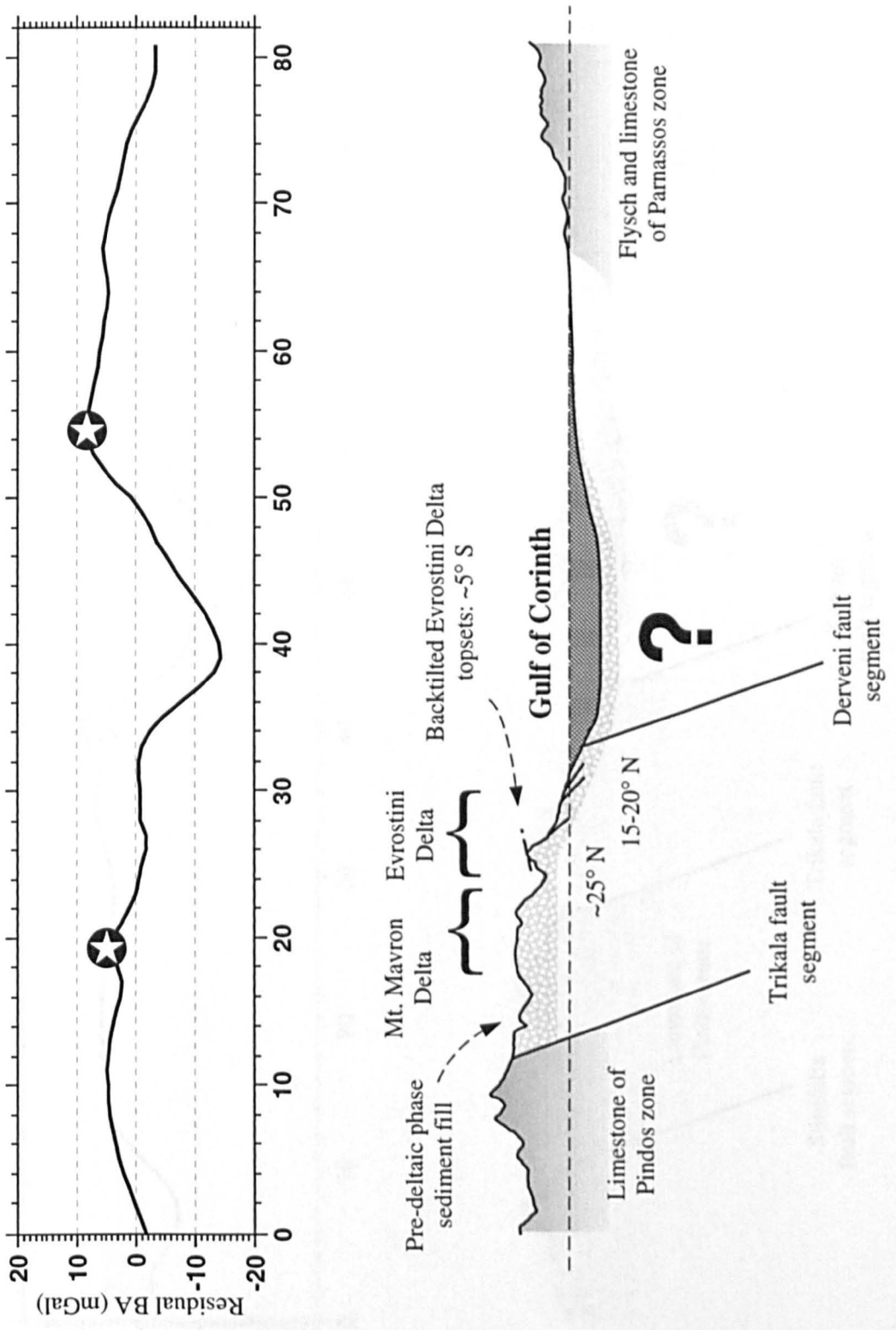

Figure 5.14: Profiles of geology and residual Bouguer anomaly for the Gulf of Corinth section 1.

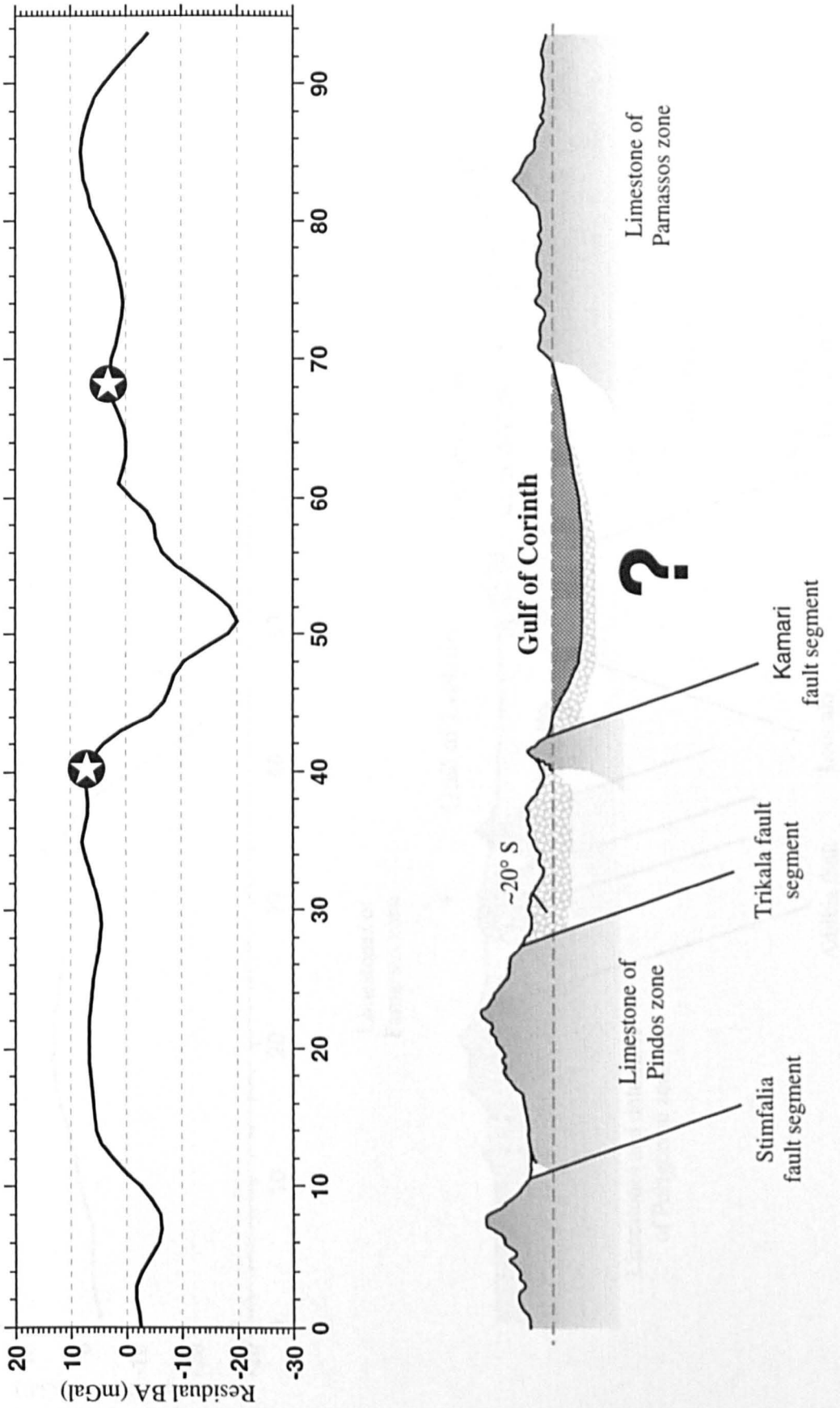

Figure 5.15: Profiles of geology and residual gravity anomaly for the Gulf of Corinth section 2.

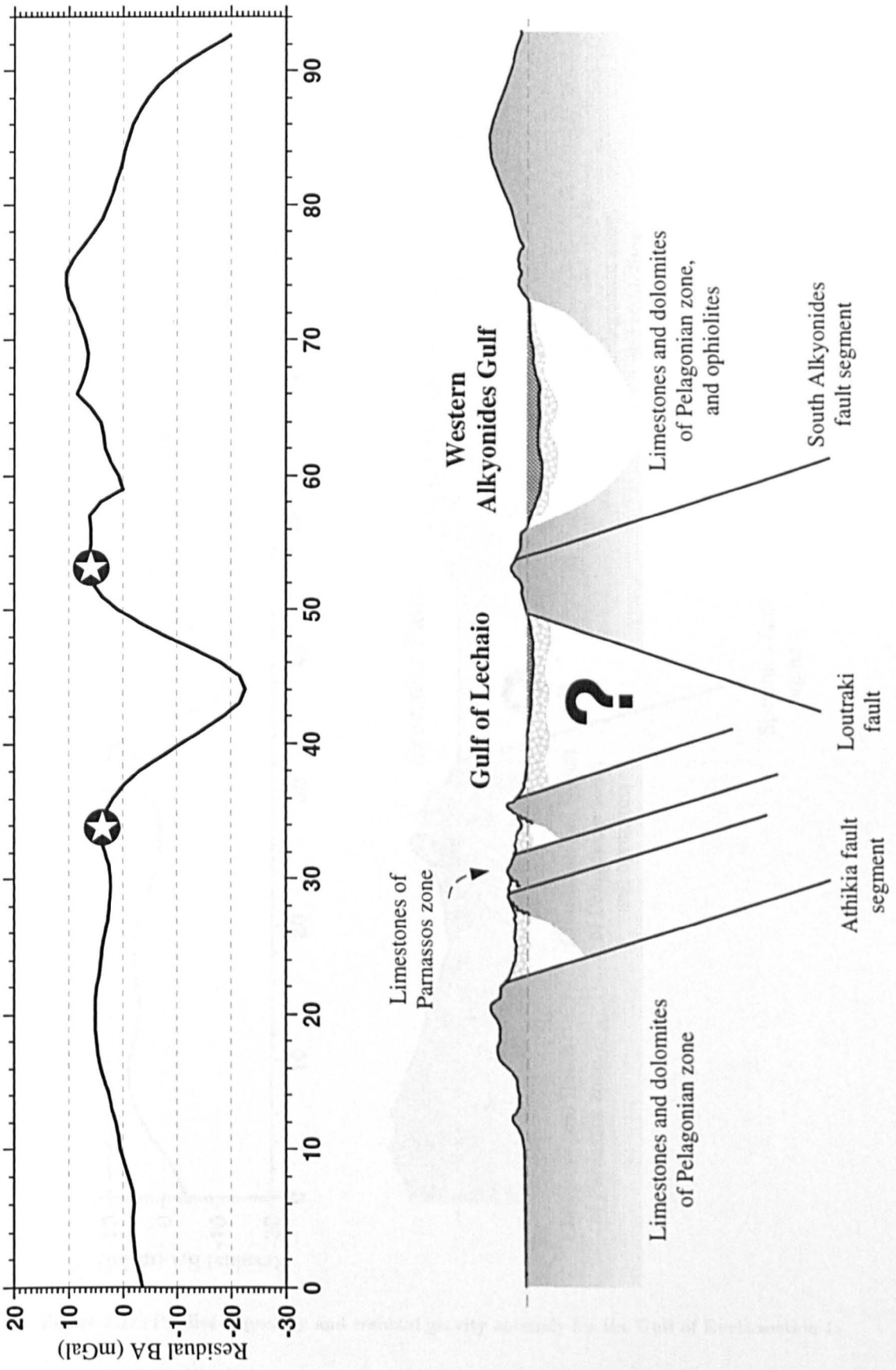

Figure 5.16: Profiles of geology and residual gravity anomaly for the Gulf of Corinth section 3.

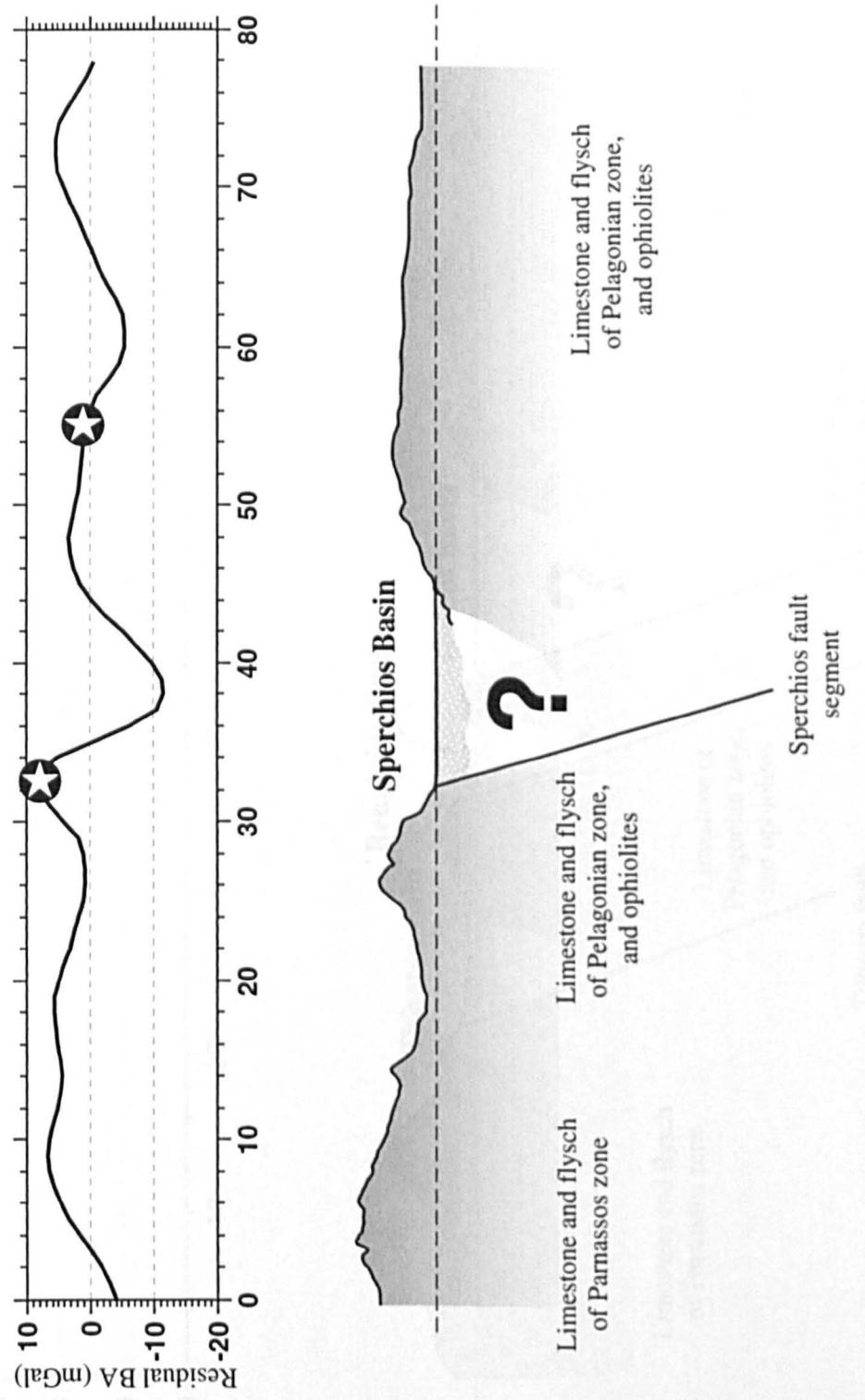

Figure 5.17: Profiles of geology and residual gravity anomaly for the Gulf of Evvia section 1.

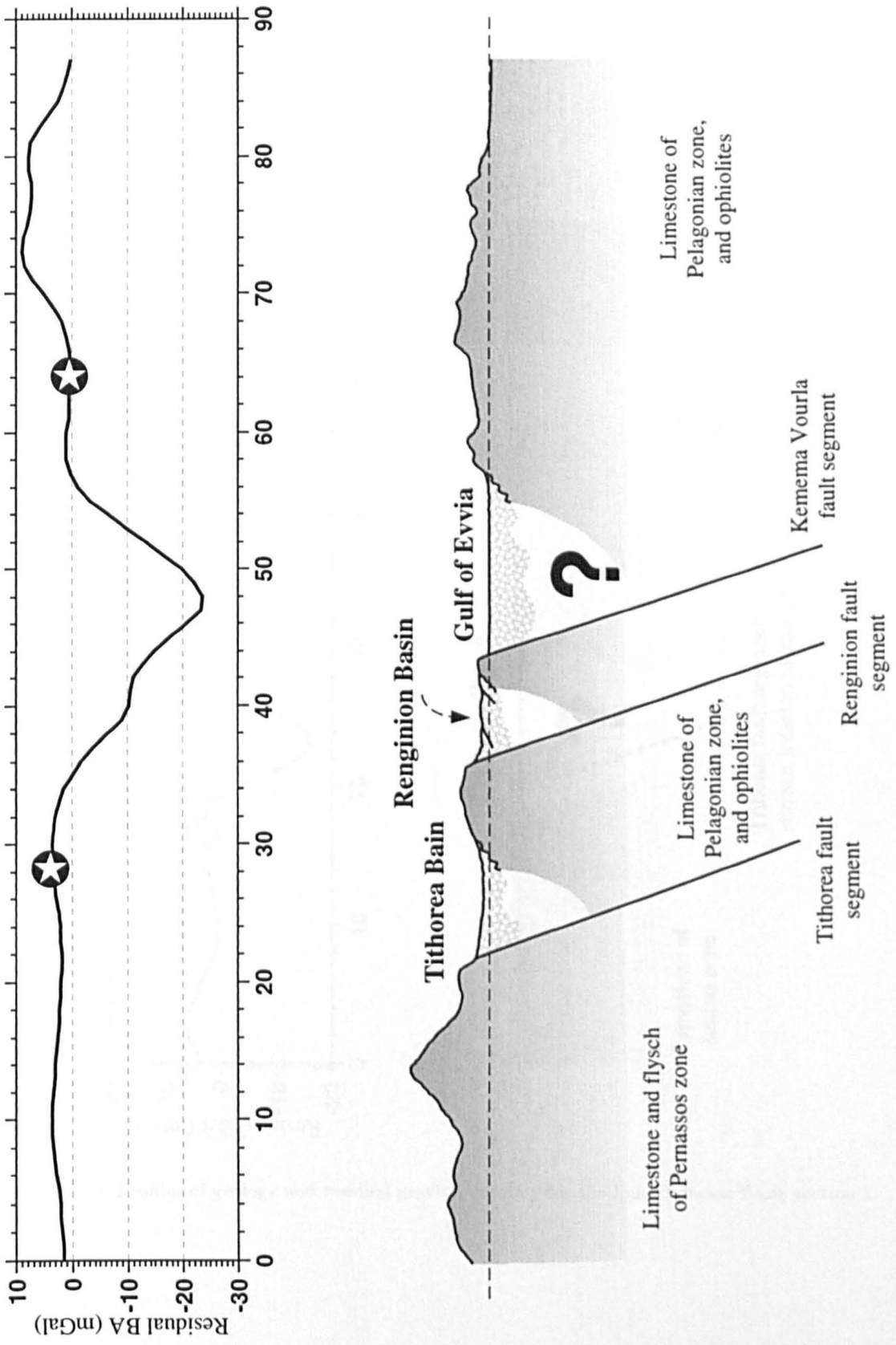

Figure 5.18: Profiles of geology and residual gravity anomaly for the Gulf of Evvia section 2.

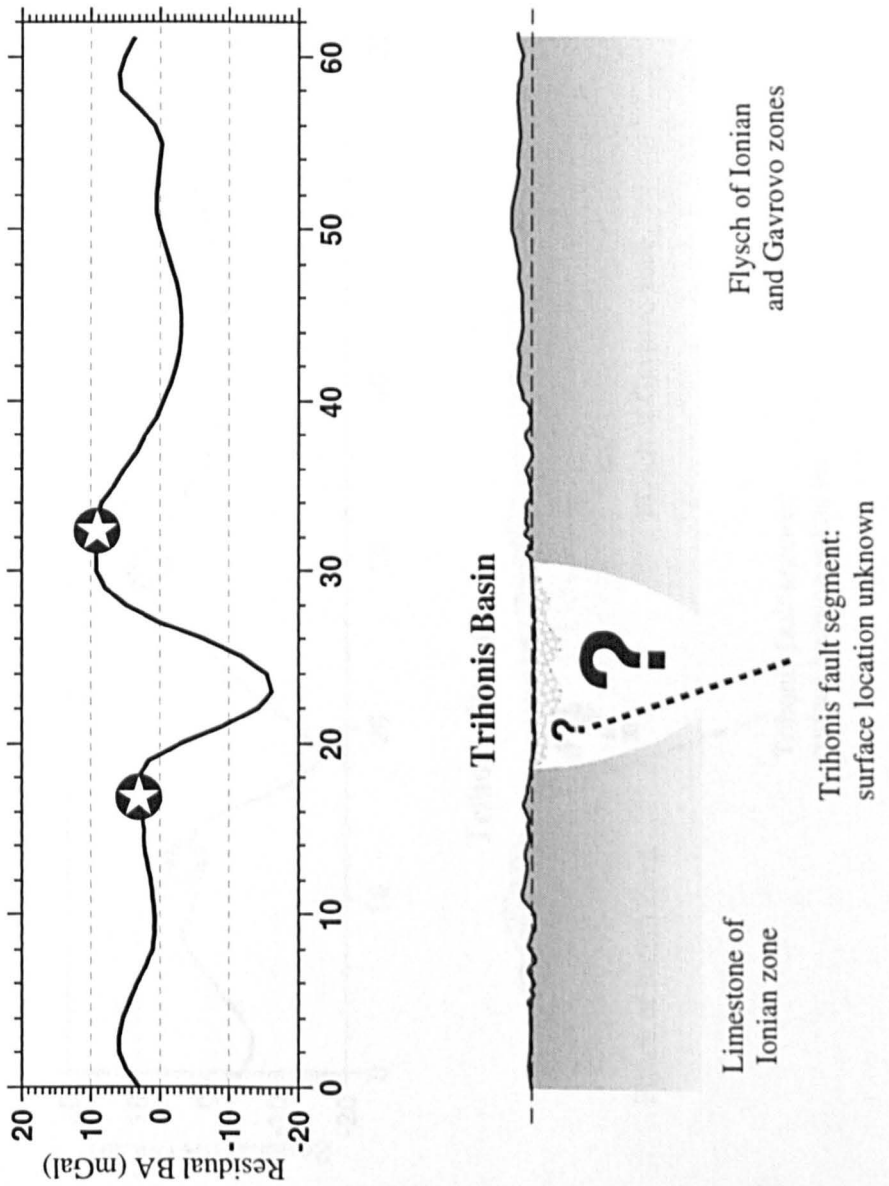

Figure 5.19: Profiles of geology and residual gravity anomaly for the Lake Trihonis Basin section 1.

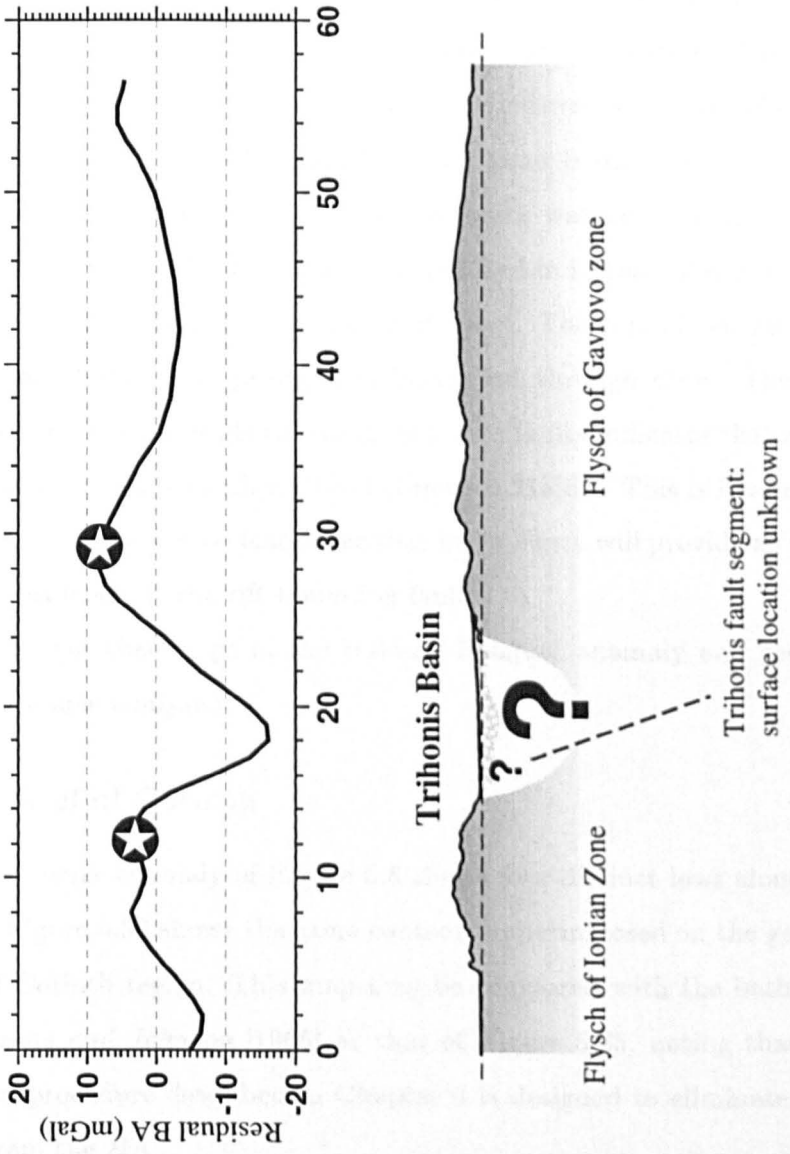

Figure 5.20: Profiles of geology and residual gravity anomaly for the Lake Trihonis Basin section 1.

ual BA will correlate with thicker sediment accumulations. Furthermore, if the apparently thicker sediment accumulations are not coincident with bathymetric or topographic highs, then we may infer a greater depth to basement. It must be emphasised that the confidence one can assign to any particular feature in the gravity field is a function of the original gravity station spacing across it.

Even where confident estimates of basin depth may be obtained, the amount of hanging wall subsidence in the rift-bounding fault segment is difficult to assess if the basin floor did not start to subside from sea level. However, with careful consideration, upper-bound estimates may be distinguished from lower-bound ones.

Prior to the onset of extension, Aegean tectonics was dominated by compression and crustal thickening so it is likely that rifts initiated in intramontane settings (Figure 5.21a[iii]), such as in the Basin and Range and Tibet. The rifts of central Greece show that rift-bounding faults have propagated basinward through time. The exposure of marine sediment on the footwalls to currently active faults indicates that subsidence in its hanging wall initiated beneath sea level (Figure 5.21a[ii]). This is illustrated in more detail by Figure 5.21b, and it is clear to see that basin depth will provide an upper-bound estimate for subsidence on the rift-bounding fault[2].

It is in this light that maps of the residual Bouguer anomaly and geology for the three regions are now analysed.

5.3.1 The Gulf of Corinth

The residual Bouguer anomaly of Figure 5.6 shows four distinct lows along the Gulf of Corinth Rift. Figure 5.22 shows the same contours superimposed on the geological map of the Gulf of Corinth region. This map may be compared with the bathymetric map of *Heezen, Ewing and Johnson* [1966] or that of Figure 5.23, noting that the gravity data reduction procedure described in Chapter 4 is designed to eliminate the effect of bathymetry from the BA.

It is perhaps surprising that there is no clear gravitational signal from the Neogene sediments exposed in the northern Peloponnese. Chapter 4 shows that the random error in both the onshore and Gulf of Corinth gravity data is due mostly to errors in the terrain correction. This error is likely to be smaller offshore than on, as the topography is both

[2]The extent to which the displacement patterns of parallel faults interfere is a function of fault spacing and effective elastic thickness.

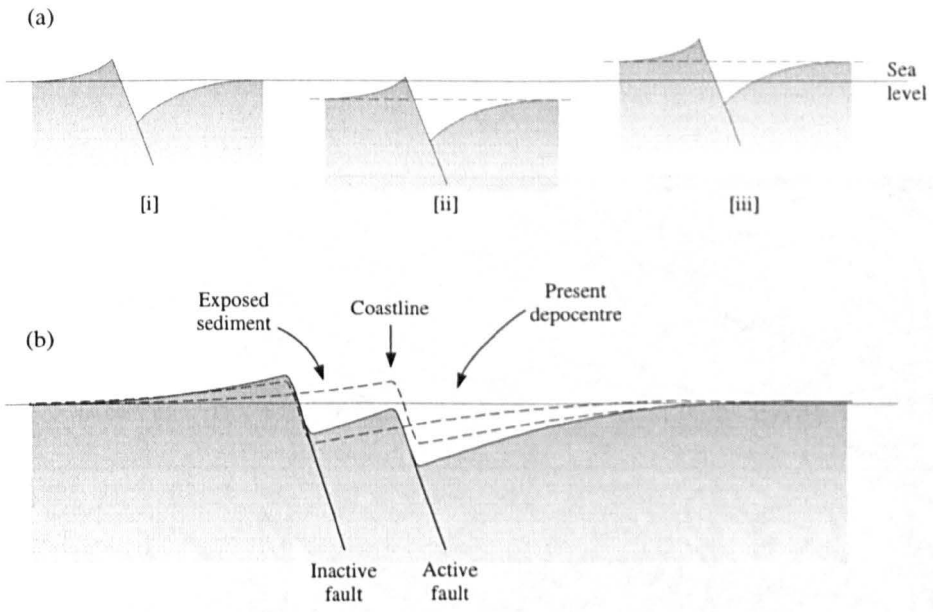

Figure 5.21: Schematic representation of how basin depth may provide either upper-bound or lower-bound estimates for hanging wall subsidence. (a) Basin depth is measured from present-day sea level, though subsidence may have initiated below [ii] or above [iii] this level. (b) A more detailed analysis of the case where subsidence initiated beneath sea level.

smoother and more distant from the point of observation. It will be seen in Figures 5.32 and 5.33 that an anomaly of 4 mGal would correspond to ~150 m of uncompacted sediment. Perhaps this is an indication of the minimum sediment thickness at the points of gravity measurement.

The largest feature in the residual Bouguer gravity runs along the Gulf of Corinth from ~22.1° in the west to ~22.9° in the east, a length of ~70 km. Two local minima are observed: one offshore from Xylocastron with amplitude 21 mGal, and one to the west with amplitude 15 mGal (Figure 5.22).

The minima to the west occurs at the offset between the Eigion and the inferred Derveni fault segments. Streams flowing through such offsets drain a greater area of catchment, and the source of the currently active Akrata delta (the River Kratis) enters the Gulf through the offset. It is tempting to assign the gravity anomaly to an increased thickness in sediment. However, such a feature is not evident in the bathymetric map of Figure 5.23 (see also the map of *Heezen, Ewing and Johnson* [1966]). The gravity anomaly may be explained by the presence of coarse, low density sediment which may retain its porosity on burial deeper than surrounding finer grained sediment. Alternatively, the residual anomaly may indicate a greater depth to basement representing subsidence in historically inactive faults (Figure 5.21b).

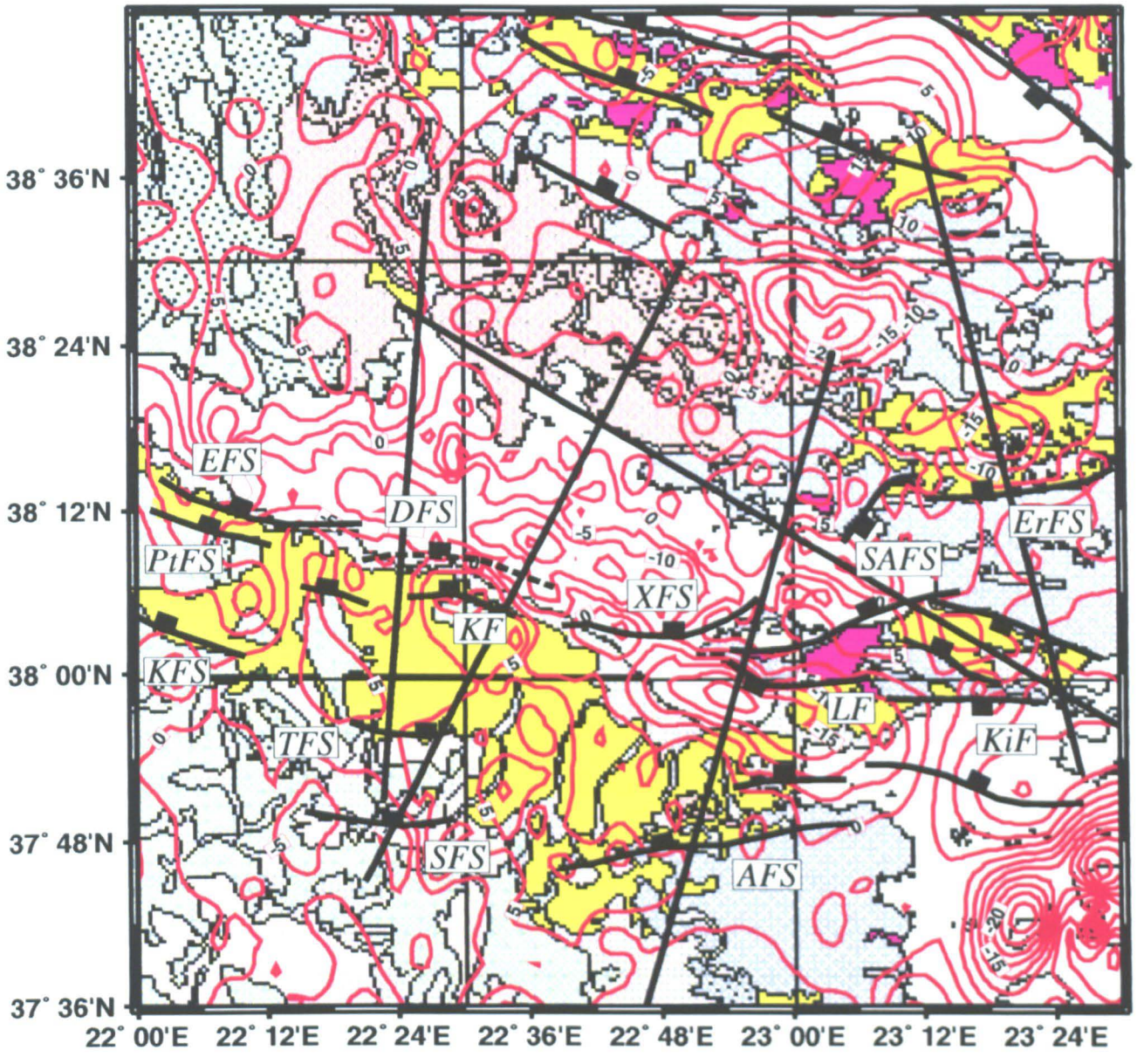

Figure 5.22: Geology map for the Gulf of Corinth region, overlain by the residual Bouguer anomaly, contoured at 5 mGal. Three distinct gravity lows are seen within the Gulf of Corinth. There are also lows across the Alkyonides Gulf, Thiva Plain, the Erithres Basin and the Megara Basin. *EFS*: Eigion fault segment. *DFS*: Derveni fault segment. *XFS*: Xylocastron fault segment. *SAFS*: South Alkyonides Fault Segment. *KFS*: Kalavrita fault segment. *PtFS*: Pteri fault segment. *KF*: Kamari fault. *TFS*: Trikala fault segment. *SFS*: Stymfalia fault segment. *LF*: Loutraki fault. *AFS*: Athikia fault segment. *KiF*: Kineta fault. For key to geological information, see Figure 3.9.

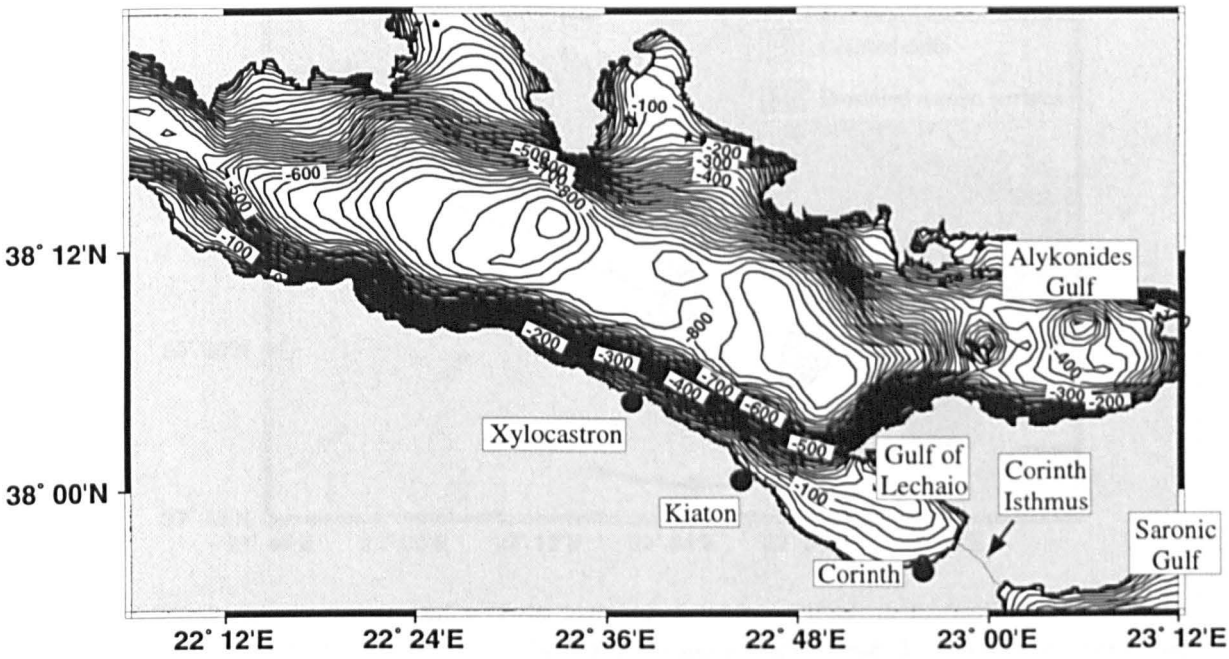

Figure 5.23: Bathymetry of the Gulf of Corinth, from 2 km DEM. Contour interval is 25 m.

The second minima to the east is located mostly in the hanging wall to the Xylocastron fault segment, but continues further west into the hanging wall of the Derveni fault. *Armijo et al.* [1996] link the Xylocastron fault with the Kamari fault that bounds the basement block west of Xylocastron, though there is field evidence to indicate that such a westward continuation does not exist [*Roberts*, 1996a]. The westward continuation of the gravity low is probably the combined effect of more than one depocentre.

The largest magnitude anomaly (~23 mGal) lies across the Gulf of Lechaio and the Corinth Isthmus. There are no data points to the east of the Isthmus (see Figure 5.6), so the nature of its continuation towards the Saronic Gulf is not constrained. The apparent closure of the residual low to the east may simply be a feature of data gridding, but its length is at least 25 km.

The smooth bathymetry of the Gulf of Lechaio and its southern continuation onshore around Corinth and Xylocastron indicates the presence of an old rift basin, controlled by the historically inactive Loutraki fault. *Collier and Dart* [1991] provide evidence for activity on this fault during the Lower Pliocene (pre 4 Ma) and show that the thickness of these early syn-rift sediments is at least 800 m. The sedimentary strata are being uplifted in the footwalls to the Xylocastron and South Alkyonides fault segments. The eustatic sea level fluctuations that are superimposed on the relatively slower tectonic uplift has produced a series of stepped erosional terraces between Xylocastron and Kiato [*Armijo*

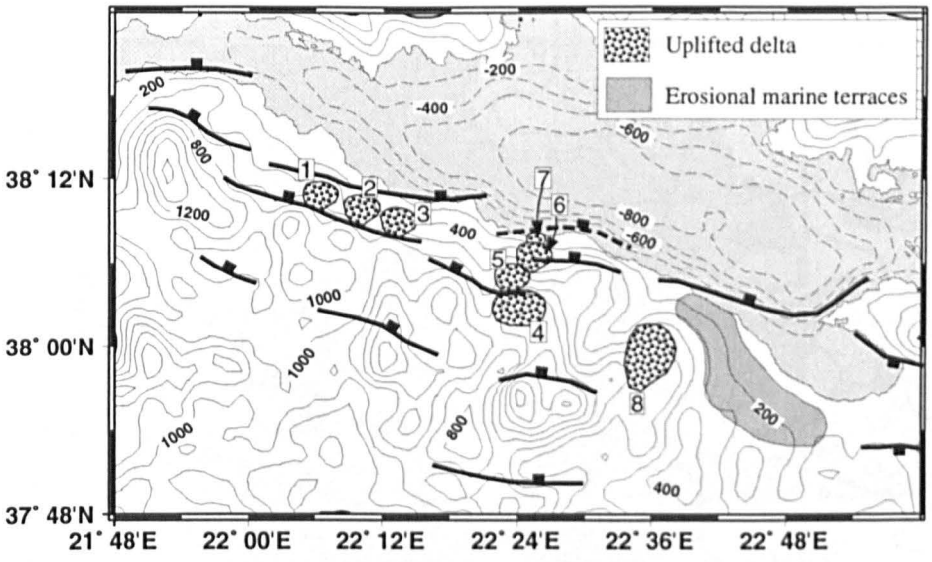

Figure 5.24: Schematic representation of the location of uplifted Gilbert deltas and erosional marine terraces in the northern Peloponnese. The fan deltas are named as followed: 1 - Selinous; 2 - Keranitis; 3 - Vouraikos; 4 - Mt. Mavron; 5 - Evrostini; 6 - Ilias; 7 - Rodea; 8 - Proto-Xylocastron. Marine terraces are seen at elevations of up to 400 m. Contour interval for topography and bathymetry is 200 m. Based on field observations, *Stephens* [1995], *Dart et al.* [1994] and *Armijo et al.* [1996].

et al., 1996; *Sébrier*, 1977] (Figure 5.24).

The fourth gravity low occurs in the Alkyonides Gulf with an amplitude of ~8 mGal. The northwesterly trend of the gravity anomaly may indicate that the anomaly represents the offshore continuation of the Megara basin. However, the high density ophiolite to the west may be complicating the signal.

The exposure of marine Neogene sediment across the northern Peloponnese indicates that the present rift-bounding faults initiated under water[3]. Using present-day sea level as the reference datum will therefore lead to upper-bound estimates for the *amount* hanging wall subsidence. There are no means currently available to directly estimate the *rate* of hanging wall subsidence.

The amount of footwall uplift may be estimated from the elevation of marine sediment, such as old delta foresets. The assumption here is that the exposed sediment is marine (or that lake level was approximately the same as sea level), which cannot be demonstrated at all locations. Where Neogene sediment can be dated, such as on the marine terraces around Corinth, the rate of uplift may be determined (e.g., *Armijo et al.* [1996]; Figure 5.24).

[3]The location of the 1995 Eigion earthquake may indicate the presence of a fault offshore from the Eigion fault segment

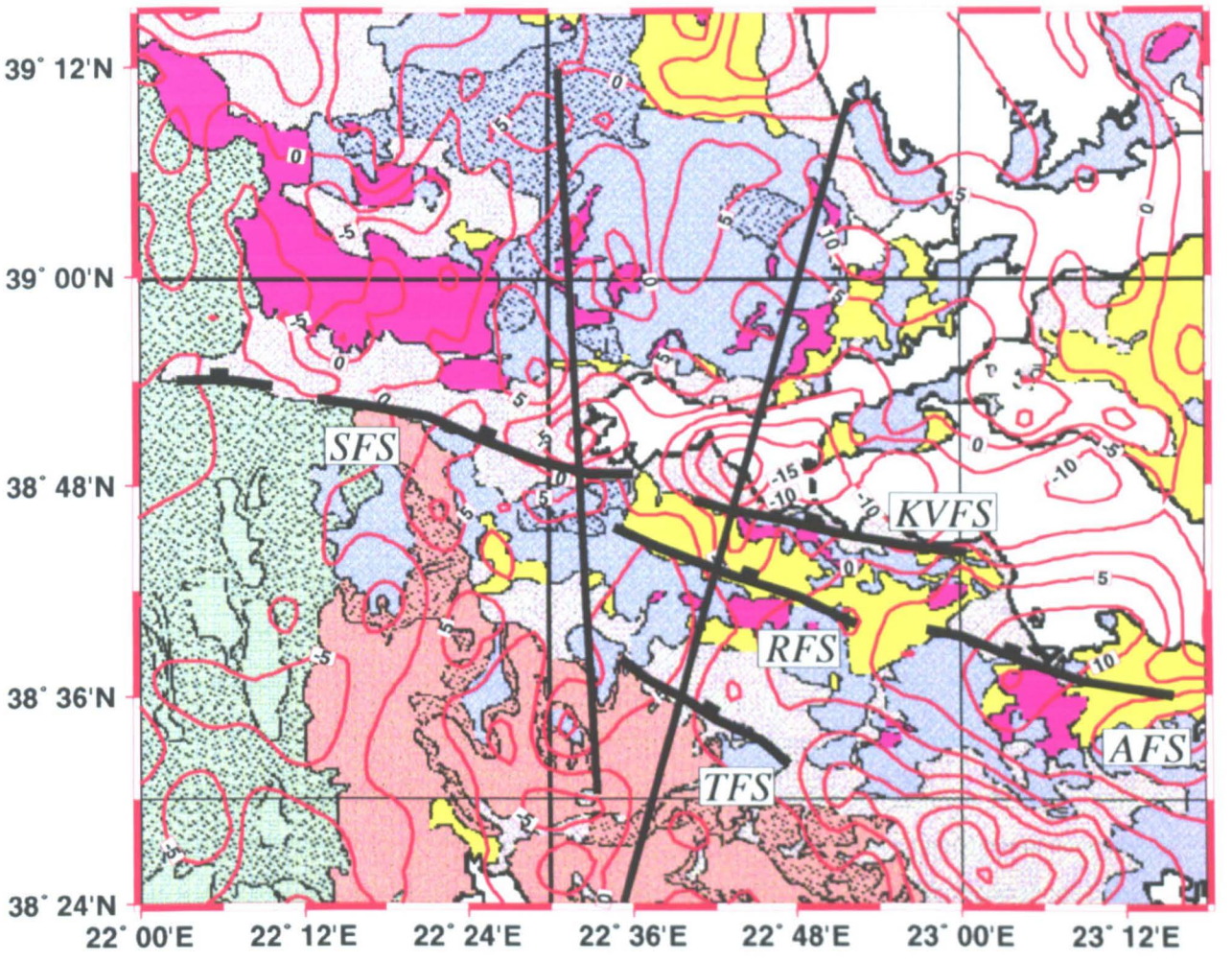

Figure 5.25: Geology map for the Gulf of Evvia region, overlain by the residual Bouguer anomaly, contoured at 5 mGal. *SFS*: Sperchios fault segment. *KVFS*: Kamena Vourla fault segment. *RFS*: Renginion fault segment. *AFS*: Atalanti fault segment. *TFS*: Tithoria fault segment. For key to geological information, see Figure 3.9.

5.3.2 The Gulf of Evvia

The residual gravity signature across the Gulf of Evvia is less clear than that for the Gulf of Corinth because there are no marine data. Even though there are relatively few data points to constrain their precise form, there are apparent lows in the hanging walls to the Sperchios (~12 mGal) and Kamena Vourla (~23 mGal) fault segments.

The Sperchios Basin clearly continues westwards to a longitude of 22.0° though there is no clear gravity signal west of 22.4°. This may be due to the presence of high density ophiolitic material beneath the lower density sediments (Figure 5.25). Finally, there is no apparent signature from the sediment in the hanging walls to the other fault segments shown in Figure 5.25, which is probably due to the low density of data coverage.

For the Kamena Vourla fault segment, basin depth may represent an lower-bound estimate for subsidence. It is located in the hanging wall of the Renginion segment, whose sediments are continental.[4] For the Sperchios segment however, subsidence initiated above sea level and basin depth will provide a lower-bound estimate for hanging wall subsidence.

5.3.3 The Lake Trihonis Basin

There is a good distribution of data across the region of interest, though the density of stations is poorer towards the east. Two residual gravity lows are confidently identified within the basin. The westerly one (~16 mGal) is ~10 km long, and the less well-constrained one to the east (~16 mGal) is ~15 km long. As described in Chapter 3, there is only indirect evidence for a fault on the southern margin of the basin. It is clear here that subsidence would have initiated in thickened crust, so basin depth is a lower-bound estimate for subsidence.

Brooks et al. [1988] suggest a scheme where the Lake Trihonis Basin is linked to the Gulf of Amvrakia Basin by left-lateral strike-slip faults. Such a model is supported by strike-slip focal mechanism solutions, by the tail of sediment at the northwestern end of the Lake Trihonis Basin (see Figure 5.26), and by the residual *BA* low that shows a similar trend.

This northwesterly trend parallels that of the pre-extensional structural grain, which might indicate the reactivation of Alpine related structures. It is clear from the geology of Figure 5.26 that these major thrust faults cross-cut the trend of the Lake Trihonis Basin, although there is no obvious gravitational signal of the thrusts or of the different isopic zones.

5.3.4 Other Basins

Residual gravity lows are also seen across the Thiva Plain (~25 mGal), the Erithres Basin (~17 mGal) and the Megara Basin (~7 mGal), although the form of the latter is constrained by few data points. These basins are not actively subsiding at present, and so are not discussed in detail. Estimates of depth to basement are provided here for completeness.

[4]This would assume that any eustatic effect is small compared to the tectonic subsidence.

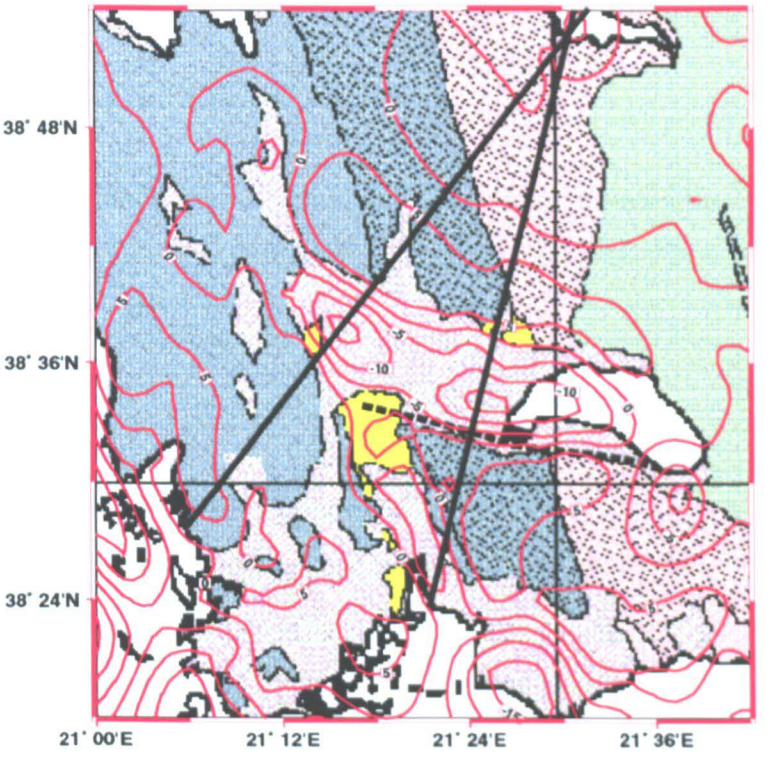

Figure 5.26: Geology map for the Lake Trihonis Basin, overlain by the residual Bouguer anomaly, contoured at 5 mGal. Two distinct gravity lows are seen. For key to geological information, see Figure 3.9.

5.4 Diagenesis, Porosity and Density

5.4.1 Theory

For the purposes of gravity modelling, we need to define density-depth relationships. Attempts to quantify porosity reduction with depth generally rely on fitting curves through observed porosity data. These data come from either the measurement of porosity in boreholes (e.g., *Gallagher and Lambeck* [1989], *Schmoker and Halley* [1982], *Sclater and Christie* [1980]), or from the analysis of sediment in compression tests (e.g., *Goldhammer* [1997]).

Although it is common to attribute porosity reduction purely to mechanical compaction, five processes control the change in porosity of a sediment from its depositional value: mechanical compaction, overpressuring, cementation, dissolution and recrystallisation (Figure 5.27) [*Gallagher*, 1989; *Thorne and Watts*, 1989]. The processes of dissolution and recrystallisation are not shown in Figure 5.27, though their effects on porosity are obvious.

For a general depth z, a volume of rock ($V(z)$) comprises a grain component ($V_g(z)$),

a cement component $(V_c(z))$, and a fluid component $(V_f(z))$, such that

$$V(z) = V_g(z) + V_c(z) + V_f(z) \; . \tag{5.4}$$

Athy [1930], *Korvin* [1984] and *Goldhammer* [1997] have shown that in the absence of cementation (i.e., $V_c(z) = 0$), porosity (Φ) decreases exponentially with depth (z) from its depositional value, Φ_0. Thus,

$$\Phi(z) = \Phi_0 e^{-cz} \tag{5.5}$$

where c determines the rate of decay with depth such that the greater the value of c, the more rapidly a sediment compacts with depth. The density of a sediment at depth z is found as

$$\begin{aligned} \rho_s(z) &= \text{mass}/\left(V_g(z) + V_f(z)\right) \\ &= \left(1 - \Phi(z)\right)\rho_g + \Phi(z)\rho_w \; . \end{aligned} \tag{5.6}$$

The second mechanism, cementation, is impossible to predict, and its influence is unlikely to be a simple function of depth. In the extreme case where $\Phi(z) = 0$ and assuming that the cement density is the same as the grain density (ρ_g), the bulk density will equal the grain density (Figure 5.27).

Overpressuring results if water cannot escape from a compacting sedimentary layer. In such cases, the weight of the overburden is partially supported by the excess pore-fluid pressure. In the extreme case where fluid movement is completely restricted, the bulk density will not change from its depositional value (Figure 5.27).

5.4.2 Application to Siliciclastic Lithologies

Most analyses of porosity reduction have focussed on the behaviour of siliciclastic sediment. Figure 5.28 shows a range of observed porosity-depth relationships for sandstone and for shale. Inconsistency in the observed trends is due to variations in lithology and in the relative influence of the five diagenetic processes.

The results of *Sclater and Christie* [1980] are based on exploration wells in the North Sea and have been widely applied. Figure 5.28 shows that their data lie towards the high porosity end of the observed trends. The results of *Gallagher and Lambeck* [1989]

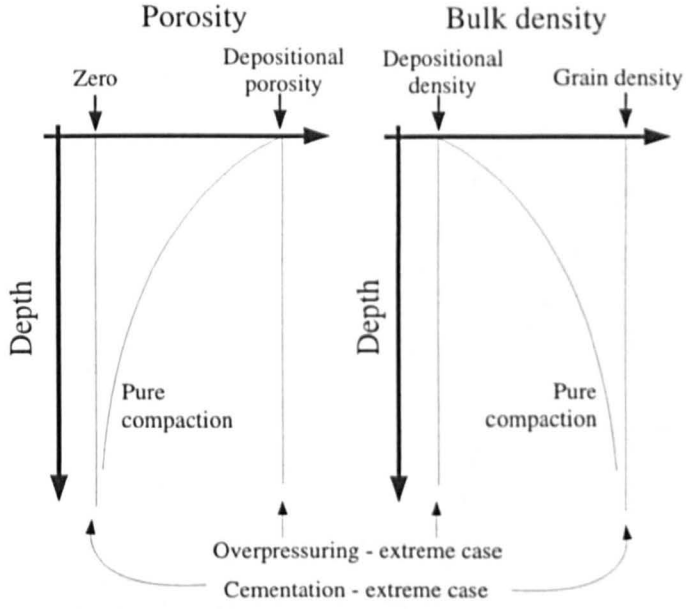

Figure 5.27: A schematic representation of the range of possible porosity-depth functions for a single lithology of known depositional porosity (Φ_0) and grain density (ρ_g). A pure compaction trend lies between trends that include cementation and overpressuring. The corresponding schematic representation of bulk density is also shown, assuming that cement density is equal to grain density. The effects of dissolution and recrystallisation are obvious, and are not represented in this diagram.

Lithology	Φ_0 (%)	c (km^{-1})	Reference
Sandstone (S1)	49.0	0.27	(1)
Sandstone (S2)	42.8	0.614	(2)
Shale (Sh1)	63.0	0.51	(1)
Shale (Sh2)	50.4	1.616	(2)

Table 5.2: Model parameters for the modelling of exponential porosity reduction with depth, corresponding to the thick lines in Figures 5.28 and 5.29. (1) [*Sclater and Christie*, 1980] and [*Cowie and Karner*, 1990]. (2) [*Gallagher and Lambeck*, 1989].

lie at the low porosity end, and are based on porosity data from the Eromanga Basin in Australia. Both studies show that the porosity varies exponentially with depth, and the parameters are shown in Table 5.2. Both sets of results are used in this study and are taken to represent extremes.

5.4.3 Application to Carbonate Lithologies

The high susceptibility of carbonates to dissolution, recrystallisation and cementation means that porosity-depth relationships are in general more complex than for siliciclastic sediment. The diagenetic potential of carbonates depends on the permeability, and so

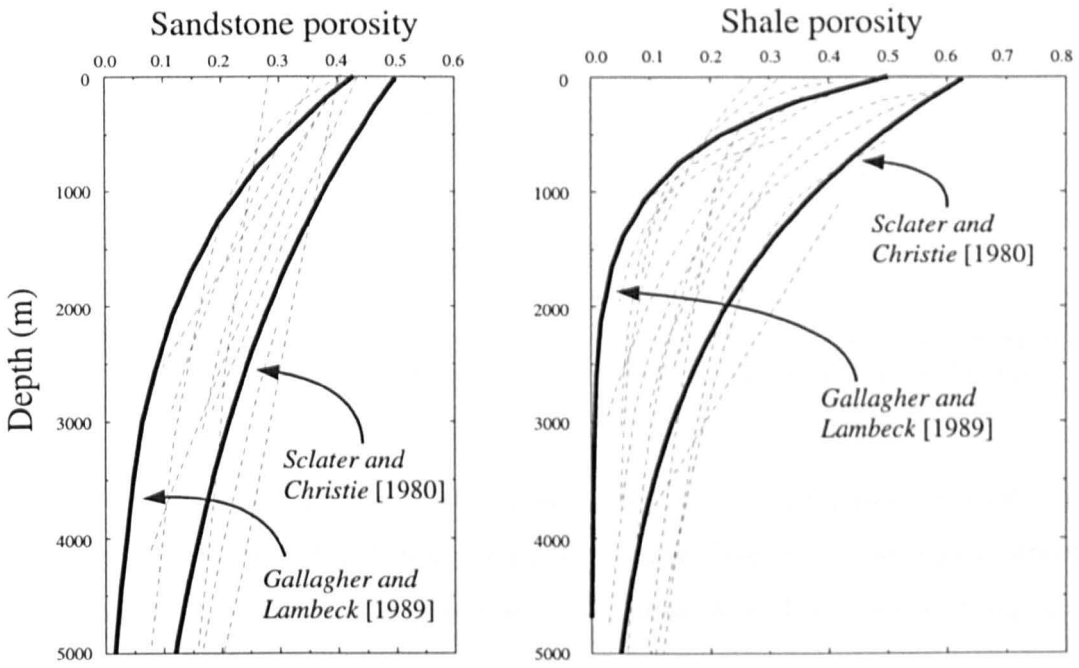

Figure 5.28: Porosity-depth curves for sandstone and shale. Dashed lines correspond to the findings of numerous studies, as presented by *Poelchau et al.* [1997]. The bolder lines (see Table 5.2 for parameters) which broadly envelope the range are those used in this study.

on grain size. Coarser grained rocks are cemented and altered more quickly than finer grained ones.

Goldhammer [1997] uses compressional testing results to find porosity depth functions for carbonate mud (i.e., marl) and carbonate sand, so the results are a description of compaction alone. Carbonate muds undergo significant compaction in the first 150 m of burial, through which a 50% porosity decrease can occur. At greater depths, compaction occurs at a slower rate (Table 5.3, Figure 5.29).

In a study of the sonic velocity of carbonate rocks from Florida, the Bahamas and Central Italy, *Anselmetti and Eberli* [1993] show that after an initial compaction, the porosity may continue to decrease due to further compaction and cementation. However, the trend is not as predictable as for siliciclastics and the porosity may actually increase due to grain dissolution. This complication is evident in the range of observed porosity-depth trends in Figure 5.29.

In spite of these observations, porosity measurements generally display a decrease with depth (Figure 5.29). *Sclater and Christie* [1980] show that the porosity-depth relationship for chalk in the North Sea shows an exponential behaviour. Similarly, *Schmoker and Halley* [1982] analyse a thick succession of carbonate rocks from South Florida that represent a wide range of depositional environments. They also show that the subsequent

Lithology	Φ_0 (%)	c (km^{-1})	Source
Chalk (L1)	70.0	0.71	(1)
General Carbonate (L2)	41.7	0.4	(2)
Carbonate sand	47.8	0.251	(3)
Carbonate mud ($z < 150$ m)	70.0	3.80	(3)
Carbonate mud ($z > 150$ m)	40.0	0.154	(3)

Table 5.3: Parameters for the modelling of exponential porosity reduction with depth, corresponding to the bold lines in Figure 5.29. (1) [*Sclater and Christie*, 1980]. (2) [*Schmoker and Halley*, 1982]. (3) [*Goldhammer*, 1997].

diagenetic effects on porosity can be characterised by an exponential function (Table 5.3, Figure 5.29). The sediment within any one rift in central Greece is expected to comprise a host of carbonate lithologies, so the results of *Schmoker and Halley* [1982] appear to be the most applicable.

5.5 Porosity Reduction and Bouguer Gravity

In order to estimate the depth to the basin floor from the amplitude of the residual BA, density increase with depth must be modelled. If the sediment infill is derived from the surrounding basement rocks of density ρ_b and porosity Φ_b such that their grain densities are equal, we can define the anomalous density relative to the basement rock. Using Equation 5.6,

$$\begin{aligned}\Delta\rho(z) &= \rho_s(z) - \rho_g \\ &= -(\Phi(z) - \Phi_b)(\rho_g - \rho_w)\ . \end{aligned} \tag{5.7}$$

If the porosity of basement rock is zero, $\Delta\rho(z)$ may be expressed from Equation 5.5 as

$$\Delta\rho(z) = -\Phi_0 e^{-cz}(\rho_g - \rho_w) \tag{5.8}$$

Equation 5.8 is used in this study. Thus, if the basement rock has porosity greater than zero, then $|\Delta\rho(z)|$ will overestimate the true density contrast.

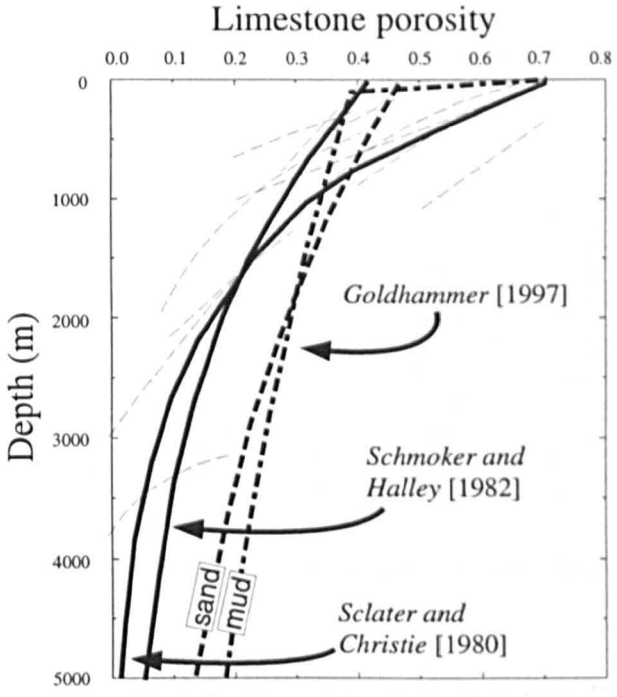

Figure 5.29: Porosity-depth curves for limestone. Dashed lines correspond to the findings of numerous studies, as presented by *Poelchau et al.* [1997]. The solid bold lines (see Table 5.2 for parameters) are those used in this study.

5.6 Grain Density and Rock Porosity Estimations

5.6.1 Basement Lithologies

Figure 3.9 shows that the main pre-rift lithologies in Central Greece are limestone, radiolarite, flysch, and ophiolitic material. Samples of these rocks were collected from the Ionian, Gavrovo, Pindos, Parnassos and Pelagonian Zones (Figures 3.7 and 3.9) and brought back to Leeds for density estimation. The flysch of these zones comprise weathered sandstones, clays and marls. Samples of sandstone were taken from the Ionian and Gavrovo Zones. An unweathered sample of ophiolite was not found in the field, although the densities of mafic rocks are well known [*Telford, Geldart and Sheriff*, 1990]. The limestone basement lithologies are seen to have very little porosity, which is probably the result of metamorphism. Indeed, the limestone basement is seen to have a marble texture in places.

Densities are estimated using a standard buoyancy technique (e.g., *Brown* [1981]). Four samples of each rock type from geographically distinct locations were used. The values in Table 5.4 represent the mean of the four density estimates. Individual errors are not presented, and the random error on single wet and dry density measurements is

Rock type	Dry ρ (kg/m^3)	Sat. ρ (kg/m^3)	Φ (%)	ρ_g (kg/m^3)
Ionian Limestone	2695	2710	1.5	2736
Gavrovo Limestone	2728	2744	1.6	2772
Pindos Limestone	2702	2715	1.3	2738
Pindos Radiolarites	2582	2653	7.1	2779
Parnassos Limestone	2688	2692	0.4	2699
Pelagonian Limestone	2784	2788	0.4	2795
Ionian Flysch (sst)	2598	2651	5.3	2743
Gavrovo Flysch (sst)	2545	2607	6.2	2713
Basalt†	3000	3000	~0	3000
Gabbro†	3030	3030	~0	3030
Peridotite†	3150	3150	~0	3150

Table 5.4: Density estimations for the basement lithologies of Central Greece. † Values taken from *Telford, Geldart and Sheriff* [1990].

negligible. Because different samples of the same rock type were taken from geographically distinct locations, the dry density measurements range within ±2% of the average given in Table 5.4. Grain densities are estimated as the ratio of dry density to $(1 - \Phi)$, and the mean grain density for basement is 2750±50 kg/m^3.

5.6.2 Syn-rift Lithologies

Carbonate conglomerates and sandstones were examined in-situ on the southern margins of the Gulf of Corinth Rift and the Gulf of Evvia Rift. However, a specimen could not be taken from the field due to the large clast size and the friable nature. Five samples of marl were collected from the eastern Gulf of Corinth Rift, south of Xylocastron and Corinth. Table 5.5 presents the range of density estimations for the Corinth marls.

The method to calculate saturated density and porosity is slightly different from that of basement rocks as the samples fall apart when saturated. The dry density was measured by coating the specimen with plastic and, assuming ρ_g to be equal to the basement bulk density, the porosity and saturated density is found.

The lowest value is presumed to represent the least compacted, and this provides us with a minimum estimate for Φ_0 for the Corinth Marl of 38%. However, no estimate can be made for the Neogene carbonate sandstones and conglomerates of the Gulf of Corinth, and no measurements exist for the sediment in the other basins throughout Central Greece. Furthermore, the relative proportions of coarse and fine grained sediment cannot be constrained. In view of these uncertainties, gravity modelling is carried out for the

Rock type	Dry ρ (kg/m^3)	Φ (%)	Sat. ρ (kg/m^3)
Sample 1	1724	38	2104
Sample 2	1794	35	2144
Sample 3	1842	33	2172
Sample 4	1917	30	2217
Sample 5	1930	30	2230

Table 5.5: Density estimations for the Corinth marls, assuming a grain density of 2750 kg/m^3. Errors in the dry density measurements are less than 1%.

range of lithological parameters (i.e., Φ_0 and c) in Tables 5.2 and 5.3.

5.7 Gravity Models for Basin Depth

Section 5.5 has shown that porosity reduction must be considered in the modelling of Bouguer gravity across rift basins. Commercially available gravity modelling packages work with discrete bodies for which single density values must be assigned. Modelling the gravity signature across the rifts of Greece would therefore require creating many thin bodies in order to approximate density variations with depth. As six sets of compaction parameters are to be tested, a less cumbersome method was sought.

Oliva and Ravazzoli [1997] present an algorithm for the computation of gravity anomalies over bodies whose density varies both laterally and vertically. Although lateral density variations may occur within the rifts of central Greece, no data exist to constrain them. *Cowie and Karner* [1990] present a Fourier domain method for sediments whose density vary as depth alone. As basin depth is the only parameter to be estimated, a more simple approach is derived here.

The shape of the rift basin may be approximated by three distinct bodies: an infinite slab, a beam with rectangular cross-section, or a beam with triangular cross-section (Figure 5.30). Both beams are infinite in the y-dimension i.e., along the strike of the rift. The floors to the basins are expected to be less uniform than represented in Figure 5.30, but the effects of upward continuation will mean that average depths are estimated. Expressions for the amplitude of the gravity anomaly over these model bodies are now derived.

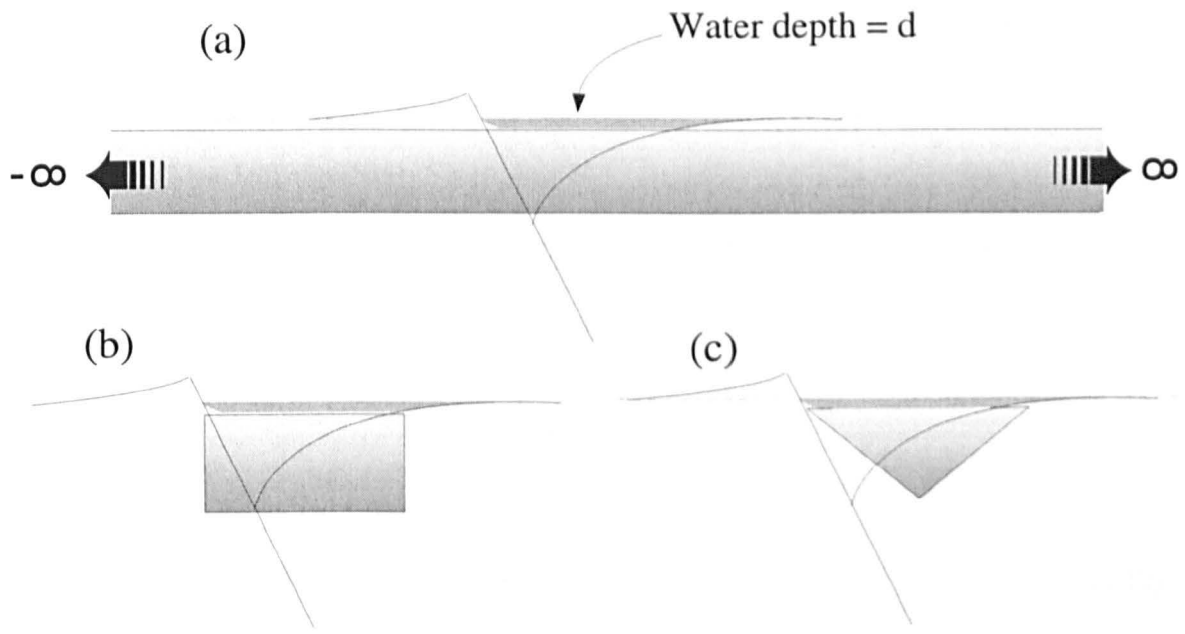

Figure 5.30: Approximations to a typical half-graben geometry. (a) The infinite slab approximation. (b) The rectangular beam approximation. (c) The triangular beam approximation.

5.7.1 Derivation of Gravity Models

The vertical component of the gravitational attraction of an element of mass m at position (x, y, z) is

$$g_{el} = \frac{Gm}{(x^2 + y^2 + z^2)^{3/2}} \cdot \tag{5.9}$$

Using Equation 5.8 this becomes

$$g_{el} = G\Phi_0(\rho_g - \rho_w)\frac{ze^{-cz}}{(x^2 + y^2 + z^2)^{3/2}}\delta x \delta y \delta z \tag{5.10}$$

This is extended to infinity in both positive and negative y to find the gravitational attraction of a line-mass.

$$\begin{aligned} g_{line} &= G\Phi_0(\rho_g - \rho_w)ze^{-cz}\delta x \delta z \int_{-\infty}^{\infty} \frac{1}{(x^2 + y^2 + z^2)^{3/2}}\, dy \\ &= 2G\Phi_0(\rho_g - \rho_w)ze^{-cz}\delta x \delta z \int_{0}^{\infty} \frac{1}{(x^2 + y^2 + z^2)^{3/2}}\, dy \\ &= 2G\Phi_0(\rho_g - \rho_w)\delta x \delta z \frac{ze^{-cz}}{x^2 + z^2}. \end{aligned} \tag{5.11}$$

This is the basic expression from which the gravitational attraction of the three distinct bodies is derived.

5.7.1.1 The Infinite Slab

Integrating Equation 5.11 in x from minus to plus infinity will give the expression for an infinite sheet, such that

$$\begin{aligned} g_{sheet} &= 2G\Phi_0(\rho_g - \rho_w)e^{-cz}\delta z \int_{-\infty}^{\infty} \frac{z}{x^2+z^2}dx \\ &= 2G\Phi_0(\rho_g - \rho_w)e^{-cz}\delta z \left[\arctan\frac{x}{z}\right]_{-\infty}^{\infty} \\ &= 2\pi G\Phi_0(\rho_g - \rho_w)e^{-cz}\delta z \ . \end{aligned} \tag{5.12}$$

The gravity of a slab of thickness s whose upper surface is at a depth b is found as

$$\begin{aligned} g_{slab} &= 2\pi G\Phi_0(\rho_g - \rho_w) \int_{b}^{b+s} e^{-cz}\ dz \\ &= \frac{2\pi G}{c}\Phi_0(\rho_g - \rho_w)\left(e^{-cb} - e^{-c(b+s)}\right) \end{aligned} \tag{5.13}$$

By expanding the exponential terms in power series, it is easily shown that g_{slab} tends to the familiar slab formula as c tends to zero.

5.7.1.2 The Rectangular Beam

To obtain an expression for a horizontal sheet of limited extent (or *strip*), Equation 5.11 is integrated between the horizontal limits a and a' (Figure 5.31) such that,

$$\begin{aligned} g_{strip} &= 2G\Phi_0(\rho_g - \rho_w)e^{-cz}\delta z \int_{-a}^{a'} \frac{z}{x^2+z^2}\ dx \\ &= 2G\Phi_0(\rho_g - \rho_w)e^{-cz}\delta z \left(\arctan\frac{a'}{z} + \arctan\frac{a}{z}\right) \ . \end{aligned} \tag{5.14}$$

If a' is equal to a, this becomes

$$g_{strip} = 4G\Phi_0(\rho_g - \rho_w)e^{-cz}\delta z \left(\arctan\frac{a}{z}\right) \ . \tag{5.15}$$

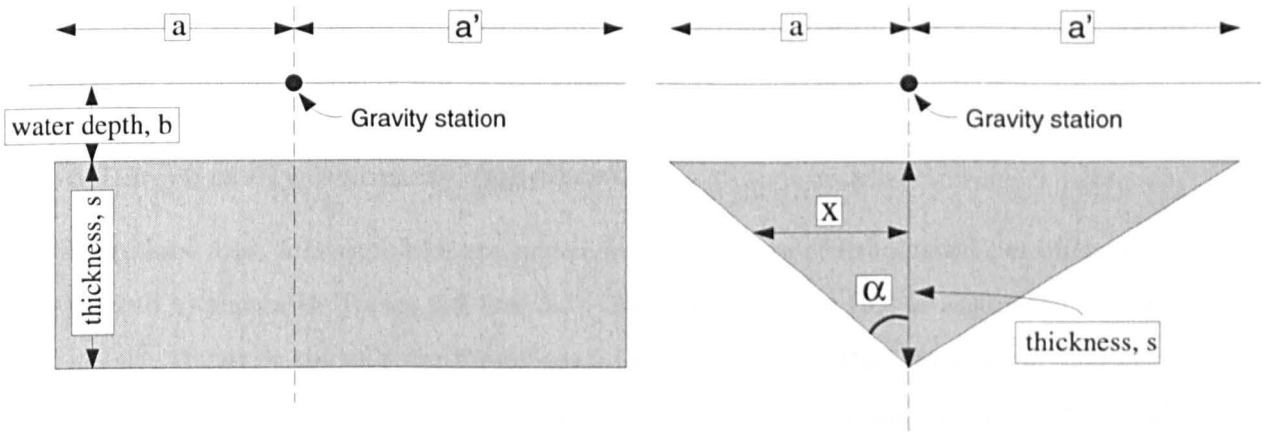

Figure 5.31: Geometry of the rectangular and triangular beams. For the analysis presented here, the dimensions a and a' are assumed to be equal.

The expression for the gravitational attraction of a rectangular beam of thickness s at a height b above its upper surface then becomes

$$g_{rect} = 4G\Phi_0(\rho_g - \rho_w) \int_b^{b+s} \arctan\left(\frac{a}{z}\right) e^{-cz}\, dz\ . \tag{5.16}$$

Because a simple analytic solution cannot be found, this integration was performed numerically using the extended trapezoidal rule [*Press et al.*, 1986].

5.7.1.3 The Triangular Beam

The geometry of the triangular beam is shown in Figure 5.31. From this,

$$\tan\alpha = \frac{a}{s} = \frac{x}{b+s-z} \tag{5.17}$$

where x is the half-width of the triangle at depth z. Substituting x for a in Equation 5.15,

$$g_{strip} = 4G\Phi_0(\rho_g - \rho_w)e^{-cz}\delta z \left(\arctan\frac{a(b+s-z)}{zs}\right)\ . \tag{5.18}$$

such that the gravitational attraction above the central point of a triangular beam is found as

$$g_{tri} = 4G\Phi_0(\rho_g - \rho_w) \int_b^{b+s} \arctan\left(\frac{a(b+s-z)}{zs}\right) e^{-cz}\, dz \tag{5.19}$$

As for the rectangular beam, this integration was performed numerically using the extended trapezoidal rule [*Press et al.*, 1986].

5.7.2 Gravity Anomaly Amplitudes

Equations 5.13, 5.16 and 5.19 are solved for the six sets of lithological parameters (i.e., Φ_0 and c) shown in Tables 5.2 and 5.3. The grain density (ρ_g) is assumed to be 2750 kg/m^3. It can be shown from Equations 5.13, 5.16 and 5.19 that the error of ± 50 kg/m^3 in ρ_g results in an error of ± 1 mGal in the calculated gravity anomaly magnitude. This is small compared to the gravity values presented in Table 5.1.

Sandstone S1 [*Sclater and Christie*, 1980] and shale Sh2 [*Gallagher and Lambeck*, 1989] represent extreme porosity-depth relationships. The form of the model curves for $2a = 10$ km are analysed for these two lithologies prior to the estimation of basin depths across central Greece. As the maximum water depth in the Gulf of Corinth is ~800 m (Figure 5.23), the lower limit of the integration, b, is varied from 0 to 1000 m. The thickness of the sediment body, s, is varied from 0 to 5000 m.

Figure 5.32 shows that, for a given magnitude of anomaly and depth, the infinite slab gives the smallest s. The decreasing magnitude here for a constant thickness is the result of exponentially decreasing porosity with depth. For the rectangular and triangular beams, the more rapid decrease with b is due to the additional effect of upward continuation. As expected, the triangular beam gives the greatest depth for any given magnitude of gravity anomaly.

The same set of plots for the rapidly compacting shale (Sh2) is shown in Figure 5.33. The same general pattern is seen, though the effect of the high c value is clear. This introduces the problem of sensitivity. Figure 5.28 shows that the density of shale Sh2 approaches that of the basement rock at depth of around 2000 m. This accounts for the near-vertical contours where the sum of b and s is 2000 m. For this analysis, a depth estimate is not assigned where the rate of increase in s with gravity anomaly magnitude exceeds 200 m/mGal

Finally, the water depth in the Gulf of Corinth reaches a maximum of 800 m. The porosity reduction curves assume that water depth is zero. Therefore, sediment is compacted less than the model assumes, resulting in a greater model density contrast. Further, the depth b is taken as the maximum water depth. Sediment at shallower depths toward the margins of the basin will also contribute to the magnitude of the observed

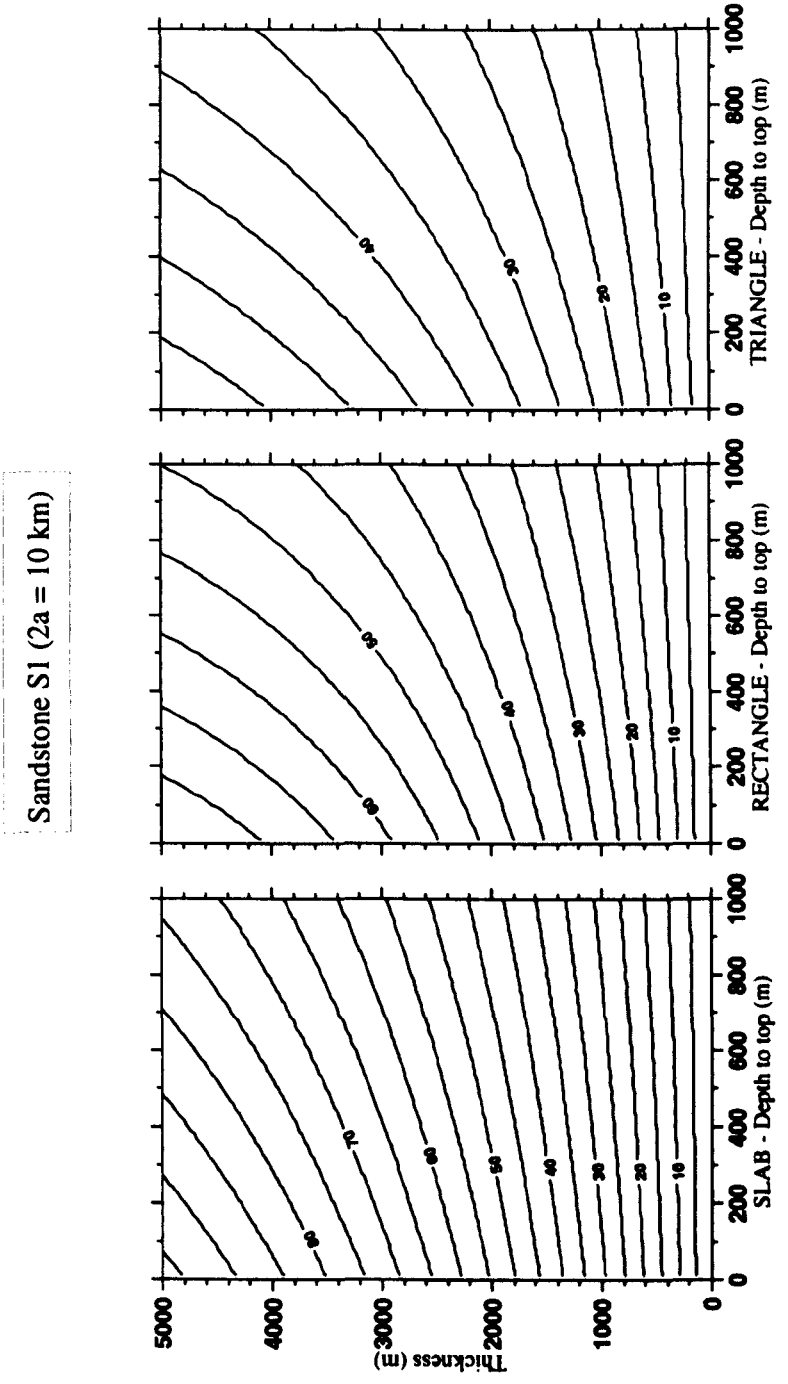

Figure 5.32: Magnitude of Bouguer anomaly predicted for (a) an infinite slab, (b) a rectangular beam, and (c) a triangular beam of sandstone S1. Porosity reduction parameters taken from *Sclater and Christie* [1980]. Width for (b) and (c) at depth b is 10 km (a = 5km). Contours in mGal.

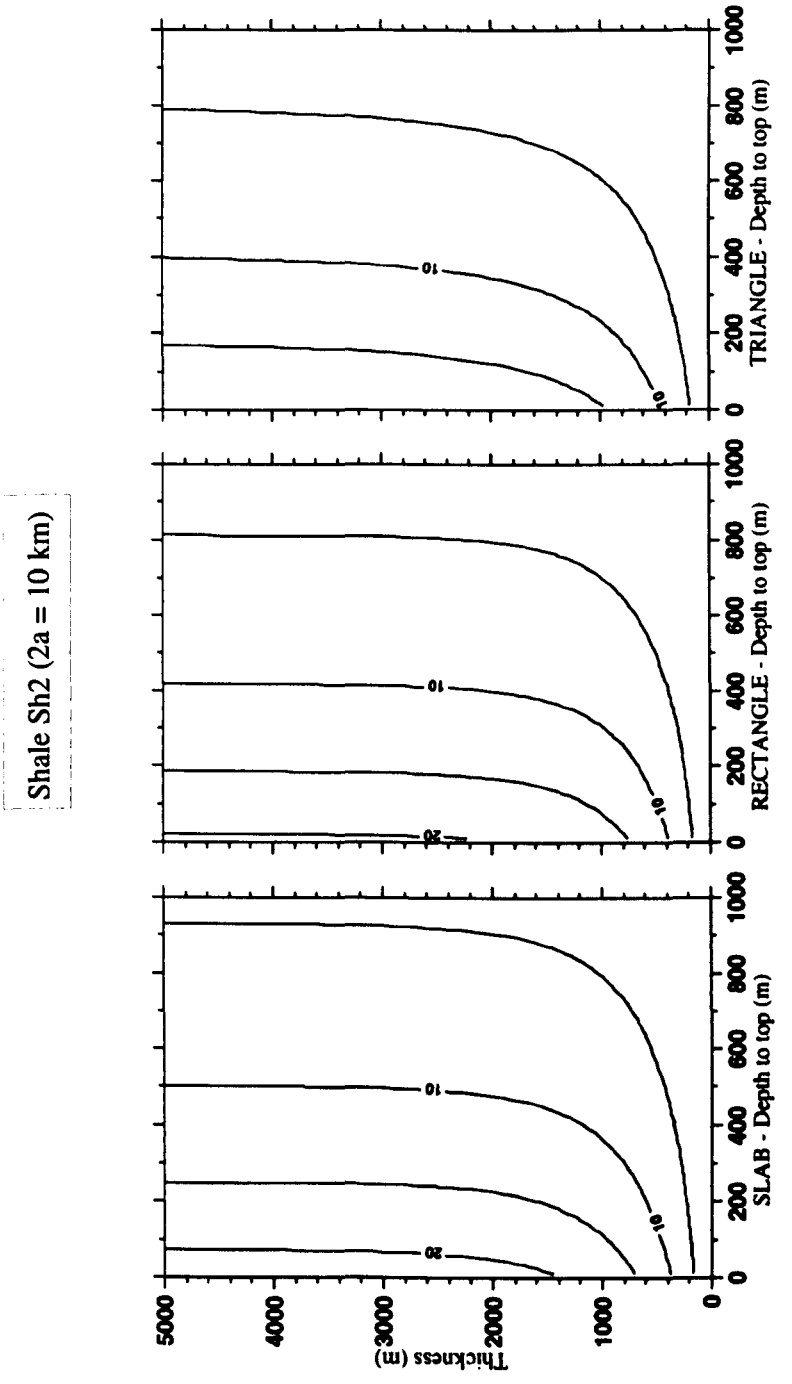

Figure 5.33: Gravity anomaly amplitude for (a) an infinite slab, (b) a rectangular beam, and (c) a triangular beam of sandstone Sh2. Parameters taken from *Gallagher and Lambeck* [1989]. Width for (b) and (c) at depth b is 10 km (a = 5km). Contours in mGal.

Anomaly	BA (mGal)		$2a$ (km)	s (m)	S1 Depths (m)		S2 Depths (m)	
	Min	Max			Min	Max	Min	Max
Corinth 1	15	21	20	800	1600	2000	2500	?
Corinth 2	21	27	20	800	2000	2400	?	?
Corinth 3	23	28	10	150	1250	1550	1950	?
Alkyonides	10	16	10	400	900	1200	1100	1800
Evvia 1	12	20	10	0	400	800	500	1100
Evvia 2	23	32	10	0	900	1500	1500	?
Trihonis 1	16	22	10	0	600	900	800	1400
Trihonis 2	16	25	10	0	600	1000	800	1700
Thiva	25	34	15	0	1000	1500	1500	?
Erithres	17	26	10	0	600	1100	900	1900
Megara	7	16	10	0	200	600	300	800

Table 5.6: Estimated basin depths assuming sandstone lithologies.

anomaly. Both of these effects result in upper-bound estimates of basin depth.

5.8 Basement Depth Estimations

The difference between the slab and the rectangular beam is greater than that between the rectangular beam and the triangular beam. This section deals only with the thicknesses of model triangular beams, such that estimates of basin depth are upper-bound. The full set of gravity curves is presented in Appendix H.

Tables 5.6, 5.7 and 5.8 summarise the depth estimates for each of the residual BA anomalies discussed in Section 5.3. The symbol '?' indicates situations where the rate of change of thickness (s) is greater than 200 m/mGal.

The porosity curve of *Schmoker and Halley* [1982] (i.e., limestone L2) is expected to best represent the behaviour of the sediment fill in the rifts of central Greece. Lithology L2 consistently gives the third deepest estimate for basin depth, after Sh2 and S2. Porosity reduction is so rapid for Sh2 that only two minimum estimates for basin depth can be made from the residual Bouguer gravity.

Within the Gulf of Corinth, the central of the three anomalies gives the greatest depth to basement of up to 3700 m. It is interesting to note that the sum of the depths estimated from the anomalies across the Corinth isthmus (up to 2200 m) and the Alkyonides Gulf (up to 1500) is very similar to that of the central Gulf of Corinth anomaly. This may imply that extension that was accommodated across the Corinth

Anomaly	BA (mGal)		$2a$ (km)	s (m)	Sh1 Depths (m)		Sh2 Depths (m)	
	Min	Max			Min	Max	Min	Max
Corinth 1	15	21	20	800	1600	2100	?	?
Corinth 2	21	27	20	800	2100	2700	?	?
Corinth 3	23	28	10	150	1050	1350	?	?
Alkyonides	10	16	10	400	800	1100	900	?
Evvia 1	12	20	10	0	300	600	600	?
Evvia 2	23	32	10	0	700	1200	?	?
Trihonis 1	16	22	10	0	500	700	?	?
Trihonis 2	16	25	10	0	500	800	?	?
Thiva	25	34	15	0	800	1200	?	?
Erithres	17	26	10	0	500	900	?	?
Megara	7	16	10	0	200	500	?	?

Table 5.7: Estimated basin depths assuming shale lithologies.

Anomaly	BA (mGal)		$2a$ (km)	s (m)	L1 Depths (m)		L2 Depths (m)	
	Min	Max			Min	Max	Min	Max
Corinth 1	15	21	20	800	1700	2400	**1900**	**2700**
Corinth 2	21	27	20	800	2400	3600	**2700**	**3700**
Corinth 3	23	28	10	150	1000	1350	**1600**	**2200**
Alkyonides	10	16	10	400	800	1200	**1000**	**1500**
Evvia 1	12	20	10	0	350	700	**500**	**1000**
Evvia 2	23	32	10	0	700	1200	**1300**	**2300**
Trihonis 1	16	22	10	0	500	700	**800**	**1200**
Trihonis 2	16	25	10	0	450	800	**800**	**1400**
Thiva	25	34	15	0	700	1200	**1300**	**2200**
Erithres	17	26	10	0	500	800	**800**	**1600**
Megara	7	16	10	0	200	500	**300**	**800**

Table 5.8: Estimated basin depths assuming carbonate lithologies. The estimates for lithology L2 (in bold) represent the best estimates.

isthmus is now accommodated by the younger South Alkyonides fault segment.

Where profiles may be taken, the depth to the floor of the Gulf of Evvia Rift is shallower than for the Gulf of Corinth. However, as this rift is also believed to be propagating towards the west, we may expect depths to be greater in the areas where no gravity data are available.

5.9 Seismic Reflection in the Gulf of Corinth

Four seismic reflection surveys have been carried out across the Gulf of Corinth. The first of these was in the eastern Gulf of Corinth in 1970. *Myrianthis* [1982] presents two lines from this survey, though only one of these is a dip line. Its location and the interpretation presented by *Myrianthis* [1982] are shown as Line 1 in Figure 5.34. A second survey was carried out in 1979, and two lines are presented by *Myrianthis* [1984] with the interpretation shown in Figure 5.34 (Lines 2 and 3).

In all three cases, the top of the Mesozoic was picked as the deepest observable reflection. A clean copy of seismic line 3 was obtained from N. Roussos (Public Petroleum Corporation of Greece, Athens, personal communication, 1995)[5] and is shown in Figure 5.35. Although the quality of the data is poor, the interpretations of *Myrianthis* [1984] appear dubious. The deepest observable reflection occurs at 2.7 seconds of two-way travel time, and not 3.3 seconds which may correspond to the second sea-bed multiple. Further, *Myrianthis* [1984] picked a *Base PlioQuaternary* event at ~2.2 s.

An estimation of basin depth may be made from the two-way travel times and an assumed velocity model for the sediment layer. As with the literature on porosity-depth relationships, there exists a range of velocity-depth relationships for a range of lithologies from a range of geographical locations.

Numerous studies have shown that the velocity of limestones shows a general increase with depth which is likely to be due to a general increase in density with depth [*Jankowsky*, 1970]. This may then be used to calculate a velocity profile using Gardner's rule [*Gardner, Gardner and Gregory*, 1974]:

$$v(z) = \left(\frac{\rho(z)}{310}\right)^4 . \tag{5.20}$$

Figure 5.36a shows this empirical relationship, and the observed relationship for four

[5]Seismic line 2 was not supplied.

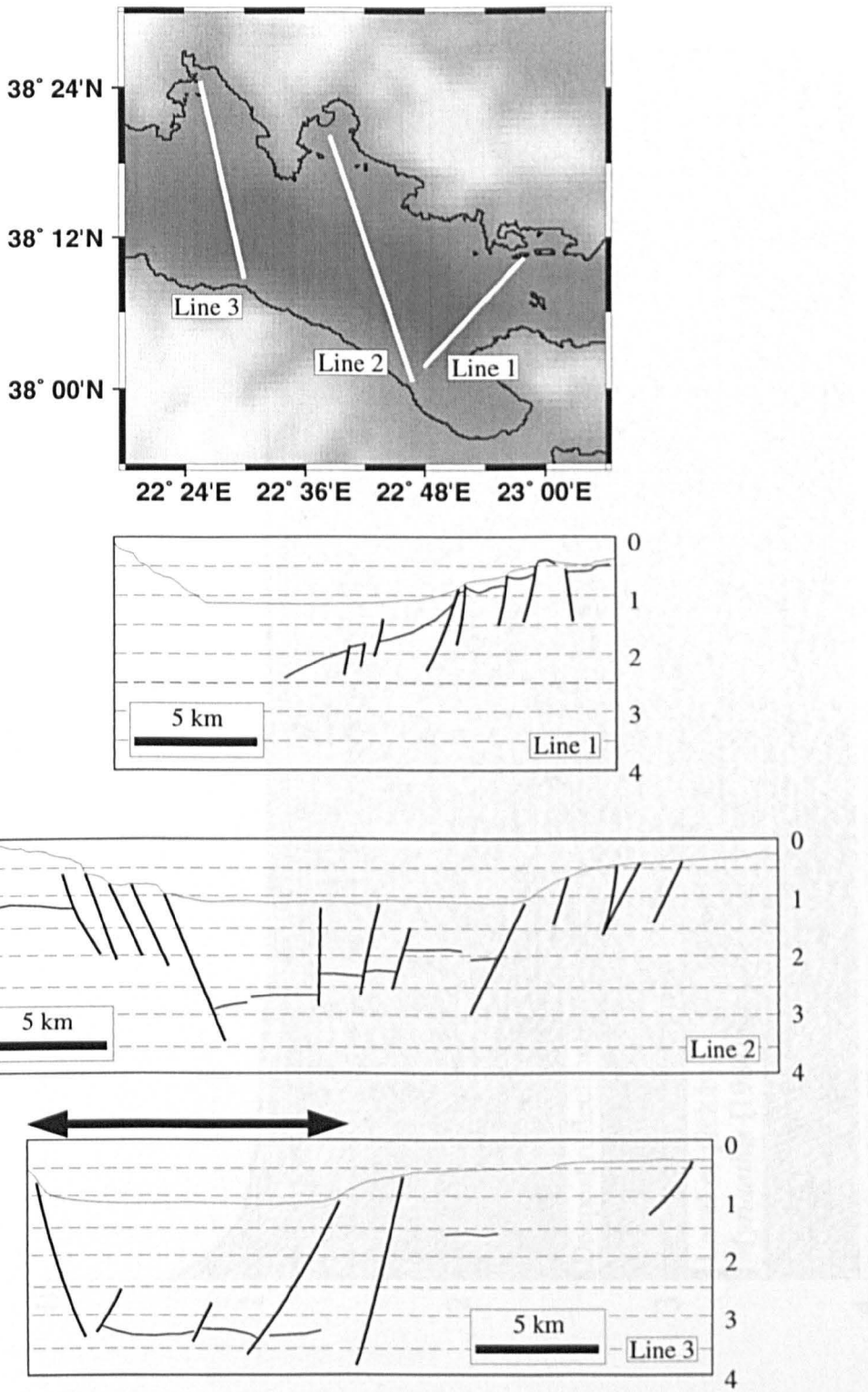

Figure 5.34: Interpretations of the seismic lines presented in *Myrianthis* [1982] (Line 1) and *Myrianthis* [1984] (Lines 2 and 3). All interpretations are represented at the same scale, and each runs from the southern shore to the northern shore. Vertical scale is in seconds of two-way travel time. The double-headed arrow above Line 3 shows the location of Figure 5.35.

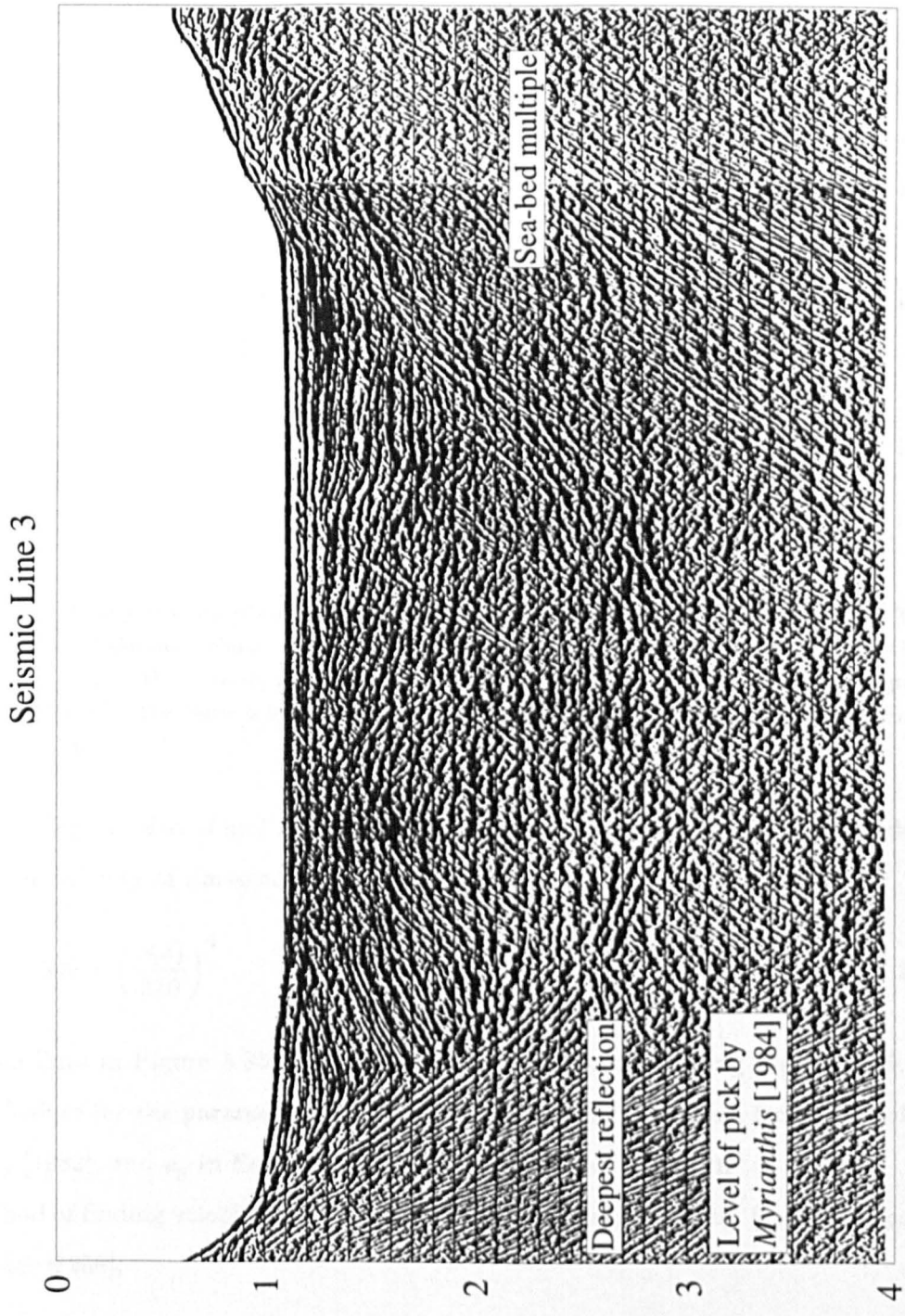

Figure 5.35: Seismic reflection line 3 to show that the deepest visible reflectors occurs at a two-way travel time of ~2.7 s. The first sea-bed multiple is clearly seen, and corresponds to the base Plio-Quaternary pick of *Myrianthis* [1984]. The top Mesozoic pick of *Myrianthis* [1984] may correspond to the second sea-bed multiple. See Figure 5.34 for location. Vertical scale in seconds of two-way travel time.

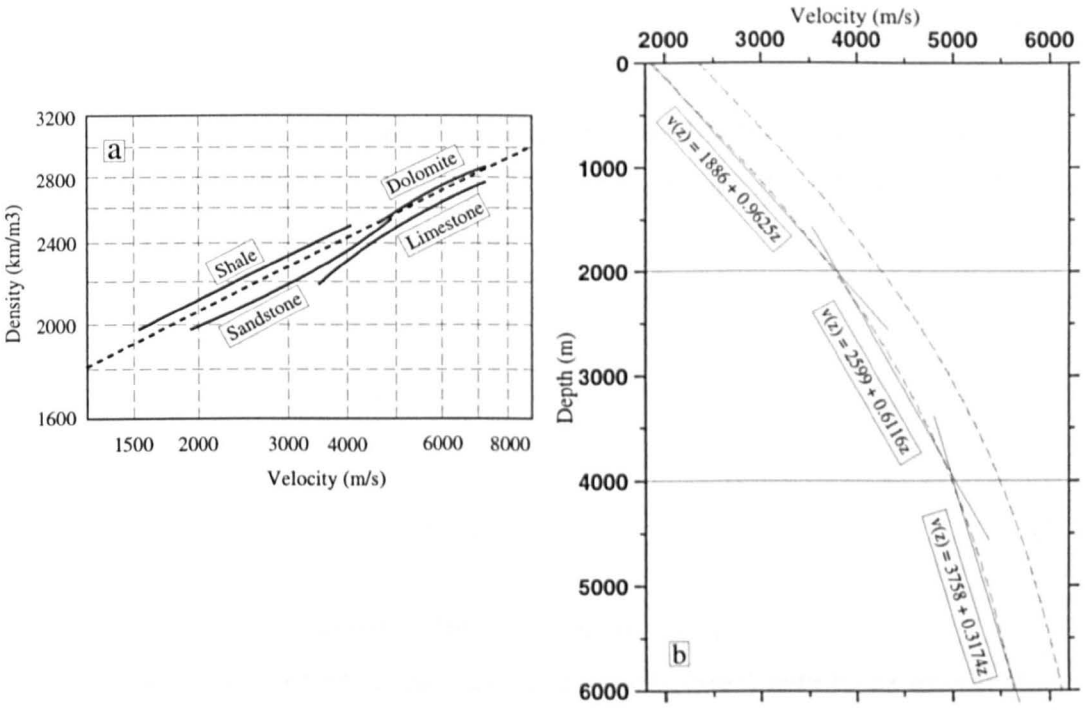

Figure 5.36: (a) Density-velocity relationships for four lithologies, from *Meckel and Nath* [1977]. The general expression of *Gardner, Gardner and Gregory* [1974] is shown by the dashed line. (b) Velocity-depth profiles assuming the porosity-depth relationship of *Schmoker and Halley* [1982] and a grain density of 2750 kg/m^3. The lower velocity curve is from Equation 5.20, and the higher velocity curve from Equation 5.21.

different lithologies [*Meckel and Nath*, 1977]. It is seen here that Gardner's rule underestimates the velocity of limestone by ~500 m/s. Thus,

$$v(z) = 500 + \left(\frac{\rho(z)}{310}\right)^4 . \tag{5.21}$$

The dashed lines in Figure 5.36b plot the velocity depth profiles using Equations 5.20 and 5.21. Values for the parameters c and Φ_0 in Equation 5.5 are taken from *Schmoker and Halley* [1982], and ρ_g in Equation 5.6 is assumed to be 2750 kg/m^3.

A method of finding velocity directly from porosity was suggested by *Wyllie, Gregory and Gardner* [1958],

$$\frac{1}{v(z)} = \frac{\Phi}{v_f} + \frac{1-\Phi}{v_m} \tag{5.22}$$

where v_f and v_m are the velocities of the pore fluids and rock matrix respectively. The basin depths estimated using this equation fall within the range defined by Equations 5.20 and 5.21, so the results are not presented.

Figure 5.36b shows that the velocity-depth curves may be approximated by three linear segments which intersect at approximate depths of 2000 m and 4000 m. These are used to depth convert the maximum two-way travel times shown in Figure 5.34.

Using Equation 5.20, the velocity profiles of four layers of thickness Δz_1, Δz_2, Δz_3 and Δz_4 are linear with depth, such that

$$\begin{aligned} v_1(z) &= u_1 + k_1 z = 1500 \\ v_2(z) &= u_2 + k_2 z = 1886 + 0.9625z \\ v_3(z) &= u_3 + k_3 z = 2599 + 0.6116z \\ v_4(z) &= u_4 + k_4 z = 3758 + 0.3174z \ . \end{aligned} \tag{5.23}$$

For Equation 5.21, 500 is added to the constants u_1 to u_4.

The thickness Δz_1 (which in this case is the water layer) may be expressed as

$$\Delta z_1 = \overline{v_1}\frac{\Delta T_1}{2} \tag{5.24}$$

where $\overline{v_1}$ is the average velocity within layer 1, and ΔT_1 is the two-way interval time. As its velocity is linear with depth, $\overline{v_1}$ is equal to $v_1(z)$ for $z = \Delta z_1/2$, so

$$\begin{aligned} \overline{v_1} &= u_1 + k_1\frac{\Delta z_1}{2} \\ &= u_1 + k_1\frac{\Delta T_1 \overline{v_1}}{4} \ . \end{aligned} \tag{5.25}$$

This may be rearranged for $\overline{v_1}$, and substituted into Equation 5.24 to give an expression for Δz_1:

$$\Delta z_1 = \frac{u_1}{1 - \left(\frac{k_1 \Delta T_1}{4}\right)}\frac{\Delta T_1}{2} \ . \tag{5.26}$$

The base of the second layer is conceptual, and its thickness may be calculated simply as

$$\Delta z_2 = 2000 - \Delta z_1 \ . \tag{5.27}$$

With the gravity modelling, assuming compaction under water to be the same as that under sediment led to an upper-bound estimate for basin depth. For this depth-conversion,

the same assumption will result in higher velocities and so also in upper-bound estimates for basin depth.

To find the two-way interval time for the second layer, ΔT_2, the average interval velocity is calculated as

$$\overline{v_2} = u_2 + k_2 \left(\Delta z_1 + \frac{\Delta z_2}{2} \right) . \tag{5.28}$$

As $\overline{v_2} = 2\Delta z_2 / \Delta T_2$, ΔT_2 is found as

$$\Delta T_2 = \frac{2\Delta z_2}{u_2 + k_2 \left(\Delta z_1 + \frac{\Delta z_2}{2} \right)} . \tag{5.29}$$

The third layer is also conceptual, and

$$\Delta z_3 = 4000 - \Delta z_1 - \Delta z_2 \tag{5.30}$$

and

$$\Delta T_2 = \frac{2\Delta z_3}{u_3 + k_3 \left(\Delta z_1 + \Delta z_2 + \frac{\Delta z_3}{2} \right)} . \tag{5.31}$$

The thickness of the fourth layer, Δz_4, is obtained in a similar way to Δz_1. Thus, as ΔT_4 is found by subtracting the interval times for shallower layers from the two-way time to the Top Mesozoic reflector,

$$\overline{v_3} = \frac{u_4 + k_4 \left(\Delta z_1 + \Delta z_2 + \Delta z_3 \right)}{1 - \frac{k_4 \Delta T_4}{4}} \tag{5.32}$$

and Δz_4 as

$$\Delta z_4 = \frac{u_4 + k_4 \left(\Delta z_1 + \Delta z_2 + \Delta z_3 \right)}{1 - \frac{k_4 \Delta T_4}{4}} \frac{\Delta T_4}{2} \tag{5.33}$$

Tables 5.9 and 5.10 summarise the results of this depth conversion for the greatest two-way travel times shown in each of the lines in Figure 5.34. The depths in Table 5.9 are found using Equation 5.20 and those in Table 5.10 from Equation 5.21.

A third seismic survey was carried out by a team of geophysicists from the IPG Paris, France, led by Dr. Alfred Hirn. Although the survey was affected by severe weather conditions, the preliminary results (A. Hirn, personal communication, 1997) indicate

Line	ΔT_1 (s)	$\Sigma\Delta T$ (m)	Δz_1 (s)	Δz_2 (m)	Δz_3 (m)	Δz_4 (m)	Basin depth (m)
Line 1	1.1	2.4	825	1175	1207		3207
Line 2	1.1	2.8	825	1175	2000	187	4187
Line 3	1.1	2.7	825	1175	1933		3933

Table 5.9: Converted depths for the Top Mesozoic reflector across the Gulf of Corinth, as picked by *Myrianthis* [1982] (line 1) and *Myrianthis* [1984] (line 2). The two-way time for line 3 is taken from Figure 5.35. Seismic velocities are estimated from Equation 5.20.

Line	ΔT_1 (s)	$\Sigma\Delta T$ (m)	Δz_1 (s)	Δz_2 (m)	Δz_3 (m)	Δz_4 (m)	Basin depth (m)
Line 1	1.1	2.4	825	1175	1620		3620
Line 2	1.1	2.8	825	1175	2000	739	4739
Line 3	1.1	2.7	825	1175	2000	453	4453

Table 5.10: Converted depths for the Top Mesozoic reflector across the Gulf of Corinth, as picked by *Myrianthis* [1982] (line 1) and *Myrianthis* [1984] (line 2). The two-way time for line 3 is taken from Figure 5.35. Seismic velocities are estimated from Equation 5.21.

that the west of the Alkyonides Gulf, the Gulf of Corinth comprises three depocentres: one in the hanging wall of the Xylocastron fault, one in the hanging wall of the Eigion fault, and one in an intermediate position that may correspond to the inferred Derveni fault. These depocentres have a basement depth of ~3 km. This pattern is similar to that in the residual Bouguer gravity (Figure 5.6) and may suggest that two minima observed in the central anomaly (shown by profile 2) represent two separate depocentres.

The most recent seismic survey was carried out in 1996 by a joint team from the Universities of Leeds and Patras, Greece [*Collier et. al., in prep*]. The survey was concentrated in the eastern Alkyonides Gulf, and focussed on the resolution of sediment architecture. However, extrapolation of basement reflectors in the north towards the South Alkyonides fault segment indicates a two-way time to basement of approximately 1.15 to 1.35 s seconds. These convert to depths of 1251 to 1451 m from Equation 5.20 and 1588 to 1863 m from Equation 5.21. These are consistent with the estimates in Table 5.8.

5.10 Summary of Basin Depth Estimates for the Gulf of Corinth

Armijo et al. [1996] date the erosional marine terraces around Corinth (see Section

Method	Basin depth (m)	Reference
Gravity forward models†	2700 - 3700	This study
Depth conversion†	4200 - 4700	This study
Seismic refl. and refr.	~3000	A. Hirn (pers. comm., 1997)
Flexural cantilever model‡	4500 - 8300	*Armijo et al.* [1996]

Table 5.11: Summary of basin depth estimates for the eastern Gulf of Corinth. † indicates an upper-bound estimates, as explained in the text. ‡ indicates a lower-bound estimate for basin depth, as subsidence may have occurred across the region prior to the formation of Xylocastron fault segment.

3.7.1.2) to find time-averaged uplift rates for the last 350 kyr. Rates and amplitudes increase towards the shore, which can be attributed to flexural uplift in the footwall to the Xylocastron fault segment. They then model the fault as a dislocation in an elastic plate overlying an inviscid lower crust, and deduce a time-averaged slip rate of 11±3 mm/yr. In order to account for the present-day elevation of the deltaic sediment across Mt. Mavron (see Figure 3.13), they argue that the fault segment initiated at ~1 Ma. The total slip is therefore 11±3 km, which corresponds to a vertical throw of 8.4±2.3 km. Their model results also predicts an uplift to subsidence ratio of between 1 to 2.7 and 1 to 3.5 . Thus, hanging wall subsidence is predicted to be 6.4±1.9 km.

The region of analysis of *Armijo et al.* [1996] roughly corresponds to the location of a residual gravity anomaly with amplitude 21 mGal, and also with seismic line 2 in Figure 5.34. Table 5.11 summarises the basin depths estimated for each, and shows that the results of the gravity modelling are very similar to the results of recent seismic experiments. The upper-bound estimates obtained by depth converting old seismic data gives depths of ~1 km deeper. However, the data are poor and errors in the interpretation of *Myrianthis* [1984] were demonstrated in Section 5.9.

The model results of *Armijo et al.* [1996] are more than double the other two. In order to account for the rapid slip rates on their model for the Xylocastron fault segment (~11 mm/yr), the authors argue that the Gulf of Corinth is evolving within the process zone of the NAF. However, extension rates in the Gulf of Corinth are measured to increase towards the west [*Davies et al.*, 1997; *Le Pichon et al.*, 1995], and the high rates may be explained by the proximity of a weak lithosphere to a *GPE* low across the Hellenic Trench (see Section 3.9.3, and references therein). These observations have prompted the following examination of marine terrace geometry.

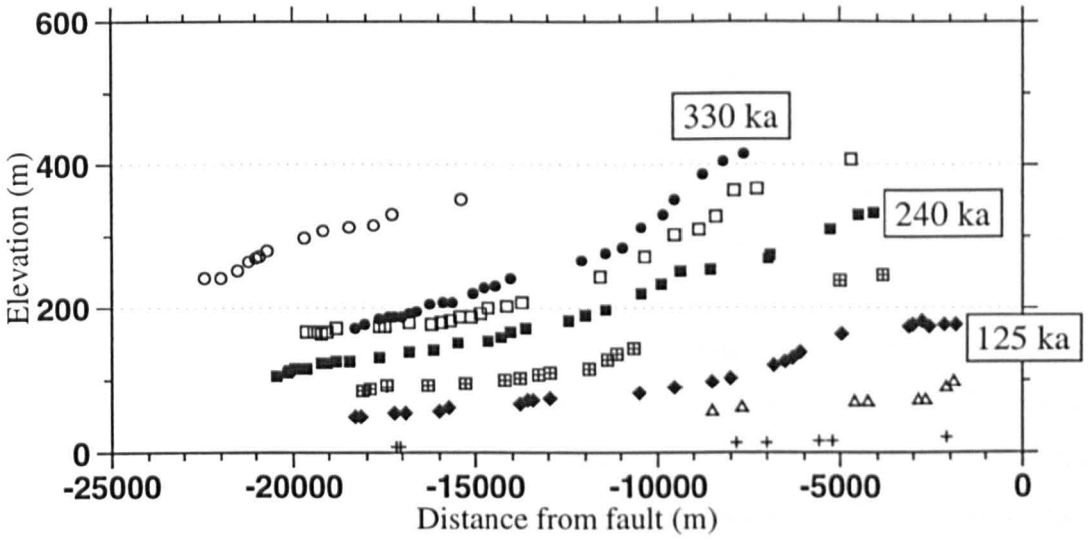

Figure 5.37: Sea Level corrected erosional marine terrace elevations in the eastern Gulf of Corinth Rift. The most prominent terraces - shown by the solid symbols - are correlated with the ~125 ka, the ~240 ka and the ~330 ka eustatic highstand. Data supplied by G. King (IPG Paris, personal communication, 1997).

5.11 Elastic Modelling in the Gulf of Corinth

5.11.1 The Marine Terraces

The process by which marine terraces form was described in Section 3.7.1.2. *Armijo et al.* [1996] present a full description of the mapping and correlation of them, and the correction for eustatic variation such that, in the absence of other mechanisms of uplift, their profiles will unflex to the same horizontal plane.

Figure 5.37 shows the sea level corrected elevations for the terraces south of the Xylocastron fault segment. The highest terrace cannot be fit by the model results of *Armijo et al.* [1996]. The reasons for this are investigated here.

5.11.2 Boundary Value Problems

Many problems in the physical sciences may be modelled as *boundary value problems*, where a region **R** is contained within a boundary **C**. In this study, we restrict analyses to two-dimensional regions, so **C** is a bounding countour. In any problem governed by partial differential equations, only some of the relevant parameters on **C** need be defined: the others emerge as part of the solution. Where analytical solutions cannot be found - because boundary conditions cannot be described by simple functions for example - a numerical solution must be sought.

In finite element models, **R** is divided into a network of elements and the object is to evaluate the solution to the problem at each node. In boundary element models, only the boundary **C** is divided into elements. The numerical solution builds on analytical solutions for simple problems, and so solutions for elements throughout **R** are found indirectly. The system of equations to be solved is much smaller than with a finite element approach.

The boundary element approach is well suited to problems of linear elasticity [*Crouch and Starfield*, 1983], and has been used previously by *King and Ellis* [1990] and *Armijo et al.* [1996] to model fault growth. The general features of the boundary element method are not described here, and further discussion may be found in *Crouch and Starfield* [1983].

5.11.3 Geometry, Boundary Conditions and Imposed Slip

The boundary of the elastic plate (**C**) is defined by two horizontal and two vertical lines. The ends of the plate are situated at a great distance from the fault (±108 km in all cases, Figure 5.38) such that their boundary conditions do not affect displacements in the region of interest. The number and spacing of the elements on **C** controls the accuracy of the final solution, and as displacements are greatest in the region of the fault, the spacing between elements is small here and increases towards the ends of the plate.

In order to calculate stresses and strains in two dimensions, either a plane strain or a plane stress approximation must be made. Plane strain indicates that the strains are restricted to a single plane, and it is usual to apply this to cases where the geometry of the body and the loading conditions are uniform over comparatively long distances in one direction [*Crouch and Starfield*, 1983]. This is also the best assumption for problems of flexure as it implies zero bending in the out-of-plane direction. Strain is taken to be zero in the y direction i.e., along the strike of the rift.

Many problems in solid mechanics involve bodies containing cracks or faults. The fault is modelled as a dislocation in the elastic plate, and the amount of slip is taken to be constant with depth. The geometry is assumed to be planar which is consistent with the observations of *Eyidogan and Jackson* [1985] and *Jackson et al.* [1982]. Many faults planes were measured throughout central Greece and dips vary between 40° and 85°, though a large majority dip between 45° and 60°. Fault dip is therefore fixed at 50o for the modelling.

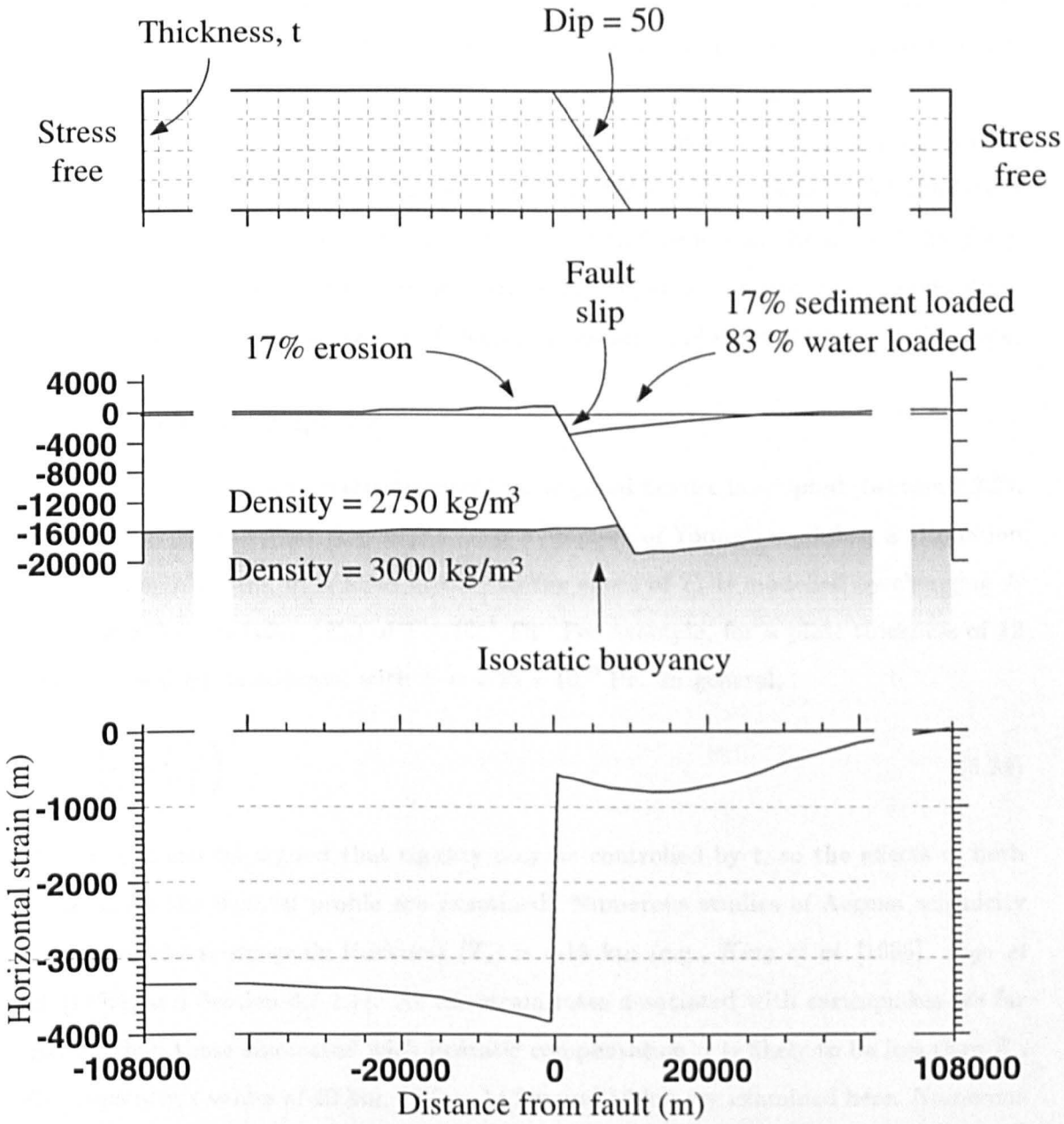

Figure 5.38: (a) Pre-slip boundary conditions for the boundary element models. (b) The geometry after co-seismic slip and post-seismic isostatic relaxation. In the running of the model, all forces are applied at the base of the plate. (c) Profile of horizontal displacement, for a fault slip of 5 km, a plate thickness (t) of 16 km and a T_e of 2 km.

For an elastic plate subjected to an extensional tectonic deviatoric stress (τ_{xx}), a normal fault slips when the shear stress along its plane exceeds a limit defined by the sum of a frictional (Mohr-Coulomb) stress [*Byerlee*, 1978; *Jaeger and Cook*, 1979] and a stress created by the flexure of the plate [*Buck*, 1993; *Forsyth*, 1992]. The model approach adopted here turns this around. Rather than computing the slip that results from a certain τ_{xx}, a slip is imposed on a fault plane of specified dip.

Crouch and Starfield [1983] and *King and Ellis* [1990] show that this strategy is valid (i.e., the shapes of the final structures are identical) if stress on the vertical boundary is zero (Figure 5.38). The shear stress is zero at the surface and at the base of the plate, and normal stress results from isostatic compensation, erosion and sediment deposition. For mathematical convenience, all of these stresses are applied at the base of the plate.

5.11.4 Isostatic Support

For this analysis, the upper-crustal model for regional flexure is adopted (Section 2.7.2). For an upper-crustal plate thickness t, T_e is a function of Young's modulus, E (Equation 2.11). Poisson's ratio, ν, is fixed at 0.25 so the effect of T_e is modelled by changing E from the reference value (E_0) of 1×10^{11} Pa. For example, for a plate thickness of 12 km, a T_e of 6 km is achieved with $E = 1.25 \times 10^{10}$ Pa. In general,

$$\frac{E}{E_0} = \left(\frac{T_e}{t}\right)^3 . \tag{5.34}$$

However, it can be argued that rigidity may be controlled by t, so the effects of both t and E on the flexural profile are examined. Numerous studies of Aegean seismicity show that the seismogenic thickness (T_s) is ~15 km (e.g., *King et al.* [1985], *Rigo et al.* [1996], and Section 3.7.1.1). As the strain rates associated with earthquakes are far greater than those associated with isostatic compensation, t is likely to be less than T_s. Consequently, t values of 10 km, 12 km, 14 km and 16 km are examined here. Numerous authors have demonstrated a local reduction in E across rifts, such that T_e is less than both T_s and t.

Isostatic compensation occurs at the base of the elastic plate. The buoyancy force per unit area, $\sigma_{Fb}(x)$, is proportional to the vertical displacement from the pre-deformational equilibrium, $w(x)$ (see Section 2.6). In one dimension,

$$\sigma_{Fb}(x) = \rho_{lc} g w(x) \tag{5.35}$$

where ρ_{lc} is the density of the lower crust. Tests show that the model results are not sensitive to density changes of up to 5%. For all results presented here, the density of the upper crust is fixed at 2750 kg/m^3, and that for the lower crust at 3000 kg/m^3.

5.11.5 Erosion and Sediment Deposition

Both erosion and deposition result in the redistribution of loads and therefore influence the flexural profile across a normal fault. The extent of both processes is controlled by local lithology, climate, topography and the rate of vertical surface displacement. In general, the greater the uplift, the greater the erosion, and the greater the subsidence, the greater the sedimentation.

Erosional profiles are generally irregular, but these irregularities are short compared to flexural wavelength. The amount of erosion is therefore modelled to be proportional to uplift. *Armijo et al.* [1996] show that erosion in the footwall is ~17% of footwall uplift, and this result is adopted here. The corresponding (unloading) stress ($\sigma_e(x)$) is therefore

$$\sigma_e(x) = \rho_{uc} g e w(x) \tag{5.36}$$

where e is the fractional erosion, fixed at 0.17 for these analyses.

Sedimentation may be modelled in a similar fashion. However, the model profiles are not very sensitive to sedimentation amounts, particularly across the footwall. For convenience, 17% of the hanging wall subsidence is filled with rock of density 2750 kg/m^3, and the remaining 83% with water (Figure 5.38). Thus, the loading stress across the hanging wall is

$$\sigma_s(x) = \rho_{uc} g e w(x) + \rho_w g (1 - e) w(x) \ . \tag{5.37}$$

5.11.6 Effect of Plate Thickness and Young's Modulus

Figure 5.39 shows the flexural profiles for 2 km increments of T_e for each of the four values for t. The most obvious features are

- flexure occurs at greater wavelengths for greater T_e
- greater uplift to subsidence ratios occur for greater T_e.

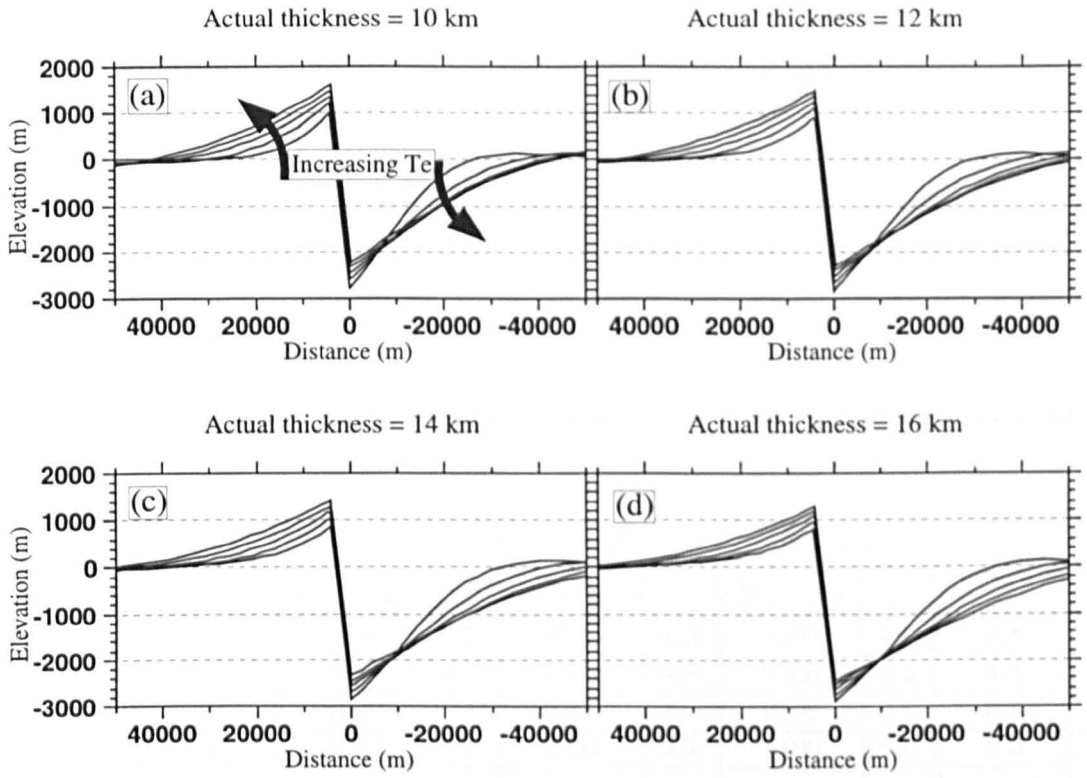

Figure 5.39: Flexure profiles for T_e = 2, 4, 6 and 8 km. (a) t = 10 km. (b) t = 12 km. (c) t = 14 km. (d) t = 16 km. Slip is 5 km and fault dip is 50° for all profiles.

The effect of variations in t for a constant T_e is shown more clearly in Figure 5.40. For greater values of t, the flexure is less tight. For example, for a plate whose true thickness is 16 km to be able to reproduce the curvature of a t = 10 km plate, Young's Modulus must be lower than the value that gives equivalent T_e (Equation 5.34). From this, we expect that

- thicker plates will give lower T_e estimates.

5.11.7 Terrace Fitting

A series of four plots - Figures 5.41 to 5.44 - compares model flexural profiles with the sea level corrected terrace elevations of Figure 5.37. The best fit curves in each case will result in estimates for

- effective elastic thickness, T_e
- the amount of slip for any one terrace

and from the age of that terrace,

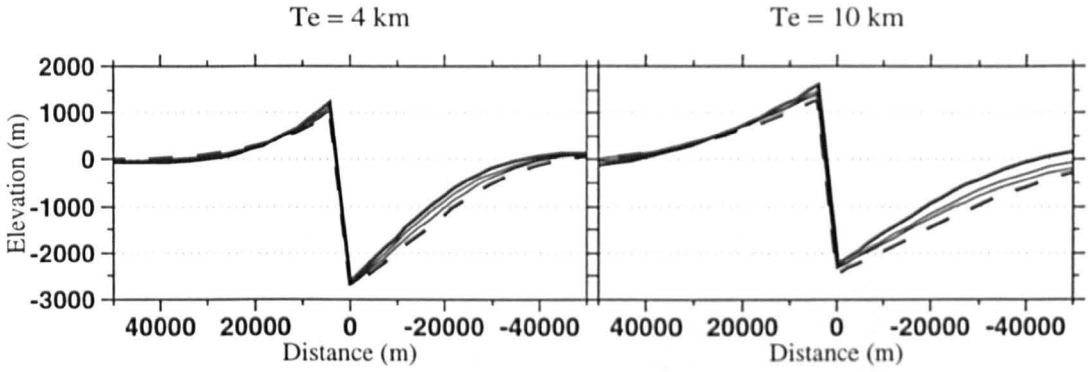

Figure 5.40: The effect of actual plate thickness, t, on the flexural profile for T_e values of 4 km and 10 km. Dashed line is for $t = 16$ km

t (km)	T_e (km)	125 ka		240 ka		330 ka		Mean v
		Slip (m)	v	Slip (m)	v	Slip (m)	v	
10	6	600	3.1	1500	4.0	2200	4.3	**3.8**
12	6	700	3.6	1600	4.3	2300	4.5	**4.1**
14	4	1000	5.1	2200	5.9	3400	6.6	**5.9**
16	4	1000	5.1	2200	5.9	3400	6.6	**5.9**
	2	1200	6.2	2800	7.5	4250	8.3	**7.3**

Table 5.12: Best fit T_e and slip from elastic models for the three dominant terraces. v is the extensional velocity (in mm/yr), calculated as (slip/age)$\cos 50°$. Thicker t results in lower T_e and faster v. For $t =$ 16 km, T_e values of 2 km and 4 km fit the data equally well.

- slip rate and extensional velocity.

The results are summarised in Table 5.12. As predicted in Section 5.11.6, the lower best-fit T_e values are obtained for greater t. Further, because smaller uplift to subsidence ratios are predicted for lower T_e, greater slip rates and extensional velocities result for thicker plates.

From Section 3.7.1.1, the age of the Xylocastron fault segment is probably less than 2 Ma. The elastic model is run through 1 Myr for each of the five average slip rates in Table 5.12, and the results are shown in Figure 5.45. As expected, there is very little difference in the profiles across the footwall, especially in the region of the marine terraces. Large differences occur in the hanging wall, however, and the results of the gravity modeling may be used to constrain the results. The following observations are made:

- Low T_e values - corresponding to thicker t - result in subsidence that is too great
- The upper-most terrace can only be fit by the high T_e, thin t models

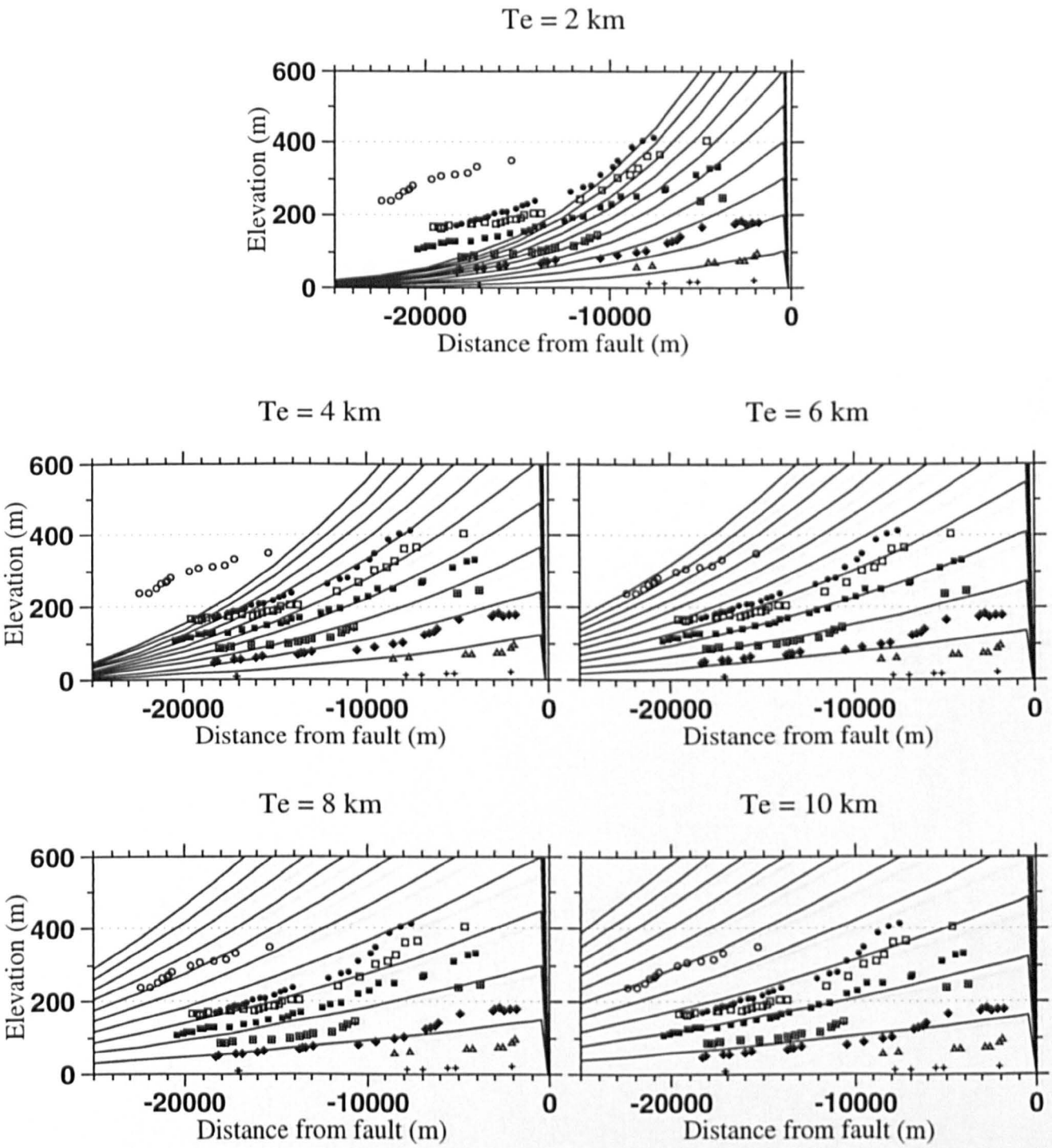

Figure 5.41: Flexural and terrace profiles for thickness t of 10 km. Five separate plots correspond to different T_e. Each plot shows flexural profiles for fault slip up to 5000 m, at intervals of 500 m.

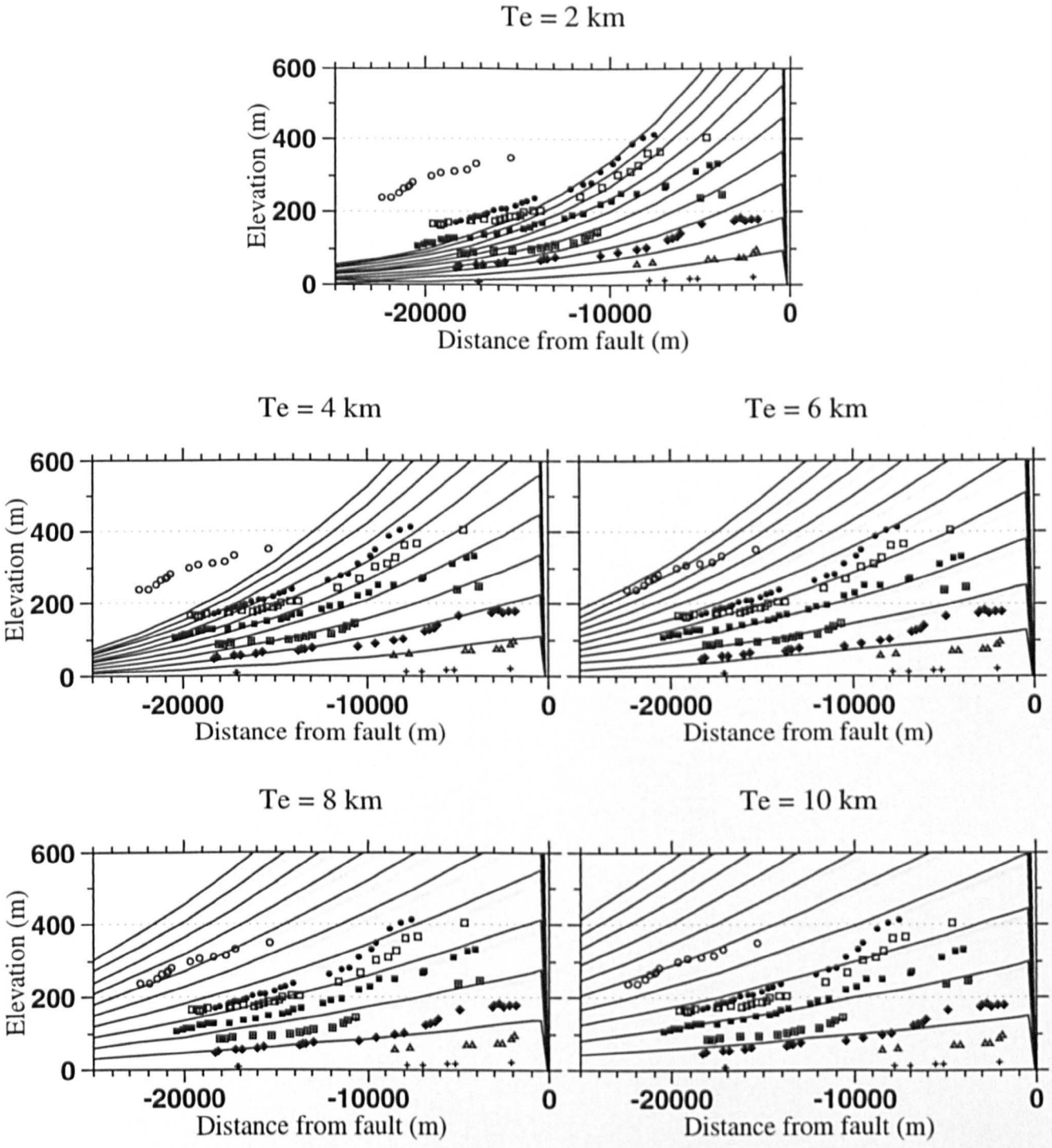

Figure 5.42: Flexural and terrace profiles for thickness t of 12 km. Five separate plots correspond to different T_e. Each plot shows flexural profiles for fault slip up to 5000 m, at intervals of 500 m.

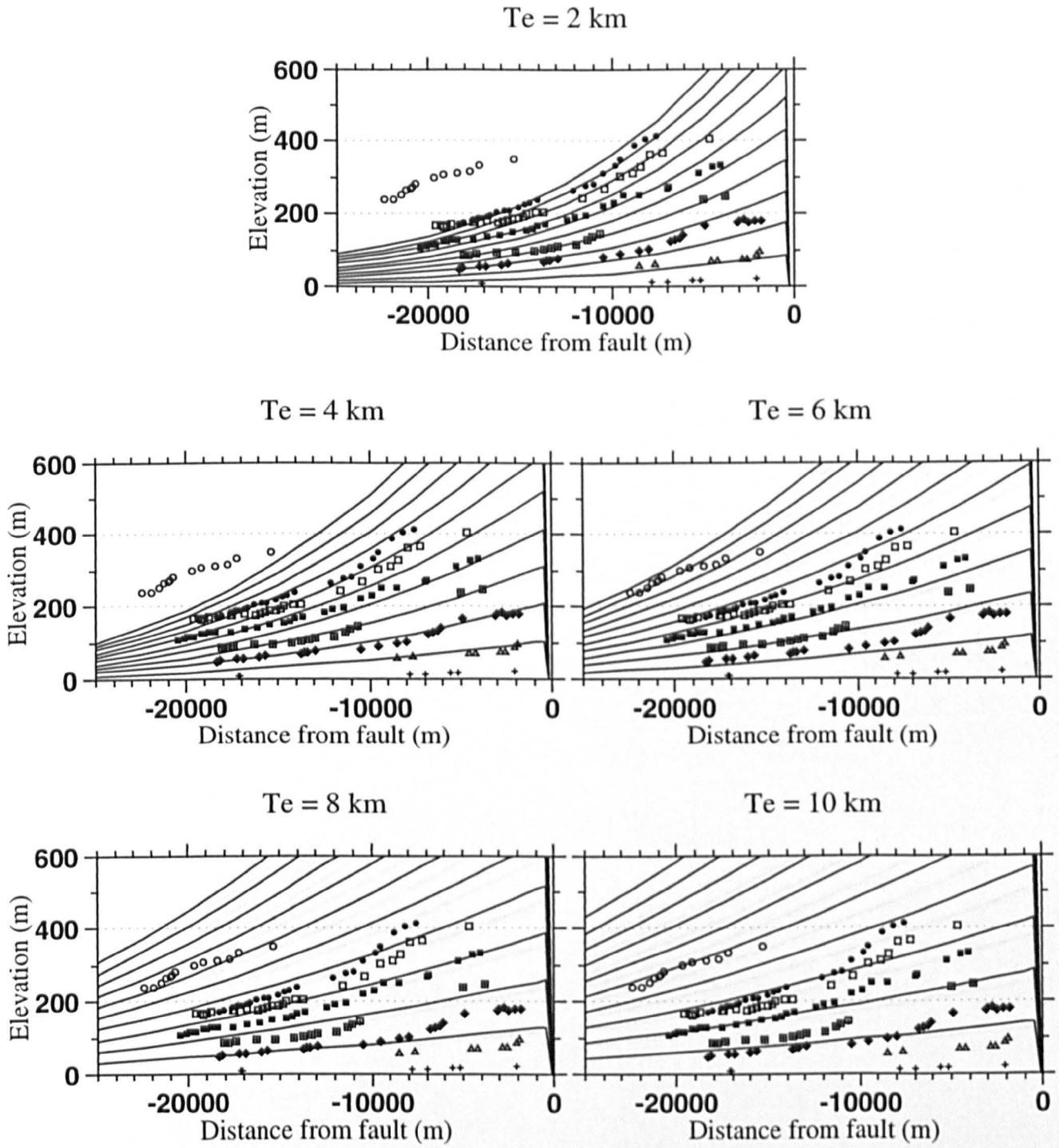

Figure 5.43: Flexural and terrace profiles for thickness t of 14 km. Five separate plots correspond to different T_e. Each plot shows flexural profiles for fault slip up to 5000 m, at intervals of 500 m.

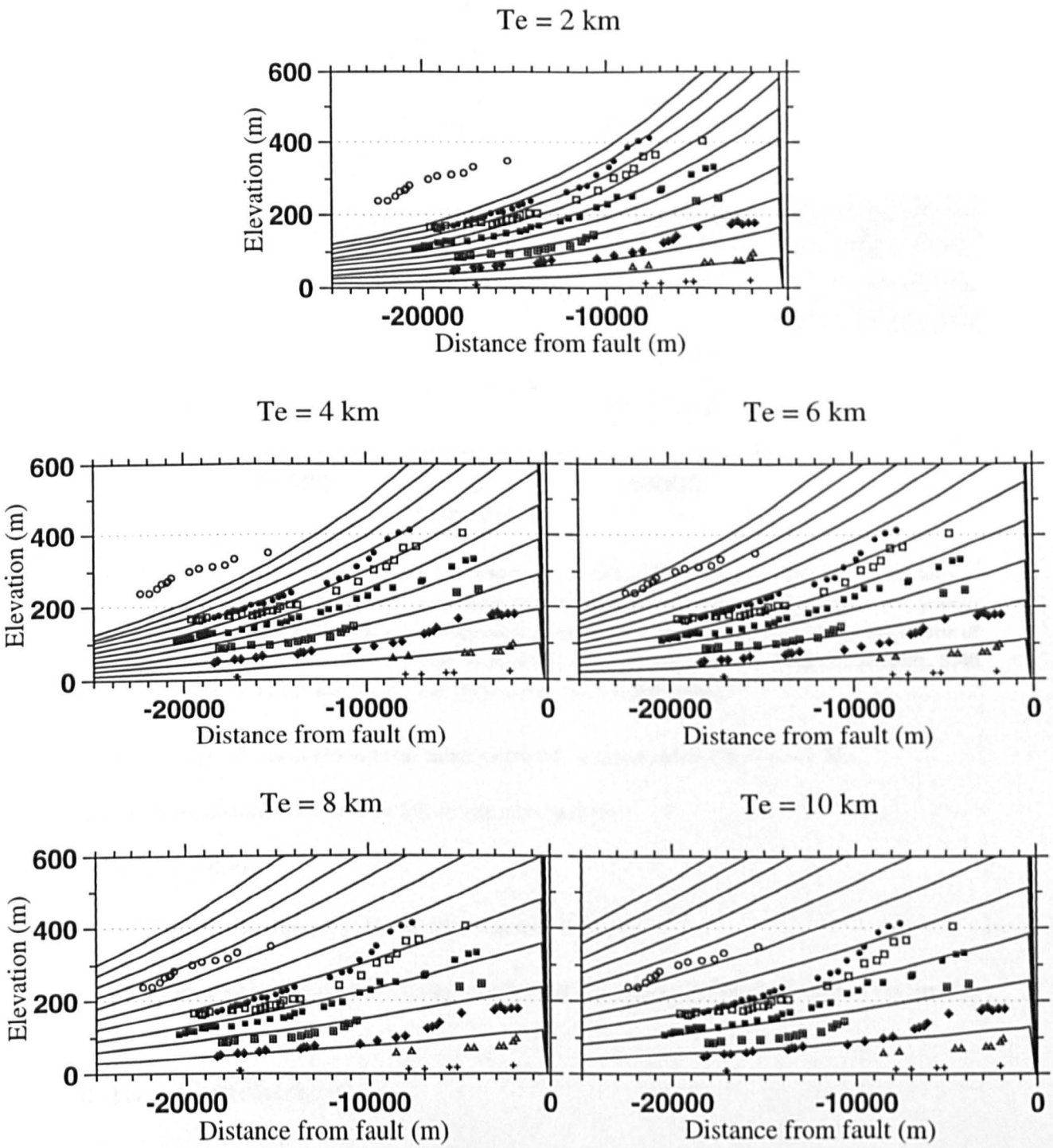

Figure 5.44: Flexural and terrace profiles for thickness t of 16 km. Five separate plots correspond to different T_e. Each plot shows flexural profiles for fault slip up to 5000 m, at intervals of 500 m.

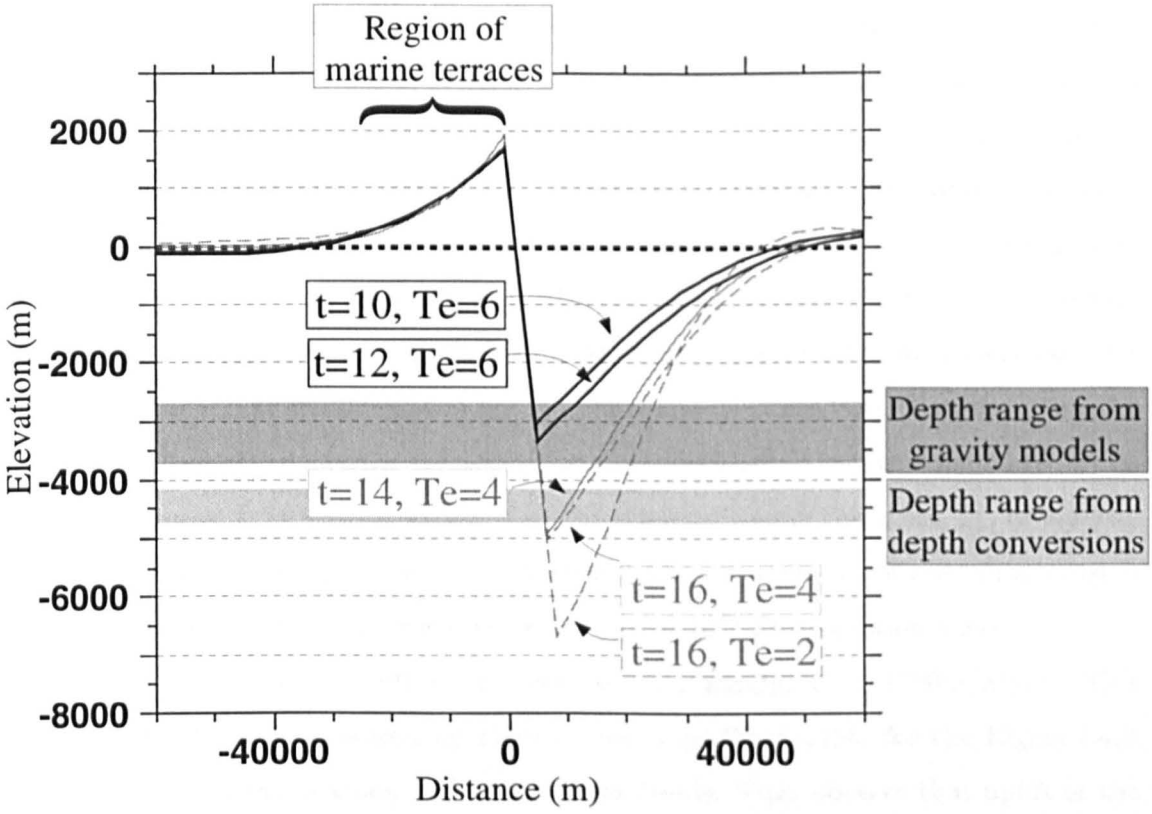

Figure 5.45: The flexural profiles for the five combinations of t and T_e based on fitting observed terrace profiles, extrapolated to 1 Myr. The dark grey zone indicates the depths obtained from the gravity models, and provides an additional and independent constraint. The light grey zone shows the results of the seismic depth conversion. The two best fit models are $t = 10$ km and $T_e = 6$ km (1690 uplift, 3340 subsidence) and $t = 12$ km and $T_e = 6$ km (1710 uplift, 3070 subsidence).

- The age of the Xylocastron fault segment is constrained to be ~1 Ma.

These observations lead to the following conclusions:

- T_e is ~6 km
- The true thickness, t, is ~3 to 5 km less than T_s.
- Extensional velocity accommodated by the Xylocastron fault segment is ~4 mm/yr

5.12 Conclusions

• Through wavenumber domain filtering, regional Bouguer gravity fields across sedimentary basins have been identified and removed to leave the gravitational signal of the buried sedimentary strata. Negative residual gravity anomalies are seen to correspond with the sedimentary basins. Where the signal in not clear, geological maps indicate the presence of shallow, high density ophiolites.

- A model has been derived for the gravitational response of buried sedimentary strata, using a range of porosity-depth relationships from the literature. With constraints on the density of lithologies in central Greece, estimates of basin depths are made from the residual gravity anomalies. The Gulf of Corinth is the deepest of the basins analysed, and is its deepest (up to 3.7 km) in the hanging wall to the Xylocastron fault segment.
- The dynamics of the Gulf of Corinth Rift had hitherto been constrained by surface observations alone. The gravity modelling results provide an additional constraint for upper-crustal flexure elastic models for the eastern Gulf of Corinth. Together with the elevations of erosional marine terraces, these models lead to estimates for the actual elastic thickness, t, of ~10 to 12 km, and the effective elastic thickness, T_e, of ~6 km. This indicates that the long-term (i.e., isostatic) Young's modulus of the upper crust is ~5 to 10 times less than the reference value (E_0) of 10^{11} Pa (Equation 5.34).
- Time-averaged rate of uplift *at the fault* is ~1.7 mm/yr (i.e., 1700m/Myr). This is similar to the rate measured by *Stewart and Vita-Finzi* [1996] for the Eigion fault segment from the radiocarbon dating of marine fossils. They observe that uplift at the fault over the last 10 ka has occurred at an average rate of 1.5 mm/yr.
- The amplitude of fault-related uplift (i.e., co-seismic plus inter-seismic) decreases to zero in the footwall over a distance of ~35 km from the normal fault.
- The ratio of footwall uplift to hanging wall subsidence increases for greater T_e. Across the eastern Gulf of Corinth, the ratio is between 1:1.8 and 1:2 (t = 10 km and t = 12 km respectively). Similar ratios are obtained in the models of *King, Stein and Rundle* [1988], and also observed across the Borah Peak [*Stein, King and Rundle*, 1988] and the Teton Range [*Byrd, Smith and Geissman*, 1994] in the Basin and Range.
- The extensional velocity is estimated to be ~4 mm/yr, which is roughly half the GPS derived velocity for a region across the eastern Gulf of Corinth. This suggests that additional processes may be active in the accommodation of strain, such as antithetic faulting and distributed deformation [*Morewood and Roberts*, 1997]. This is consistent with the findings of *Davies et al.* [1997] who conclude that, for the south-western Aegean as a whole, only 20 to 50 % of the observed strain over the last century can be accounted for by recorded earthquakes.

Chapter 6

Coherence Analysis

6.1 Introduction

This chapter analyses the stochastic relationship between the Bouguer gravity and the topography as a function of wavelength. This relationship - which may be expressed as either an *admittance* or a *coherence* - is modelled using thin elastic plate whole-lithospheric flexure to map effective elastic thickness (T_e) across the Aegean continental lithosphere. The admittance [*Lewis and Dorman*, 1970; *McNutt*, 1983] is firstly introduced, and its limitations in estimating T_e are highlighted. The coherence between gravity and topography [*Forsyth*, 1985] is shown to be a more robust method, and is applied to the Aegean gravity and topography data.

One of the limitations of conventional coherence analyses stems from the nature of the Fourier transform. Spatial resolution is limited because information about a signal at a particular wavelength is represented on a global scale. Continuous wavelet transforms (CWTs) are designed to overcome this problem, and are applied to the data to resolve their coherence as a function of wavelength and position.

6.2 Loading the Continental Lithosphere

The lithosphere is loaded wherever lateral density changes occur on or within it (Chapter 2). The most important of these are at the Earth's surface and at the moho (e.g., *Ebinger et al.* [1989]). For example, pure-shear crustal thinning in response to extension can result in both surface and moho loads whose ratio will depend on the depth of necking [*Kooi*, 1991]. The pure-shear model of *McKenzie* [1978a] implies a necking depth of zero, such that all initial loading occurs at the moho.

Loads can take the form of topography, igneous intrusions, thermal anomalies or compositional variations. However, in the isostatic model, it is assumed that the initial surface and moho loads may be represented by topography on the two interfaces, $H_I(\mathbf{k})$ and $W_I(\mathbf{k})$ respectfully, where $\mathbf{k}$ is two-dimensional wavenumber [*Forsyth*, 1985]. Figure 6.1 shows how the final topographies, $H(\mathbf{k})$ and $W(\mathbf{k})$, represent superpositions of loads and isostatic compensations. Thus,

$$H(\mathbf{k}) = H_T(\mathbf{k}) + H_B(\mathbf{k}) \tag{6.1}$$

and

$$W(\mathbf{k}) = W_T(\mathbf{k}) + W_B(\mathbf{k}) \; . \tag{6.2}$$

The ratio of moho to initial surface loading - which will vary with $\mathbf{k}$ - is an important factor in interpretations of observed admittance and coherence. *Forsyth* [1985] defines this ratio as

$$f(\mathbf{k}) = \frac{\Delta\rho W_I(\mathbf{k})}{\rho_c H_I(\mathbf{k})} \tag{6.3}$$

where ρ_c and ρ_m are the densities of the crust and mantle respectively, and $\Delta\rho = (\rho_m - \rho_c)$. Thus when $f = 1$, the *weights* of the initial surface and moho loads are equal. Many analyses of isostatic compensation have assumed either $f = 0$ (e.g., *Banks, Parker and Huestis* [1977], *Lewis and Dorman* [1970], *McKenzie and Fairhead* [1997], *McNutt and Parker* [1978]), $f = \infty$ (e.g., *McKenzie* [1978a], *McNutt* [1983]) or $f = 1$ (e.g., *Kogan et al.* [1994]). In reality, f will fall between 0 and ∞, and will vary with $\mathbf{k}$.

Assuming the lithosphere to deform as a thin elastic plate, *Forsyth* [1985] shows that the initial loads $H_I(\mathbf{k})$ and $W_I(\mathbf{k})$ can be calculated from $H(\mathbf{k})$ and $W(\mathbf{k})$ for an assumed

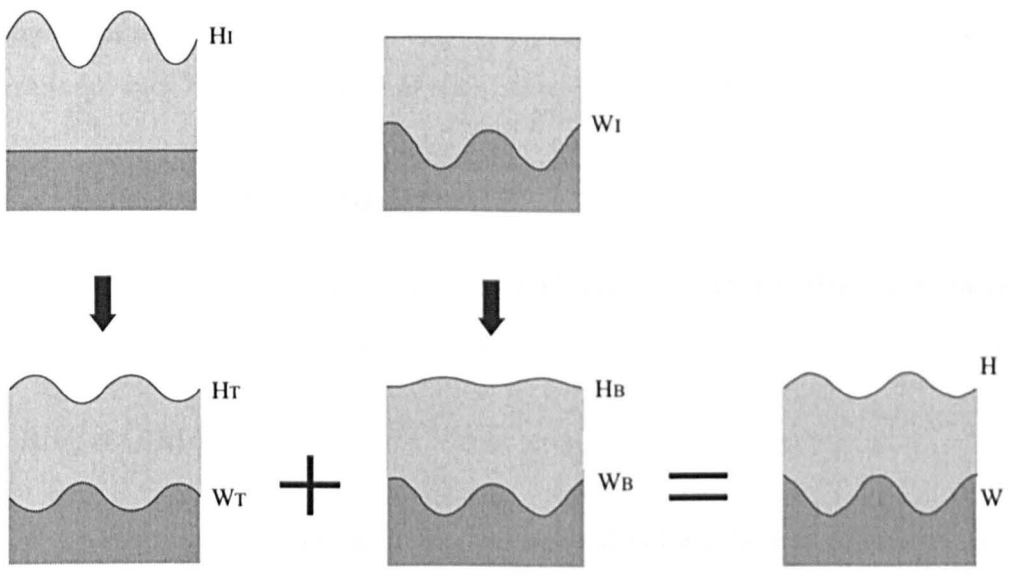

Figure 6.1: The isostatic model. Light shading represents the crust, and darker shading the mantle. Initial loads may be imparted on the surface ($H_I(\mathbf{k})$) and the moho ($W_I(\mathbf{k})$). Isostatic compentation of $H_I(\mathbf{k})$ produces a surface topography $H_T(\mathbf{k})$ and moho topography $W_T(\mathbf{k})$. Similarly, compensation of $W_I(\mathbf{k})$ results in $H_B(\mathbf{k})$ and $W_B(\mathbf{k})$. The final topographies - $H(\mathbf{k})$ and $W(\mathbf{k})$ - represent superpositions. From [*Forsyth*, 1985].

flexural rigidity, D. Thus,

$$H_I(\mathbf{k}) = \left(H(\mathbf{k}) + W(\mathbf{k})\frac{\Delta\rho}{\rho_0\phi}\right)\left(\frac{\rho_0 + \Delta\rho\xi}{\Delta\rho}\right)\left(\frac{\phi}{\phi\xi - 1}\right) \tag{6.4}$$

and

$$W_I(\mathbf{k}) = \left(H(\mathbf{k}) + W(\mathbf{k})\frac{\rho_0}{\Delta\rho\phi}\right)\left(\frac{\Delta\rho + \rho_0\phi}{\rho_0}\right)\left(\frac{\xi}{\phi\xi - 1}\right) \tag{6.5}$$

where

$$\phi = \phi(k) = 1 + \frac{Dk^4}{\rho_c g} \qquad \text{and} \qquad \xi = \xi(k) = 1 + \frac{Dk^4}{\Delta\rho g} \tag{6.6}$$

and $k = |\mathbf{k}| = 2\pi/\lambda$, where λ is wavelength. The components of relief may then be found as

$$\begin{aligned} H_T(\mathbf{k}) &= \frac{\xi(\Delta\rho/\rho_0)W(\mathbf{k}) + \phi H(\mathbf{k})}{\phi\xi - 1} \\ H_B(\mathbf{k}) &= H(\mathbf{k}) - H_T(\mathbf{k}) \\ W_B(\mathbf{k}) &= W_I(\mathbf{k}) + H_B(\mathbf{k}) \\ W_T(\mathbf{k}) &= W(\mathbf{k}) - W_B(\mathbf{k})\ . \end{aligned} \tag{6.7}$$

An important assumption here is that the processes producing the initial loads are uncorrelated, such that $H_I(\mathbf{k})$ and $W_I(\mathbf{k})$ have a random difference in phase.

6.3 The Gravity Admittance

The Fourier transforms of Bouguer gravity, $B(\mathbf{k})$, and topography, $H(\mathbf{k})$, may be related by a linear transfer function, $\hat{Q}(\mathbf{k})$, such that

$$B(\mathbf{k}) = \hat{Q}(\mathbf{k})H(\mathbf{k}) \; . \tag{6.8}$$

$\hat{Q}(\mathbf{k})$ is the observed admittance. In the presence of noise it is best estimated as

$$\hat{Q}(\mathbf{k}) = \frac{B(\mathbf{k})H^*(\mathbf{k})}{H(\mathbf{k})H^*(\mathbf{k})} \tag{6.9}$$

where the asterisk denotes the complex conjugate.

Calculation of the gravity admittance is usually carried out in 2D and the flexural response of the lithosphere is assumed to be isotropic.[1] The admittance function is therefore real and symmetric in both the space and wavenumber domains. Assuming isotropy, the products in Equation 6.9 are averaged in concentric **k**-space annuli, such that

$$\hat{Q}(\bar{k}) = \frac{\langle B(\mathbf{k})H^*(\mathbf{k})\rangle}{\langle H(\mathbf{k})H^*(\mathbf{k})\rangle} \tag{6.10}$$

where the angle brackets indicate binning and averaging in discrete annuli, and $\bar{k}$ is the average one dimensional wavenumber within each annulus.

Forsyth [1985] derives an expression for the admittance that is predicted for given $H_T(\mathbf{k})$ and $H_B(\mathbf{k})$. If $H_I(\mathbf{k})$ and $W_I(\mathbf{k})$ are uncorrelated in space, then

$$\hat{Q}(k) = -2\pi G\rho_c e^{-kz_m} \frac{\phi H_B(k)^2 + (H_T(k)^2/\xi)}{H_T(k)^2 + H_B(k)^2} \tag{6.11}$$

where z_m is the average moho depth within the area of analysis. As $H_T(k)$ and $H_B(k)$ may be related by an expression in D and f (see Equation 12 of *Forsyth* [1985]), $\hat{Q}(k)$

[1] As shown in Section 2.4.3, it might be expected that the flexural response of the lithosphere is not isotropic such that T_e varies with azimuth, and also with the sense of flexure (Figure 2.5).

may expressed as

$$\hat{Q}(k) = -2\pi G\rho_c e^{-kz_m}\left(\frac{\phi f^2\rho_c^2}{\xi^2\Delta\rho^2}+\frac{1}{\xi}\right)\left(\frac{f^2\rho_c^2}{\xi^2\Delta\rho^2}+1\right)^{-1} . \tag{6.12}$$

Figure 6.2a shows the function $\hat{Q}(k)$ for various T_e for the two extreme cases of loading, i.e., when $f(k) = 0$ and $f(k) = \infty$. Figure 6.2b shows the admittance as a function of f for a T_e of 20 km and a moho depth of 35 km. Most analyses of admittance assume $f = 0$. It can be seen from Figure 6.2 that the T_e inferred by assuming such a surface loading model will be seriously underestimated where there is a significant initial moho load. This important point has been overlooked by *McKenzie and Fairhead* [1997] who assume f to be zero and so obtain low values for T_e. Figure 6.3a shows the predicted admittance for a series of T_e values for $f = 1$.

6.4 The Gravity Coherence

The coherence between the real signals is defined as the squared power of their cross-spectrum normalised by the power of each signal. Modelling the coherence between Bouguer gravity and topography with thin elastic plate flexure has become the standard method for estimating continental T_e. The observed coherence is formulated as

$$\gamma_0^2(\bar{k}) = \frac{\langle B(\mathbf{k})H^*(\mathbf{k})\rangle^2}{\langle H(\mathbf{k})H^*(\mathbf{k})\rangle\langle B(\mathbf{k})B^*(\mathbf{k})\rangle} \tag{6.13}$$

where $B(\mathbf{k})$ and $H(\mathbf{k})$ are the Fourier transforms of Bouguer anomaly and topography. Coherence then is simply a measure of the difference in phase between Bouguer gravity and surface topography. The amplitude of moho topography, $W(\mathbf{k})$, is found from the downward continuation of Bouguer anomaly to depth z_m;

$$W(\mathbf{k}) = \frac{B(\mathbf{k})e^{kz_m}}{2\pi G\Delta\rho} . \tag{6.14}$$

If the difference in phase between the initial surface and moho loads is random, we can eliminate the cross terms and express the predicted coherence from Equations 6.1, 6.2, 6.13 and 6.14 as

$$\gamma_0^2(\bar{k}) = \frac{\langle H_T(\mathbf{k})W_T(\mathbf{k}) + H_B(\mathbf{k})W_B(\mathbf{k})\rangle^2}{\langle H_T(\mathbf{k})^2 + H_B(\mathbf{k})^2\rangle\langle W_T(\mathbf{k})^2 + W_B(\mathbf{k})^2\rangle} . \tag{6.15}$$

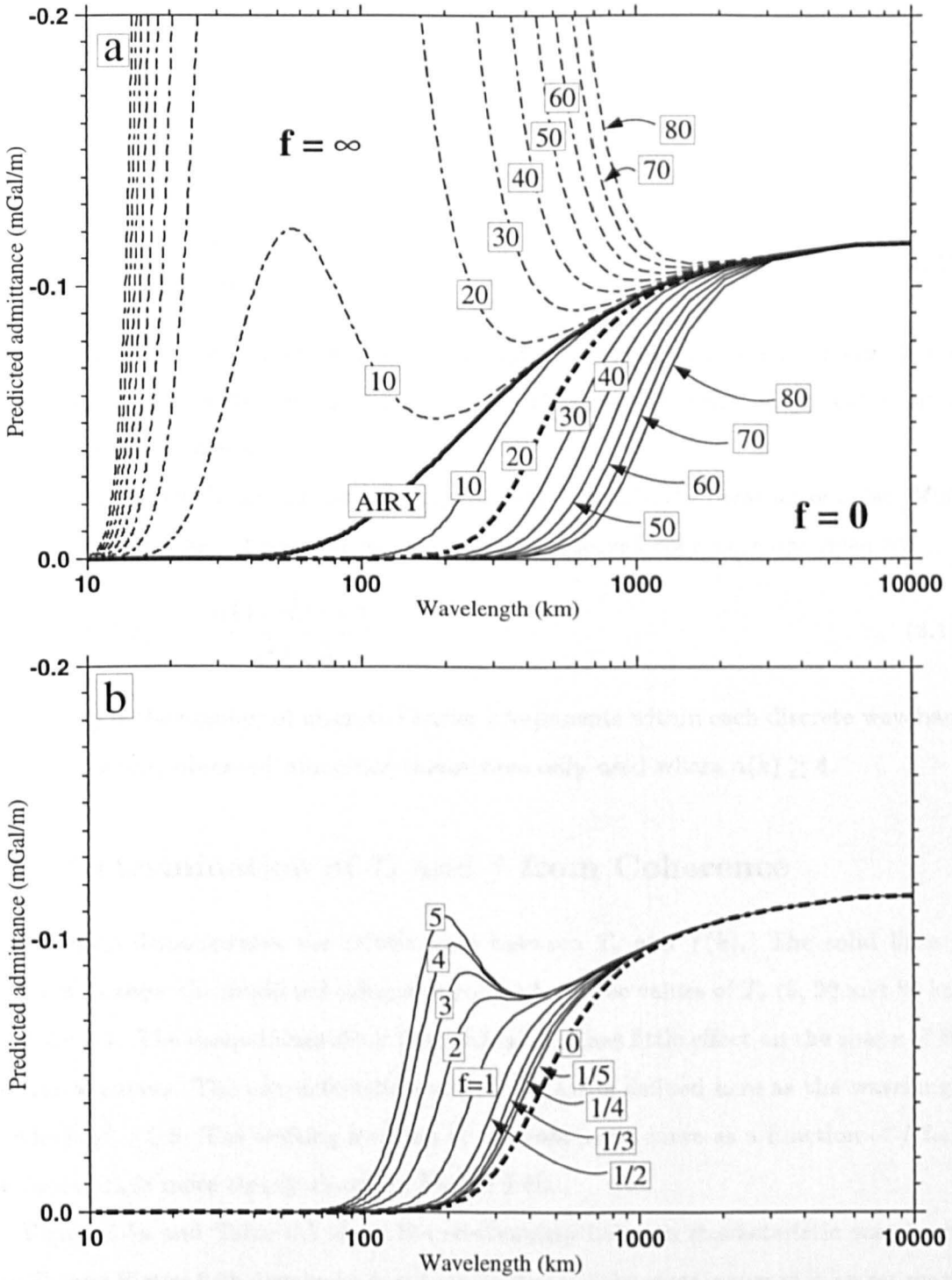

Figure 6.2: Predicted admittance curves calculated from Equation 6.12. (a) As a function of T_e for pure surface loading (solid lines) and pure moho loading (thin dashed lines). Surface and subsurface loading are indistinguishable for $T_e = 0$. (b) As a function of f for T_e of 20 km and a moho depth of 35 km. The bold dashed line is the same as that in (a).

Using Equations 6.4, 6.5 and 6.7, the predicted coherence may be found as a function of T_e and f, such that

$$\gamma_0^2(\bar{k}, f, T_e) = \frac{1 + P\left(\frac{P\phi^2}{\xi^2} + \frac{2\phi}{\xi}\right)}{1 + P\left(\phi^2 + \frac{1}{\xi^2} + \frac{P\phi^2}{\xi^2}\right)} \tag{6.16}$$

where

$$P = P(\bar{k}) = \left(\frac{f\rho_c}{\Delta\rho}\right)^2 . \tag{6.17}$$

Plots of this predicted coherence function for equal surface and sub-surface loads ($f = 1$) are shown in Figure 6.3b. The stronger the plate, the greater the wavelength of transition from low to high coherence.

In practice, the observed coherence is positively biased in the presence of noise [*Munk and Cartwright*, 1966]. Unbiased estimates of the observed coherence are given by

$$\gamma^2(\bar{k}, f, T_e) = \frac{n(\bar{k})\gamma_0(\bar{k})^2 - 1}{n(\bar{k}) - 1} \tag{6.18}$$

where $n(\bar{k})$ is the number of discrete Fourier components within each discrete waveband bin. In all cases, observed coherence values were only used where $n(\bar{k}) \geq 4$.

6.5 Determination of T_e and f from Coherence

This section demonstrates the relationship between T_e and $f(k)$. The solid lines in Figure 6.4a show the predicted coherence curves for three values of T_e (5, 20 and 80 km) for $f(k) = 1$. The dashed lines show that changing f has little effect on the shape of the coherence curves. The *characteristic wavelength* (λ_c) is defined here as the wavelength at which $\gamma^2 = 0.5$. The shifting location of the coherence curve as a function of f for a particular T_e is more clearly shown in Figure 6.4b.

Figure 6.5a and Table 6.1 show the relationship between characteristic wavelength and T_e, and Figure 6.5b demonstrates the magnitude of the error incurred in an estimated T_e by incorrectly assigning a constant f. Figure 6.5b shows that, for characteristic wavelengths greater than 50 km, the percentage error relative to the value for $f = 1$ is relatively constant with wavelength. Some coherence studies have assumed $f = 1$ (e.g., *Kogan et al.* [1994]). In such cases, a T_e estimate may be obtained by comparing

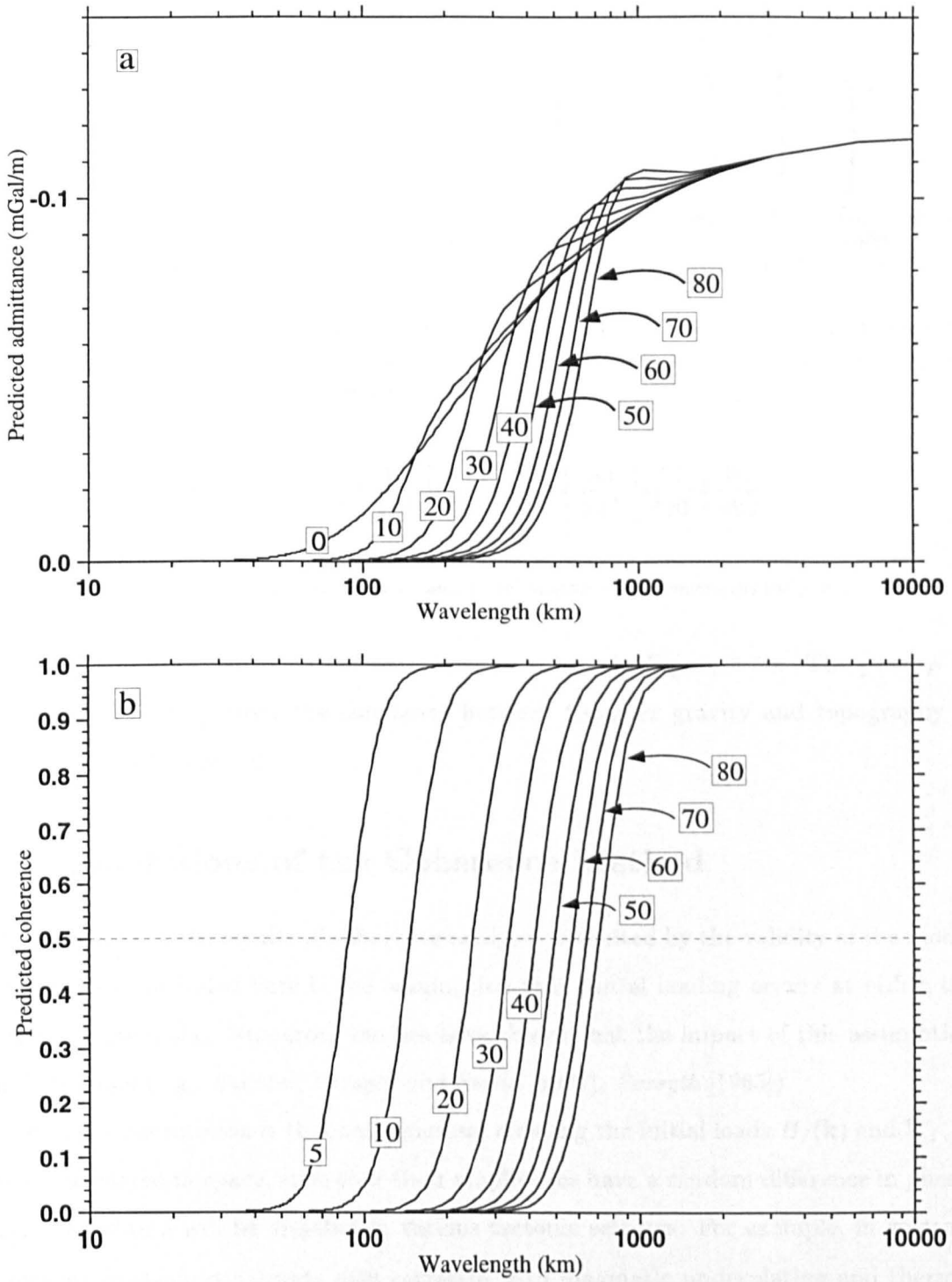

Figure 6.3: (a) Predicted admittance curves for a range of T_e values. Calculated from Equation 6.12. $f = 1$ for all curves. (b) Predicted coherence curves for a range of T_e values. Calculated from Equation 6.16. $f = 1$ for all curves.

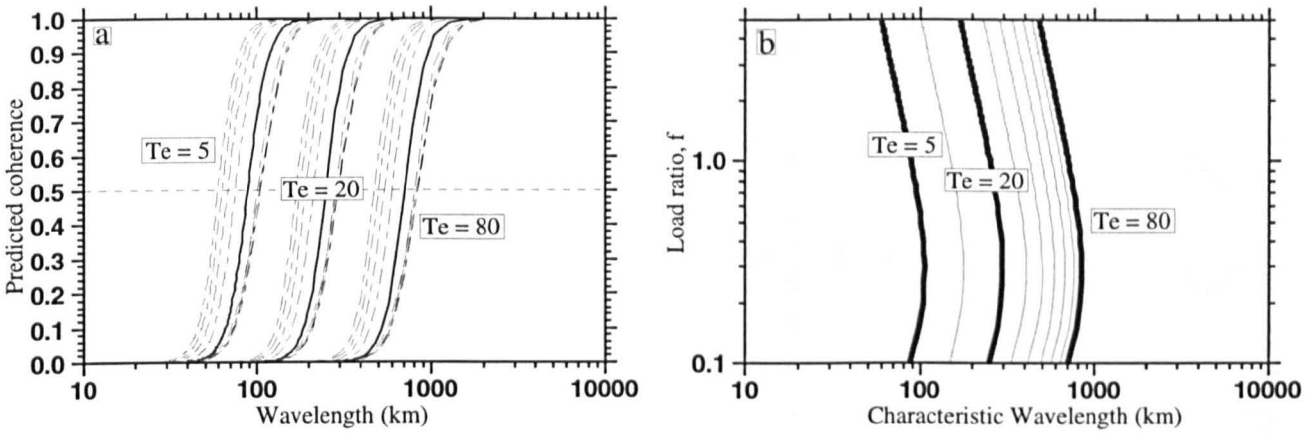

Figure 6.4: (a) Predicted coherence curves for T_e = 5, 20 and 80 km. Solid line represent curves for $f = 1$. Dashed lines correspond to f values of 5, 4, 3, 2, 1/2, 1/3, 1/4 and 1/5. (b) Locus of $\{\lambda_c, f\}$ for T_e = 5, 10, 20, 30, 40, 50, 60, 70 and 80 km.

T_e (km)	5	10	15	20	30	40	50
λ_c (km)	90	150	200	250	340	420	495

Table 6.1: Conversions between T_e and λ_c (characteristic wavelength) for $f = 1$.

observed coherence values to the set of curves shown in Figure 6.3b. The process of estimating T_e and f from the coherence between Bouguer gravity and topography is represented in Figure 6.6.

6.6 Limitations of the Coherence Method

The reliability of the results of coherence analyses is limited by the validity of the model assumptions. Included here is the assumption that initial loading occurs at either the surface or the moho. Numerous studies have shown that the impact of this assumption on T_e is small (e.g., *Bechtel, Forsyth and Swain* [1987], *Forsyth* [1985]).

A major assumption is that the processes creating the initial loads $H_I(\mathbf{k})$ and $W_I(\mathbf{k})$ are uncorrelated in space, such that their amplitudes have a random difference in phase. Such a condition will be violated in various tectonic settings. For example, in volcanic provinces, volcanic constructs may correlate with magmatic underplating and thermal loads. A similar problem may also be significant for extensional loading if the depth of pure-shear necking lies within the crust (ie., $0 < f < \infty$). *Macario, Malinverno and Haxby* [1995] show that when the initial loading is correlated, the transition from low to high coherence occurs over a greater range of wavelengths. As the correlation increases

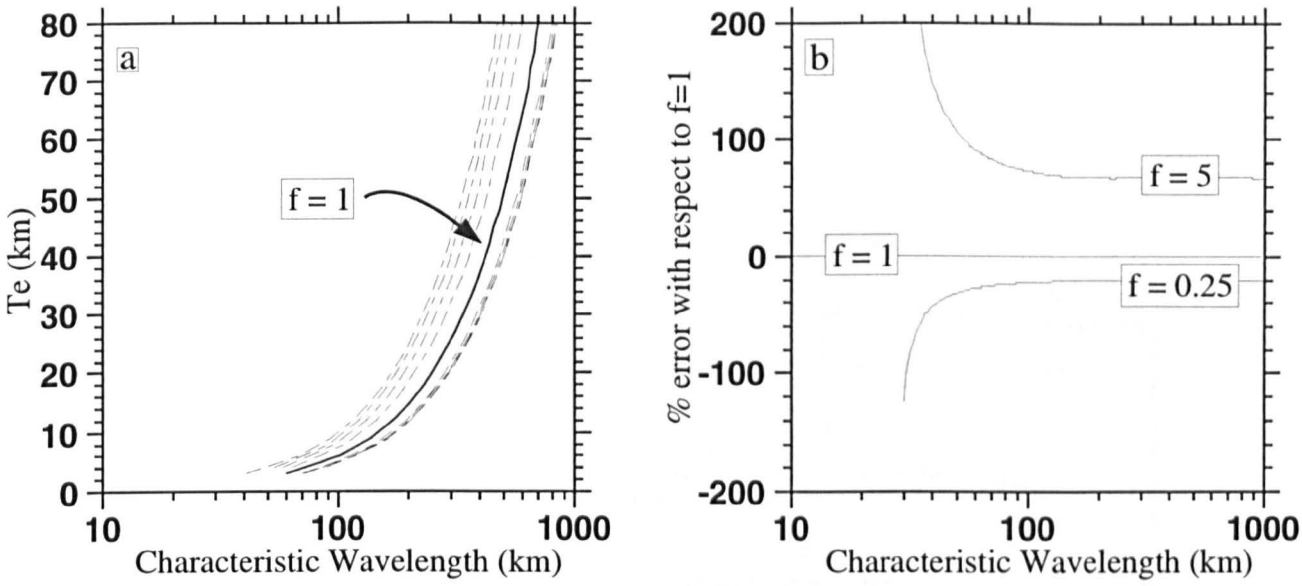

Figure 6.5: (a) T_e as a function of characteristic wavelength (λ_c) for f = 5, 4, 3, 2, 1, 1/2, 1/3, 1/4 and 1/5. (b) Percentage difference in T_e as a function of λ_c for the same range in f. Note that for λ_c greater than ~50 km, the percentage differences are relatively constant. The behaviour for $\lambda_c < 50$ km reflects the instability of the predicted coherence function for very low T_e.

from zero, coherence is observed at shorter wavelengths. Because T_e is estimated by minimising RMS errors, there is a downward bias in the estimated value. Thus, if the initial surface and moho loading are not independent, the best-fit estimates of T_e will represent underestimates.

Macario, Malinverno and Haxby [1995] do not investigate correlations as a function wavelength. In extensional settings where the depth of necking lies within the crust, the correlation between $H_I(\mathbf{k})$ and $W_I(\mathbf{k})$ is expected to be greater at the wavelengths of crustal thinning, posing a potentially more serious problem than short wavelength features such as volcanoes.

Studies of plate flexure ignore the effect of in-plane deviatoric stress on the bending moment and thus on plate rigidity. Deviatoric stress effects actual plate rigidity (see Chapter 2), so if the stress is anisotropic, the rigidity will likewise be anisotropic. For the Fourier coherence technique, the spectra are averaged in concentric annuli prior to estimating coherence, so an average T_e will result. It will be seen that tensor and polarized wavelets allow for the analysis of coherence - and so the estimation of T_e - with direction, although this is not performed in this study.

A central assumption in the coherence method is that the coherence between topography and free-air gravity is close to unity at short wavelengths. If this is not the case,

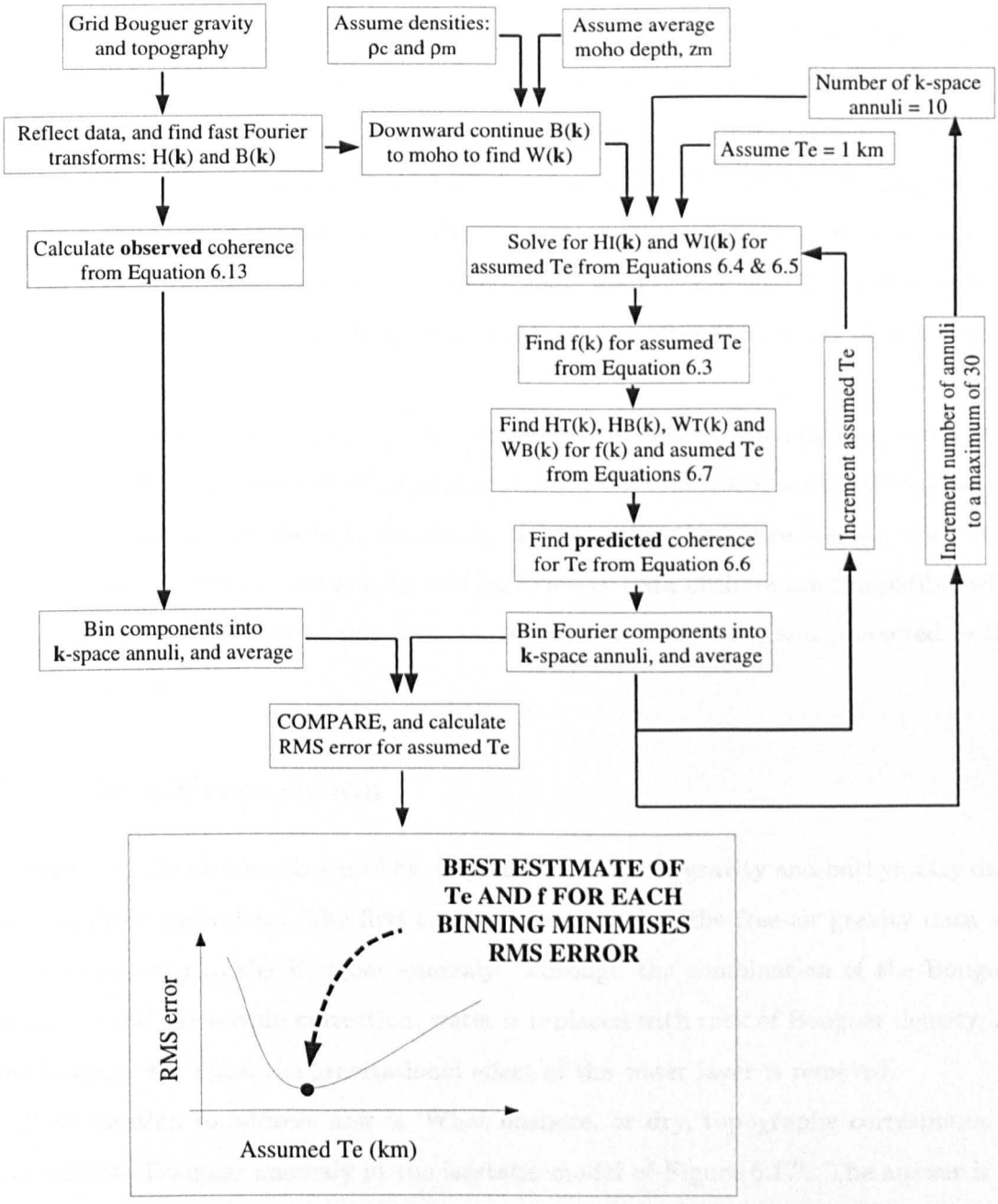

Figure 6.6: Flow diagram to demonstrate the estimation of T_e and f from datasets of Bouguer gravity and topography using the Fourier coherence method. Estimates of ρ_c, ρ_m and z_m are required.

the coherence between Bouguer gravity and topography will result in overestimates of T_e. *McKenzie and Fairhead* [1997] believe that this situation could arise across cratons where short wavelength topography has been removed by erosion, and is expected to be less of a problem in actively deforming regions. Chapter 2 (Section 2.7.3) describes the situation where lower crustal flow might result in reduced coherence at short wavelengths.

Most investigations of flexural rigidity using the coherence method have employed the conventional FFT to estimate spectra, where the analysing basis functions are sinusoids. As such, the FFT displays no spatial localisation within the window of analysis (see Section 6.13.1). As the coherence analysis must assume a uniform rigidity within the window, the resulting T_e estimate represents some kind of average. The CWT method provides a solution to this problem and is introduced after the results of the Fourier method are presented.

A final problem is specific to regions of submerged continental lithosphere, such as the Aegean Sea. The coherence method as described by *Forsyth* [1985] is directly applicable to onshore regions. In order to obtain T_e estimates for the entire Aegean area, it is important to ensure that the gravity and bathymetry data offshore are compatible with those onshore. A solution to this problem is found in this study, and presented in the following section.

6.7 Data Preparation

A solution to the problem is found by mapping the offshore gravity and bathymetry data to an onshore equivalent. The first step is to ensure that the free-air gravity data are correctly reduced to the Bouguer anomaly. Through the combination of the Bouguer correction and the terrain correction, water is replaced with rock of Bouguer density, ρ_B (see Chapter 4). Thus, the gravitational effect of the water layer is removed.

The question to address now is 'What onshore, or dry, topography corresponds to that offshore Bouguer anomaly in the isostatic model of Figure 6.1?'. The answer is to replace the water column with a layer of rock of equivalent load. For bathymetry $b(x,y)$, the equivalent layer or rock, $r(x,y)$, with density ρ_B is

$$r(x,y) = \frac{\rho_w}{\rho_B}|b(x,y)| \ . \tag{6.19}$$

The corresponding topography, which is referred to here as the *effective topography*,

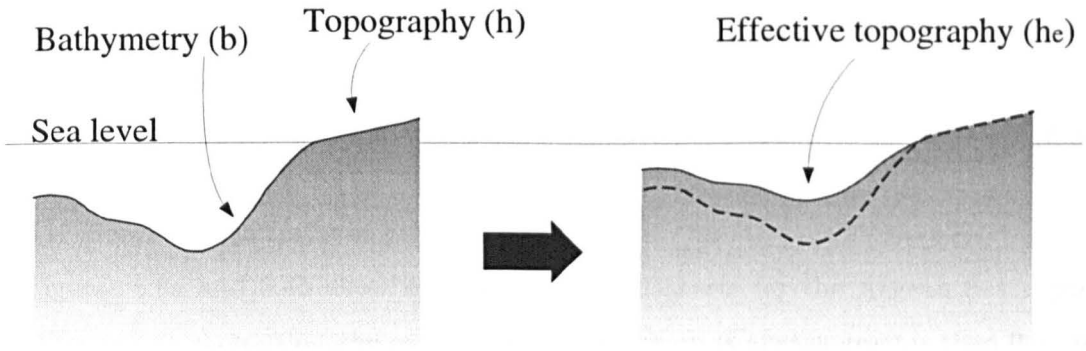

Figure 6.7: Calculation of effective topography from bathymetry.

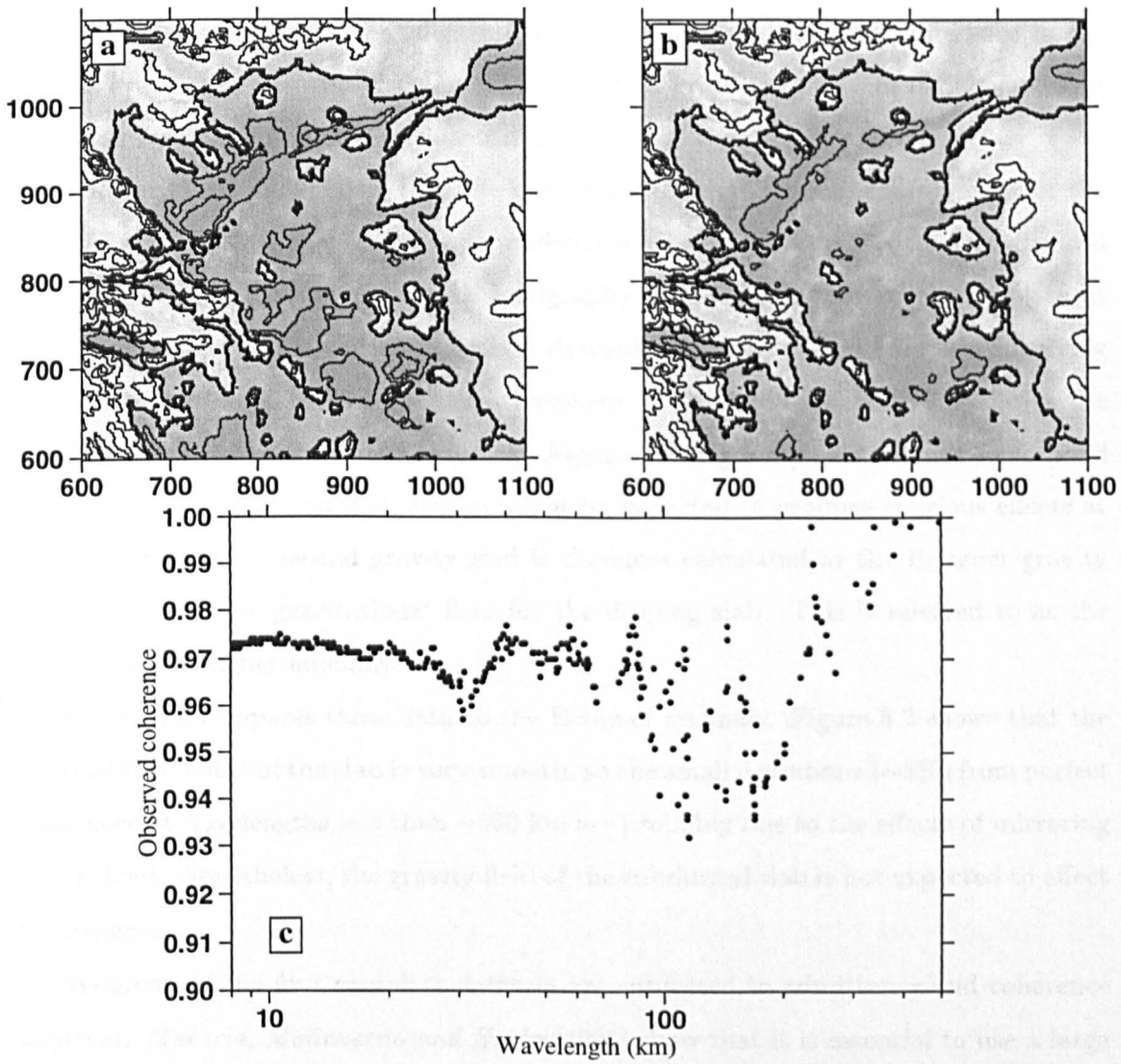

Figure 6.8: (a) Topography and bathymetry. (b) Topography and effective topography. Contour interval = 500 m. (c) Coherence between datasets of (a) and (b).

$h_e(x,y)$, is calculated as

$$\begin{aligned} h_e(x,y) &= b(x,y) + r(x,y) \\ &= \frac{\rho_B - \rho_w}{\rho_B} b(x,y) \ . \end{aligned} \tag{6.20}$$

This is shown schematically in Figure 6.7.

Figures 6.8a and 6.8b show maps of the two datasets for the Aegean Sea region, and Figure 6.8c shows that the coherence between them is always greater than 0.9. We therefore expect there to be little difference in the estimated T_e values.

Chapter 4 describes the compilation of gravity and topography data. The gravity data were gridded to 4 km using the BLOCKMEAN and SURFACE algorithms of GMT. Both the topography and the effective topography are used, and the difference in the results are analysed in this chapter. The final data grids are 1344 km in the east-west direction by 1456 km in the north-south direction.

Ebinger et al. [1989] show that the admittance observed across the plateaux of the East African rift is more negative than predicted at wavelengths greater than the flexural wavelength. As the long wavelength topography cannot be supported by the plate, it is interpreted to be the consequence of a dynamic compensation mechanism involving mantle convection at the base of the lithosphere. *Tsokas and Hansen* [1997] derive the gravitational field for the slab beneath the Aegean. This gravity field will not correspond to any isostatic compensation, and so might be expected to produce spurious effects at long wavelength. A second gravity grid is therefore calculated as the Bouguer gravity anomaly minus the gravitational field for the dipping slab. This is referred to as the *slab-reduced* Bouguer anomaly.

Figure 6.9 compares these data to the Bouguer anomaly. Figure 5.2 shows that the gravitational effect of the slab is very smooth, so the small deviations (~3%) from perfect coherence at wavelengths less than ~500 km are probably due to the effects of mirroring (see below). Nonetheless, the gravity field of the subducted slab is not expected to affect T_e estimates.

Windows of the four complete datasets are subjected to admittance and coherence analyses. *Macario, Malinverno and Haxby* [1995] show that it is essential to use a large enough window to obtain coherence estimates at long wavelengths. If the windowed area is too small, then T_e estimates are biased to higher values. It is clear that larger

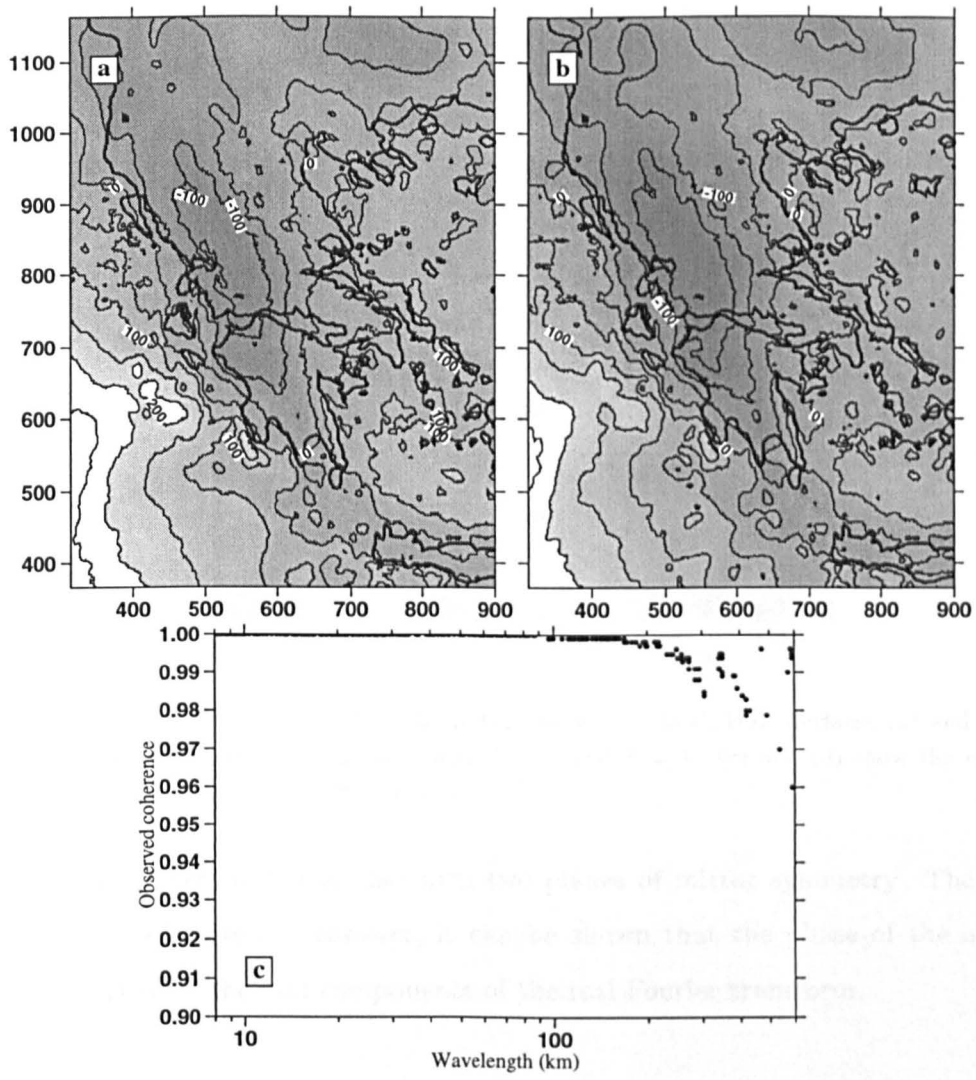

Figure 6.9: (a) The complete Bouguer anomaly. (b) The slab-reduced Bouguer gravity field. Note that the extent of these data is limited to the size of the study area of *Tsokas and Hansen* [1997]. Contour interval = 50 mGal. (c) The coherence between the two Bouguer gravity fields. The gravitational effect of the subducted slab will not affect the estimation of T_e across the overriding plate.

windows are required to resolve greater T_e values. For the Fourier method, there is thus a trade-off between result reliability and spatial resolution. This problem is readdressed with wavelet transforms in Section 6.13.

In order to minimise the edge effects when performing the FFT on windows of data, the windows of gravity and topography are reflected firstly about its southern margin, and subsequently about its western margin. Mirrored boundary conditions are favoured over tapering to avoid artificial coherence at the wavelength of the taper [*McNutt*, 1983]. Observed admittance and coherence values at wavelengths greater that the dimensions of the window are not considered in these analyses.

The input data to the FFT algorithm are therefore real and even, such that the

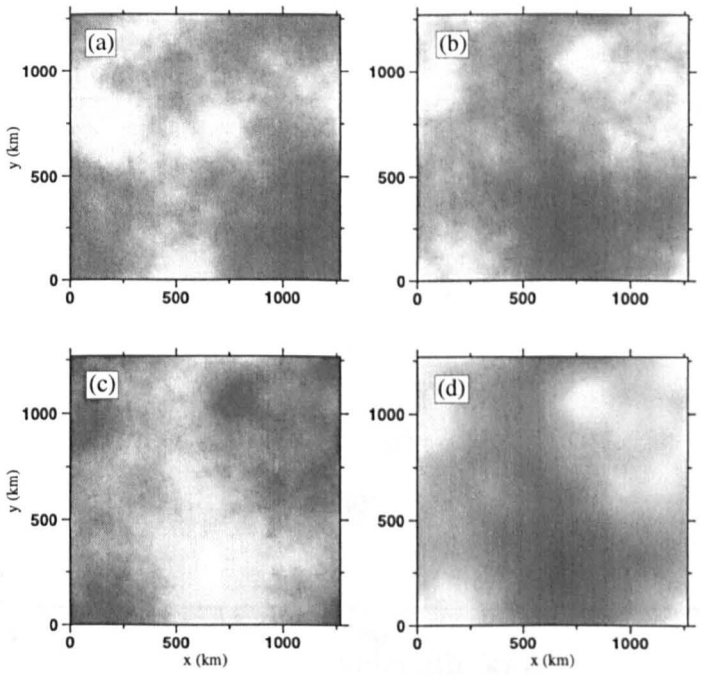

Figure 6.10: (a) Initial surface load, H_I. (b) Initial sub-surface load, W_I. Surfaces (a) and (b) are statistically uncorrelated, and are generated with $\beta = 3$ and $f = 1$. (c) and (d) show the resulting topography and Bouguer gravity for $T_e = 10$km.

resulting FFT is even and real, also with two planes of mirror symmetry. The phase spectrum is therefore zero. However, it can be shown that the phase of the original signal is contained in the odd components of the real Fourier transform.

6.8 Coherence for Synthetic Data

Fourier analyses of real topography have shown that its power decays approximately as a power law [*Goff*, 1990; *Huang and Turcotte*, 1989]

$$HH^*(k) \propto k^{-\beta} \tag{6.21}$$

over large ranges in k, where the exponent β is $\sim$3 and H is the 2D Fourier transform of an area of topography. For this test, synthetic loads H_I and W_I have been created for $\beta = 3$. The load ratio f is taken to be 1, and the two signals are uncorrelated at all wavelengths. These loads are then emplaced on a lithosphere whose T_e is 10 km. The resulting topography $h(x,y)$ and Bouguer gravity $BA(x,y)$ are shown in Figure 6.10.

Figure 6.11 shows that the observed coherence is very similar to that predicted for $T_e = 10$ and $f = 1$. However, the predicted load ratio spectra, $f(\bar{k})$, differ for different

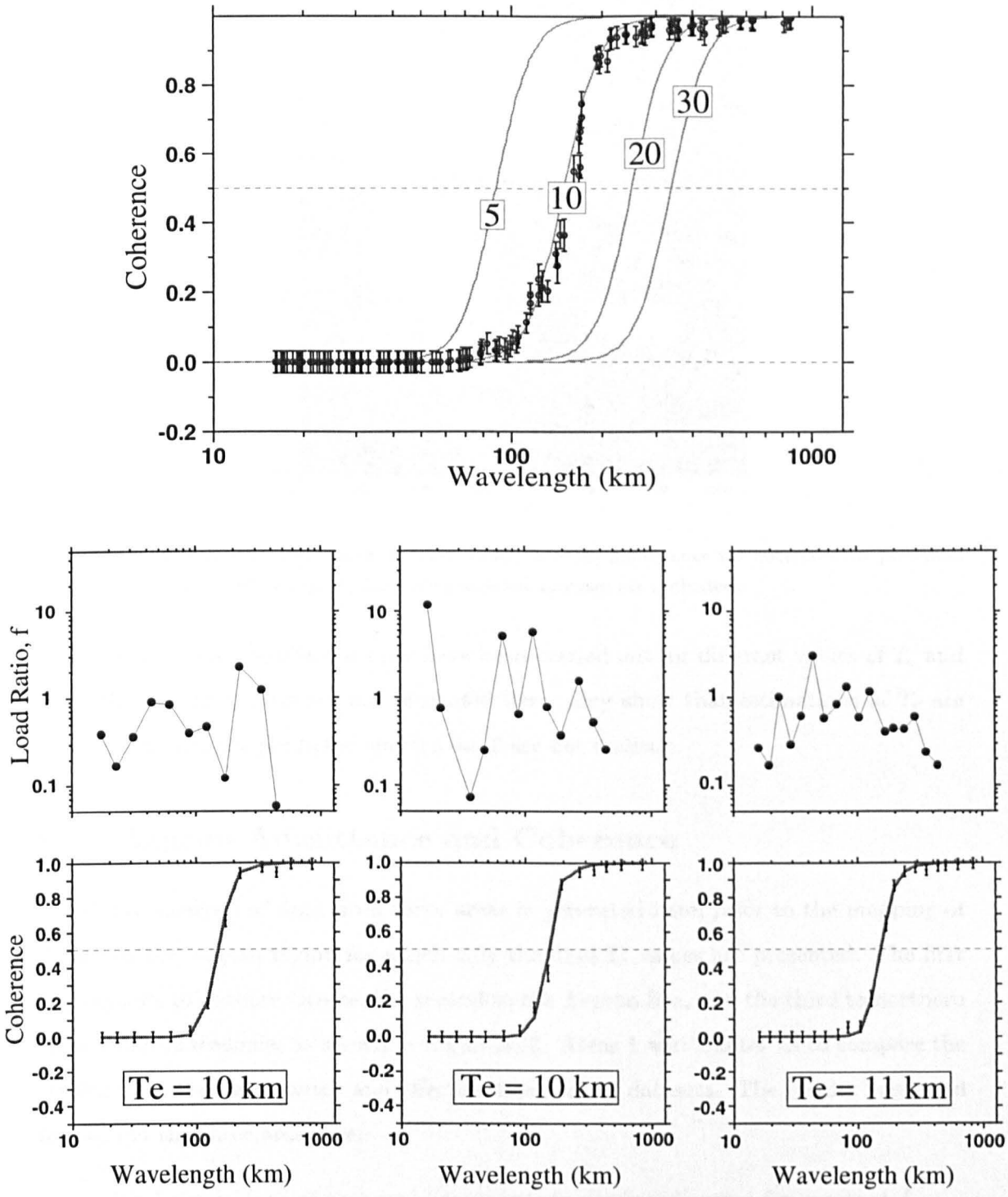

Figure 6.11: The results of performing the coherence analysis on the synthetic topography and gravity datasets. The top plot shows the observed coherence for all realisations of the spectral averaging where $n(\bar{k}) \geq 4$. Feinter lines show predicted coherence curves for $f = 1$. The lower plots shows observed coherence points and the best-fit predicted coherence curve, obtained with the cited T_e and the plotted load-ratio spectrum.

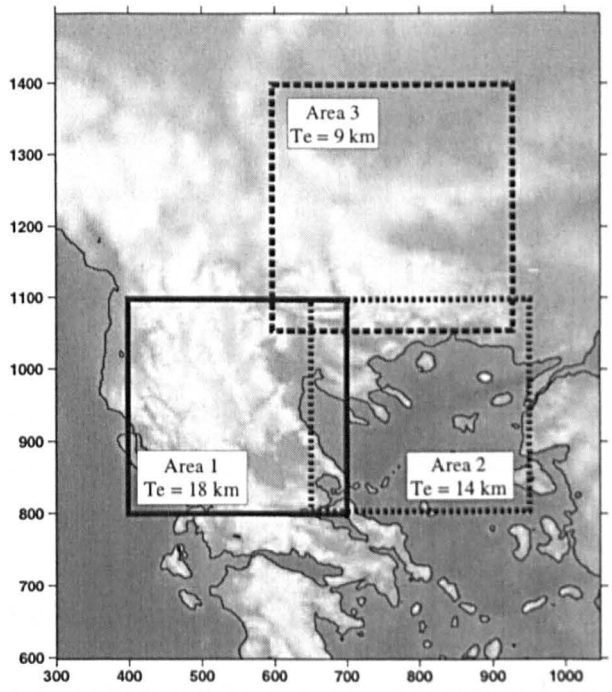

Figure 6.12: DEM showing location of the three areas where the admittance and coherence are presented in full. The estimates of average T_e from the presented analyses are indicated.

numbers of annuli. Additional tests have been carried out for different values of T_e and f. Although the results are not presented here, they show that estimations of T_e are robust, but that the predicted spectra for f are not realistic.

6.9 Aegean Admittance and Coherence

A detailed analysis of data from three areas is presented here, prior to the mapping of T_e across the Aegean region for which only the final T_e values are presented. The first corresponds to onshore Greece, the second to the Aegean Sea, and the third to northern Greece and Macedonia, as shown in Figure 6.12. Areas 1 and 2 allow us to compare the results from the bathymetry and effective topography datasets. The results presented for each of the three areas are:

- visual comparison of observed admittance to predicted curves for constant f
- visual comparison of observed coherence to predicted curves for constant f
- estimates of the T_e from minimising RMS errors for each data pair
- analyses of best-fit predicted coherence curves and the corresponding f.

Figure 6.6 shows that assumptions of density and moho depth must be made. It can be shown from Equations 6.16 and 6.17 that density contrasts ($\Delta\rho$) of 350 kg/m^3 and 650 kg/m^3 result in only a 2% error in the predicted coherence at λ_c. From *Makris* [1984], ρ_c and ρ_m are assigned the values 2850 kg/m^3 and 3350 kg/m^3 respectively.

Crustal thickness is poorly constrained across the Aegean. The preliminary map of Figure 3.8 shows that z_m ranges from ~25 km across the Southern Aegean to ~45 km in the Hellenides. In the absence of better data, z_m is held constant at 35 km for both the Fourier and the wavelet analyses. Although this is an overestimate for the Aegean sea by between 5 and 10 km, *Forsyth* [1985] shows that this will have a negligible effect on the form of the predicted coherence.

6.9.1 Area 1 - Onshore Greece

The admittance between gravity and topography is shown in Figure 6.13. Like all subsequent figures displaying observed admittance and coherence, this figure superimposes the estimates calculated for several realisations of the spectral averaging corresponding to the 21 different sets of annuli (see Figure 6.6). Only points where $n(\bar{k}) \geq 4$ are plotted. Because most of Area 1 is onshore, it is expected that there should be little difference between results obtained from the topography and the effective topography. The observed admittance for the Bouguer gravity is almost identical to that for the slab reduced gravity, indicating that the influence of the slab is not observed at the wavelengths of lithospheric flexure.

A match with the predicted curves for $f = 1$ cannot be made for wavelengths greater than ~200 km. A better match may be made if the initial load ratio is increased, and Figure 6.13b corresponds to $f = 10$. The T_e value is not obvious from these plots. This sensitivity of admittance to f is a major limitation of the admittance technique in estimating T_e.

Coherence is less sensitive to f, and Figure 6.14 shows that the T_e is approximately 15 km. As for the admittance, there is no systematic difference between the results from topography and the effective topography. It is also clearly seen that the coherence estimates for the slab-reduced Bouguer gravity are almost identical to those for the *BA*. The slab-reduced gravity is no longer considered in this thesis.

The process outlined in Figure 6.6 is carried out on the two remaining data pairs. Figure 6.15a shows that T_e estimates using topography range between 16 km and 25

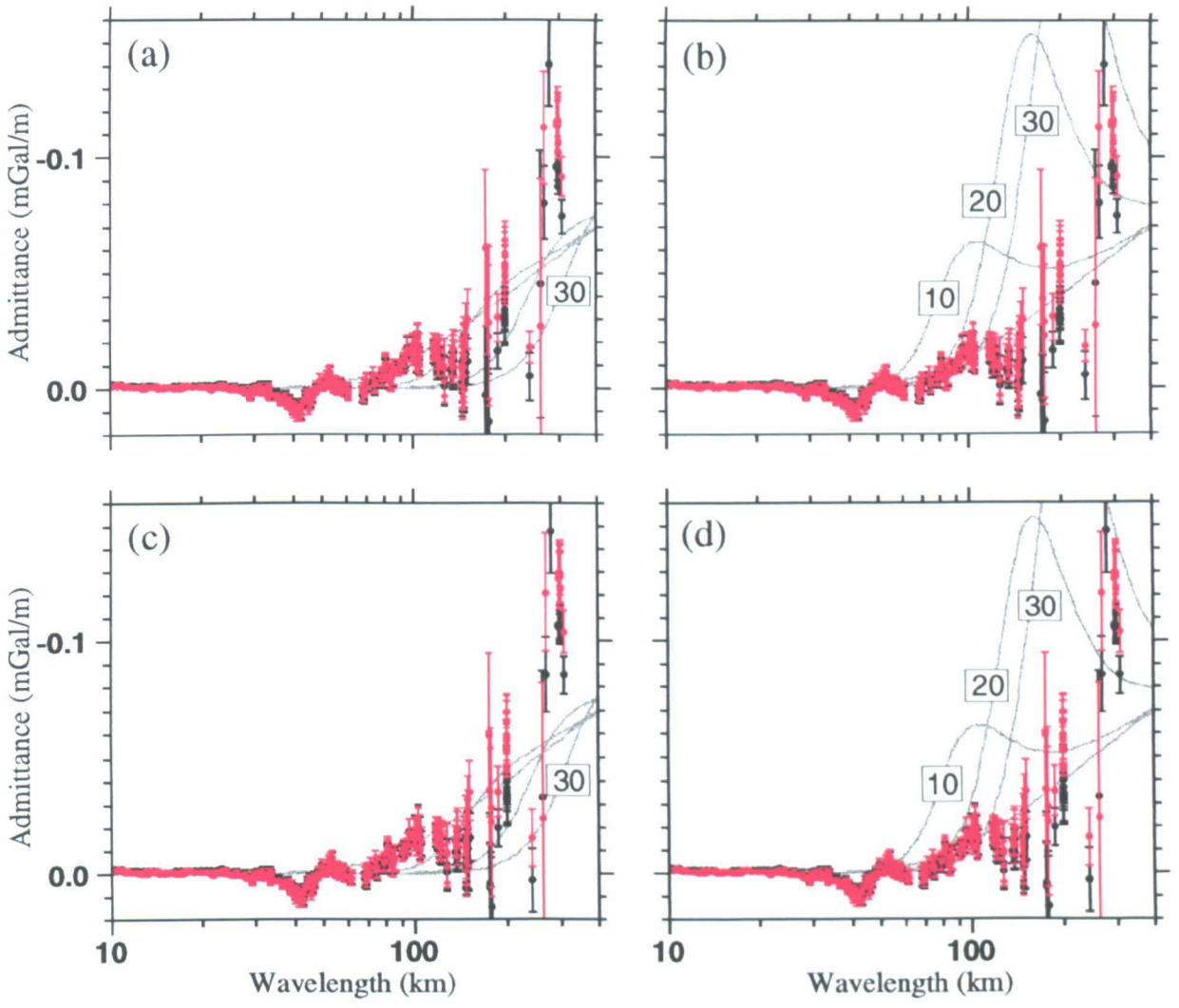

Figure 6.13: Observed admittance for Area 1. (a) Black shows observed admittance for topography and Bouguer gravity, and red for effective topography and Bouguer gravity. Feinter lines represent the admittance predicted for T_e values 0, 10, 20 and 30 km, with $f = 1$. (b) As (a), though predicted curves are for $f = 10$. (c) Black shows observed admittance for topography and slab-reduced Bouguer gravity, and red for effective topography and slab-reduced Bouguer gravity. Feinter lines are the admittance predicted for T_e values 0, 10, 20 and 30 km, with $f = 1$. (d) As (c), though predicted curves are for $f = 10$. Error bars represent one standard deviation.

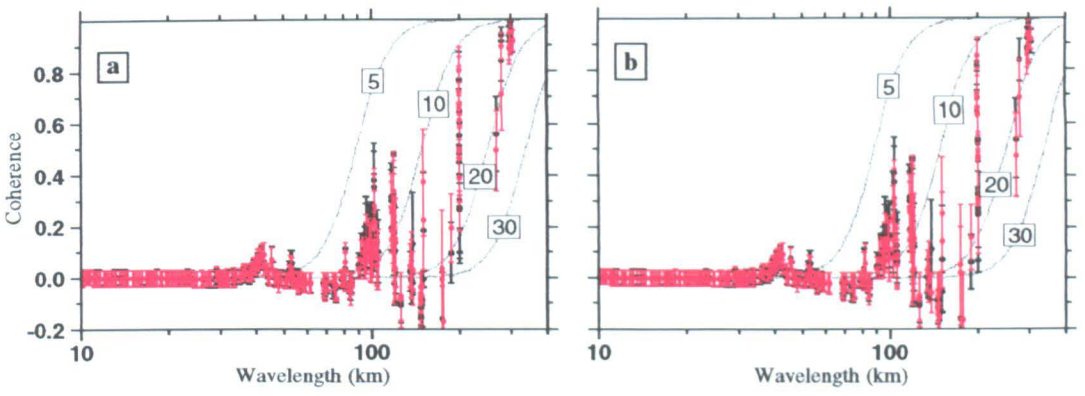

Figure 6.14: Observed coherence for Area 1. (a) Black shows observed coherence for topography and Bouguer gravity, and red for effective topography and Bouguer gravity. (b) Black shows observed coherence for topography and slab-reduced Bouguer gravity, and red for effective topography and slab-reduced Bouguer gravity. The feinter curves in each of the plots correspond to predicted admittance curves for T_e values 5, 10, 20 and 30 km with $f = 1$ (see Figure 6.3). The slab-reduced gravity has a negligible effect on the coherence. Error bars represent one standard deviation.

km, and the curve of RMS error is flat in places. This is not the case when the effective topography is used (Figure 6.15b). The RMS minima are much more clearly defined, and there is a smaller range of the best-fit T_e values.

Figures 6.16 and 6.17 show predicted coherence curves for the onshore Greece region. As was seen with the results with synthetic data, there is no common pattern in $f(\bar{k})$ across different realisations of the spectral averaging.

6.9.2 Area 2 - The Aegean Sea

The same sequence of plots are shown for the Aegean Sea region, though the slab-reduced BA is no longer considered. The observed admittance (Figures 6.18a and 6.18b) for the effective topography is more negative than for topography at wavelengths greater than ~100 km. Such a difference is not observed in the coherence (Figure 6.18c), and the T_e is expected to be approximately 15 km. This is confirmed in the RMS plots of Figure 6.19, though lower RMS values, narrower troughs and less scatter in the T_e estimates are observed for the coherence with effective topography.

6.9.3 Area 3 - Macedonia

As this area is entirely onshore, only one data pair exists. As with the the Aegean areas, the admittance (Figures 6.22a and 6.22b) gives no clear T_e value. However, Figure 6.22c shows that the T_e is approximately 10 km, and this is confirmed by the clear pattern in the RMS curves. As before, there is no consistent pattern in the loading ratio spectra.

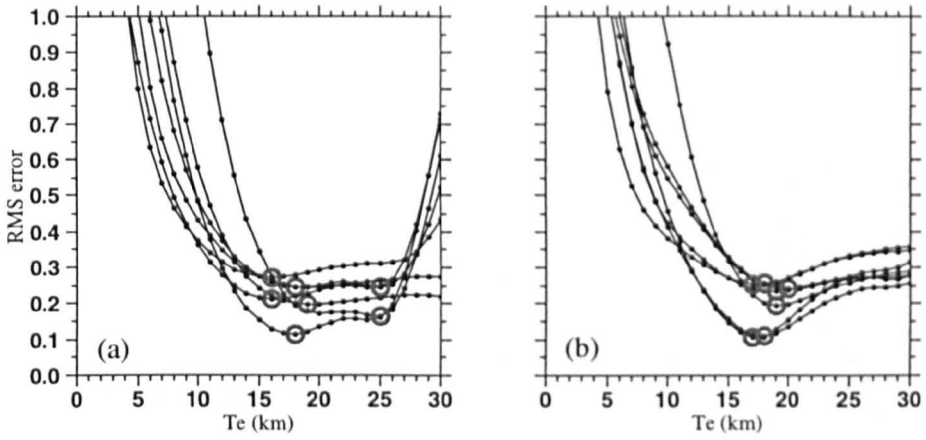

Figure 6.15: The RMS error in the fit between observed and predicted coherence for Area 1, as a function of assumed T_e for all seven realisations of the spectral averaging where $n(\bar{k}) \geq 4$. The best estimate T_e minimises this error, and are circled in each case. (a) Topography-bathymetry and Bouguer gravity. (b) Effective topography and Bouguer gravity.

The errors in the observed admittance and coherence values are significantly less than for the two areas to the south. It is also clear that the observed coherence curves are more shallow than predicted, which may indicate that T_e is not constant across the area.

6.10 Error in T_e Estimates from Coherence

Error in T_e estimations result from numerous sources. These are listed below as either a random (though not necessarily Gaussian) or a systematic source of error.

Random Errors

- Assigning a uniform T_e to a window in which the true rigidity is not constant.
- Annular averaging of spectra in regions of anisotropic in-plane deviatoric stress.
- Artificial power in gravity and topography resulting from the mirroring of long wavelength signal.
- Noise in the original gravity data.

Systematic Errors

- Assuming a random phase difference between initial loading.
- No coherence between free-air anomaly and topography at short wavelengths.

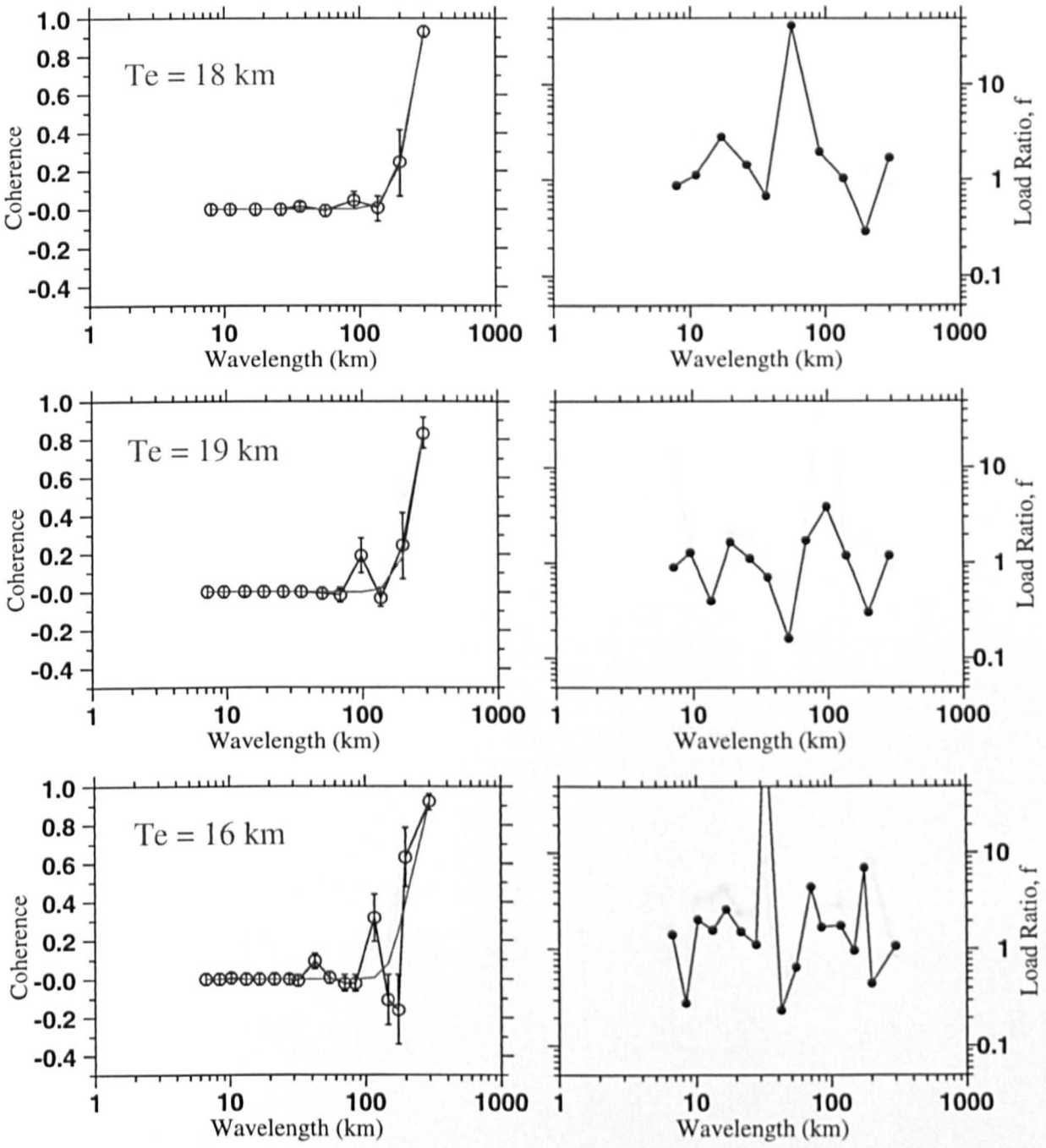

Figure 6.16: Best-fit predicted coherence curves for Area 1, for three realisations of the spectral averaging of topography and Bouguer gravity. Black circles represent the observed coherence, and the best fit predicted coherence is shown in red. The corresponding T_e value is printed, and the corresponding $f(\bar{k})$ is plotted to the right. Error bars represent one standard deviation.

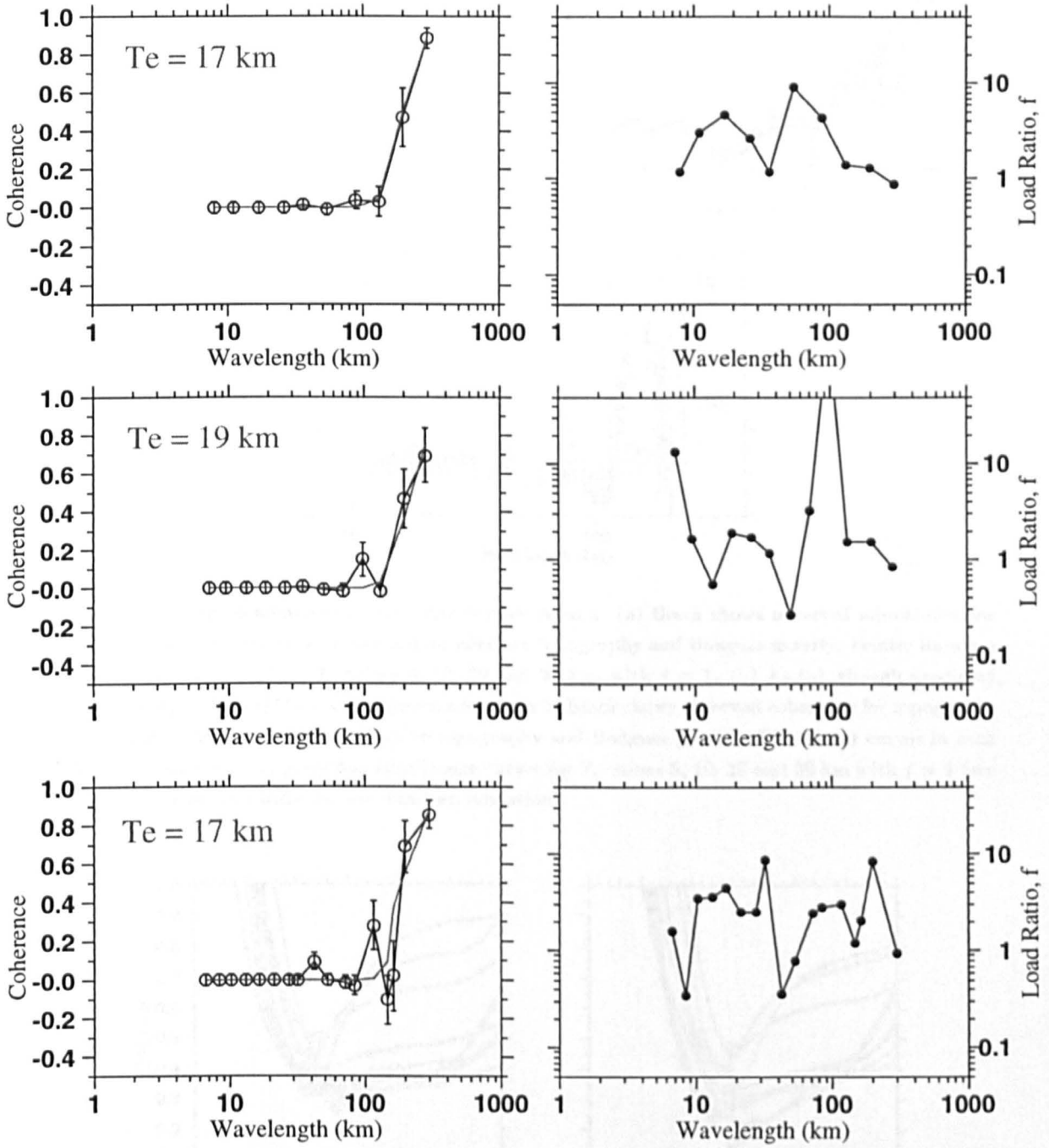

Figure 6.17: Best-fit predicted coherence curves for Area 1, for three realisations of the spectral averaging of effective topography and Bouguer gravity. Black circles represent the observed coherence, and the best fit predicted coherence is shown in red. The corresponding T_e value is printed, and the corresponding $f(\bar{k})$ is plotted to the right. Error bars indicate one standard deviation.

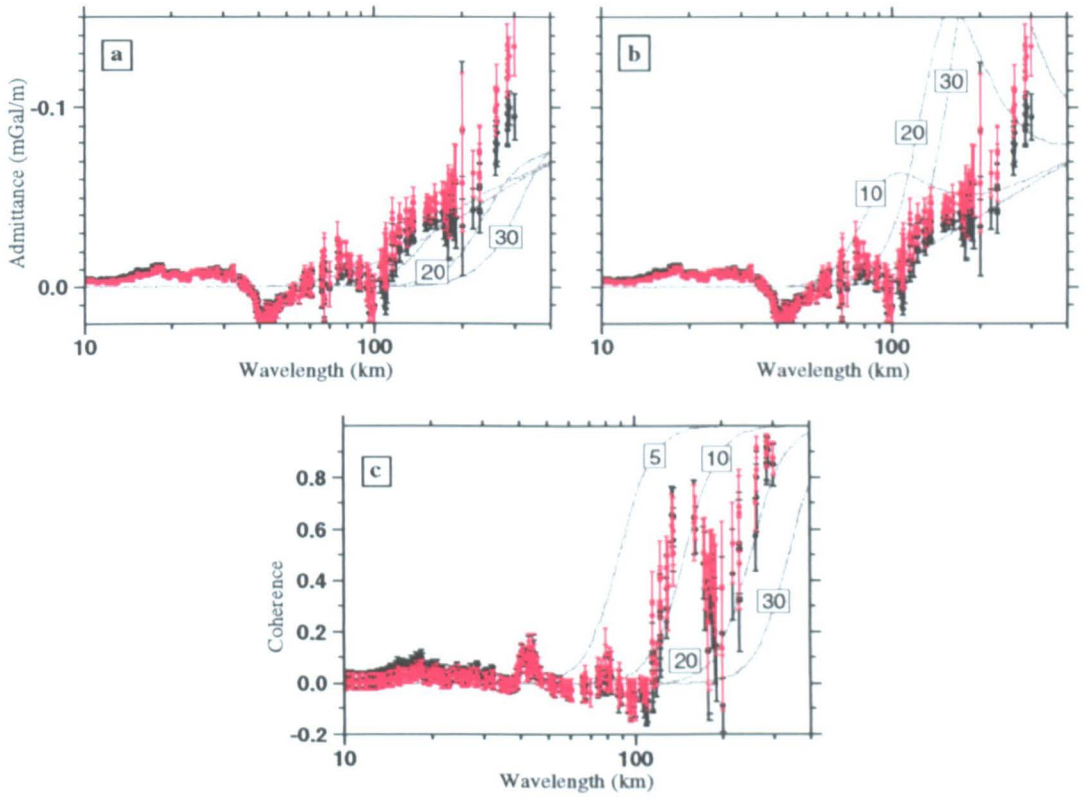

Figure 6.18: Observed admittance and coherence for Area 2. (a) Black shows observed admittance for topography and Bouguer gravity, and red for effective topography and Bouguer gravity. Feinter lines are the admittance predicted for T_e values 0, 10, 20 and 30 km, with $f = 1$. (b) As (a), though predicted curves are for $f = 10$. (c) Observed coherence for Area 2. Black shows observed coherence for topography and Bouguer gravity, and red for effective topography and Bouguer gravity. The feinter curves in each of the plots correspond to predicted admittance curves for T_e values 5, 10, 20 and 30 km with $f = 1$ (see Figure 6.3). Error bars indicate one standard deviation.

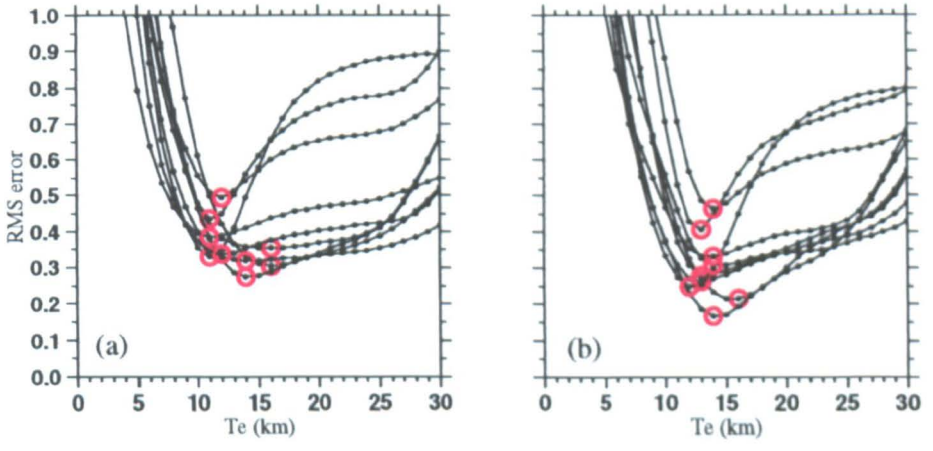

Figure 6.19: The RMS error in the fit between observed and predicted coherence for Area 2, as a function of assumed T_e. The best estimates for T_e minimises this error and are circled in each case. (a) Topography-bathymetry and Bouguer gravity. (b) Effective topography and Bouguer gravity, resulting in a sharper minimum.

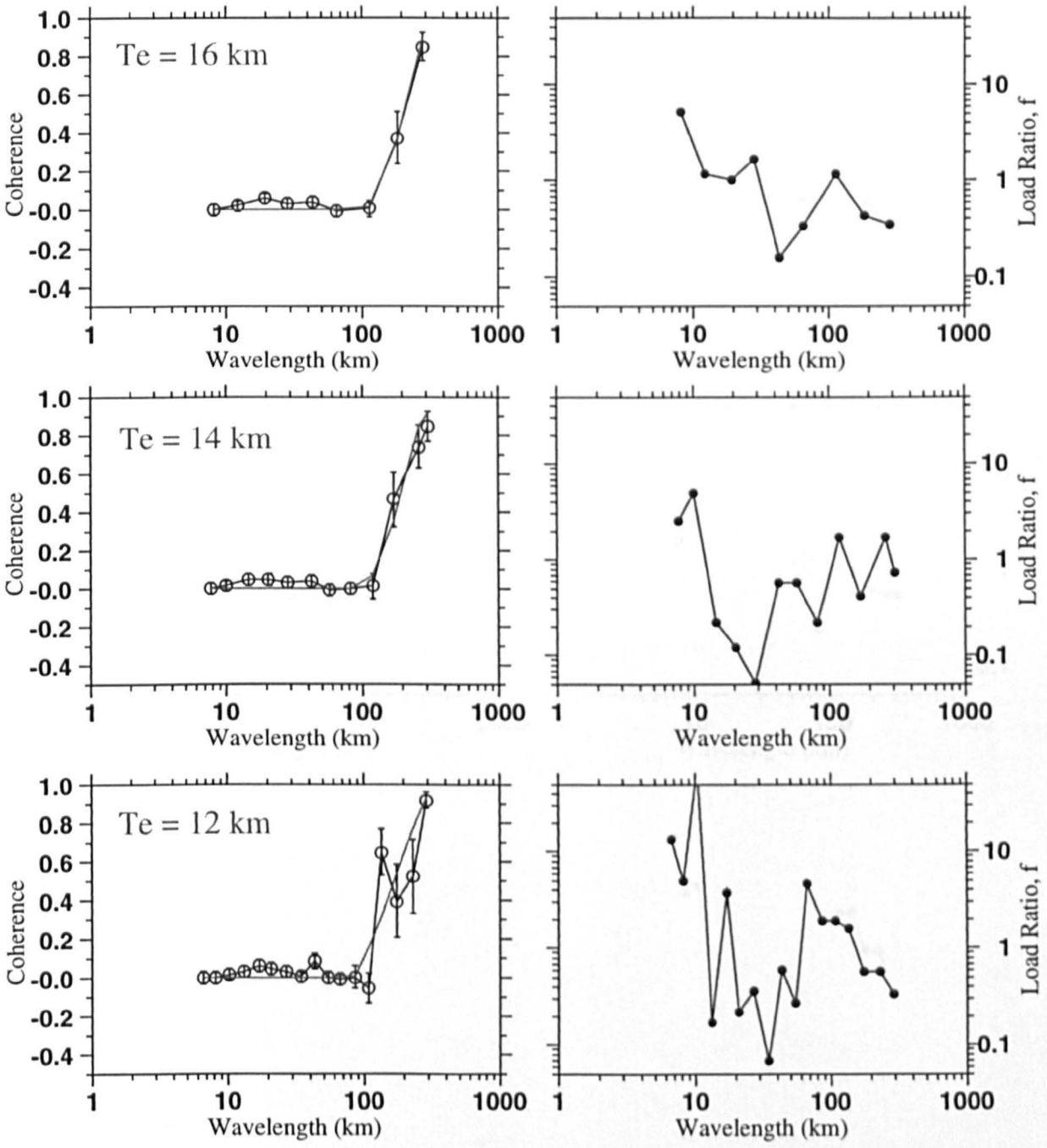

Figure 6.20: Best-fit predicted coherence curves for the Area 2 for three realisations of the spectral averaging of topography and Bouguer gravity. Black circles represent the observed coherence, and the best fit predicted coherence is shown in red. The corresponding T_e value is printed, and the corresponding $f(\bar{k})$ is plotted to the right. Error bars indicate one standard deviation.

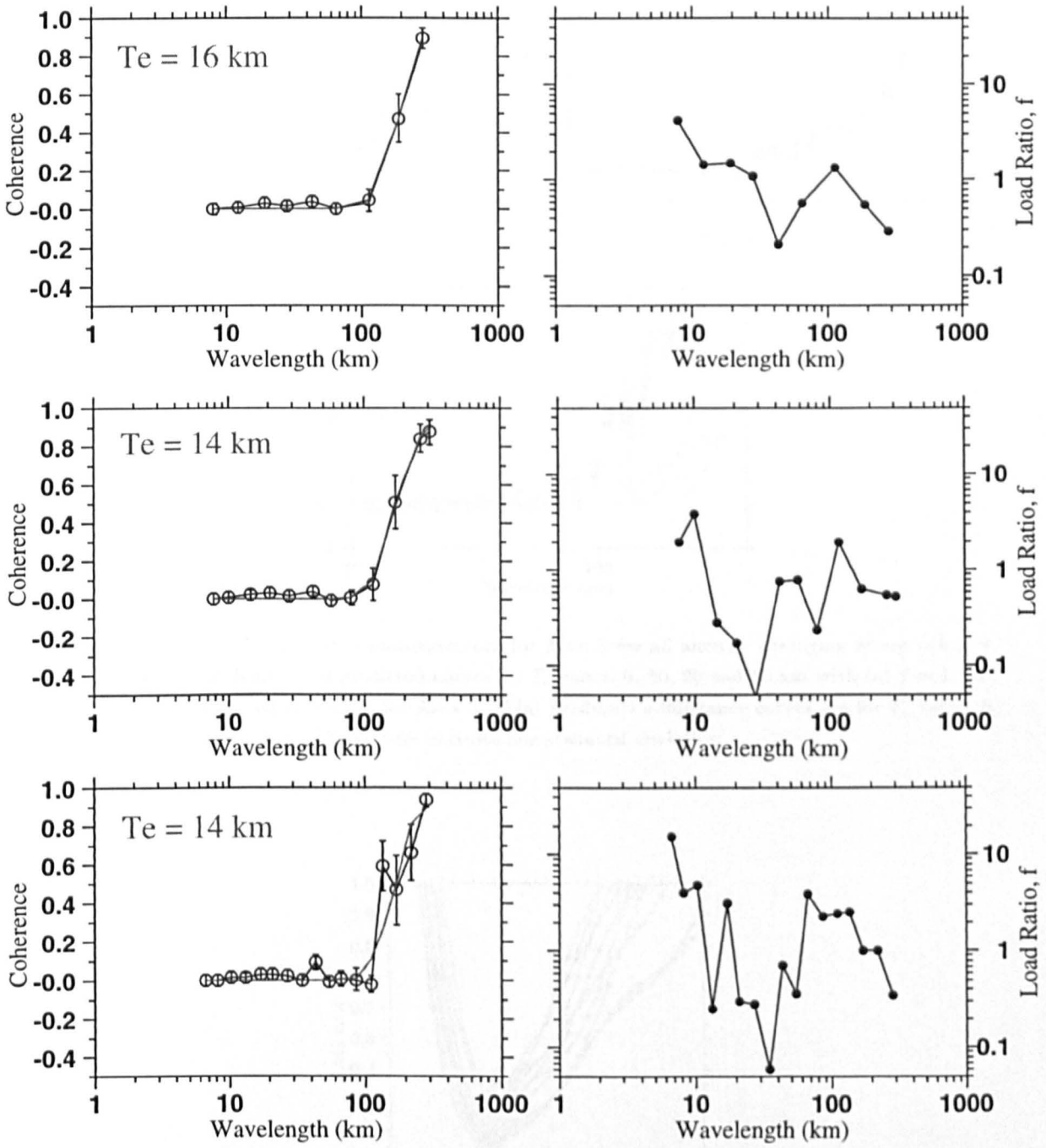

Figure 6.21: Best-fit predicted coherence curves for the Area 2, for three realisations of the spectral averaging of effective topography and Bouguer gravity. Black circles represent the observed coherence, and the best fit predicted coherence is shown in red. The corresponding T_e value is printed, and the corresponding $f(\bar{k})$ is plotted to the right. Error bars indicate one standard deviation.

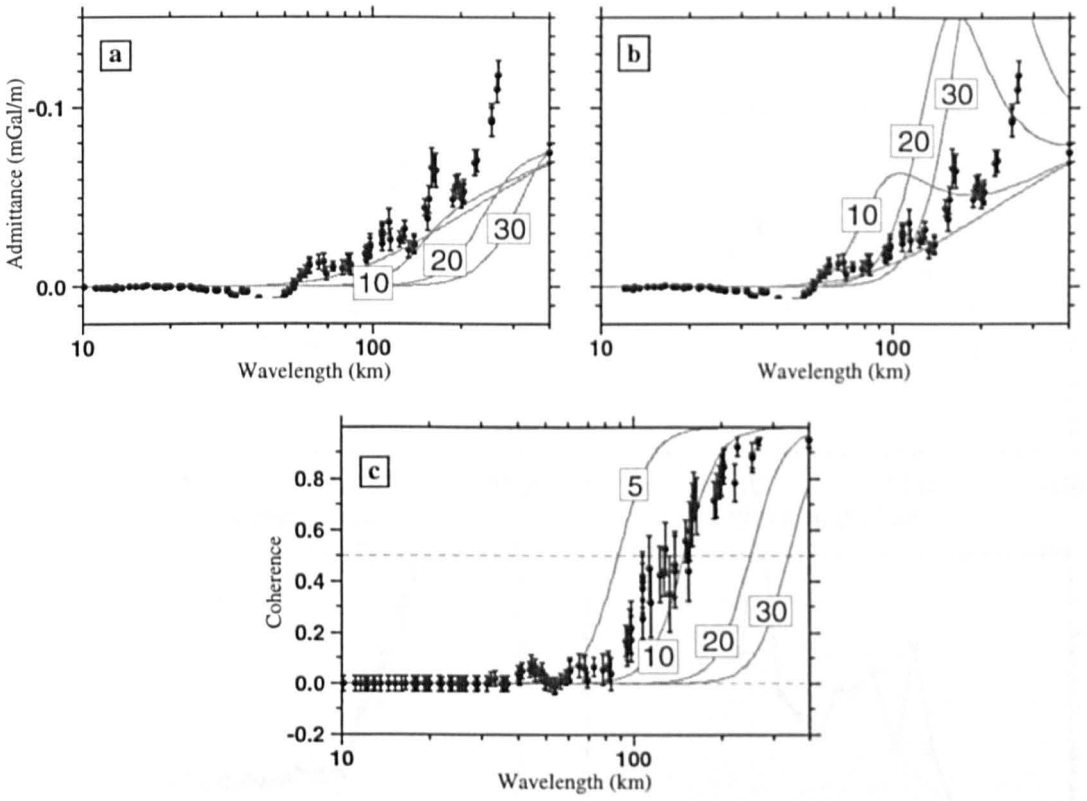

Figure 6.22: Observed admittance and coherence for Area 3 for all annular averaging where $n(\bar{k} \geq 4$. For (a) and (b), the feint set of predicted curves for T_e values 0, 10, 20 and 30 km with (a) $f = 1$, and (b) $f = 10$. (c) Observed coherence for Area 3. Feint predicted admittance curves are for T_e values 5, 10, 20 and 30 km with $f = 1$. Error bars indicate one standard deviation.

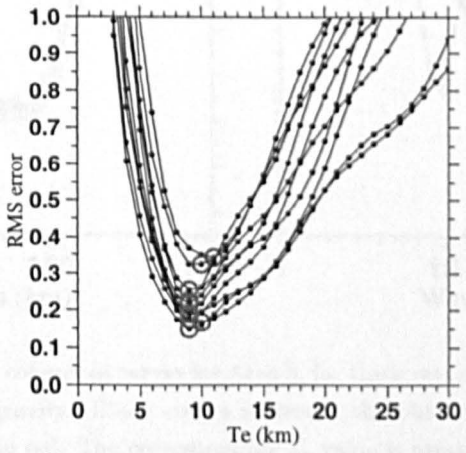

Figure 6.23: The RMS error in the fit between observed and predicted coherence for Area 3, as a function of assumed T_e. The best estimate T_e minimises this error, and are circled in each case 70% of the ten estimates give Te as 9 km.

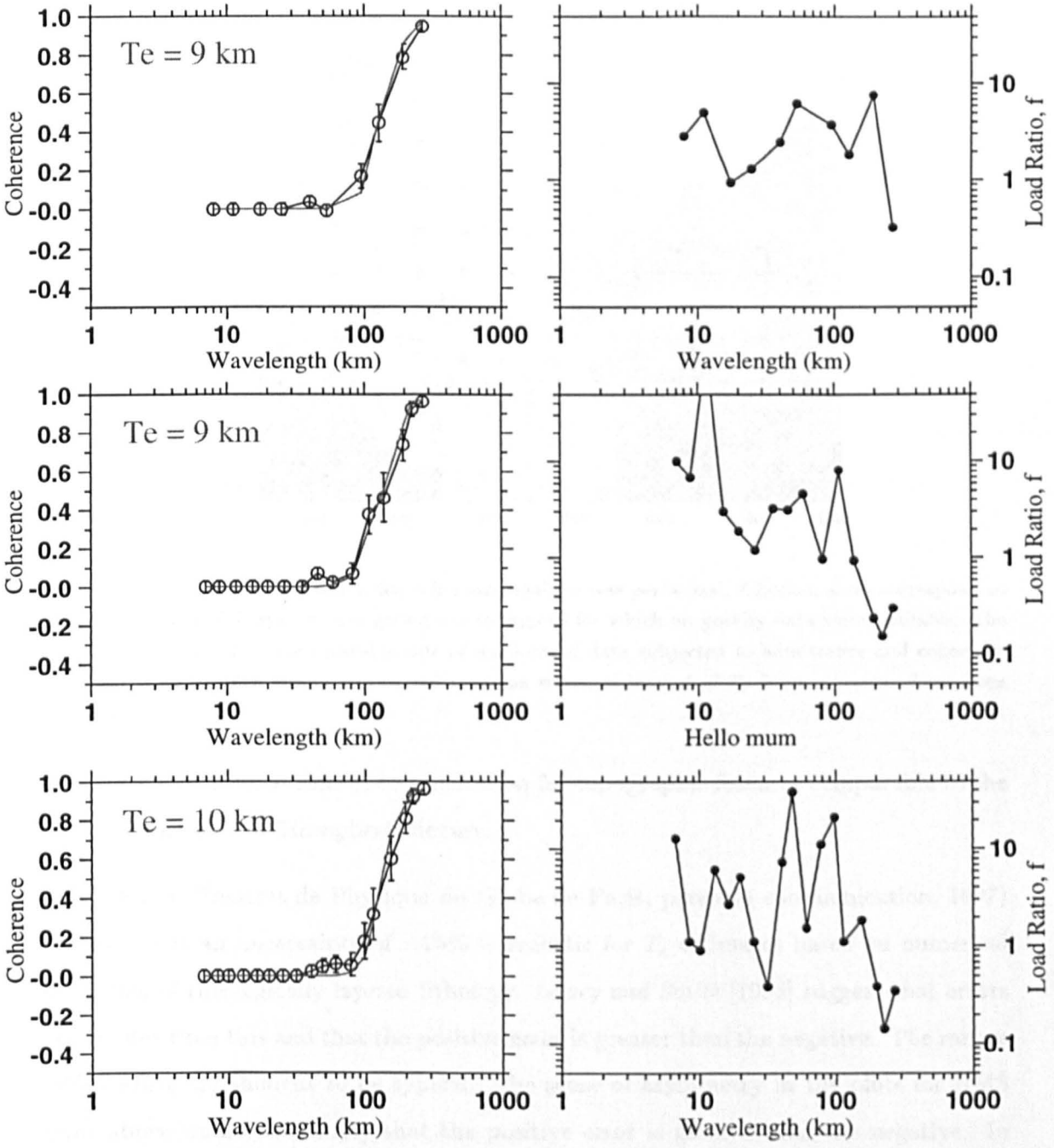

Figure 6.24: Best-fit predicted coherence curves for Area 3, for three realisations of the spectral averaging of topography and Bouguer gravity. Black circles represent the observed coherence, and the best fit predicted coherence is shown in red. The corresponding T_e value is printed, and the corresponding $f(\bar{k})$ is plotted to the right. Error bars indicate one standard deviation.

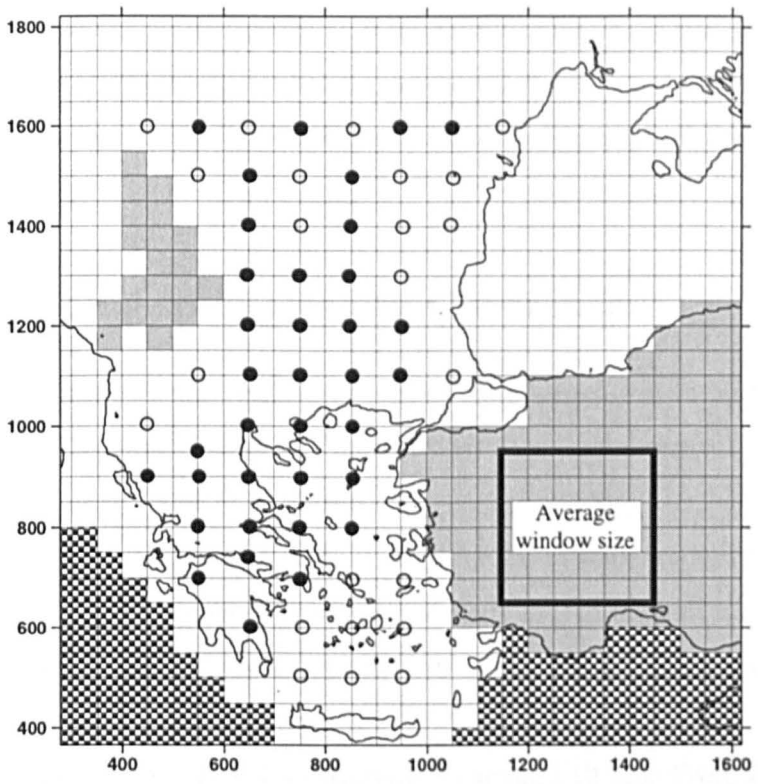

Figure 6.25: The area across which the coherence analysis was performed. Checked areas correspond to regions of oceanic lithosphere, and grey areas to regions for which no gravity data were available. The 59 circles correspond to the central points of windows of data subjected to admittance and coherence analyses. The 36 filled circles correspond to areas where estimated of T_e from coherence have been obtained.

- Dynamic mechanisms of compensation for topographic features comparable to the wavelengths of lithospheric flexure.

E. Burov (Institut de Physique du Globe de Paris, personal communication, 1997) suggests that an uncertainty of ±25% is realistic for T_e estimates based on numerical modelling of rheologically layered lithology. *Lowry and Smith* [1995] suggest that errors are greater than this and that the positive error is greater than the negative. The ranges -40%/+70% are thought to be typical. The sense of asymmetry in the plots for RMS error above would also imply that the positive error is greater than the negative. In addition, the error resulting from an assumed constant f compared to $f = 1$ (Figure 6.5) shows the same sense.

Previous methods have estimated the analytical errors by varying T_e away from the best-fit value, and defining the range such that the number of error bars within the transitional waveband cut by the corresponding predicted curve is the same as for the best-fit curve (e.g., *Bechtel, Forsyth and Swain* [1987]). In this thesis, the best T_e

estimate is assigned as the mode (i.e., most frequently occurring) of the estimated values from minimising the RMS errors, and the extreme values define the range. The range -15%/+30% is representative of the observed scatter, so individual estimates are not cited.

6.11 T_e Mapping from Gravity Coherence

A total of 60 data windows were examined across the dataset whose central points are regularly spaced at 100 km intervals (Figure 6.25). This arrangement was chosen to avoid biasing in the analysis of T_e variability.

A T_e value was not assigned to a node if only one point appeared within the transitional waveband, nor if the observed coherence did not exceed 0.75. If no suitable curve was obtained, either the window was expanded or the location of the node was shifted by up 50 km.

Initial results showed that T_e values decrease to around 10 km. From Figure 6.4, the characteristic wavelength for this is ~150 km. The initial box size used for each node was therefore 250 km, and the final box size scaled with T_e such that the transition from low to high coherence was accurately defined. Thus, there is a fundamental correlation between T_e values and window size (i.e., spatial resolution). Minimising this problem is the motivation behind applying the wavelet transform (see below).

6.12 Fourier Coherence Results

• Figure 6.25 shows that in 39% of cases, the observed coherence is poor and a T_e estimate cannot be made. Many of these windows lie in the central and southern Aegean Sea. A possible explanation for this is that the isostatic model assumed for the coherence analyses does not apply. This is supported by the conclusions of Chapter 4 (Section 4.13).

•There is little difference in the T_e resulting from topography-bathymetry and effective topography.

• The strongest lithosphere in the area analysed is seen to exist across the southern Carpathians Chain, with T_e values of ~25 to 30 km. This is consistent with the modelling results of *Stewart and Watts* [1997].

• Across the Aegean province, T_e is observed to vary between 10 and 20 km. In mainland

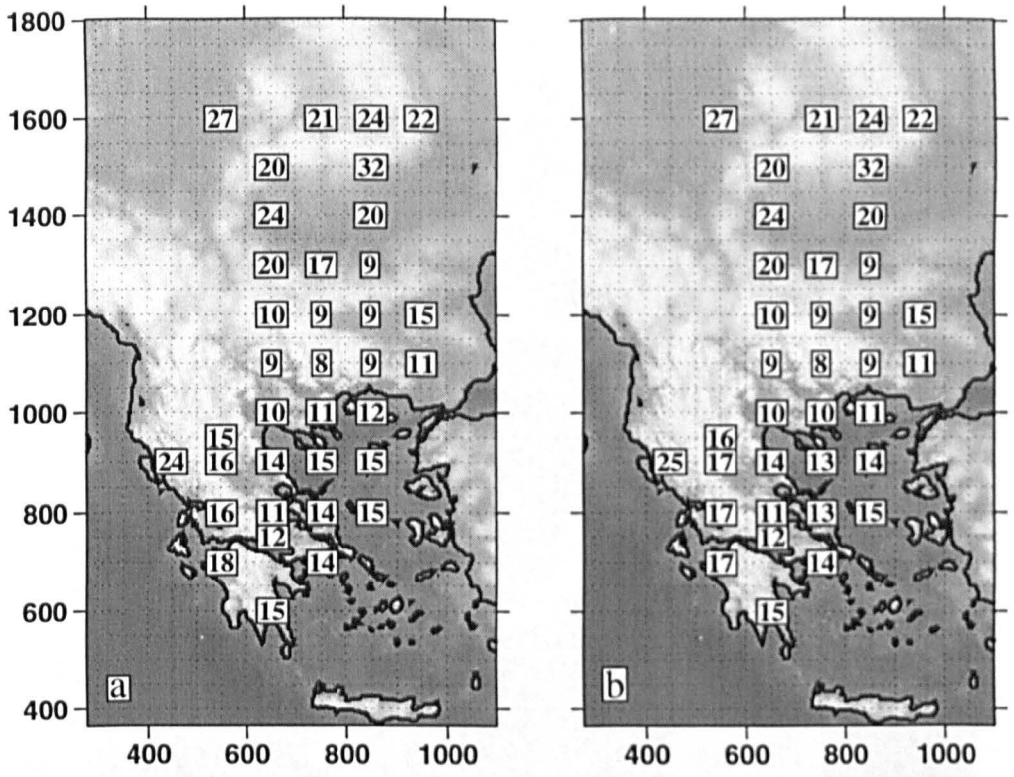

Figure 6.26: Posted values of best fit T_e. (a) Coherence with topography. (b) Coherence with effective topography.

Greece, the trend of the contours in T_e are roughly parallel to the Hellenide Chain, across which T_e exceeds 20 km.

• The weakest lithosphere is observed to exist across the Rhodope complex and the Balkan Mountains, where T_e is ~8 to 12 km. This is consistent from the observation in Chapter 4 (Section 4.12) that the Rhodope Mountains are coincident with a Bouguer gravity low. *Roy et al.* [1996] constrained T_e to fall to ~3km across the narrow peak of the Balkan chain. To resolve a T_e of 10 km, the window function for the Fourier transform is ~200 km square. We do not expect short wavelength variations in T_e such as those observed by *Roy et al.* [1996] to be resolved in the Fourier coherence results.

• The problem resulting from the limited spatial resolution of the windowed Fourier transform is also demonstrated by Figure 6.18c. T_e across the northern Aegean Sea is ~15 km (i.e., $\lambda_c \approx 200$ km). However, the northern part of the Area 2 window (see Figure 6.12) lies within a zone where T_e falls to less than 10 km. This results in high coherence at wavelengths of between 100 and 150 km. The wavelet method is applied to improve the spatial resolution in observed coherence.

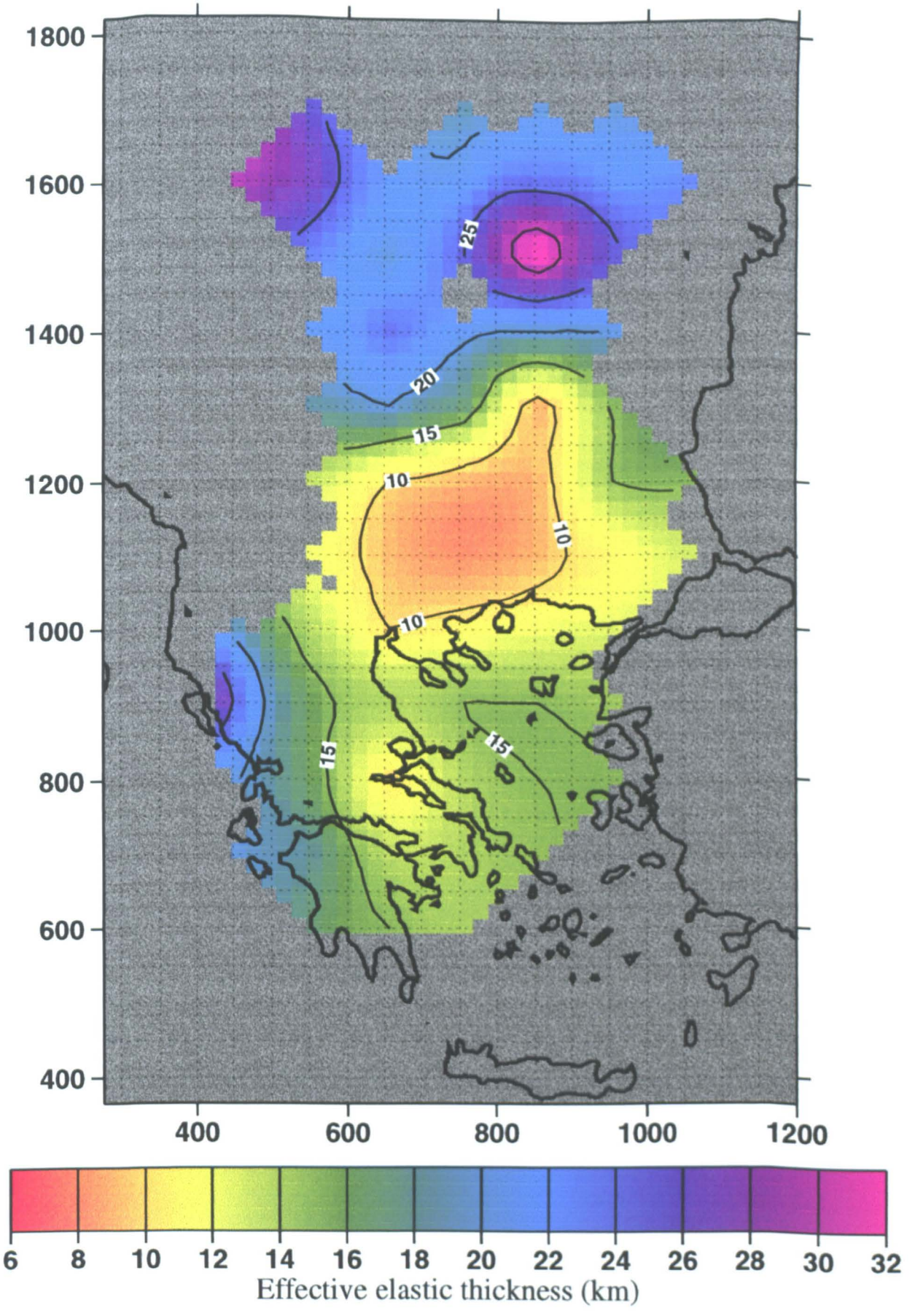

Figure 6.27: Gridded effective elastic thickness values. Observed coherence was estimated using topography and Bouguer gravity. Contour interval = 5 km.

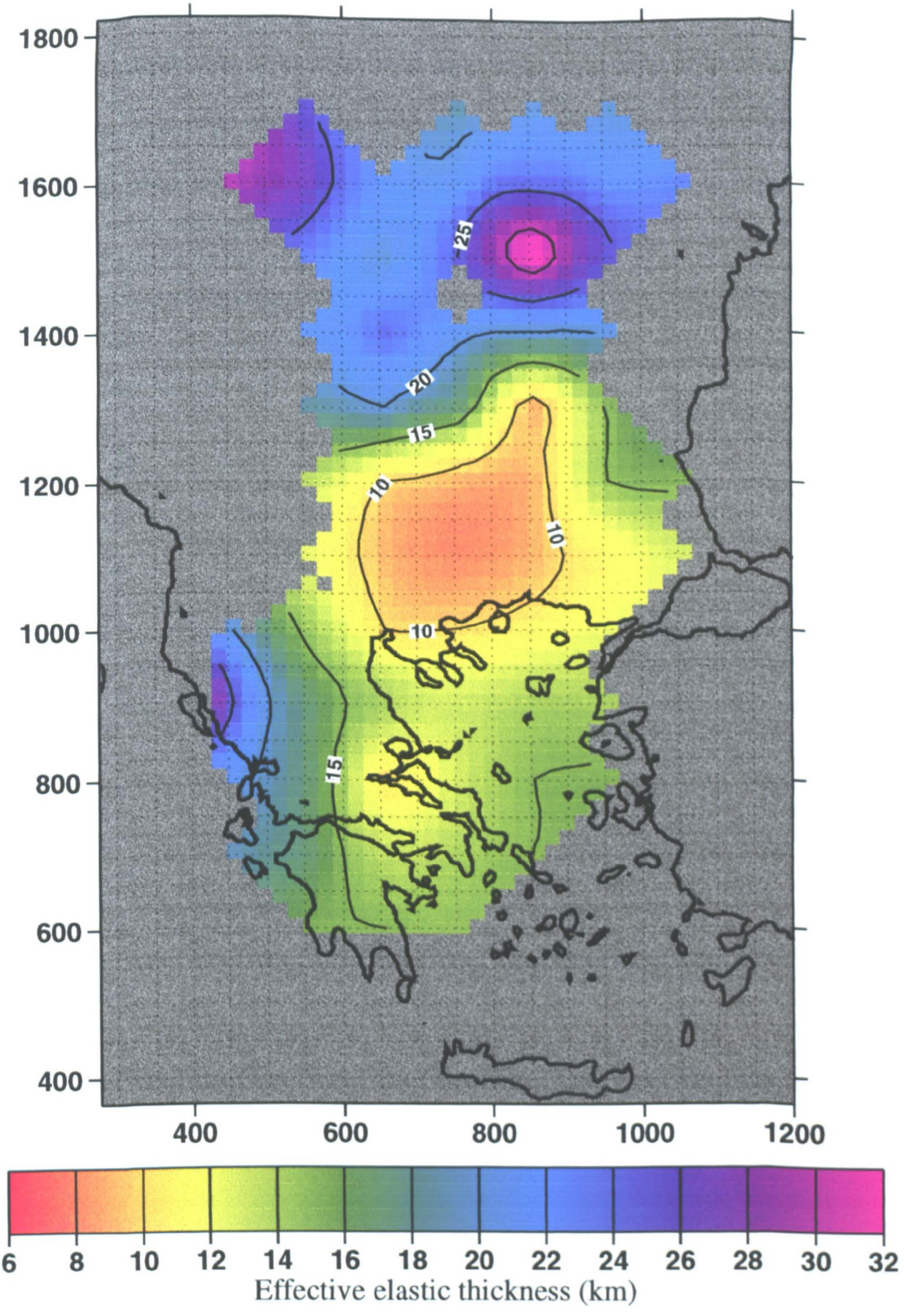

Figure 6.28: Gridded effective elastic thickness values. Observed coherence was estimated using effective topography and Bouguer gravity. Contour interval = 5 km.

6.13 The Continuous Wavelet Transform in One Dimension

6.13.1 From Fourier to Wavelets

Wavelet analysis is a relatively new branch of mathematics, so a short introduction to the theory precedes their application to coherence across the Aegean. The discussion of spectral methods has so far been limited to the Fourier transform. There are limitations with the Fourier method that have implications for the resolution of the spatial variability in T_e. These are easily seen from the expression of the Fourier transform. For a one dimensional function $f(x)$, the Fourier transform is given by

$$\begin{aligned}\mathcal{F}(f) = F(k) &= \int_{-\infty}^{\infty} f(x) e^{-ikx}\, dx \\ &= \int_{-\infty}^{\infty} f(x)\left(\cos(ikx) + i\sin(ikx)\right)\, dx \end{aligned} \tag{6.22}$$

where e^{-ikx} corresponds to a family of real and imaginary sinusoids. Integration is performed through all space, and so gives no information regarding *where* in space a spectral component of wavenumber k occurs. Consequently, the Fourier transform of signals (a) and (b) in Figure 6.31 would give equivalent results. There is therefore zero spatial resolution with the Fourier transform, making it unsuitable for analyses of non-stationary signals.

A modification is provided by the windowed Fourier transform (or the short-time Fourier transform) to simultaneously give information about a signal in both the space domain and the wavenumber domain, which has been used to map spatial variability in T_e (Figures 6.27 and 6.28). Equation 6.22 is modified to

$$F(k, x') = \int_{-\infty}^{\infty} f(x) w(x - x') e^{-ikx}\, dx \tag{6.23}$$

where x' is the position of the centre of a box-car window function, w. The width in space (or support) of this window controls the resolution of the Fourier transform in both the space and wavenumber domains. The narrower the window, the better the resolution in space and the poorer the resolution in the wavenumber domain. This is a consequence of the Uncertainty Principle which states that the simultaneous resolution

of both wavenumber and space cannot be exact (e.g., *Meyer* [1992]).

Narrow windows are required in order to obtain good spatial localisation (i.e., to resolve spatial variability), and wide windows are required in order to obtain good wavenumber localisation. The aim of *multiresolution analyses* (MRAs) is to achieve both these so that high wavenumbers are analysed across a short lengthscale, and low wavenumbers across a large lengthscale.

Scaling wavelets provide ideal functions for this, and allow high-wavenumber variations to be resolved well in space - though poorly in wavenumber - and low wavenumber variations to be resolved well in wavenumber - though poorly in space.[2] This simultaneous localisation in both domains allows for the description of spectral behaviour around a *single point* of interest, and is illustrated in Figure 6.29(b).

The 1D continuous wavelet transform (CWT) is given by

$$\mathcal{W}(f) = \mathcal{W}(f;a,b) = |a|^{-N/2} \int_{-\infty}^{\infty} f(x)\Psi^* \left(\frac{x-b}{a}\right) dx \tag{6.24}$$

where the asterisk denotes the complex conjugate and N are the number of dimensions. The function $\Psi(x,a,b)$ denotes a *family* of wavelets, which may be either real or complex. We restrict ourselves in this thesis to wavelets that are real in space (although wavelets with odd order are imaginary in wavenumber - see Equation 6.36), so the complex conjugate in Equation 6.24 may be omitted. The wavelets are formed by stretching (or dilating) and translating the *mother* (or basic) wavelet, $\Psi(x,1,0)$, subject to a normalising factor that depends on the dilation a. Wavelet dilation is given by a, and b relates to the position of the analysing wavelet in space. Thus the function $f(x)$ is transformed into a function of two variables, a and b.

It is important to note here that because the lithosphere acts as a low-pass filter, there is an upper limit to the spatial resolution of T_e regardless of the spectral method used. For example, for a T_e of 10 km, the characteristic wavelength is ~150 km (Figure 6.5). However, the advantage of using the CWT is that short wavelength information is only analysed local to b (Figure 6.29).

[2] This is ideal where signals have high wavenumber components for short distances, and low wavenumber components for long distances.

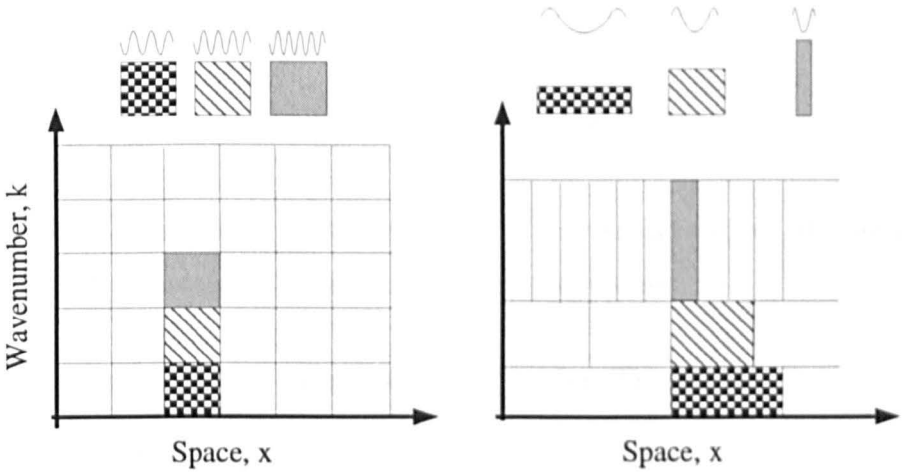

Figure 6.29: Heisenberg diagrams showing the space-wavenumber resolution of (a) the windowed Fourier and (b) the continuous wavelet transforms.

6.13.2 Gaussian Derivative Wavelets

Not all oscillating functions of compact support qualify as wavelets. There is an admissibility condition on $\Psi(x)$ which states that its mean (zeroth-order moment, or dc value) must be zero. In general, the derivative of any smoothing function is a wavelet. Differentials of Gaussian smoothing functions provide excellent simultaneous localisation in both space and wavenumber, and may be expressed analytically in both domains. For a standard deviation (or width) a, the Gaussian is given by

$$\Phi_a(x) = \frac{1}{a\sqrt{2\pi}} \exp\left(-\frac{x^2}{2a^2}\right) \tag{6.25}$$

and is shown in Figure 6.30. A wavelet of order n is then found by differentiating $\Phi_a(x)$ n times. Thus,

$$\Psi_a^{(n)} = a^n \frac{d^n}{dx^n} [\Phi_a(x)] \tag{6.26}$$

where the normalising factor a^n ensures that the wavelets are "mass"-preserving (i.e., L1 norm). The second order and the fourth order wavelets are used in this study. These are given by

$$\Psi_a^{(2)} = a^2 \frac{d^2}{dx^2} [\Phi_a(x)] = -\left(1 - \frac{x^2}{a^2}\right) \Phi_a(x) \tag{6.27}$$

and

$$\Psi_a^{(4)} = a^4 \frac{d^4}{dx^4} \left[\Phi_a(x)\right] = -\left(\frac{3a^2 - 6a^2x^2 + x^4}{a^5}\right) \Phi_a(x) \ . \tag{6.28}$$

and are shown in Figure 6.30. The second order Gaussian-derivative ("d2gauss") wavelet is commonly used, and is known as the Mexican-hat wavelet.

6.13.3 Visualising the Continuous Wavelet Transform

6.13.3.1 The Space Domain

For the n^{th}-order wavelet $\Psi^{(n)}$ of some fixed dilation a, the CWT of a function $f(x)$ is found as

$$\begin{aligned} \mathcal{W}(f;b) &= |a|^{-N/2} \int_{-\infty}^{\infty} f(x) a^n \frac{d^n}{dx^n} \left[\Phi_a(x-b)\right] \, dx \\ &= \frac{a^n}{|a|^{N/2}} \frac{d^n}{dx^n} \int_{-\infty}^{\infty} \left[f(x) \Phi_a(x-b)\right] \, dx \end{aligned} \tag{6.29}$$

Convolution between two real signals $f(x)$ and $g(x)$ is defined by the integral

$$c(b) = \int_{-\infty}^{\infty} f(x) g(b-x) \, dx \ . \tag{6.30}$$

Replacing g with Φ_a, this may be expressed as

$$c(b) = -\int_{-\infty}^{\infty} f(x) \Phi_a(x-b) \, dx \ . \tag{6.31}$$

which is directly proportional to the negative of the CWT. Thus,

$$\mathcal{W}(f;b) \propto \frac{d^n}{dx^n} \left[f(x) \otimes \Phi_a(x)\right] \tag{6.32}$$

where $\otimes$ denotes the convolution in the space domain. Three examples of CWTs are shown for simple signals in Figure 6.31. The alternating positive and negative peaks with b may now be understood.

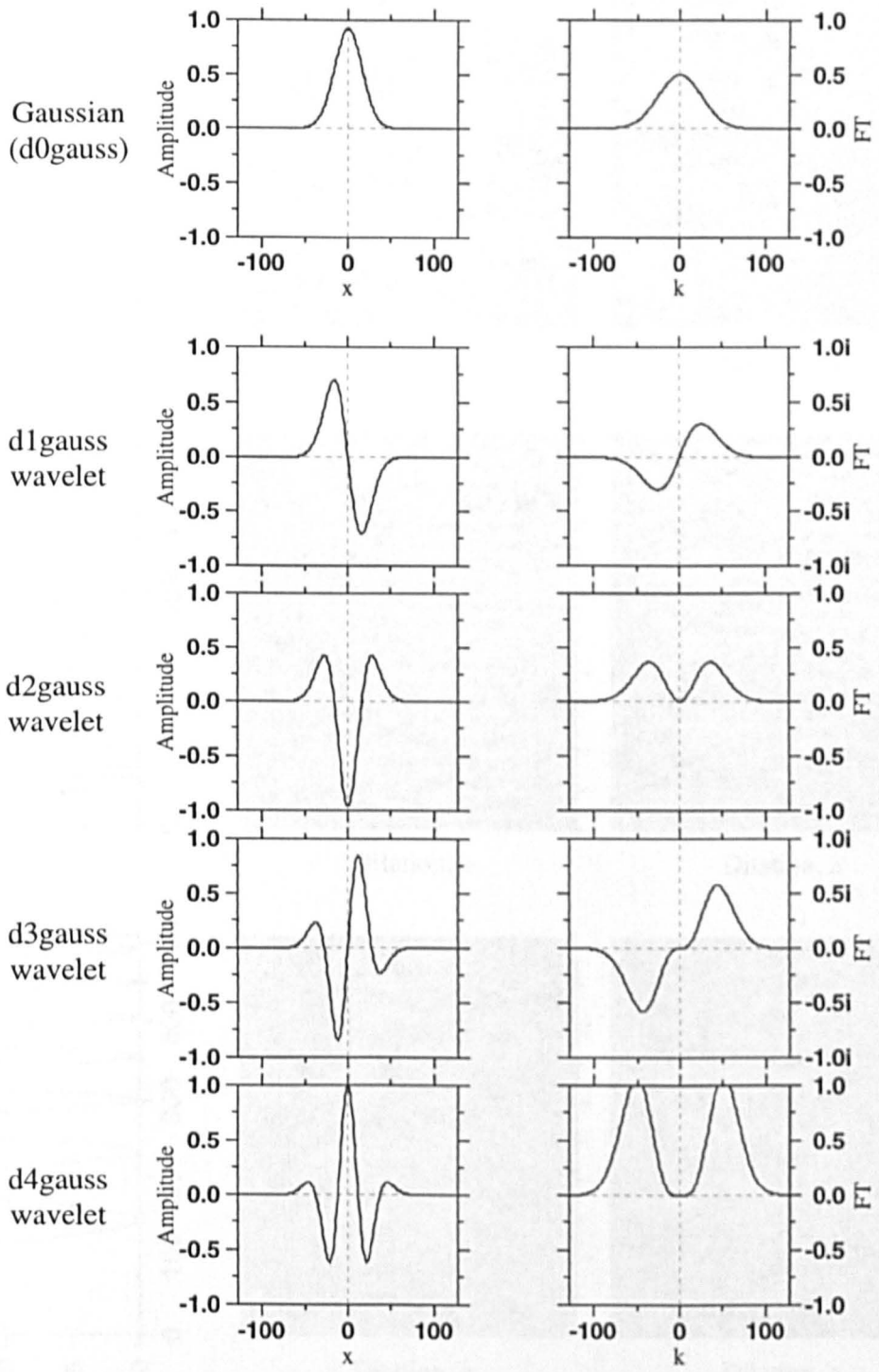

Figure 6.30: One dimensional space and wavenumber domain representations of the Gaussian smoothing function and its derivatives. Note the unimodal, band-pass nature of wavelets in the wavenumber domain.

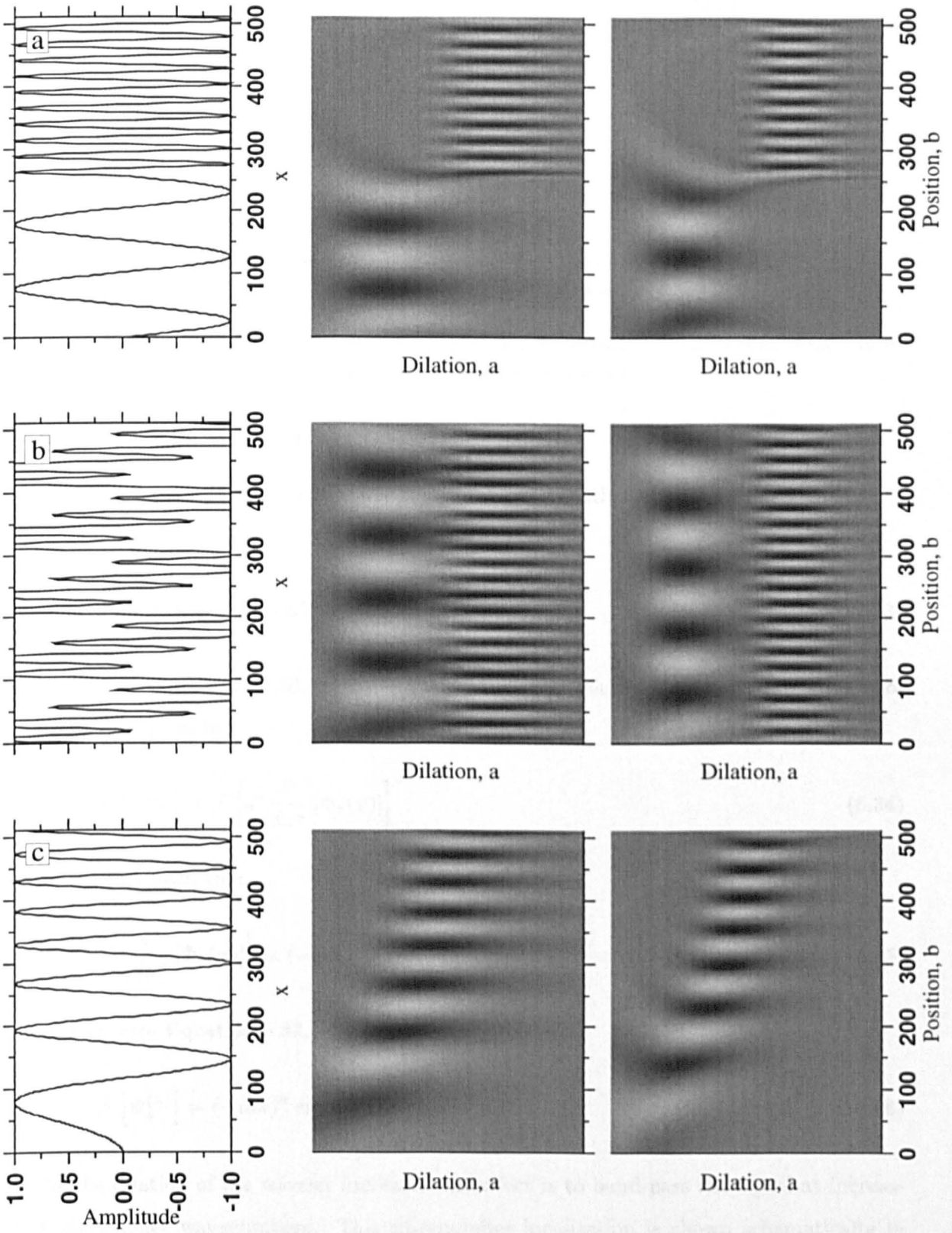

Figure 6.31: The one dimensional CWT for simple signals. (a) The addition of two sinusoids. (b) Two adjacent sinusoids. (c) A chirp. The second row of plots shows the results for a second order wavelet, and the bottom row is for a fourth order wavelet, demonstrating the improved wavenumber localisation.

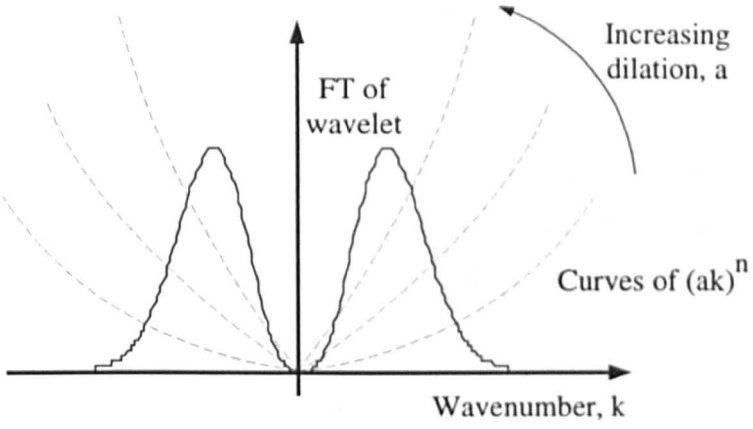

Figure 6.32: The effect of wavelet dilation in the wavenumber-domain. As the dilation of the wavelet increases, the effect is to band-pass the signal at increasingly smaller k.

6.13.3.2 The Wavenumber Domain

The Fourier transform of the Gaussian smoothing function of Equation 6.25 is itself a Gaussian in k:

$$\mathcal{F}\left[\Phi_a(x)\right] = \exp\left(-a^2k^2/2\right) \tag{6.33}$$

as is shown in Figure 6.30. From Equation 6.26, the Fourier transform of a wavelet of order n is given by

$$\mathcal{F}\left[\Psi_a^{(n)}\right] = \mathcal{F}\left[a^n \frac{d^n}{dx^n}\left[\Phi_a(x)\right]\right] \ . \tag{6.34}$$

It can be shown that

$$\mathcal{F}\left[\frac{d^n}{dx^n}\left[\Phi_a(x)\right]\right] \equiv (-iak)^n \, \mathcal{F}\left[\Phi_a(x)\right] \tag{6.35}$$

and so from Equation 6.33,

$$\mathcal{F}\left[\Psi_a^{(n)}\right] = (-iak)^n \exp\left(-a^2k^2/2\right) \ . \tag{6.36}$$

As the dilation of the wavelet increases, the effect is to band-pass the signal at increasingly smaller wavenumbers. This wavenumber localisation is shown schematically in Figure 6.32. It is also seen that wavelets with odd n are imaginary in wavenumber.

6.14 The CWT in Two Dimensions

6.14.1 Radial Wavelets

Radial wavelets are the most commonly used wavelets in 2D. As their name suggests, they are radially symmetric in both space and wavenumber. They are formed by differentiating the radial Gaussian smoothing function, $\Phi_a(x,y)$, where

$$\Phi_a(x,y) = \frac{1}{a\sqrt{2\pi}} \exp\left(-\frac{\sqrt{x^2+y^2}}{2a^2}\right) . \tag{6.37}$$

Thus, a radial wavelet of dilation a and order n is found as

$$\Psi_a^{(n)} = a^n \nabla^n \left[\Phi_a(x,y)\right] \tag{6.38}$$

where ∇^n denotes $\frac{\partial^n}{\partial x^n} + \frac{\partial^n}{\partial y^n}$. Second and fourth order radial wavelets are shown in Figure 6.33.

The wavenumber domain representation is found as

$$\begin{aligned} \mathcal{F}\left[\Psi_a^{(n)}\right] &= \mathcal{F}\left[a^n \nabla^n \left[\Phi_a(x)\right]\right] \\ &= (-iak)^n \mathcal{F}\left[\Phi_a(x)\right] \end{aligned} \tag{6.39}$$

where k is the modulus of two dimensional wavenumber. They therefore act as radially symmetric band-pass filters (Figure 6.34).

6.14.2 Tensor Wavelets

The second order tensor wavelet is derived here and the extension to higher orders is trivial. The radially symmetric Gaussian of dilation a is differentiated in tensors

$$\Psi_a^{(2)} = \begin{pmatrix} \frac{\partial^2}{\partial x^2} & \frac{\partial^2}{\partial x \partial y} \\ \frac{\partial^2}{\partial y^2 x^2} & \frac{\partial^2}{\partial y^2} \end{pmatrix} \left[\Phi_a(x,y)\right] \tag{6.40}$$

to produce the space-domain patchwork effect shown in Figure 6.33. It is clear that the number of tensor wavelets is equal to $(n+1)$. In the wavenumber domain , the three

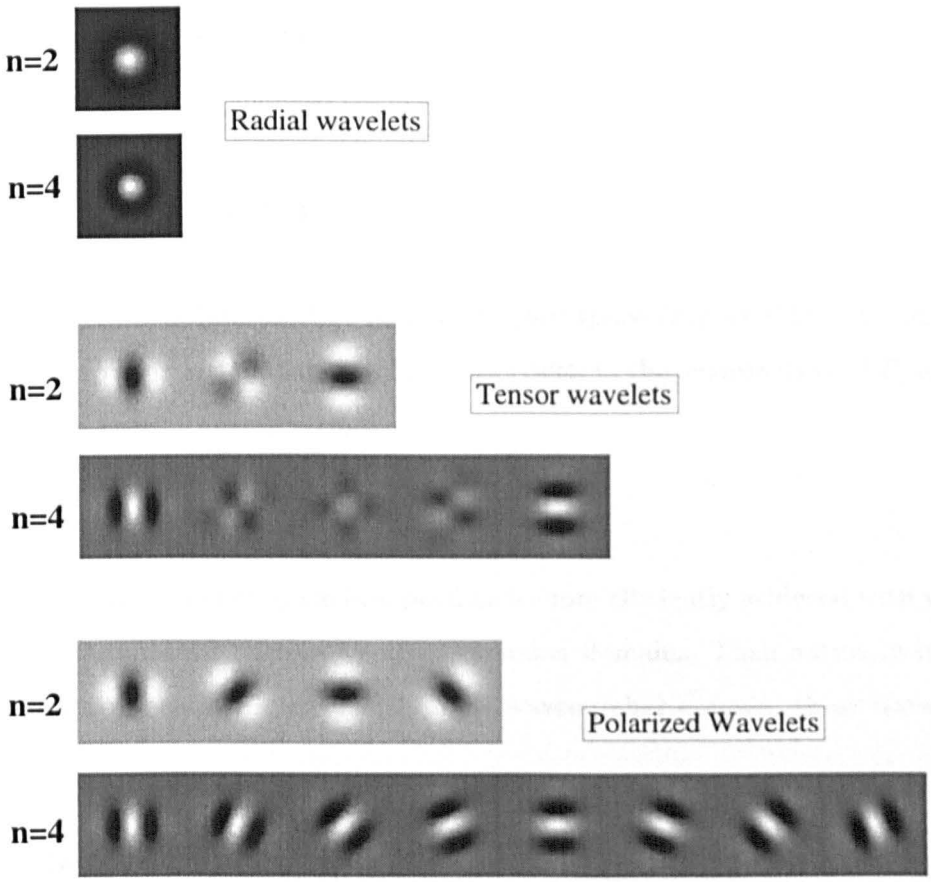

Figure 6.33: Space domain appearance of second and fourth order two dimensional wavelets.

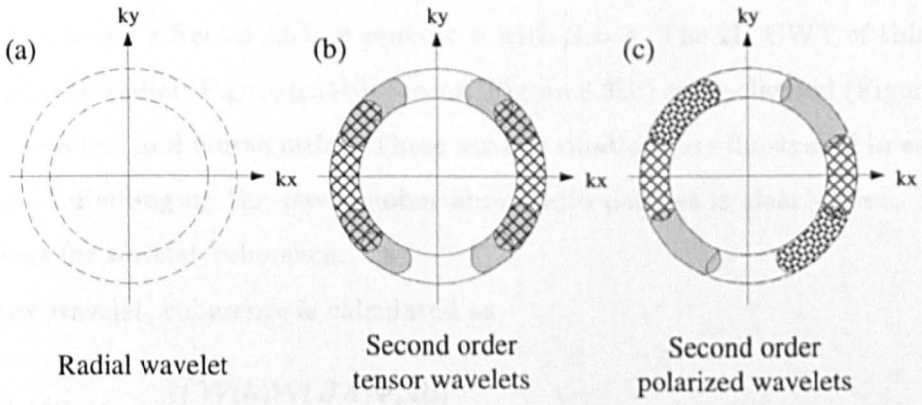

Figure 6.34: Schematic representation of the nature of second and fourth order two dimensional wavelets in the wavenumber domain.

second order wavelets are given by

$$\mathcal{F}\left[a^2\frac{\partial^2\Phi_a}{\partial x^2}\right] = -a^2k_x^2\mathcal{F}\left[\Phi_a\right]$$
$$\mathcal{F}\left[a^2\frac{\partial^2\Phi_a}{\partial x\partial y}\right] = -a^2k_xk_y\mathcal{F}\left[\Phi_a\right]$$
$$\mathcal{F}\left[a^2\frac{\partial^2\Phi_a}{\partial y^2}\right] = -a^2k_y^2\mathcal{F}\left[\Phi_a\right] \ . \tag{6.41}$$

and the effect is to isolate patches in wavenumber space (Figure 6.34). Second order tensor wavelets were used by *Stark and Hartley* [1994] in the examination of T_e variation across the Basin and Range Province.

6.14.3 Polarized Wavelets

The division of wavenumber space into patches is more efficiently achieved with wavelets that are polarized in both the space and wavenumber domains. Their nature in the space domain is clearly seen in Figure 6.33. In the wavenumber domain, these wavelets are found as

$$\mathcal{F}\left[\Psi_a(x,y)\right] = (-iak')^n exp\left(-a^2k^2/2\right) \tag{6.42}$$

where k' is rotated to the chosen polarization direction (Figure 6.34). The number of polarization directions is set here to $2n$.

6.14.4 Wavelet Types and Wavelet Coherence

Figure 6.35a shows a fractal surface generated with $\beta = 3$. The 2D CWT of this surface is obtained with radial (Figure 6.35b), tensor (Figure 6.35c) and polarized (Figure 6.35d) wavelets of second and fourth order. Three wavelet dilations are illustrated in each case. The effect of dividing up the wavenumber annuli into patches is clearly seen. This has implications for wavelet coherence.

For any wavelet, coherence is calculated as

$$\gamma_\psi^2(a,\mathbf{b}) = \frac{\left[\int \mathcal{W}(h)\mathcal{W}(BA)\Phi_s d\mathbf{b}\right]^2}{\int \mathcal{W}(h)^2\Phi_s db_1 \int \mathcal{W}(BA)^2\Phi_s db_2} \tag{6.43}$$

where $\mathbf{b}$ is the 2D position vector. For the $(n+1)$ tensor and $2n$ polarized wavelets, the resulting coherence is combined to produce a single (i.e., radial) coherence curve at each

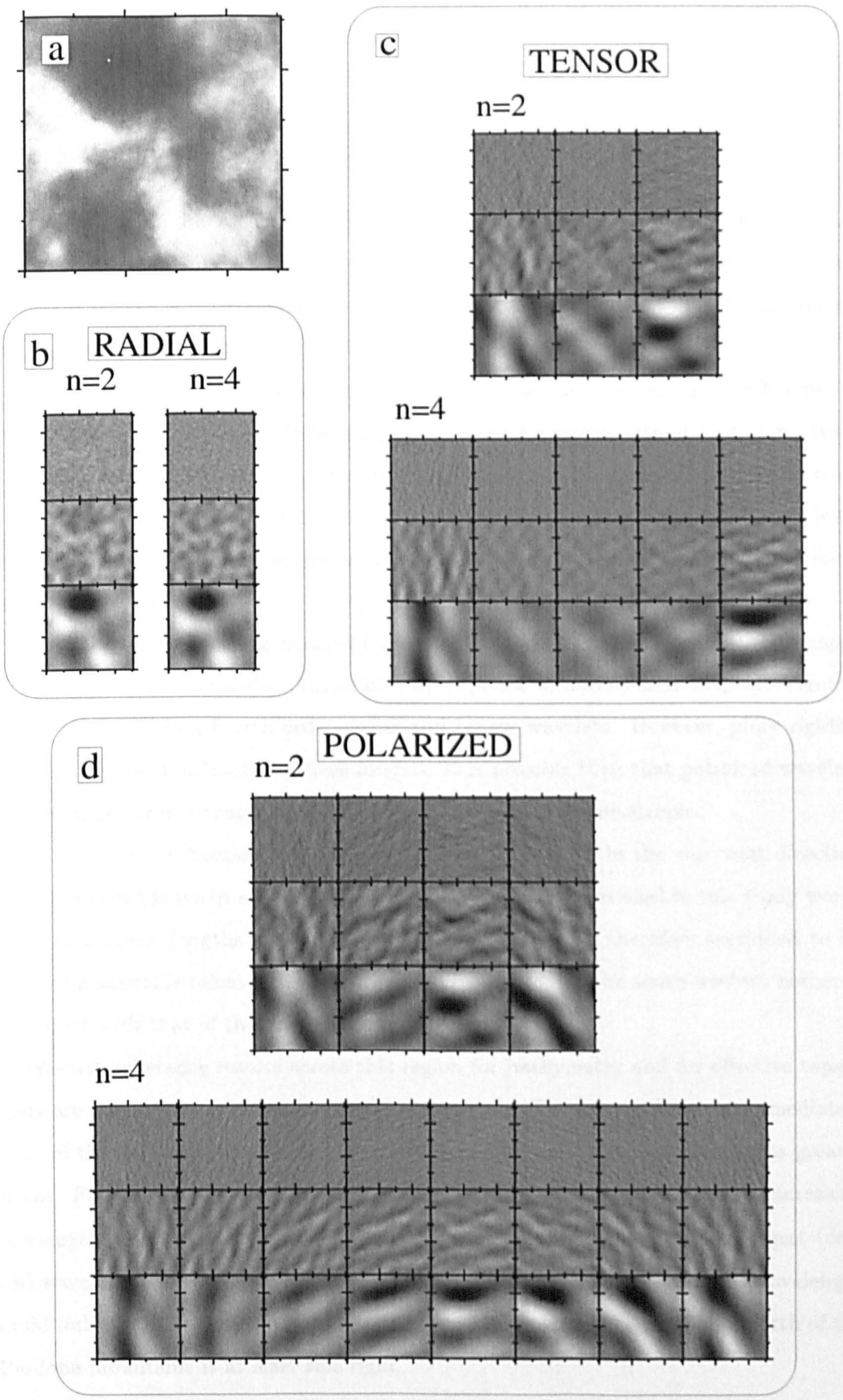

Figure 6.35: (a)Synthetic topography, generated with exponent $\beta = 3$. (b), (c) and (d) show the CWT for radial, tensor and polarized wavelets respectively. Note the effect of dividing the k-space annuli.

position (b_1, b_2) in the grid. For radial wavelets, the spectra are averaged in wavenumber annuli *prior* to estimating the coherence.

6.15 Wavelet Coherence Results

Before looking at the Aegean, the coherence is estimated for a number of synthetic topography and gravity datasets to test the resolution of the wavelet method. Figure 6.10 showed synthetic data sets generated for T_e = 10 km (and f =1). Results for all six wavelets are shown in Figure 6.36.

Six logarithmically spaced dilations are presented in each case and 50% coherence is observed at the fourth finest, indicating a characteristic wavelength of ~140 km. From Figures 6.4 and 6.5, this is consistent with the T_e of 10 km. For each of the three wavelet types, it is clear that the fourth order wavelet best resolves the transition from low to high coherence. This result serves as a control for the analyses of synthetic data for a lithosphere of varying T_e.

A series of datasets are generated for spatially varying T_e. The results are presented in Appendix J, and the main conclusion is that spatial variability in lithospheric rigidity is best resolved using fourth order radial and tensor wavelets. However, plate rigidity does not vary with azimuth in these models. It is possible then that polarized wavelets may work better in situations where lithospheric rigidity is anisotropic.

As described in Section 6.7, the data grids are 1344 km in the east-west direction by 1456 km in the north-south direction. The CWT algorithm used in this study works with grids whose lengths are powers of two. The data are therefore regridded to 10 km, and a subset is taken that measures 1270 by 1270 km. The south-western corner is coincident with that of the larger rectangular grid.

Wavelet coherence results across this region for bathymetry and for effective topography are shown in Figures 6.37 and 6.38 respectively. The low rigidity area immediately north of the Aegean is clearly seen by the high coherence values for wavelengths greater 60 km. Figure 6.39 shows the results across this area in more detail. With increasing wavelength, areas of high coherence extend across mainland Greece. The largest (central) wavelength analysed across the study area is 320 km. Coherence at this wavelength would indicate T_e values of less than 30 km, indicating that the lithosphere north of the Rhodope Mountains is at least this rigid.

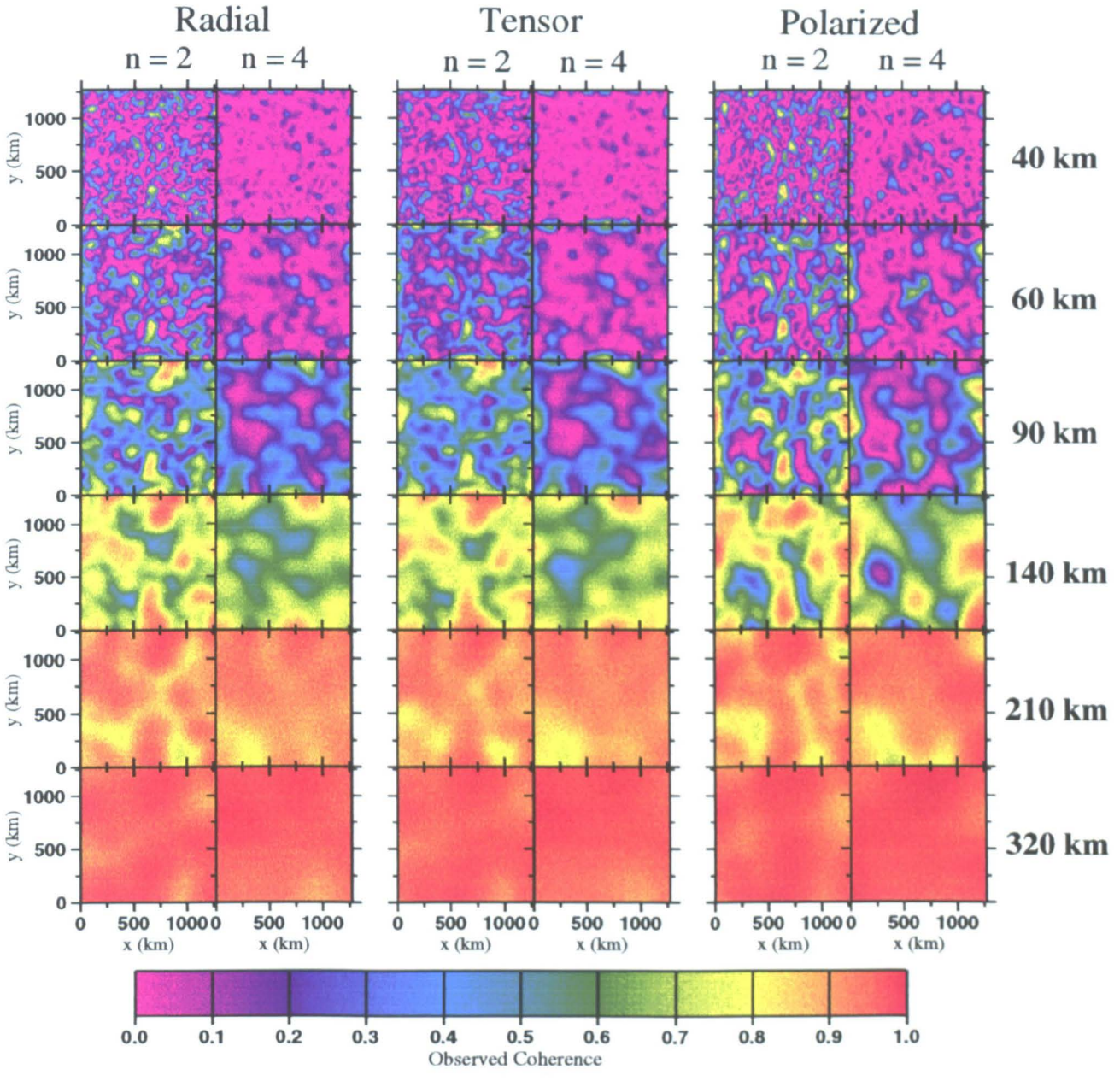

Figure 6.36: Wavelet coherence for synthetic gravity and topography data. Panels show results for second and fourth order radial, tensor and polarized wavelets. The central wavelength for each of the six slices is shown down the right.

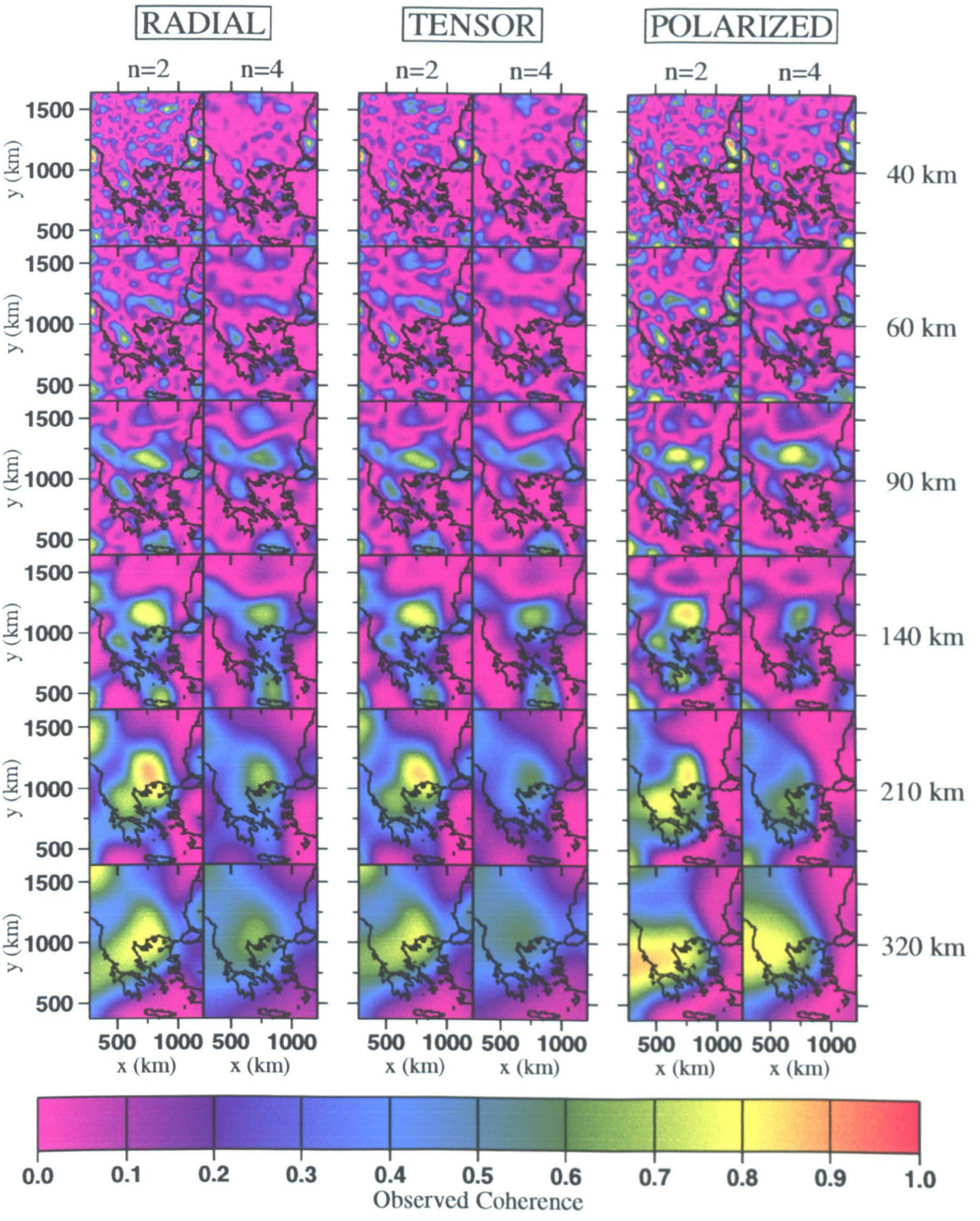

Figure 6.37: Wavelet coherence for the Aegean using bathymetry across the offshore. Panels show results for second and fourth order radial, tensor and polarized wavelets. The central wavelength for each of the six slices is shown down the right.

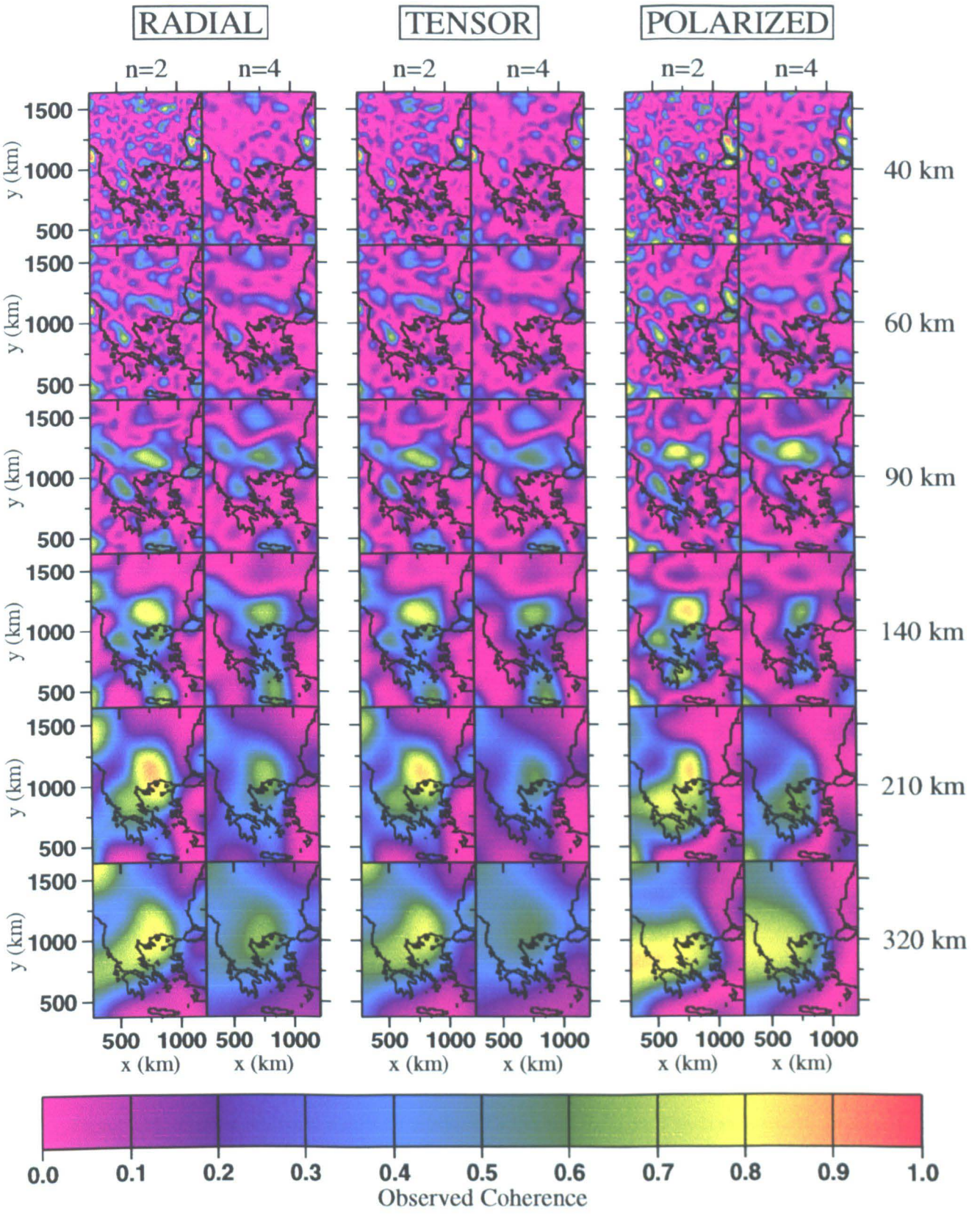

Figure 6.38: Wavelet coherence results for the Aegean using effective topography across the offshore. Panels show results for second and fourth order radial, tensor and polarized wavelets. The central wavelength for each of the six slices is shown down the right.

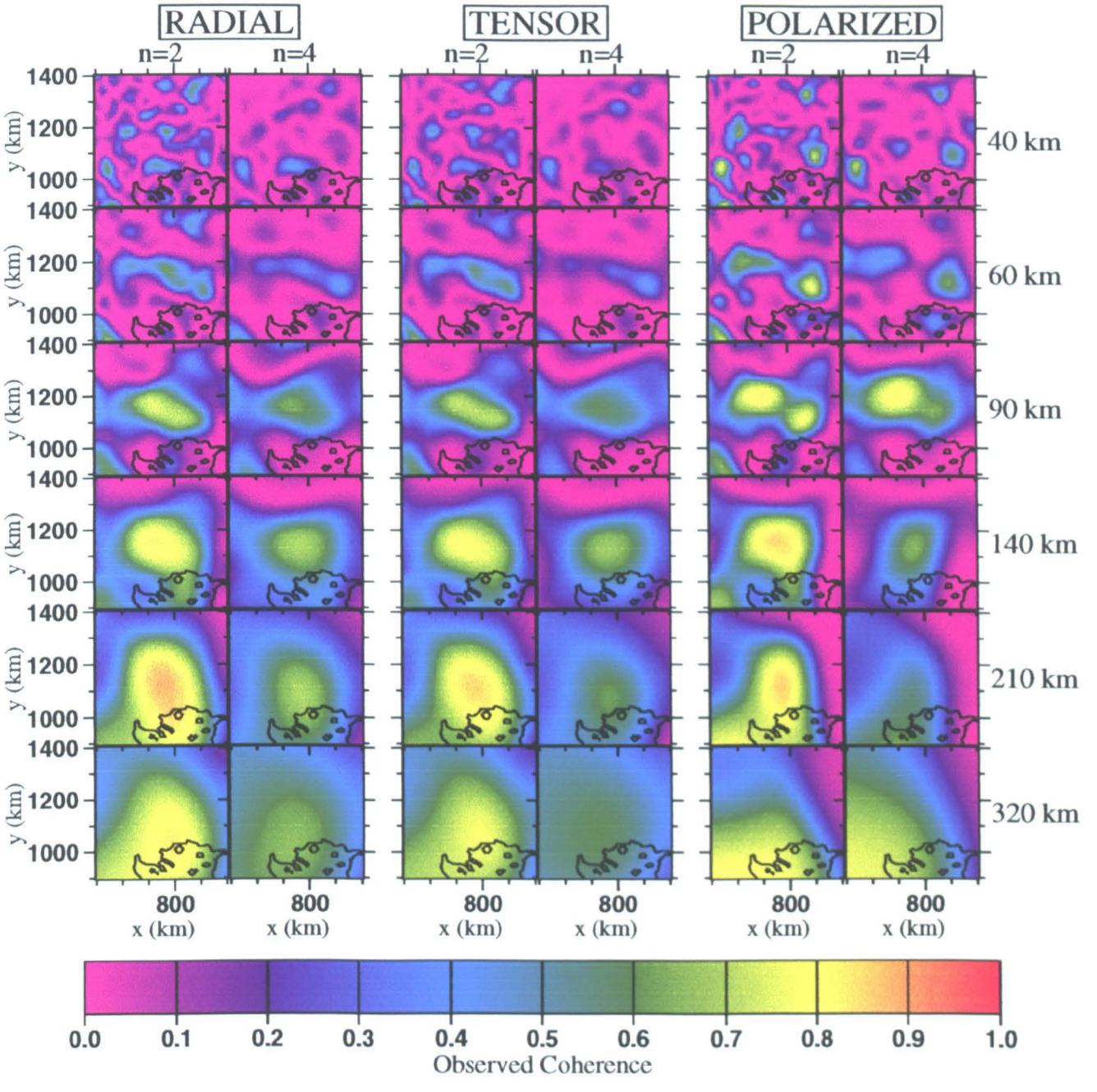

Figure 6.39: Wavelet coherence results for northern Greece and Bulgaria. Panels show results for second and fourth order radial, tensor and polarized wavelets. The central wavelength for each of the six slices is shown down the right.

6.16 A Comparison of Fourier and Wavelet Coherence

This thesis presents the first comparison of the Fourier and wavelet coherence methods. The broad-scale patterns seen in Figures 6.37 and 6.38 are similar to those observed with the Fourier analysis. To assess the extent of any differences at shorter lengthscales, the area immediately north of the Aegean Sea is focussed on. This region gave the lowest T_e values (8 to 12 km) from the Fourier coherence.

The observed coherence in Figure 6.18, as well as the results of *Roy et al.* [1996], highlighted the limitations of spatial resolution associated with the Fourier method (see Section 6.12). The ability of the continuous wavelet transform to resolve spatial variability in coherence is examined in Figure 6.40. High coherence at wavelengths shorter than ~100 km indicates T_e values of less than 5 km. The weakest portions of the lithosphere are indicated by those areas which display high coherence at the shortest wavelengths, and which remain coherent with increasing wavelength. At the longest wavelengths, the observed coherence begins to resemble the T_e map obtained from the Fourier method, for which the window size is ~200 km. We can conclude therefore that the resolution of spatial variability in coherence is greatly improved with the wavelet technique.

Figure 6.40 shows that the narrow Balkan chain lies outside the region of lowest rigidity. The Rhodope core complex is located across a region of extremely weak lithosphere which is seen to be elongated in an east-west direction, parallel to the trend of normal faulting.

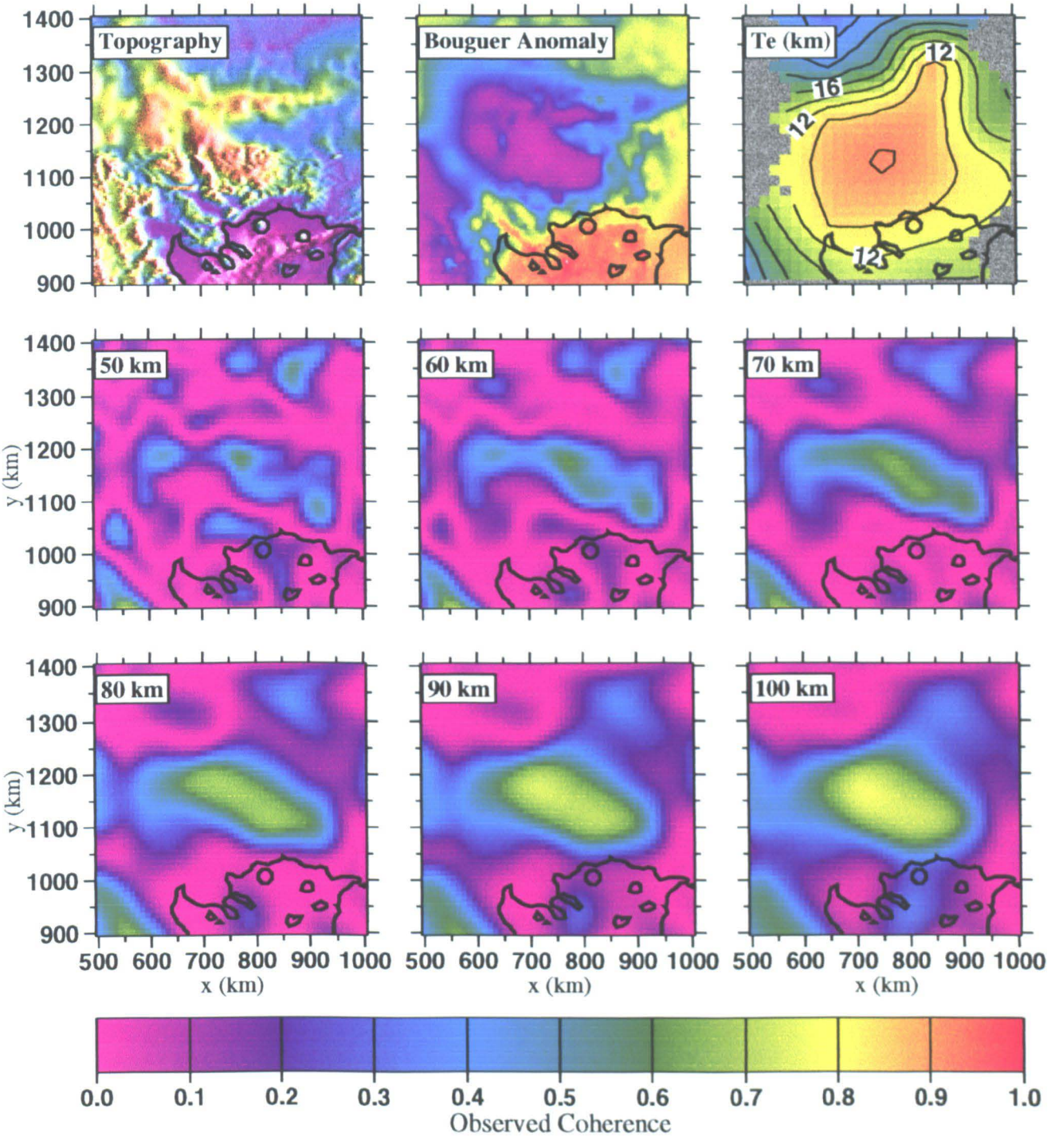

Figure 6.40: Topography, Bouguer gravity, T_e and wavelet coherence across northern Greece and Bulgaria. T_e map is extracted from Figure 6.28. Wavelet coherence is found with a second order radial wavelet, and its central wavelength is indicated within each plot.

6.17 Conclusions

- T_e is 15 km or weaker across zones undergoing diffuse extension, and increases to over 20 km towards the western coast of Greece.
- No coherence is observed across the central and Southern Aegean. This may be due to the action of dynamic mechanisms of isostatic compensation.
- The strongest lithosphere is observed across the southern Carpathians, where T_e is ~25 to 30 km.
- The weakest lithosphere is observed across the Rhodope Mountains. The Fourier coherence method resolves a broad, roughly circular zone across which T_e decreased to 8 km.
- The improved spatial resolution of the wavelet coherence method has been demonstrated, and has led to significant results across the Rhodope Mountains:

1. T_e across the Rhodope complex decreases to less than 5 km
2. The weak area, shown by high coherence at 60 to 70 km, is ~100 km wide and trends in an east-west direction. This is parallel to the trend of the normal faults that bound the core complex.

Chapter 7

Discussion and Conclusions

7.1 Introduction

The results of previous studies of the Aegean province have greatly influenced our understanding of continental extensional tectonics. Although the style of surface deformation is known to be controlled by the rheology of the lithosphere, a systematic investigation of the rheology of the Aegean lithosphere had not been carried out. This has formed the primary objective of this thesis, which is timely given the recent and ongoing research concerning the seismically and geodetically measured strain.

Gravity data from across the Aegean province had been collected prior to this study in a number of onshore and offshore surveys, including two across the Gulf of Corinth in the early 1980s. As part of this thesis, additional data were collected in mainland Greece in order that the individual sources could be merged. The end product is the best gravity data set currently available for the Aegean. Together with topography data, this formed the basis from which the aims of this thesis were addressed.

This chapter firstly examines what the effective elastic thickness (T_e) estimates across the Aegean tell us about the rheology of the lithosphere, and discusses its relationship with the seismogenic thickness, T_s. Discussion then focuses on the the role that rheology has to play in the spatial and temporal variations of rifting style, and compares the Aegean with the Tibetan Plateau and the Basin and Range. Finally, a summary of the conclusions from previous chapters are listed.

7.2 T_e and Rheology

From the theoretical considerations in Chapter 2, the effective elastic thickness is controlled by

- Yield stress (σ_y), and so
    1. geothermal gradient
    2. crustal thickness
    3. composition
    4. strain rate ($\dot{e}$)
- plate curvature ($\frac{d^2w}{dx^2}$)
- in-plane deviatoric stress (τ_{xx}^N).

Recent numerical models for the rheology of continental lithosphere [*Burov and Diament*, 1995a; *Lavier and Steckler*, 1997] have shown that T_e values predicted from these parameters match observed T_e. Moreover, these studies show that the geothermal gradient exerts the primary control on rheology and T_e. The results of this thesis provide observational evidence for this theoretical result.

GPS observations reveal the spatial variations in $\dot{e}$ across Mainland Greece and, from Section 2.2.3.4, greater $\dot{e}$ should result in higher ductile yield stress, and so stronger T_e. Although the size of the region analysed by *Davies et al.* [1997] is comparable to the average window size for the Fourier coherence analysis, $\dot{e}$ is expected to decrease to the north of the GPS network. There is little evidence for a corresponding decrease in T_e.

The magnitude of the influence of τ_{xx}^N is difficult to assess from the results of this thesis, as is the effect of $\frac{d^2w}{dx^2}$, although the latter may in part explain the T_e of 6 km obtained across the flexed flanks of the Gulf of Corinth Rift.

Figure 7.1 presents maps of surface heat flow, q_s, and T_e. Across mainland Greece, a decrease in q_s towards the west to ~40 mW/m^2 correlates with an increase in T_e to values greater than 20 km. Although the trend of the contours in both plots is similar to the trend of isopic zones (Figure 3.7), it seems unlikely that compositional variation could account for this east-west gradient. Additionally, the sense of the gradient is opposite to that which would be expected if crustal thickness was the primary control on rheology.

From a review of global seismicity, *Molnar and Chen* [1983] show that seismogenic thickness, T_s, is also primarily controlled by temperature, and approximately coincides

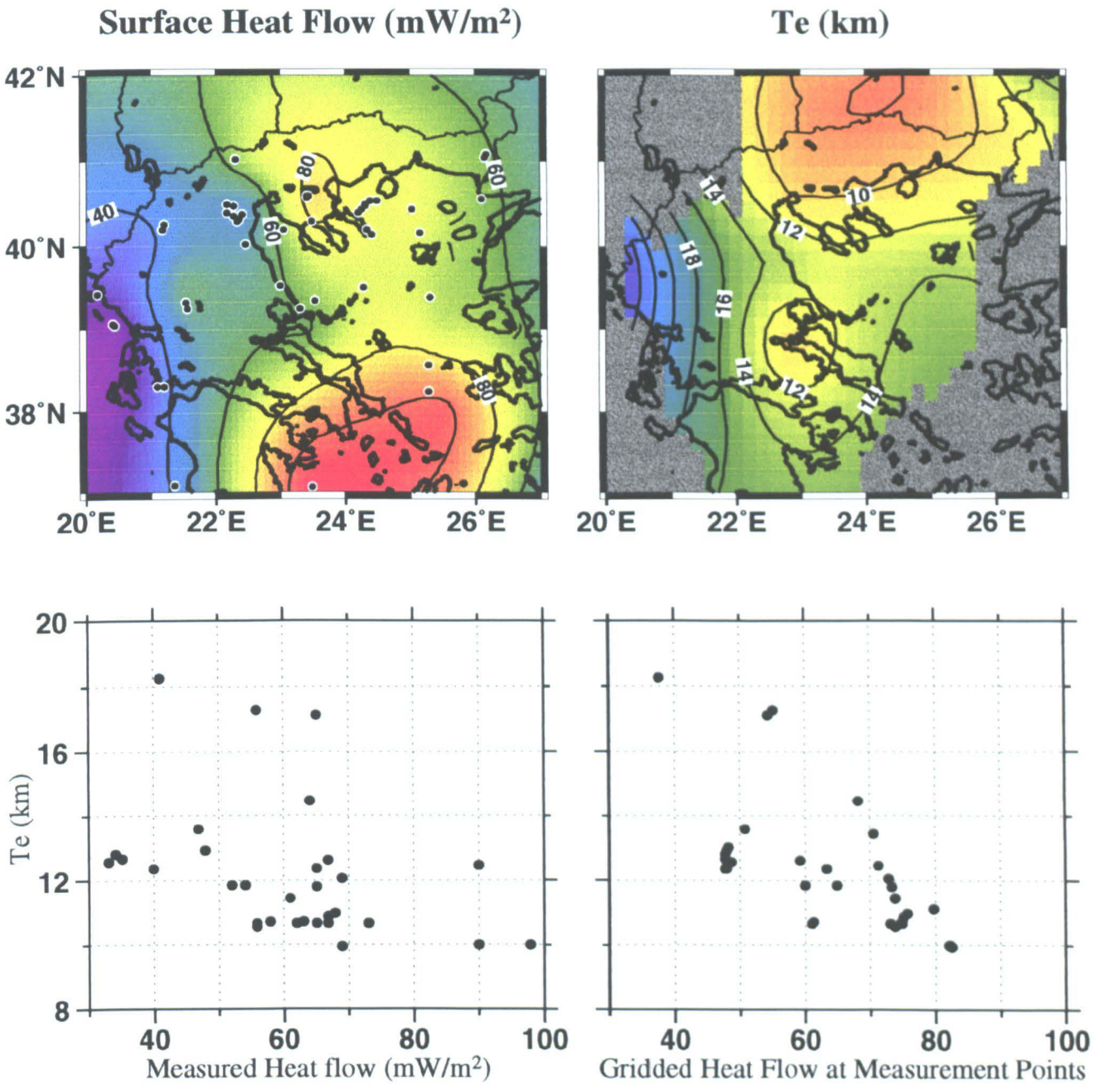

Figure 7.1: Maps of surface heat flow (in mW/m^s) and T_e (in km, using effective topography across the offshore). Plots demonstrate the dependence of lithospheric rheology on geothermal gradient.

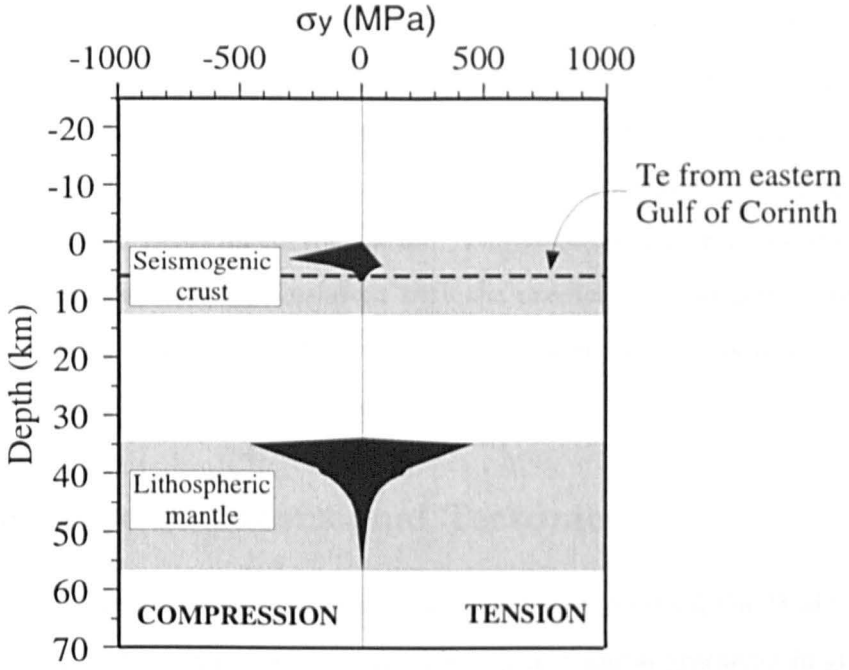

Figure 7.2: Yield stress profiles for the Aegean lithosphere, calculated for T_s = 12 km, T_c = 35 km, q_s = 80 mW/m^2 and $\dot{\epsilon} = 2 \times 10^{-15}$ s^{-1}. Crust is assumed to have a quartz rheology, and the mantle an olivine rheology. For a curvature equivalent to that of the earth, this yield stress profile predicts a T_e of 15 km, consistent with the results of this thesis. Supplied by E. Burov (Institut de Physique du Globe de Paris, personal communication, 1997).

with the 350±100°C isotherm. This has led some authors (e.g., *McKenzie and Fairhead* [1997]) to suggest that T_e and T_s should always be similar, so implying that the strength of the mantle contributes nothing to overall lithospheric rheology. However, *Lavier and Steckler* [1997] show that observed T_e values greater than crustal thicknesses are consistent with predicted T_e values, and can only be explained by the coupled flexure of the crust and strong mantle.

Chapter 6 presents the results of a coherence analysis, the aim of which was to map the spatial variability in lithospheric rheology. A primary result of this thesis is that where the surface is extending, the effective elastic thickness is less than 20 km. On the basis of observations of T_s, surface heat flow, crustal thickness and strain rate, E. Burov (Institut de Physique du Globe de Paris, personal communication, 1997) constructed a yield stress profile for the Aegean lithosphere (Figure 7.2). For a curvature equivalent to that of the earth, this yield stress profile predicts a T_e of 15 km, which is consistent with the T_e estimates made in this thesis. Therefore, despite the similarity between T_e and T_s for the Aegean, the mantle is contributing to flexural strength.

An estimation of the magnitude of this contribution can be made from the results of the gravity and elastic modelling in the Gulf of Corinth, presented in Chapter 5. Here, upper crustal T_e is modelled to be 6 km. Thus, upper-crustal T_e is less than T_s, which is to be expected as the strain rates associated with earthquakes are far greater than those associated with isostatic compensation. The contribution to lithospheric T_e from the mantle is therefore ~9 km, consistent with the prediction of significant ductile yield stress in the mantle (Figure 7.2). However, caution must be expressed here as different isostatic models are assumed in Chapters 5 and 6.

7.3 The Style of Extensional Tectonics

The driving force for the extensional tectonics across the Aegean, the Basin and Range and the Tibetan Plateau appears to be provided by horizontal gradients in gravitational potential energy (GPE) [*Davies et al.*, 1997; *England and Molnar*, 1997b; *Jones, Unruh and Sonder*, 1996], and each may be thought of as a collapsing orogen. Further similarities between these provinces exist:

- T_s of 10 to 15 km
- fault lengths of ~20 to 30 km
- half-graben widths of <30 km
- similar ratios of footwall uplift to hanging wall subsidence
- high q_s, locally exceeding 100 mW/m^2.

From this study, it can now be said that T_e in each province is low, as indicated on Figure 7.3.

Extensional strain across mainland Greece and western Turkey is accommodated by diffuse rifting. From the models of *Buck* [1991], *Hopper and Buck* [1996] and *Benes and Davy* [1996], this may indicate that the lower crust beneath the rifts is flowing at a fast enough rate to partially restore any local GPE gradients generated by thinning.

The spacing of the rifts across the Tibetan Plateau is ~150 to 200 km, compared to ~35 km for the Basin and Range. *Armijo et al.* [1996] make the suggestion that the spacing across Tibet must therefore be controlled by mantle processes. Indeed, a long wavelength periodicity of ~200 km is seen in the Bouguer anomaly across the Basin and

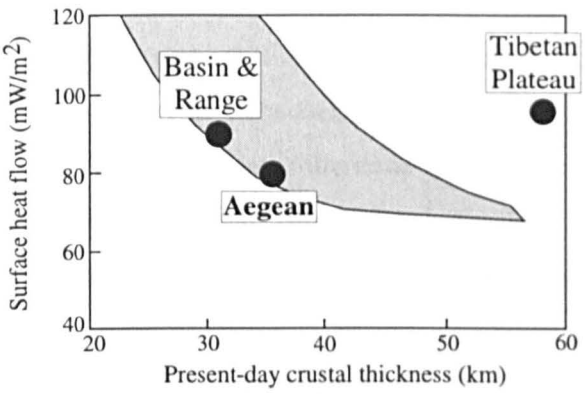

(a)

PROVINCE	Te estimate (km) Coh.	Mod.	tr (Ma)	β
Tibetan Plateau	-	1 - 3	8	<1.1
Aegean	**<15**	**6**	**20**	**<2.0**
Basin & Range	5 - 15	2 - 4	40	<2.0

(b)

Figure 7.3: (a) Plots showing the location of the Basin and Range, the Tibetan and the Aegean provinces on the extensional mode plot of *Buck* [1991]. Note that the x-axis is *present-day* crustal thickness. (b) shows the T_e estimates for each province (from both coherence and forward modelling methods), the time of onset of extensional strain, t_r, and the extension factor, β. See Table 2.2.

Range, which could be interpreted to represent a remnant of an early stage process. By analogy, *Armijo et al.* [1996] suggest that the 50 to 70 km rift spacing across mainland Greece and Turkey is also mantle controlled.

The present-day heat flow and crustal thicknesses are plotted on Figure 7.3, which also indicates the time of onset of rifting, t_r, the extension factor, β, and the range of observed T_e values. It seems possible that these regions represent different stages of a similar extensional process. The Tibetan Plateau is extending well within the core complex field, and as such we expect surface rifting to be localised. However, the localisation is controlled by the weak rheology of the lower crust rather than by strength in the mantle.

A scheme for tectonic evolution consistent with the theory and the results presented in this thesis comes from a consideration of spatial and temporal variations in lithospheric rheology. Aegean extension initiated in a back-arc setting in thickened crust at ~20 Ma. Weak rheologies meant that the extensional strain of the collapsing orogen was accommodated by the formation of core complexes. As extension continued, crustal thickness decreased which led to an increase in the effective lower crustal viscosity by thinning the lower crustal channel. Extension evolved to a diffuse mode, as seen today across Greece and western Turkey (Figure 7.3). All extension has occurred in response to the same GPE gradient across the Hellenic Trench (Appendix B).

This scheme is consistent with our understanding of the evolution of lithospheric rheology, the age of diffuse rifting (5 to 16 Ma) and the constraints on rheology from

estimates of T_e. The T_e across the extending regions of mainland Greece is ~10 to 15 km, similar to the diffuse Basin and Range. The Rhodope core complex in northern Greece may provide a modern analogue for the initial extension across central and southern Aegean. Wavelet coherence across this region reveal a localised zone of very low T_e, probably <5 km. Such a weak rheology is consistent with the idea that the lower crust is very weak, so promoting the development of a core complex.

7.4 Conclusions

• Existing gravity data from both the onshore and offshore have been collated. Gravity field work and the establishment of a network of base stations allowed for the calibration of individial data sources. The inclusion of the recently published offshore data of *Sandwell and Smith* [1997] allowed for the analysis of greater wavelengths. This is crucial if the isostatic process is to be resolved. From the analysis of maps and profiles:

1. β values for the Aegean are ~1.2 to 1.5

2. The regional form of the Cyclades appears to be anomalous, as there is no negative Bouguer anomaly across the broad positive topography. This region is coincident with elevated surface heat flow, low P-wave velocity, a positive geoid anomaly, and low gravity coherence. This is evidence that dynamic processes are in operation.

• Gravity data across the rifts in central Greece allow for a direct assessment of basin depth. Along the Gulf of Corinth, the residual Bouguer gravity indicates the presence of four areas of locally increased basin depth. A model is derived for the gravitational effect of a sediment pile whose porosity decreases exponentially with depth of burial. From this, subsidence in the hanging wall to the Xylocastron fault segment is between 2.7 and 3.7 km. This provides excellent constraint for elastic models of erosional marine terrace elevations, and the following conclusions can be made for a model of upper-crustal flexure:

1. The footwall flexes with a T_e of ~6 km, a rigidity that is considerably less than the T_e estimates for discrete rifts such as the East African and Baikal rifts, and similar to estimates across the Basin and Range province, the archetypal diffuse rift.

2. Time-averaged rate of uplift at the fault (i.e., co-seismic plus inter-seismic) is ~1.7 mm/yr.

3. The amplitude of fault-related uplift decreases to zero in the footwall over a distance of ~35 km from the normal fault.

4. The ratio of footwall uplift to hanging wall subsidence increases for greater T_e. Across the eastern Gulf of Corinth, the ratio is between 1:1.8 and 1:2.

5. Extensional velocity is estimated at ~4 mm/yr which is roughly half that rate measured with the GPS [*Davies et al.*, 1997], consistent with their observation that geodetic strains exceed estimates based on the summation of seismic moment.

• This thesis presents the first assessment of the spatial variability in lithospheric rheology across the Aegean province. The following points summarise the conclusions from coherence mapping:

1. The weakest lithosphere lies across the Rhodope complex in northern Greece and southern Bulgaria, indicated by T_e values of less than 10 km. Locally, T_e decreases to less than 5 km, and is weakest in a narrow (~100 km) zone that trends parallel to normal faulting.

2. The strongest lithosphere occurs across the Southern Carpathian Mountains, indicated by T_e values of ~25 to 30 km.

3. T_e is 15 km or weaker in the regions undergoing diffuse extension, similar to estimates obtained across the Basin and Range province.

4. Geothermal gradient exerts the major control on lithospheric rigidity across the Aegean.

• The first comparison between coherence results using windowed Fourier transforms and the continuous wavelet transform is presented in this thesis, and shows the following:

1. CWTs are able to resolve short-wavelength spatial variations. This is a consequence of the simultaneous localisation in space and wavenumber of the wavelet basis functions

2. With the Fourier method, the window size must be reduced at each node in order to gain maximum spatial resolution. Due to the scaling properties of wavelets,

no such input is required. The final results are therefore less biased and may be obtained with greater efficiency.

Appendix A

Physics of Gravitational Potential Energy

A.1 Airy Isostasy and Stress

In general, the stress tensor (σ_{ij}) may be decomposed into a *deviatoric* component (τ_{ij}) and an *isotropic* component (κ_{ij}), such that

$$\sigma_{ij} = \tau_{ij} + \kappa_{ij} \tag{A.1}$$

where

$$\begin{aligned} \kappa_{ij} &= \frac{1}{3}\sigma_{kk}\delta_{ij} \\ &= -p\,\delta_{ij}\ . \end{aligned} \tag{A.2}$$

and σ_{kk} is the sum of the diagonal components of σ_{ij}, p is the mean normal stress (or *pressure*) and δ_{ij} is the Kronecker identity matrix. Ignoring variation in y, this is more simply expressed as

$$\sigma_{xx} = \tau_{xx} - p \tag{A.3}$$

and

$$\sigma_{zz} = \tau_{zz} - p \tag{A.4}$$

where x and z are the horizontal and vertical coordinate axes, assumed to coincide with the axes of principal stress.

As the forces involved in accelerations are very small compared to gravitational forces [*England and Jackson*, 1989], we may assume that the equilibrium equations apply (see *Ranalli* [1987] for their derivation). The relation between stress and body forces for a medium of density ρ is given by

$$\frac{\partial \sigma_{xx}}{\partial x} + \frac{\partial \sigma_{xz}}{\partial z} = 0 \tag{A.5}$$

and

$$\frac{\partial \sigma_{xz}}{\partial x} + \frac{\partial \sigma_{zz}}{\partial z} = -\rho g \ . \tag{A.6}$$

Following *Dalmayrac and Molnar* [1981], *England and McKenzie* [1983] and *Molnar and Lyon-Caen* [1988] who ignore deviations from horizontality, the top surface of the earth's lithosphere ($z = 0$) is assumed to be free from normal and shear stress. Thus, $\sigma_{zz}|_{z=0} \approx \sigma_{xz}|_{z=0} \approx 0$. We also assume that the base of the lithosphere ($z = L$) is free from shear stress: $\sigma_{xz}|_{z=L} \approx 0$.

Integrating Equation A.5 through lithospheric depth, we get

$$\int_0^L \frac{\partial \sigma_{xx}}{\partial x}\, dz + \int_0^L \frac{\partial \sigma_{xz}}{\partial z}\, dz = 0 \tag{A.7}$$

where the second term is zero. If $\sigma_{xx}(x, z)$ is a well behaved function, we get

$$\frac{\partial}{\partial x} \int_0^L \sigma_{xx}\, dz = 0 \ . \tag{A.8}$$

Assuming Airy isostasy, the shear on all vertical planes (i.e., σ_{xz}) is zero. Equation A.6 then becomes

$$\frac{\partial \sigma_{zz}}{\partial z} = -\rho(x, z) g \tag{A.9}$$

and

$$\sigma_{zz}(z) = -g \int_0^z \rho(x, z)\, dz \ . \tag{A.10}$$

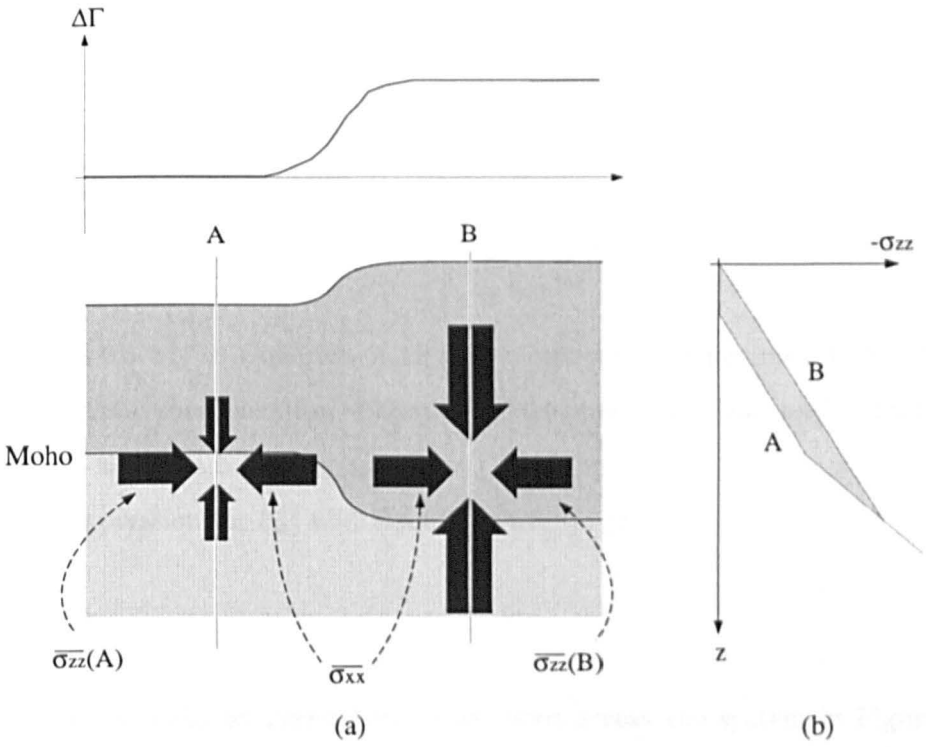

Figure A.1: (a) Sketch of the state of stress across a locally compensated plateau, with $F_d = 0$. $\overline{\sigma_{xx}}$ is constant across the system, such that the vertically averaged horizontal deviatoric stress ($\overline{\tau_{xx}}$) varies and controls the deformation of the region. $\Delta\Gamma$ describes the difference in GPE relative to that at reference column A. (b) Profiles of the vertical normal stress for two columns (A and B), assuming that isostatic compensation occurs about the moho (i.e., $\rho_f = \rho_m$). Density differences due to thermal processes are ignored.

This leads to the result that σ_{zz} is equal to the negative of weight per unit area of overlying rock (i.e., σ_{zz} is compressional). This condition is often assumed to hold in geological processes, but is not valid where the elastic support of lithosphere is significant [*Molnar and Lyon-Caen*, 1988]. The function describing the difference in σ_{zz} with depth is

$$\Delta\sigma_{zz}(z) = -g \int_0^z \Delta\rho(x,z)\, dz \tag{A.11}$$

where $\Delta\rho(x,z)$ is the difference in density between two columns.

Because stress cannot be measured at depth within the lithosphere, deformation is considered to occur in a thin viscous sheet in response to vertical averages of stress.

These are indicated by overbars (Equations A.12).

$$\overline{\sigma_{xx}} = \frac{1}{L}\int_0^L \sigma_{xx}\, dz \qquad \text{and} \qquad \overline{\sigma_{zz}} = \frac{1}{L}\int_0^L \sigma_{zz}\, dz$$

$$\overline{\tau_{xx}} = \frac{1}{L}\int_0^L \tau_{xx}\, dz \qquad \text{and} \qquad \overline{\tau_{zz}} = \frac{1}{L}\int_0^L \tau_{zz}\, dz\ . \tag{A.12}$$

The expression for $\overline{\sigma_{zz}}$ in Equation A.12 is the vertical force per unit area that arises from local isostatic compensation within the lithosphere. *England and Jackson* [1989] loosely refer to this as a buoyancy force.

From the expression for $\overline{\sigma_{xx}}$ and Equation A.8, we get

$$\frac{\partial \overline{\sigma_{xx}}}{\partial x} = 0\ . \tag{A.13}$$

Therefore, the vertically averaged horizontal stress across the system in Figure A.1 is constant. The depth integral of σ_{xx} is often cited as a force (F_x) [*Houseman and England*, 1986; *Sonder et al.*, 1987], where

$$\begin{aligned} F_x &= \int_0^L \sigma_{xx}\, dz \\ &= L\overline{\sigma_{xx}} \end{aligned} \tag{A.14}$$

Thus, high ranges or plateaus transmit a constant horizontal force across the entire length of the feature. This is a simple consequence of isostatic equilibrium.

A.2 Horizontal Deviatoric Stress

In general, extensional deformation occurs where $\overline{\sigma_{xx}} > \overline{\sigma_{zz}}$, and compressional deformation where $\overline{\sigma_{xx}} < \overline{\sigma_{zz}}$. From Equations A.3 and A.4, and assuming incompressibility such that $\overline{\tau_{xx}} = -\overline{\tau_{zz}}$,

$$\overline{\tau_{xx}}(x) = \frac{\overline{\sigma_{xx}} - \overline{\sigma_{zz}}}{2} \tag{A.15}$$

such that the average horizontal deviatoric stress is equal to half the difference between the average horizontal and vertical normal stresses. Extensional deformation therefore occurs where $\overline{\tau_{xx}} > 0$, and compressional deformation where $\overline{\tau_{xx}} < 0$. As $\overline{\sigma_{xx}}$ is constant

with x (Equation A.13), $\overline{\tau_{xx}}(x)$ clearly varies with position.

For columns A and B in (Figure A.1), the difference in $\overline{\tau_{xx}}$ is expressed as

$$\Delta\overline{\tau_{xx}} = \overline{\tau_{xx}}(B) - \overline{\tau_{xx}}(A) \; . \tag{A.16}$$

From Equation A.15 and noting that $\overline{\sigma_{xx}}$ is the same for columns A and B, we get

$$\begin{aligned} \Delta\overline{\tau_{xx}} &= -\frac{1}{2L}\int_0^L \sigma_{zz}(B)\, dz + \frac{1}{2L}\int_0^L \sigma_{zz}(A)\, dz \\ &= -\frac{1}{2L}\int_0^L \Delta\sigma_{zz} \; . \end{aligned} \tag{A.17}$$

The difference in horizontal deviatoric stress between two isostatically compensated columns is therefore proportional to the integral of the difference in the vertical normal stress between them. This is the area between the two curves in Figure A.1b. Ignoring lateral variations in crustal and mantle density,

$$\int_0^L \Delta\sigma_{zz}\, dz = \frac{g\rho_c}{2}\left(1 - \frac{\rho_c}{\rho_m}\right)(\Delta T_c)^2 \tag{A.18}$$

A.3 Gravitational Potential Energy

By virtue of its position in a gravitational field, a mass (δm) has gravitational potential energy (GPE). This is equivalent to the negative of the work done on δm by the gravitational force in bringing δm from infinity to its position in the field at r above the centre of the Earth with mass M (e.g., *Turcotte and Schubert* [1982]). Thus,

$$\begin{aligned} GPE &= \int_\infty^r \frac{GM\delta m}{r^2} dr \\ &= -\frac{GM\delta m}{r} \end{aligned} \tag{A.19}$$

where G is the gravitational constant. If $g(r)$ is the Earth's gravitational acceleration at r, then $g(r) = -GM/r^2$ and

$$\begin{aligned} GPE &= \delta m\, g(r) r \\ &= \rho(r) \delta V\, g(r) r \\ &= \rho(r)\, \delta x \delta y \delta r\, g(r) r \ . \end{aligned} \tag{A.20}$$

Γ is defined as the GPE per unit of surface area, so Equation A.20 becomes

$$\Gamma = \frac{GPE}{\delta x \delta y} = \rho(r) g(r) r\ \delta r \ . \tag{A.21}$$

The GPE per unit area of lithosphere is then the depth integral of Equation A.21. Changing variables from r to z, where z is the distance down from the surface of the Earth, the difference in GPE per unit area between two lithospheric columns to a depth z is therefore

$$\Delta\Gamma = -\int_0^z \Delta\rho(z) g(z) z\ dz \ . \tag{A.22}$$

If isostatic equilibrium prevails, then we need only integrate from 0 to the base of the lithosphere, L. Assuming $g(z)$ to be constant through this depth,

$$\Delta\Gamma = -\int_0^L \Delta\rho(z) g z\ dz \ . \tag{A.23}$$

Performing the integration in Equation A.17 (by parts) and substituting Equation A.11, we obtain

$$\begin{aligned} \int_0^L \Delta\sigma_{zz}\ dz &= \left\{ z \Delta\sigma_{zz} \right\}_0^L - \left(\int_0^L -\Delta\rho(z) g z\ dz \right) \\ &= \int_0^L \Delta\rho(z) g z\ dz \end{aligned} \tag{A.24}$$

From Equations A.23 and A.24,

$$\Delta\Gamma = -\int_0^L \Delta\sigma_{zz}\ dz \ . \tag{A.25}$$

Thus, the difference in the GPE per unit area between columns A and B in Figure A.1a is equal to the negative of the area between the curves in Figure A.1b. From equations A.17 and A.25,

$$\Delta\overline{\tau_{xx}} = \frac{1}{2L}\,\Delta\Gamma \ . \tag{A.26}$$

Therefore, the difference in the horizontal deviatoric stress between two columns of isostatically compensated lithosphere is proportional to the difference in their gravitational potential energy per unit of surface area.

Appendix B

Geometry of the Subducted Slab

Section 3.9 shows that the rate of subduction of the African oceanic lithosphere is controlled largely by the rate of rate of motion of the southern Aegean. This appendix investigates the simple idea that the change in slab dip seen in Figure 3.5 could result from changes in that rate.

The major assumption here is that the rate at which the slab sinks down through the mantle is directly proportional to the time since subduction. This ignores possible differences in thermal structure along the plate. I assume that the steeper portion was subducted at a velocity s_1 and the more recent, shallower portion at s_2. These are each the vector sum of the velocities of Aegean motion (Ag_1 or Ag_2) and African motion relative to Eurasia. The velocity Ag_1 is assumed to be the same as today, and Section 3.9 shows this to be ~50 mm/yr towards the south-west. The African plate is moving towards the north at 10 mm/yr, so the vector sum is ~57 mm/yr. The length of the shallow-dipping portion is ~200 km, so the convergence velocity is modelled to have increased to this value at ~3.5 Ma.

If d is the depth a portion of slab sinks in a time t (note this assumes the elastic strength of the slab is negligible), then

$$\begin{aligned} d &= s_1 t \sin 15 \\ d &= s_2 t \sin 45 \end{aligned} \qquad \text{(B.1)}$$

which combine to give

$$s_1 = s_2 \frac{\sin 15}{\sin 45} \,. \qquad \text{(B.2)}$$

This gives a pre-3.5Ma convergence velocity of 21 mm/yr. If the rate of African motion has remained constant, then Ag_1 is estimated as 14 mm/yr. As the length of the steeper portion is ~750 km, these velocities applied for 35 Myr. However, despite there being no evidence for a second slope change, it will be shown that the Aegean has only been extending since 20 to 25 Ma.

If these model assumptions are valid, we can say that the slab has been subducting for at least the last 40 Myr. Less than 5 Myr ago, the velocity of motion of the southern Aegean increased from 14mm/yr to 50 mm/yr. This is roughly coincident with the time at which the North Anatolian Fault propagated into the Aegean. Thus, if the motion af Anatolia is transferred to the Hellenic Trench, this may have begun at ~3.5 Ma.

However, the model is poorly constrained. Furthermore, the results of *Houseman and Gubbins* [1997] for the shape of subducted slabs shows that the balance between internal buoyancy forces and the viscous stresses associated with deformation can produce a wide variety of geometries. Perhaps the safest conclusion to draw is that, taking the present-day rate of convergence and the total slab length, Hellenic subduction has been active for at the very least 15 Myr. However, it seems more than likely that extension across the Aegean, which began at 20 to 25 Ma, has always occurred in a back-arc setting.

Appendix C

Gravity Base Station Descriptions

Gravity Base Station Description

Station name: Athens (East Air Terminal)
Established by: E. Lagios
Date established: 3/86 to 4/86
Longitude: 23.7419 Latitude: 37.8900
Elevation: ~30 m
Method of elevation determination: Unknown
Absolute gravity value: 980042.605 ±0.010 mGal
Established by tying with: Italy

Comments: See *Hipkin et. al.* [1988], Geophysical Journal, 92, p. 143-8

Description: Agios Trias is ~200 m from the East Terminal of Athens Airport. Base station was established on the northern side if the church, 60 cm from the foot of the steps. Four metal pins mark the precise location.

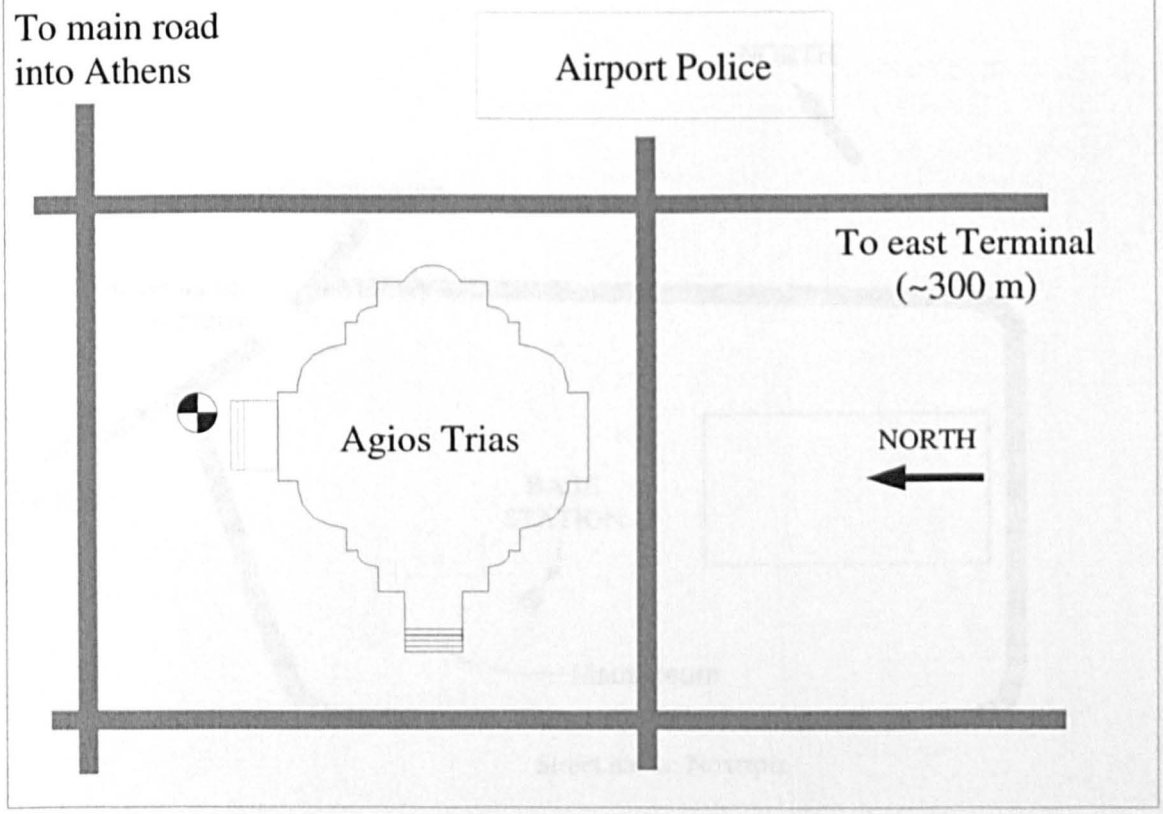

Gravity Base Station Description

Station name: Corinth
Established by: T. King
Date established: 23/5/97 and 27/9/95
Longitude: 22.9308 Latitude: 37.9394
Elevation: 8.63 m (ground level)
Method of elevation determination: Determined by HMGS
Absolute gravity value: 979996.884 ±0.014 mGal
Established by tying with: Athens IGSN71

Comments: At the site of the HMGS gravity base station, for which no gravity value was provided.
6 ties on 23/5/97, 7 ties on 27/9/95

Description: At mausoleum, on road to Kiato from centre of Corinth.
Base is against the low, NE facing wall, to SE of main entrance.
Plaque on low wall, 0.36 m above ground.

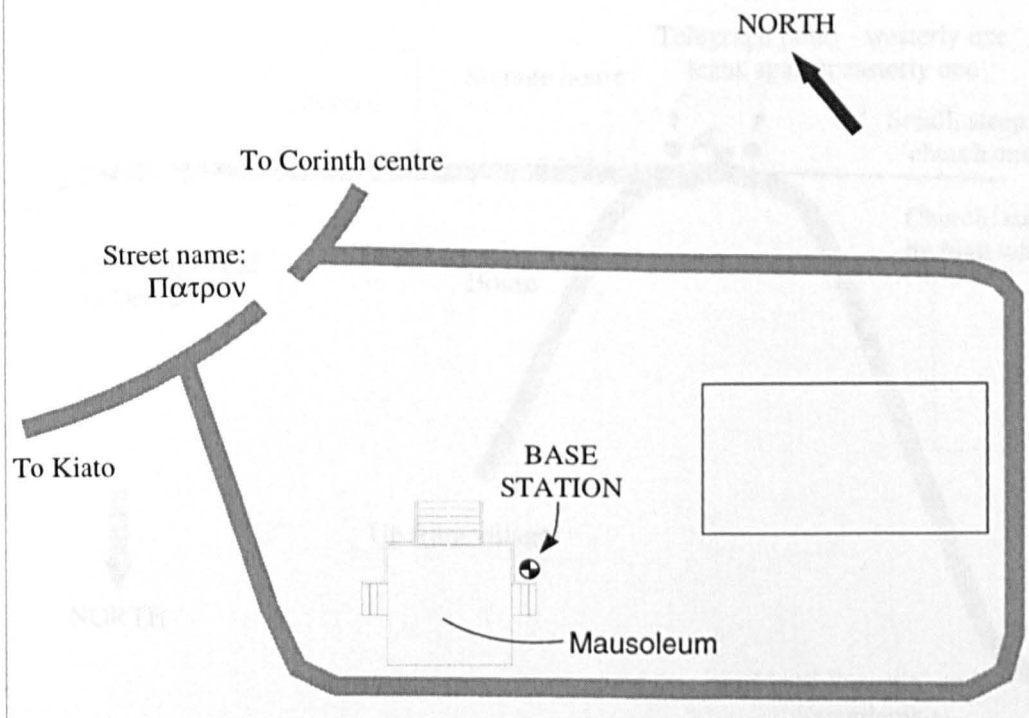

Gravity Base Station Description

Station name: Rozena
Established by: T. King
Date established: 29/5/94 and 3/10/95
Longitude: 22.3983 Latitude: 38.1200
Elevation: 169 m
Method of elevation determination:Barometric looping from nearby trig pillar
Absolute gravity value: 979935.560 ±0.015 mGal
Established by tying with: Corinth

Comments: 6 ties on 29/5/94, and 6 ties on 3/10/95.
Value quoted above is that for 3/10/95.

Description: In the village of Rozena, below the main church.
Base established exactly between 2 telegraph poles.

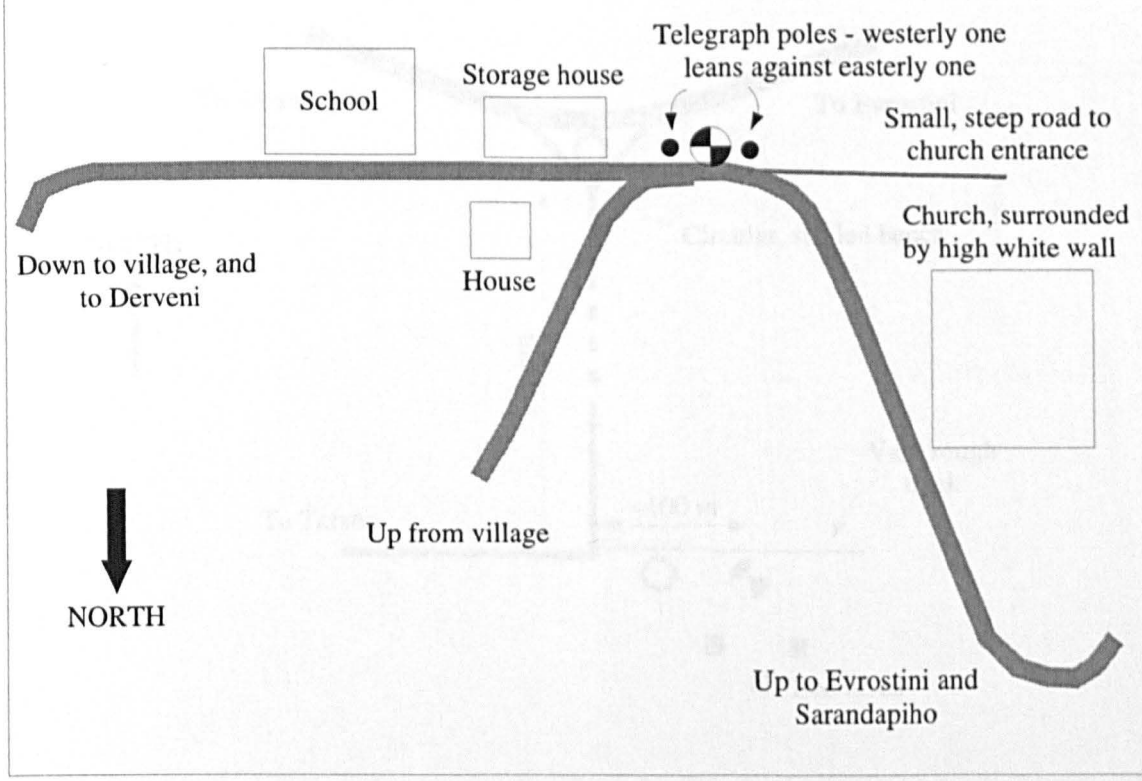

Gravity Base Station Description

Station name: Sarandapiho
Established by: T. King
Date established: 1/6/94 ans 1/10/95
Longitude: 22.3817 Latitude: 38.0150
Elevation: 1416 m
Method of elevation determination: Determined by HMGS
Absolute gravity value: 979682.937 ±0.017 mGal
Established by tying with: Rozena

Comments: Gravity meter placed **on** the 1416 m trig pillar.
Quoted value is that for 1/10/95.

Description: Driving south form Evrostini towards Sarandapiho, turn left at triangular junction. Trig pillar is ~2km from junction, 100 m along a track off to the left, where the main track towards Tarsos bends right.

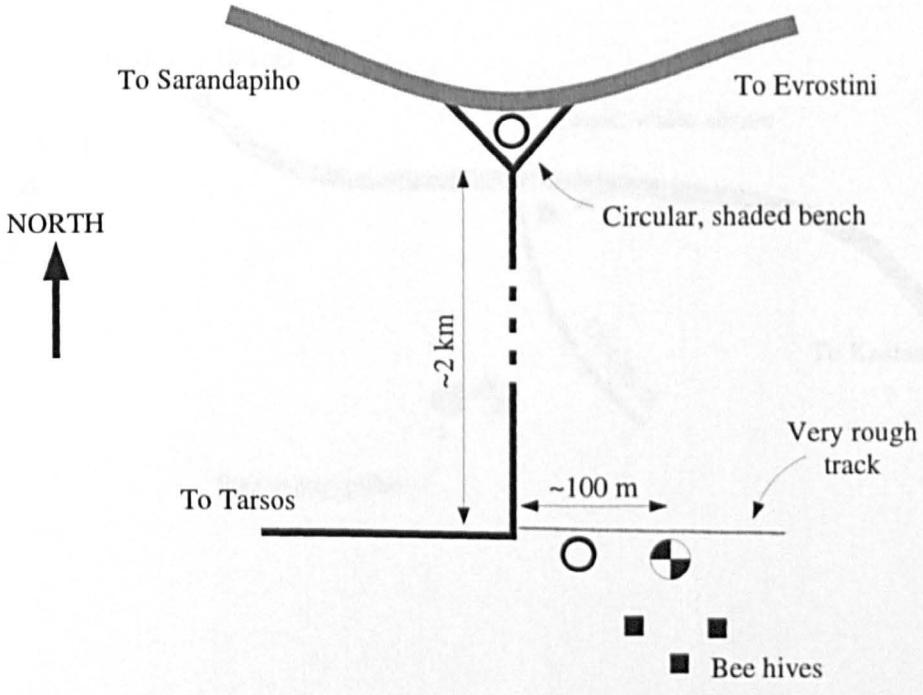

Gravity Base Station Description

Station name:Mossia
Established by: T. King
Date established: 6/6/94
Longitude: 22.3467 Latitude: 37.8817
Elevation: 908 m
Method of elevation determination: Determined by HMGS
Absolute gravity value: 979769.413 ± 0.020
Established by tying with: Sarandapiho

Comments: Base established at ground level due to windy conditions.

Description: Base station located 1 m from 909 m trig pillar, just off the road connecting Mossia and Kastania

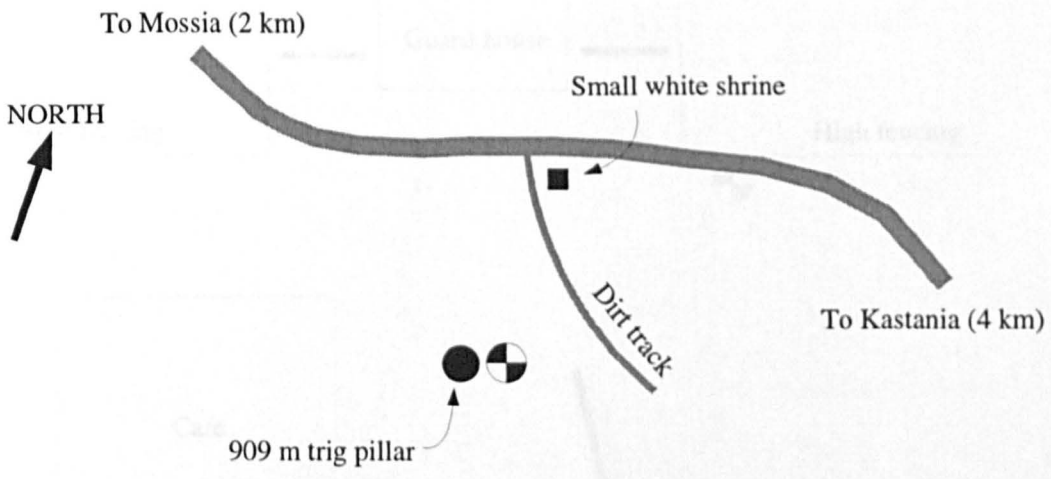

Gravity Base Station Description

Station name: Tripolis
Established by: T. King
Date established: 24/5/95
Longitude: 22.3969 Latitude: 37.5264
Elevation: 670 m
Method of elevation determination: Determined by HMGS
Absolute gravity value: 979781.921 ±0.015 mGal
Established by tying with: Corinth

Comments: Air base not marked on 1:50000 topography maps

Description: Head north out of Tripolis, and follow signs towards the northeasrt for "Αεροδρομιο", which is ~3 km outside Tripolis. To the right of the guard house is a low, circular pillar (0.35 m high). Base established on the pillar

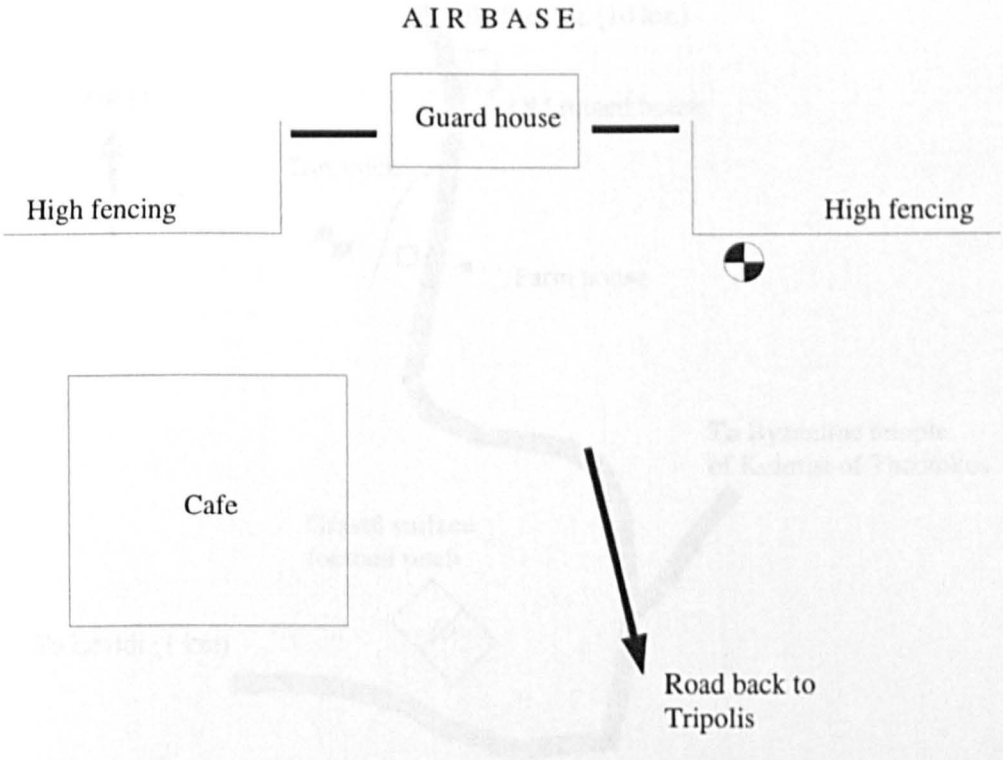

Gravity Base Station Description

Station name: Levidi
Established by: T. King
Date established: 25/6/94
Longitude: 22.3100 Latitude: 37.6950
Elevation: 704 m
Method of elevation determination: Determined be HMGS
Absolute gravity value: 979783.071 ±0.020 mGal
Established by tying with: Tripolis

Comments: Base established on the 704 m trig pillar

Description: Driving from Levidi towards Kandilla, the 704 m trig pillar can be seen to the west from the road, ~2 km from Levadi.

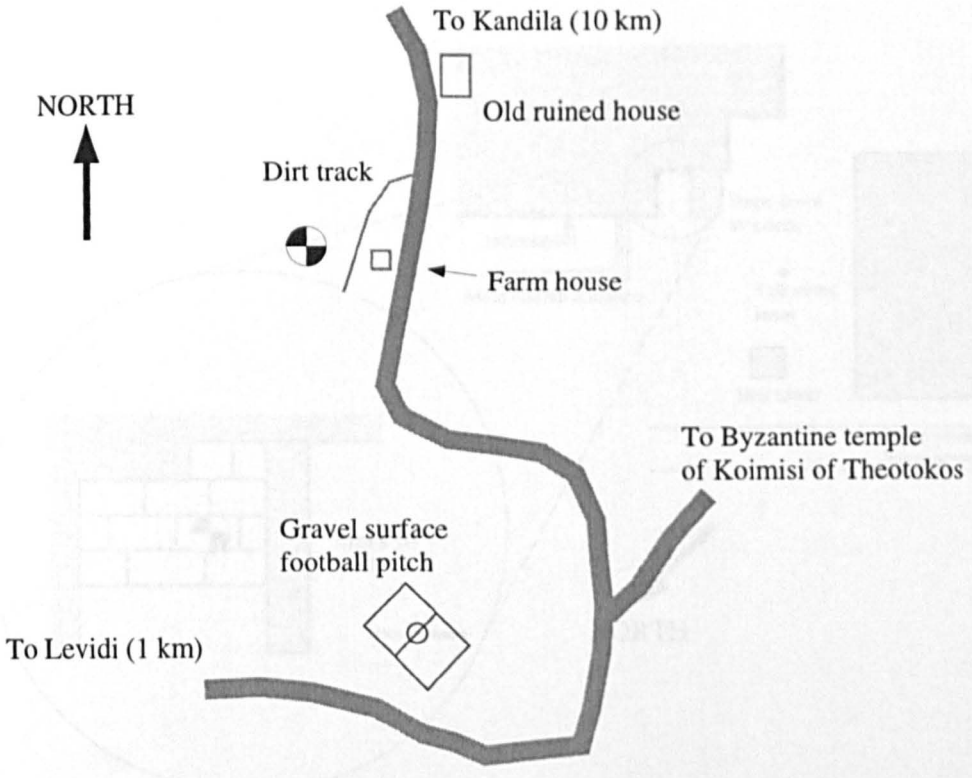

Gravity Base Station Description

Station name: Patras
Established by: T. King
Date established: 25/5/95
Longitude: 21.7260 Latitude: 38.2312
Elevation: 4.7 m
Method of elevation determination: Barometric levelling from shore and trig pillars
Absolute gravity value: 979882.674 ±0.020 mGal
Established by tying with: Corinth

Comments:

Description: Agios Andreas is situated near to the ferry terminal.
Base established at north-eastern side of Agios Andreas, to the south-west of the main gravity entrance. The groud is paved, and the base is at the very centre of the paving shown in the diagram

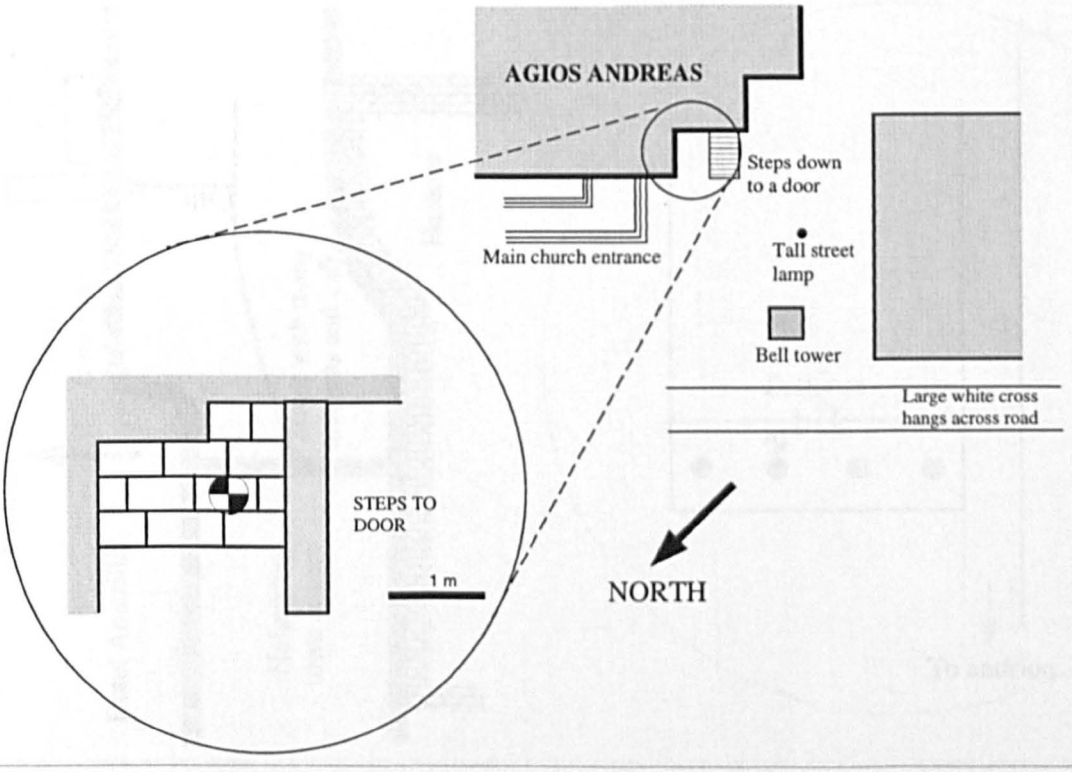

Gravity Base Station Description

Station name: Nafpaktos
Established by: T. King
Date established: 29/5/95
Longitude: 21.8307 Latitude: 38.3950
Elevation:
Method of elevation determination:
Absolute gravity value: 979910.755
Established by tying with: Patras

Comments: No elevation estimate made.

Description: Base established at the enrtance to Agios Dimitrios, behind the second column from the left (when facing the entrance). Edge of base plate is 10 cm from edge of column.

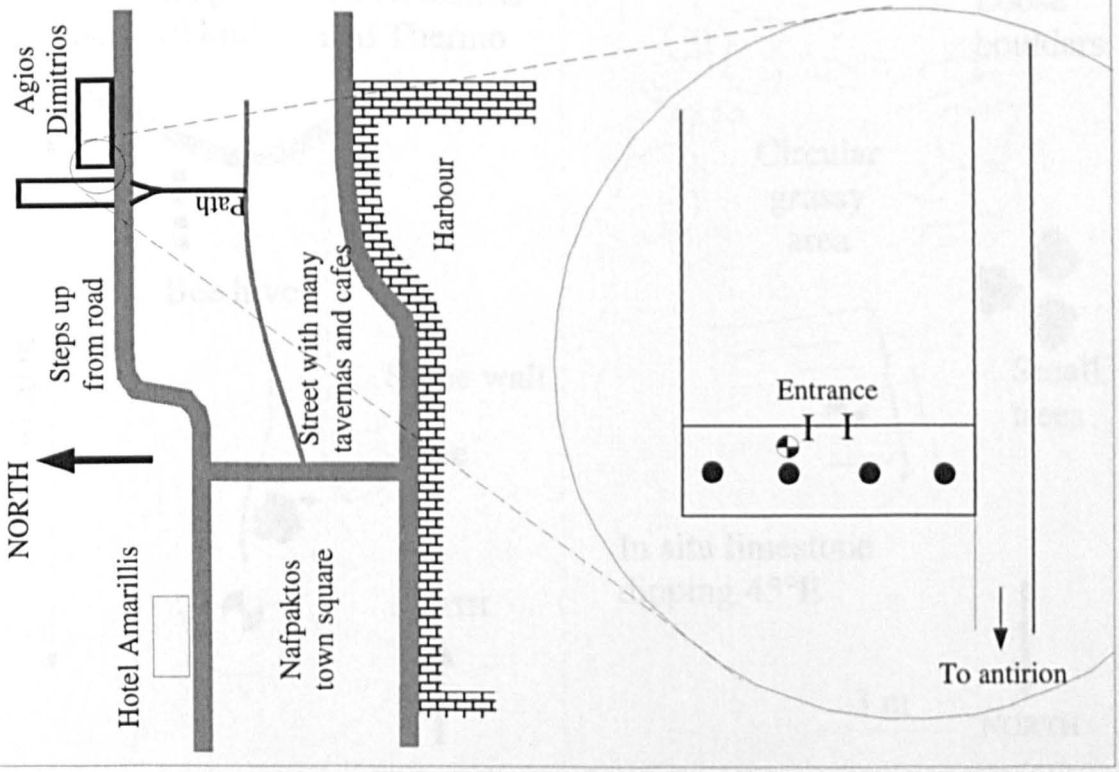

Gravity Base Station Description

Station name: Nerosirtis
Established by: T. King
Date established: 12/6/94
Longitude: 21.6522 Latitude: 38.6785
Elevation: 994.5 m
Method of elevation determination: Differential GPS from Prousos
Absolute gravity value: 979721.873 ±0.025 mGal
Established by tying with: Thermo

Comments: Thermo gravity value taken from difference relative to Nafpaktos, in Lagios [1985].
Most easily approached from South (Thermo).

Description: Very obvious spur is ~2 km by road from Nerostirtis. Base established at its southern end, on the lase outcrop of limestone before a circular grassy area.

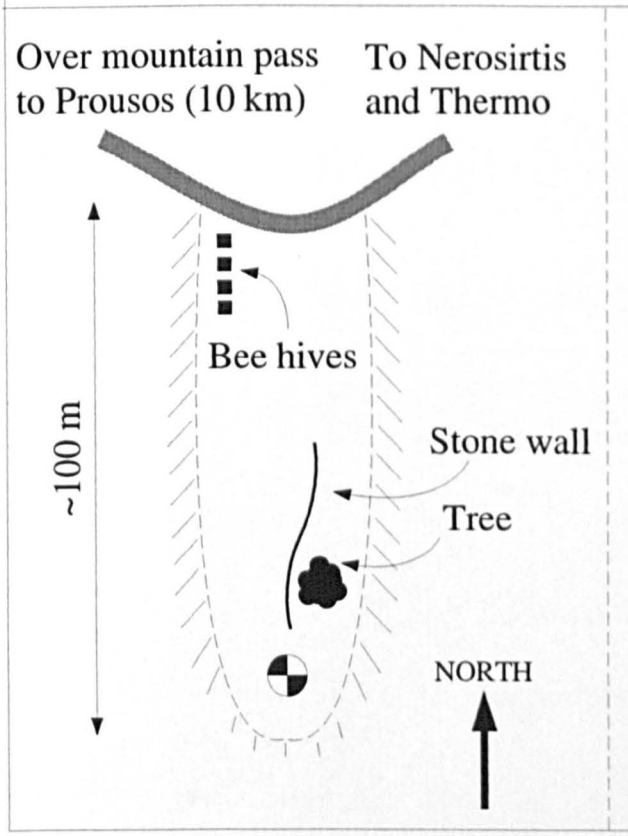

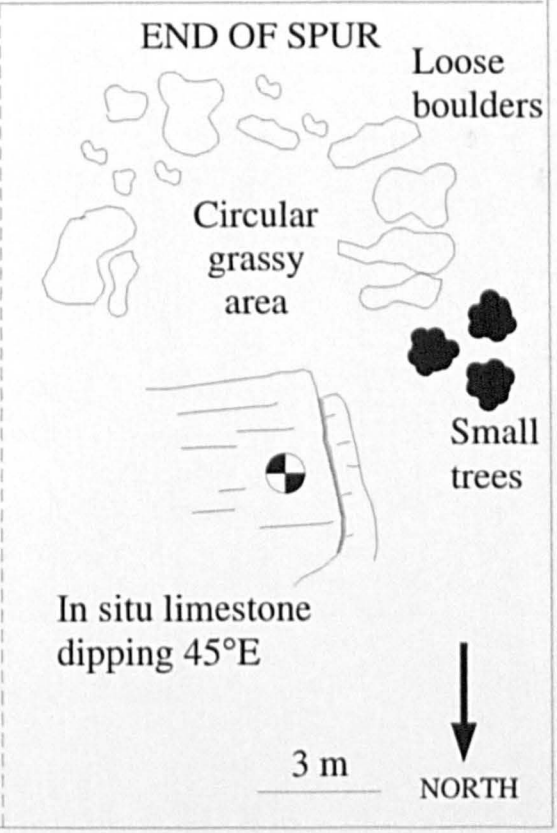

Appendix D

GPS Station Descriptions

GPS Station Description

Station name: Proussos
Established by: T. King
Date established: 20/5/94
Longitude: 21.6518 Latitude: 38.7346
Elevation of ground level above OSU91A geoid: 792.4 m
Height of geoid above WGS84 ellipse: 30.2
CPDOP: 10.2
Carrier phase measurements: 1330
Established by differencing with: Karpenissi (GPS station 13)

Comments:

Description: 0.5 km south of Proussos, a wooden bridge crosses a stream before the track climbs into the mountains. Just before the bridge, a rough track leads down into the valley. A large sign stands at the junction. The GPS site is 4.9 m form the first (eastern) post, and 3.8 m from the second one.

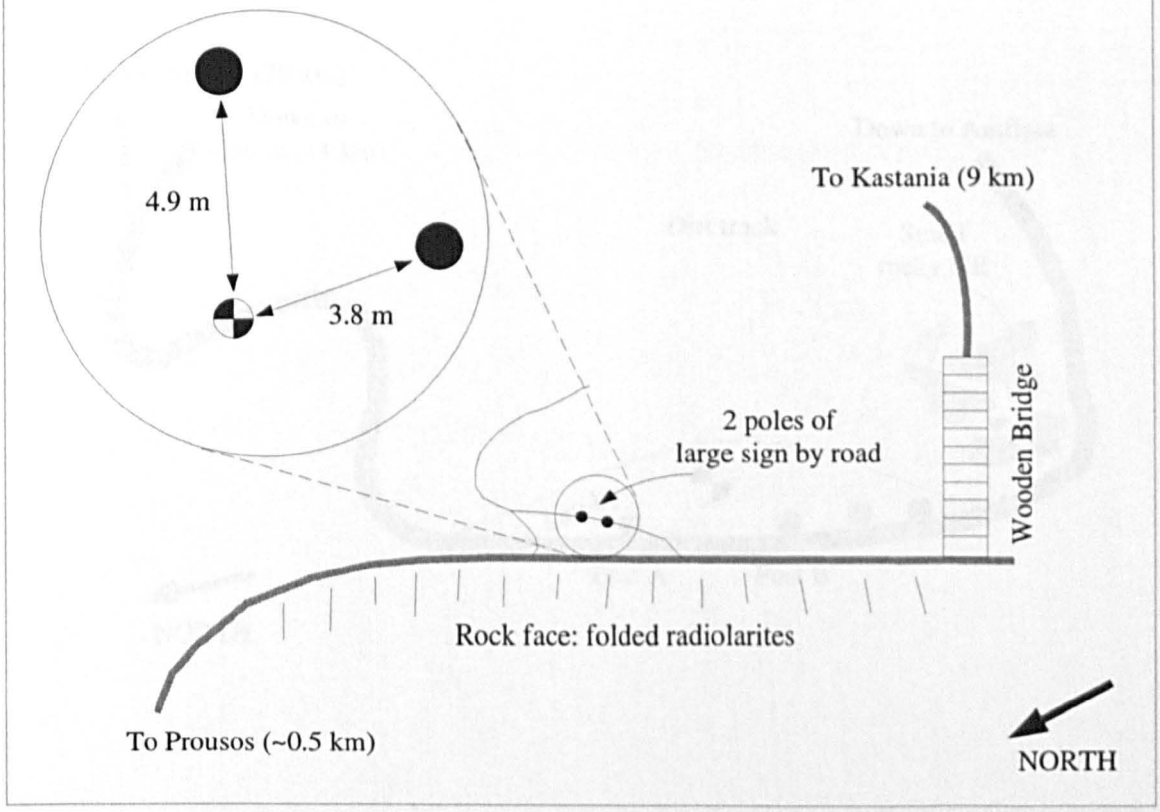

GPS Station Description

Station name: GTA
Established by: T. King
Date established: 22/5/94
Longitude: 22.3762 Latitude: 38.6323
Elevation of ground level above OSU91A geoid: 874.9 m
Height of geoid above WGS84 ellipse: 33.9 m
CPDOP: 8.6
Carrier phase measurements: 1499
Established by differencing with:Lamia (Station 19)

Comments: Immediate terrain is flat, so precise relocation may not be necessary.

Description: Station located at the highest point on the road from Gravia to Amfissa. Antenna placed between two concrete posts (~80 cm high): 23.9 m from Post A, and 28.0 m from Post B.

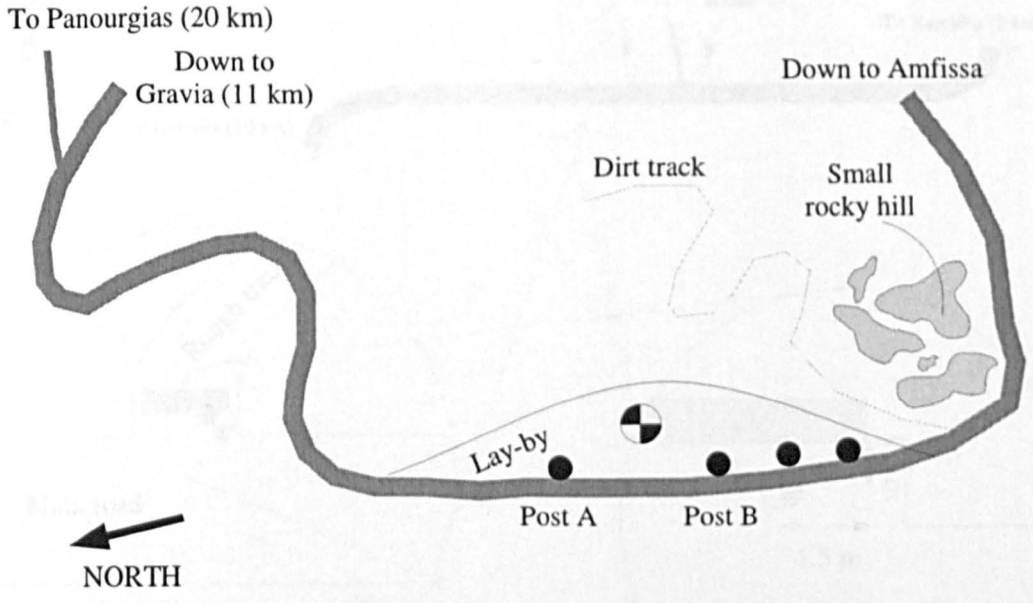

GPS Station Description

Station name: Kandilla
Established by: T. King
Date established: 7/6/94
Longitude: 22.3630 Latitude: 37.7512
Elevation of ground level above OSU91A geoid: 653.0 m
Height of geoid above WGS84 ellipse: 31.7
CPDOP: 9.4
Carrier phase measurements: 1499
Established by differencing with: Karteri (GPS station 62)

Comments: Immediate terrain is flat, so precisr relocation may not be necessary

Description: Station is located beside the road between Kandilla and Levadia. A concrete slab (10 m long, 0.5m wide) froms the entrance to a rough, stoney track, near to the 55 km marker. The slab is 1 m from the main road, and the GPS site is midway between, 1.5 m in form the slab's eastern end.

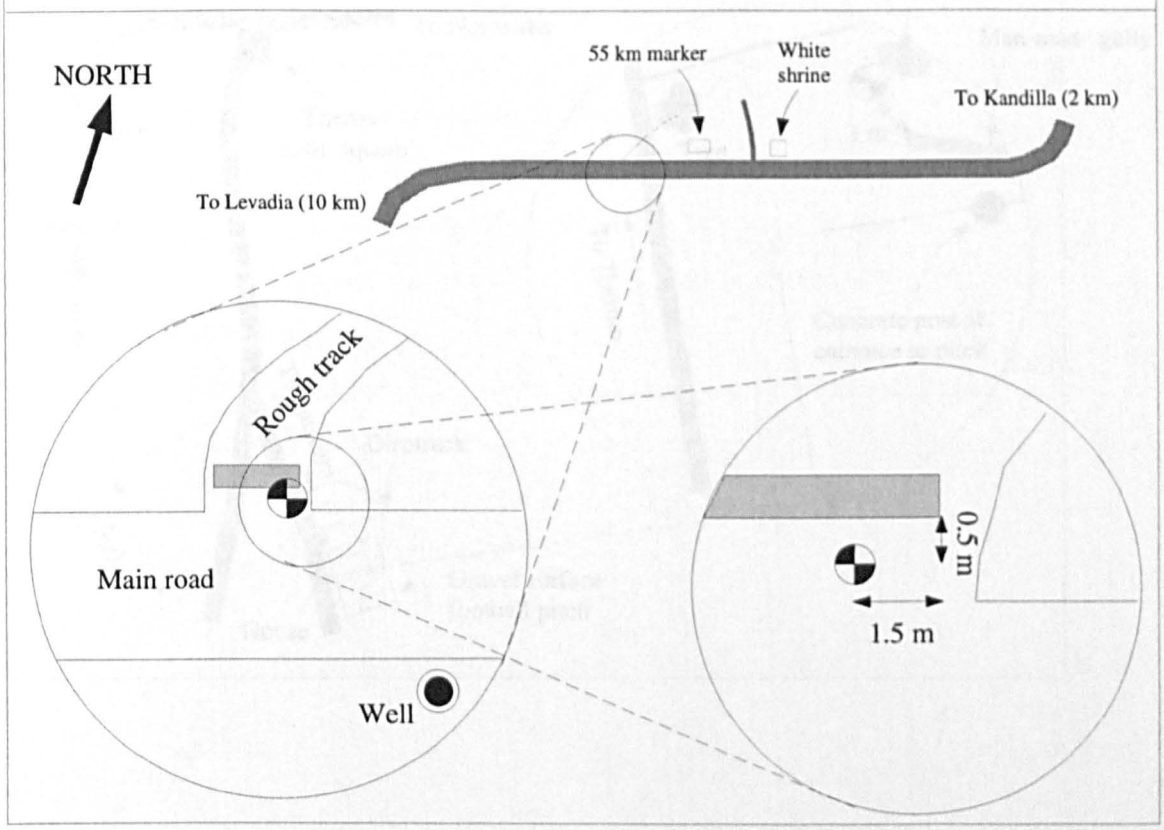

GPS Station Description

Station name: Thermo
Established by: T. King
Date established: 11/6/94
Longitude: 21.6522 Latitude: 38.6785
Elevation of ground level above OSU91A geoid: 352.3
Height of geoid above WGS84 ellipse: 29.3
CPDOP: 10.9
Carrier phase measurements: 1128
Established by differencing with: Nerosirtis

Comments:

Description: Follow signs for "Museum"south of Thermo. ~0.5 km south of Thermo, follow fork to left (east). GPS station is ~300 m down this road, near to a gravel-surface football pitch. Precise location is 3 m from a man made gully, next to an outcrup of limestone.

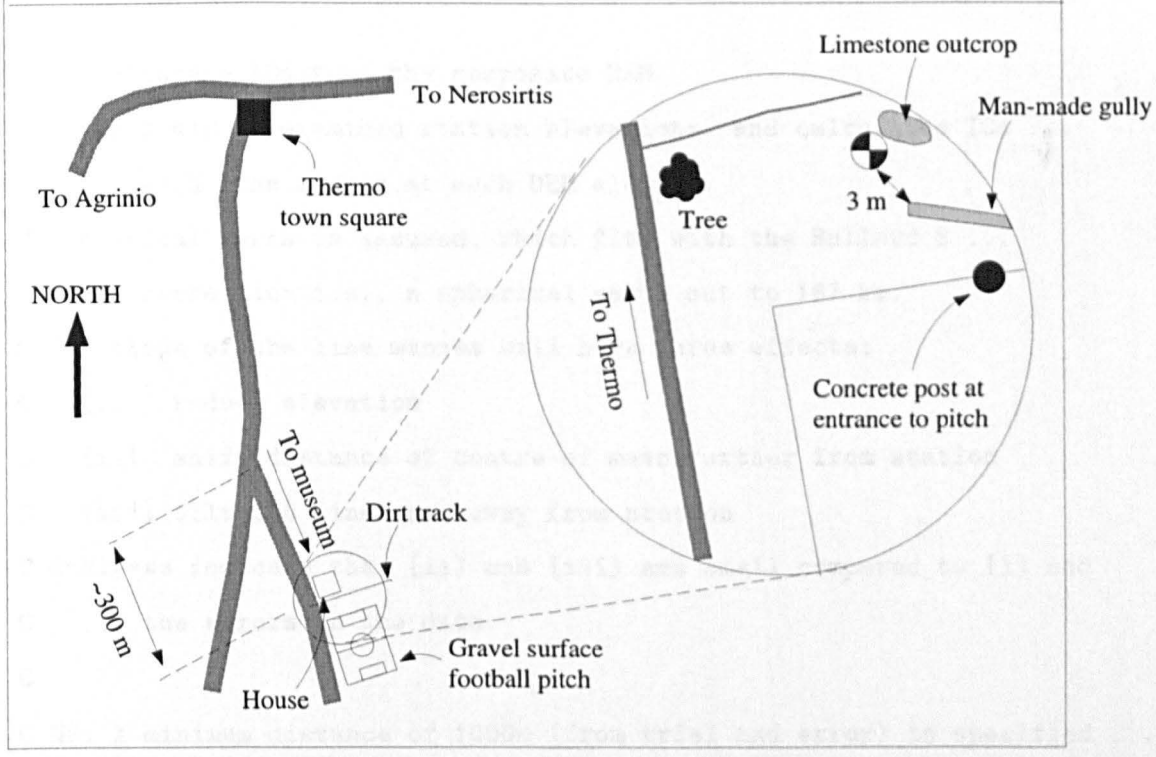

Appendix E

Terrain Correction Calculation

```
C       1         2         3         4         5         6         7

      PROGRAM TCCALC
      IMPLICIT NONE

C To calculate TCs from the composite DEM
C Takes field deteremined station elevations, and calculates TCs ...
C   ... with line masses at each DEM element.
C A sperical earth is assumed, which fits with the Bullard B ...
C   ... correction i.e., a spherical earth out to 167 km.
C The slope of the line masses will have three effects:
C   [i]   reduce elevation
C   [ii]  shift distance of centre of mass further from station
C   [iii] tilt the line mass away from station
C Analyses indicate that [ii] and [iii] are small compared to [i] and
C   ... the errors in the data.
C
C NB. A minimum distance of 1000m (from trial and error) is specified ...
C  ....(as well as the maximum of 167 km).
C ie., If DIST is very small, TC becomes unrealistically large.
C
C The DEM is a composite of  (coded 1 or 2):
```

```
C  [1] 2 km DEM
C  [2] ETOPO5, to fill in the surrounding area such that all gravity ...
C   ... stations have at least 167 km of DEM all around.
C   NB. The Bouguer slab out to 167 km is curved. Thus, TCs must be ...
C   ... calculated out to the distance R.theta = 167000.
C
C There are 4 general cases:
C  CASE 1 - Land gravity station, land DEM element
C  CASE 2 - Land gravity station, marine DEM element
C  CASE 3 - Marine gravity station, land DEM element
C  CASE 4 - Marine gravity station, marine DEM element
C NB. A marine case is assumed for negative elevations.
C
C Gravity station file format:
C  GLON GLAT GELEV TCOLD
C  TCOLD is that from the original data-set, where calculated.
C
C  DEM format:
C  CODE(1/2) DLON DLAT DELEV


      DOUBLE PRECISION GLON,GLAT,GELEV,TCOLD,DLON,DLAT,DELEV
      DOUBLE PRECISION GCOLAT,DCOLAT,TC,DELTC
      DOUBLE PRECISION DH1,DH2,DROP,A
      DOUBLE PRECISION X,Y,DELTA,DIST,SEP
      DOUBLE PRECISION R,RHOR,RHOW,G,PI
      CHARACTER*25 GRAVIN,DEMIN,FILEOUT
      INTEGER I,J,CODE,NUMBER


      G=6.6732E-11
      R=6371000.0
      RHOR=2670.0
      RHOW=1030.0
```

```
      PI=4.0*ATAN(1.0)

      PRINT*, '    Names of gravityfile, DEMfile and outputfile?'
      READ*, GRAVIN,DEMIN,FILEOUT

      OPEN (UNIT=1,FILE=GRAVIN)
      OPEN (UNIT=3,FILE=FILEOUT)

CCCCCCCCCCCCCCCCCCCCCCCCCCCCCCCCCCCCCCCCCCCCCCCCC
CCCCCCCCC  Start of TC calculations CCCCCCCCCC
CCCCCCCCCCCCCCCCCCCCCCCCCCCCCCCCCCCCCCCCCCCCCCCCC

C Each point of the gravity station file is dealt with in turn.

      DO 100 I=1,1000000
       READ (1,200,END=900) GLON,GLAT,GELEV,TCOLD
        GLON=GLON*PI/180.0
        GLAT=GLAT*PI/180.0

        OPEN (UNIT=2,FILE=DEMIN)

        TC=0.0
        NUMBER=0

        DO 1100 J=1,1000000
         READ (2,1200,END=1900) CODE,DLON,DLAT,DELEV
         DLON=DLON*PI/180.0
         DLAT=DLAT*PI/180.0

         IF (CODE.EQ.1) THEN
          X=0.023
          Y=0.018
         ENDIF
```

```
      IF (CODE.EQ.2) THEN
       X=5.0/60.0
       Y=5.0/60.0
      ENDIF

      X=X*PI/180.0
      Y=Y*PI/180.0

C The difference in cell area beteween a flat and a curved area is ...
C  ... almost zero. Variable A is therefore the flat area.

      A=(2.0*R*SIN(X/2.0))*(2.0*R*SIN(Y/2.0))*COS(DLAT)

C     PRINT*,'A = ',A,' and should be close to ',(R*X)*(R*Y)*COS(DLAT)

C This simple equation for DELTA only works if both points are ...
C  ... in the eastern half of northern hemisphere.

      GCOLAT=(PI/2.0)-GLAT
      DCOLAT=(PI/2.0)-DLAT
      DELTA=ACOS((SIN(GCOLAT)*COS(GLON)*SIN(DCOLAT)*COS(DLON)) +
     1      (SIN(GCOLAT)*SIN(GLON)*SIN(DCOLAT)*SIN(DLON)) +
     2      (COS(GCOLAT)*COS(DCOLAT)))

      SEP=R*DELTA
      DIST=R*SIN(DELTA)
      DROP=(R*COS(DELTA))-R

      IF (SEP.GE.1000 .AND. SEP.LE.167000) THEN

      NUMBER = NUMBER+1

      IF (GELEV.GE.0.0 .AND. DELEV.GE.0.0) GOTO 2100
```

```
      IF (GELEV.GE.0.0 .AND. DELEV.LT.0.0) GOTO 2200
      IF (GELEV.LT.0.0 .AND. DELEV.GE.0.0) GOTO 2300
      IF (GELEV.LT.0.0 .AND. DELEV.LT.0.0) GOTO 2400
      ELSE
       DELTC=0.0
       GOTO 3000
      ENDIF

C CASE 1 - Land gravity station, land DEM element

2100  DH1=ABS(GELEV-DELEV-DROP)
      DELTC=RHOR*G*A*
     1          ((1/(SQRT((SEP**2.0)+(DROP**2.0))))-
     2          (1/(SQRT((SEP**2.0)+(DH1**2.0)))))
       GOTO 3000

C CASE 2 - Land gravity station, marine DEM element

2200  DH1=ABS(GELEV-DROP)
      DH2=ABS(GELEV-DELEV-DROP)
      DELTC=RHOR*G*A*
     1          ((1/(SQRT((SEP**2.0)+(DROP**2.0))))-
     2          (1/(SQRT((SEP**2.0)+(DH1**2.0)))))
      DELTC=DELTC + ((RHOR-RHOW)*G*A*
     1          ((1/(SQRT((SEP**2.0)+(DH1**2.0))))-
     2          (1/(SQRT((SEP**2.0)+(DH2**2.0))))))
       GOTO 3000

C CASE 3 - Marine gravity station, land DEM element

2300  DH1=ABS(DELEV+DROP)
      DH2=ABS(GELEV+DROP)
      DELTC=RHOR*G*A*((1/DIST)-
```

```
     1          (1/(SQRT((DIST**2.0)+(DH1**2.0)))))
        DELTC=DELTC - (RHOR*G*A*
     1          ((1/DIST)-(1/(SQRT((DIST**2.0)+(DROP**2.0))))))
        DELTC=DELTC - ((RHOR-RHOW)*G*A*
     1          ((1/(SQRT((DIST**2.0)+(DROP**2.0))))-
     2          (1/(SQRT((DIST**2.0)+(DH2**2.0))))))
         GOTO 3000

C CASE 4 - Marine gravity station, marine DEM element

2400     DH1=ABS(DROP+DELEV)
         DH2=ABS(DROP+GELEV)
         DELTC=(RHOR-RHOW)*G*A*
     1          ((1/(SQRT((DIST**2.0)+(DH2**2.0))))-
     2          (1/(SQRT((DIST**2.0)+(DH1**2.0)))))
         GOTO 3000

3000     TC=TC + DELTC

1100    CONTINUE

1900    GLON=GLON*180.0/PI
        GLAT=GLAT*180.0/PI
        WRITE (3,3100) GLON,GLAT,GELEV,TCOLD,(TC*1.0E+5)
        CLOSE(2)

         PRINT*, I,NUMBER
100     CONTINUE

900     PRINT*, '   End of gravity station file at line ',I-1

       CLOSE(1)
       CLOSE(3)
```

```
200     FORMAT (F8.4,1X, F8.4,1X, F8.2,1X, F10.4)
1200    FORMAT (I1,1X, F8.4,1X, F8.4,1X, F8.2)
3100    FORMAT (F8.4,1X, F8.4,1X, F8.2,1X, F10.4,1X, F10.4)


        STOP
        END
```

Appendix F

Data Listing

LON	LAT	ELEV	G_OBS	G_REF	G_ATM	FAC	BC+CC	TC
21.7950	38.9167	940.00	979764.232	980073.688	0.7804	290.0840	106.2780	5.2355
21.7984	38.9053	969.60	979761.259	980072.688	0.7776	299.2186	109.6145	3.2632
21.7533	38.8683	719.60	979800.732	980069.438	0.8014	222.0686	81.4152	8.5404
21.7367	38.8450	669.60	979803.416	980067.375	0.8062	206.6386	75.7700	9.6488
21.7317	38.8217	585.30	979807.765	980065.312	0.8143	180.6236	66.2482	16.3427
21.7100	38.7967	504.10	979822.978	980063.062	0.8221	155.5653	57.0719	26.1860
21.6518	38.7346	792.70	979767.010	980057.625	0.7944	244.6272	89.6652	7.5627
21.6683	38.7550	707.90	979788.621	980059.438	0.8025	218.4579	80.0943	7.2356
21.7817	38.8583	857.60	979772.191	980068.562	0.7882	264.6554	96.9867	4.5039
21.7617	38.9383	1368.70	979675.487	980075.625	0.7405	422.3808	154.5407	6.9283
21.7217	38.9750	794.10	979795.919	980078.875	0.7942	245.0593	89.8232	3.6708
22.4293	38.6721	402.50	979939.253	980052.062	0.8319	124.2115	45.5836	9.7306
22.3762	38.6323	875.20	979836.962	980048.562	0.7865	270.0867	98.9716	8.8137
22.4233	38.6550	592.80	979898.659	980050.562	0.8135	182.9381	67.0956	8.5666
22.4517	38.7000	392.90	979941.087	980054.562	0.8329	121.2489	44.4978	3.4660
22.4567	38.7517	614.30	979899.127	980059.125	0.8115	189.5730	69.5244	3.3137
22.4480	38.7807	526.10	979912.731	980061.688	0.8200	162.3545	59.5586	5.0881
22.3109	39.1247	523.10	979961.660	980092.125	0.8203	161.4287	59.2195	1.3947
22.3117	39.1433	467.30	979973.849	980093.750	0.8257	144.2088	52.9116	1.5393
22.2950	39.1567	185.90	980031.814	980094.938	0.8528	57.3687	21.0676	1.4391
22.2767	39.1917	132.30	980048.774	980098.000	0.8579	40.8278	14.9958	0.8012
22.2817	39.2433	203.30	980040.669	980102.625	0.8512	62.7384	23.0383	0.7376
22.2783	39.2467	180.30	980045.870	980102.875	0.8534	55.6406	20.4333	0.5833
22.4283	38.9067	182.40	979996.604	980072.812	0.8532	56.2886	20.6712	2.2306

22.4150	38.9367	287.40	979977.664	980075.438	0.8431	88.6916	32.5601	2.0981
22.3767	38.9900	754.10	979883.279	980080.188	0.7980	232.7153	85.3093	3.7020
22.3386	39.0311	514.60	979937.278	980083.812	0.8211	158.8056	58.2588	1.1554
22.3150	39.0783	470.70	979952.101	980088.000	0.8253	145.2580	53.2961	0.8714
22.3983	38.1200	169.00	979935.560	980003.500	0.8545	52.1534	19.1534	8.0059
22.4050	38.1350	14.30	979971.530	980004.812	0.8688	4.4130	1.6215	7.7149
22.3817	38.0150	1416.30	979682.937	979994.250	0.7362	437.0702	159.8915	9.1622
22.4100	38.0933	625.80	979845.447	980001.125	0.8104	193.1219	70.8234	6.3677
22.3933	38.0700	684.80	979831.205	979999.125	0.8047	211.3293	77.4863	9.0476
22.3883	38.0717	919.80	979790.754	979999.250	0.7823	283.8503	104.0007	6.6058
22.3600	37.9850	941.30	979784.971	979991.625	0.7802	290.4852	106.4246	6.9769
22.3433	37.9367	1037.30	979750.288	979987.438	0.7712	320.1108	117.2434	4.8829
22.3467	37.9617	858.00	979790.919	979989.625	0.7881	264.7788	97.0318	6.7454
22.3433	37.9500	832.30	979795.856	979988.562	0.7906	256.8478	94.1329	7.2811
22.3433	37.9350	989.10	979762.901	979987.250	0.7757	305.2363	111.8122	4.9299
22.3333	37.9083	773.20	979800.645	979984.938	0.7962	238.6095	87.4648	4.7366
22.3467	37.8817	908.30	979769.413	979982.562	0.7834	280.3014	102.7041	4.3670
22.4303	37.8497	633.90	979836.584	979979.812	0.8096	195.6215	71.7383	6.1170
22.3867	37.8650	874.30	979780.872	979981.125	0.7866	269.8090	98.8701	4.9781
21.6678	38.5745	347.20	979845.803	980043.500	0.8373	107.1459	39.3276	2.5441
21.6522	38.6785	994.80	979721.873	980052.688	0.7752	306.9953	112.4546	4.0460
21.6567	38.7150	1386.80	979647.116	980055.875	0.7389	427.9665	156.5755	7.5699
21.6633	38.7000	953.20	979734.021	980054.562	0.7791	294.1575	107.7660	4.5680
21.6533	38.6800	997.10	979724.770	980052.812	0.7750	307.7051	112.7138	4.0487
21.6550	38.6567	1008.10	979721.032	980050.750	0.7740	311.0997	113.9533	4.8851
21.6683	38.6317	848.00	979753.330	980048.500	0.7891	261.6928	95.9039	4.2622
21.6550	38.6067	481.70	979820.110	980046.312	0.8243	148.6526	54.5397	3.2701
21.6467	38.5467	302.20	979849.743	980041.062	0.8416	93.2589	34.2352	4.5355
21.6583	38.5100	60.00	979900.897	980037.812	0.8647	18.5160	6.8023	2.9974
21.6617	38.4833	424.10	979829.840	980035.438	0.8298	130.8773	48.0266	3.7277
21.6733	38.4633	277.00	979863.223	980033.688	0.8441	85.4822	31.3829	1.3554
21.7017	38.4533	131.60	979891.172	980032.812	0.8580	40.6118	14.9164	3.2200
21.8307	38.3950	0.00	979910.755	980027.688	0.8700	0.0000	0.0000	3.3951
21.7667	38.3300	1.70	979901.708	980021.938	0.8699	0.5246	0.1928	1.6714
21.7533	38.3583	65.10	979895.655	980024.438	0.8642	20.0899	7.3804	1.8629
21.7317	38.3917	265.80	979862.596	980027.375	0.8452	82.0259	30.1150	2.4904
21.7417	38.3633	225.30	979866.331	980024.875	0.8491	69.5276	25.5296	1.9642
21.7367	38.4317	330.60	979847.617	980030.875	0.8389	102.0232	37.4493	1.7752

22.4400	38.8583	10.80	980022.481	980068.562	0.8691	3.3329	1.2246	2.9480
22.4467	38.8283	15.90	980017.369	980065.875	0.8687	4.9067	1.8029	3.9386
22.4467	38.7917	74.10	980002.584	980062.625	0.8634	22.8673	8.4005	7.6211
22.4367	38.8967	57.00	980022.658	980071.938	0.8650	17.5902	6.4623	2.3691
22.3783	38.5300	175.00	979961.515	980039.562	0.8539	54.0050	19.8330	13.1539
22.4033	38.5600	500.50	979904.022	980042.188	0.8225	154.4543	56.6650	5.2565
22.3783	38.6000	733.00	979860.874	980045.750	0.8001	226.2038	82.9278	5.4935
22.4150	38.4933	86.70	979984.020	980036.312	0.8622	26.7556	9.8285	7.4351
22.4367	38.4533	30.10	979997.937	980032.812	0.8674	9.2889	3.4128	4.5980
22.4283	38.4367	7.90	979999.770	980031.375	0.8694	2.4379	0.8958	3.9687
22.4117	38.4133	30.80	979992.864	980029.312	0.8674	9.5049	3.4922	3.2042
22.3783	38.3817	18.20	979989.878	980026.500	0.8685	5.6165	2.0636	4.6445
22.3833	38.3567	54.10	979981.441	980024.312	0.8653	16.6953	6.1335	3.1040
22.3969	37.5264	670.00	979781.921	979951.500	0.8061	206.7620	75.8152	2.5597
22.3100	37.6950	704.30	979783.017	979966.250	0.8028	217.3470	79.6879	6.8912
22.4033	37.5600	667.20	979791.901	979954.438	0.8064	205.8979	75.4990	2.9119
22.3800	37.5933	654.10	979795.278	979957.375	0.8076	201.8553	74.0196	4.6909
22.3500	37.6150	702.20	979783.493	979959.250	0.8030	216.6989	79.4508	8.5718
22.3250	37.7217	671.50	979792.953	979968.562	0.8060	207.2249	75.9845	4.1879
22.3629	37.7512	653.20	979802.690	979971.188	0.8077	201.5775	73.9180	5.3745
22.4050	37.7983	1160.90	979710.606	979975.312	0.7597	358.2537	131.1629	4.2458
22.3917	37.7717	941.90	979748.050	979972.938	0.7802	290.6703	106.4922	4.9427
22.2967	37.6750	862.20	979742.860	979964.500	0.7877	266.0749	97.5055	7.4760
22.3167	37.6400	793.30	979757.171	979961.438	0.7943	244.8124	89.7329	8.7151
21.7260	38.2312	4.70	979882.674	980013.250	0.8696	1.4504	0.5329	1.8930
21.7390	38.2058	29.80	979875.681	980011.062	0.8675	9.1963	3.3788	2.7318
21.7373	38.1880	93.50	979864.419	980009.438	0.8616	28.8541	10.5992	3.1491
21.7285	38.1643	207.00	979853.424	980007.375	0.8508	63.8802	23.4573	2.4809
21.7352	38.1413	259.30	979842.182	980005.375	0.8458	80.0200	29.3792	2.5008
21.7023	38.1093	109.30	979864.101	980002.562	0.8601	33.7300	12.3897	1.8494
21.7402	38.0723	200.50	979849.633	979999.312	0.8514	61.8743	22.7212	2.3744
22.2912	38.9202	57.30	980002.923	980074.000	0.8650	17.6828	6.4963	3.4116
22.2110	38.9437	77.10	979999.357	980076.062	0.8631	23.7931	8.7405	2.8635
22.1713	38.9252	103.60	979975.782	980074.438	0.8607	31.9710	11.7438	3.0509
22.1552	38.9017	172.60	979959.510	980072.375	0.8541	53.2644	19.5612	3.9455
22.2167	38.8982	120.60	979973.938	980072.062	0.8591	37.2172	13.6701	4.8594
22.2658	38.8980	99.80	979988.632	980072.062	0.8610	30.7983	11.3131	5.6333

Appendix G

Contoured Gravity Maps

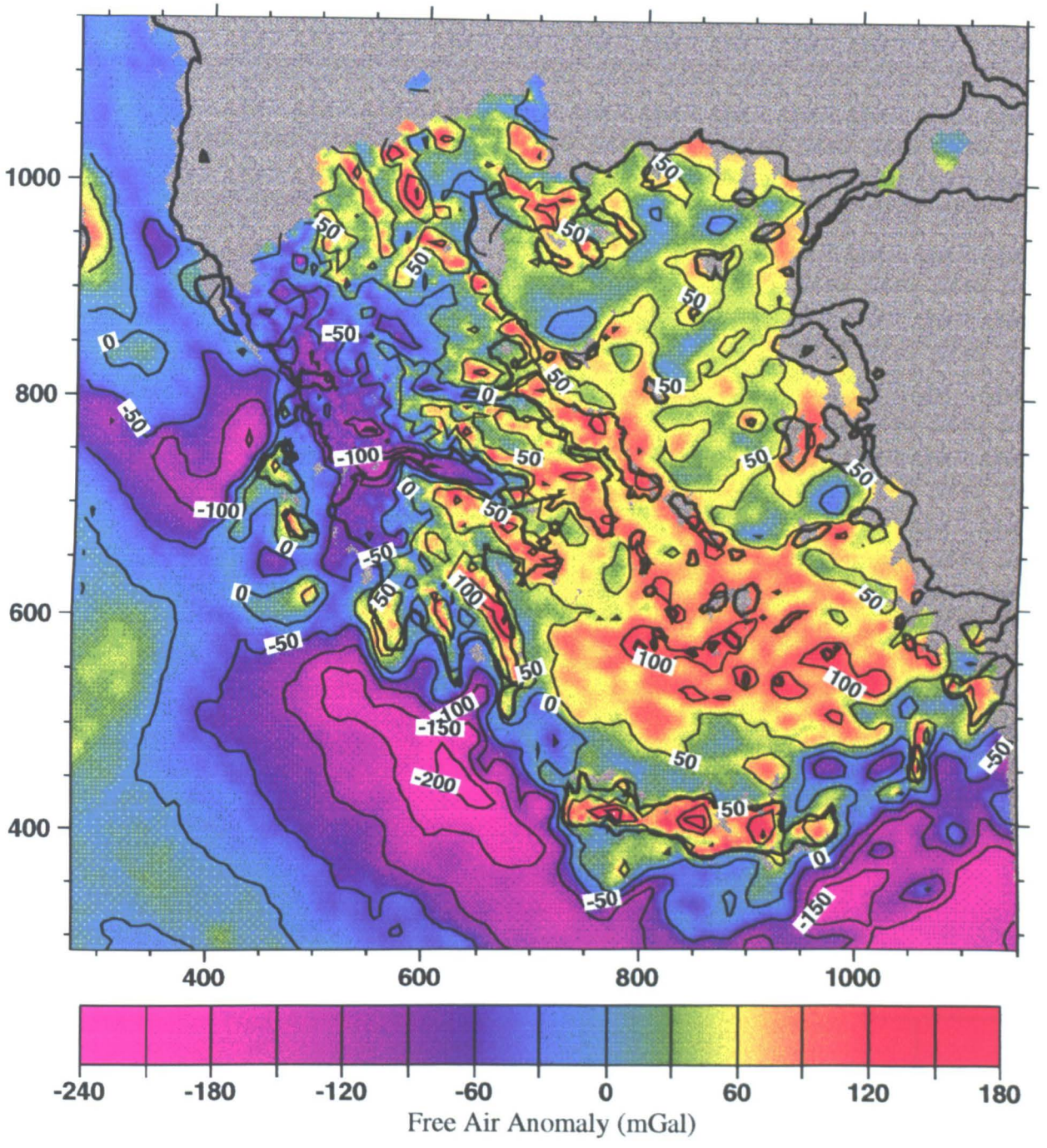

Figure G.1: Contoured free-air gravity anomaly. Contour interval = 50 mGal.

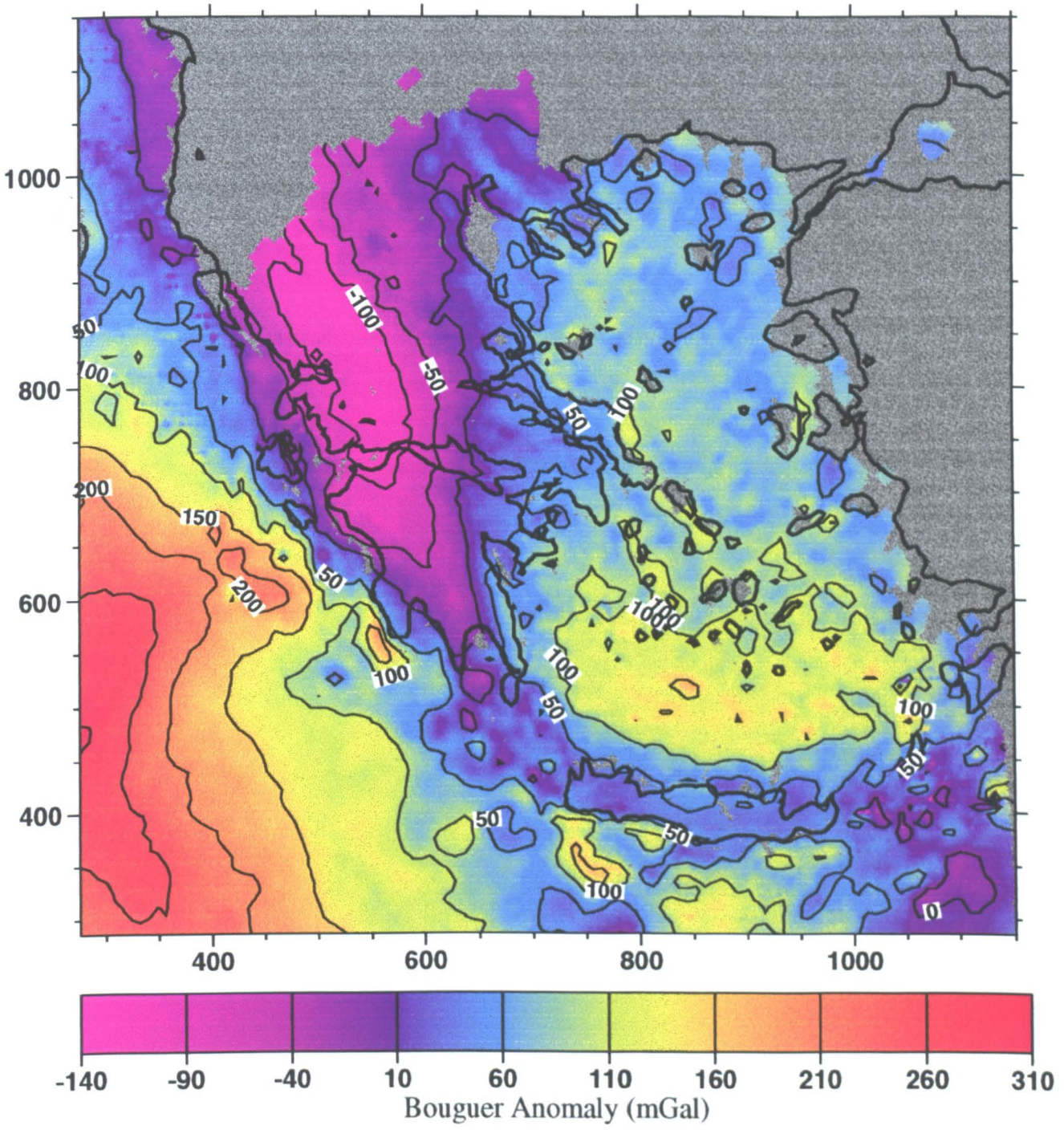

Figure G.2: Contoured Bouguer anomaly gravity. Contour interval = 50 mGal.

Appendix H

Model Gravity Anomaly Curves

The following six sets of plots are used to find the estimated basin depths presented in Chapter 5 (see Tables 5.6, 5.7 and 5.8). It is shown in Section 5.7 that the triangular beam is a good approximation to a half-graven geometry, and in Section 5.7.2 that - of the three model geometries considered - the triangular beam gives the greatest estimates for basin depth.

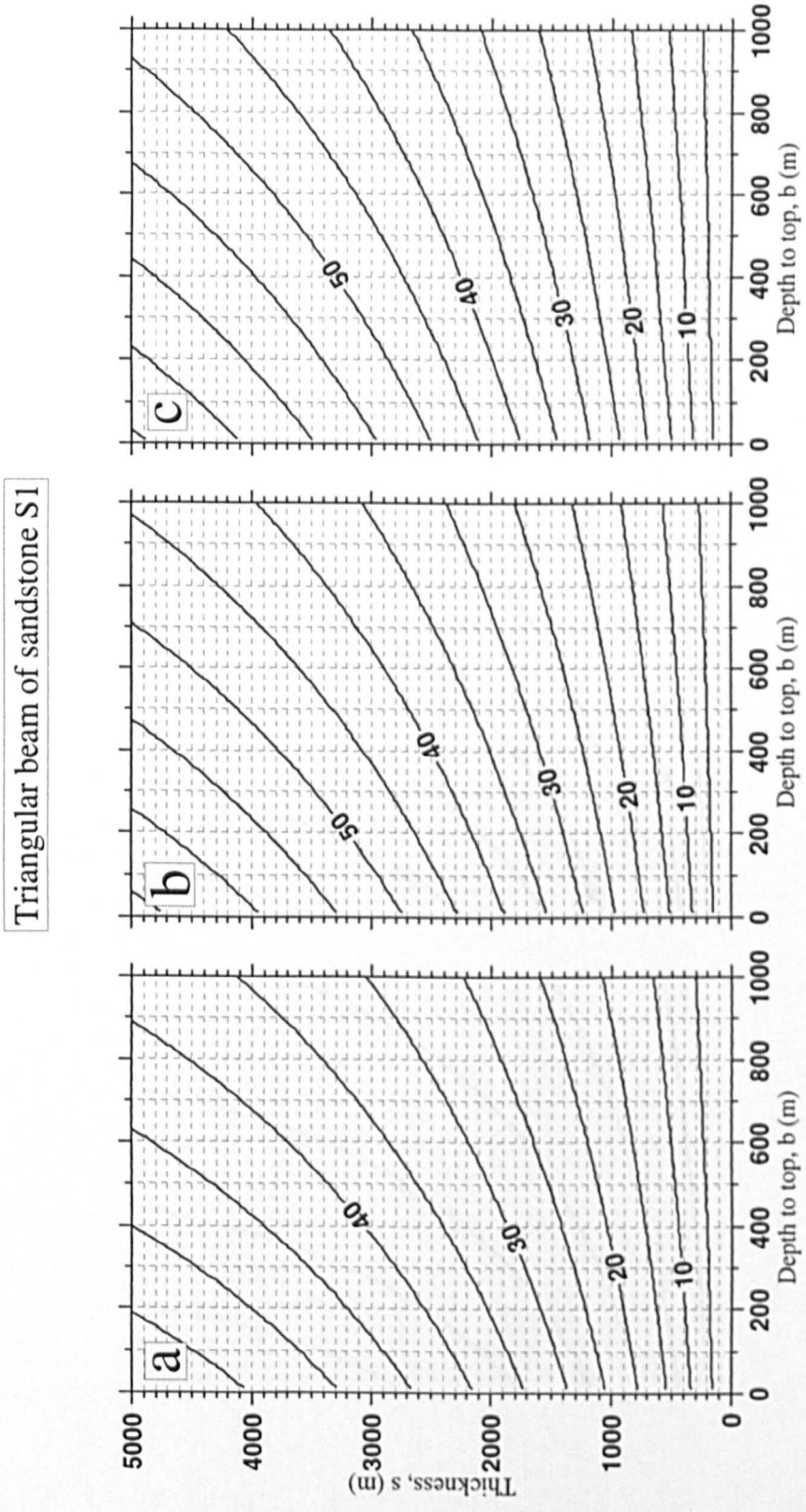

Figure H.1: Gravity anomaly magnitudes for a triangular beam of sandstone S1. Parameters taken from *Sclater and Christie* [1980]. Widths ($2a$) are (a) 10 km, (b) 15 km, and (c) 20 km. Contours in mGal.

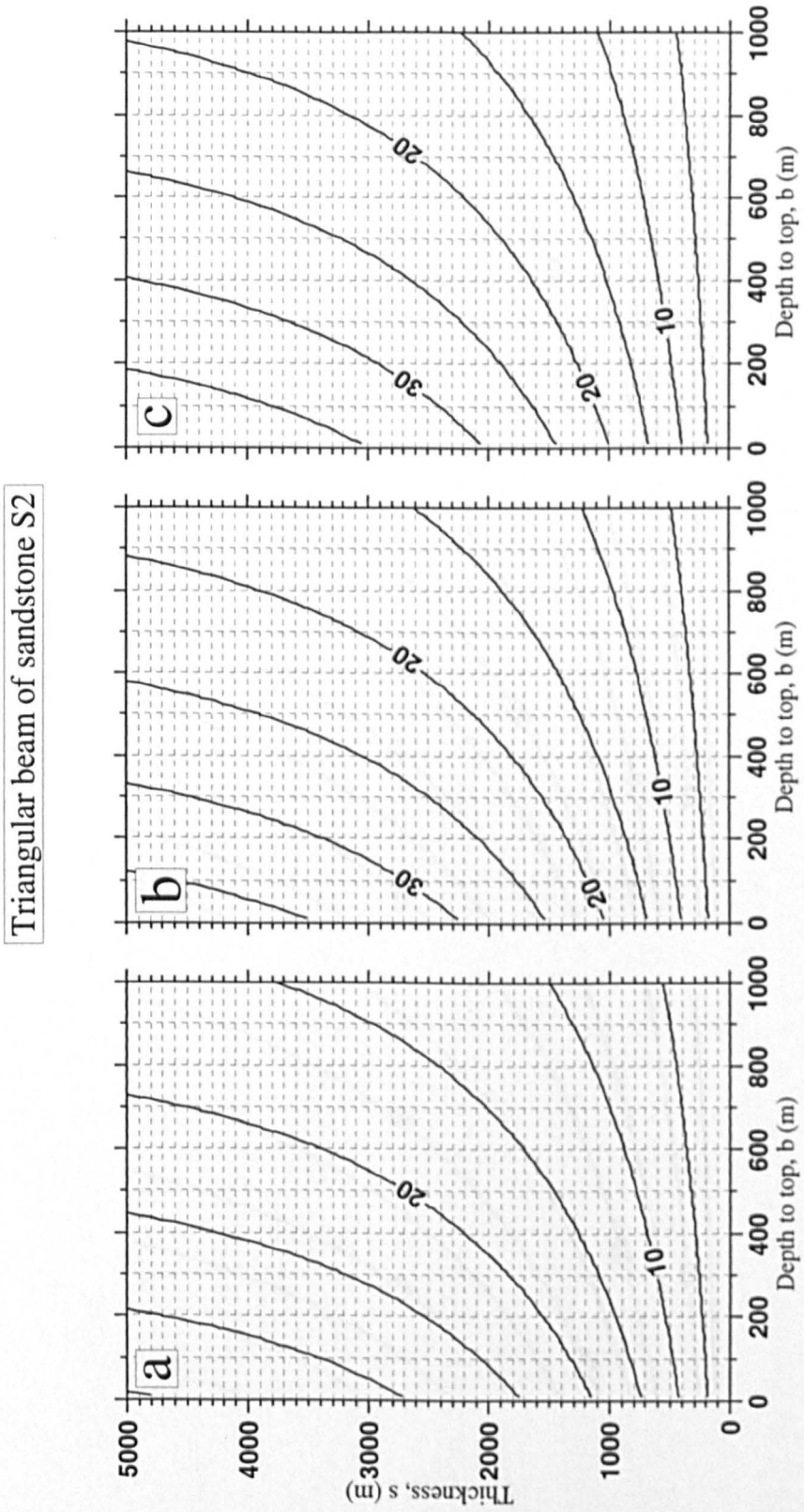

Figure H.2: Gravity anomaly magnitudes for a triangular beam of sandstone S2. Parameters taken from *Gallagher and Lambeck* [1989]. Widths ($2a$) are (a) 10 km, (b) 15 km, and (c) 20 km. Contours in mGal.

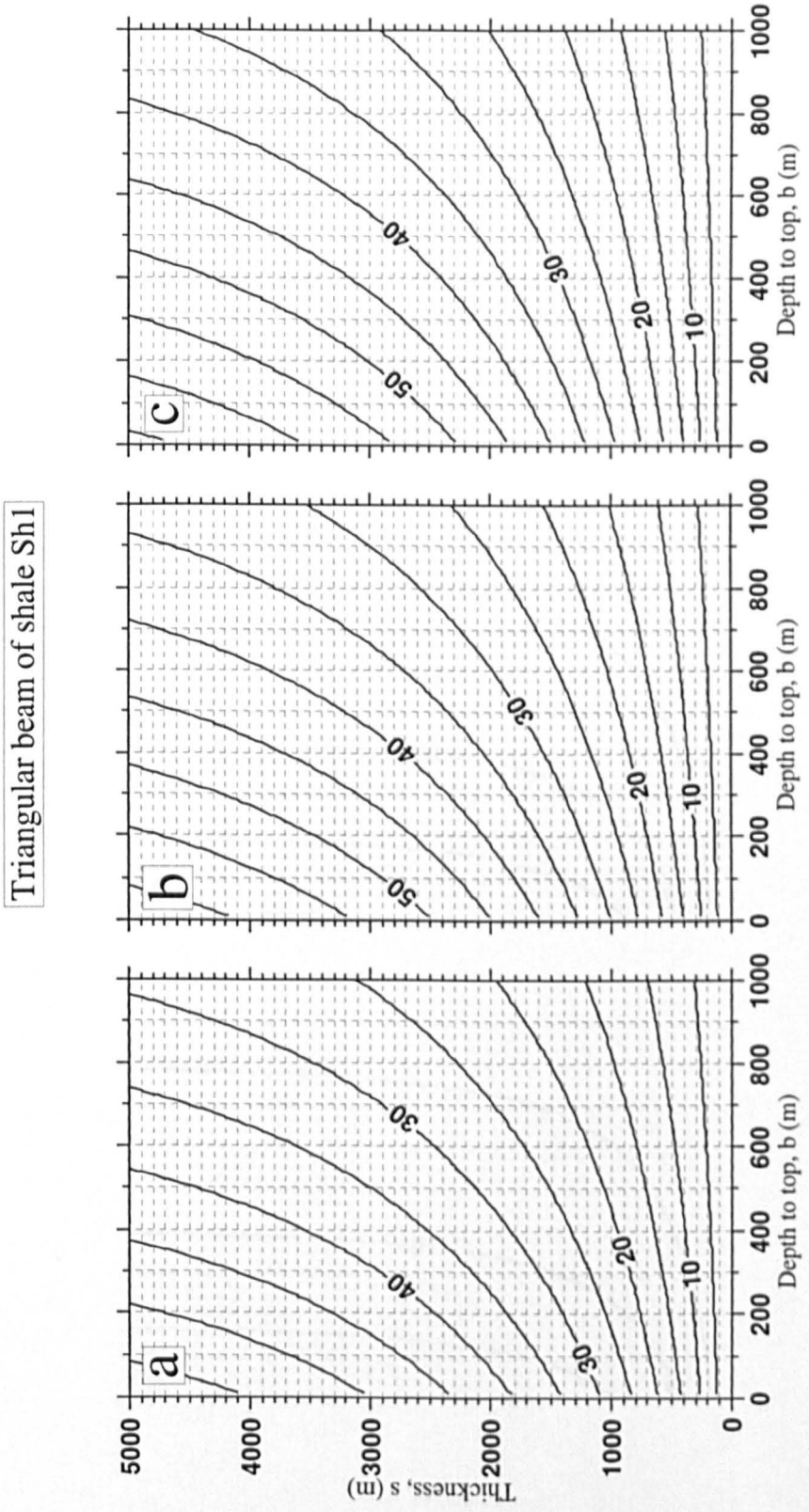

Figure H.3: Gravity anomaly magnitudes for a triangular beam of shale Sh1. Parameters taken from *Sclater and Christie* [1980]. Widths ($2a$) are (a) 10 km, (b) 15 km, and (c) 20 km. Contours in mGal.

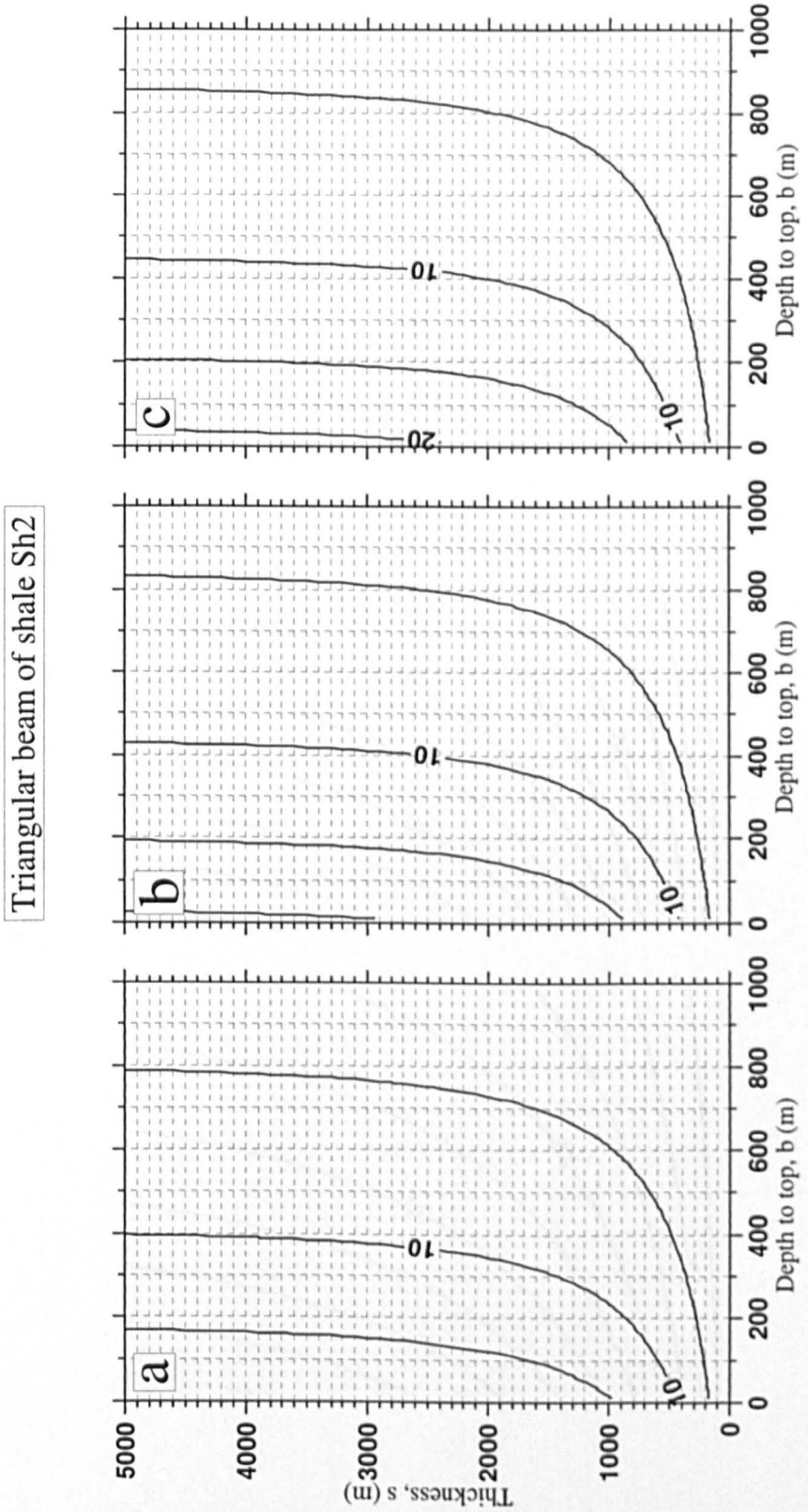

Figure H.4: Gravity anomaly magnitudes for a triangular beam of shale Sh2. Parameters taken from *Gallagher and Lambeck* [1989]. Widths ($2a$) are (a) 10 km, (b) 15 km, and (c) 20 km. Contours in mGal.

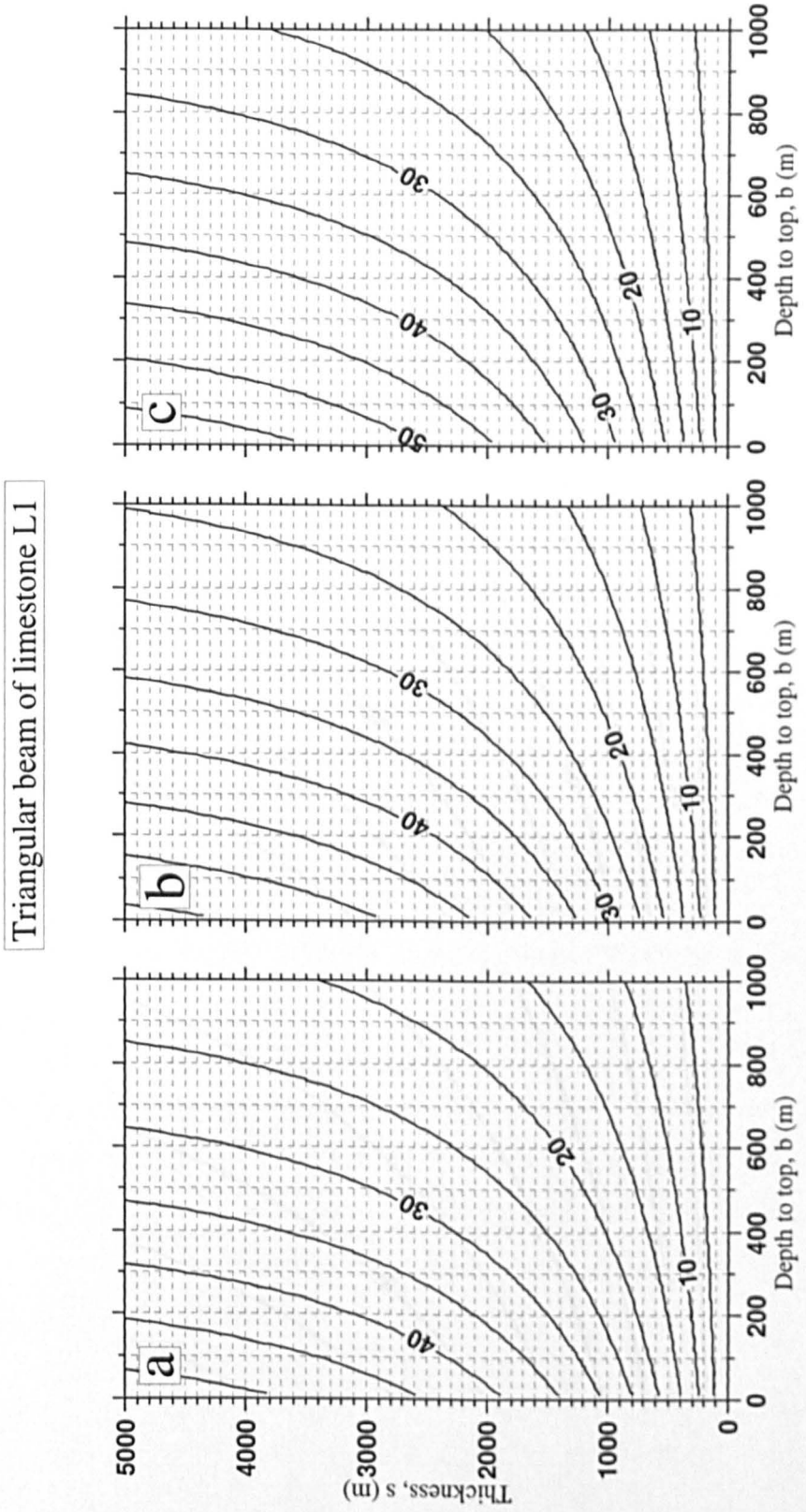

Figure H.5: Gravity anomaly magnitudes for a triangular beam of carbonate L1. Parameters taken from *Schmoker and Halley* [1982]. Widths ($2a$) are (a) 10 km, (b) 15 km, and (c) 20 km. Contours in mGal.

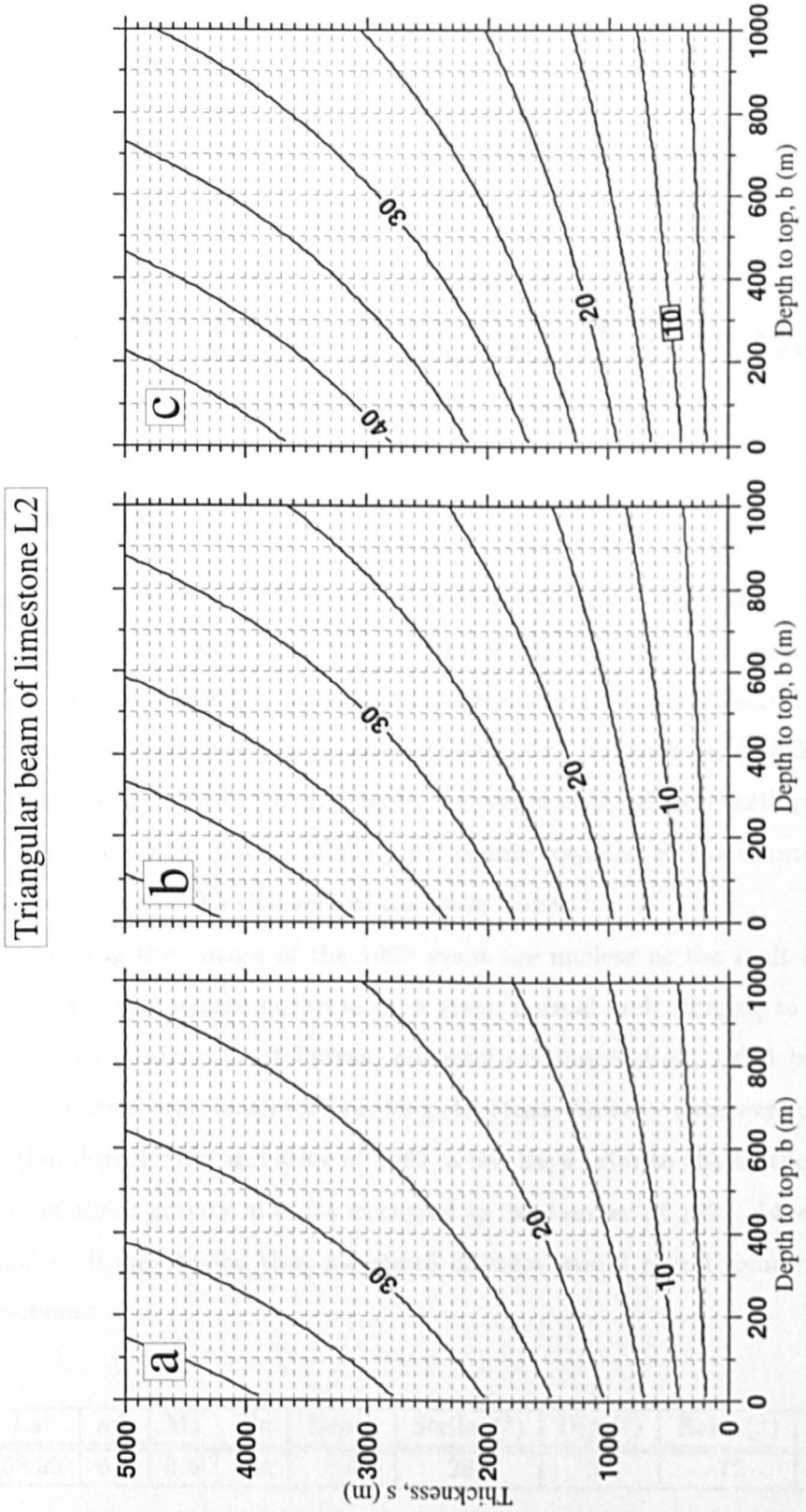

Figure H.6: Gravity anomaly magnitudes for a triangular beam of carbonate L2. Parameters taken from *Sclater and Christie* [1980]. Widths ($2a$) are (a) 10 km, (b) 15 km, and (c) 20 km. Contours in mGal.

Appendix I

Coseismic Gravitational Response

I.1 Motivation

Davies et al. [1997] compare GPS measured geodetic strains with earthquake moment release in central Greece, and show that the western Gulf of Corinth has a significant seismic deficit. In June of 1995, a major earthquake occurred in the western Gulf (Table I.1. The apparent seismic deficit is roughly equivalent to ten such earthquakes [*Clarke et al.*, 1997]. GPS experiments are ongoing in the region of the Eigion earthquake, in an attempt to characterise the nature of the post-seismic response to the normal faulting, and so infer something of the rheology of the lower crust.

Details regarding the nature of the 1995 event are unclear as the fault is offshore. It is likely that the earthquake occurred on a steep normal fault dipping to the north. However, N. Melis (University of Patras, personal communication, 1996) believes the event to have occurred on a southward dipping structure. Gravity data were collected in the same region during May and June of 1995, a few days prior to the earthquake. The reoccupation of these gravity stations occurred in September of 1995, 14 weeks after the earthquake. It was hoped that measured changes would reveal something of the coseismic response.

Lon	Lat	mb	Ms	Mo	Depth	Strike (°)	Dip (°)	Rake (°)	Slip (°)
22.20	38.36	6.1	6.5	244	6.5	281	23	-72	11

Table I.1: Focal mechanism solution for the 1995 Eigion earthquake, from *Baker et al.* [1997]. Mo is in MNm, and depth in km.

Base station	Established from:	Post-seismic gravity (mGal)	Change (mGal)
ATH	-	980042.605±0.010	Assumed zero
CORI	ATH	979996,884±0.014	-0.007±0.016
ROZE	CORI	97995.560±0.015	-0.061±0.022
SARA	ROZE	979682.937±0.017	-0.126±0.030

Table I.2: Base station ties made after the 1995 Eigion earthquake. Negative changes in gravity indicate a reduction in observed gravity.

I.2 Results

Before resurveying the gravity stations, the base stations values were re-established. Three ties were performed and the results are shown in Table I.2.

The gravity value at the Athens base station is assumed to remain the same through the 14 week period, and the lack of seismic activity in the Athens region suggests that this is a valid assumption to make. Indeed, there was no resolvable change in absolute gravity as the Corinth base station (Table I.2). This region has not experienced a major earthquake since 1981. For the ROZE and SARA base stations, the measured differences in gravity were great compared to observational errors.

As described in Chapter 4, the stations north of the Gulf of Corinth were not tied directly to Athens. Because of this, gravity differences are expressed relative to any change that may have occurred at the station furthest from the epicentre (the Amfissa gravity base station, AMFI). Figure I.1 shows the locations of the gravity stations that were re-occupied, together with profiles of the observed gravity change.

I.3 Interpretation

Coseismic changes in observed gravity (Δg_c) may be due to the coseismic elevation change (Δh_c). This may be expressed as

$$\begin{aligned} \Delta g_c &= \left(2\pi \times 10^5 G\rho\Delta h_c\right) - (0.3086\Delta h_c) \\ &= -0.1967\Delta h_c \end{aligned} \tag{I.1}$$

where Δh_c is in metres and Δg_c is in mGal. The Bouguer density (2670 kg/m^3) is used here for ρ. Figure I.2(a) shows the gravity changes across the gulf, assuming that there was no actual change at AMFI. The equivalent profile in Δh_c is shown in Figure I.2(b).

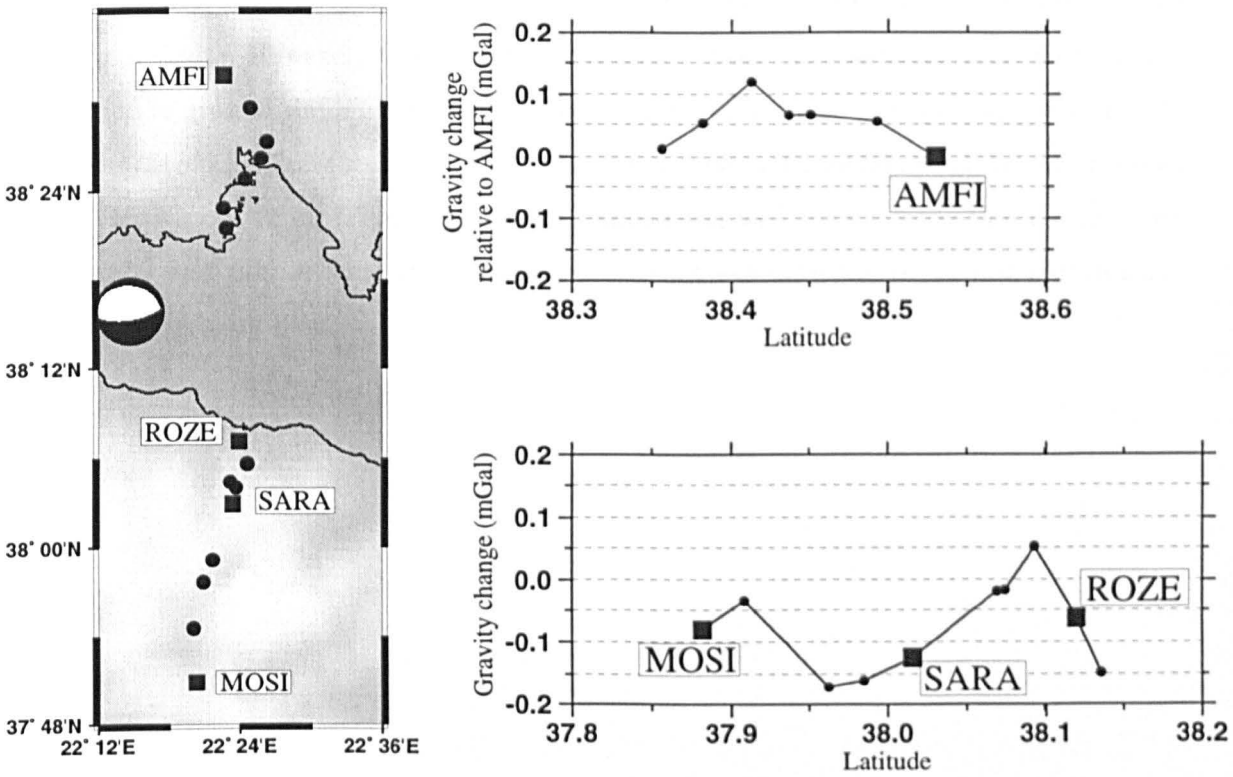

Figure I.1: The topographic map shows the locations of the gravity stations that were re-occupied after the 1995 Eigion eathquake. The blue squares indicate base stations. Of these, ROZE and SARA were re-established by tying with ATH via CORI. The plots show the measured gravity differences.

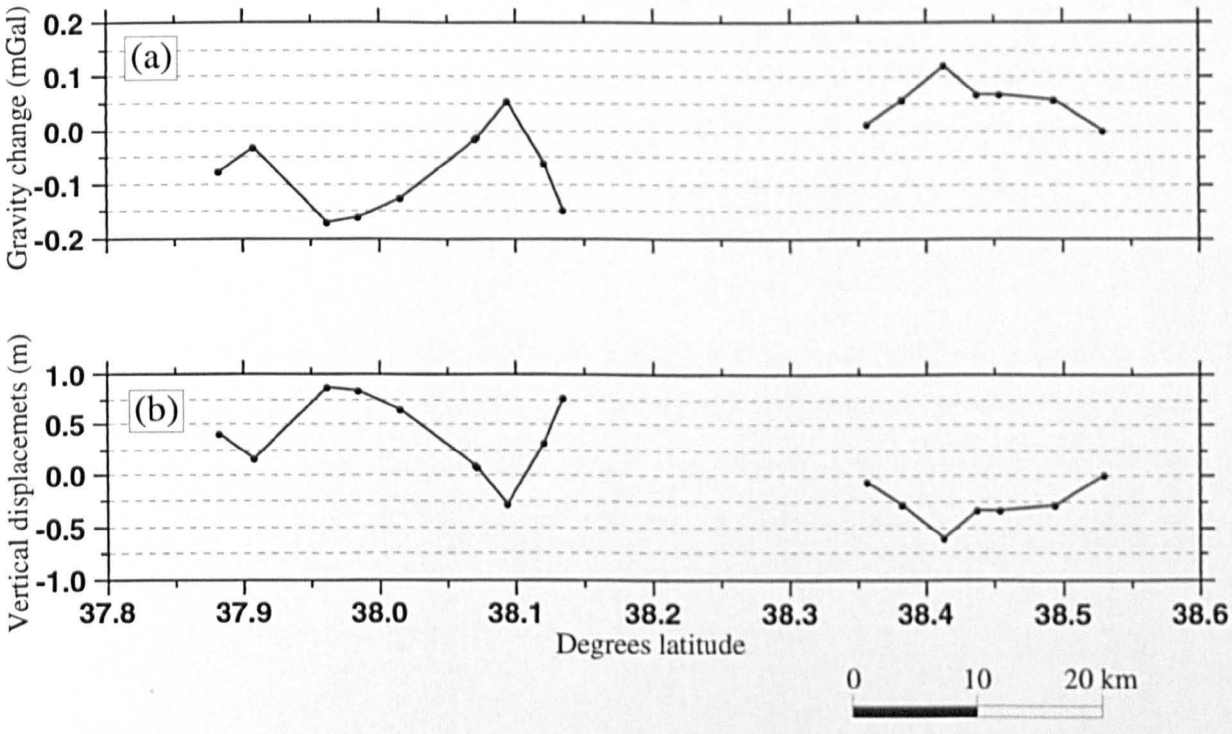

Figure I.2: Profiles of gravity change and equivalent elevation change

This may indicate that the 1995 Eigion earthquake occurred on a northward dipping normal fault. However, there may be other processes in operation here, such as the motion of ground water. For example, for a sedimentary rock of 20 percent porosity, the thickness of an infinite slab of ground water to produce a 0.1 mGal change in the observed gravity is only 12 m. Therefore, without additional well data information to constrain the pre- and post-seismic water levels, we cannot evaluate the co-seismic deformation from the gravity field.

Appendix J

Spatial Resolution of CWT Coherence

This section examines the ability of the wavelet method to resolve spatial variations in plate rigidity. The top and bottom loads from Figure 6.10 are applied to a series of five model lithospheres and the resulting Bouguer gravity and topography are calculated.[1] Wavelets are then used on these data to map observed coherence as a function of position and dilation, and the results compared to model input.

The first example models a lithosphere with a sharp ramp in T_e from 5 km in the west to 20 km in the east. From Figure 6.5a and Table 6.1, high coherence is expected a lengthscales greater than 90 km and 250 km respectively. For all three wavelet types, the sharpest resolution in both space and lengthscale is obtained with the fourth order wavelet. This is also seen in each of the following examples. The change from high to low coherence is more rapid across the eastern half, as predicted by the uncertainty principle.

The second example is comparable to this. Similar observations can be made, but the transition is less well defined in space because the amplitude of the ramp is reduced. High coherence is predicted at lengthscales greater than 90 km in the west and 150 km in the east, which matches the observations well. The third model is a constant gradient in T_e, such that λ_c should increase from 90 km in the west to 200 km in the east. Figure J.3 shows that high coherences are seen closer to the eastern margin for greater wavelet dilations.

[1] Data grids of topography and Bouguer gravity were supplied by J. Stewart, University of Oxford.

A feature in common to each of these results is that radial and tensor wavelets resolve both the spatial and lengthscale variations better than polarized wavelets. The same is true for the corner and window models, as shown in Figures J.4 and J.5.

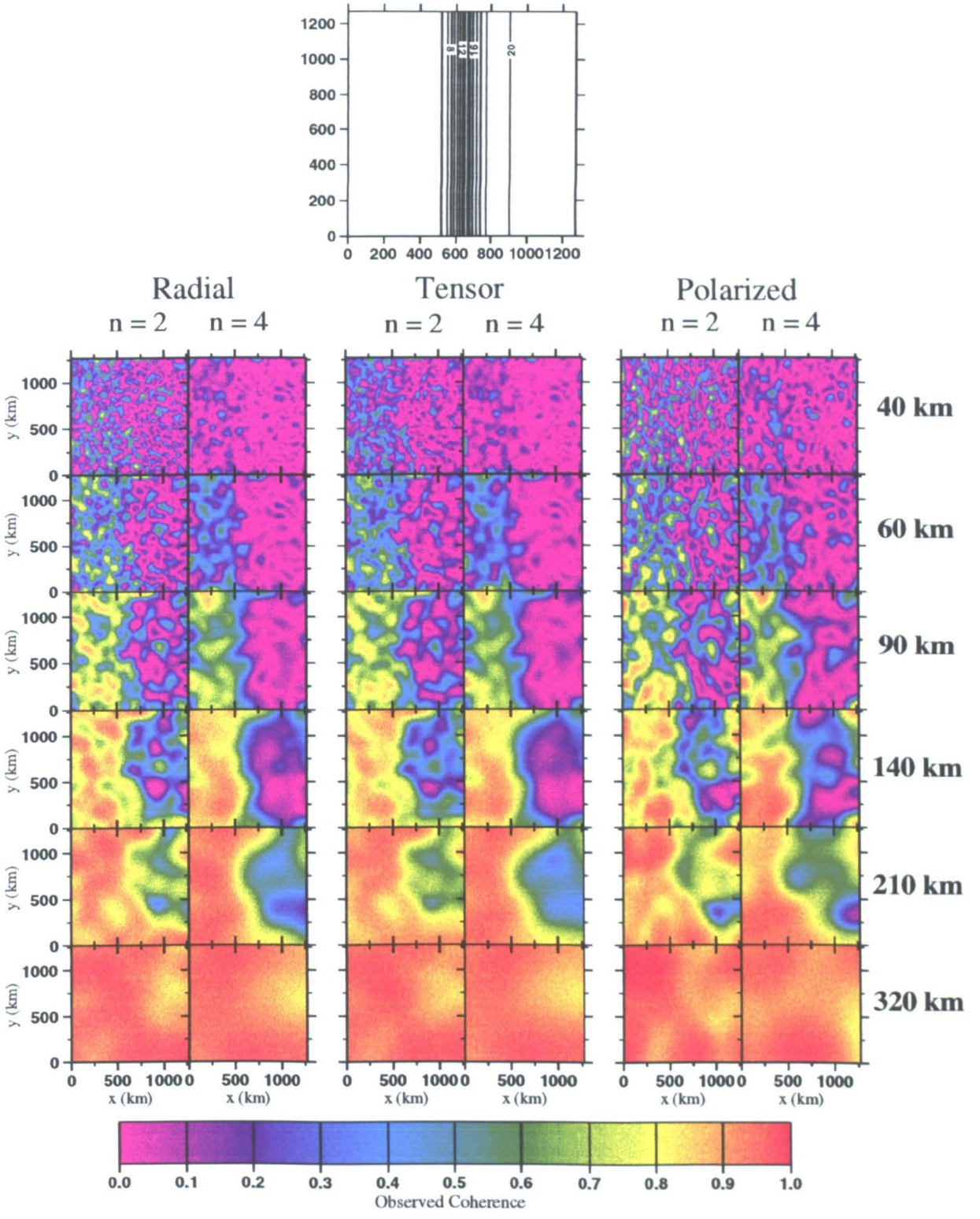

Figure J.1: Wavelet coherence across a 15 km T_e ramp model

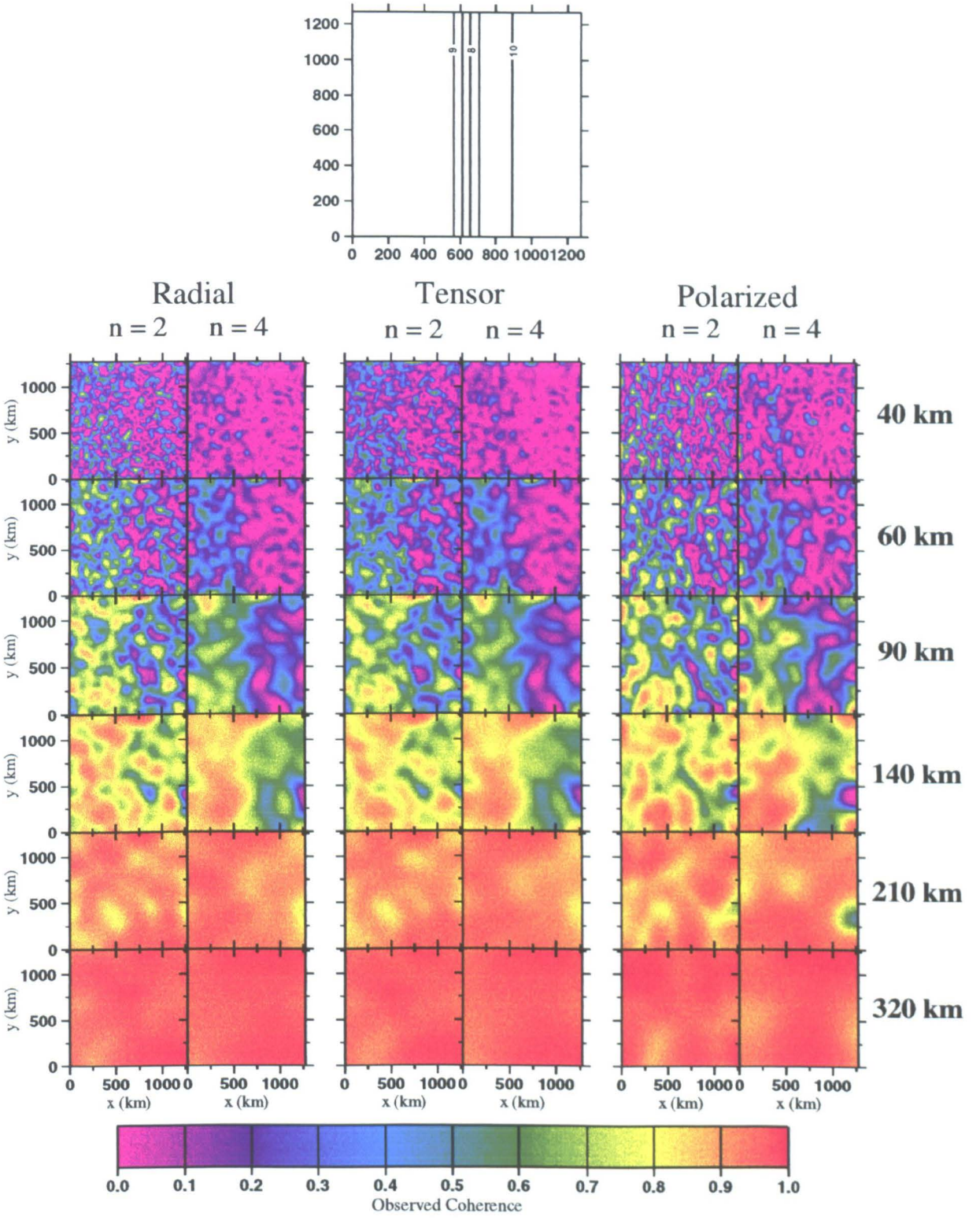

Figure J.2: Wavelet coherence across a 5 km T_e ramp model

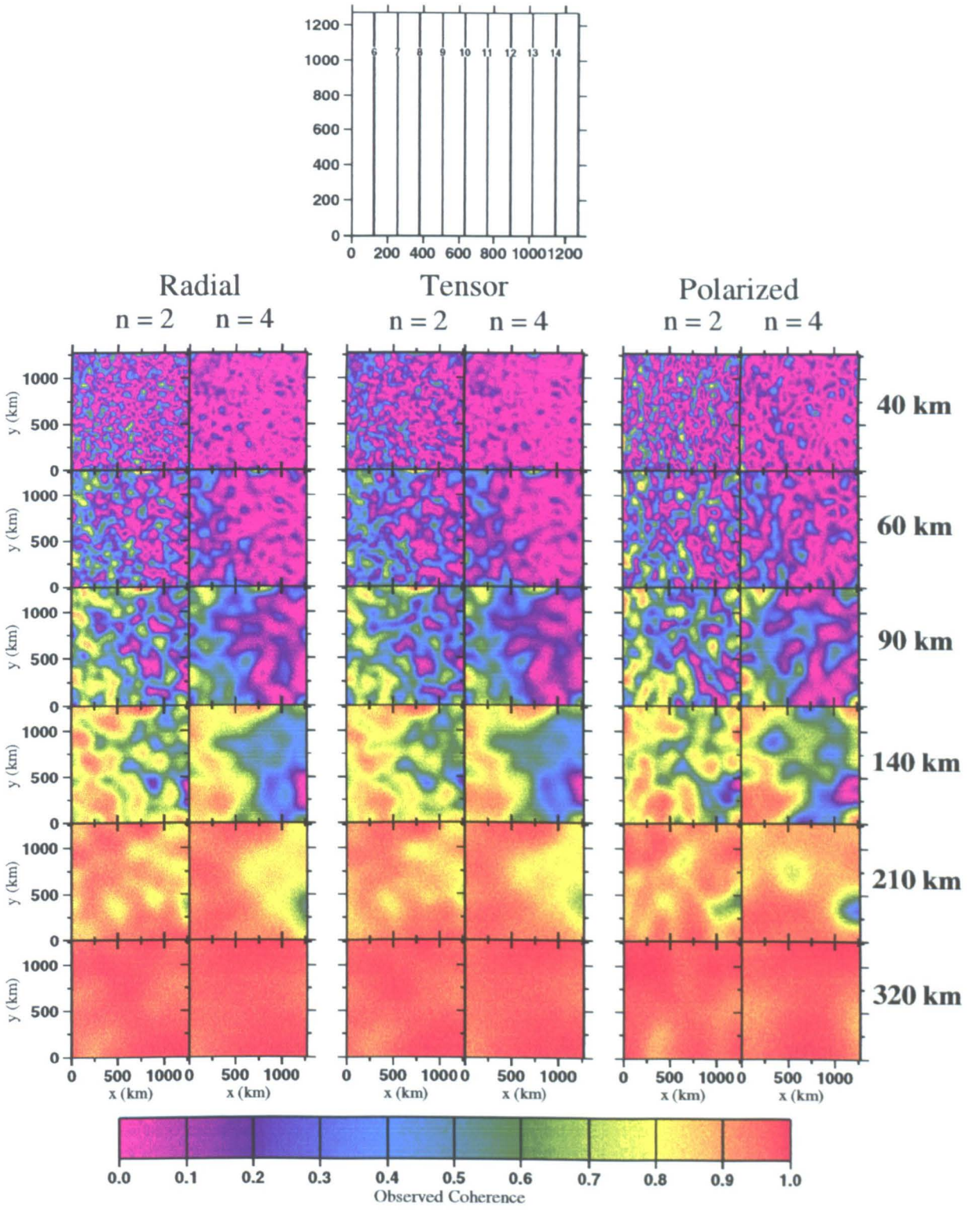

Figure J.3: Wavelet coherence across a gradual T_e gradient model

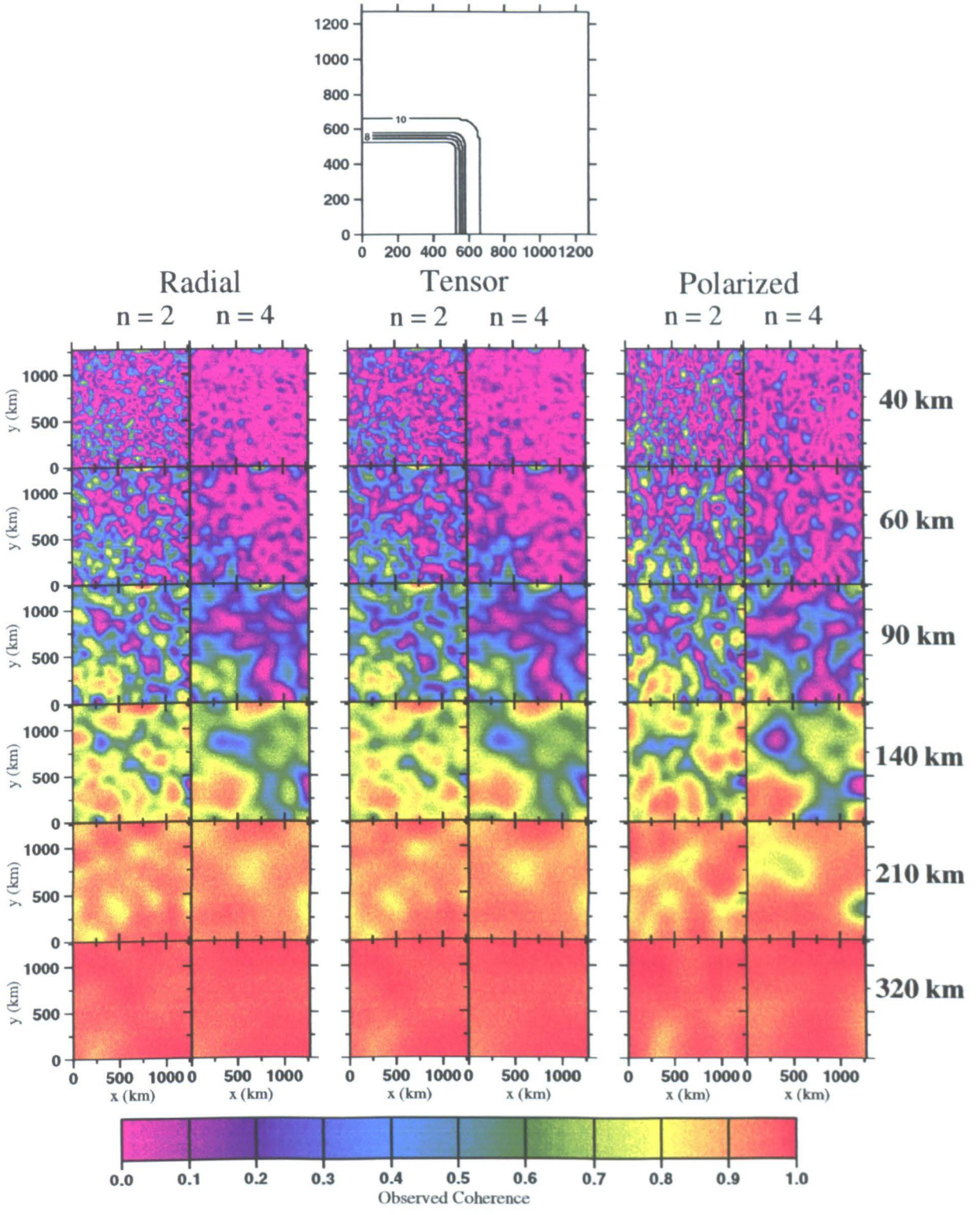

Figure J.4: Wavelet coherence across a 5 km T_e corner model

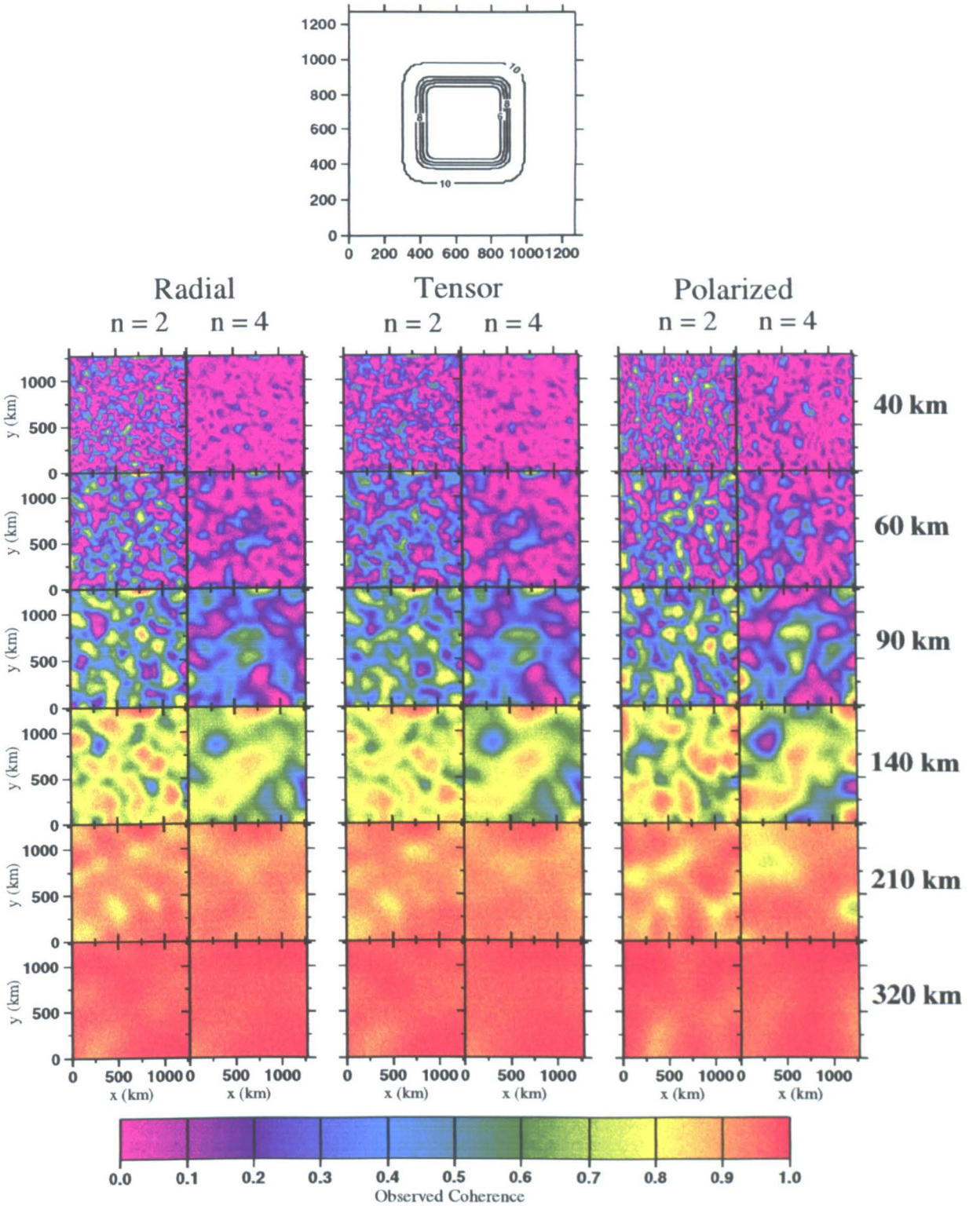

Figure J.5: Wavelet coherence across a 5 km T_e window model

List of References

Airy, G. B., On the computation of the effect of the attraction of mountain-masses as disturbing the apparent astronomical latitude of stations of geodetic surveys, *Philos. Trans. R. Soc.*, **145**, 101–104, 1855.

Alberello, D., C. Tamburelli, D. Babbucci and M. Viti, Plate convergence, crustal delamination, extrusion tectonics and minimization of shortening work as main controlling factors of the recent Mediterranean deformation pattern, *Annali di Geofisica*, **40**(3), 611–634, 1997.

Alvarez, F., J. Virieux and X. Le Pichon, Thermal consequences of lithospheric extension: the initial rifting phase, *Geophys. J. R. astron. Soc.*, **78**, 389–411, 1984.

Anderson, D. L., Lithosphere, asthenosphere and perisphere, *Rev.Geophys.*, **33**, 125–149, 1995.

Anderson, H. and J. Jackson, Active tectonics of the Adriatic region, *Geophys. J. R. astr. Soc.*, **91**, 937–993, 1987.

Angelier, J., N. Lybéris, X. Le Pichon, E. Barrier and P. Huchon, The tectonic development of the Hellenic Arc and the Sea of Crete: a synthesis, *Tectonophysics*, **86**, 159–196, 1982.

Anselmetti, F. S. and G. P. Eberli, Controls on sonic velocity in carbonates, *Pure and Applied Geophysics*, **141**, 287–323, 1993.

Armijo, R., H. Lyon-Caen and D. Papanastassiou, East-west extension and Holocene normal-fault scarps in the Hellenic arc, *Geology*, **20**, 491–494, 1992.

Armijo, R., B. Mayer, G. C. P. King, A. Rigo and D. Papanastassiou, Quaternary evolution of the Corinth Rift and its implications for the Late Cenozoic evolution of the Aegean, *Geophys. J. Int.*, **126**, 11–53, 1996.

Artemjev, M. E. and E. V. Artyushkov, Structure and isostasy in the Baikal Rift and the mechanism of rifting, *J. Geophys. Res.*, **76**, 1197–1211, 1971.

Athy, L. F., Density, porosity and compaction of sedimentary rocks, *Amer. Assoc. Petrol. Geol. Bull.*, **14**, 1–24, 1930.

Atzemoglou, A., D. Kondopoulou, S. Papamarinopoulos and S. Dimitriadis, Paleomagnetic evidence for block rotations in the western Greek Rhodope, *Geophys. J. Int.*, **118**, 221–230, 1994.

Aubouin, J., Geosynclines, in *Developments in Geotechnics, Part 1*, Elsevier, New York, 1965.

Baker, C., D. Hatzfeld, H. Lyon-Caen, E. Papadimitriou and A. Rigo, Earthquake mechanisms of the Adriatic Sea and Western Greece, *Geophys. J. Int.*, **131**, 559–594, 1997.

Banks, R. J., R. L. Parker and S. P. Huestis, Isostatic compensation on a continental scale: local versus regional mechanisms, *Geophys. J. R. astr. Soc.*, **51**, 431–452, 1977.

Barford, N. C., Experimental Errors: Precision, Error and Truth, 1985, (second edition).

Barka, A., The North Anatolian fault zone, *Annales Tectonicae*, **6**, 164–195, 1992.

Barka, A. and R. Reilinger, Active tectonics of the Eastern Mediterranean region: deduced from GPS, neotectonic and seismicity data, *Annali di Geofisica*, **40(3)**, 587–610, 1997.

Barrell, J., The strength of the Earth's crust, IV, Heterogeneity and rigidity of the crust as measured by departures from isostasy, *J. Geol.*, **22**, 289–314, 1914.

Bassi, G., Factors controlling the style of continental rifting: insights from numerical modelling, *Earth. Planet. Sci. Lett.*, **105**, 430–452, 1991.

Bassi, G., Relative importance of strain rate and rheology for the mode of continental extension, *Geophys. J. Int.*, **122**, 195–210, 1995.

Bechtel, T. D., D. W. Forsyth, V. L. Sharpton and R. A. F. Grieve, Variations in effective elastic thickness of the North American lithosphere , *Nature*, **343**, 636–638, 1990.

Bechtel, T. D., D. W. Forsyth and C. J. Swain, Mechanisms of isostatic compensation in the vicinity of the East African Rift, Kenya, *Geophys. J. R. astr. Soc.*, **90**, 445–465, 1987.

van der Beek, P., Flank uplift and topography at the central Baikal Rift (SE Siberia): a test of kinematic models for continental extension, *Tectonics*, **16**(1), 122–136, 1997.

Beekman, P., *Tectonic modelling of thick-skinned compressional intraplate deformation*, University of Amsterdam, PhD Thesis, 1994.

Benes, V. and P. Davy, Modes of continental lithospheric extension: experimental verification of strain localization processes, *Tectonophysics*, **254**, 69–87, 1996.

Billiris, H., D. Paradissis, G. Veis, P. England, W. Featherstone, B. Parsons, P. Cross, P. Rands, M. Rayson, P. Sellers, V. Ashkenazi, M. Davison, J. Jackson and N. Ambraseys, Geodetic determination of tectonic deformation in central Greece from 1900 to 1988, *Nature*, **350**, 124–129, 1991.

Bird, P., Lateral extrusion of lower crust from under high topography in the isostatic limit, *J. Geophys. Res.*, **96**, 10275–10286, 1991.

Blackwell, D. D. and J. L. Steele, Geothermal map of North America, scale 1:5,000,000, Boulder, Colo., 1992.

Block, L. and L. H. Royden, Core complex geometries and regional scale flow in the lower crust, *Tectonics*, **9**, 557–567, 1990.

Bodine, J. H., M. S. Steckler and A. B. Watts, Observations of flexure and the rheology of oceanic lithosphere, *J. Geophys. Res.*, **86**, 3965–3707, 1981.

Bott, M. H. P., Modelling the formation of a half graben using realistic upper crustal rheology, *J. Geophys. Res.*, **102**, 24605–24617, 1997.

Bott, M. H. P. and N. J. Kusznir, The origin of tectonic stress in the lithosphere, *Tectonophysics*, **105**, 1–13, 1984.

Bourne, S. J., P. C. England and B. Parsons, The motion of crustal blocks by flow of the lower lithosphere and implications for slip rates of continental strike-slip faults, *Nature*, **391**, 655–659, 1998.

Brace, W. F. and D. L. Kohlstedt, Limits on lithospheric stress imposed by laboratory experiments, *J. Geophys. Res.* , **85**, 6248–6252, 1980.

Braile, L. W., G. R. Keller, R. F. Wendlandt, P. Morgan and M. A. Khan, The East African rift system, in *Continental Rifts: Evolution, Structure and Tectonics*, edited by K. H. Olsen, Developments in Geotectonics, **25**, pp. 213–231, Elsevier, 1995.

Braun, J. and C. Beaumont, A physical explanation of the relation between flank uplifts and the breakup unconformity at rifted continental margins, *Geology*, **17**, 760–764, 1989.

de Bremaecker, J., P. Huchon and X. Le Pichon, The deformation of the Aegea: a finite element study, *Tectonophysics*, **86**, 197–211, 1982.

Brooks, M., J. E. Clews, N. S. Melis and J. R. Underhill, Structural development of Neogene basins in western Greece, *Basin Research*, **1**, 129–138, 1988.

Brooks, M. and G. Ferentinos, Tectonics and sedimentation in the Gulf of Corinth and the Zakinthos and Kefallinia channels, Western Greece, *Tectonophysics*, **101**, 25–54, 1984.

Brown, E. T., *Rock Characterization, Testing and Monitoring*, ISRM Suggested Methods, Pergamon Press, 1981.

Buck, W. R., Small-scale convection induced by passive rifting: the cause for uplift of rift shoulders, *Earth. Planet. Sci. Lett.*, **77**, 213–234, 1986.

Buck, W. R., Modes of continental lithospheric extension, *J. Geophys. Res.*, **96**, 20161–20178, 1991.

Buck, W. R., Effect of lithospheric thickness on the formation of high- and low-angle normal faults, *Geology*, **21**, 933–936, 1993.

Buck, W. R., F. Martinez, M. S. Steckler and J. R. Cochran, Thermal consequences of lithospheric extension: pure and simple, *Tectonics*, **7**, 213–234, 1988.

Burov, E. B. and M. Diament, Flexure of the continental lithosphere with multilayer rheology, *Geophys. J. Int.*, **109**, 449–468, 1992.

Burov, E. B. and M. Diament, The effective elastic thickness (Te) of continental lithosphere: What does it really mean?, *J. Geophys. Res.*, **100**, 3905–3927, 1995a.

Burov, E. B. and M. Diament, Isostasy, effective elastic thickness (EET) and inelastic rheologies of continents and oceans, *Geology*, **24**, 419–422, 1995b.

Byerlee, J. D., Friction on rocks, *Pure and Applied Geophysics*, **116**, 615–626, 1978.

Byrd, O. D., R. B. Smith and J. W. Geissman, The Teton fault, Wyoming: Topographic signature, neotectonics, and mechanisms of deformation, *J. Geophys. Res.*, **99**, 20095–20122, 1994.

Carter, N. L. and M. C. Tsenn, Flow properties of continental lithosphere, *Tectonophysics*, **136**, 27–63, 1987.

Cartwright, D. E. and R. J. Tayler, New computation of the tide-generating potential, *Geophys. J. R. astr. Soc.*, **23**, 34–74, 1971.

Chapin, D. A., The theory of the Bouguer anomaly: a tutorial, *The Leading Edge*, **May**, 361–363, 1996.

Clarke, P. J., R. R. Davies, P. C. England, B. E. Parsons, H. Billiris, D. Paradissis, G. Veis, P. H. Denys, P. A. Cross, V. Ashkenazi and R. Bingley, Geodetic estimate of seismic hazard in the Gulf of Korinthos, *Geophys. Res. Lett.*, **24**, 1303–1306, 1997.

Cloetingh, S. and E. B. Burov, Thermomechanical structure of European continental lithosphere: constraints from rheological profiles and EET estimates., *Geophys. J. Int.*, **124**, 695–723, 1996.

Cloetingh, S. and H. Kooi, Intraplate stresses and dynamic aspects of rifted basins, *Tectonophysics*, **226**, 167–185, 1993.

Cloetingh, S., J. D. van Wees, P. A. van der Beek and G. Spadini, Role of pre-rift rheology in kinematics of extensional basin formation - constraints from thermomechanical models of Mediterranean and intracratonic basins, *Marine and Petroleum Geology*, **12**, 793–807, 1995.

Cochran, J. R., Effects of finite rifting times on the development of sedimentary basins, *Earth. Planet. Sci. Lett.*, **66**, 289–302, 1983.

Collier, R. E. L. and C. J. Dart, Neogene to Quaternary rifing, sedimentation and uplift in the Corinth Basin, Greece, *J. Geol. Soc.*, **148**, 1049–1065, 1991.

Comninakis, P. E. and B. C. Papazachos, Space and time distribution of the intermediate focal depth earthquakes in the Hellenic arc, *Tectonophysics*, **70**, 35–47, 1980.

Cooper, R. F. and D. L. Kohlstedt, Rheology and structure of olivine basalt partial melts, *J. Geophys. Res.*, **91**, 9315–9323, 1986.

Cowie, P. A. and G. D. Karner, Gravity effect of sediment compaction: examples from the North Sea and Rhine Graben, *Earth Planet. Sci. Lett.*, **99**, 141–153, 1990.

Crouch, S. L. and A. M. Starfield, *Boundary element methods in solid mechanics, with applications in rock mechanics and geological engineering*, Allen and Unwin, 1983.

Curtis, A., P. England and R. Davies, Local and regional components of western Aegean deformation extracted from 100 years of geodetic displacement measurements, *Geophys. J. Int.*, **130**, 623–639, 1997.

DMA, Report by the Defence Mapping Agency Aerospace Center: "WGS84 Ellipsoidal Gravity Formula and Gravity Anomaly Conversion Equations", Aug., 1987.

Dalmayrac, B. and P. Molnar, Parallel thrust and normal faulting in Peru and constraints on the state of stress, *Earth Planet. Sci. Lett.*, **55**, 473–481, 1981.

Dart, C. J., R. E. L. Collier, R. L. Gawthorpe, J. V. A. Keller and G. Nichols, Sequence stratigraphy of (?)Pliocene-Quaternary syn-rift Gilbert-type fan deltas, northern Peloponnesos, Greece, *Marine and Petroleum Geology*, **11**, 545–560, 1994.

Davies, R. R., P. C. England, B. E. Parsons, H. Billiris, D. Paradissis and G. Veis, Geodetic Strain of Greece in the Interval 1892-1992, *J. Geophys. Res.*, **102**, 24571–24588, 1997.

DeMets, C., R. G. Gordon, D. F. Argus and S. Stein, Current plate motions, *Geophys. J. Int.*, **101**, 425–478, 1990.

Dewey, J. F. and A. M. C. Şengör, Aegean and surrounding regions: Complex multiplate and continuum tectonics in a convergent zone, *Geological Society of America Bulletin, Part 1*, **90**, 84–92, 1979.

Dinter, D. A. and L. Royden, Late Cenozoic extension in northeastern Greece: Strymon Valley detachment system and Rhodope metamorphic core complex, *Geology*, **21**, 45–48, 1993.

Dobrin, M. B. and C. H. Savit, *Introduction to Geophysical Prospecting* (fourth edition), McGraw-Hill, 1988.

Doglioni, C., C. Busatta, G. Bolis, L. Marianini and M. Zanella, Structural evolution of the eastern Balkans (Bulgaria), *Marine and Petroleum Geology*, **13**, 225–251, 1996.

Dorman, L. M. and B. T. R. Lewis, Experimental isostasy, 1. Theory of the determination of the earth's isostatic response to a concentrated load, *J. Geophys. Res.*, **75**, 3357–3365, 1970.

Doutsos, T., N. Komtopoulos and D. Frydas, Neotectonic evolution of northwestern continental Greece, *Geologische Rundschau*, **76**(2), 433–450, 1987.

Doutsos, T., N. Komtopoulos and G. Poulimenos, The Corinth-Patras rift as the initial stage of continental fragmentation behind an active island arc (Greece), *Basin Research*, **1**, 177–190, 1988.

Ebinger, C. J., T. D. Bechtel, D. W. Forsyth and C. O. Bowin, Effective elastic thickness beneath the East African and Afar Plateaus and dynamic compensation of the uplifts, *J. Geophys. Res.*, **94**, 2883–2901, 1989.

Ebinger, C. J., G. D. Karner and J. K. Weissel, Mechanical strength of extended continental lithosphere: constraints from the Western Rift system, Africa, *Tectonics*, **10**, 1239–1256, 1991.

Eliet, P. P. and R. L. Gawthorpe, Drainage development and variations in sediment supply within rift basins: examples from the active Sperchios Basin, central Greece, *J. Geol. Soc.*, **152**, 883–893, 1995.

England, P. and G. Houseman, Extension during continental convergence, with application to the Tibetan Plateau, *J. Geophys. Res.*, **94**, 17561–17579, 1989.

England, P. and D. McKenzie, Correction to: a thin viscous sheet model for continental deformation, *Geophys. J. R. astr. Soc.* , **73**, 523–532, 1983.

England, P. and P. Molnar, The field of crustal velocity in Asia calculated from Quaternary rates of slip on faults, *Geophys. J. Int.*, **130**, 551–582, 1997a.

England, P. and P. Molnar, Active deformation in Asia: from kinematics to dynamics, *Science*, **278**(5338), 647–650, 1997b.

England, P. C., Constraints on extension of continental lithosphere, *J. Geophys. Res.*, **88**, 1145–1152, 1983.

England, P. C. and J. A. Jackson, Active deformation of the continents, *Ann. Rev. Earth Planet. Sci*, **17**, 197–226, 1989.

Ervin, C. P., Short note: theory of the Bouguer anomaly, *Geophysics*, **42**, 1468, 1977.

Eyidogan, H. and J. A. Jackson, A seismological study of normal faulting in the Demirci, Alasehir and Gediz earthquakes of 1969-70 in western Turkey: implications for the nature and geometry of deformation in the continental crust, *Geophys. J. R. astr. Soc*, **81**, 569–607, 1985.

Fletcher, R. C. and B. Hallet, Unstable extension of the lithosphere: a mechanical model for Basin-and-Range structure, *J. Geophys. Res.*, **88**, 7457–7466, 1983.

Forsyth, D. W., Subsurface loading and estimates of the flexural rigidity of continental lithosphere, *J. Geophys. Res.*, **90**, 12623–12632, 1985.

Forsyth, D. W., Finite extension and low angle normal faulting, *Geology*, **20**, 27–30, 1992.

Francheteau, J., C. Jaupart, X. Shen, W. Kang, D. Lee, J. Bai, H. Wei and H. Deng, High heat flow in southern Tibet, *Nature*, **307**, 32–36, 1984.

Gallagher, K., An examination of some uncertainties associated with estimates of sedimentation rates and tectonic subsidence, *Basin Research*, **2**, 97–114, 1989.

Gallagher, K. and K. Lambeck, Subsidence, sedimentation and sea-level changes in the Eromanga Basin, Australia, *Basin Research*, **2** , 115–151, 1989.

Galloway, W. E. and D. K. Hobday, in *Terrigenous Clastic Depositional Systems*, p. 423 pp, Springer, 1983.

Gardner, G. H. F., L. W. Gardner and A. R. Gregory, Formation velocity and density - the diagnostic basics for stratigraphic traps, *Geophysics*, **18**, 271–288, 1974.

Gautier, P. and J. Brun, Ductile crust exhumation and extensional detachments in the central Aegean (Cyclades and Evvia Islands), *Geodinamica Acta (Paris)*, **7**(2), 57–85, 1994.

Georgadas, D. and E. Lagios, Remeasurement of the national gravity base station network in Peloponnese, *Annales Géologiques des Pays Helléniques*, **31**, 136–145, 1982.

Giese, P., K. J. Ruetter, V. Jacobshagen and R. Nicolich, Explosion seismic crustal studies in the Alpine-Mediterranean region and their implications to tectonic processes, in *Alpine-Mediterranean Geodynamics*, edited by H. Berkhemer, Geodyn. Ser., **7**, 1982.

Goetze, C. and B. Evans, Stress and temperature in the bending lithosphere as constrained by experimental rock mechanics, *Geophys. J. R. astr. Soc.*, **59**, 463–478, 1979.

Goff, J. A., Comment on "Fractal mapping of digitized images: application to the topography of Arizona and comparisons with synthetic images" by J. Huang and D. L. Turcotte, *J. Geophys. Res.*, **95**, 5158–5160, 1990.

Goldhammer, R. K., Compaction and decompaction algorithms for sedimentary carbonates, *J. Sed. Res.*, **67**, 26–35, 1997.

Hager, B. H., Mantle viscosity: a comparison of models from postglacial rebound and from the geoid, plate driving forces, and advected heat flux, in *Glacial Isostasy, Sea-Level and Mantle Rheology*, edited by R. Sabadini, K. Lambeck and E. Boschi, NATO ASI Series, **334**, pp. 493–513, 1991.

Haines, J., Continental mechanics, *Nature*, **391**, 634, 1998.

Hassani, R. and J. Chéry, Anelasticity explains topography associated with Basin and Range normal faulting, *Geology*, **24**, 1096–1098, 1996.

Hatzfeld, D., I. Kassaras, D. Panagiotopaulos, D. Amorese, K. Makropoulos, G. Karakaisis and O. Coutant, Microseismicity and strain pattern in northwestern Greece, *Tectonics*, **14**, 773–785, 1995.

Hatzfeld, D. and C. Martin, Intermediate depth seismicity in the Aegean defined by teleseismic data, *Earth Planet, Sci. Lett.*, **113**, 267–275, 1992.

Hatzfeld, D., J. Martinod, G. Bastet and P. Gautier, An analog experiment for the Aegean to describe the contribution of gravitational potential energy, *J. Geophys. Res.*, **102**, 649–659, 1997.

Heezen, B. C., M. Ewing and H. L. Johnson, The Gulf of Corinth floor, *Deep-Sea Res.*, **13**, 381–411, 1966.

Higgs, B., Syn-sedimentary structural controls on basin deformation in the Gulf of Corinth, Greece, *Basin Research*, **1**, 155–165, 1988.

Hipkin, R. G., The earth's gravity field: "what?"; "what for?" and "what next?", paper presented at Geodesy From Space: The Earth's Gravity Field, RAS 'G' Meeting, London, March, 1995.

Hipkin, R. G., E. Lagios, D. Lyness and P. Jones, Reference gravity stations on the IGSN71 standard in Britain and Greece, *Geophysical Journal*, **92**, 143–148, 1988.

Hopper, J. R. and W. R. Buck, The initiation of rifting at constant tectonic force: role of diffusion creep, *J. Geophys. Res.*, **98**, 16213–16221, 1993.

Hopper, J. R. and W. R. Buck, The effect of lower crustal flow on continental extension and passive margin formation, *J. Geophys. Res.*, **101**, 20175–20194, 1996.

Houseman, G. and P. England, A dynamic model of lithospheric extension and sedimentary basin formation, *J. Geophys. Res.*, **91**, 719–729, 1986.

Houseman, G. A. and D. Gubbins, Deformation of subducted oceanic lithosphere, *Geophys. J. Int.*, **131**, 535–551, 1997.

Huang, J. and D. L. Turcotte, Fractal mapping of digitized images: application to the topography of Arizona and comparisons with synthetic images, *J. Geophys. Res.*, **94**, 7491–7495, 1989.

Hubert, A., R. Armijo, B. Meyer, G. King, F. Gasse and A. Barka, Slip rate of the North Anatolian Fault, Turkey, *Eos, Transactions, American Geophysical Union*, **78**(49), 715, 1997.

Jackson, J., Relations between faulting and continuous deformation on the continents, *Annali di Geofisica*, **36**, 3–11, 1993.

Jackson, J., Active tectonics of the Aegean region, *Ann. Rev. Earth. Planet. Sci.*, **22**, 239–271, 1994.

Jackson, J. and D. McKenzie, The relationship between plate motions and seismic moment tensors, and the rates of active deformation in the Mediterranean and the Middle East, *Geophysical Journal*, **93**, 45–73, 1988.

Jackson, J. A., G. Gagnepain, G. Houseman, G. C. P. King, P. Papadimitriou, C. Soufleris and J. Virieux, Seismicity, normal faulting, and the geomorphological development of the Gulf of Corinth (Greece): the Corinth earthquakes of February and March 1981, *Earth Planet. Sci. Lett.*, **57**, 377–397, 1982.

Jackson, J. A., A. J. Haines and W. E. Holt, The horizontal deformation field in the deforming Aegean Sea region from the moment tensors of earthquakes, *Journal of Geophysical Research*, **97**, 17657–17684, 1992.

Jaeger, J. C. and N. G. W. Cook, *Fundamentals of rock mechanics*, John Wiley & Sons, New York, 1979.

Jankowsky, W., Empirical investigation of some factors affecting elastic wave velocities in carbonate rocks, *Geophys. Prosp.*, **18**, 103–118, 1970.

Jestin, F., P. Huchon and J. M. Gaulier, The Somail plate and the East African rift system: present-day kinematics, *Geophys. J. Res.*, **116**, 637–654, 1994.

Jin, Y., M. K. McNutt and Y. Zhu, Evidence from gravity and topography data for folding of Tibet, *Nature*, **371**, 669–674, 1994.

Jolivet, L., J. P. Brun, P. Gautier and S. Lallemant, 3D-kinematics of extension in the Aegean from the early Miocene to the present: insights from the ductile crust, *Bull. Soc. Géol. Fr.*, **165**, 195–209, 1994.

Jones, C. H., J. R. Unruh and L. J. Sonder, The role of gravitational potential energy in active deformation in the southwestern United States, *Nature*, **381**, 37–41, 1996.

Jones, C. H., B. P. Wernicke, G. L. Farmer, J. D. Walker, D. S. Coleman, L. W. McKenna and F. V. Perry, Variations across and along a major continental rift: an interdisciplinary study of the Basin and Range Province, western USA, *Tectonophysics*, **213**, 57–96, 1992.

Kahle, H. G., M. V. Muller, S. Meuller and G. Veis, The Kephalonia transform-fault and the rotation of the Apulian platform - evidence from satellite geodesy, *Geophys. Res. Lett.*, **20**, 651–654, 1993.

Karato, S., M. S. Paterson and J. D. Fitzgerald, Rheology of synthetic olivine aggregates: influence of grain size and water, *J. Geophys. Res.*, **91**, 8151–8176, 1986.

Karner, G. D. and A. B. Watts, Gravity anomalies and flexure of the lithosphere at mountain ranges, *J. Geophys. Res.*, **88**, 10449–10477, 1983.

Kaufman, P. S. and L. H. Royden, Lower crustal flow in an extensional setting: costraints from the Halloran Hills region, eastern Mojave Desert, California, *J. Geophys. Res.*, **99**, 15723–15739, 1994.

Keen, C. E., The dynamics of rifting: deformation of the lithosphere by active and passive driving forces, *Geophys. J. R. astron. Soc.*, **80**, 95–120, 1985.

Keller, G. R., M. H. P. Bott, R. F. Wendlandt, D. I. Doser and P. Morgan, The Baikal rift system, in *Continental Rifts: Evolution, Structure and Tectonics*, edited by K. H. Olsen, Developments in Geotectonics, **25**, pp. 325–341, Elsevier, 1995.

King, G. C. P. and M. Ellis, The origin of large local uplift in extensional regions, *Nature*, **438**, 689–693, 1990.

King, G. C. P., D. Oppenheimer and F. Amelung, Block versus continuum deformation in the western United States, *Earth. Planet. Sci. Lett.*, **128**, 55–64, 1994.

King, G. C. P., Z. X. Ouyang, P. Papadimitriou, A. Deschamps, J. Gagnepain, G. Houseman, J. A. Jackson, C. Soufleris and J. Virieux, The evolution of the Gulf of Corinth Rift (Greece): an aftershock study of the 1981 earthquakes, *Geophys. J. R. astr. Soc.*, **80**, 55–64, 1985.

King, G. C. P., R. S. Stein and J. B. Rundle, The growth of geological structures by repeated earthquakes, *J. Geophys. Res.*, **93**, 13307–13318, 1988.

Kirby, S. H., W. B. Durham and L. A. Stern, Mantle phase changes and deep-earthquake faulting in subducting lithosphere, *Science*, **252**, 216–224, 1991.

Kirby, S. H. and A. K. Kronenberg, Rheology of the lithosphere: selected topics, *Reviews of Geophysics*, **25**(6), 1219–1244, 1987.

Kissel, C., O. Averbuch, D. F. D. Lamotte, O. Monod and S. Allerton, First paleomagnetic evidence for post-Eocene rotation of Western Taurides thrust belt east of the Isparta re-entrant (southwest Turkey), *Earth Planet. Sci. Lett.*, **117**, 1–14, 1993.

Kissel, C. and C. Laj, Tertiary geodynamical evolution of the Aegean arc: a paleomagnetic reconstruction, *Tectonophysics*, **146**, 183–201, 1988.

Kogan, K. G., J. D. Fairhead, G. Balmino and E. L. Makedonskii, Tectonic fabric and lithospheric strength of northern Eurasia based on gravity data, *Geophys. Res. Lett.*, **21**, 2653–2656, 1994.

Kohlstedt, D. L., B. Evans and S. J. Mackwell, Strength of the lithosphere: constraints imposed by laboratory experiments, *J. Geophys. Res.*, **100**, 17587–17602, 1995.

Kooi, H., *Tectonic modelling of extensional basins: the role of lithospheric flexure, intraplate stress and relative sea-level change*, University of Amsterdam, PhD Thesis, 1991.

Kooi, H. and S. Cloetingh, Lithospheric necking and regional isostasy at extensional basins, 2: stress induced vertical motions and relative sea-level changes, *J. Geophys. Res.*, **97** , 17573–17591, 1992.

Kooi, H., S. Cloetingh and J. Burrus, Lithospheric necking and regional isostasy at extensional basins, 1: subsidence and gravity modelling with an application to the Gulf of Lions margin (SE France), *J. Geophys. Res.*, **97**, 17553–17571, 1992.

Korvin, G., Shale compaction and statistical physics, *Geophys. J. R. astr. Soc.*, **28**, 35–50, 1984.

Kruse, S., M. McNutt, J. Phipps-Morgan, L. Roden and B. Wernicke, Lithospheric extension near Lake Mead, Nevada: a model for ductile flow in the lower crust, *J. Geophys. Res.*, **96**, 4435–4456, 1991.

Kusznir, N. J., G. Marsden and S. S. Egan, A flexural-cantilever simple-shear/pure-shear model of continental lithospheric extension: applications to the Jeanne d'Arc Basin, Grand Banks and Viking Graben, North Sea, in *The Geometry of Normal Faults*, edited by A. M. Roberts, G. Yielding and B. Freeman, Geological Society Special Publication, **56**, pp. 41–60, 1991.

Kusznir, N. J. and R. G. Park, The extensional strength of continental lithosphere: its dependence on geothermal gradient, and crustal composition and thickness, in *Continental Extensional Tectonics*, edited by M. P. Coward, J. F. Dewey and P. L. Hancock, Geological Society Special Publication, **28**, pp. 35–52, 1987.

LaFehr, T. R., An exact solution for the gravity curvature (Bullard B) correction, *Geophysics*, **56**, 1179–1184, 1991a.

LaFehr, T. R., Standardization in gravity reduction, *Geophysics*, **56**, 1170–1178, 1991b.

Lagios, E., A gravity network in central Greece for secular gravity studies, *Pure and Applied Geophysics*, **123**, 81–90, 1985.

Lagios, E., S. Chailas, R. G. Hipkin and J. Drakopoulos, *Gravity and topographic data banks of Greece*, Department of Geophysics and Geothermy, University of Athens, Publication No. 4/94, 1994.

Lagios, E., R. G. Hipkin, A. Angelopoulos and S. Nikolaou, *The gravity anomaly map of Greece - a recompilation*, Institute of Geology and Mineral Exploration of Greece, 1988.

Lallemant, S. J., C. Truffert, L. Jolivet, P. Henry, N. Chamot-Rooke and B. De Voogd, Spatial transition from compression to extension in the Western Mediterranean ridge: a synthesis incorporating new sea-beam data, *Tectonophysics*, **60**, 1–42, 1994.

Lavier, L. L. and M. S. Steckler, The effect of sedimentary cover on the flexural strength of continental lithosphere, *Nature*, **389**, 476–479, 1997.

Le Pichon, X., Land-locked oceanic basins and continental collision: the eastern Mediterranean as a case example, in *Mountain Building Processes*, edited by K. J. Hsü, pp. 201–211, 1982.

Le Pichon, X. and J. Angelier, The Hellenic arc and trench system: a key to the evolution of the Eastern Mediterranean area, *Tectonophysics*, **60**, 1–42, 1979.

Le Pichon, X., N. Chamot-Rooke, S. Lallemant, R. Noomen and G. Veis, Geodetic determination of the kinematics of Central Greece with respect to Europe: implications for eastern Mediterranean tectonics, *Journal of Geophysical Research*, **100**, 12675–12690, 1995.

Lewis, B. T. R. and L. M. Dorman, Experimental isostasy 2: an isostatic model for the USA derived from gravity and topographic data, *J. Geophys. Res.*, **75**, 3367–3386, 1970.

Logatchev, N. A. and Y. A. Zorin, Evidence and causes of the two-stage development of the Baikal rift, *Tectonophysics*, **143**, 225–234, 1987.

Love, A. E. H., *A Treatise on the Mathematical Theory of Elasticity* (fourth edition), Dover, 1944.

Lowry, A. R. and R. B. Smith, Flexural rigidity of the Basin and Range-Colorado Plateau-Rocky Mountain transition from the coherence analysis of gravity and topography, *J. Geophys. Res.*, **99**, 20123–20140, 1994.

Lowry, A. R. and R. B. Smith, Strength and rheology of the western U. S. Cordillera, *J. Geophys. Res.*, **100**, 17947–17963, 1995.

Lyon-Caen, H., R. Armijo, J. Drakopoulos, J. Baskoutass, N. Delibassis, R. Gaulon, V. Kouskouna, J. Latoussakis, K. Makropoulos, P. Papadimitriou, D. Papanastassiou and G. Pedotti, The 1986 Kalamata (South Peloponnese) Earthquake: Detialed Study of a Normal Fault, Evidences for East-West Extension in the Hellenic Arc, *J. Geophys. Res.*, **93**, 14967–15000, 1988.

Lysak, S. S., The Baikal rift heat flow, *Tectonophysics*, **45**, 87–93, 1987.

Macario, A., A. Malinverno and W. F. Haxby, On the robustness of elastic thickness estimates using the coherence method, *J. Geophys. Res.*, **100**, 15163–15172, 1995.

Magellan, *Professional Products Operations Manual*, Magellan, 1992.

Makris, J., Geophysical Investigation of the Hellenides, *Hamburger Geophysikalische Einzelschriften*, **34**, 125 pp, 1977.

Makris, J., Geophysics and geodynamics implications for the evolution of the Hellenides, in *Geological Evolution of the Mediterranean Basin*, edited by D. J. Stanley and P. C. Wezel, pp. 231–248, Springer-Verlag, New York, 1984.

Mascle, J. G. and E. Chaumillon, Pre-collisional geodynamics of the Mediterranean Sea: the Mediterranean Ridge and the Tyrrhenian Sea, *Annali di Geofisica*, **40**(3), 569–586, 1997.

Mascle, J. G. and L. Martin, Shallow structure and recent evolution of the Aegean Sea: a synthesis based on continuous reflection profiles, *Marine Geology*, **94**, 271–299, 1990.

Masek, J. G., B. L. Isacks and E. J. Fielding, Rift flank uplift in Tibet: evidence for a viscous lower crust, *Tectonics*, **13**, 659–667, 1994.

Maus, S. and V. Dimri, Depth estimation from the scaling power spectrum of potential fields?, *Geophys. J. Int.*, **124**, 113–120, 1996.

McAdoo, D. C., C. F. Martin and S. Polouse, Seasat observation of flexure: evidence for a strong lithosphere, *Tectonophysics*, **116**, 209–222, 1985.

McKenzie, D., Active tectonics of the Mediterranean region, *Geophys. J. R. astr. Soc.*, **30** , 109–185, 1972.

McKenzie, D. P., Some remarks on the development of sedimentary basins, *Earth Planet. Sci. Lett.*, **40**, 25–32, 1978a.

McKenzie, D. P., Active tectonics of the Alpine-Himalayan belt: the Aegean Sea and surrounding areas, *Geophys. J. R. astr. Soc.*, **55**, 217–254, 1978b.

McKenzie, D. P., A possible mechanism for epeirogenic uplift, *Nature*, **307**, 616–618, 1984.

McKenzie, D. P. and M. J. Bickle, The volume and composition of melt generated by extension of the lithosphere, *J. Petrol.*, **29**, 625–679, 1988.

McKenzie, D. P. and J. D. Fairhead, Estimates of the effective elastic thickness of the continental lithosphere from Bouguer and free air gravity anomalies, *J. Geophys. Res.*, **102**, 27523–27552, 1997.

McNutt, M. K., Influence of plate subduction on isostatic compensation in northern California, *Tectonics*, **2**, 399–415, 1983.

McNutt, M. K. and R. L. Parker, Isostasy in Australia and the evolution of the compensation mechanism, *Science*, **199**, 773–775, 1978.

Meckel, L. D. and A. K. Nath, Geological considerations for stratigraphic modeling and interpretation, in *Seismic Stratigraphy - Applications to Hydrocarbon Exploration*, edited by C. E. Payton, AAPG Memoir, **26**, pp. 417–438, 1977.

Melis, N. S., M. Brooks and R. G. Pearce, A microearthquake study in the Gulf of Patras region, western Greece, and its seismotectonic interpretation, *Geophys. J. R. astr. Soc.*, **98**, 515–524, 1989.

Mercier, J. L., Extensional-compressional tectonics associated with the Aegean arc: comparisons with the Andean Cordillera and south Peru-north Bolivia, *Philosophical Transactions of the Royal Society of London*, **300**, 337–355, 1981.

Mercier, J. L., R. Armijo, P. Tapponnier, E. Carey-Gailhardis and H. Tonglin, Change from Tertiary compression to Quaternary extension in southern Tibet during the India-Asia collision, *Tectonics*, **6**, 275–304, 1987.

Mercier, J. L., D. Sorel and P. Vargely, Extensional tectonic regimes in the Aegean basin during the Cenozoic, *Basin Research*, **2**, 49–71, 1989.

Meyer, Y., *Wavelets and Applications*, Springer-Verlag, 1992.

Mitrovica, J. X., Haskell [1935] revisited, *J. Geophys. Res.*, **101**, 555–569, 1996.

Molnar, P. and W. P. Chen, Focal depths and fault plane solutions of earthquakes under the Tibetan Plateau, *J. Geophys. Res.*, **88**, 1180–1196, 1983.

Molnar, P., P. C. England and J. Martinod, Mantle dynamics, uplift of the Tibetan plateau, and the Indian monsoon, *Rev. Geophys.*, **31(4)**, 357–396, 1993.

Molnar, P. and H. Lyon-Caen, Some simple physical aspects of the support, structure, and evolution of mountain belts, in *Processes in Continental Lithospheric Deformation*, edited by S. P. Clark, Geol. Soc. Am. Spec. Pap., **218**, pp. 179–207, 1988.

Morelli, C., C. Gantar, T. Honkasalo, R. K. McConnell, I. G. Tanner, B. Szabo, U. Uotila and C. T. Whalen, The International Gravity Standardization Net 1971 (IGSN71), Paris, 1974.

Morelli, C., M. Pisani and C. Gantar, Geophysical studies in the Aegean Sea and in the Eastern Mediterranean, *Boll. Geofis. Teor. Appl.*, **18**, 127–167, 1975.

Morewood, N. C. and G. P. Roberts, Geometry, kinematics and rates of deformation in a normal fault segment boundary, central Greece, *Geophys. Res. Lett.*, **24**, 3081–3084, 1997.

Morgan, P. and R. Meissner, Heat flow and thermal regimes in the continental United States, in *Geophysical Framework of the Continental United States*, edited by L. C. Pakiser and W. D. Mooney, Geol. Soc. Am. Mem., **172**, pp. 493–522, 1989.

Mposkos, E. and A. Liati, Metamorphic evolution of metapelites in the high-pressure terrane of the Rhodope zone, northern Greece, *Canadian Mineralogist*, **31**, 401–424, 1993.

Munk, W. H. and D. E. Cartwright, Tidal spectroscopy and prediction, *Phil. Trans. R. Soc. London*, **259**, 533–589, 1966.

Mutter, J. C., W. R. Buck and C. M. Zehnder, Convective partial melting, 1: a model for the formation of thick basaltic sequences during the initiation of spreading, *J. Geophys. Res.*, **93**, 1031–1048, 1988.

Myrianthis, M. L., Geophysical study of the epicentral area of Alkyonides Islands earthquakes, Central Greece, *Geophysical Transactions of Eötvös Loránd Institute of Hungary*, **28**(2), 5–17, 1982.

Myrianthis, M. L., Graben formation and associated seismicity in the Gulf of Korinth (Central Greece), in *The Geological Evolution of the Eastern Mediterranean*, edited by J. Dixon and A. H. F. Robertson, **17**, pp. 701–707, Geol. Soc. London Spec. Publ, 1984.

Nyblade, A. A., H. N. Pollack, D. L. Jones, F. Podmore and M. Mushayandebvu, Terrestrial heat flow in east and southern Africa, *J. Geophys. Res.*, **95**, 17371–17384, 1990.

Oliva, S. E. and C. L. Ravazzoli, Complex polynomials for the computation of 2D gravity anomalies, *Geophysical Prospecting*, **45**, 809–818, 1997.

Oral, M. B., R. E. Reilinger, M. N. Toksöz, R. W. King, A. A. Barka, I. Kinik and O. Lenk, Global positioning system offers evidence of plate motions in eastern Mediterranean, *EOS, Transactions, Americal Geophysical Union*, **76**(2), 9–11, 1995.

Ori, G. G., Geologic history of the extensional basin of the Gulf of Corinth (?Miocene-Pleistocene), Greece, *Geology*, **17**, 918–921, 1989.

Ori, G. G., M. Roveri and G. Nichols, Architectural patterns in large-scale Gilbert-type delta complexes, Pleistocene, Gulf of Corinth, Greece, in *The Three-Dimensional Facies Architecture of Terrigenous Clastic Sediments and its Implications for Hydrocarbon Discovery and Recovery*, edited by A. D. Miall and N. Tyler, Concepts in Sedimentology and Paleontology, **3**, pp. 207–216, 1992.

Papazachos, C. B., P. M. Hatzidimitriou, D. G. Panagiotopoulos and G. N. Tsokas, Tomography of the crust and upper mantle in southeast Europe, *J. Geophys. Res.*, **100**, 12405–12422, 1995.

Papazachos, C. B. and G. Nolet, P and S deep velocity structure of the Hellenic area obtained by robust nonlinear inversion of travel times, *J. Geophys. Res.*, **102**, 8349–8367, 1997.

Parsons, B. and J. Sclater, An analysis of the variation of ocean floor bathymetry and heat flow with age, *J. Geophys. Res.*, **82**, 803–827, 1977.

Parsons, T., The Basin and Range province, in *Continental Rifts: Evolution, Structure and Tectonics*, edited by K. H. Olsen, Developments in Geotectonics, **25**, pp. 277–324, Elsevier, 1995.

Pawlowski, R. S., Preferential continuation for potential field anomaly enhancement, *Geophysics*, **60**, 390–398, 1995.

Petit, C., E. Burov and J. Déverchère, On the structure and mechanical behaviour of the extending lithosphere in the Baikal rift from gravity modelling, *Earth. Planet. Sci. Lett.*, **149**, 29–42, 1997.

Poelchau, H. S., D. R. Baker, T. Hantschel, B. Horsfield and B. Wygrala, Basin simulation and the design of the conceptual basin model, in *Petroleum and Basin Evolution: Insights from Petroleum Geochemistry, Geology and Basin Modeling*, edited by D. H. Welte, B. Horsfield and D. R. Baker, Springer, 1997.

Pollack, H. N., S. J. Hurter and J. R. Johnson, Heat flow from the Earth's interior: analysis of the global data set, *Rev. Geophys.*, **31**, 267–280, 1993.

Pratt, J. H., On the attraction of the Himalaya Mountains and of the elevated regions beyond them, upon the plumb line in India, *Philos. Trans. R. Soc.*, **145**, 53–100, 1855.

Press, W. H., B. R. Flannery, S. A. Teukolsky and W. T. Vetterling, *Numerical Recipies*, Cambridge University Press, 1986.

Prodehl, C., S. Meuller and V. Haak, The European Cenozoic rift system, in *Continental Rifts: Evolution, Structure and Tec tonics*, edited by K. H. Olsen, Developments in Geotectonics, **25**, pp. 133–212, Elsevier, 1995.

Ranalli, G., *Rheology of the Earth: Deformation and Flow Processes in Geophysics and Geodynamics*, Allen and Unwin, Boston, 1987.

Ranalli, G., Rheology and deep tectonics, *Annali di Geofisica*, **40**(3), 671–680, 1997.

Rigo, A., H. Lyon-Caen, R. Armijo, A. Deschamps, K. Makropoulos, P. Papadimitriou and I. Kassaras, A microseismicity study in the western part of the Gulf of Corinth (Greece): implications for large-scale normal faulting mechanisms, *Geophys. J. Int.*, **126**, 663–688, 1996.

Robbins, S. L., Reexamination of the values used as constants in calculating rock density from borehole gravity data, *Geophysics*, **46**, 208–210, 1981.

Roberts, G. P., Non-characteristic normal faulting surface ruptures from the Gulf of Corinth, Greece, *J. Geophys. Res*, **101**, 25255–25267, 1996a.

Roberts, G. P., Variation in fault-slip directions along active and segmented fault systems, *Journal of Structural Geology*, **18**(6), 835–845, 1996b.

Roberts, G. P. and I. Koukouvelas, Structural and seismological segmentation of the Gulf of Corinth fault: implications for models of fault growth, *Annali di Geofisica*, **39**, 619–646, 1996.

Roberts, S. C., *Active normal faulting in central Greece and western Turkey*, University of Cambridge, PhD Thesis, 1988.

Roberts, S. C. and J. Jackson, Active normal faulting in central Greece: an overview, in *The Geometry of Normal Faults*, edited by A. M. Roberts, G. Yielding and B. Freeman, Geological Society Special Publication, **56**, pp. 125–142, 1991.

Robertson, A. and J. Dixon, Introduction: aspects of geological evolution of the Eastern Mediterranean, in *The Geological Evolution of the Eastern Mediterranean*, edited by J. Dixon and A. Robertson, **17**, pp. 1–74, Geol. Soc. London Spec. Publ , 1984.

Roy, M., L. H. Royden, B. C. Burchfiel, T. Tzankov and R. Nakov, Flexural uplift of the Stara-Planina Range, Central Bulgaria, *Basin Research* , **8**, 143–156, 1996.

Royden, L. and C. E. Keen, Rifting processes and thermal evolution of the continental margin of eastern Canada determined from subsidence curves, *Earth. Planet. Sci. Lett.*, **51**, 343–361, 1980.

Ruppel, C., Extensional processes in continental lithosphere, *J. Geophys. Res.*, **100**, 24187–24215, 1995.

Ruppel, C., M. Kogan and M. McNutt, Implications of new gravity data for Baikal rift zone structure, *Geophys. Res. Lett.*, **20**, 1635–1638, 1993.

Sandwell, D. T. and W. H. F. Smith, Marine gravity anomaly from Geosat and ERS-1 satellite altimetry, *J. Geophys. Res.*, **102**, 10039–10054, 1997.

Scheirer, D., D. Forsyth and A. Hosford, Multitaper estimates of lithospheric strength of the Basin and Range Province, paper presented at Spring Meeting of the American Geophysical Union, San Francisco, 1995.

Schmidt, J. F. J., in *Studien über Vulnacs und Erdbeben (Studies of Volcanos and Earthquakes)*, pp. 68–83, Leipzig, 1881.

Schmoker, J. W. and R. B. Halley, Carbonate porosity versus depth: a predictable relation for south Florida, *AAPG Bulletin*, **66**, 2561–2570, 1982.

Scholz, C. H., the brittle-plastic transition and the depth of seismic faulting, *Geol. Rundsch.*, **77**, 319–328, 1988.

Scholz, C. H., Comments on models of earthquake recurrence, in *Proceedings of Conference XLV, "Fault Segmentation and Controls of Rupture Initiation and Termination"*, edited by D. P. Schwartz and R. H. Sibson, U.S. Geol. Surv. Open-file Rep., **89-315**, pp. 350–360, 1989.

Sclater, J. G. and P. A. F. Christie, Continental stretching: an explanation of the post-mid-Cretaceous subsidence of the Central North Sea basin, *J. Geophys. Res.*, **85**, 3711–3739, 1980.

Sébrier, M., *Tectonique récente d'une traversale à l'Arc Egéen: le Golfe de Corinthe et ses régions périphériques*, Univ. Paris-Sud, France, PhD Thesis, 1977.

Seger, M. and J. Alexander, Distribution of Plio-Pleistocene and modern coarse-grained deltas south of the Gulf of Corinth, Greece, in *Tectonic Controls and Signatures in Sedimentary Successions*, edited by L. E. Frostick and R. J. Steel, International Association of Sedimentologists Special Publication, **20**, pp. 37–48, Oxford, 1993.

Seyitoğlu, G., B. C. Scott and C. C. Rundle, Timing of Caenozoic extensional tectonics in west Turkey, *Journal of the Geological Society of London*, **149**, 533–538, 1992.

Smith, D. E., R. Kolenkiewicz, J. W. Robbins, P. J. Dunn and M. H. Torrence, Horizontal crustal motion in the central and eastern Mediterranean inferred from satellite laser ranging measurements, *Geophysical Research Letters*, **21**, 1979–1982, 1994.

Sokoutis, D., J. P. Brun, J. Vandendriessche and S. Pavlides, The metamorphism and migmatization of the Xanthe-Echinos metamorphic complex, Central Rhodope, Greece, *J. Geol. Soc.*, **150**, 243–246, 1993.

Sonder, L. J., P. C. England, B. P. Wernicke and R. L. Christiansen, A physical model for Cenozoic extension of western North America, in *Continental Extensional Tectonics*, edited by M. P. Coward, J. F. Dewey and P. L. Hancock, Geological Siciety Special Publication, **28**, pp. 187–201, 1987.

Spakman, W., M. J. R. Wortel and N. S. Vlaar, The Hellenic subduction zone: a tomographic image and its geodynamical implications, *Geophysical Research Letters*, **15**, 60–63, 1988.

Spector, A. and F. S. Grant, Statistical methods for interpreting aeromagnetic spectra, *Geophysics*, **35**, 293–302, 1970.

Stark, C. P. and R. W. Hartley, Estimating local flexural rigidity using wavelet coherence, *Eos, Transactions, American Geophysical Union*, **75(44)**, 1994.

Stark, C. P. and J. Stewart, Mechanical lithospheric strength and loading using wavelet transform admittance and coherence, *Eos, Transactions, American Geophysical Union*, **78**(46), 35, 1997.

Stein, R. S., G. C. P. King and J. B. Rundle, The growth of geological structures by repeated earthquakes 2. Field examples of continental dip-slip faults, *J. Geophys. Res.*, **95**, 13319–13331, 1988.

Stephens, C., *Mass flow sedimentation adjacent to rift basin margins, Central Greece*, University of Leeds, PhD Thesis, 1995.

Stewart, I. and C. Vita-Finzi, Coastal uplift on active normal faults - the Eliki Fault, Greece, *Geophys. Res. Lett.*, **23**, 1853–1856, 1996.

Stewart, J. and A. B. Watts, Gravity anomalies and spatial variations of flexural rigidity at mountain ranges, *J. Geophys. Res.*, **102**, 5327–5352, 1997.

Straub, C. and H. G. Kahle, Global positioning estimates of crustal deformation in the Marmara Sea region, northwest Anatolia, *Earth and Planetary Science Letters*, **121**, 495–502, 1994.

Taymaz, T., J. A. Jackson and D. P. McKenzie, Active tectonics of the north and central Aegean Sea, *Geophys. J. Int.*, **106**, 433–490, 1991.

Telford, W. M., L. P. Geldart and R. E. Sheriff, *Applied Geophysics* (second edition), Cambridge University Press, 1990.

Thorne, J. A. and A. B. Watts, Quantitative analysis of North Sea subsidence, *AAPG Bulletin*, **73**(1), 88–116, 1989.

Truffert, C., N. Chamot-Rooke, S. Lellamant, B. De Voogd, P. Huchon and X. Le Pichon, The crust of the western Mediterranean Ridge from deep seismic and gravity modelling, *Geophys. J. Int.*, **114**, 360–372, 1993.

Tsokas, G. N. and R. O. Hansen, A study of the crustal thickness and the subducting lithosphere in Greece from gravity data, *J. Geophys. Res.*, **102**, 20585–20597, 1997.

Turcotte, D. L. and G. Schubert, *Geodynamics: Applications of Continuum Physics to Geological Problems*, John Wiley, 1982.

Upcott, N. M., R. K. Mukasa, C. J. Ebinger and G. D. Karner, Along-axis segmentation and isostasy in the Western Rift, East Africa, *J. Geophys. Res.*, **101**, 3247–3268, 1996.

Veis, G., H. Billiris, B. Nakos and D. Paradissis, Tectonic strain in Greece from Geodetic measurements, *C. R. Acad. Sci. Athens*, **67**, 129–166, 1992.

Vening-Meinesz, F. A., Une nouvelle méthod pour la réduction isostatique régionale de l'intensité de la pesanteur, *Bull. géod*, **39**, 1931.

Wdowinski, S. and G. J. Axen, Isostatic rebound due to tectonic denudation: a viscous flow model of a layered lithosphere, *Tectonics*, **11**(2), 303–315, 1992.

van Wees, J. D. and S. Cloetingh, A finite-difference technique to incorporate sparial variations in rigidity and planar faults into 3-D models for lithospheric flexure, *Geophys. J. Int.*, **117**, 179–195, 1994.

Weissel, J. K. and G. D. Karner, Flexural uplift of rift flanks due to mechanical unloading of the lithosphere during extension, *J. Geophys. Res.*, **94**, 13919–13950, 1989.

Westaway, R., Quaternary elevation change of the Gulf of Corinth in central Greece, *Phil. Trans. R. Soc. Lond.*, **354**, 1125–1164, 1996.

Wyllie, M. R. J., A. R. Gregory and G. H. F. Gardner, An experimental investigation of factors affecting elastic wave velocities in porous media, *Geophysics*, **23**, 459–493, 1958.

Yoshioka, S. and M. J. R. Wortel, Three-dimensional numerical modeling of detachment of subducted lithosphere, *J. Geophys. Res.*, **100**, 20223–20244, 1995.

Zoback, M. L., R. E. Anderson and G. A. Thompson, Cainozoic evolution of the state of stress and style of tectonism of the Basin and Range province of the western United States, *Phil. Trans. R. Soc. London*, **A300**, 407–434, 1981.

Zuber, M. T. and E. M. Parmentier, Lithospheric necking: a dynamic model for rift morphology, *Earth Planet. Sci. Lett.*, **77**, 373–383, 1986.

Zuber, M. T., E. M. Parmentier and R. C. Fletcher, Extension of continental lithosphere: a model for two scales of Basin and Range deformation, *J. Geophys. Res.*, **91**, 4826–4838, 1986.